



UNIVERSITÄT
DES
SAARLANDES

FARADAIC MATERIALS AND PROCESSES

FOR THE ELECTROCHEMICAL SEPARATION

OF ALKALI AND ALKALINE EARTH METAL IONS

Dissertation
zur Erlangung des Grades
des Doktors der Naturwissenschaften
der Naturwissenschaftlich-Technischen Fakultät
der Universität des Saarlandes

von

Lei Wang

Saarbrücken
Februar 2023

Tag des Kolloquiums: 11. Mai 2023

Dekan: Prof. Dr. Ludger Santen

Berichterstatter: Prof. Dr. Volker Presser
Prof. Dr.-Ing. Markus Gallei
Prof. Dr. Choonsoo Kim

Akad. Mitglied: Dr. Oliver Janka

Vorsitz: Prof. Dr. mont. Christian Motz

Abstract

As industrial and agricultural activities expand along with a growing global population, numerous regions are experiencing shortages of water and essential metals. To address these challenges, electrochemical separation methods utilizing electroactive materials and interfaces offer an efficient and straightforward approach to water purification and targeted ion extraction. Although carbon-based materials have been extensively studied and have the advantages of stability and low cost, they suffer from low desalination capacity, particularly for high-salinity water, and low selectivity. This dissertation investigates the potential of Faradaic materials and processes for electrochemical ion/water separation, as well as ion/ion separation, with a focus on alkali and alkaline earth metal ions, which are vital for industrial development but challenging to separate. The study includes synthesizing several Faradaic materials to achieve high ion removal capacity in seawater desalination. This work also develops a strategy to exploit the nuanced differences of ion intercalation kinetics in 2D material to achieve specific ion separation. The study also examines the selectivity and stability of LiFePO_4 and presents new ways to optimize its performance. Finally, the study establishes a novel electrochemical process based on redox flow batteries, which promises a more efficient and continuous extraction of lithium ions from seawater.

Zusammenfassung

Mitwachsender Weltbevölkerung, Industrie und Landwirtschaft werden zunehmend mehr Regionen einer Knappheit an Wasser und relevanten Elementen unterworfen. Entgegenwirkend bieten elektrochemische Trennverfahren unter Verwendung elektroaktiver Materialien und Grenzflächen einen effizienten und einfachen Ansatz zur Wasserreinigung und gezielten Ionenextraktion. Ausführlich untersuchte Kohlenstoffmaterialien welche Vorteile von Stabilität und niedrigen Kosten aufweisen, liefern nur eine geringe Selektivität und Entsalzungskapazität, insbesondere für Wasser mit hohem Salzgehalt. Diese Dissertation untersucht das Potenzial faraday'scher Materialien und Prozesse für die elektrochemische Ionen/Wasser- sowie Ionen/Ionen-Trennung, mit einem Fokus auf Alkali- und Erdalkalimetallionen, die für die industrielle Entwicklung von entscheidender Bedeutung, aber schwierig zu trennen sind. Die Studie umfasst die Synthese faraday'scher Materialien, um hohe Ionenentfernungskapazitäten im Kontext der Meerwasserentsalzung zu erreichen. Zudem wurde eine Strategie entwickelt, um die differenzierenden Unterschiede der Ioneninterkalationskinetik in 2D-Material für eine spezifische Ionentrennung auszunutzen. Die Studie untersucht auch die Selektivität und Stabilität von LiFePO_4 und zeigt neue Möglichkeiten zur Optimierung seiner Leistung auf. Schließlich wird ein neuartiger elektrochemischer Prozess auf Basis von Redox-Flow-Batterien etabliert, der eine kontinuierlichere Extraktion von Lithium-Ionen aus Meerwasser verspricht.

Acknowledgments

I want to express my appreciation to my supervisor, Prof. Volker Presser, who provided me the chance to work at the INM - Leibniz Institute for New Materials. Without his support and patient guidance, I could not experience the charm of science and could not accomplish paper publications. The thesis is funded by the China Scholarship Council (CSC) with the award number 201906260277. I also appreciate Prof. Markus Gallei from Saarland University for his kind support during my doctoral study and for being the second reviewer of the thesis.

During my study at INM, I was honored and fortunate to meet many creative and friendly colleagues. They gave me lots of help and assistance when I encountered problems in scientific work and daily life. I thank Dr. Yuan Zhang, Dr. Qingsong Wang, Dr. Samantha Husmann, Dr. Mesut Aslan, Dr. Hwirim Shim, Dr. Pattarachai Srimuk, Dr. Emmanuel Pamet , Dr. Sarah Saleem, Dr. Kaitlyn Prenger, Zeyu Fu, Stefanie Arnold, Bowen Dong, Yunjie Li, Panyu Ren, Cansu K k, Mohammad Torkamanzadeh, and Jean Gustavo Ruthes, for their scientific help, fruitful discussion and all the memorable time that we spent together. I also want to thank Robert Drumm, Andrea Jung, Alexander May, Dr. Kasten Moh, and all the people in the workshop of INM for their continuing kind aid.

The world would not have been imagined without our great collaborators. I want to thank Prof. Guido Kickelbick, Prof. Michael Naguib, Prof. Guang Feng, Prof. Zhaoyin Wen, Dr. Oliver Janka, Dr. Ben Breitung, and Dr. Jun Jin for their effort and support in the collaborations. I learned a lot from the discussion with them, and the collaborations broadened my horizons.

Finally, with my love, I thank my parents, girlfriend, and relatives for their love, support, and encouragement throughout my doctoral studies, which is one of the motivations to keep me moving forward.

Contents

1. Motivation.....	1
2. Alkali/alkaline earth ions separation: state of the art.....	2
2.1 Ion separation technologies.....	2
2.1.1 Ion/water separation technologies.....	2
2.1.1.1 Thermal-energy-based technologies.....	2
2.1.1.2 Mechanical-energy-based technologies.....	3
2.1.1.3 Electrical-energy-based technologies.....	4
2.1.2 Ion/ion separation technologies.....	5
2.1.2.1 Ion/ion separation based on physical mechanisms.....	6
2.1.2.2 Ion/ion separation based on chemical mechanisms.....	10
2.2 Electrochemical ion separation.....	12
2.2.1 Mechanism of ion/water separation.....	12
2.2.2 Mechanism of ion/ion separation.....	20
2.3 Cell architectures of electrochemical ion separation.....	22
2.3.1 Symmetric architectures.....	22
2.3.2 Asymmetric architectures.....	22
2.3.3 Membrane-based architectures.....	24
2.4 Faradaic materials for ion separation.....	30
2.4.1 1D (tunnel) materials.....	30
2.4.2 2D (layered) material.....	31
2.4.3 3D-structured material.....	33
3. Approach and overview.....	39
4. Peer-reviewed research papers.....	42
4.1 From capacitive deionization to desalination batteries and desalination fuel cells.....	43
4.2 Dual-use of seawater batteries for energy storage and water desalination.....	53
4.3 MXene/activated-carbon hybrid capacitive deionization for permselective ion removal at low and high salinity.....	80
4.4 Antimony alloying electrode for high-performance sodium removal: how to use a battery material not stable in aqueous media for saline water remediation.....	102
4.5 Time-dependent cation selectivity of titanium carbide MXene in aqueous solution.....	122
4.6 Electrochemical lithium recovery with lithium iron phosphate: what causes performance degradation and how can we improve the stability?.....	141
4.7 Redox flow battery for continuous and energy-effective lithium recovery from aqueous solution.....	160
5. Conclusion and outlook.....	177
6. References.....	180

1. Motivation

Water is the essential substance of our daily life. However, more people are encountering challenges in obtaining potable water. According to a report from the United Nations, about two-thirds of the global population will confront a potable water crisis by 2050.[1] To address this issue, many technologies, such as multi-stage flash[2], multi-effect distillation[3], reverse osmosis[4], and electrodialysis[5], have been developed to separate water from salt ions. For most water bodies, this pertains to the removal of alkali and alkaline earth metal cations. Currently, reverse osmosis is the most widely used technology for industrial desalination, with an energy consumption of 2-4 kWh/m³. [6, 7] Reverse osmosis is a relatively energy-intensive, which is an issue when meeting the enormous demand for remediated water.[8] In addition, achieving highly selective and high-yield ion separation, which exploits valuable ions, is difficult with traditional technologies. Therefore, electroactive materials and interfaces offer a new avenue for refining water resources, including water purification and valuable-ions extraction. Carbon materials are the earliest and most deeply studied. As nanoporous carbon materials store ions via the formation of the electrical double-layer, the related electrochemical technology is called capacitive deionization (CDI).[9] Benefiting from its ion-storage mechanism, CDI has higher energy efficiency and lower cost than traditional desalination technologies. The desalination capacity of CDI is 5-30 mg_{NaCl}/g, and the energy consumption is 10-40 Wh/mol_{NaCl}. [10] However, typical carbon materials cannot desalinate in high-salinity water due to the co-ions effect[11]; carbon materials also do not exhibit any promising performance in cations separation, especially between alkali and alkaline earth metal ions.[12]

Faradaic materials, which store ions through redox reactions, are promising candidates for replacing carbon materials.[13] The first work that used Faradaic materials for water purification emerged in 2012.[14] This work applied sodium manganese oxides and silver for the sodium-capture and chloride-capture electrodes. Afterward, many researchers reported related works with different Faradaic materials for immobilizing sodium, such as NaTi₂(PO₄)₃[15], Na_{0.44}MnO₂[16], MXene[17], and Prussian blue[18]. Compared with carbon materials, the desalination capacity of Faradaic materials is much higher (50-150 mg_{NaCl}/g). Many Faradaic materials also manifest better ion selectivity (with selectivity factors above 30). However, Faradaic materials suffer from limited stability and, in some cases, environmental toxicity, thereby being unable to meet the practical demand.[19] Additionally, the use of Faradaic materials in ion-selective extraction is a more widely explored research topic. Thus, there is a strong need for developing new Faradaic materials with higher performance, stability, and low cost in ion/water separation (i.e., water purification) and investigating the cation selectivity performance of various Faradaic materials. This dissertation explores the design of novel Faradaic materials for water remediation and studies the ion/ion separation performance of different Faradaic materials. A new electrochemical process for specific ion extraction (Li⁺) will be developed.

2. Alkali/alkaline earth ions separation: state of the art

2.1 Ion separation technologies

Separation is the process that distinguishes one substance from its mixture. It is a crucial method in modern industry to purify products, recycle resources, and mine specific ions.[20] The separation process requires particular devices or selective materials that utilize co-existing species' chemical or physical differences. The most uncomplicated separation process is between two different phases, such as isolating ions from water. However, separating ions with similar chemical or physical properties is harder. The following section introduces the separation process between alkali/alkaline-earth metal ions and water (named ion/water separation) and selectively detaching one alkali/alkaline-earth metal ion from others (defined as ion/ion separation).

2.1.1 Ion/water separation technologies

Alkali/alkaline-earth metal ions are the main dissolved cations in natural salinity. The total dissolved salt concentration needs to be lowered below 250 mg/L to obtain drinking water quality.[21] According to the driven force, ion/water separation technologies could be classified into thermal-energy-based, mechanical-energy-based, and electrical-energy-based technologies, as shown in **Figure 1**.

2.1.1.1 Thermal-energy-based technologies

Thermal-energy-based technology, also known as thermal distillation, is presumably the earliest technology humankind has explored for separating ions from water. The general principle of this technology is evaporating the water in the salinity via heating and then undergoing a condensing process. Depending on different operations and architectures, thermal distillation develops into multi-stage flash distillation (MSF), multi-effect distillation (MED), membrane distillation (MD), and vapor compression (VC).[22] The former two are the best-known and most widespread thermal distillation technologies.

MSF accounts for ca. 10% of the technology used in global desalination plants.[23] A typical MSF plant is comprised of several stages (generally 20-30), each containing a heat exchanger and a condensate collector (**Figure 1A**). The pre-heated saline flows through brine heaters, where the hot saline receives additional heat until the temperature reaches 90-110 °C. Afterward, the hot saline returns to the first stage, where the temperature and pressure are lower than the saline. Some saline flashes on because hot saline has a higher temperature than boiling at the first stage. The generated vapor loses latent heat to the saline water in the heat exchanger tubes and is collected in a tray. A typical MSF has a capacity of 50000 m³/d to 70000 m³/d and an energy consumption of 18.3-28.5 kWh/m³, the latter of

which includes 15.8-23.5 kWh/m³ (30% energy recovery) of thermal energy and 2.5-5.0 kWh/m³ of electrical energy.[22]

Although MED faced scaling problems early on, it has become the preferred technology among thermal desalination technologies.[24] In the MED process, the saline feed water is pre-heated and flows proportionally into the various vessels (**Figure 1B**). The hot feed water is then sprayed on the evaporator tubes.[25] The low-pressure steam in the evaporator tubes loses its energy to the feed water and causes it to evaporate. The produced vapor then further heats the evaporator. In the following stages, similar processes happen. The vapor from the last stage will condense into fresh water (cooled by the feed water) in the final condenser. Attributed to a lower water boiling temperature (70 °C to 90 °C) compared to MSF, MED could consume less energy. To generate 1 m³ of drinking water (with a typical capacity of 5000 m³/d to 50000 m³/d), MED consumes 14.2-21.6 kWh, of which 12.2-19.1 kWh is thermal energy (30% energy recovery) and 2.0-2.5 kWh is electrical energy.[26, 27]

2.1.1.2 Mechanical-energy-based technologies

Mechanical-energy-based technologies generally utilize pressure to force the feed water to penetrate the semi-permeable membrane. Based on the pore size of the membrane, the technologies could be classified as microfiltration (MF, 0.1-10 µm), ultrafiltration (UF, 0.01-1 µm), nanofiltration (NF, 1-100 nm), and reverse osmosis (RO, <1 nm).[28] Determined by the pore size, structure, and composition of the membranes, only RO could remove the dissolved alkali and alkaline earth metal ions in water, and NF membrane generally shows good rejection to divalent ions but not monovalent ions.[29, 30] RO is the most widespread desalination technology on a large scale, accounting for 65% of the global constructed capacity due to its lower energy consumption than thermal desalination technologies.[31] Another advantage of RO is that it is adapted to various feed waters such as brackish water (salinity 1-10 g/L) and seawater (salinity ~35 g/L) and that its production capacity varies from 1 m³/d (household water purifier) to 500000 m³/d (industrial desalination plant).[32] A typical RO plant contains pre-treatment devices, pumps, membranes, energy recovery devices (ERD), and after-treatment devices (**Figure 1C**).[33] During the operation, the saline first flows through the pre-treatment devices to remove suspended impurities, colloids, and organisms. Subsequently, the water is pressurized to typically 55-82 bar (seawater desalination), forcing water to pass through the membrane. The purified water goes through the after-treatment plant for disinfection and sterilization. The hydraulic energy of a highly pressured concentrated stream could be recovered via ERD (e.g., centrifugal-type devices and isobaric chamber devices)[34] and be transferred back to the feed water. Benefitting from ERD, the energy consumption of RO could be decreased to ~40%.[35] A typical seawater reverse osmosis (SWRO) desalination device requires 2-5 kWh (net consumption) to process

1 m³ seawater. Doing the same using brackish water, reverse osmosis (BWRO) would only require 0.5-2.5 kWh/m³ because of the lower osmotic pressure of brackish water.[6, 36]

In addition to the technologies that overcome the osmotic pressure, another technology, forward osmosis (FO), utilizes the osmotic pressure gradient as the driving force. In this process, one side of the membrane is the feed solution, while the other side is a draw solution with a higher osmotic pressure than the feed water. The water would penetrate the membrane, thereby diluting the draw solution and concentrating the feed water. At the early stage, FO studies were conducted utilizing RO membranes.[37] The research on synthesizing FO membranes started around 2000, and most FO membranes are now asymmetric.[38, 39] Typical asymmetric membrane contains a 0.1-1 μm dense layer (determining permeability selectivity) and a 100–200 μm supporting layer (providing mechanical strength).[38] Moreover, some studies indicate that the pore structure and hydrophilicity of the supporting layer are also crucial to the transport mechanism.[40, 41] The material for FO membranes varies from organic compounds (such as cellulose derivatives[42], polyethersulfone[43], polysulfone[44]) to inorganic compounds (like graphene oxide[41], SiO₂[45], and MXene[46]). The organic FO membranes are well-studied and commercially purchased. The inorganics are added to enhance the performance (e.g., hydrophilicity and water flux[47]) and to enable new properties (e.g., conductivity[48]). FO is synergetically combined with other desalination technologies (e.g., RO) by being the pre-treatment process to reduce the system costs.[49] Recently, FO has also been implemented as the core component to treat wastewater on an industrial scale.[50]

2.1.1.3 Electrical-energy-based technologies

Electrical-energy-based technologies include electrodialysis (ED) and technologies that immobilize ions in the electrodes, such as CDI and FDI (introduced in the following sections). ED is the only one used on an industrial scale, accounting for ca. 4% of the global constructed capacity.[51] ED plants contain several ion exchange membranes (IEMS) stacked between the cathode and anode, as shown in **Figure 1D**. The cation exchange membrane (CEM) and anion exchange membrane (AEM) are alternately installed, for which, in between, there is a channel for water to flow. During the operation, a voltage (higher than water splitting voltage) is applied on the electrodes to produce OH⁻ and H⁺ at the cathode and anode areas, respectively. The cations and anions in the feed water will migrate through CEM/AEM to maintain charge balance, producing concentrated and diluted water. The typical capacity of ED is 100-145000 m³/d, and the net energy consumption varies from 0.5 kWh/m³ to 17 kWh/m³, depending on the salinity of the feed water.[27, 52]

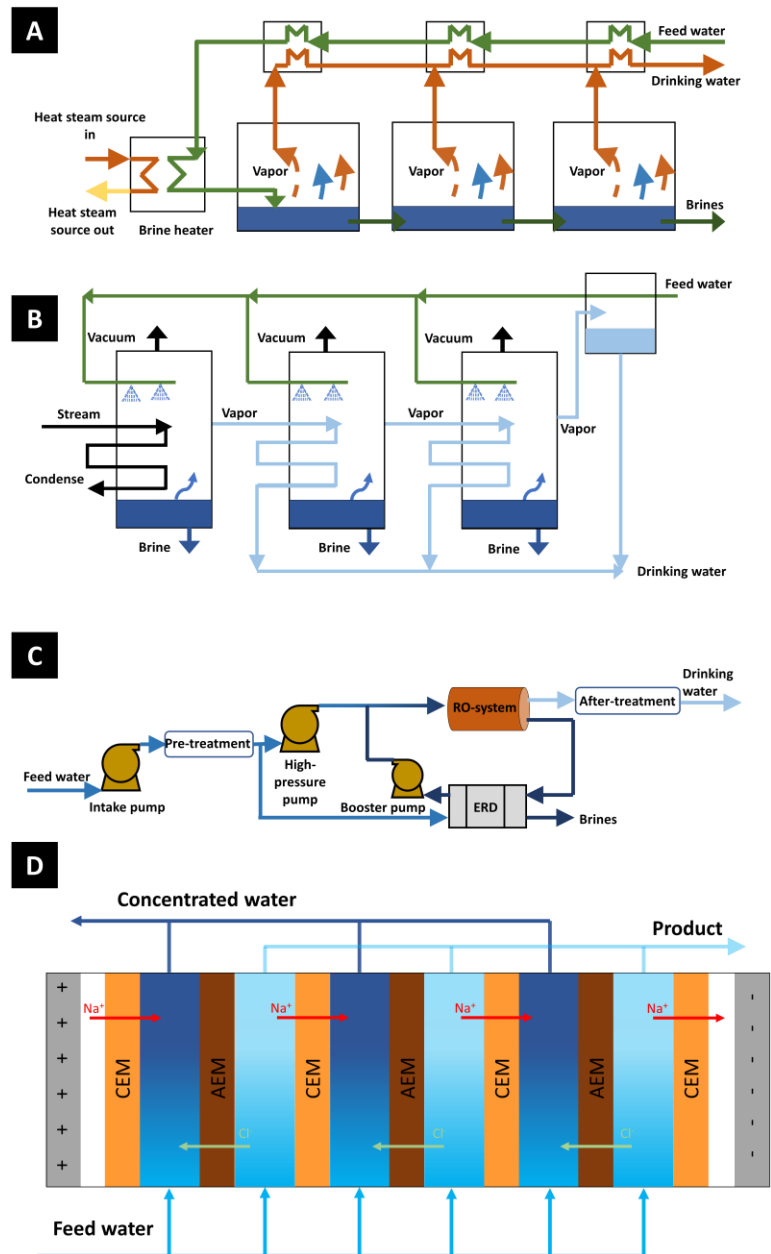


Figure 1: Scheme of MSF (A), MED (B), RO (C), and ED (D).

2.1.2 Ion/ion separation technologies

Common alkali and alkaline-earth metal ions in natural aqueous solutions are Li⁺, Na⁺, K⁺, Mg²⁺, and Ca²⁺.^[53] Metal or compounds containing these elements are essential for industrial production. For example, lithium salts are indispensable raw materials for lithium-ion batteries, while sodium compounds are central to industries producing glass, paper, and soap. However, similar physical natures and chemical behaviors bring challenges for separating a specific ion from its mixture. The ion/ion separation technologies of alkali/alkaline earth metal ions can be classified into physical-nature-based technologies and chemical-nature-based technologies according to the separation mechanism.

2.1.2.1 Ion/ion separation based on physical mechanisms

Technologies based on physical mechanisms separate a specific alkali/alkaline-earth metal ion from others by enlarging and utilizing physical property differences such as ionic size, mobility, and dehydration energy (**Figure 2**). These include capillary electrophoresis (CE), adsorption, and membrane separation.

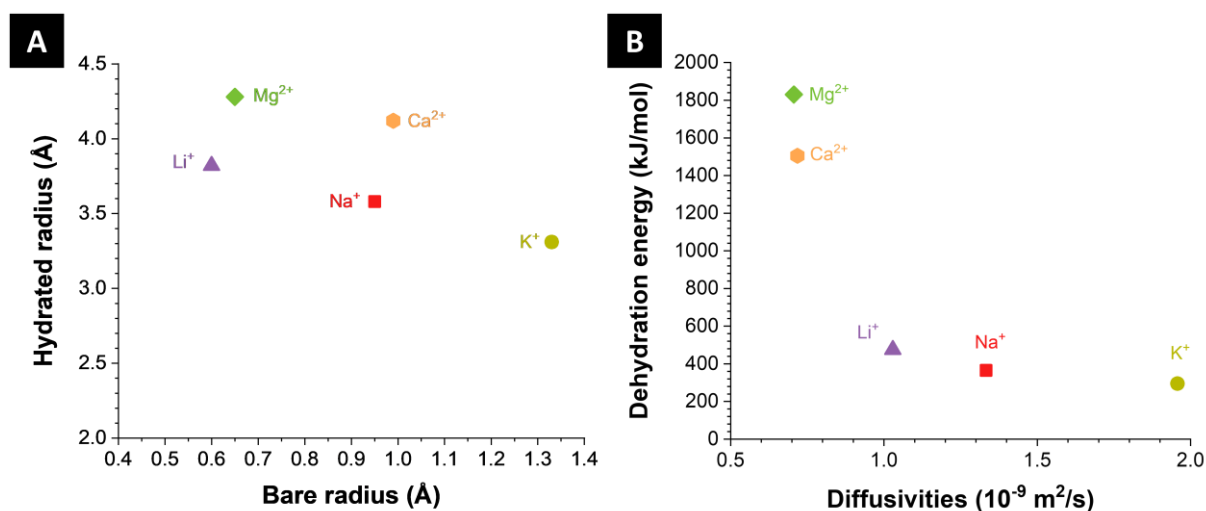


Figure 2: Physical properties of alkali/alkaline-earth metal ions: (A) ionic and hydration radius, and (B) dehydration energy and diffusivities. Data from reference [53]

Capillary electrophoresis

Capillary electrophoresis separates alkali/alkaline earth metal ions by utilizing different mobilities of ions in the media (under a high electrical field), as shown in **Figure 3A**. The velocity of the ions, v , is determined by the electrophoretic migration velocity (v_p), the velocity of electroosmotic flow (v_o), and the applied electric field (**Equation 1**). [54] v_o depends on the charge of the capillary wall. The polarity of charge determines the direction of electroosmotic flow, and the charge number dictates the magnitude of the flow. [55] Generally, v_o is far higher than v_p , so all cations and anions would thus migrate from positive to negative electrodes. Anions stay longer than cations of their conflicting electrophoretic mobilities, and most anions can be easily separated due to significant differences in their equivalent ionic conductivities. [56] In contrast, the mobility of some alkali/alkaline earth metal ions is too close to distinguish (e.g., Ca²⁺ and Mg²⁺). Thus, some weak complexing agents, e.g., ethylenediaminetetraacetic acid [57] and tartaric acid [58], are generally added to affect the mobility of some cations. Due to the low volume of the capillary (generally $< 0.1 \mu\text{L}$), CE is more suitable for analyzing the alkali/alkaline earth metal content in samples not enriching one specific element. [55]

$$v = v_p + v_o = (\mu_p + \mu_o) \times E \quad \text{Equation 1}$$

where v and v_p are the velocity and electrophoretic migration velocity of ions, respectively; v_o is the velocity of electroosmotic flow; μ_p is the electrophoretic mobility of ions; μ_o is the coefficient of electroosmotic flow, and E is the electric field gradient.

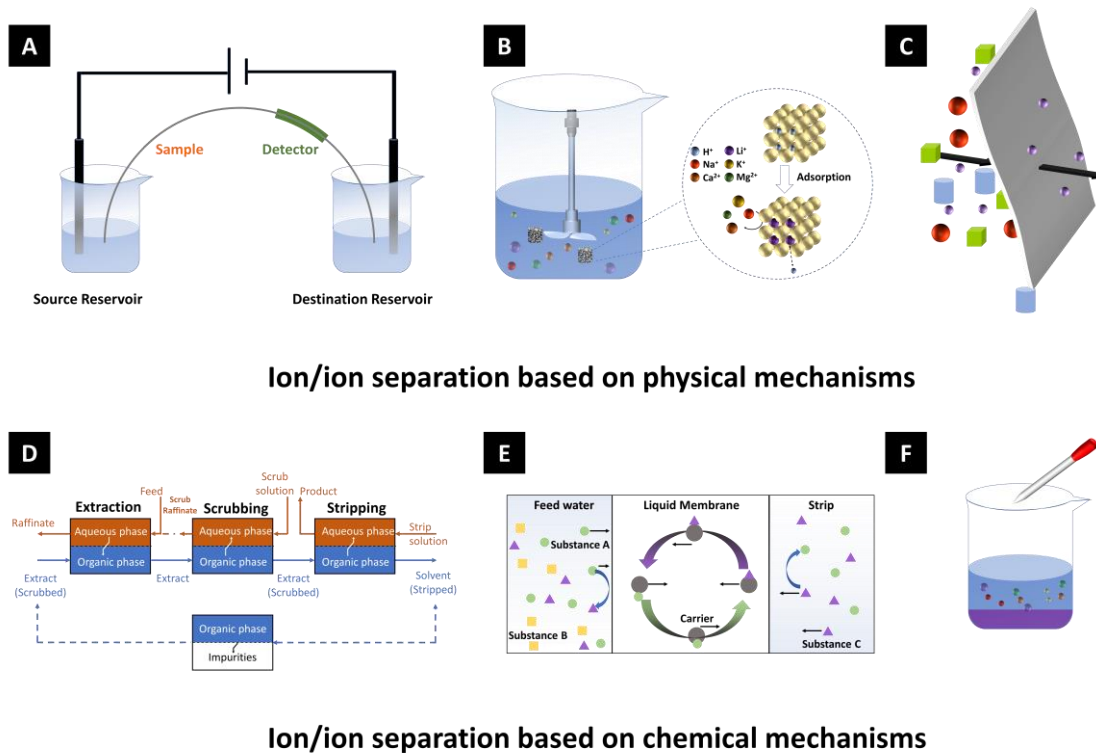


Figure 3: Scheme of ion/ion separation technologies based on physical mechanisms: (A) capillary electrophoresis, (B) adsorption method, (C) membrane separation process, and ion/ion separation technologies based on chemical mechanisms: (D) liquid-liquid extraction, (E) supported liquid membrane (F) precipitation.

Adsorption method

Adsorption methods accomplish ion/ion separation by relying on the ion sieve sorbents (**Figure 3B**). Ion sieve sorbents contain vacant sites formed by stripping target ions from the precursors. Therefore, vacant sites only accommodate ions with the same or smaller ionic diameters than the target ion. Among Li^+ , Na^+ , K^+ , Ca^{2+} , and Mg^{2+} , Li^+ has the smallest ionic diameter. Thus, only Li^+ can be reinserted in vacant lithium-ion sieves (LIS) sites, which are formed by replacing Li^+ with H^+ from the precursor.[59] After immersion in the feed water, ion exchange processes between the H^+ in the LIS and Li^+ in the water (e.g., H_2TiO_3)[60] and other redox processes (e.g., between $\lambda\text{-MnO}_2$ and LiOH)[61, 62] will occur. LIS will generally be regenerated by acid and accompanied by the production of lithium salts. Popular LIS is the family of lithium manganese oxides (LMO-type) and lithium titanium oxides (LTO-type). Most LMO-type LIS have spinel structures obtained from the precursors of LiMn_2O_4 [63], $\text{Li}_2\text{Mn}_2\text{O}_5$ [64], or

$\text{Li}_4\text{Mn}_5\text{O}_{12}$ [65]. LTO-type LIS contains H_2TiO_3 and $\text{H}_4\text{Ti}_5\text{O}_{12}$, which are derived from Li_2TiO_3 (layered structure) [66] and $\text{Li}_4\text{Ti}_5\text{O}_{12}$ (spinel structure) [67], respectively. LMO-type LIS manifests a lithium uptake capacity between 10-40 mg/g with a capacity fading of about 10% after 5 cycles.[59] The low stability of LMO-type LIS may be due to the dissolution of Mn during the adsorption/desorption process.[68] The reported capacity of LTO-type LIS ranges from 30 $\text{mg}_{\text{Li}}/\text{g}$ to 100 $\text{mg}_{\text{Li}}/\text{g}$, with slight capacity fading after 5 cycles.[69, 70] The better stability of LTO-type LIS benefits from larger Ti-O bonding energy.[59]

Apart from LIS, some studies use potassium-ion sieves (PIS) to extract K^+ from aqueous solutions. Yuan et al. synthesized membrane-type PIS with a molecular sieve (composed of 76% $\text{Na}_6\text{Al}_6\text{Si}_{10}\text{O}_{32}\cdot 12\text{H}_2\text{O}$ and 24% $\text{K}_2\text{Al}_2\text{Si}_3\text{O}_{10}\cdot 3\text{H}_2\text{O}$) on $\alpha\text{-Al}_2\text{O}_3$ -supporting layer.[71] The channel of this PIS ranges between 0.6 nm to 0.7 nm, which is larger than the hydration diameter of K^+ but less than those of Na^+ , Ca^{2+} , and Mg^{2+} . It thereby exhibits a good selectivity towards K^+ with selectivity factors of 94 (K^+/Na^+), 161 ($\text{K}^+/\text{Mg}^{2+}$), and 1186 ($\text{K}^+/\text{Ca}^{2+}$). Pan et al. synthesized Birnessite-type potassium manganese oxides, $\text{K}_{0.5}\text{MnO}_{4.3}\cdot 3\text{H}_2\text{O}$, by heating a mixture of ocean manganese nodules and KMnO_4 and then oxidizing the products with $(\text{NH}_4)_2\text{S}_2\text{O}_8$. [72] The adsorption capacity of $\text{K}_{0.5}\text{MnO}_{4.3}\cdot 3\text{H}_2\text{O}$ in seawater brine is 22.1 mg/g with a selectivity factor of 109 (K^+/Na^+).

All in all, the adsorption method has the advantage of high selectivity and facile operation processes. However, it's operation processes require many chemicals to regenerate the adsorbents or to maximize the adsorption capacity.[73]

Membrane separation

In the separation process, membranes serve as the barrier, hindering the transport of cations except for the target cation (**Figure 3C**). Membrane separation has the advantage of clean production, small footprints, and simple operation in continuous mode.[74]

The ion/ion separation via the different membranes depends on distinct mechanisms. Cation transportation in cation exchange membranes (CEM) could be explained by the solution-diffusion model, with a concentration or an electrical potential gradient as the driving force[75]. The ion selectivity between two cations, therefore, depends on the ion concentration (ion exchange) and the mobility of cations in the membrane phase.[76] Ion exchange relates to the valence and size of ions. Generally, CEM shows an affinity for cations with higher valences or larger ionic diameters (with the same valences).[75] The mobility of the cations relies on the inherent ionic mobilities and the interaction between the cations and the fixed negatively charged groups. The preference could be switched from divalent cations to monovalent cations by coating a positively charged surface (electrostatic repulsion)[77] or a highly cross-linked layer (steric hindrance).[78] Besides the properties of CEM, the diffusion boundary layer adjacent to a membrane (determined by the operations) also

affects the selectivity. The work of Kim et al. shows that the boundary layer prefers K^+ over Ca^{2+} due to its higher diffusivity.[79] With a higher current density, the transport number of K^+ in the boundary layer rises.

A typical nanofiltration membrane contains negatively charged functional groups in neutral solutions.[80] Similar to CEM, the negatively charged functional groups prefer divalent cations over monovalent cations. However, the steric hindrance and dielectric exclusion reduce the transport of divalent cations more than monovalent cations (**Figure 4**). Consequently, nanofiltration membranes generally manifest a high affinity for monovalent cations.[81] Positively charged nanofiltration membranes that could be prepared from amine-containing polycations (e.g., polyethylenimine and poly(N,N-dimethylaminoethyl methacrylate))[82] have been developed to enhance the selectivity towards monovalent cations.[29, 83] Zhang et al. synthesized a positively charged nanofiltration membrane via interfacial polymerization with polyethylenimine and trimesoyl chloride. The selectivity factor (Li^+/Mg^{2+}) is triple that of the negatively charged membrane (10 vs. 3).[84]

In addition, decreasing the pore size of the nanofiltration membrane could improve the selectivity between monovalent cations and divalent cations or even possess the selectivity between monovalent cations and monovalent cations.[85, 86] Wen et al. fabricated a sub-nanometer polyethylene terephthalate membrane (average pore radius of ca. 0.3 nm) by irradiating a commercial membrane utilizing heavy ions with high energy and subsequently exposing it to UV radiation for 3 h.[87] The transport rate of monovalent is more than 1000 times that of divalent cations. Furthermore, the transport rate order of monovalent cations follows $Li^+ > Na^+ > K^+ > Cs^+$. Abraham et al. studied the influence of interlayer spacing on the transport of cations.[88] With an interlayer spacing of 1.0 nm, Li^+ , Na^+ , and K^+ show similar permeation rates at least 100 times higher than those of Ca^{2+} and Mg^{2+} . When the interlayer spacing decreases to 0.9 nm, the permeation rate of all the cations declines but exhibits the selectivity order of $K^+ > Na^+ > Li^+ \gg Ca^{2+} > Mg^{2+}$. Moreover, no ion concentration can be detected in the permeate after 5 days as the interlayer spacing decreases to 0.6 nm. The improved selectivity performance is attributed to the enhanced dielectric exclusion effect, which forms different energy barriers for cations transport. The energy barriers are mainly determined by the dehydration energy and are also related to the interaction between the ions and membrane materials (specific frictional and viscous interactions).[85] Frictional effects originate from the collisions between cations and the rough surface of the membrane, and viscous interactions stem from the chemical affinity between the cations and the pore materials. Both these effects increase the energy barriers of ion transport in the pores.[89] However, the high affinity between the cations and pore materials can also facilitate partitioning into the pores.[85]

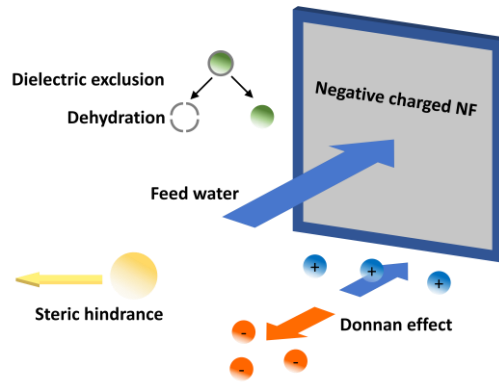


Figure 4: Steric hindrance, Donnan effect, and dielectric exclusion in nanofiltration membrane.

Recently, solid superionic conductor materials have been used as another type of membrane to separate alkali and alkaline earth metal ions. The diffusion of cations in this kind of membrane is similar to hopping from one site to another adjacent site and passing through periodic bottleneck points (an energy barrier that separates two local minima along the minimum energy pathway)[90]. The activation energy for different cations to pass through the bottlenecks is distinct, so the membrane could manifest selectivity towards one specific ion. Solid superionic conductor membranes generally exhibit superior selectivity even facing the challenge of super high concentration differences between target cations and competing cations (e.g., Li^+ and Na^+ in seawater), benefiting from the repeatable lattice structure with angstrom bottleneck size.[91] For instance, Li et al. utilized a lithium superionic conductor (LISICON) membrane, $\text{Li}_{0.33}\text{La}_{0.56}\text{TiO}_3$, in the electro dialysis system to extract lithium from seawater.[92] After 100 h of treatment, the Li^+ concentration increases from 0.21 mg/L to 9.01 g/L with a selectivity factor of more than $45 \cdot 10^6$ ($\text{Li}^+/\text{Mg}^{2+}$) and $1.7 \cdot 10^6$ (Li^+/Na^+). However, this kind of membrane suffers from low penetration flux and poor mechanical properties.[93] Supported liquid membranes isolate target ions depending on their chemical properties in a similar way to the liquid-liquid extraction method. It will thus be introduced in the following subsection.

2.1.2.2 Ion/ion separation based on chemical mechanisms

Liquid-liquid extraction

Liquid-liquid extraction (LLE) is the process of repartitioning a solute from one liquid to another liquid phase (generally from water to an organic solution), as shown in **Figure 3D**. Complex agents (called extractants) are generally required to extract dissolved metal ions from water to organic solutions (named diluent).[94] The formed hydrophobic complexes are extracted into the diluent, and the targeted ion are stripped out by adding other chemicals (e.g., HCl[95, 96], water[97]). Benefiting from the different affinities of the complex agents, LLE is able to extract a specific ion from the mixture.

Depending on the different mechanisms, the extractants can be classified into chelating, acidic, and solvating extractants. Chelating extractants can directly form complexes with alkali/alkaline earth metal ions. For instance, crown ethers and their derivatives are well-known extractants to separate alkali/alkaline earth metal ions. They could form multidentate complexes between uncombined electron pairs of oxygen atoms and cations. The size of crown ethers' cavities and ion diameters determine the selectivity of crown ethers.[98] Acidic extractants, such as organic phosphoric acid derivatives, extract alkali/alkaline earth metal ions via the ion exchange between the H⁺ and metal ions.[99] Organic phosphoric acids generally show an affinity for divalent cations over monovalent cations.[94] The extraction process with solvating extractants involves transferring metal ions into the organic phases with an inorganic anion and ultimately forming a salt with solvating extractants (**Equation 2**). Note that sometimes two kinds of extractants could be used simultaneously to enhance the selectivity performance. For example, chelating extractants (β -diketone) and solvating extractants (trioctylphosphine oxide) are used together to improve the selectivity of lithium.[100] LLE could accomplish continuous operations and produce high-purity products (higher than 90%) but has the drawbacks of the loss of extractants, volatility of some organics, and high cost of the reagents.[73]



where, M, X, and B represent metal ions, inorganic anions, and solvating extractants, respectively. The top line on B refers to the organic phase.

One possible approach to address the issues of LLE is embedding organic liquid in the pores of polymer support, which is referred to as a supported liquid membrane (SLM). The organic liquid is the extractant and sometimes includes diluent (adjusting the viscosity) and modifier (preventing the formation of another phase).[101] The organic liquid remains in the pores due to the capillary forces. SLM isolates the two aqueous phases, the feed water and the stripping solution. The cations in the feed water are selectively extracted by the extractants through the organic/feed water interface and are carried to another side of the membrane. Once there, the cations are exchanged by another charged species (**Figure 3E**). Like LLE technology, the performance of SLM (e.g., extraction efficiency and selectivity) also depends on the organic extractants. So far, many extractants such as α -acetyl-m-dodecylacetophenone (combined with tri-octyl phosphine oxide),[102] di-2-ethyl hexyl phosphoric acid (with TBP),[103] and [C₄mim][NTf₂](with TBP)[104], have been used in the SLM. Compared to other organics, ionic liquids exhibit better stability due to their high viscosity and strong hydrophobicity, which could inhibit solvent leakage.[74]

Precipitation

Precipitation transforms a dissolved solute into an insoluble solid. Among Li^+ , Na^+ , K^+ , Ca^{2+} , and Mg^{2+} , Na^+ and K^+ can co-exist with almost all inorganic anions in the water.[105] In contrast, Li^+ , Ca^{2+} , and Mg^{2+} would all form a precipitate with some anions. Therefore, it is possible to extract Li^+ from the mixed solution containing other alkali and alkaline earth metal ions on a large scale. An et al. developed a two-step process to extract lithium from brines of Salar de Uyuni, Bolivia, composed of saturated Na^+ , Cl^- , SO_4^{2-} , 0.7-0.9 g/L Li^+ , and 15-18 g/L Mg^{2+} . [106] Mg^{2+} and SO_4^{2-} are removed by adding lime until $11.3 > \text{pH} > 8.0$, forming $\text{Mg}(\text{OH})_2$ and CaSO_4 sediment. The residual Mg^{2+} and Ca^{2+} are precipitated with $\text{C}_2\text{O}_4^{2-}$. The supernatant is then evaporated until the concentration of Li^+ is 20 g/L, and the final product Li_2CO_3 (99.5% purity) is produced by adding CO_3^{2-} . Hamzaoui et al. precipitated 60% Li^+ of the brines by using Al^{3+} (Al/Li molar ratio = 5) and KOH (adjusting pH to 7). [107] The choice of precipitant should be determined according to the feed water composition. Precipitation is a rapid and easy-operation approach, but it consumes lots of chemicals and requires several steps to obtain high-quality products.

2.2 Electrochemical ion separation

2.2.1 Mechanism of ion/water separation

Electrochemical ion/water separation via ion immobilization inside the electrode or at the fluid/solid electrode interface can be accomplished by forming an electrical double-layer (EDL), pseudocapacitance, and Faradaic (battery-like) processes. The latter two involve redox reactions, where the distinguishing difference is kinetics.

Electrical double-layer

The EDL formation is an electrostatic process at the fluid/solid interface of an electrode in contact with an electrolyte. The first EDL model was proposed by Helmholtz in 1879.[108] He claimed that at the electrode/electrolyte interface, all ions with opposite charges to the electrode distribute parallel to the electrode at a small distance (H). The model was successively modified by Gouy and Chapman in 1910[109] and 1913[110], respectively. They considered the mobility of ions and the coupled effect of diffusion and electrostatic forces. Specifically, they stated that ions distribute in a large area called the diffuse layer. They assume ions are point charges, and their equilibrium concentration follows the Boltzmann distribution (**Equation 3**). [111] The ion concentration decreases progressively as the distance to the electrode/electrolyte interface increases. Because the diffuse layer's width is imprecise, an evaluation parameter, the Debye length, is introduced to describe the characteristic distance for the counterion concentration and potential to decay by the factor e (in the low-voltage limit of the theory and for a single planar surface).[9]

In 1924, Otto Stern combined the Helmholtz and Gouy-Chapman models and described EDL as two layers: the Stern layer (or Helmholtz layer) and the diffuse layer (**Figure 5A**).^[112] The Stern layer is not accessible to ions and is occupied by the solvent sphere. The distribution of ions in the diffuse layer, however, follows the Gouy-Chapman model.

$$c_i = c_{i\infty} \times \exp\left(\frac{-z_i \times e \times \Psi}{k_B \times T}\right) \quad \text{Equation 3}$$

where c_i and $c_{i\infty}$ are the molar ion concentration in EDL and bulk, respectively; z_i is the valency; T is the absolute temperature; e is the elementary charge; Ψ is the local electric potential in the diffuse layer, and K_B is the Boltzmann constant.

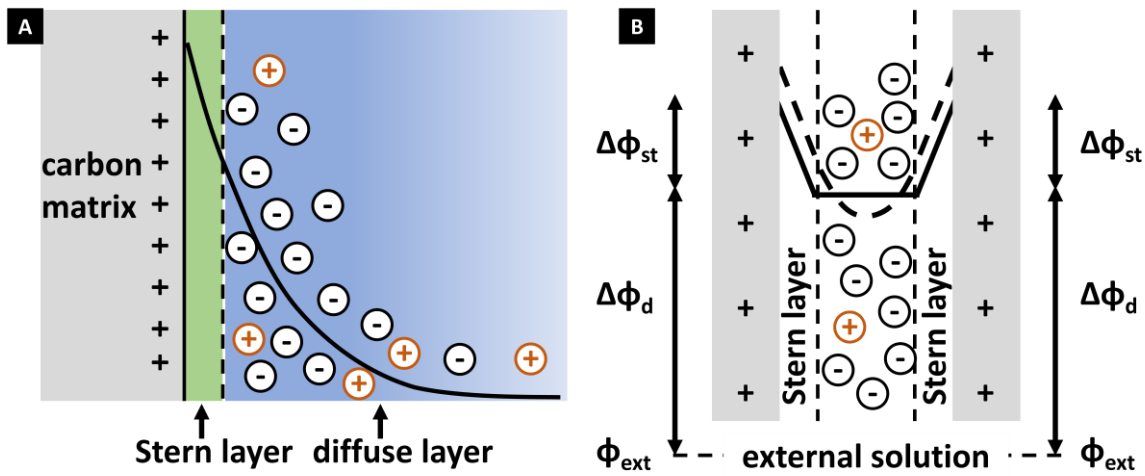


Figure 5: Schematics of (A) the Gouy-Chapman-Stern model and (B) the modified Donnan model.

The Stern-Gouy-Chapman model works well in a non-overlapped EDL, which indicates that the pores are far larger than the Debye length. When the EDL overlaps, however, the Stern-Gouy-Chapman must be modified.^[113] Biesheuvel et al. proposed a modified Donnan model to describe the interior volume of the nanopores of carbon material (**Figure 5B**).^[114] Based on the classic Donnan mode, this work included two modifications. First, it included a charge-free stern layer between the electrolyte and electrode, indicating that the ionic charge cannot be infinitely close to the electronic charge. Second, it included an additional force that attracts ions transforming from the interparticle pores (pores between the particles) into the intraparticle pores (pores inside the material particles). The concentration of ion j in the micropores in the material particles ($c_{j,mi}$) and the charges density of micropores (σ_{mi}) follow **Equation 4** and **Equation 5**, respectively. Different from the Stern-Gouy-Chapman model, the ion concentration in the modified Donnan model refers to the ion in the whole volume of micropores (intraparticle pores). This modified Donnan model could validly describe the equilibrium ion adsorption and charge in micropores (intraparticle pores), matching many experimental datasets reasonably well.^[115-117]

$$c_{j,mi} = c_{mA} \times \exp(-z_j \times \Delta\phi_d + \mu_{att}) \quad \text{Equation 4}$$

where c_{mA} represents the ion concentration in interparticle pores; z_j equals + 1 and -1 for Na^+ and Cl^- , respectively, $\Delta\Phi_d$ stands for the Donnan potential difference between the interparticle and intraparticle, and μ_{att} is the additional force.

$$\sigma_{mi} = \frac{-C_{St,vol} \times \Delta\phi_{St} \times V_T}{F} \quad \text{Equation 5}$$

where $C_{St,vol}$ represents volumetric Stern layer capacity; $\Delta\Phi_{St}$ and V_T are the potential drops in the Stern layer and thermal potential, respectively, and F stands for the Faraday constant.

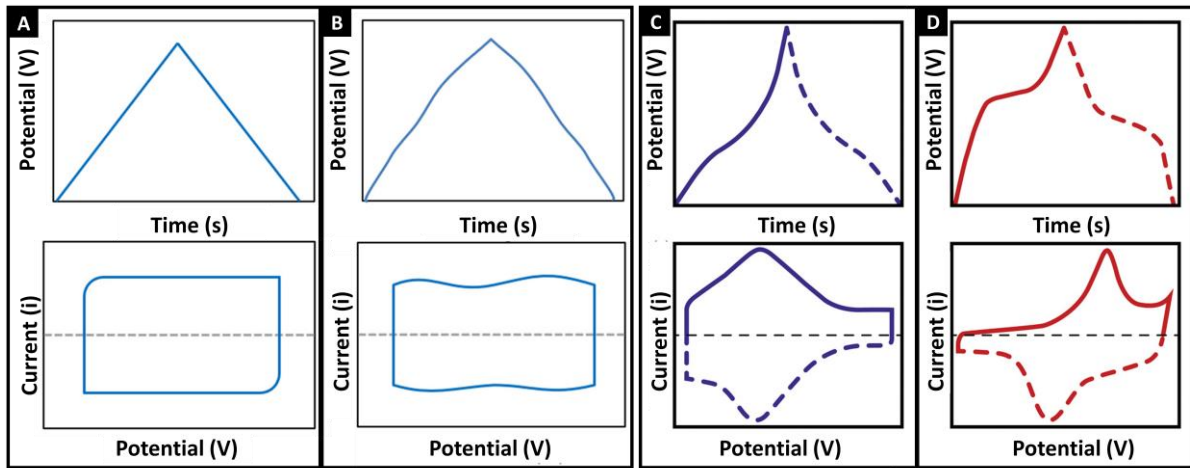


Figure 6: Typical cyclic voltammograms and galvanostatic cycling with potential limitation profiles of capacitive(A), pseudocapacitive (B, C), and battery-like materials (D). The curve in Panel C only follows the wide definition of pseudocapacitance. Panel A and B are reproduced from Ref. [118], Copyright 2019, John Wiley and Sons; Panel C and D are adapted from Ref.[119], Copyright 2019, John Wiley and Sons.

The electrochemical behavior of the capacitive material, which stores ions by the EDL, has unique characteristics. The ideal cyclic voltammetric (CV) curve is rectangular (**Figure 6A**), originating from the relationship between the current (i) and scan rate (v), $i = Cv$, where C is the capacitance. If a constant current is applied to the electrode, the potential has a linear relationship with time (**Figure 6A**). This means that the capacitance (the ratio between the accumulated charge and the potential) is constant. The gravimetric capacitance of carbon materials ranges from 50-200 F/g, depending on the pore sizes, functional groups, and electrolytes.[120, 121] As the EDL is formed at the electrodes/electrolytes interface, the capacitive materials have fast kinetics generally measured by Electrochemical Impedance Spectroscopy (EIS). The ideal Nyquist plot (one of the plotting forms of EIS results) of the capacitive material shows a 90° line parallel to the y-axis at the low-frequency region and no semi-circle at the high-frequency area (**Figure 7**).[122]

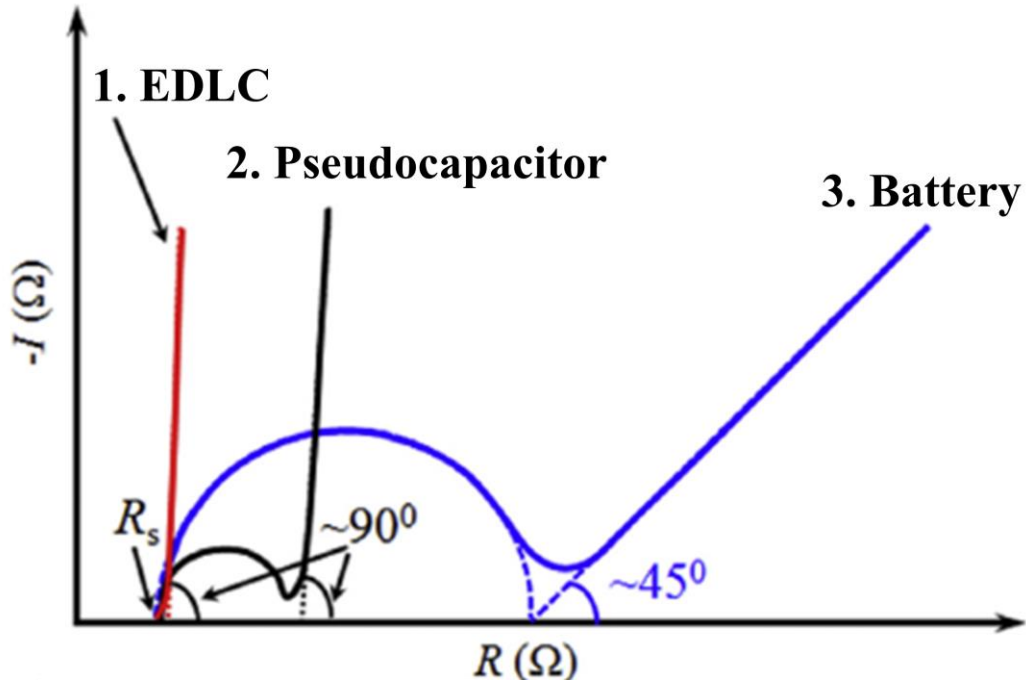


Figure 7: Typical Nyquist plot of capacitive, pseudocapacitive, and battery-behavior materials, reproduced from Ref.[122] Copyright 2018, Elsevier.

Pseudocapacitive behavior redox reaction

The term pseudocapacitive refers to a seemingly capacitive electrochemical process that emanates from charge transfer processes across the interface between the electrode and electrolyte (Faradaic process).[123] In the late 20th century, Conway first proposed three types of possible pseudocapacitive behavior, monolayer adsorption, redox reaction on the electrode surface, and solid-solution intercalation (**Figure 8**).[124-126] The species adsorbed on the electrode in a monolayer is generally the intermediate during forming bulk substances, similar to the adsorbed H⁺ during H₂ evolution and the metal atom layer during the deposition.[124] Redox reaction on the electrode surface refers to ions adsorbed on or near the electrode surface coinciding with charge transfer, such as the Faradaic reaction of hydrous RuO₂ in sulfuric acid.[127] Solid-solution intercalation appears when ions intercalate into the layers or tunnels of the material undergoing charge transfer but have no kinetic limitations. Conway assumed that the adsorbed species follow the Langmuir-type electrosorption isotherm (**Equation 6**). This equation could be transformed into a Nernst equation type, as shown in **Equation 7**. Thus, the pseudocapacitance (C) can be derived, as shown in **Equation 8**.

$$\frac{\theta}{1-\theta} = K \times C_A \times \exp\left(\frac{V \times F}{R \times T}\right) \quad \text{Equation 6}$$

where θ is the surface coverage of adsorbed species; C_A is the concentration of species in the electrolyte, K is the ratio of the forward and reverse reaction rate constant; V stands for the potential; F and R are Faraday and the ideal gas constants, respectively.

$$E = E^0 + \frac{RT}{F} \times \ln \left(\frac{1}{K \times C_A} \times \frac{\theta}{1-\theta} \right) \quad \text{Equation 7}$$

where E and E⁰ stand for the equilibrium potential and standard potential, respectively; T is the temperature.

$$C = q \times \frac{d\theta}{dV} = \frac{q \times F}{R \times T} \times \theta \times (1 - \theta) \quad \text{Equation 8}$$

where q is the amount of the transferred charge.

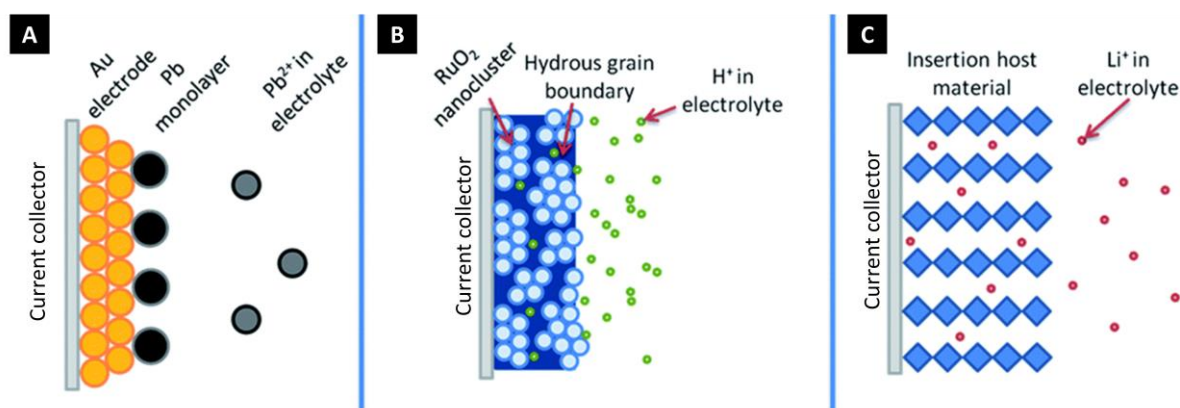


Figure 8: Three kinds of mechanisms of pseudocapacitive behavior (A) Monolayer adsorption, (B) redox pseudocapacitance, and (C) intercalation pseudocapacitance, adapted from Ref. [127] Copyright 2014, The Royal Society of Chemistry.

With the development of material science, especially nanomaterials, more explanations about pseudocapacitive processes and the definition of pseudocapacitance are provided. Augustyn et al. proposed the concept of intrinsic and extrinsic pseudocapacitance to explain the pseudocapacitive behavior of nanomaterials.[127]

- Intrinsic pseudocapacitive materials exhibit behavior that is not limited by particle sizes, morphologies, and electrochemical kinetics. For example, rod-like, petal-shaped, and irregular MnO₂ particles exhibit pseudocapacitive behavior despite their pseudocapacitances being different.[128] The cyclic voltammograms of electrodes composed of 35 nm and 7 nm Nb₂O₅ are similar with the same potential range. The only difference is the area (i.e., the pseudocapacitance).[129]
- Extrinsic pseudocapacitive materials transform from battery to pseudocapacitive behavior when the particle sizes are reduced to nanometers (e.g., LiCO₂[130]).

A broad interpretation of pseudocapacitive is that pseudocapacitance originates from fast and reversible redox reactions that are not limited by solid-state diffusion.[121, 123, 127] However, Brousse et al. stated that only materials with nearly constant pseudocapacitance in a wide potential range could be defined as pseudocapacitive material.[131] This definition aims to prevent the increasing number of published papers with seemingly high gravimetric capacitance (thousands of F/g),

which has obvious redox peaks. Recently, Ando et al. proposed a distinguishing method based on a mechanistic standpoint and the interaction between the cations and electrodes during the process.[132] They claimed that the electrochemical behavior is capacitive when cations intercalate in MXene with a complete hydration shell. The pseudocapacitive behavior occurs when (partially desolvated) cations intercalate in-between the layers of MXene. Their orbit couple with the orbit of MXene (especially surface-termination species), causing the charge redistribution. The charge transfer encourages depletion of the electrostatic potential difference at the electrode/electrolyte interface, producing pseudocapacitance.[132] The definition and detailed mechanism of pseudocapacitive behavior are still inconclusive, attracting the research community to explore them.[123]

In CV measurements, the pseudocapacitive process shows a nearly rectangular shape (e.g., MnO_2), as shown in **Figure 6B**. [121] Some pseudocapacitive materials (following the broad definition of pseudocapacitance) may also manifest kinetic limited broad/distributed charge transfer peaks.[123, 127] These peaks are minor images with slight potential differences between the oxidation and reduction peaks (**Figure 6C**)[127], which could also have a larger and distinct peak position difference at high scan rates.[133] The potential-time curve of pseudocapacitive material under constant current is almost linear without any obvious plateaus but does have some inflection points.[119]. Apart from the CV and GCPL measurement, the EIS results of pseudocapacitive materials show unique properties, which is essential evidence to distinguish them from capacitive and battery-behavior materials. The Nyquist plots contain a semi-circle at the high frequency, which corresponds to the charge transfer process. The low-frequency region exhibits a line with an angle of ca. 90° against the X-axis (**Figure 7**), reflecting the fast kinetics of pseudocapacitive processes since they occur at/near the surface of the electrodes.[123, 134]

Battery-behavior redox reaction

Unlike pseudocapacitive processes, the kinetics of battery-behavior redox processes are controlled by solid-state diffusion. Consequently, the voltammogram of battery behavior contains at least one pair of redox peaks. The potential of the cathodic and anodic peaks generally differs (**Figure 6D**). Under a constant applied current, there are plateaus in the potential-time curve, which is also a defining characteristic of battery-behavior materials (**Figure 6D**). [135] Note that the plateaus may disappear or become indistinct under high specific currents.[118] The typical Nyquist plot of battery materials contains a semi-circle at high frequency and a straight line with 45° angle at low frequency (**Figure 7**). The diameter of the semi-circle of battery materials is generally larger than pseudocapacitive materials, suggesting a larger charge transfer resistance. And the straight line at low frequency indicates that the batteries' materials are limited by the diffusion process.[136] Therefore, the electrochemical measurement should be conducted using a wide range of scan rates or specific currents. The results of

various electrochemical measurements should be comprehensively considered to distinguish pseudocapacitive and battery-behavior material. Limited by the diffusion rate, one charge/discharge cycle of battery-behavior processes may take ca. from tens of minutes to several hours, which is much more than that of capacitive materials (tens of seconds) and pseudocapacitive materials (several minutes).[123, 137] The charge/ion storage ability (per mass) of battery-behavior redox reactions varies from hundreds to thousands of mAh/g (depending on the reaction mechanism), which is higher than EDL.[137]

Battery-behavior redox reactions include intercalation, conversion, and alloying reactions (**Figure 9A**).[138] Intercalation reaction refers to guest ions (often cations, such as Li^+ , Na^+ , K^+ , and Mg^{2+}) being inserted into appropriate sites of the host material's crystal structure, accompanied by uptaking electronics at the particular redox center, which is generally the d-orbital of the transition metals.[139] During the intercalation reaction, the structure of the host material experiences minimal changes compared with the conversion and alloying reactions.[123] The intercalation reactions of battery behavior are limited by kinetics different from that of pseudocapacitive behavior. Many intercalation materials, such as LiFePO_4 [140], lithium/sodium manganese oxides[141], and Prussian blue/Prussian blue analogues [142], have been studied in rechargeable ion batteries. Some can be directly applied in the aqueous electrolyte, which will be introduced in Chapter 2.4. Intercalation materials generally exhibit better stability than conversion and alloying materials. However, the limited amount of transferred charge in the intercalation reaction leads to a relatively lower capacity than conversion and alloying materials).[143]

Alloying reactions can occur between alkali/alkaline earth metal ions with metal or semi-metal (group IVA and VA), producing binary alloy accompanied by multi-charge transferring.[144] During alloying, the electrode materials undergo several structural changes, accompanied by forming and breaking chemical bonds and often following several intermediate steps.[145, 146] Alloying materials may provide a superior theoretical capacity ($\gg 400$ mAh/g) as they benefit from multi-electronic reactions.[147] However, due to the formation of the many intermediates, alloying materials undergo very large volume expansion (e.g., 420% for Sn[148], 390% for Sb[149]), which leads to rapid capacity fading.[150] In addition, the low redox potential of alloying materials (-2.5 V to -1.0 V vs. SHE) renders them unsuitable to directly serve as electrodes in ion/water separation.

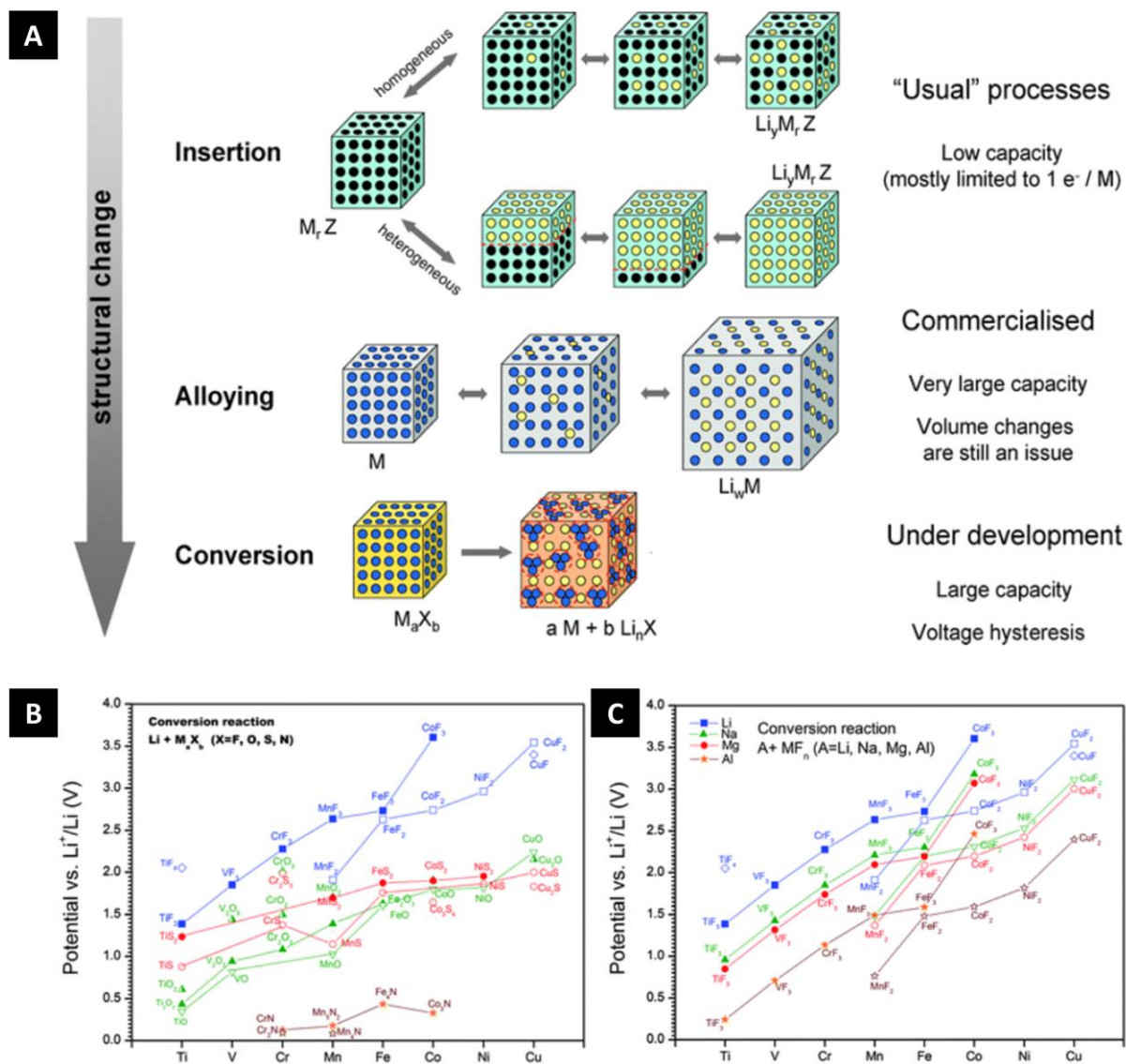


Figure 9: (A) Schematic image of intercalation, alloying, and conversion reaction, adapted from Ref [138], Copyright 2009, The Royal Society of Chemistry, the calculated electromotive force of conversion reactions between selected binary transition metal compounds and Li (B) and between selected binary transition metal fluorides and Li, Na, Mg, or Al (C), adapted from Ref [151], Copyright 2011, The Royal Society of Chemistry.

Conversion reactions occur between the binary transition metal compound and alkali/alkaline earth metal ions.[138] Therefore, metallic nanoparticles and alkali/alkaline earth metal compounds can form, as shown in **Equation 9**. The latter only shows the ultimate product of conversion reactions. They generally experience various transformations (i.e., intermediates) during the charge/discharge processes. Because transition metals are reduced to metallic states in conversion reactions, the resulting capacity (>200 mAh/g)[152] is higher than in intercalation reactions. Conversion materials could be either cathodes or anodes in rechargeable ion batteries. The potential of conversion material (-2.5-0.5 V vs. SHE) depends on the component of the transition metal compound, the valence of the

transition metal, and the kind of alkali/alkaline earth metal ions. With the same transition metal and valence, the electrode potential follows the order of phosphide < nitrate < sulfate < oxide < fluoride, as shown in **Figure 9B**.^[151] Metals with higher oxidation states have higher electrode potential. With the same transition metal compound, such as fluoride, the electrode potential follows the order of Al < Mg < Na < Li (**Figure 9C**).^[151] Conversion materials suffer from voltage hysteresis due to low kinetics and low stability due to volume expansion (similar to alloying materials) and interaction with electrolytes.^[152] Moreover, because the products of conversion reactions have a high solubility, can react with water, and have a low redox potential of alloying extraction, the conversion and alloying material cannot be used directly in ion/water separation.^[153, 154] However, some research has used alloying material for water desalination with unique cell structures, which will be introduced in Section 2.3



Equation 9

where M represents the single or mix of transition metals' X is the sole or combination of anions from the group of oxygen, halogens, chalcogenides, and pnictides; n stands for the oxidation stage of X.

2.2.2 Mechanism of ion/ion separation

Electrochemical methods could selectively extract one specific cation from the mixtures by employing materials with an affinity for the target cation or installing a selective membrane between electrodes and feed water. Depending on the target ions, the membrane could be CEMs, nanofiltration membranes, or ceramic membranes, which have been overviewed in Section 2.1.2.1. For the electrodes, the intrinsic characteristics (e.g., the crystal structure, lattice sizes, and pore size distribution) determine which cation is preferred and how good the selectivity performance is.

The selectivity of unmodified material depends on the required energy of cations for entering their pores (capacitive materials) or carrying out the redox reactions with electrodes (Faradaic material). Ions exist in an aqueous solution in the form of hydration ions. When the pore size is far larger than the hydration diameters of all alkali/alkaline-earth metal ions, the hydrated cations can freely enter the pores without dehydration.^[85, 155] In this case, the valence of cations strongly influences the resulting ion selectivity. This means that divalent cations are preferred compared with monovalent cations.^[156] The selectivity between monovalent and monovalent cations is weak (generally lower than 2) ^[157, 158], and the selectivity originates from the ion volume expulsion. This means that ions with smaller hydration diameters are preferred.^[159] Some studies also reported a kinetics-dependent selectivity phenomenon with capacitive materials. Zhao et al. calculated the ionic composition in the porous electrodes whereby the electrolyte contained 5 mM NaCl and 1 mM CaCl₂.^[115] The Ca²⁺/Na⁺ ratio increased from ca. 1/5 (charging time, ~100 s) to ca. 3/1 (charging time, ~800 s), and the Na⁺ flux

decreased rapidly to negative as the charging time increased, suggesting the ion exchange between Ca^{2+} and Na^+ . The work of Gueyes et al. shows a similar conclusion.[160]

As the pore size decreases to the subnanometer range (Ångström scale), the cations require energy to partially desolvate or rearrange the hydration sphere to enter the pores.[161] The required energy for different cations is different due to their different hydration diameters, the number of hydrated molecules, and dehydration energy (**Figure 2**). Consequently, the materials exhibit selectivity towards a specific ion with a lower hydration diameter and dehydration energy [162]. For instance, Zhang et al. studied the selectivity of carbon cloth with sub-nanopores and narrow pore distribution (89% pore volume at the pore size less than 0.7 nm) in the electrolyte containing equimolar Li^+ , Na^+ , K^+ , Cs^+ , Ca^{2+} , and Mg^{2+} . [12] The electrodes show an affinity for K^+ and Cs^+ with selectivity factors (vs. Na^+) of 3.5 and 3.8, respectively. Unlike common micropore carbon, the carbon cloth prefers the uptake of Na^+ rather than Ca^{2+} and Mg^{2+} .

The size of interstitial sites for cation intercalating into the crystal structure of Faradaic materials is generally much less than the hydration diameter of alkali and alkaline earth metal ions. Therefore, cations lose almost all the water shells before entering the structure of materials.[163] The dehydration energy, Coulomb repulsions, and Steric hindrance effect (related to the ionic size) influence the required energy for the reaction reflected on the different redox potentials in cyclic voltammograms.[164] For example, ions with smaller hydration energy have more positive redox potential to intercalate in TiS_2 (e.g., the redox potential difference between Cs^+ and Mg^{2+} , 164 mV). By controlling the potential range for charging and discharging, Srimuk et al. accomplished selective uptake of both Cs^+ and Mg^{2+} depending on the operational settings.[165] Na^+ , which has a higher ionic diameter than Li^+ , has a more negative potential (ca. -0.2 V at the same concentration) to intercalate in $\text{LiFePO}_4/\text{FePO}_4$ than Li^+ . [166] Additionally, LiFePO_4 kinetically prefers the uptake of Li^+ due to the lower migration energy barrier of Li^+ than Na^+ . [167] Therefore, LiFePO_4 could uptake Li^+ from a mixture of Li^+ and Na^+ with high selectivity over hundreds with proper operation conditions (e.g., cell voltage, concentration ratio in the feed water, specific current).[168, 169] Note that the interlayer spacing of some intercalation pseudocapacitive material (e.g., MoS_2 , MXene) is between the ionic diameter and hydration diameter of alkali and alkaline-earth metal ions. Thus, they also exhibit similar selectivity performance (including kinetics-dependent selectivity) to capacitive materials with Angstrom scale pores.[170, 171]

Apart from the above mechanism, ion/ion separation could arrive by modifying materials with functional groups which have affinities for specific cations. This approach is widely used in selectively extracting heavy metals[172] and is also reported for alkali and alkaline-earth metal separation in some research. Kim coated the carbon electrode with nanosized calcium chelating resin to selectively mine

Ca²⁺ from the mixture of Ca²⁺ and Na⁺. [173] Compared with uncoated carbon, the selectivity factor increased by 94-184%.

2.3 Cell architectures of electrochemical ion separation

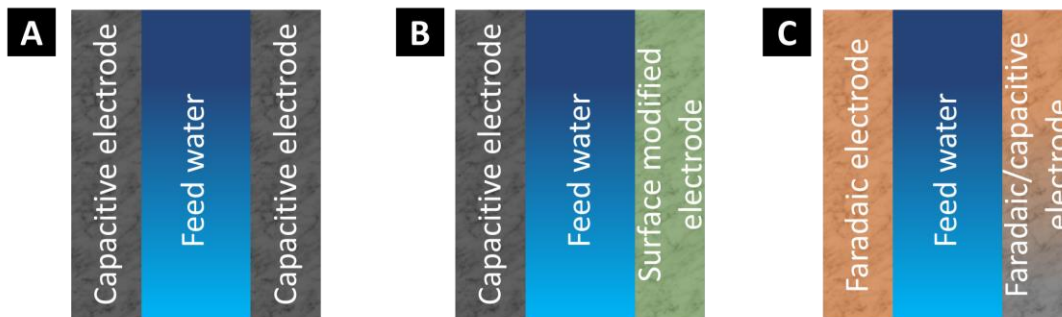
Electrochemical ion/water separation and ion/ion separation have similar cell architectures that could switch by changing the properties of some components, for example, electrodes and membranes. Therefore, the cell architectures are introduced without special distinguishment. In this section, the cell architectures are divided into three categories based on whether the cell contains a membrane and whether the cathode and anode are the same.

2.3.1 Symmetric architectures

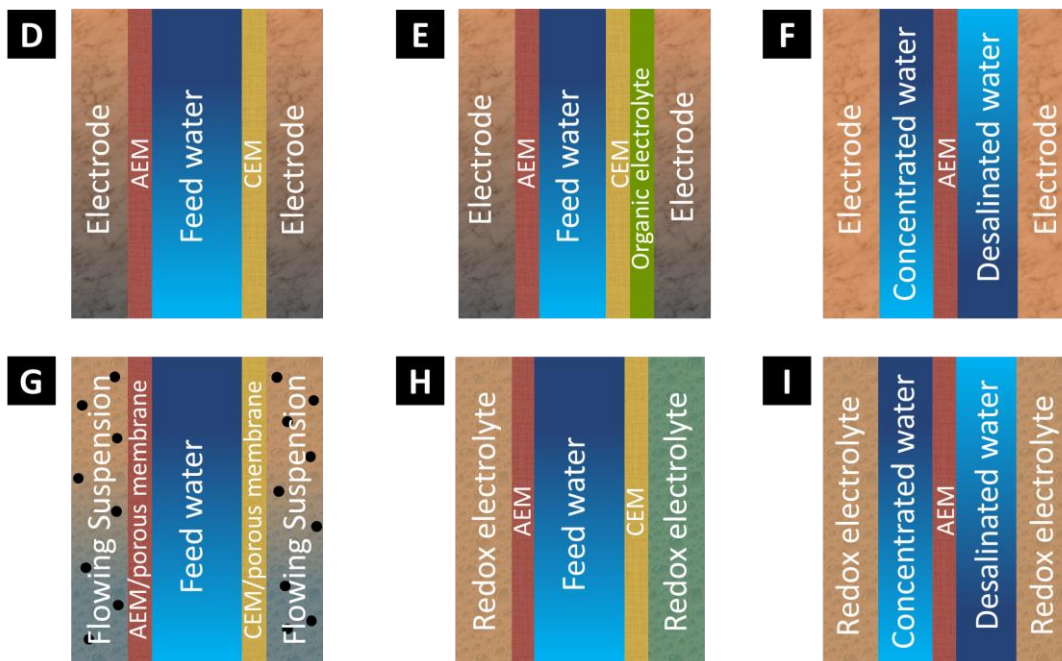
A symmetric-electrode-based setup contains two symmetric electrodes (generally capacitive behavior or pseudocapacitive material) that could uptake cations and anions. The electrodes are parallel with a gap in between for water flow, defined as flow by mode (**Figure 10A**). On a laboratory scale, the cell is usually a cube with a section size between 5x5 cm² to 10x10 cm² or a column with a diameter of less than 10 cm. There could be one pair of electrodes with a thickness of 100-500 μm or several pairs stacked together. The water channel inside could be open or filled with thin porous layers such as a glass fiber membrane. Apart from this water-flowing mode, another water-flowing mode where water could also possibly flow directly through the porous electrodes was first proposed by Newman and Johnson. Compared with the flow by mode, flow through mode has a higher desalination rate but requires a high porous electrode or high porous current collector with large macropores to ensure smooth water flow [174].

2.3.2 Asymmetric architectures

Since some materials have an affinity for storing cations while others manifest better anion uptake performance, pairing dissimilar materials as electrodes can enhance the system's performance. Some capacitive and pseudocapacitive material brings chemical charges due to the surface functional group [175, 176]. They could thus adsorb counter ions (with opposite charges to the chemical charges of the material) without external charge. The intrinsic chemical charge on the material would affect the potential distribution of the electrodes and the system's performance. Assuming a symmetric cell contains two carbon electrodes with negatively charged functional groups, both electrodes will adsorb cations to maintain charge neutrality before charging the cell. After applying an external voltage, the potential of the positive electrode would first reach the potential of zero charge (E_{PZC}). During this period, the adsorbed cations, via the chemical charge, will be expelled from the electrode. After the



Non-membrane architecture



Membrane-based architecture

Figure 10: Schematic image of different architecture: (A) Flow-by symmetric cell, (B) asymmetric cell with surface modified material, (C) desalination battery, (D) membrane capacitive deionization, (E) Bi-electrolyte desalination battery, (F) rocking-chair desalination battery, (G) flow electrode capacitive deionization, (H) redox flow battery desalination, (I) redox flow battery desalination with continuous mode.

potential crosses over E_{PZC} , the electrode would uptake the anions. Consequently, some charges do not contribute to removing the ions from water, and the positive electrode would go to more positive potentials, which would quickly oxidize electrodes.[177] However, if the chemically charged electrodes only serve as either positive or negative electrodes (i.e., pairing with other material to compose asymmetric cells), the system’s performance would be enhanced (**Figure 10B**). For example, Uwayid et al. employed oxidized or sulfonated activated carbon cloth as the cathode, and non-functionalized activated carbon cloth served as the anode.[178] Compared with the symmetric setup (with both non-

functionalized electrodes), the asymmetric cell shows a better desalination performance of 16.2 mg_{NaCl}/g for oxidized activated carbon cloth) and 13.4 mg_{NaCl}/g for the sulfonated cathode than the non-functionalized cathode (8.7 mg_{NaCl}/g). Gao et al. utilized positively charged carbon xerogel as a cathode and negatively charged carbon xerogel as an anode.[179] Without charging, the system could also uptake ions from water, and the cell releases the ions into the electrolyte during the charging process. Because the salt adsorption and desorption processes are opposite to typical CDI, the system is named inverted capacitive deionization (iCDI). After 50 cycles, the desalination capacity of iCDI slightly decays while that of symmetric CDI decreases from 1.0 mg_{NaCl}/g to 0.5 mg_{NaCl}/g.

Asymmetric cell architectures are the most common setup for battery-behavior materials because this type of material can almost only have redox reactions with cations or anions. They are also referred to as desalination batteries (**Figure 10C**). This concept was first introduced by Pasta et al. in 2012, where Na_{2-x}Mn₅O₁₀ supplies the cathode, and Ag serves as the anode.[14] During the charging process, Na⁺ intercalates in Na_{2-x}Mn₅O₁₀, and Cl⁻ reacts with Ag, forming AgCl. The discharging process is the opposite. This system consumes 0.29 Wh to desalinate 1 L seawater (25% salt removal). Subsequently, in 2013, Lee et al. used the same cell architecture but employed a lithium-selective electrode, λ-MnO₂, as the anode to achieve liquid extraction from brine.[180] Many Faradaic materials have been studied as cation uptake electrodes (selective and non-selective), which will be introduced in the next chapter. Anion-uptake electrodes are limited in Ag/AgCl[181], Bi/BiOCl[16], and layered double hydroxides[182] due to the weak electrochemical activity of Cl⁻ at a limited potential window (no water splitting). Besides pairing two Faradaic materials as electrodes, one Faradaic material and one capacitive material can also fulfill ion separation (hybrid capacitive deionization, HCDI). The first reported work using this setup was in 2014 by Lee et al., where Na₄Mn₉O₁₈ was paired with activated carbon.[183] HCDI combines the advantages of using a Faradaic material and capacitive material to some extent and achieves a relatively high ion-uptake capacity, rate, and low cost simultaneously (analogy to hybrid capacitors). Most studies on HCDI also focus on Faradaic materials for uptaking cations. Capacitive materials (generally carbon) serve as anion-uptake electrodes.[174] Thus, HCDI commonly faces the same problem of irreversible carbon oxidation. This problem can be solved by adding ion exchange membranes or synthesizing the cathode materials, which adapt low voltage operation.[184]

2.3.3 Membrane-based architectures

In the above cell architectures, the electrodes directly contact the feed water. Adding a permselective or selective membrane between the feed water and electrodes brings remarkable improvements and unique functions. Lee et al. first installed ion exchange membranes (IEMs), separating electrodes and feed water, and named the system membrane capacitive deionization (MCDI, **Figure 10D**). Compared with CDI, the salt removal capacity of MCDI increases by 19%.[185] Implementing IEMs could also

enhance the charge efficiency to above 80% (in low-salinity water) and enable capacitive materials to desalinate high-salinity water since IEMs can effectively block the migration of co-ions from electrodes to feed water (i.e., eliminating the co-ion effects).[186, 187]

The isolated space formed by membranes on the electrode sides enables the use of different electrolytes around electrodes rather than feed water. Kim et al. first used organic electrolytes as the supporting electrolyte in the side channel isolated from feed water by a CEM, as shown in **Figure 10E**. [188] Utilizing organic electrolytes extends the cell voltage to 2.4 V, which overcomes the limitation of cell voltage for aqueous electrolytes originating from the stability window of water. The desalination capacity is also significantly improved to 64 mg_{NaCl}/g, benefiting from the high cell voltage. However, the performance reduces by 38% after 25 cycles due to water penetration to the organic electrolyte. Using ceramic membranes could effectively solve this problem. For instance, Zhang et al. applied a sodium superionic conductor (NASICON) membrane to detach organic electrolytes from seawater and used sodium metal as the anode. [189] In the first ten cycles, the system removed 10.76% of the sodium in seawater with a Coulombic efficiency of 91.5%. Ceramic membranes also showed promising selectivity towards specific ions (with a selectivity factor higher than thousands)[92, 190]. Thus, some research extracted lithium from seawater or brines with this setup. For example, Yang et al. reported a lithium extraction device comprised of LiClO₄-propylene carbonate (catholyte) and seawater (anolyte) that are separated by a LISICON membrane. [191] Due to the high selectivity of LISICON membranes towards Li⁺, only lithium metal can be detected on the surface of the cathode. [191] Unlike MCDI, rocking-chair-type desalination batteries implement one AEM in the middle, forming two water streams (**Figure 10F**). The electrodes here only store cations. Thus, only Faradaic materials serve as electrodes. During operation, one electrode is oxidized and releases cations into the electrolyte, while the other is reduced and stores cations in the electrodes. Anions would pass through the AEM and maintain the charge balance. Ultimately, the ionic strength in one water stream rises, and the mirror image decreases in the other ionic strength. The cation-capture electrodes in this system could be different materials or the same materials at different states (i.e., one at the oxidation state, the other at the reduction state). With different materials, the system could fulfill energy storage and release. Utilizing the same electrodes could reduce the required voltage. The system is also suitable for employing two anion-capture electrodes and a CEM in the middle. [192, 193] Without the IEM, rocking-chair desalination batteries could not complete water purification. However, they could fulfill the extraction of specific ions by using two cation-capture electrodes with different selectivity. For example, Trócoli et al. applied LiFePO₄ and nickel hexacyanoferrate (NiHCF) as electrodes. [194] LiFePO₄ has selectivity towards Li⁺ while NiHCF is incompatible with Li⁺. During the charging process, delithiated LiFePO₄ selectively uptakes Li⁺ from feed water, while NiHCF(III) releases other cations (Na⁺,

K⁺). During the discharge process, LiFePO₄ releases Li⁺ into the recovery solution, and NiHCF(II) uptakes other cations rather than Li⁺.

Besides solid electrodes, liquids or suspensions flowing in the isolated channel could also serve as electrodes. In 2013, Jeon proposed using flowing carbon suspension instead of solid carbon electrodes and named it flow electrode capacitive deionization (FCDI).[195] In their setup, the water channel is in the middle, and the adjacent two channels for the suspension electrode are isolated from the water channel by IEMs (**Figure 10G**). The IEMs can be substituted by other kinds of membranes. For example, Nativ et al. replaced one CEM with a nanofiltration membrane. The system does not show selectivity towards Na⁺ in the mixture of equimolar Na⁺ and Mg²⁺. [196] Hatzell et al. also proposed a system without using IEMs.[197] Their system does not contain the water flow channel, and the two suspension-electrode channels are separated by a porous separator to block the suspensions. Filters were also installed at the end of the channels to obtain the desalinated water and recycle the suspension particles. During the charging operation of FCDI, the cations and anions migrated through corresponding IEMs and ultimately were immobilized on the suspended materials or existed in the aqueous phase. In other words, the ions attracted from the feed water to the suspensions due to the produced extra ions, for example, H⁺ and OH⁻. [198] The latter phenomenon is caused by the Faradaic reactions on the carbon electrodes or competitive electrosorption of non-targeted ions (e.g., H⁺/OH⁻). [199] This mechanism will become invalid if the FCDI system does not contain the permselective membranes. Compared with static-electrode systems, FCDI avoids the mass-loading problem. Higher mass loading in the static electrodes means more ions can be immobilized in a specific area, while the higher mass is loaded, the thicker electrode would be, which leads to low kinetics. Therefore, FCDI can remove almost all the ions from feed water in a typical lab-scale cell.

The performance of FCDI relates to flow electrodes, operation mode, and conditions. Typical FCDI electrodes are the suspension of carbon-based material such as activated carbon[200], reduced graphene oxides[201], carbon nanotubes[202], or Faradaic material such as sodium vanadium fluorophosphate[203], nickel hexacyanoferrate[204] (active materials) in aqueous electrolyte. The mass ratio of active materials is generally in the range of 5-20 mass%. The higher the mass loading of active material is, the faster salts could be removed due to the promoting electron transporting network. When the carbon content increases from 10 mass% to 20 mass%, the desalination rate can accelerate from 0.3 μmol/cm²/min to 1.2 μmol/cm²/min.[205]

Going beyond about 20 mass% mass loading is challenging for carbon suspensions to still enable flowability and avoid clogging.[206, 207] An effective way to decrease the viscosity of the suspensions with a high mass loading of active material is by adding surfactants. Lee et al. studied the influence of several surfactants, sodium lignosulfonate, tetrapropylammonium iodide, (ferrocenylmethyl) dodecyldimethyl-ammonium bromide, and the mixture of sodium lignosulfonate and

tetrapropylammonium iodide (molar ratio of 50:50).[208] The viscosity of the suspensions (20 mass% activated carbon in 1 M Na₂SO₄) reduces from ca. 36 mPa S to ca. 14 mPa S at the shear rate of 1000 1/s after adding 5 mM surfactants (the lowest viscosity among these four surfactants). Doornbusch et al. proposed a fluidized bed capacitive deionization to increase the mass loading of active material in the suspensions.[209] The fluidized bed reactor contains carbon beads (diameter > 100 μm), and the flow direction in the reactor is opposite to the gravity. The beads could inhibit the flowing of the particles, whereas the liquid was relatively difficult to restrain using the beads. Consequently, a dense flowing suspension was formed in the electrode compartment with a 35% mass loading, despite an 8.3% mass loading of the initial suspension (before flowing in the reactor), and the mass loading in other compartments was low (ca. 2.5 mass%).[209]

Another approach to facilitate electron transport is adding conductive additives to the flow electrodes, especially Faradaic materials as the active material.[210] Common conductive additives include solid ones such as carbon black, carbon nanotubes, and aqueous electron-mediators such as hydroquinone, which could carry out rapidly reversible redox reactions.[211] The content of conductive additives varies from 1 mass% to 10 mass%, depending on the conductivity of active materials.[211] The electrolytes in the flow electrodes are generally non-redox electrolytes such as NaCl and NaSO₄. Higher concentration means higher conductivity of the suspension but may reduce the stability of active materials and cause counterion back diffusion and co-ion leakage.[205, 212]

FCDI can be operated in an isolated closed-cycle (ICC), short-circuited closed-cycle (SCC), or single-cycle (SC) mode. ICC is the earliest studied mode, where the slurry at the positive and negative sides are circulated separately (**Figure 11A**). Electrode regeneration can be accomplished by reversing the polarization in one or a second cell. The former is an analogy to the charging and discharging process, while the latter could continuously remove ions from water (**Figure 11B**). Flow electrodes are regenerated differently in SCC mode. In SCC mode, the positively and negatively charged slurries are mixed in an outer reservoir where the charge neutralization takes place, thus releasing adsorbed ions (**Figure 11C**). By adjusting the flow rates, SCC enables continuous water desalination. SC mode has the simplest setup. Compared to SCC mode, SC mode discards the external mixing reservoir. Instead, the positively charged suspension directly flows into the opposing side and circulates back (**Figure 11D**). Hence, counterion uptake and co-ion release coincide. The released co-ions could draw the counterion from the feed water to the suspension to maintain the charge neutrality, benefiting from the IEMs. If the membrane does not have permselectivity, some charge will be lost in the process of releasing the co-ions. SCC and SC could, however, utilize the electrostatic energy during the regeneration process. Thus, lower energy is consumed than in the ICC mode (< 60%)[213]. However, SCC and SC mode suffers from ions constant ion accumulation in the flow electrodes that would harm the stability of active materials. Rommerskirchen et al. proposed installing an AEM to divide the feed water into two

streams.[214] Thus, the released chloride ions migrate into one feed water stream instead of staying in the flow electrodes. Consequently, a stream of desalinated water and a stream of concentrated water is constantly produced.

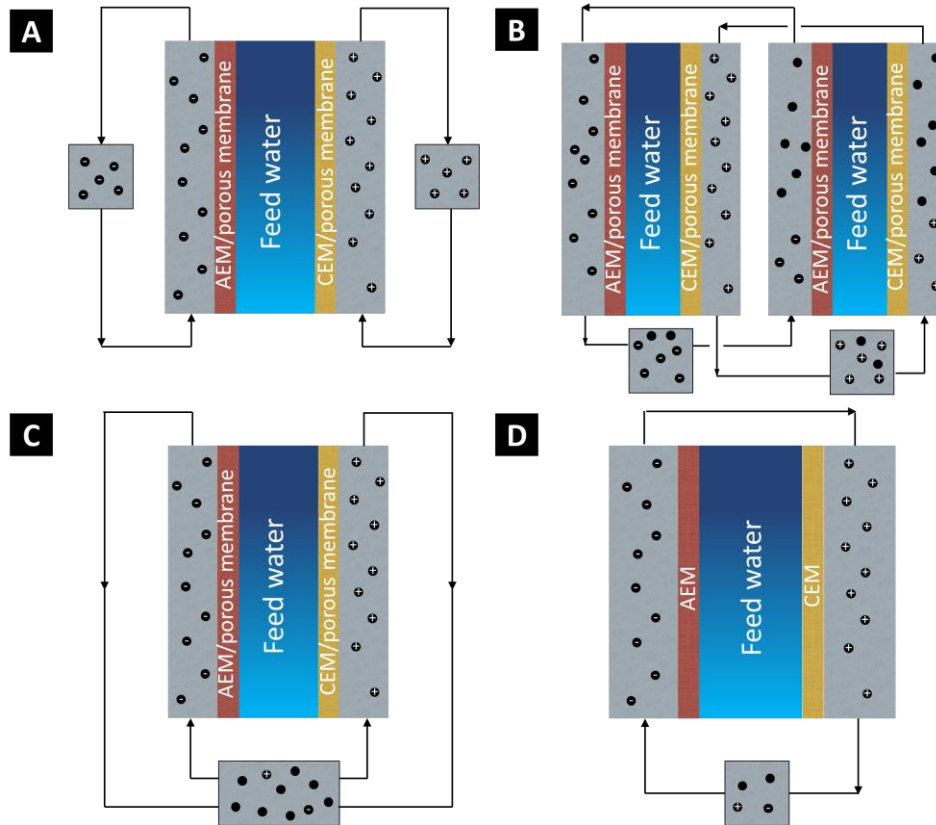


Figure 11: Scheme of (A) ICC, (B) ICC mode with two cells, (C) SCC, and (D) SC mode of FCDI.

A derivation of FCDI called redox-flow desalination or redox-flow-battery desalination (RFD) utilizes redox electrolytes and porous electrodes instead of material suspension, resulting in lower resistance and energy consumption. Additionally, the RFD does not face tube blockage problems. **Figure 10H** shows the typical setup of RFD, containing catholyte with $X^{(m+1)-}/X^{m-}$ redox couple and anolyte with $Y^{n+}/Y^{(n+1)+}$ couple. The anolyte and catholyte are isolated from feed water by an AEM and a CEM, respectively, like the ICC mode of FCDI. During the charging process, the anolyte is oxidized and produces more positive charges at the anode compartment, which draws more anions from the feed water to keep the charge balanced. On the other end, the catholyte is reduced, allowing the cations to migrate from the feed water into the catholyte. The regeneration of redox electrolytes requires reversed polarizations. The regeneration of redox electrolytes requires reversed polarizations. Either the desalination or regeneration process is thermodynamically favorable depending on the redox potential of the anolyte or catholyte). Thereby, RFD can store and release energy similar to redox flow batteries.[215] RFD can also operate in a symmetric mode where the same redox couple serves as the catholyte and anolyte. This setup is shown in **Figure 10I**. RFD can also continuously uptake ions by

circulating the catholyte and anolyte. The oxidized anolyte could be reduced in the catholyte chamber and vice versa. Symmetric RFD setup only requires low cell voltage to overcome the overpotential, IR drop, and membrane potential, [216] whereas there is no energy storage or release in the symmetric setup.[217] Redox electrolytes are the key component in RFD. An ideal electrolyte requires high stability, suitable redox potential, non-toxicity, fast kinetics, and low cost. Until now, various aqueous redox couples such as I^-/I_3^- [218], $Fe(CN)_6^{4-}/Fe(CN)_6^{3-}$ [219], V^{3+}/V^{2+} [215] and organic redox couples such as methyl viologen[220], 4-hydroxy-2,2,6,6-tetramethylpiperidin-1-oxyl (TMPO)[221], 1,1'-bis[3-(trimethylammonio)propyl]ferrocene dichloride-based (BTMAP-Fc)[222] have been studied (**Figure 12A**). The redox electrolyte with simple metal ions like I^- and V^{2+} suffer easily from membrane crossover caused by the nonideal permselectivity of the membrane.[223] The membrane crossover could result in capacity fading, increased overpotential, and lower voltage and charge efficiency.[220, 224, 225] Moreover, the crossover of redox electrolytes may contaminate the water.[216] Aqueous organic redox electrolytes show more potential than inorganic electrolytes due to their high tunability and stability.[192]

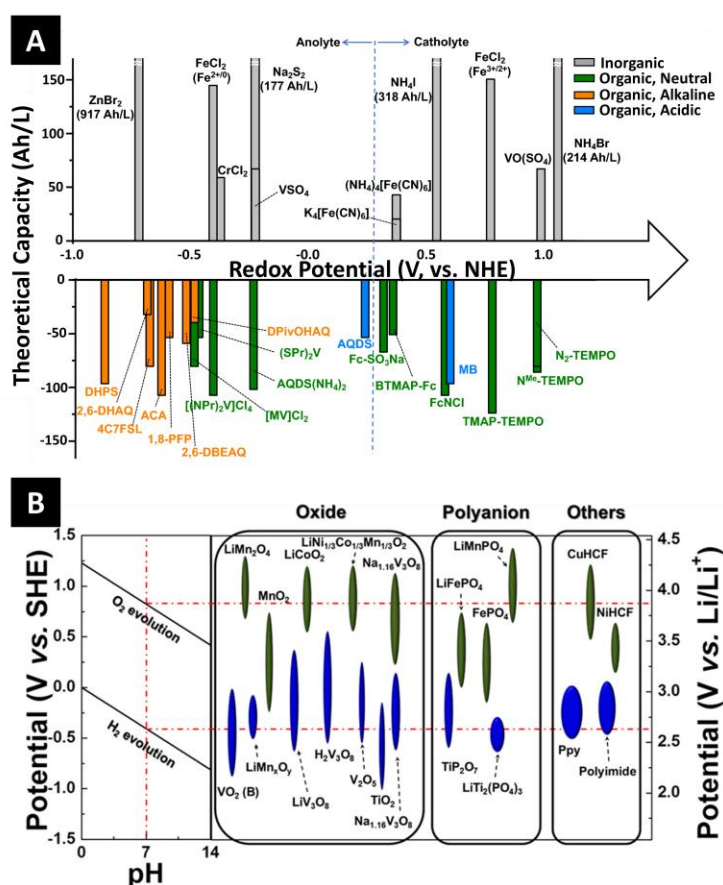


Figure 12: (A) Potential of some inorganic and organic redox electrolytes, adapted from Ref [226] Copyright 2022, Springer Nature, (B) Representative Faradaic materials suitable for aqueous electrolytes, adapted from Ref [153], Copyright 2014, American Chemical Society.

2.4 Faradaic materials for ion separation

Faradaic materials suitable for ion/water or ion/ion separation should meet several parameters. First, the material should be chemically, electrochemically, and mechanically stable in aqueous solutions. Second, the redox potential should not exceed the H₂ and O₂ evolution potential range. Third, if the redox potential is close to the H₂/O₂ evolution potential, the material should resist the consequent pH change. **Figure 12B** shows the possible Faradaic materials in ion separation. Finally, we classify Faradaic materials according to their crystal framework into 1D (tunnel), 2D (layered), and 3D materials. We will also introduce their properties and the properties and performance of representative materials.

2.4.1 1D (tunnel) materials

α -MnO₂

The structural unit of α -MnO₂ comprises double chains of corner-sharing [MnO₆] octahedrons, forming the 2x2 (4.6 Å) and 1x1 (1.8 Å) tunnel (parallel to the *c*-axis).[227] α -MnO₂ exhibits a pseudocapacitive behavior in neutral electrolytes (e.g., NaCl, Na₂SO₄) with a specific capacitance ranging from 100 F/g to 300 F/g due to differences in measure conditions.[227, 228] The pseudocapacitive behavior mainly originates from the cation intercalation into the tunnel.[229] Benefitting from the high capacitance, α -MnO₂ also exhibits good desalination performance. The desalination capacity of poorly crystallized α -MnO₂ reaches 9.9 mg_{NaCl}/g in 20 mM NaCl, reported in the work of Leong et al.[228] Byles et al. synthesized α -MnO₂ via a hydrothermal method and achieved a desalination capacity of 22.1 mg_{NaCl}/g.[230] By increasing the size of the tunnel (to 2xn tunnel, n = 2,3,4), the capacity increased to 27.8 mg_{NaCl}/g. The capacity of α -MnO₂ can also be enhanced via doping other transition metal elements, as reported by Xu et al.[231] Note that α -MnO₂ can also adsorb cations without any charge. At pH = 6, the adsorption capacity of α -MnO₂ in individual alkali hydroxide solutions exhibits an order of Rb⁺ ≈ K⁺ > Na⁺ > Li⁺ > Cs⁺. [232]. However, they did not explore the selectivity in the mixed solution.

Na_{0.44}MnO₂

Crystallographically, the structure of Na_{0.44}MnO₂ (also named Na₄Mn₉O₁₈) is constructed from double and triple chains of edge-sharing [MnO₆] octahedra and a single chain of corner-sharing [MnO₅] pyramids, forming a large S-shaped tunnel and a small tunnel.[233] There are five Mn sites and three Na sites in the Na_{0.44}MnO₂ structure. Mn³⁺ occupy Mn(1), Mn(2) sites, and Mn⁴⁺ occupy the others. Two sodium sites (Na(2) and Na(3) sites) are located in the S-shaped tunnel, whereas the other (Na(1)) occupies the small tunnel.[234]

Na_{0.44}MnO₂ is a battery-behavior material. In the range of 0-0.8 V vs. Ag/AgCl, it exhibits three cathodic peaks and three anodic peaks approximately at 0.1 V, 0.4 V, and 0.6 V (formal potential).[235] Due to

the low sodium content, $\text{Na}_{0.44}\text{MnO}_2$ shows a capacity of less than 50 mAh/g in Na^+ -contained neutral solutions[236], yielding a desalination capacity of less than 50 $\text{mg}_{\text{NaCl}}/\text{g}$. [183] Despite its unsatisfying capacity, $\text{Na}_{0.44}\text{MnO}_2$ demonstrates good stability with capacity retention higher than 80% after 200 cycles. [237, 238] The outstanding stability may benefit from the robust crystal structure. [239] Another advantage of $\text{Na}_{0.44}\text{MnO}_2$ is its high selectivity towards Na^+ . Kim et al. investigated the selectivity of $\text{Na}_{0.44}\text{MnO}_2$ in the mixed solution of NaCl, KCl, MgCl_2 , and CaCl_2 (30 mM of each). [240] The selectivity factor of Na/K, Na/Ca, and Na/Mg are $(13\pm 2):1$, $(7\pm 4):1$, and $(8\pm 3):1$, respectively. [240] Yoon et al. utilized $\text{Na}_{0.44}\text{MnO}_2$ to remove the NaCl impurity (20 mM) in KCl (4 M). [235] After three cycles, ca. 36% NaCl is removed, and the purity of KCl increases to 99.8%.

2.4.2 2D (layered) material

MXenes

MXenes are the family of two-dimensional transition metal carbides, nitrides, and carbonitrides that are generally synthesized by etching their corresponding MAX phase. The latest works have shown the importance of surface functionality going to the degree of assigning the name oxycarbides to some MXenes. [241] The formula of MXene is $\text{M}_{n+1}\text{X}_n\text{T}_x$ ($n= 1-4$, x is various), where M stands for early transition metal elements (e.g., Ti, V, Cr, Nb, Mo, or Zr); X represents carbon and/or nitrogen, and T_x is the terminal functional group. [242] MXenes can contain two or more M elements. [243] Depending on the distribution of two M elements, MXenes could be classified as ‘solid solution’ (random distribution), i-MXenes (forming alternating chains of M' and M'' atoms in the same M layer), or o-MXenes (at different atomic layers and out-plane ordering), shown in **Figure 13A**. [244] Note that the M'' of most i-MXenes can be selectively etched, forming the MXenes with ordered vacancies (e.g., $\text{Mo}_{1.33}\text{C}$, $\text{W}_{1.33}\text{C}$). [245, 246] The structure of MXenes is hexagonal close-packed (the same as corresponding MAX phases), where M elements are closed-packed, and X atoms locate in the octahedral sites. [247] i-MXenes have monoclinic or orthorhombic structures due to the in-plane atomic rearrangement of i-MAX phases. [248, 249]

Benefiting from the presence of terminal functional groups (e.g., OH, F, O), MXenes prefer to uptake cations rather than anions. Also, because of their catalytic properties for oxygen evolution, the potential window of MXenes generally does not exceed ca. 0.3 V vs. Ag/AgCl in neutral electrolytes. [250] MXenes manifest intercalation pseudocapacitive behavior (**Figure 13B**) with a capacitance range of 80-250 F/g. [251] Srimuk et al. first studied the performance of MXenes in electrochemical desalination. [17] In 5 mM NaCl, $\text{Ti}_3\text{C}_2\text{T}_x$ manifests a desalination performance of ca. 13 $\text{mg}_{\text{NaCl}}/\text{g}$. Subsequently, they reported a study that utilized $\text{Mo}_{1.33}\text{CT}_x$ as the electrodes to desalinate brackish water (5 mM NaCl). [252] The desalination capacity was low at 5 $\text{mg}_{\text{NaCl}}/\text{g}$, but it was stable throughout 40 cycles (**Figure 13C**). The interlayer spacing and terminal function group also affect the

performance of MXenes.[253, 254] Chen et al. compared the performance of Na⁺ intercalated Ti₃C₂T_x and normal Ti₃C₂T_x. [255] Benefiting from extended interlayer spacing (from 0.98 nm to 1.21 nm), the Na⁺ intercalated Ti₃C₂T_x shows a desalination capacity of 12.2 mg_{NaCl}/g, which is 78% higher than that of normal Ti₃C₂T_x. Guo et al. investigated the influence of terminal functional groups by treating Ti₃C₂T_x with Ar plasma.[256] After the treatment, no F functional groups exist, and the capacity reaches 26.8 mg_{NaCl}/g, which is much higher than the NaOH-treated Ti₃C₂T_x (8.9 mg_{NaCl}/g). The performance of MXenes could also be enhanced via delamination[257] or the creation of a 3D network[258] to eliminate the adverse effect of MXene sheet stacking. Besides serving as electrodes individually, many hybrids of MXenes and other materials, such as MoS₂[259], metal oxides[260], and polymers[261], have been reported.

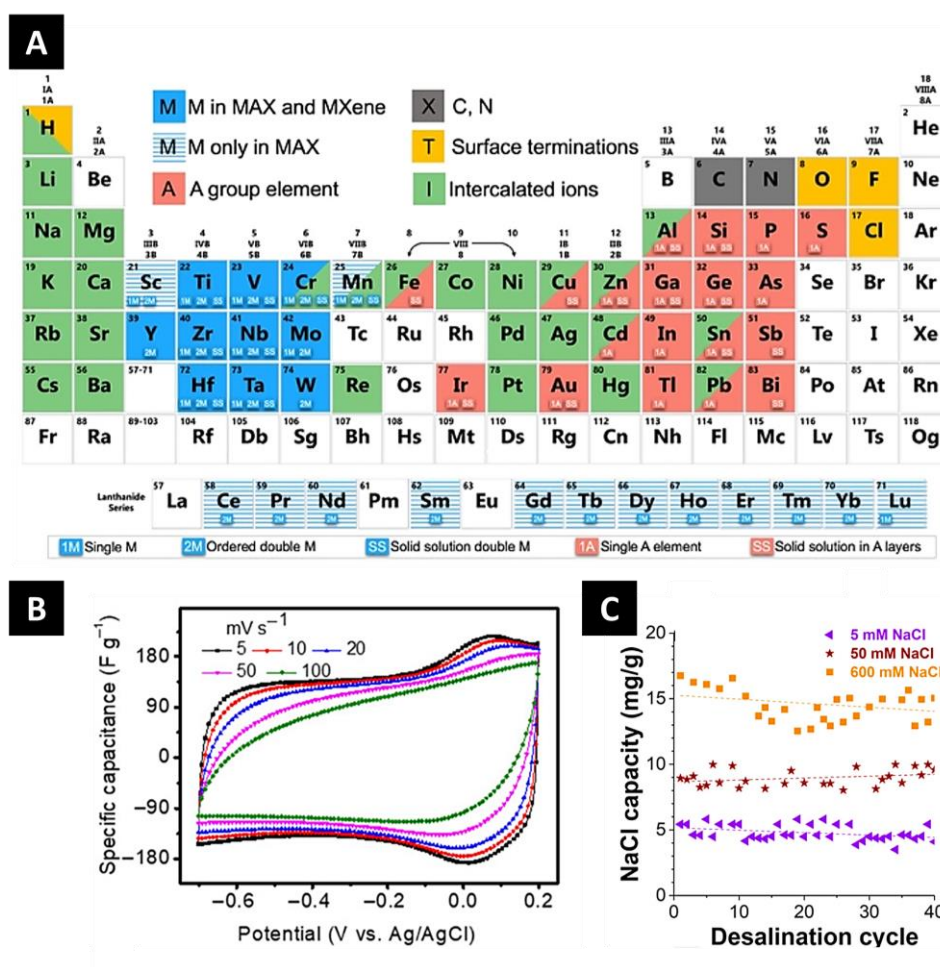


Figure 13: (A) Schematic image of MXenes structure, adapted from Ref[262], Copyright 2019, American Chemical Society, (B) Electrochemical performance of MXene electrode in 1 M NaCl, reproduced from Ref [263], Copyright 2020, John Wiley and Sons, (C) Desalination performance of Mo_{1.33}CT_x in NaCl with different concentration, adapted from Ref [252], Copyright 2018, American Chemical Society.

MXenes show cation selectivity when used in electrodes within multiple cations. Sun et al. studied the performance of $\text{Ti}_3\text{C}_2\text{T}_x$ in a mixture of 2 mM Ca^{2+} , 2 mM Mg^{2+} , and 2 mM Na^+ . [256] The uptake capacity of Ca^{2+} is 9.8 and 2.6 times higher than the uptake capacity of Na^+ and Mg^{2+} , respectively. The study of Wang et al. indicates that the $\text{Ti}_3\text{C}_2\text{T}_x$ has a kinetics-dependent selectivity in a mixed solution of equimolar Li^+ , Na^+ , K^+ , Ca^{2+} , and Mg^{2+} (10 mM of each). [171] At the beginning of the charging period, species with higher ionic mobility, such as K^+ , are preferred, while the uptake capacities of divalent cations (Ca^{2+} and Mg^{2+}) are ultimately higher than those of monovalent cations. The selectivity of MXenes mainly depends on the dehydration energy barriers and kinetics. The intercalation distance of MXenes (e.g., $\text{Ti}_3\text{C}_2\text{T}_x$, ca. 0.57 nm) is smaller than the hydration diameters of alkali and alkaline-earth metal ions, resulting in partial desolvation before intercalating in MXenes. However, the intercalation distance will increase as the cations intercalate in MXenes, which weakens the size effect [264].

2.4.3 3D-structured material

Prussian blue analogs

Prussian blue analogs (PBAs) are the umbrella term for transition-metal hexacyanoferrates, with a formula of $\text{A}_x\text{M}[\text{Fe}(\text{CN})_6] \cdot z\text{H}_2\text{O}$, where A and M are the alkali ions and transition metal elements, respectively. [265] Most PBAs (guest-ion-deficient PBAs) have a face-center cubic structure containing A elements at 8c sites. M elements coordinate with the N atoms, while Fe elements are octahedrally neighboring to C atoms, forming a 3D framework with open ionic channels and large interstitial spaces (e.g., $\text{FeFe}(\text{CN})_6$, ca. 4.6 Å), thereby permitting the intercalation of even trivalent cations. [266] Water molecules could coordinate M elements neighbored by vacancies. [267] Some PBAs have monoclinic structures (generally guest-ion-enriched PBAs), and some have rhombohedral structures. [268, 269] PBAs are battery-type materials with a theoretical capacity range of 80-200 mAh/g, related to their composition and redox process. [270] Their electrochemical behavior could be mono- or multi-electronic redox reactions depending on the highest valence of the M element. Generally, when the highest valence of M is two, e.g., Cu and Ni, only one charge is transferred during the intercalation process, which corresponds to the oxidation of Fe^{2+} to Fe^{3+} . If M contains multiple oxidation states like Fe, Mn, and Co, the redox process could be double charge transferred (i.e., the oxidation/reduction of Fe and M). [271] The reported capacity range of mono-charge-transferred PBAs is 50-70 mAh/g, and that of two-charge-transferred PBAs is 80-110 mAh/g. [269] In contrast, mono-charge-transferred PBAs exhibit better stability than two-charge-transferred PBAs because the oxidation/reduction of M elements may cause a more considerable lattice volume change than Fe. [272] In addition, M elements also influence the position of redox potential. The higher ionic potential (the ratio between the charge and effective diameter) M has, the more positive the redox peak representing the oxidation/reduction of $\text{Fe}^{3+}/\text{Fe}^{2+}$ locates. [273]

PBAs are very attractive for electrochemical water purification (i.e., ion/water separation). This first reported work about PBAs regarding water desalination was in 2017.[274] The simulation work indicates that using two nickel hexacyanoferrate (NiHCF) electrodes could reduce the concentration of NaCl from 0.7 M to 0.2-0.3 M. Subsequently, Lee et al. studied the performance of NiHCF coupled with sodium iron hexacyanoferrate in a rocking-chair desalination battery.[275] The system shows a desalination capacity of 59.9 mg_{NaCl}/g with an energy consumption of 0.34 Wh/L. So far, many works have explored the desalination performance of PBAs (in NaCl), inclusive of Prussian blue[18], sodium cobalt hexacyanoferrate[276], sodium manganese hexacyanoferrate[277], and their hybrid of carbon materials[278], MXene[279], and polymers[280]. The desalination capacity of PBAs varies from 10 mg_{NaCl}/g to 100 mg_{NaCl}/g, determined by the material properties and operating conditions.[269, 271] Besides pure NaCl, some work reported using PBAs to remove Ca²⁺ from water. For instance, Sebti et al. investigated the Ca²⁺ uptake capacity of K_{0.04}Cu[Fe(CN)₆]_{0.68} and K_{0.06}Mn[Fe(CN)₆]_{0.65}. [277] In 1000 mg/L Ca²⁺ solution, the uptake capacity of K_{0.04}Cu[Fe(CN)₆]_{0.68} and K_{0.06}Mn[Fe(CN)₆]_{0.65} are 46 mg/g and 37 mg/g, respectively.

For ion selectivity, NiHCF and sodium copper hexacyanoferrate (CuHCF) have been studied. Choi et al. studied the electrochemical behavior of K_{0.03}Cu[Fe(CN)₆]_{0.65}·0.43H₂O in individual 1 M NaCl, KCl, CaCl₂, and MgCl₂ and its selectivity in simulated brackish water.[281] The positions of redox peaks in NaCl, KCl, CaCl₂, and MgCl₂ are 0.56 V, 0.69 V, 0.68 V, and 0.63 V vs.Ag/AgCl, respectively. The similar potential results in a similar uptake capacity in brackish water, where the highest uptake capacity (K⁺) is 1.7 times the lowest (Mg²⁺). Singh et al. explored the selectivity of NiHCF in an equimolar solution of Na⁺, Ca²⁺, and Mg²⁺. [282] The selectivity factors of Na/Mg and Na/Ca, in this case, are 25:1 and 15:1, respectively. They also found that NiHCF exhibits voltage hysteresis in Mg²⁺-containing electrolytes but none in Na⁺-containing electrolytes, thereby demonstrating the sluggish kinetics of Mg²⁺ intercalation. The work of Porada et al. indicated that NiHCF prefers K⁺ compared with Na⁺, with a selectivity factor of 3.[283] Trócoli et al. compared the uptake capacity of NiHCF towards Li⁺, Na⁺, K⁺, and Mg²⁺ in the binary electrolyte.[194] The selectivity factors of Na/Li, K/Li, and Mg/Li are 17:1, 11:1, and 0.8:1, respectively. According to the reported works, we could conclude that the selectivity of NiHCF is related to the dehydration energy of cations, which act as part of energy barriers for cation intercalation. Although the dehydration energies of Na⁺ and Li⁺ are close, PBAs prefer Na⁺ over Li⁺ because the intercalation of partially dehydrated Li⁺ may cause structure degradation.[284]

Polyanionic phosphates

The well-known 3D framework built on transition metal ions and polyanions (PO₄³⁻) is olivine-type phosphates (AMPO₄) and NASICON-type phosphates (A_xMM'(PO₄)₃), where A stands for Li, Na, or K. M and M', on the other hand, represent transition metal ions. LiFePO₄ is a widely used olivine-type

phosphate widely studied in lithium-ion batteries and lithium recovery. LiFePO_4 has an orthorhombic structure containing $[\text{FeO}_6]$ octahedra and $[\text{LiO}_6]$ octahedra linked by PO_4 tetrahedra.[285] Li ions diffuse in the crystal structure in a zigzag 1D diffusion path along the b-axis direction, which is limited by the a-b plane (**Figure 14A**).[286] However, the Li/Fe anti-site defects easily block the diffusion path. When the Li^+ encounters the anti-site defects in the diffusion path, Li^+ likely migrates to the adjacent diffusion channel through the anti-site defects and continues to diffuse along the 1D diffusion path due to a lower energy barrier than proceeding the diffusion along the original path.[287, 288] The anti-site defects would thus decrease the apparent lithium diffusion rate. The content of anti-site could be reduced through ion doping or optimizing the synthesis process.[289, 290]

Due to the single-phase transformation, LiFePO_4 exhibits one pair of redox peaks in organic and aqueous electrolytes, forming FePO_4 with the same structure as LiFePO_4 (6.81% of volume change)[291]. The formal potential of LiFePO_4 in 1 M LiCl was determined to be 0.2 V vs. Ag/AgCl.[292] LiFePO_4 also shows electrochemical activity in Na^+ -contained electrolytes. The potential of Na^+ intercalation is more negative than Li^+ intercalation, indicating that the intercalation of sodium ions requires more energy than lithium (**Figure 14B**).[166] The unbalanced number of the anodic and cathodic peaks is caused by forming an intermediate phase ($\text{Na}_{0.7}\text{FePO}_4$) during the oxidation process.[293] Additionally, the potential difference between the anodic and cathodic peaks in Na^+ -based electrolytes is larger than in Li^+ -based electrolytes, suggesting a more sluggish diffusion rate of Na^+ due to the higher diffusion energy barrier (**Figure 14C**).[167] Because Mg^{2+} has a similar ionic radius to Li^+ , Mg^{2+} could also intercalate into FePO_4 . However, the capacity and reversibility are inferior due to the high coulomb repulsions and the formation of an amorphous phase.[294, 295] In the electrolyte containing large ionic diameter, e.g., K^+ , FePO_4 scarcely has electrochemical activity (**Figure 14B**).[166] The first use of LiFePO_4 for lithium recovery was reported by Pasta et al. in 2012.[296] Their results indicated that LiFePO_4 showed selectivity towards Li^+ with a selectivity factor of 2621 even though the Na/Li is 10000 (molar ratio). Subsequently, Trócoli et al. utilized LiFePO_4 to recover lithium from the Atacama brine.[168] The selectivity factors of Li/Na, Li/Mg, and Li/K at 0.5 mA/cm² are 29000, 9000, and 36000, respectively. Additionally, the selectivity of LiFePO_4 can be improved by surface modification. Kim et al. modified the surface of LiFePO_4 with mussel-inspired polydopamine.[297] The modified LiFePO_4 electrode could enrich the Li^+ from 1% (molar ratio) to 43.3% in a binary electrolyte of Li^+ and Na^+ . In contrast, the concentration of Li^+ increases to 2.64% with pristine LiFePO_4 . Liu et al. coated a 3 nm amorphous TiO_2 layer on LiFePO_4 via atomic layer deposition.[298] The TiO_2 -coated LiFePO_4 could extract lithium from seawater with a selectivity factor of 18000:1.

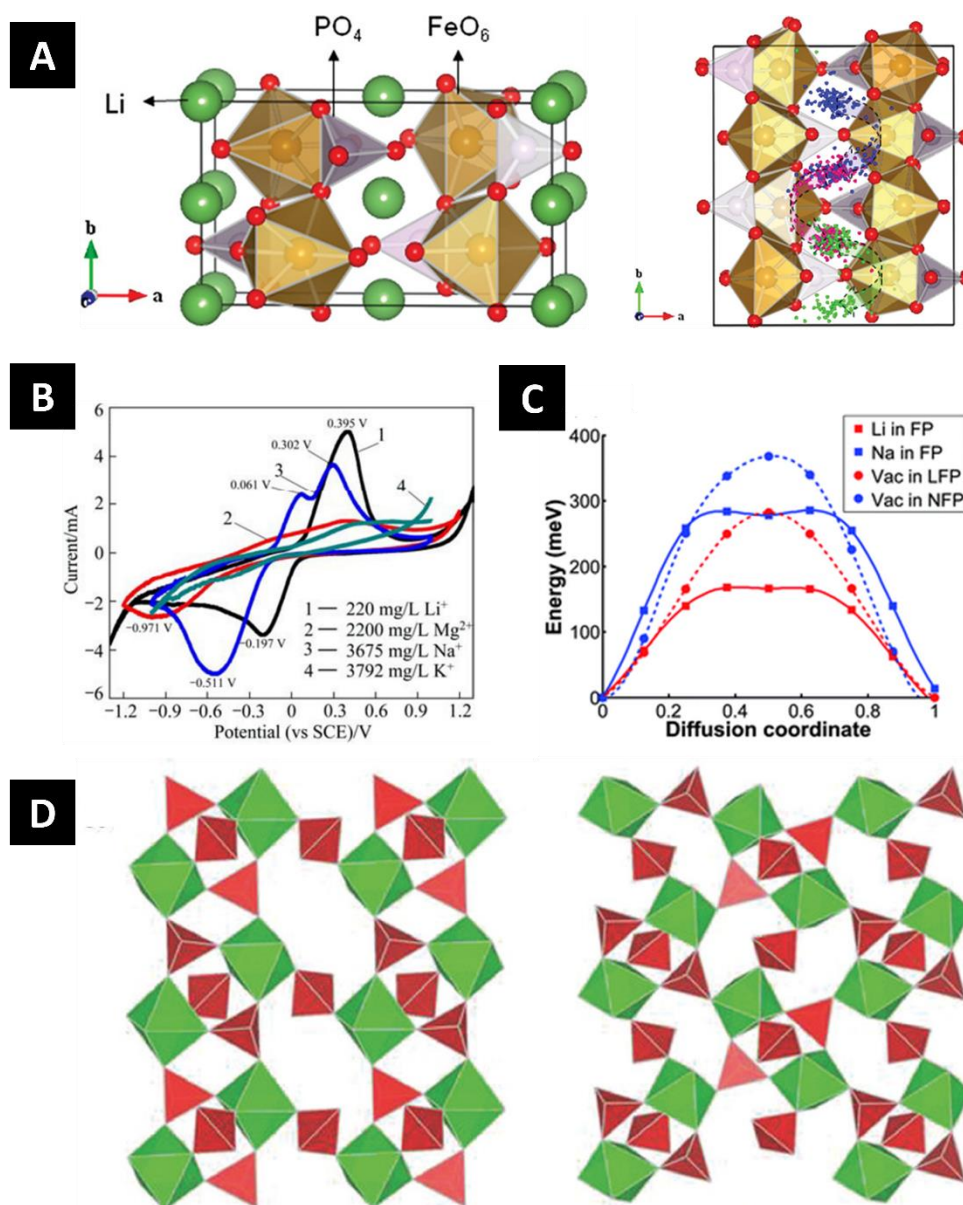


Figure 14: (A) Schematic crystal structures and diffusion path of Li⁺ in LiFePO₄, adapted from Ref [288], Copyright 2011 American Chemical Society, (B) electrochemical behavior of LiFePO₄ in various electrolyte, reproduced from Ref [166], Copyright 2013, Elsevier, (C) calculated diffusion barrier of Na and Li in LiFePO₄, adapted from Ref [167], Copyright 2011, Royal Society of Chemistry, (D) the rhombohedral (left) and monoclinic (right) structure of NASICON type phosphate, reproduced from Ref [299], Copyright 2017, John Wiley and Sons.

The NASICON-type phosphates are constructed by corner-shared MO₆ and M'O₆ octahedrons connecting three PO₄ tetrahedrons, which compose a basic unit.[300] There are two possible structures, rhombohedral and monoclinic, of NASICON-type phosphate.[299] In rhombohedral structure, [MO₆]₂[PO₄]₃ is parallel to the c-axis, while in monoclinic structure, [MO₆]₂[PO₄]₃ exhibits a zigzag alignment (**Figure 14D**).

Until now, three kinds of NASICON-type phosphates, $\text{NaTi}_2(\text{PO}_4)_3$, $\text{Na}_3\text{Fe}_2(\text{PO}_4)_3$, and $\text{Na}_3\text{V}_2(\text{PO}_4)_3$, have been explored for water purification. All three of these materials show single pair of redox peaks in the sodium-contained electrolyte under a safe potential window though V has multiple oxide states.[301-303] The redox peaks of $\text{NaTi}_2(\text{PO}_4)_3$ located at ca. -0.8 V vs. Ag/AgCl in 1 M NaCl, while those of $\text{Na}_3\text{Fe}_2(\text{PO}_4)_3$ and $\text{Na}_3\text{V}_2(\text{PO}_4)_3$ are more positive at ca. -0.2 V and +0.45 V, respectively.[301, 303, 304] The reported desalination performance of NASICON-type phosphate ranges from 70 $\text{mg}_{\text{NaCl}}/\text{g}$ to 130 $\text{mg}_{\text{NaCl}}/\text{g}$. [15, 304, 305] NASICON-type materials have also been used in the aqueous electrolyte containing other alkali and alkaline earth metal ions (e.g., Li^+ , Mg^{2+})[306], but it has not been applied for the purpose of ion separation.

LiMn_2O_4

Spinel LiMn_2O_4 is constructed by cubic close-packed O, where Li and Mn occupy 8a tetrahedral and 16d octahedral sites, respectively. Lithium ions diffuse in the structure by hopping between 8a tetrahedral sites mediated by 16c octahedral sites with an activation energy of 0.35-0.4 eV (**Figure 15A**).[307] The cyclic voltammogram of LiMn_2O_4 contains two pairs of oxidation/reduction peaks at approximately 0.72 V and 0.85 V vs. Ag/AgCl measured in 0.1 M LiNO_3 [308], suggesting that the intercalation/deintercalation of Li^+ in LiMn_2O_4 experiences two steps.[309] The fully delithiated product is $\lambda\text{-MnO}_2$, which also has the spinel structure.[310] No reversible reduction redox peaks exist in electrolytes with Na^+ , K^+ , Ca^{2+} , or Mg^{2+} , indicating that these cations hardly intercalate in LiMn_2O_4 (**Figure 15B**)[311] because these cations (excluding Mg^{2+}) have too large ionic diameters to diffuse in the framework of LiMn_2O_4 . Although Mg^{2+} has a similar ionic diameter to Li^+ , the high dehydration causes it to be more energetically hard to be extracted.[312] $\lambda\text{-MnO}_2$ selectively uptakes lithium also already without applying a charge as an adsorbent.

LiMn_2O_4 has been widely studied for lithium recovery and was first published by Kanoh et al.[313] In their study, $\lambda\text{-MnO}_2$ and Pt supply electrodes, and the electrolyte contains Li^+ and all alkaline earth metal ions (except Be and Ra). Only Li^+ and slight Mg^{2+} and Ca^{2+} are extracted with a selectivity factor of 250:1 (Li/Mg) and 125:1 (Li/Ca). Zhao et al. explored the selectivity performance of LiMn_2O_4 in a simulated brine.[314] The lithium extract capacity is 22 $\text{mg}_{\text{Li}^+}/\text{g}$, and the selectivity factor Li/Na, Li/Mg, and Li/Ca reaches ca.300, ca.70, and ca.110, respectively. Joo et al. utilized $\lambda\text{-MnO}_2$ and Ag as electrodes to extract lithium ions from desalination concentrate on a pilot scale (**Figure 15C**).[315] After the treatment, the content of lithium rose from 0.0048% to 88%.

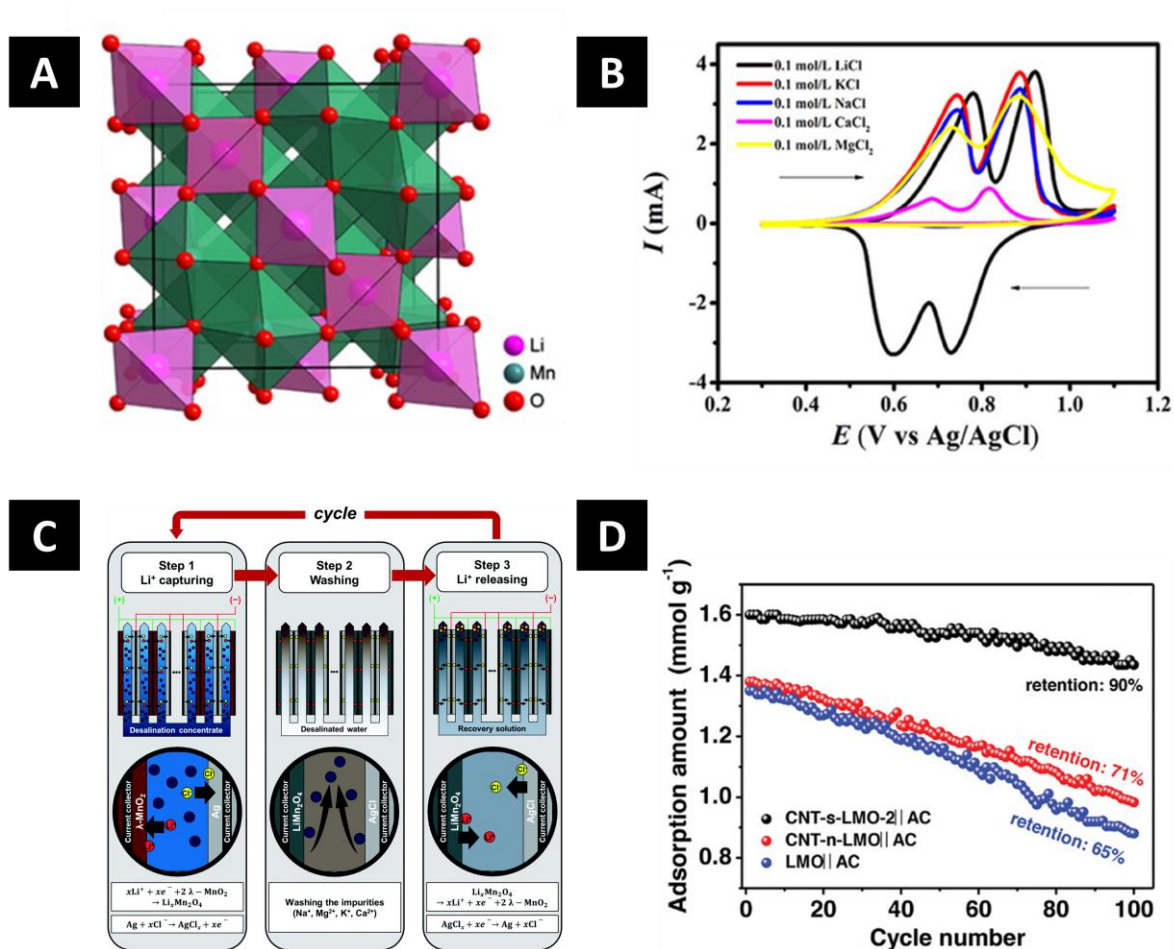


Figure 15: (A) Schematic image of a LiMn_2O_4 structure, adapted from Ref [307], Copyright 2013, Elsevier, (B) cyclic voltammograms of LiMn_2O_4 measured in different electrolytes, adapted from Ref [311], Copyright 2019, John Wiley and Sons, (C) schematic description of the electrochemical lithium extraction setup with $\lambda\text{-MnO}_2$ and Ag on a pilot-scale, reproduced from Ref [315], Copyright 2019, Royal Society of Chemistry, (D) stability performance of LiMn_2O_4 and CNT-strung LiMn_2O_4 , reproduced from Ref [316], Copyright 2022, John Wiley and Sons.

LiMn_2O_4 suffers from an unstable capacity and Mn loss due to the Mn^{3+} disproportionation reaction in the acid solution [317] and Jahn-Teller distortion. [318] Without modification, the capacity retention of LiMn_2O_4 (or $\lambda\text{-MnO}_2$) after 100 cycles is usually lower than 75%. [311, 319] The stability of LiMn_2O_4 can be enhanced by forming a hybrid with other materials (like carbon), surface modification, ion doping, and crystal plane adjustment. [320] For instance, Shang et al. prepared CNT-strung LiMn_2O_4 , which increased the capacity retention from 65% (pristine LiMn_2O_4) to 90% after 100 cycles (Figure 15D). [316] Zhou et al. designed a truncated octahedral LiMn_2O_4 with (111) facets as the dominant crystallographic planes, which inhibited the Mn loss. [321] A small portion of (100) facets favor lithium diffusion. The capacity retention after 30 cycles of truncated octahedral LiMn_2O_4 is much higher (85.2%) compared with octahedral LiMn_2O_4 (77.9%) and cubic LiMn_2O_4 (47.3%).

3. Approach and overview

Electrochemical ion separation is a promising technology to remediate water (i.e., ion/water separation) and extract valuable resources (i.e., ion/ion separation) due to its high energy efficiency and facile operation. Faradaic materials and processes are also attractive because of their charge storage/ion uptake capacity and high selectivity towards specific ions. These virtues outperform capacitive materials and processes such as nanoporous carbons in capacitive deionization. Although much research has been conducted, most works stay in the ion/water separation area, and some issues of Faradaic material, such as relatively low stability, low kinetics, and environmental toxicity, remain. Therefore, it is crucial to synthesize new material with higher capacity, stability, selectivity (in ion/ion separation area), low cost, and low toxicity to develop novel cell architectures.

My Ph.D. work first addresses the Faradaic desalination of seawater and sodium chloride aqueous solutions ([first segment](#)), explores Faradaic cation separation via Ti_3C_2 MXene ([second segment](#)), and then focuses specifically on one cation ([third segment](#)), namely Faradaic lithium-ion separation, as shown in **Figure 16**.

In the [first segment](#), we first overviewed the recent advances in electrochemical desalination technologies as the basement of further research (**Chapter 4.1**). According to the cation storage mechanism, we classify the electrochemical desalination technology into three generations. The merits and demerits of each generation are summarized and introduced. We reviewed the state of the art of a particular system, namely seawater batteries with dual use of energy storage and water desalination (**Chapter 4.2**). This review introduces the components and evaluation index of seawater batteries. Finally, the relationship between components and the performance is analyzed, and the approaches to enhance the performance are summarized.

After comprehending the current study and issues of electrochemical cation separation (ion/water) technologies, we investigate the sodium-uptake performance of a 2D pseudocapacitive material, Ti_3C_2 MXene, paired with activated carbon as the other electrode (**Chapter 4.3**). The asymmetric cell enables effective ion/water separation of saline water from a low concentration (20 mM) to a high concentration (600 mM). The desalination capacity at 600 mM is about $9 \text{ mg}_{\text{NaCl}}/\text{g}_{\text{electrodes}}$ with a charge efficiency of $96\pm 4\%$, implying that the permselectivity of MXene will 'force' activated carbon to uptake only counter ions, thereby overcoming the co-ion expulsion effect. That means that common activated carbon could also work in high saline water without an IEM if paired with a permselective electrode. This would reduce the system's total cost. At low concentrations, the capacity is about $11 \text{ mg}_{\text{NaCl}}/\text{g}_{\text{electrodes}}$ with a charge efficiency of $114\pm 7\%$. The measured value above 100% charge efficiency is due to the surface charges in the MXene interlayers, where a chemical and electrochemical component towards ion removal is combined.

To obtain a higher sodium-uptake capacity, we applied the alloying material Sb/C as a Na⁺-uptake electrode for ion/water separation by using a multi-channel bi-electrolyte cell architecture (**Chapter 4.4**). Sb/C is immersed only in an organic electrolyte, which is separated from the feed water by NASICON membranes and accomplishes the Na⁺ uptake. The Cl⁻ ions are immobilized by the activated carbon electrode via electrosorption. The system manifests a high Na⁺-uptake capacity of 294 mg_{Na⁺}/g_{Sb} with a charge efficiency of around 74% in 600 mM NaCl at 200 mA/g.}

In the **second segment**, the focus moves away from general cation removal and specifically addresses Faradaic materials and processes for cation separation. As an important part of Faradaic material, pseudocapacitive materials are intriguing, especially 2D materials. It is indispensable to understand the interaction between kinetic ion preference (by mobility) and inherent preference (by charge/dehydration energy) for better utilization. Thus, we studied the ion selectivity behavior of Ti₃C₂T_x MXene toward alkali and alkaline earth cations (**Chapter 4.5**). Ti₃C₂T_x MXene displays a kinetics-dependent selectivity feature. The affinity order is K⁺ > Na⁺ > Ca²⁺ ≈ Mg²⁺ > Li⁺ up to about 50 min, whereas Ca²⁺ and Mg²⁺ are preferred at the end. The preference at the beginning depends on dehydration energy. Afterward, the uptake capacity of Ca²⁺ and Mg²⁺ grows, which is because the divalent cations replace the monovalent cations. In situ X-ray diffraction manifests the structure changes of MXene during the cycling. In the second cycle, the (002) reflection of Ti₃C₂T_x is symmetric, whereas, after 10 cycles, the reflection becomes asymmetric related to the coexistence of cations with a different coordination number of water molecules.

After general considerations toward cation separation, the work focuses on Lithium-ions. Specifically, I explored separating Li⁺ from other alkali and alkaline earth cations due to the increasing demand for lithium (**third segment**). In **Chapter 4.6**, we studied the stability of LiFePO₄ during electrochemical lithium extraction. To avoid the influence of other materials on the consequences, we experimented with a rocking chair cell configuration with LiFePO₄ and delithiated LiFePO₄ as the electrodes. We found that some ions in the electrolyte, such as Ca²⁺, exacerbate the capacity fading of LiFePO₄. In contrast, the effects of some ions like Na⁺ and Mg²⁺ on the stability of LiFePO₄ are not apparent. Dissolved oxygen in the electrolyte also aggravates the decay of LiFePO₄ due to the irreversible oxidation of LiFePO₄. We propose two solutions to this problem: bubbling nitrogen in the electrolyte and carbon coating. The capacity retention rises from 47% to 70% within 10 cycles after flushing nitrogen in the electrolyte. The retention further increases to 82% after coating carbon on LiFePO₄ particles. To further enhance the lithium extraction rate and archive continuously mining lithium ions from aqueous solutions, we proposed a new cell configuration, lithium-ion extraction redox flow batteries (**Chapter 4.7**). The system contains LISICON membranes for selective uptake of Li⁺ and redox electrolyte couples, Fe[CN]₆⁴⁻/Fe[CN]₆³⁻ (Li⁺ transport barrier and migration force). The system exhibits a high selectivity towards Li⁺, with a Li⁺ purity of 93.5% in the extracts, associated with a superior selectivity factor (Li/Mg) of ca.

50000:1. The energy consumption of this system is 2.5 Wh/g_{Li+}, at least 7-times less than that of other reported system with similar performances for lithium extraction from seawater, benefiting from low operation voltage (0.6 V).

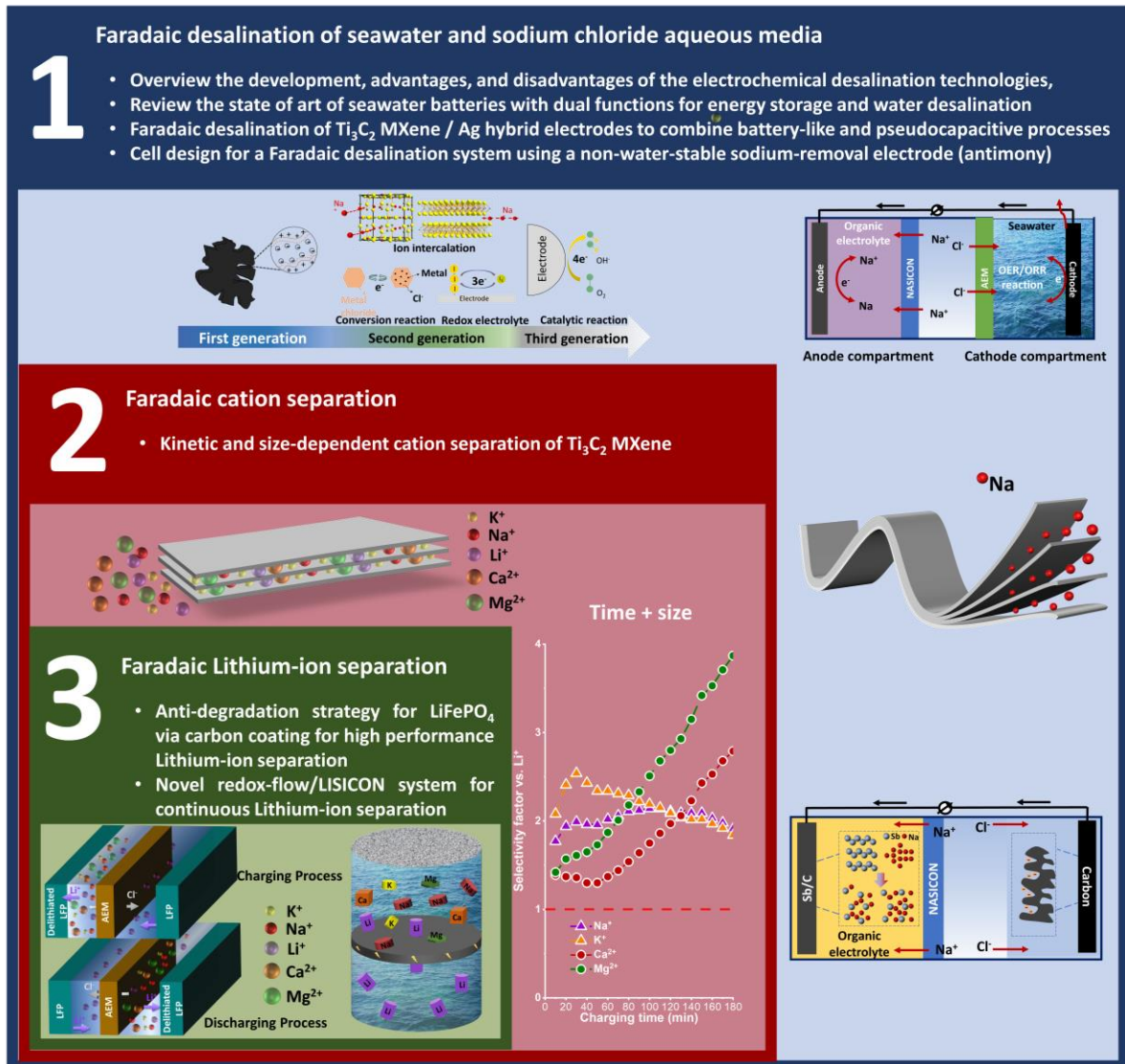


Figure 16: Overview of three segments of this doctoral thesis. First segment: the top two images are adapted from Ref. [10], Copyright 2021, Elsevier, and Ref. [322], Copyright 2021, John Wiley and Sons, respectively; the image at the right bottom corner is adapted from Ref. [323], Copyright 2021, Royal Society of Chemistry. Second segment: images at the bottom right corner are reprinted from Ref. [171] Copyright 2022, John Wiley and Sons. Third segment: the image at the left is adapted from Ref. [292] Copyright 2021, Royal Society of Chemistry.

4. Peer-reviewed research papers

- 4.1. From capacitive deionization to desalination batteries and desalination fuel cells
- 4.2. Dual-use of seawater batteries for energy storage and water desalination
- 4.3. MXene/activated-carbon hybrid capacitive deionization for permselective ion removal at low and high salinity
- 4.4. Antimony alloying electrode for high-performance sodium removal: how to use a battery material not stable in aqueous media for saline water remediation
- 4.5. Time-dependent cation selectivity of titanium carbide MXene in aqueous solution
- 4.6. Electrochemical lithium recovery with lithium iron phosphate: what causes performance degradation and how can we improve the stability?
- 4.7. Redox flow battery for continuous and energy-effective lithium recovery from aqueous solution

4.1 From capacitive deionization to desalination batteries and desalination fuel cells

Lei Wang,^{1,2} Yuan Zhang,^{1,2} Karsten Moh,¹ Volker Presser,^{1,2}

¹ INM - Leibniz Institute for New Materials, D2 2, 66123, Saarbrücken, Germany

² Department of Materials Science & Engineering, Saarland University, Campus D2 2, 66123, Saarbrücken, Germany

Citation:

L. Wang, Y. Zhang, K. Moh, V. Presser, FROM CAPACITIVE DEIONIZATION TO DESALINATION BATTERIES AND DESALINATION FUEL CELLS, **Current Opinion in Electrochemistry**, 29 (2021) 100758.

DOI: <https://doi.org/10.1016/j.coelec.2021.100758>

Own contribution:

Conceptualization, Visualization, Writing-Original Draft, Writing - Review & Editing



Review Article

From capacitive deionization to desalination batteries and desalination fuel cells

Lei Wang^{1,2}, Yuan Zhang^{1,2}, Karsten Moh¹ and Volker Presser^{1,2}**Abstract**

The considerable growth of the world population, concomitant with an increase in environmental pollution, aggravates the antinomy between supply and demand for drinking water. Various desalination technologies have been developed to address this issue, allowing for abundant saltwater as a source for drinking water. Electrochemical desalination attracts more and more attention due to its high energy efficiency, facile operation, and low cost. Especially within the last decade, tremendous scientific progress on electrochemical desalination technologies has been made. This article reviews the development of electrochemical desalination technologies and introduces a facile classification into three generations based on the different working principles. The cell architecture, metrics, advantages, and disadvantages of other electrochemical desalination technologies are introduced and compared.

Addresses

¹INM - Leibniz Institute for New Materials, D2 2, 66123, Saarbrücken, Germany

²Department of Materials Science & Engineering, Saarland University, Campus D2 2, 66123, Saarbrücken, Germany

Corresponding author: Presser, Volker (volker.presser@leibniz-inm.de)

Current Opinion in Electrochemistry 2021, 29:100758

This review comes from a themed issue on **Electrochemical Materials and Engineering (2021)**

Edited by **Fabio La Mantia**

For complete overview about the section, refer [Electrochemical Materials and Engineering \(2021\)](#)

Available online 30 April 2021

<https://doi.org/10.1016/j.coelec.2021.100758>

2451-9103/© 2021 Elsevier B.V. All rights reserved.

Keywords

Electrochemical desalination, Desalination batteries, Capacitive deionization, Metal air desalination.

Introduction

Water scarcity is one of the grand challenges of the 21st century. In 2018, about 3 billion people did not have access to clean, potable water [1], and by 2025, approximately two-thirds of the world's population may have to live under water-stressed conditions [2]. Water

technology is not just crucial to generate drinking water but is equally essential for agriculture, mining, and industrial production. Various water purification technologies have been developed to address this issue, such as multistage flash [3], reverse osmosis [4], forward osmosis [5], and electro dialysis [6]. Among them, reverse osmosis has been widely used for water desalination of brackish water and seawater on an industrial scale [7]. Although the cost has been reduced significantly from 20 kWh/m³ to 2–4 kWh/m³ [8], reverse osmosis remains energy-intensive to meet the enormous demand for remediated water [4].

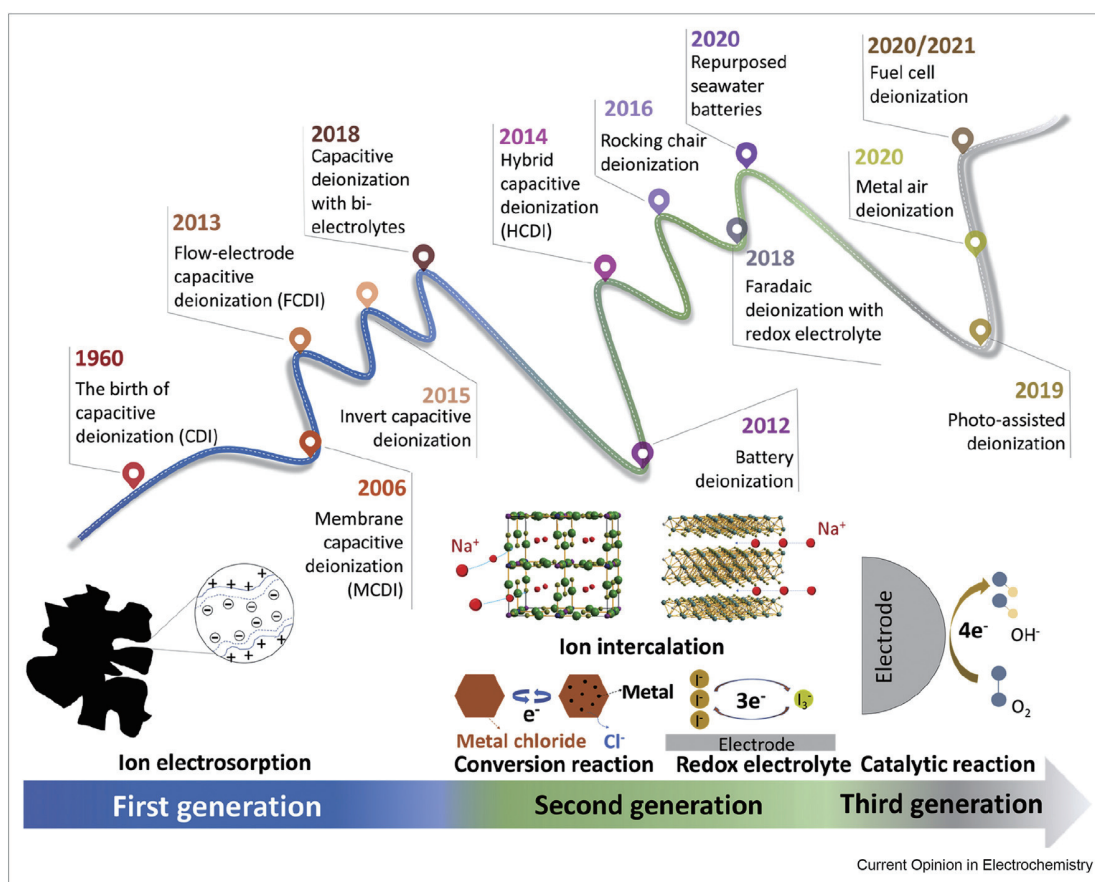
To decrease the energy consumption and improve the desalination performance, some of the desalination technology, based on other electrochemical principles, such as electrosorption [9], reversible electro–redox reaction [10], and electrocatalysis [11–13], have rapidly emerged as promising alternatives to the traditional desalination technologies for their high industrial application potential. In this paper, these emerging technologies are systematically divided into three generations according to their ion-removal mechanism (collectively referred to as electrochemical desalination technologies). The principle, merits, and limitations of the three generations are introduced and future perspectives on the emerging trends in electrochemical desalination technologies are discussed.

First-generation: carbon electrodes and ion electrosorption

In 1960, Blair and Murphy [14] opened the carbon ages of electrochemical desalination by using porous carbon electrodes. This technology can be classified as first-generation (Figure 1). A first-generation cell is known as capacitive deionization (CDI) because of the mechanism of ion electrosorption [15]. The cell contains one carbon electrode pair and a single middle channel for the feed water (Figure 2A). When the cell is charged, the ions are removed from the water and immobilized via electrosorption in the electrical double layer at the fluid/solid interface in the electrodes' pores (Figure 1), introduced by Johnson and Newman [16].

CDI electrodes usually use nanoporous carbon with facile ion access to a large pore volume and specific

Figure 1



The timeline and working principle of the first-, second-, and third-generation of electrochemical desalination methods. The terms deionization and desalination is used interchangeably in the literature.

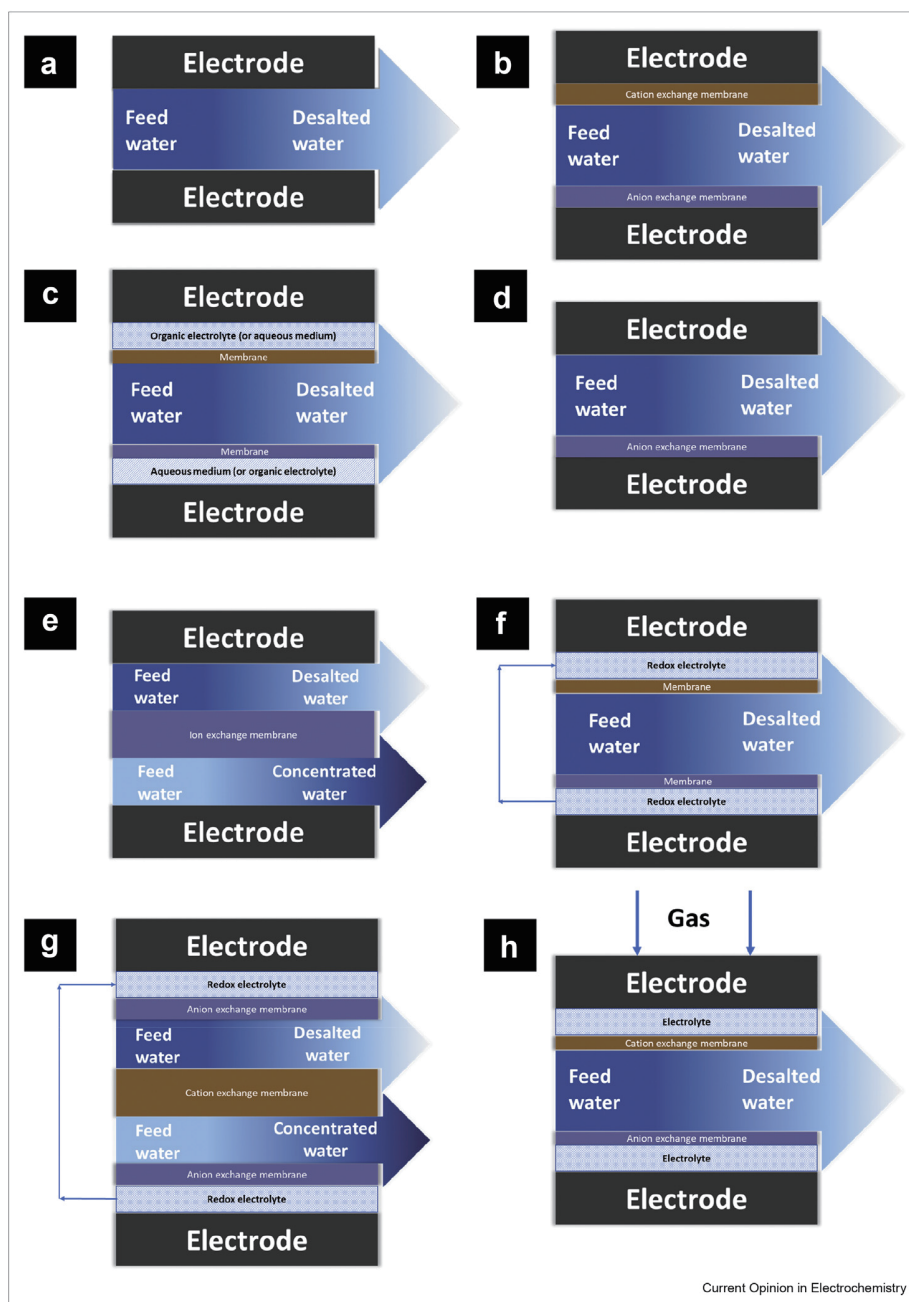
surface area. Even in the uncharged state, the pores are already populated by some ions. Expelling ions with the same charge as the electrode (co-ions) while attracting ions with the opposite charge (counter-ions) achieve facile charge storage. Still, it fails to accomplish any desalination as long as the ratio between counter ions and co-ions 1:1 [17]. This issue prevails for feed water with high salinity. In seawater, for instance, the desalination capacity of activated carbon (with an average pore size of more than 1 nm) is only around 1 mg/g with a charge efficiency (ratio of salt removal over charge) of about 10% [18]. However, micropores smaller than 1 nm become increasingly permselective and enable CDI to operate even in saline media with high molarity [19].

The desalination capacity is limited by the specific capacitance of carbon, around 0.1 F/m² [20]. Thus optimizing the cell voltage [21] is also important. When applying higher cell voltage, there may be water splitting and carbon oxidation [22], which reduces the charge

efficiency and causes significant performance degradation. Besides, inverting the CDI process by modifying the carbon surface with chemical charge can mitigate the oxidation of the anode and consequently improve stability [23]. Ions are immobilized via the chemical charge of surface groups and released when an electric potential is applied [24].

The first-generation electrochemical desalination is a promising technology, with a desalination capacity of (5–30 mg_{NaCl}/g_{electrodes}) and low energy consumption (10–40 Wh/mol_{NaCl}) for low to medium brackish water (0.1–1 g/L) but does not work sufficiently well in seawater (Figure 3). Commonly, it has a desalination rate of 0.03–0.6 mg_{NaCl}/g_{electrode}/s (Table 1), which greatly depends on the operation parameters such as the feedwater salinity, charge/discharge rate, flow rate, and so on, apart from the pore size effect [9,25]. The first-generation also exhibits stable desalination performance (80–97% desalination capacity retention after several hundred cycles) analogous to the long life

Figure 2



Cell architectures: conventional capacitive deionization (a), membrane capacitive deionization (b), bielectrolyte deionization (c), hybrid capacitive deionization (d), sodium ion desalination (e), desalination based on redox-electrolyte (f), photo-redox desalination (g), metal-air batteries desalination (h).

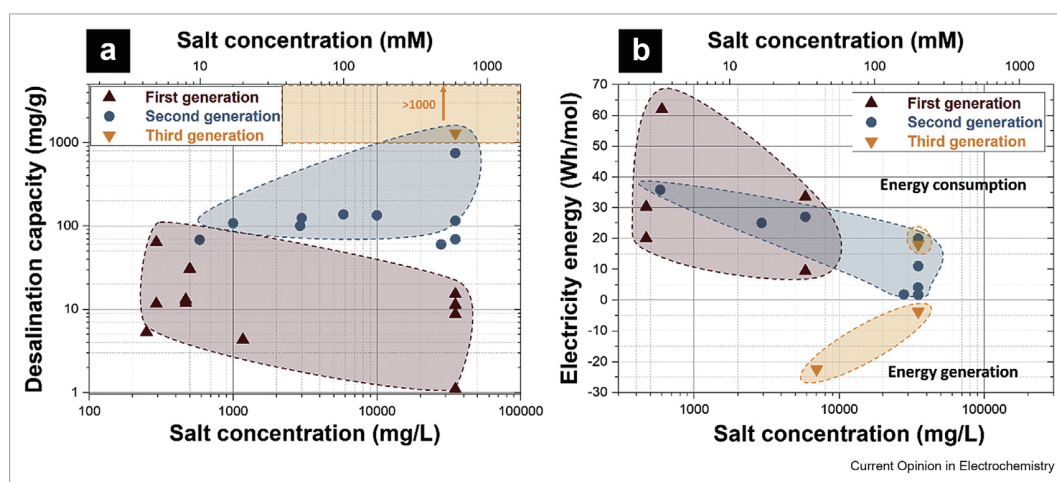
span of electrical double layer capacitors (Table 1) [26].

First-generation 1.1: ion-exchange membranes

To enhance the performance of CDI, in 2006, Lee *et al.* [27] proposed a membrane capacitive deionization (MCDI) technology. In this case, ion-exchange

membranes (IEMs) are added between the electrode pair and the water channel (Figure 2B). Implementing a pair of IEMs provides permselectivity to the nonpermeable carbon electrodes and suppresses the detrimental Faradaic side reactions, such as oxygen reduction at the cathode [28]. Compared with conventional CDI, the desalination capacity of MCDI for remediation of

Figure 3



The desalination capacity (a) and electricity energy consumed (positive value) and energy generated (negative value) (b) of different generations at various concentrations. Data adapted from [9,10,18,33,41,44,46,48,53,54,58–69].

water with low ionic molarity are improved [29] to 15–30 $\text{mg}_{\text{NaCl}}/\text{g}_{\text{electrodes}}$, with charge efficiency higher than 80% [18,30,31]. Besides, MCDI allows for seawater desalination [32]. The high cost of IEMs raises the desalination costs.

MCDI with multichannel structures allows for more diversity in cell designs. In 2018, a CDI cell containing two different electrolytes was introduced (Figure 2C) [33]. By immersing one electrode in the organic electrolyte, the cell voltage could reach 2.4 V, significantly improving the desalination capacity to 64 $\text{mg}_{\text{NaCl}}/\text{g}_{\text{electrodes}}$.

First-generation 1.2: suspension electrodes

Owing to the limited system capacities of immobile solid electrodes (M)CDI systems require electrode regeneration (discharging) once the electrode pores are saturated for ion adsorption, which leads to inefficiency of (M)CDI technology. To overcome this, flow electrode capacitive deionization was introduced by Jeoh et al. in 2013 (Figure 1) [34]. The basic concept of suspension electrodes dates back to Bertel Kastening and Faul [35]. With a separated regeneration process of the electrodes, the electrode suspension's mobility enables electrode regeneration during desalination and allows continuous operation [36].

Second-generation: desalination batteries

To overcome the intrinsic capacitance limitations of carbon, one needs to move beyond. In 2012, Pasta et al. [37] used a pair of Faradaic electrodes, namely, $\text{Na}_2\text{-xMn}_5\text{O}_{10}$ and Ag, to desalinate seawater. Unlike the first-generation, the second-generation (desalination

batteries) applies Faradaic materials to store ions in the crystallographic sites, between the electrode material's atomic planes, or immobilized through a conversion reaction (Figure 1). This ion-storage mechanism of Faradaic materials enables higher desalination capacity (Figure 3A) as they have higher charge storage capacities than carbon electrodes. Besides, desalination batteries allow for higher charge efficiency due to intrinsic permselectivity, which enables effective and efficient desalination at the seawater salinity and beyond [38].

Different kinds of Faradaic materials have been used as electrodes. Most of them are intercalation-type materials, such as sodium manganese oxides [39], $\text{NaTi}_2(\text{PO}_4)_3$ [40], $\text{Na}_3\text{V}_2(\text{PO}_4)_3$ [10], Prussian blue [41], and MXenes, [42]. Commonly they are used as cathodes, providing a desalination capacity of around 50–150 $\text{mg}_{\text{NaCl}}/\text{g}_{\text{electrodes}}$ in the feed water with the salinity of 1–35 g/L (Figure 3A). Similar to MXenes or different transition metal dichalcogenides, some materials also enable intercalation of anions [43]. Often, conversion materials such as Ag [44], Bi [45], or BiOCl [46] are chosen as the anode to store chloride. Attributed to the conversion reaction, these materials generally have a higher capacity (100–150 $\text{mg}_{\text{NaCl}}/\text{g}_{\text{electrode}}$) but reduced performance stability, compared with intercalation-type materials. Recently, the water-sensitive electrode (such as metallic sodium [47]), and alloying material (e.g. antimony [48]) are also applied in the desalination, using sodium super ion conductor. Compared with the first-generation, the Faradaic materials suffer commonly from lower desalination rates (because of the slow ions diffusion rates in bulk material) [41] and lower stability (due to irreversible

Table 1
The desalination rates, stability, technology-readiness level, and key-aspects of the three generations of electrochemical desalination technologies.

Generation of electrochemical desalination technology	Materials and technologies	Feed water salinity (mg/L)	Operation mode ^a	Desalination rates (mg _{NaCl} /g _{electrode} /s, or other)	Desalination capacity retention (%)	Cycle number	Reference	Technology-readiness level TRL ^b	Key aspects
First-generation	Block copolymer-based porous carbon fibers/block copolymer-based porous carbon fibers, CDI	500	C.V., 1.0 V	0.63	No obvious decrease	30	[9]	6–8	For CDI, scale-up; For MCDI, the cost control of the ion exchange membrane and scale-up
	H ₂ activated carbon/H ₂ activated carbon, CDI	292.5	C.V., 1.2 V	0.1	90%	100	[68]		
	Activated carbon/Activated carbon, MCDI	35100	C.C., 250 mA/g + C.V., 1.0 V	~0.05	97	180	[18]		
	Activated carbon cloth/Activated carbon cloth, bi-electrolyte	292.5	C.C., 30 mA/g	0.015	62	25	[33]		
	Na ₃ V ₂ (PO ₄) ₃ -graphene aerogel/AgCl-graphene aerogel, DEDI	1000	C.C., 100 mA/g	0.035	86	50	[10]	3–5	The synthesis of the electrode material with low cost, high capacity, and high selectivity
Second-generation	Na ₃ V ₂ (PO ₄) ₃ /AgCl, DEDI	1000	C.C., 100 mA/g	–	73	50	[10]		
	Prussian blue/PANI//C, hybrid cell	500	C.C., 100 mA/g	0.03	No obvious decrease	250	[41]		
	Ag//AgCl, CID	35100	C.C., 100 mA/g	0.38	61	15	[44]		
	BiOI–CNF//Bi–CNF	3000	C.C., 500 mA/g	0.52	90	30	[46]		
	Sb/C/C, bi-electrolyte	35100	C.C., 200 mA/g	–	51	40	[48]		
	Zn//K ₃ Fe(CN) ₆	35000	C.C., 1.3 mA/cm ²	2.0 mg _{NaCl} /cm ² /h	–	–	[62]		
Third-generation	Na _{0.44} MnO ₂ /BiOI, EDI	760	C.C., 100 mA/g	0.021	~61%	50	[64]		
	Na ₃ V ₂ (PO ₄) ₃ /C//AC	5850	C.V., 1.0 V	0.07 mg _{NaCl} /g _{NVP} /s	–	–	[65]		
	Zinc air desalination	35100	C.C., 1 mA/cm ²	1.8 mg _{NaCl} /cm ² /h	93	20	[58]	3–5	The design of catalytic electrodes.
	Fuel cell desalination	35100	no power supply	1.8 mg _{NaCl} /cm ² /h	–	–	[12]		

MCDI, membrane capacitive deionization.

^a C.C. and C.V. are the abbreviation of constant current and constant voltage, respectively.

^b It is estimated according to the criteria announced by the European Union [70].

processes) [25]. These challenges can be addressed by optimization of the crystal structure, reducing the particle size to the nanometer range, and hybridizing with conductive materials [25].

Hybrid CDI (Figure 2D) was introduced by Lee et al., in 2014 (Figure 1) [49]. In HCDI, a Faradaic electrode is coupled with a capacitive electrode, and a rapid ion removal rate is achieved. Technically, this was already explored by Blair and Murphy (where activated carbon and a silver electrode were used) [14]. Asymmetric systems require careful adjustment of mass ratio and operating potential windows of the two electrodes to optimize the desalination performance [50].

Standard desalination batteries use dual-ion architectures, with each electrode takes up one charge species. It is also possible to have a pair of the same electrodes with different oxidation and reduction states, which uptake or release the same ion kind at the same time. This cell concept requires an IEM to separate two flow channels. Charge compensation of the electrolyte is accomplished via ion transport across the IEM, yielding an increase of ionic strength in one channel and the mirror-image decrease in ion concentration in the other (Figure 2E). This concept was demonstrated for chloride-ion desalination [44,51], and sodium-ion desalination [52].

Second-generation 2.1: redox electrolytes

Besides solid electrodes, redox electrolytes have also been applied (Figure 2F) [53]. Redox electrolytes benefit from high redox kinetics and better stability compared with solid Faradaic electrodes [54]. Typical values for the desalination capacities are about 70–90 $\text{mg}_{\text{NaCl}}/\text{g}_{\text{electrodes}}$ [53–55]. Such systems also allow a continuous operation to desalinate water [56]. Taking the redox couple of ferricyanide/ferrocyanide as the example, during the charging process, the ferrocyanide is oxidized into ferricyanide on the anode's surface and then anions are attracted to balance the charge. On the cathode side, ferricyanide is reduced to ferrocyanide, and sodium immigrates from the feed water to the electrolyte. By cycling the redox electrolyte from the anode side to the cathode side (or by using a second cell), continuous operation can be achieved.

Third-generation: catalytic interface reactions

Recently, the third-generation of electrochemical desalination is budding, introducing catalytic material and redox couples into the multichannel system. In 2019, Chen et al. [57] developed a photo-redox desalination generator using LEG4 dye-modified TiO_2 as the photoanode and a mixture of 2,2,6,6-tetramethyl piperidinyloxy (TEMPO) and NaCl as the electrolyte. The system contains two AEMs placed at the anode and cathode and one CEM in the middle of two

water channels (Figure 2G). Under irradiation with visible light, the TEMPO is oxidized into TEMPO^+ , attracting the chloride in the feed water to pass the membrane to the electrolyte. This generator is driven by light energy, which enables water desalination and energy release simultaneously.

Apart from the photocatalytic materials, the electrocatalytic reaction for the redox couple is also applied in water desalination. Srimuk et al. [58] introduced a zinc air desalination cell consisting of a MoS_2 cathode for the oxygen reduction reaction (ORR) and Zn/Zn^{2+} redox couple at the anode, with a feedwater channel in the middle separated by a pair of IEMs (Figure 2H). When the cell is discharged, Na^+ and Cl^- immigrate from the feed water into the anolyte and catholyte with a desalination rate of 0.9–1.0 $\text{mg}_{\text{NaCl}}/\text{cm}^2_{\text{IEM}}$ (Figure 3). Bhat et al. [11] used Pt/C electrodes to utilize the H_2/H^+ redox couple as an energy carrier and the neutralization energy of NaOH and HCl as fuels; thereby, the cell removes NaCl to balance the charge of the electrocatalytic H_2/H^+ reaction under the acidic and alkali environment. The NaCl concentration decreased from 4 M to about 1 M with a low energy consumption of 13.6 $\text{kJ}/\text{mol}_{\text{NaCl}}$ in 22 h. Zhang et al. used a pair of Pt/C electrodes, by applying the electrocatalytic reaction of H_2/H^+ and O_2/OH^- , by removing 1 g of NaCl at a desalination rate of 18 $\text{g}_{\text{NaCl}}/\text{m}^2_{\text{IEM}}/\text{h}$; 67 mWh of electric energy is generated. Meanwhile, NaOH and HCl are produced at the anolyte and catholyte [12].

Perspective

Over three generations of technological development, electrochemical desalination technologies have diversified both in device types and target applications. Apart from commonly required improvement, such as the establishment of more reasonable performance metrics, synthesis of novel IEMs, and so on, the future study of three generations could focus on different aspects, according to different technologies-readiness levels.

Owing to its relatively low ion storage capacity, the first-generation seems not suitable for desalinating the seawater alone. But it is greatly beneficial when combined with other technologies, such as nanofiltration. How to extend it from lab scale to the full scale could be studied. Accompanying issues, such as the setup of commercial benchmarks or the blockage of the electrode by fouling, need to be addressed.

The second-generation benefits from higher capacity and efficiency but suffers from limited redox potential window and stability. A material-characterization-performance database should be established for better exploration of stable, low-cost materials. The study of selective electrodes toward specific ions could also be an

attractive research branch. The third-generation has high-performance desalination potential, but designing robust catalytic interfaces, reducing energy consumption, and improving the desalination rate may be challenging in more demanding water environments.

Declaration of competing interest

The authors declare that they have no known competing financial interests or personal relationships that could have appeared to influence the work reported in this article.

Acknowledgements

The authors acknowledge support from the RAG-Stiftung for the MERLIN project and thank Eduard Arzt (INM) for his continued support. L.W. acknowledges funding from the China Scholarship Council (CSC) via award number 201906260277.

References

Papers of particular interest, published within the period of review, have been highlighted as:

* of special interest

** of outstanding interest

1. *Water U: Sustainable Development Goal 6 synthesis report on water and sanitation*. 2018.
 2. Cosgrove CE, Cosgrove WJ: *The dynamics of global water futures: driving forces 2011-2050, report on the findings of phase one of the UNESCO-WWAP water scenarios project to 2050*. UNESCO; 2012. 9230010359.
 3. Lv H, Wang Y, Wu L, Hu Y: **Numerical simulation and optimization of the flash chamber for multi-stage flash seawater desalination**. *Desalination* 2019, **465**:69–78.
 4. Park K, Kim J, Yang DR, Hong S: **Towards a low-energy seawater reverse osmosis desalination plant: a review and theoretical analysis for future directions**. *J Membr Sci* 2020, **595**:117607.
 5. Firouzjaei MD, Seyedpour SF, Aktij SA, Giagnorio M, Bazrafshan N, Mollahosseini A, Samadi F, Ahmadalipour S, Firouzjaei FD, Esfahani MR, Tiraferri A, Elliott M, Sangermano M, Abdelrasoul A, McCutcheon JR, Sadrzadeh M, Esfahani AR, Rahimpour A: **Recent advances in functionalized polymer membranes for biofouling control and mitigation in forward osmosis**. *J Membr Sci* 2020, **596**:117604.
 6. Al-Amshawee S, Yunus MYBM, Azoddein AAM, Hassell DG, Dakhil IH, Hasan HA: **Electrodialysis desalination for water and wastewater: a review**. *Chem Eng J* 2020, **380**:122231.
 7. Qasim M, Badrelzaman M, Darwish NN, Darwish NA, Hilal N: **Reverse osmosis desalination: a state-of-the-art review**. *Desalination* 2019, **459**:59–104.
 8. Meerganz von Medeazza GL: **“Direct” and socially-induced environmental impacts of desalination**. *Desalination* 2005, **185**:57–70.
 9. Liu T, Serrano J, Elliott J, Yang X, Cathcart W, Wang Z, He Z, Liu G: **Exceptional capacitive deionization rate and capacity by block copolymer-based porous carbon fibers**. *Sci Adv* 2020, **6**: eaaz0906.
 10. Zhao W, Ding M, Guo L, Yang HY: **Dual-ion electrochemical deionization system with binder-free aerogel electrodes**. *Small* 2019, **15**:1805505.
 11. Bhat ZM, Pandit D, Ardo S, Thimmappa R, Kottaichamy AR, Christudas Dargily N, Devendrachari MC, Ottakam Thotiyil M: **An electrochemical neutralization cell for spontaneous water desalination**. *Joule* 2020, **4**:1730–1742.
- This paper introduced a novel concept of electrochemical desalination based on hydrogen reduction and evolution. In 22 h, NaCl concentration decreases from 4 M to 1 M with a low energy consumption of 13.6 kJ/mol. And as time increases, the concentration of NaCl will continuously go down. This conception opens up an unprecedented pathway for the obtain of drinking water
12. Zhang Y, Wang L, Presser V: **Electrocatalytic fuel cell desalination for continuous energy and freshwater generation**. *Cell Rep Phys Sci* 2021.
 13. Atlas I, Khalla SA, Suss ME: **Thermodynamic energy efficiency of electrochemical systems performing simultaneous water desalination and electricity generation**. *J Electrochem Soc* 2020, **167**:134517.
 14. Blair JW, Murphy GW: **Electrochemical demineralization of water with porous electrodes of large surface area**. In *ACS publications*; 1960.
 15. Farmer J, Fix D, Mack G: *Capacitive deionization of water: an innovative new process*. CA (United States): Lawrence Livermore National Lab.; 1995.
 16. Johnson A, Newman J: **Desalting by means of porous carbon electrodes**. *J Electrochem Soc* 1971, **118**:510.
 17. Suss ME, Presser V: **Water desalination with energy storage electrode materials**. *Joule* 2018, **2**:10–15.
 18. Zhang Y, Srimuk P, Aslan M, Gallei M, Presser V: **Polymer ion-exchange membranes for capacitive deionization of aqueous media with low and high salt concentration**. *Desalination* 2020, **479**:114331.
 19. Bi S, Zhang Y, Cervini L, Mo T, Griffin JM, Presser V, Feng G: **Permselective ion electrosorption of subnanometer pores at high molar strength enables capacitive deionization of saline water**. *Sust Ener Fuels* 2020, **4**:1285–1295.
- This paper demonstrates the carbon electrode, without any modification, could also work in high salinity water when the pores are less than 1 nm. This provides a new avenue about how to use the carbon electrode in high salinity water.
20. Jäckel N, Simon P, Gogotsi Y, Presser V: **The increase in capacitance by subnanometer pores in carbon**. *ACS Energy Lett* 2016, **1**:1262–1265.
 21. Lu D, Cai W, Wang Y: **Optimization of the voltage window for long-term capacitive deionization stability**. *Desalination* 2017, **424**:53–61.
 22. Zhang C, He D, Ma J, Tang W, Waite TD: **Faradaic reactions in capacitive deionization (CDI) - problems and possibilities: a review**. *Water Res* 2018, **128**:314–330.
 23. Gao X, Omosabi A, Landon J, Liu K: **Surface charge enhanced carbon electrodes for stable and efficient capacitive deionization using inverted adsorption-desorption behavior**. *Energy Environ Sci* 2015, **8**:897–909.
 24. Tu Y-H, Liu C-F, Wang J-A, Hu C-C: **Construction of an inverted-capacitive deionization system utilizing pseudocapacitive materials**. *Electrochem Commun* 2019, **104**:106486.
 25. Srimuk P, Su X, Yoon J, Aurbach D, Presser V: **Charge-transfer materials for electrochemical water desalination, ion separation and the recovery of elements**. *Nat Rev Mat* 2020, **5**:517–538.
 26. Liu J, Wang J, Xu C, Jiang H, Li C, Zhang L, Lin J, Shen ZX: **Advanced energy storage devices: basic principles, analytical methods, and rational materials design**. *Adv Sci* 2018, **5**:1700322.
 27. Lee J-B, Park K-K, Eum H-M, Lee C-W: **Desalination of a thermal power plant wastewater by membrane capacitive deionization**. *Desalination* 2006, **196**:125–134.
 28. Kim N, Lee J, Kim S, Hong SP, Lee C, Yoon J, Kim C: **Short review of multichannel membrane capacitive deionization: principle, current status, and future prospect**. *Appl Sci* 2020, **10**:683.
 29. Hassanvand A, Chen GQ, Webley PA, Kentish SE: **A comparison of multicomponent electrosorption in capacitive deionization and membrane capacitive deionization**. *Water Res* 2018, **131**:100–109.

30. Liu D, Ning X-a, Hong Y, Li Y, Bian Q, Zhang J: **Covalent triazine-based frameworks as electrodes for high-performance membrane capacitive deionization**. *Electrochim Acta* 2019, **296**:327–334.
31. Shi P, Wang C, Sun J, Lin P, Xu X, Yang T: **Thermal conversion of polypyrrole nanotubes to nitrogen-doped carbon nanotubes for efficient water desalination using membrane capacitive deionization**. *Separ Purif Technol* 2020, **235**: 116196.
- This paper synthesized the hybrid of polyaniline and Prussian blue. This material exhibits excellent stability (with no fading during 250 cycles) and a high salt removal rate. Density functional theory (DFT) calculations were further conducted to investigate the interaction between polyaniline and Prussian blue, contributing to this material's good rate performance.
32. Tang K, Kim Y-h, Chang J, Mayes RT, Gabitto J, Yiacoumi S, Tsouris C: **Seawater desalination by over-potential membrane capacitive deionization: opportunities and hurdles**. *Chem Eng J* 2019, **357**:103–111.
33. Kim C, Srimuk P, Lee J, Presser V: **Enhanced desalination via cell voltage extension of membrane capacitive deionization using an aqueous/organic bi-electrolyte**. *Desalination* 2018, **443**:56–61.
34. Jeon S-i, Park H-r, Yeo J-g, Yang S, Cho CH, Han MH, Kim DK: **Desalination via a new membrane capacitive deionization process utilizing flow-electrodes**. *Energy Environ Sci* 2013, **6**: 1471–1475.
35. Kastening B, Faul W: **Herstellung von Wasserstoffperoxid durch kathodische Reduktion von Sauerstoff**. *Chem Ing Tech* 1977, **49**: 911-911.
36. Rommerskirchen A, Linnartz CJ, Egidi F, Kendir S, Wessling M: **Flow-electrode capacitive deionization enables continuous and energy-efficient brine concentration**. *Desalination* 2020, **490**:114453.
37. Pasta M, Wessells CD, Cui Y, La Mantia F: **A desalination battery**. *Nano Lett* 2012, **12**:839–843.
38. Metzger M, Besli MM, Kuppan S, Hellstrom S, Kim S, Sebt E, Subban CV, Christensen J: **Techno-economic analysis of capacitive and intercalative water deionization**. *Energy Environ Sci* 2020, **13**:1544–1560.
- This work conducted a techno-economic analysis of electrochemical desalination technology. It compares the cost, volume, and energy consumption of membrane capacitive deionization, hybrid capacitive deionization, and sodium intercalation desalination by establishing the module. The results show that sodium intercalation desalination technology only needs 27% costs and 20% device volume of membrane capacitive with a similar desalination performance. This work points out the potential direction in the industrial application of electrochemical desalination technology.
39. Zhao Y, Liang B, Zong M, Duan M, Li K, Lv C: **Different crystallographic sodium manganese oxides for capacitive deionization: performance comparison and the associated mechanism**. *Environ Sci: Nano* 2019, **6**:3091–3101.
- This work reveals the relation between the crystal structure of sodium manganese oxides (NMO) and its electrochemical capacity and desalination performance. It shows the layered NMO has a better behavior than the tunnel NMO and the P2-group layered NMO is better than O3-group layered NMO. According to the postmortem XPS measurement, the different performance between these three materials is due to the different levels of Mn⁴⁺/Mn³⁺ species.
40. Han C, Meng Q, Cao B, Tian G: **Enhanced hybrid capacitive deionization performance by sodium titanium phosphate/reduced porous graphene oxide composites**. *ACS Omega* 2019, **4**:11455–11463.
41. Shi W, Liu X, Deng T, Huang S, Ding M, Miao X, Zhu C, Zhu Y, Liu W, Wu F, Gao C, Yang S-W, Yang HY, Shen J, Cao X: **Enabling superior sodium capture for efficient water desalination by a tubular polyaniline decorated with prussian blue nanocrystals**. *Adv Mater* 2020, **32**:1907404.
42. Chen B, Feng A, Deng R, Liu K, Yu Y, Song L: **MXene as a cation-selective cathode material for asymmetric capacitive deionization**. *ACS Appl Mater Interfaces* 2020, **12**: 13750–13758.
43. Karthikeyan P, Elanchezhiyan SS, Preethi J, Talukdar K, Meenakshi S, Park CM: **Two-dimensional (2D) Ti₃C₂T_x MXene nanosheets with superior adsorption behavior for phosphate and nitrate ions from the aqueous environment**. *Ceram Int* 2021, **47**:732–739.
44. Srimuk P, Husmann S, Presser V: **Low voltage operation of a silver/silver chloride battery with high desalination capacity in seawater**. *RSC Adv* 2019, **9**:14849–14858.
45. Chang J, Duan F, Su C, Li Y, Cao H: **Removal of chloride ions using a bismuth electrode in capacitive deionization (CDI)**. *Environ Sci: Water Research & Technology* 2020, **6**: 373–382.
46. Liu Y, Gao X, Wang Z, Wang K, Dou X, Zhu H, Yuan X, Pan L: **Controlled synthesis of bismuth oxychloride-carbon nanofiber hybrid materials as highly efficient electrodes for rocking-chair capacitive deionization**. *Chem Eng J* 2021, **403**: 126326.
47. Kim N, Park J-S, Harzandi AM, Kishor K, Ligaray M, Cho KH, Kim Y: **Compartmentalized desalination and salination by high energy density desalination seawater battery**. *Desalination* 2020, **495**:114666.
48. Arnold S, Wang L, Budak Ö, Aslan M, Srimuk P, Presser V: **Antimony alloying electrode for high-performance sodium removal: how to use a battery material not stable in aqueous media for saline water remediation**. *J Mater Chem* 2021, **9**: 585–596.
- This paper introduced an alloying material, previously considered not suitable for aqueous electrolyte, for desalination batteries. Attributed to the high capacity of antimony, the hybrid desalination cell provides a high desalination capacity of 294 mg_{Na} g_{Sb}⁻¹ (748 mg_{NaCl} g_{Sb}⁻¹). The convergence of battery desalination and seawater batteries is a synergistic and dynamic research domain.
49. Lee J, Kim S, Kim C, Yoon J: **Hybrid capacitive deionization to enhance the desalination performance of capacitive techniques**. *Energy Environ Sci* 2014, **7**:3683–3689.
50. Torkamanzadeh M, Wang L, Zhang Y, Budak Ö, Srimuk P, Presser V: **MXene/activated carbon hybrid capacitive deionization for permselective ion removal at low and high salinity**. *ACS Appl Mater Interfaces* 2020, **12**: 26013–26025.
51. Grygolowicz-Pawlak E, Sohail M, Pawlak M, Neel B, Shvarev A, de Marco R, Bakker E: **Coulometric sodium chloride removal system with nafion membrane for seawater sample treatment**. *Anal Chem* 2012, **84**:6158–6165.
52. Smith KC, Dmello R: **Na-ion desalination (NID) enabled by Na-blocking membranes and symmetric Na-intercalation: porous-electrode modeling**. *J Electrochem Soc* 2016, **163**: A530.
53. Kim N, Hong SP, Lee J, Kim C, Yoon J: **High-desalination performance via redox couple reaction in the multichannel capacitive deionization system**. *ACS Sustainable Chem Eng* 2019, **7**:16182–16189.
54. Lee J, Srimuk P, Carpiere S, Choi J, Zornitta RL, Kim C, Aslan M, Presser V: **Confined redox reactions of iodide in carbon nanopores for fast and energy-efficient desalination of brackish water and seawater**. *ChemSusChem* 2018, **11**: 3460–3472.
55. Lee J, Srimuk P, Zornitta RL, Aslan M, Mehdi BL, Presser V: **High electrochemical seawater desalination performance enabled by an iodide redox electrolyte paired with a sodium superionic conductor**. *ACS Sustainable Chem Eng* 2019, **7**: 10132–10142.
56. Ramalingam K, Liang M, Pyae NLW, Aung SH, Oo TZ, Srimuk P, Ma J, Presser V, Chen F, Waite TD: **Self-sustained visible-light-driven electrochemical redox desalination**. *ACS Appl Mater Interfaces* 2020, **12**:32788–32796.
57. Chen F, Karthick R, Zhang Q, Wang J, Liang M, Dai J, Jiang X, Jiang Y: **Exploration of a photo-redox desalination generator**. *J Mater Chem* 2019, **7**:20169–20175.
- This work introduced a new architecture of electrochemical desalination, a photo-redox catalysis desalination generator. This cell utilizes the electrolyte's redox reaction driven by the photo-excited

semiconductor and removes the salt by electrostatic force. The utilization of solar energy effectively reduced the energy consumption and cost of electrochemical desalination.

58. Srimuk P, Wang L, Budak Ö, Presser V: **High-performance ion removal via zinc–air desalination.** *Electrochem Commun* 2020, **115**:106713.
59. Qu Y, Campbell PG, Gu L, Knipe JM, Dzenitis E, Santiago JG, Stadermann M: **Energy consumption analysis of constant voltage and constant current operations in capacitive deionization.** *Desalination* 2016, **400**:18–24.
60. Chen Y-J, Liu C-F, Hsu C-C, Hu C-C: **An integrated strategy for improving the desalination performances of activated carbon-based capacitive deionization systems.** *Electrochim Acta* 2019, **302**:277–285.
61. Gao X, Omosebi A, Landon J, Liu K: **Enhanced salt removal in an inverted capacitive deionization cell using amine modified microporous carbon cathodes.** *Environ Sci Technol* 2015, **49**: 10920–10926.
62. Desai D, Beh ES, Sahu S, Vedharathinam V, van Overmeere Q, de Lannoy CF, Jose AP, Völkel AR, Rivest JB: **Electrochemical desalination of seawater and hypersaline brines with coupled electricity storage.** *ACS Energy Lett* 2018, **3**: 375–379.
63. Lee J, Kim S, Yoon J: **Rocking chair desalination battery based on prussian blue electrodes.** *ACS Omega* 2017, **2**:1653–1659.
64. Chen F, Huang Y, Guo L, Sun L, Wang Y, Yang HY: **Dual-ions electrochemical deionization: a desalination generator.** *Energy Environ Sci* 2017, **10**:2081–2089.
65. Cao J, Wang Y, Wang L, Yu F, Ma J: **Na₃V₂(PO₄)₃@C as faradaic electrodes in capacitive deionization for high-performance desalination.** *Nano Lett* 2019, **19**:823–828.
66. Wei X, Zhao Y, Liang B, Mo X, Li K: **Core-shell nanoparticles of Prussian blue analogues as efficient capacitive deionization electrodes for brackish water desalination.** *Separ Purif Technol* 2020:117899.
67. Srimuk P, Lee J, Tolosa A, Kim C, Aslan M, Presser V: **Titanium disulfide: a promising low-dimensional electrode material for sodium ion intercalation for seawater desalination.** *Chem Mater* 2017, **29**:9964–9973.
68. Krüner B, Srimuk P, Fleischmann S, Zeiger M, Schreiber A, Aslan M, Quade A, Presser V: **Hydrogen-treated, sub-micrometer carbon beads for fast capacitive deionization with high performance stability.** *Carbon* 2017, **117**:46–54.
69. Dai J, Win Pyae NL, Chen F, Liang M, Wang S, Ramalingam K, Zhai S, Su CY, Shi Y, Tan SC, Zhang L, Chen Y: **Zinc-air battery-based desalination device.** *ACS Appl Mater Interfaces* 2020, **12**: 25728–25735.
70. **Technology readiness levels (TRL); extract from Part 19 - commission decision C. 4995..** In *European commission, 2014*; 2014.

4.2 Dual-use of seawater batteries for energy storage and water desalination

Stefanie Arnold,^{1,2} Lei Wang^{1,2} and Volker Presser^{1,2,3}

¹ INM - Leibniz Institute for New Materials, D2 2, 66123, Saarbrücken, Germany

² Department of Materials Science & Engineering, Saarland University, Campus D2 2, 66123, Saarbrücken, Germany

³ Saarene - Saarland Center for Energy Materials and Sustainability, Campus C4 2, 66123 Saarbrücken, Germany

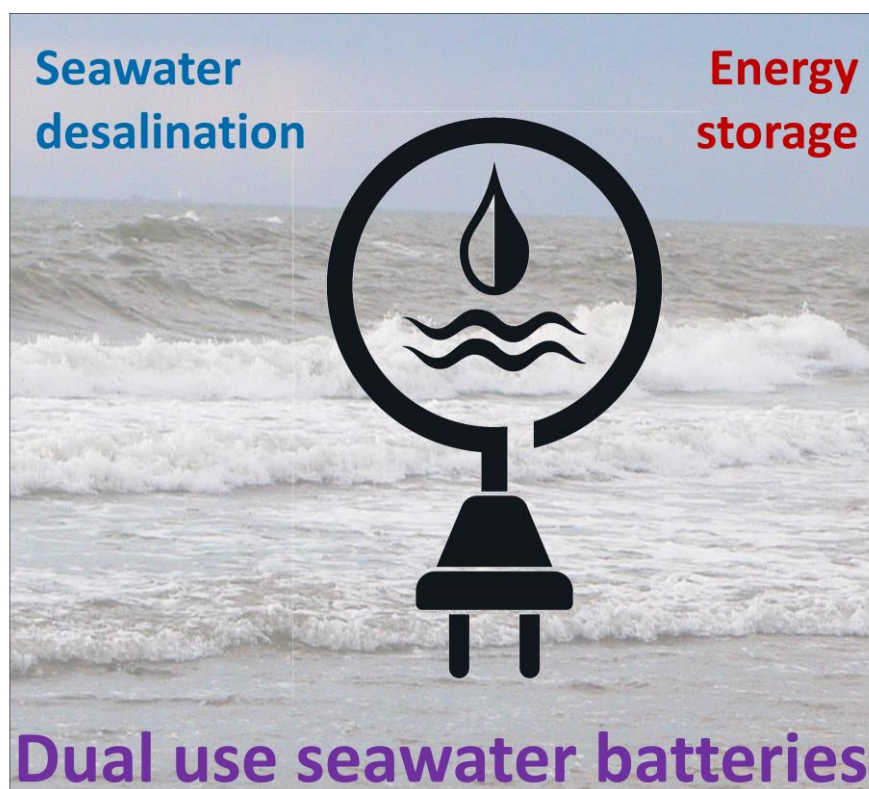
Citation:

S. Arnold, L. Wang, V. Presser, DUAL-USE OF SEAWATER BATTERIES FOR ENERGY STORAGE AND WATER DESALINATION, **Small**, 18 (2022) 2107913.

DOI: <https://doi.org/10.1002/smll.202107913>

Own contribution:

Conceptualization, Visualization, Writing-Original Draft, Writing - Review & Editing



Dual-Use of Seawater Batteries for Energy Storage and Water Desalination

Stefanie Arnold, Lei Wang, and Volker Presser*

Seawater batteries are unique energy storage systems for sustainable renewable energy storage by directly utilizing seawater as a source for converting electrical energy and chemical energy. This technology is a sustainable and cost-effective alternative to lithium-ion batteries, benefitting from seawater-abundant sodium as the charge-transfer ions. Research has significantly improved and revised the performance of this type of battery over the last few years. However, fundamental limitations of the technology remain to be overcome in future studies to make this method even more viable. Disadvantages include degradation of the anode materials or limited membrane stability in aqueous saltwater resulting in low electrochemical performance and low Coulombic efficiency. The use of seawater batteries exceeds the application for energy storage. The electrochemical immobilization of ions intrinsic to the operation of seawater batteries is also an effective mechanism for direct seawater desalination. The high charge/discharge efficiency and energy recovery make seawater batteries an attractive water remediation technology. Here, the seawater battery components and the parameters used to evaluate their energy storage and water desalination performances are reviewed. Approaches to overcoming stability issues and low voltage efficiency are also introduced. Finally, an overview of potential applications, particularly in desalination technology, is provided.

1. Introduction

The global shift toward sustainability has intensified the development of new materials and technologies, constant improvement, and creative redesign.^[1,2] The large-scale implementation

S. Arnold, L. Wang, V. Presser
INM – Leibniz Institute for New Materials
Campus D22, 66123 Saarbrücken, Germany
E-mail: volker.presser@leibniz-inm.de

S. Arnold, L. Wang, V. Presser
Department of Materials Science and Engineering
Saarland University
Campus D22, 66123 Saarbrücken, Germany

V. Presser
Saarene – Saarland Center for Energy Materials and Sustainability
Campus C42, 66123 Saarbrücken, Germany

 The ORCID identification number(s) for the author(s) of this article can be found under <https://doi.org/10.1002/smll.202107913>.

© 2022 The Authors. Small published by Wiley-VCH GmbH. This is an open access article under the terms of the Creative Commons Attribution License, which permits use, distribution and reproduction in any medium, provided the original work is properly cited.

DOI: 10.1002/smll.202107913

of renewable, green energy goes hand-in-hand with the digitalization of our power distribution grid and the rigorous use of energy storage technologies.^[3] Electrochemical energy storage (EES) plays a crucial role in this context, from enabling mobile computing and communication to large-scale intermittent power storage.^[4] The so-far best-researched lithium-ion batteries are known for their comparably high energy density, long shelf life, and high energy efficiency.^[5] Accordingly, they have become an essential power source for consumer electronics, portable devices, and electric vehicles. However, lithium-ion batteries mainly face two issues. First, lithium is a limited resource on our planet, which induces a future hard limitation to lithium-ion battery technology proliferation.^[6] This shortage has increased the global quest to explore alternative lithium sources, such as hydrothermal water, seawater, and mining water.^[7–9] Second, lithium-ion batteries' high cost and safety issues make it hard to meet the continuously increasing demand for electronic devices, both portable electronic devices and large-scale stationary devices.^[5,10] The high cost comes from the limited availability and exceeding the demand for lithium, nickel, and cobalt (in addition to price fluctuations due to fluctuating trade markets).^[11] The safety concern arises from the toxicity of cobalt and the flammable organic electrolytes. Interesting energy storage systems beyond lithium attract attention and have been explored in past years.^[12,13]

Over the last years, several alternatives to lithium-ion batteries have been researched. In particular, the pure focus is placed on naturally occurring alkali metal ions such as sodium and potassium, which offers the possibility of low-cost energy storage systems.^[14–16] Simultaneously, multivalent charge carriers such as Mg²⁺, Zn²⁺, Al³⁺, and others are investigated, which theoretically transfer more than one electron, thus offering the possibility of a higher specific capacity and a higher energy density.^[17–20] Especially sodium-ion batteries have received particular attention since 2011, as sodium is one of the most abundant elements on earth, offering the potential for low-cost energy storage systems.^[21–24] Sodium is abundant in seawater and can be easily extracted from it. Another advantage is that Na-ion batteries do not require cobalt, which is still needed in Li-ion batteries. Most of the cobalt used today to make Li-ion batteries is mined in socially and environmentally challenged regions.^[25,26] Thus, developing a promising

post-lithium energy storage technology with all its changes and optimizations represents an approach to the UN's Sustainable Development Goals (SDGs) claims. For example, direct contributions can be made to the areas outlined in the SDGs, which include the following indicators and measures: sustainable water management, sustainable consumption, production and development of communities, climate change mitigation, sustainable use of the oceans and terrestrial ecosystems, and affordable and clean energy. Sodium-ion-based and other beyond-lithium technologies can capitalize on know-how and materials available from decades of lithium-ion battery research and development.^[27] In contrast, the Na-ion battery technology is still under development.^[28,29] Researchers are working to increase its lifespan, shorten its charging time, and make batteries that deliver many watts of power.

Besides energy storage, sustainable water use is another vital part of sustainable development in the 21st century. According to the United Nations, ≈3 billion people currently have limited access to safe drinking water.^[30] Two out of three humans will face water-stressed situations worldwide by 2050.^[31] The oceans account for about 97% of the Earth's water, which has the great potential to be the drinking, agricultural, and industrial water resources. This particularly applies to the emerging global hydrogen economy, where seawater is an abundant source of water used for hydrogen production.^[32] So far, various desalination technologies have been explored, which could be divided into thermal methods (i.e., multieffect distillation,^[33] multistage flash distillation^[34]), membrane-based processes (such as reverse osmosis^[35]), and electrochemical methods (like electrodialysis,^[36] capacitive deionization,^[37] desalination batteries,^[9,38] desalination fuel cells^[39,40]), according to the mechanism. Reverse osmosis is dominant in desalination with an energy consumption of 3–5 kWh m⁻³, which consumes more than 70% of the energy of the whole seawater desalination plants.^[41,42] More energy-efficient technologies are required for large-scale seawater desalination.

A derivative of the rechargeable sodium-ion battery (NIB) is the rechargeable seawater battery, which could carry out simultaneous energy storage and desalination due to its unique configuration. Seawater, covering about two-thirds of our planet and a sodium concentration of around 470 mM, is a quasi-abundant resource of sodium ions.^[43] The first commercial primary seawater batteries, which means cells that cannot be recharged, were developed in 1943.^[44] The research field was re-energized with a focus on secondary (rechargeable) seawater batteries in 2014.^[45,46] Aqueous rechargeable sodium-ion batteries are a promising and environmentally friendly way to store electrochemical energy by circulating seawater as a low-cost electrolyte; they eliminate many of the safety problems of organic electrolytes.^[18]

A typical rechargeable seawater battery contains an organic electrolyte side and an aqueous electrolyte side, separated by the solid sodium diffusion membrane.^[43] The organic parts resemble the typical NIB with elemental sodium as an anode. If the seawater battery is contacted with seawater, the catholyte's free and abundant sodium ions can migrate into the anode compartment during the charging process. They are ultimately stored as elemental sodium metal. At the cathode side, the oxygen evolution reaction

(OER, $4\text{OH}^- \leftrightarrow \text{O}_2 + 2\text{H}_2\text{O} + 4\text{e}^-$, $E = 0.77\text{ V vs SHE}$) produces a theoretical cell voltage of 3.48 V.^[45] The sodium ions are rereleased and transferred to the seawater during the subsequent discharge, and the dissolved oxygen is reduced (oxygen reduction reaction, ORR).

Since the rechargeable seawater batteries entered the market in 2014,^[47] most works have optimized the performance, including the anode and cathode materials, anolyte and catholyte, and cell architecture.^[45] However, there is a lack of systematic review that analyzes the relationship between the components of rechargeable seawater batteries, their application in desalination systems, and their performance. This may correlate with a separation between the energy storage and electrochemical water desalination communities; in our view, both communities are strongly linked and situated within the critical water/energy research nexus. The realization that batteries are electrochemical ion management/ion storage devices is a key to unlocking unseen synergy between the battery and desalination communities.^[48] Dual functionality may help to address, at the same time, storing intermittently available renewable energy and providing clean, potable water to residential areas and agriculture. A growing amount of desalinated water will also significantly advance the large-scale production of green hydrogen.

We provide a review to meet the need for crossing disciplines and application areas along with sustainable electrochemical application and exemplify the synergy and dual-use application for the intriguing system of seawater batteries. This review introduces the component and properties of rechargeable seawater batteries and explores the possible reason for the demerits. Subsequently, we summarized the adopted approaches to overcome these drawbacks, including the materials design, cell-structure adjustment, and parameters optimization. Additionally, the applications of rechargeable seawater batteries are presented. Finally, the challenges faced by rechargeable seawater batteries and prospects for their further development are discussed.

2. Rechargeable Seawater Batteries

Conventional seawater batteries enable the storage of electrochemical energy by combining a sodiation/desodiation anode and an electrolysis cathode. This concept mandates an open-cell architecture to be able to constantly supply fresh seawater as the catholyte during the charge–discharge process. Based on the evaluation and continuous improvement of the cell parts, the electrochemical performance such as the stability, power, voltage efficiency, Coulombic efficiency, and other parameters of the resulting cell is then evaluated and reflects the current state of the art.

2.1. Rechargeable Seawater Battery Design and Components

To combine the individual components of a seawater battery into a functioning and efficient cell, it is necessary first to optimize and examine all the individual elements. The essential components of the seawater battery are electrode materials

(cathode and anode), electrolyte (anolyte, catholyte), current collector, ceramic solid electrolyte, electrocatalyst, and the general cell type. The following sections explain the requirements for the individual components, what needs to be considered and optimized, and the current research state.

2.1.1. Anode

A seawater battery basically consists of an anode in an organic electrolyte and a seawater cathode with a current collector. This design allows its use both as an energy storage system and for water desalination (Figure 1). A high-performance seawater battery needs an optimized anode compartment, including electrolyte and electrode material.^[43,49–51] The cell's anode in the past consisted of an organic electrolyte and an electrode material used as a negative electrode. In addition to the ability to uptake

ions reversibly, anode materials and the associated anode compartments must fulfill several criteria. Apart from avoiding side reactions leading to cell swelling and failure, the anode material must combine good conductivity, a suitable electrochemical stability window at a low voltage range, and low cost and toxicity.^[52] Elemental sodium is highly abundant and frequently used as an electrode material, with a very high theoretical capacity of 1166 mAh g^{-1} .^[43,53–56] However, uncontrolled growth of sodium dendrites hinders safe battery operation, ruptures separators, and shortens the device lifetime while still exhibiting low Coulombic efficiency and battery performance.^[57–61] Finally, light metals or alloy materials such as magnesium or aluminum promise access to a high theoretical specific capacity (Mg: 2200 mAh g^{-1} , Al: 2980 mAh g^{-1}) and can be considered as possible electrodes as well.^[62,63]

The wealth of materials developed initially for high-performance electrodes of sodium-ion batteries can be capitalized on.

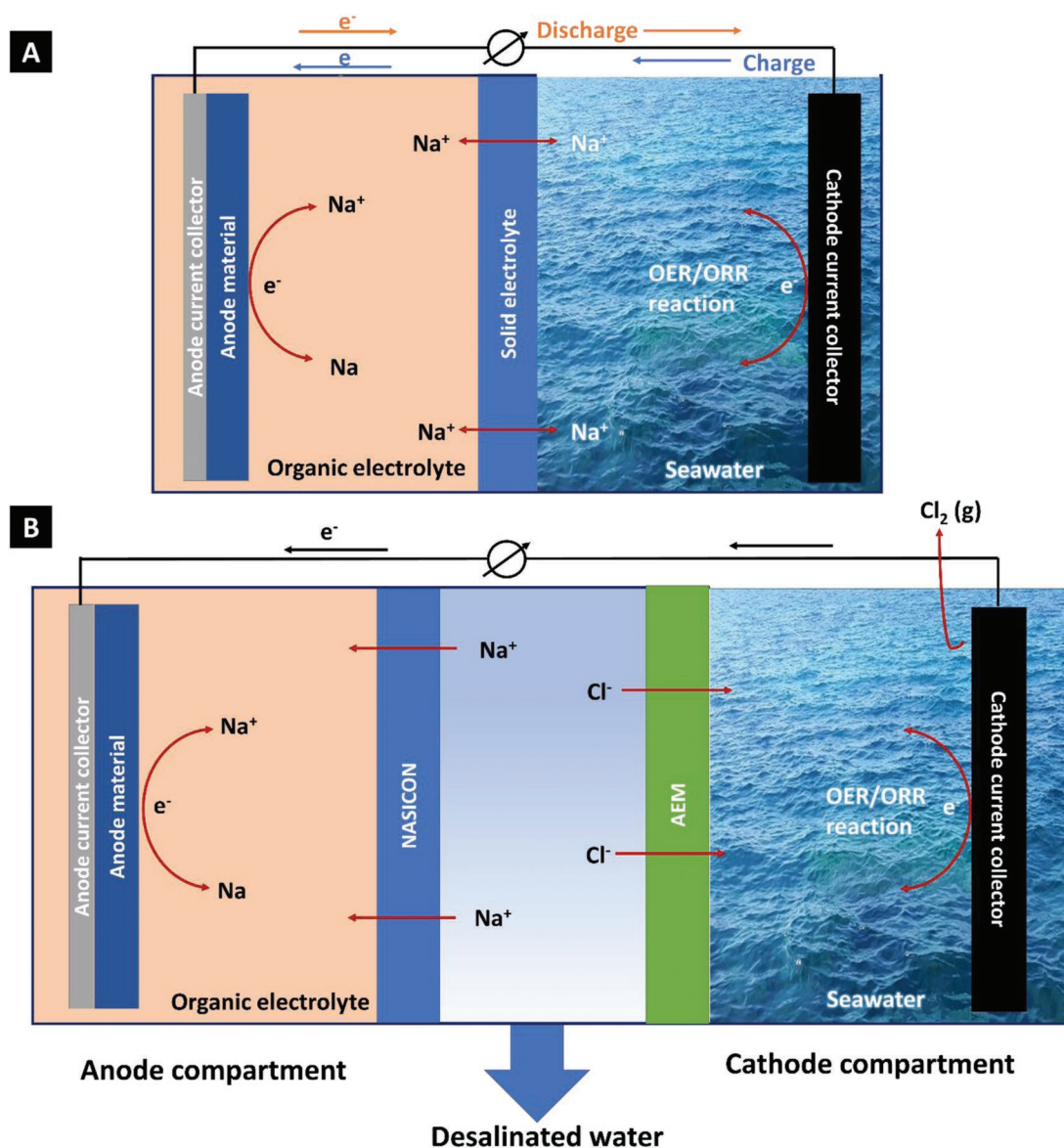


Figure 1. The operation principle of seawater battery A) for energy storage and B) for water desalination.

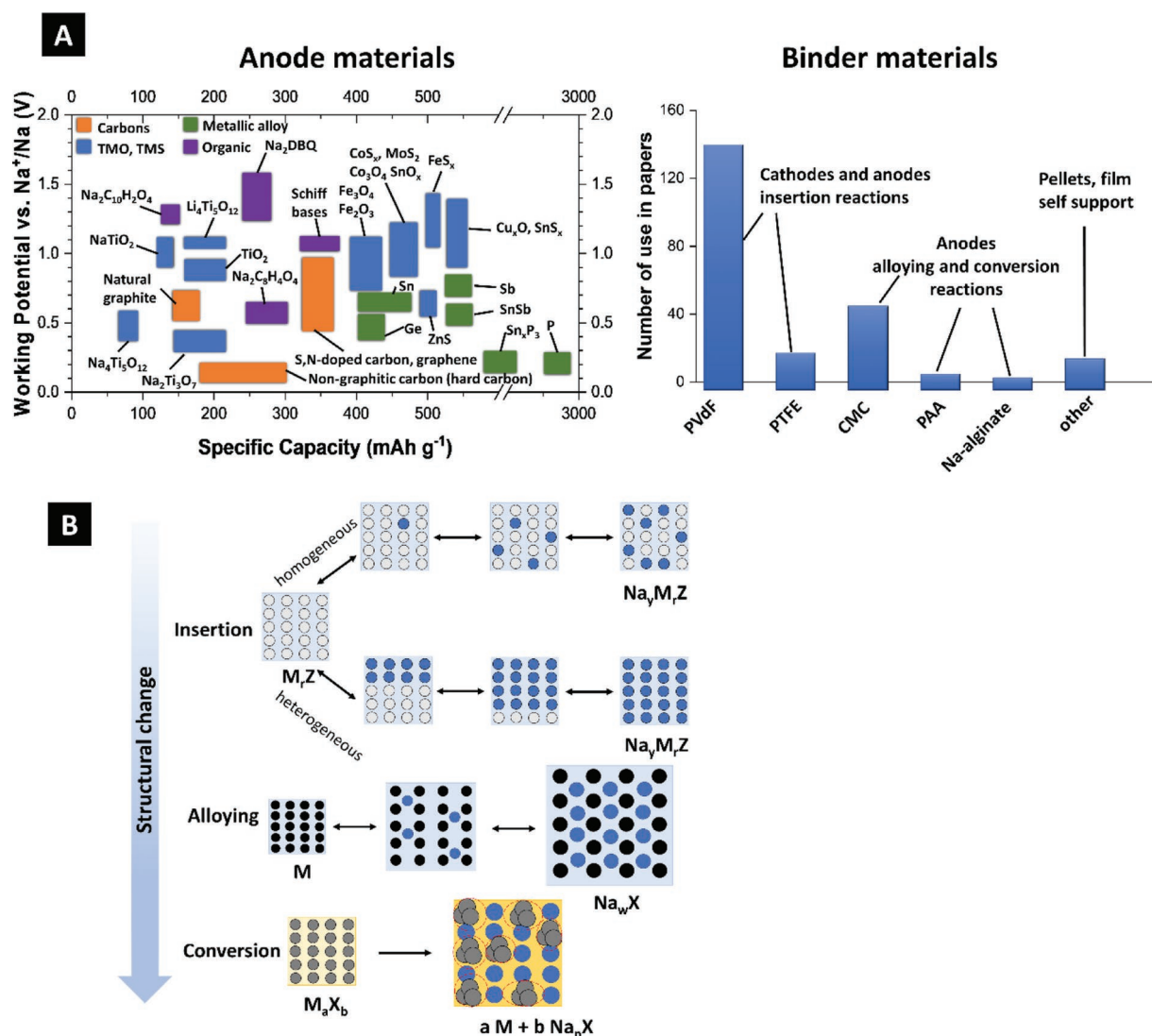


Figure 2. Overview of anode materials for sodium-ion batteries. A) Representation of the theoretical capacities of different anode materials and respective binder use in sodium-ion batteries. Adapted with permission.^[214] Copyright 2017, Royal Society of Chemistry. B) Schematic representation of varying reaction mechanisms observed in electrode materials. Adapted with permission.^[214] Copyright 2009, Royal Society of Chemistry. Abbreviation: PTFE = polytetrafluoroethylene, PVdF = polyvinylidene difluoride; CMC = carboxymethyl cellulose, PAA = polyacrylic acid, Na₂DBQ = disodium salt of 2,5-dihydroxy-1,4-benzoquinone.

Figure 2 schematically presents different reaction mechanisms of electrode materials and the expected theoretical capacities of these materials in sodium-ion batteries. Different types of anode materials interact with sodium in specific ways, including intercalation or conversion and alloying reactions. A commonly used intercalation material such as hard carbons can be adopted from its use in NIBs.^[51,64–68] Other cation intercalation materials are TiO₂, Li₄Ti₅O₁₂, or Na₂Ti₃O₇, the associated theoretical capacities of 335,^[69] 175,^[70] and 177 mAh g⁻¹,^[71] respectively. Nevertheless, these values are moderate compared to large charge transfer capacities associated with processes such as alloying and conversion reactions.

Alloying materials form Na-rich intermetallic compounds through alloying reactions and promise high-capacity materials due to their specific reaction mechanism.^[72] However, these materials have a significant volume expansion during

sodiation and desodiation, potentially leading to capacity fading.^[73,74] The strong forces can break the electrode and damage the electrode material. Some approaches are already known to prevent this rapid loss of capacity. For example, the volume change can be buffered, and composites can maintain the conductive path in the electrode with carbon or other layer-like structures. Successful applications in seawater batteries include Sn-C^[75] in an ionic liquid electrolyte or red phosphorous.^[49]

Conversion-type materials accomplish reversible charge storage via a phase transformation.^[76] The solid-state reactions result in new compounds with new properties. Conversion materials also exhibit a relatively large voltage hysteresis, providing low energy efficiency during charge/discharge cycling.^[77,78] Conversion materials also suffer from a significant volume change during cycling.^[79] As already reported material in a seawater

battery, Sb_2S_3 is a model material with a multistep conversion and alloying charge storage process.^[80] In a seawater full-cell, the synthesized antimony sulfide nanoparticle aggregates provided a specific capacity of 470–485 mAh g^{-1} at a discharge voltage of about 1.9 V after 50–70 charging and discharging cycles (corresponding Coulombic efficiency: 83–88%).^[81] By contrast, the initial discharge capacity was relatively low.^[81]

Comparing the specific capacities by using alloying or conversion-based materials in contrast to intercalation anode materials, one obtains values about 4–5 times as high. Typical carbon materials in seawater batteries provide a capacity of about 100–200 mAh g^{-1} , which is much smaller than alternative systems, such as red phosphorus (900 mAh g^{-1} ; **Table 1**).^[49]

2.1.2. Cathode

The unique design of seawater batteries and the underlying electrochemical processes make it impossible to use common battery electrode materials found in sodium-ion batteries. Also, the wettability of the cathode current collector and seawater catholyte must be considered to improve the battery performance (voltage efficiency).^[82] Since an electrocatalytic process is used, the cathode employs only seawater and a current collector. Referring to standard seawater data, the amount of salt in one liter of water reaches about 35 g.^[83] In addition to the main component of sodium chloride, many other cations and anions are found in standard seawater, such as magnesium, calcium, potassium, sulfates, bicarbonates, and fluorides (**Figure 3A**).^[83] The composition of seawater varies from place to place, depth to depth, and time to time, depending on the respective climate, conditions, and environment. Since there is no typical solid electrode in this system, a current collector is still required at this point. Electrons released from the anode part during deintercalation/dealloying are carried away via the current collector. The current collector also carries the cathode reactions (oxygen evolution reactions and oxygen reduction reactions) and is required for the associated charge transport. Compared to organic batteries with solid cathodes, the current collector requires special properties like the stability in saltwater, which is indispensable for their use in seawater batteries.^[53,84] Besides high electronic conductivity and electrochemical and mechanical stability, other criteria such as large surface area, uniformly distributed transport area, and a low mass are also considered.

Copper and aluminum foils are typical current collectors in alkali metal batteries. Depending on the potential, it can be decided which current collector can be used without forming alloys and other byproducts by also considering the cost-effectiveness. Since these metals are usually not stable in the presence of NaCl and after application of a potential, carbon-based collectors are the most common in seawater batteries.^[45] A seawater battery current collector offers sites for the cathode reactions and ensures the charge transport. This mandates a large interface surface area, good electrochemical stability, and high electrical conductivity. An attractive current collector material should also be cost-effective and, ideally, based on an environmentally friendly material. These requirements are, in large parts, met by carbon-based current collectors. Carbons

are abundantly available and offer high corrosion resistance in seawater, predestined for use in the former primary seawater batteries with the ORR and HER (hydrogen evolution reaction).^[85,86] Yet, the limited mechanical stability of carbon provides a limitation to its application.^[47]

There are different carbon materials explored on the cathode side.^[45] Carbon felts, which did not exhibit the previously explored weaknesses of carbon current collectors, showed mechanical stability, high flexibility, and conductivity.^[64,84] Figure 3B–D shows scanning electron images of carbons commonly used as cathodes. Senthilkumar et al. investigated the cathode side porous carbon with defects and oxygen functional obtained from bio-organic waste (grapefruit peels).^[87] The resulting materials provided efficient OER/ORR activities, a discharge capacity of 191–196 mAh g^{-1} , and 96–98% Coulombic efficiency over 100 cycles of the full-cell.

Zhang et al. used an electrolytic carbon sponge with an open design and a highly interconnected and macroporous framework.^[84] The bifunctional electrocatalytic OER and ORR activities yielded a low charge–discharge voltage gap, high voltage efficiency, high-power density, and long-term cycling stability.^[84] In another work by Park et al., activated carbon cloth was used as a current collector on the cathode side and compared to the performance of a low surface area carbon felt.^[64] In addition to the OER/ORR electrolytic activity, the carbon cloth electrode provides electrical double-layer formation. The hybrid electrochemical process improved the voltage/energy efficiency (86%) and power performance (16 mA cm^{-2}) of high surface area carbon cloth as the current collector for seawater batteries.^[64]

2.1.3. Ceramic Membranes

A sodium-ion-conducting membrane separates the anode and cathode compartments of seawater batteries. Such membrane materials are commonly employed as solid electrolytes in solid-state batteries.^[88] The stability of the membrane against different types of liquid electrolytes has to be preserved to guarantee stability in organic and aqueous solutions. Essential for the application in an electrochemical system is applying a high current and stability in a relatively wide electrochemical potential window for the highest possible capacity without degrading parts of the cell.^[89,90] In general, the solid electrolytes in seawater batteries also need to provide high sodium-ion conductivity, robust mechanical property, and ultralow porosity to avoid the penetration of electrolytes.

There are three main types of solid electrolytes that have the possibility of selective Na ion transport: ceramics, polymers, and inorganic composite.^[91–94] Given the mechanical stability and effective separation of the organic/aqueous sides, inorganic compounds and ceramic membranes are commonly used as solid electrolytes in seawater batteries. The most often used membrane materials are the inorganic $\beta''\text{-Al}_2\text{O}_3$ or sodium superionic conductor (NASICON) because of the high ion mobility and chemical stability.^[54,88] A general issue of ceramic membranes is their mechanical brittleness, which imposes specific considerations onto seawater battery design and scalability.

$\beta''\text{-Al}_2\text{O}_3$ is a layered fast ionic conductor closely related to the widely studied class of $\beta\text{-Al}_2\text{O}_3$ (**Figure 4A**). It consists of

Table 1. Comparison and summary of different parameters seawater battery in the state-of-the-art literature. CC: current collector.

Anode	Cathode/cathode current collector	Solid electrolyte	Liquid electrolyte	Mechanism	Cell setup	Capacity	Coulombic efficiency/voltage efficiency	Refs.
Prepatterned Cu/Al current collector (anode-free)	Seawater carbon felt	NASICON (Na ₃ Zr ₂ Si ₂ PO ₁₂)	1 M NaOTf in DME	–	2465-type coin cells	n.a.	98%	[127]
Sodium with nickel mesh	Seawater Ag foil	NASICON (Na ₃ Zr ₂ Si ₂ PO ₁₂)	1 M NaCF ₃ SO ₃ in TEGDME	OER/ORR	Seawater test cells (421Energy Co., Ltd)	n.a.	98.6-98.7% 90.3%	[111]
Hard carbon:Super-P carbon black:PVdF 8:1:1	Seawater carbon paper	1 mm thick β'-Al ₂ O ₃ 3 mm thick NASICON (Na ₃ Zr ₂ Si ₂ PO ₁₂)	1 M NaCF ₃ SO ₃ in TEGDME	OER/ORR	Seawater cell in water was from (421Energy Co Ltd)	≈10 mAh g ⁻¹ ≈120 mAh g ⁻¹ at 0.05 mA cm ⁻²	91%	[88]
Activated carbon fiber coated with Na metal	Simulated seawater carbon felt Pt wire Ag/AgCl Ref	PE separator NASICON (Na ₃ Zr ₂ Si ₂ PO ₁₂)	1 M NaCF ₃ SO ₃ in TEGDME	OER/ORR	Coin cells	20 mAh g ⁻¹ 0.6 mA (0.3 mA cm ⁻²)	n.a.	[194]
Na metal attached to Ni taps	Air cathode S-rGO-CNT-Co powder coating with PVdF on carbon felt electrocatalyst	NASICON (Na ₃ Zr ₂ Si ₂ PO ₁₂) PE separator	1 M NaCF ₃ SO ₃ in TEGDME	OER/ORR	Pouch cells	n.a.	n.a.	[112]
Hard carbon:Super-P carbon black:PVdF 8:1:1 On Cu foil	Ti mesh carbon Carbon paper	0.8 mm-thick NASICON (Na ₃ Zr ₂ Si ₂ PO ₁₂)	1 M NaCF ₃ SO ₃ in TEGDME	OER/ORR	–	296 mAh g ⁻¹ 0.025 mA cm ⁻²	98%	[129]
Na metal on stainless-steel CC	Seawater	NASICON membrane	1 M NaCF ₃ SO ₃ in TEGDME	–	Seawater battery coin cells	37 mAh g ⁻¹ 0.5 mA cm ⁻²	Na-BP-DME 99.5% over 10 cycles	[52]
Al, Mg, and Zn	NiHCF crystals:carbon black:PVdF 7:2:1 on carbon cloth	–	Seawater	–	Two electrode cells	57 mAh g ⁻¹ At 1 A g ⁻¹	n.a.	[55]
Na foil and Na/carbon composite on PAN-based carbon cloths	Seawater carbon felt	NASICON (Na ₃ Zr ₂ Si ₂ PO ₁₂)	1 M NaCF ₃ SO ₃ in TEGDME	–	Coin cell seawater battery	40 mAh g ⁻¹ At 1 mA	98%	[218]
Na metal or hard carbon Ni tap CC	Seawater Ti mesh and a sheet of carbon paper	0.8 mm thick NASICON (Na ₃ Zr ₂ Si ₂ PO ₁₂)	1 M NaCF ₃ SO ₃ in TEGDME	OER/ORR	–	190 mAh g ⁻¹ hard carbon 0.05 mA cm ⁻²	~96–98%	[87]
Using Na metal	Seawater heat-treated carbon felt	PE Hong-type NASICON (Na _{1+x} Zr ₂ Si _x P _{3-x} O ₁₂ , x = 2)	1 M NaCF ₃ SO ₃ in TEGDME	OER/ORR	2465-coin-cell seawater battery	n.a.	n.a.	[56]
Pristine or graphene-coated Cu	Seawater carbon felt	1 mm thick NASICON (Na _{1+x} Zr ₂ Si _x P _{3-x} O ₁₂ , x = 2)	1 M NaOTf-DME	–	Modified 2465-type coin cell flow cell	n.a.	95%	[219]
Sn-C:Super-P carbon black:PVdF 8:1:1	Seawater carbon paper	NASICON (Na ₃ Zr ₂ Si ₂ PO ₁₂)	1 M solution of NaClO ₄ in EC/DEC And sodium bis(trifluoromethanesulfonyl) imide (NaTFSI) and N-butyl-N-methyl-pyrrolidiniumbis(trifluoromethanesulfonyl)imide (Pyr14TFSI)	–	n.a.	~325 mAh g ⁻¹ Sn 312 mAh g ⁻¹ Sn 0.05 mA cm ⁻²	55% 1 st cycle 91%	[75]
Sodium metal/carbon cloth composite	Pyridinic-N catalyst, in a carbon cloth CC	1 mm thick NASICON (Na ₃ Zr ₂ Si ₂ PO ₁₂)	1 M NaCF ₃ SO ₃ in DME	OER/ORR	Coin cell anode Seawater flow battery tester	n.a.	n.a.	[169]

Table 1. Continued.

Anode	Cathode/cathode current collector	Solid electrolyte	Liquid electrolyte	Mechanism	Cell setup	Capacity	Coulombic efficiency/voltage efficiency	Refs.
Na metal or hard carbon:carbon black:Super-P:PvDF 8: 1:1 Ni taps CC	CMO nanoparticles: carbon black Super-P:PvDF 8:1:1 Air-electrode CMO catalyst	NASICON ($\text{Na}_{1+x}\text{Zr}_2\text{Si}_x\text{P}_3\text{O}_{12}$, $x = 2$)	1 M NaCF_3SO_3 in TEGDME	OER/ORR	Pouch cell seawater	190 mAh g^{-1} hard carbon 0.01 mA cm^{-2}	>96% energy 85%	[68]
Na metal foil	Carbon felt catalyst and CC	0.8 mm thick NASICON ($\text{Na}_{1+x}\text{Zr}_2\text{Si}_x\text{P}_3\text{O}_{12}$, $x = 2$)	1 M NaCF_3SO_3 in TEGDME	OER/ORR	Coin cell	n.a.	n.a.	[54]
Hard carbon:Super-P carbon black:PvDF 8:1:1	Seawater carbon paper	NASICON ($\text{Na}_3\text{Zr}_2\text{Si}_2\text{PO}_{12}$)	1 M NaClO_4 in EC/PC 1 M NaCF_3SO_3 in TEGDME		Flowing-seawater cell	118 mAh g^{-1} 125 mAh g^{-1} 0.05 mA cm^{-2} .	n.a.	[67]
Na metal at Ni mesh	90 wt% PNC-electrocatalyst:PvDF 9:1 carbon felt CC	0.8 mm thick NASICON ($\text{Na}_3\text{Zr}_2\text{Si}_2\text{PO}_{12}$)	1 M NaCF_3SO_3 in TEGDME	OER/ORR	Pouch cell of seawater batteries	n.a.	n.a.	[166]
Sodium metal or hard carbon	P2-type $\text{Na}_{0.5}\text{Co}_{0.5}\text{Mn}_{0.5}\text{O}_2$ layered electrocatalyst:SP-carbon:PvDF 8:1:1 carbon felt CC	Celgard NASICON	1 M NaCF_3SO_3 in TEGDME	OER/ORR	Coin cell Flow cell tester	183 mA h g^{-1} at 0.1 mA	85% Coulombic efficiency 80% voltage efficiency	[66]
Hard carbon: SuperC45: CMC 8:1:1 On Cu foil	Seawater Carbon felt	NASICON ($\text{Na}_3\text{Zr}_2\text{Si}_2\text{PO}_{12}$)	0.1 M NaFSI –0.6 M $\text{Pyr}_{13}\text{FSI}$ –0.3 M $\text{Pyr}_{13}\text{TFSI}$ and 0.1 M NaFSI –0.6 M $\text{Pyr}_{13}\text{FSI}$ –0.3 M $\text{Pyr}_{13}\text{TFSI}$ with 5 wt% EC 1 M NaCF_3SO_3 in TEGDME	OER/ORR	Coin cell	290 mA h g^{-1} hard carbon 1.0 C (= 300 mA g^{-1})	ILE-EC 98% energy efficiency (80.5%) 76.3% for the LE	[124]
Sodium or hard carbon:SuperP:PvDF 8:1:1 Ni mesh	Seawater NiHCF:SuperP:PvDF 8:1:1	0.8 mm thick NASICON	1 M NaCF_3SO_3 in TEGDME	OER/ORR	Pouch cell	56 mA h g^{-1} 20 mA h g^{-1}	95% to 98%	[65]
Sodium anode Hard carbon Ti mesh	Seawater activated carbon cloth (ACC) and carbon felt (CF; PAN-based, CNF)	PE 1 mm thick NASICON ($\text{Na}_{1+x}\text{Zr}_2\text{Si}_x\text{P}_3\text{O}_{12}$, $x = 2$)	1 M NaCF_3SO_3 in TEGDME	OER/ORR	Coin cell	16.2 mA cm^{-2}	energy efficiency of 78% ACC-seawater battery CF-seawater battery (60%)	[64]
Na metal or a-Sb ₂ S ₃ electrode	Natural seawater air electrode	0.8 mm thick NASICON ($\text{Na}_{1+x}\text{Zr}_2\text{Si}_x\text{P}_3\text{O}_{12}$, $x = 2$)	1 M NaClO_4 dissolved in a mixture of EC/DEC (1:1) with 5 wt% FEC	OER/ORR	Seawater flow cells (421Energy Co., Ltd)	470–485 mA h g^{-1} 0.05 mA cm^{-2}	83–88%	[81]
Red phosphorus: SuperP:polyacrylic acid 7:1:2 Al foil CC Or Na	Natural seawater carbon felt	NASICON ($\text{Na}_3\text{Zr}_2\text{Si}_2\text{PO}_{12}$)	1 M NaClO_4 in EC:DEC + 5%FEC	OER/ORR	Coin cell	900 mA h g^{-1} composite 200 mA g^{-1} composite	>92%	[49]
Na metal Stainless steel	Natural seawater Activated carbon cloth (ACC-5092-20, Kynol)	PE NASICON ($\text{Na}_3\text{Zr}_2\text{Si}_2\text{PO}_{12}$)	1 M NaCF_3SO_3 in TEGDME	OER/ORR	Coin cell	n.a.	n.a.	[53]

Table 1. Continued.

Anode	Cathode/cathode current collector	Solid electrolyte	Liquid electrolyte	Mechanism	Cell setup	Capacity	Coulombic efficiency/voltage efficiency	Refs.
Liquid anodes (Na-BPs, Na-PYRs, and Na-BP-PYRs) and the red phosphorus Semiliquid anodes (P/C@Na-BP-PYRs and the P/C@LE)	0.47 M NaCl carbon fabric	NASICON ($\text{Na}_3\text{Zr}_2\text{Si}_2\text{PO}_{12}$)	LE: 1 M NaPF_6 in DEGME	OER/ORR	2465-type seawater coin cells seawater flow cell testers	7.5 mAh cm^{-2} 0.5 mA cm^{-2}	n.a.	[124]

alumina blocks arranged in a spinel structure in between which the mobile sodium cations are postured in conductor planes.^[95] β' - Al_2O_3 is characterized by a higher proportion of sodium ions than other compounds in this class, which can be explained by the structural arrangement of the conduction planes, which comprises a network of sodium ions in the stoichiometric compound.

Kim et al. compared β' - Al_2O_3 with a type of NASICON in a rechargeable seawater battery using a hard carbon anode and seawater as the catholyte.^[88] It has been shown that protonated H_3O^+ species in β' - Al_2O_3 are allowed to pass through the conduction band into the anode compartment of the seawater battery, which in the end leads to not

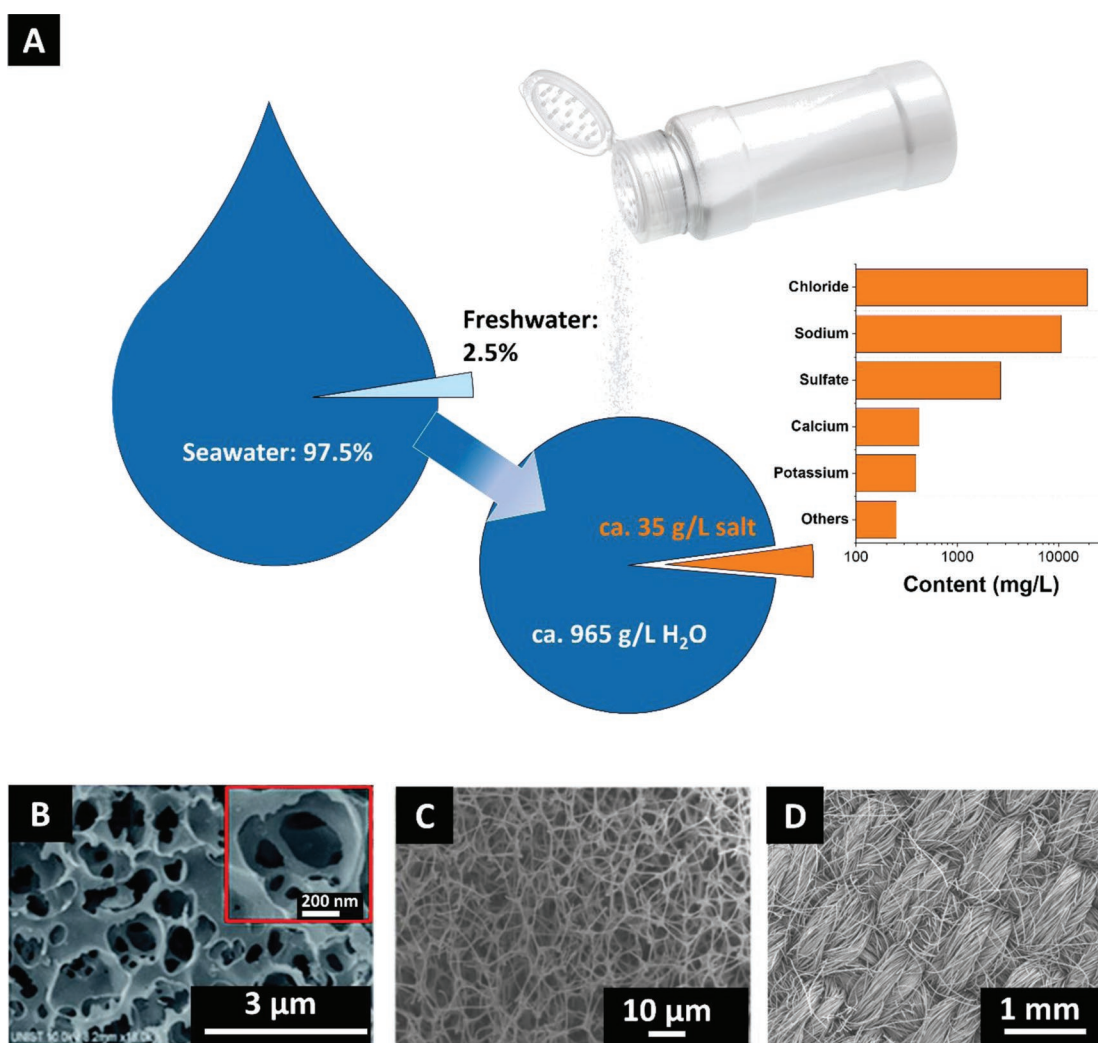


Figure 3. A) Main components and distribution of different ions in natural seawater. Scanning electron images of carbonaceous materials used as cathode current collector in seawater battery B) carbon felt, Reproduced with permission.^[87] Copyright 2018, Elsevier, and C) carbon sponge. Reproduced with permission.^[84] Copyright 2019, Elsevier, and D) carbon cloth. Reproduced with permission.^[64] Copyright 2019, Elsevier.

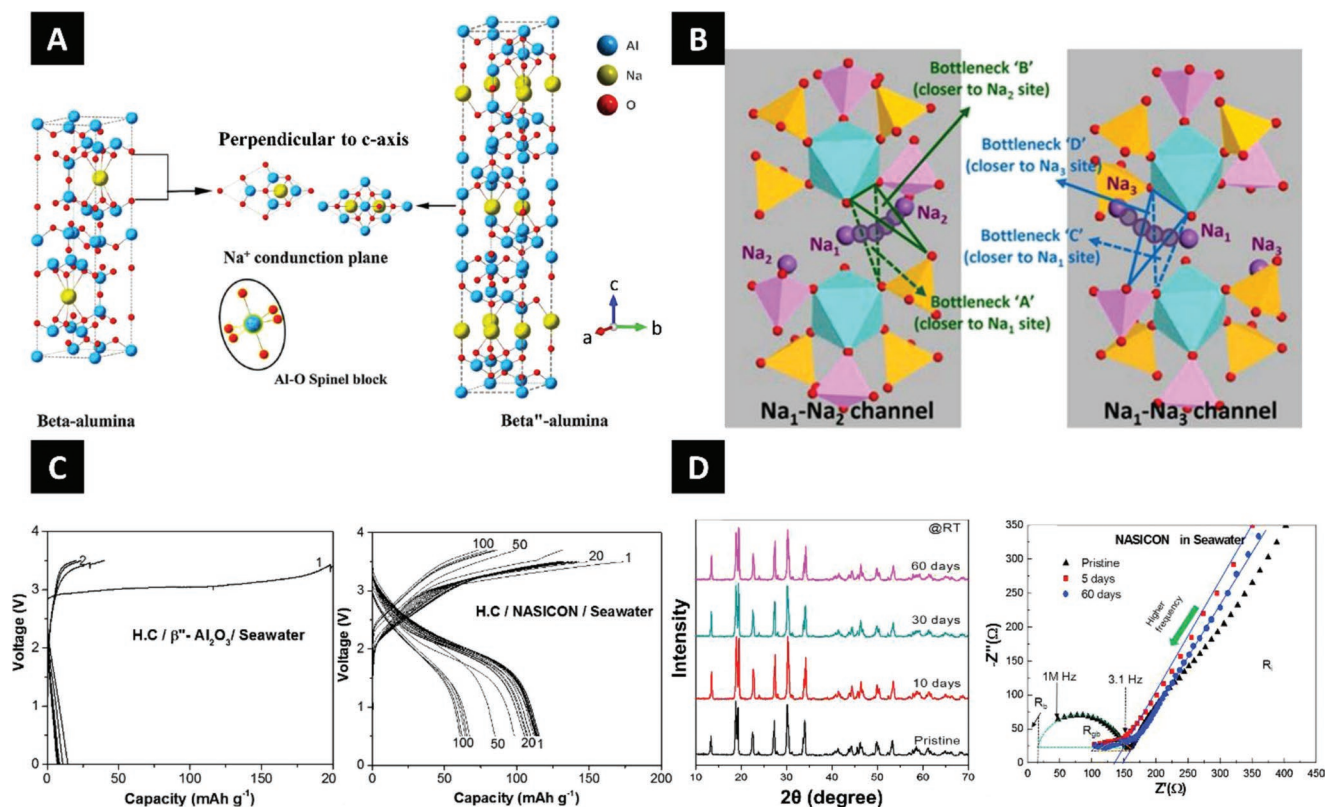


Figure 4. A) The structure of β - Al_2O_3 and β' - Al_2O_3 . Reproduced with permission.^[216] Copyright 2020, Elsevier. B) The structure of $\text{Na}_3\text{Zr}_2\text{Si}_2\text{PO}_{12}$. Reproduced with permission.^[217] Copyright 2016, American Chemical Society. C) The performance of rechargeable seawater batteries with β' - Al_2O_3 (left) and NASICON (right) as the solid membrane. Reproduced with permission.^[88] Copyright 2016, Elsevier. D) Structural changes of β' - Al_2O_3 and NASICON membranes during stability testing. Reproduced with permission.^[88] Copyright 2016, Elsevier.

satisfactory matched performance. NASICON-structured materials are desirable because they exhibit high structural stability and fast ionic conductivity ($10^{-3} \text{ S cm}^{-1}$) because of their suitable tunnel size for sodium-ion migration in a 3D framework (Figure 4B).

In general, there are mainly two different NASICON types found for seawater batteries. The Hong-type NASICON ($\text{Na}_{1+x}\text{Zr}_2\text{Si}_x\text{P}_{3-x}\text{O}_{12}$) offers the advantage compared to the von Alpen-type ($\text{Na}_{1+x}\text{Zr}_{2-x/3}\text{Si}_x\text{P}_{3-x}\text{O}_{12-x/3}$) NASICON that it can be produced at lower temperatures (1250°C), even compared to β - Al_2O_3 ($\geq 1600^\circ\text{C}$ β - Al_2O_3 , $\geq 1300^\circ\text{C}$ Alpen-type NASICON), and still achieves very high densification.^[96,97] In some works, the density ($\leq 78\%$) of the synthesized NASICON membranes only insufficiently prevents water from penetrating the membrane. For this reason, the remaining open pore channels are filled with epoxy resin.^[90,98] A recent report by Go et al. reported that a vA-NASICON ($\text{Na}_{3.1}\text{Zr}_{1.55}\text{Si}_{2.3}\text{P}_{0.7}\text{O}_{11}$) has even better and more suitable properties compared to the Hong-type NASICON.^[99] Due to the changed composition and the microstructure, higher ionic conductivity and a lower grain boundary resistance can be obtained. In addition to the higher bend strength, an improved voltage efficiency and higher power output for use in a seawater battery could be demonstrated in this way.^[99]

NASICON structures are known for their use as materials in sodium-ion batteries, both as electrode material and solid

electrolytes. Goodenough and Hing discovered this electrode material and showed the formula $\text{Na MMA}(\text{XO}_4)$, where M and MA represent metals and X are silicon, phosphorus, or sulfur.^[100,101] Due to the diverse use and the different structure of NASICON structures, a unique and targeted design is possible. Their open framework allows them to intercalate up to four sodium ions, making them a promising electrode material in sodium-ion batteries.^[102] With their fast ionic diffusion, relatively high structural facile production/synthesis, stability in different solvents, and rich structural diversity, they are also attractive for seawater batteries. The catholyte, seawater, provides an ample supply of sodium ions to be transported across the NASICON membrane. Corrosion is inevitable even for NASICON, which provides much higher stability than β' - Al_2O_3 membranes (Figure 4C,D).

In the work of Kim et al., NASICON membranes were immersed in seawater for several days.^[88] A slight change in the crystalline structure was observed due to changes in intensity ratios in the subsequent X-ray analysis, which was also reported in other publications.^[103,104] A proposed mechanism can be attributed to a topotactic ion exchange between Na^+ and H_3O^+ ions at the surface of the NASICON grains.^[103,104] Many factors influence this behavior, such as the applied current density, which at high rates (2 mA cm^{-2}) causes structural degradation with irreversible phase deformation and Na^+ extraction.^[54] However, further detailed investigations need to be carried out

in the future to better understand this process (and membrane degeneration in general).

2.1.4. Liquid Electrolyte

Besides the solid electrolyte (membrane), a thorough selection of the liquid electrolyte is of defining importance. In sodium-ion batteries, an inorganic conductive salt dissolved in organic solvents is mainly used to guarantee ionic conductivity between the electrodes. The key points that apply here, such as a wide electrochemical stability window, thermal stability, or a low electronic conductivity, can only address the needs of the seawater battery to a minimal extent. However, this type of electrolyte shows relatively low stability at low potentials, so the Coulombic efficiency is generally low in the first cycles. The solid electrolyte interphase (SEI), the protective cover layer at the electrode surface, is also formed due to electrolyte decomposition.^[105] The ideal liquid electrolyte would combine high ion mobility, high electrochemical stability, low cost, natural abundance, and low environmental impact.

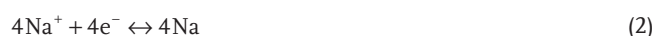
The electrolyte stability and SEI formation are essential in seawater batteries' operation and stability. The SEI is a passivating and isolating boundary layer that, ideally, protects the active material from direct contact with the electrolyte.^[105] The SEI prevents continuous and degradative reactions between the electrolyte and the electrode material depending on the applied potential and type of electrode material.^[106] The SEI is formed during the first cycle because of the (initial) instability stability of organic electrolytes at low potentials.^[107] Applying organic electrolytes leads to forming a solid and dense SEI at the anode and protects the electrolyte from further decomposition.^[108] An ideal SEI should have a low electronic but high alkali-ion conductivity, an appropriate thickness, good flexibility, and uniform morphology.^[109,110] If this layer is too thick, the cell's capacity will decrease. However, especially in the early stage of seawater battery research, an electrolyte adapted from the NIB was often used in the anode compartment; that was later revised and replaced because its properties could not lead to high performance in seawater batteries.

An organic electrolyte that has been one of the most successful in seawater batteries is a 1 M sodium trifluoromethanesulfonate (NaCF₃SO₃) solution in tetraethylene glycol dimethyl ether (TEGDME)^[53,64,111,112] since the SEI layer seems beneficial with the TEGDME-based electrolyte.^[67] A disadvantage for the anode section is the occurrence of side reactions with resulting gas evolution in this compartment during cycling. This causes a swelling of this cell section; therefore, the battery cell cannot run for a long time and in stable conditions but rather breaks down relatively quickly.^[113] It is not an easy task to solve this problem due to the high reactivity of the commonly used metallic sodium anode. Thereby, achieving long performance stability remains a tall challenge. Lee et al. developed an alternative system using sodium-biphenyl-dimethoxyethane (Na-BP-DME) as a redox-active.^[52] This approach allows the chemical and electrochemical stability of the anode side to be optimized, which ultimately represents a decisive advantage for practical applications. Compared with the conventional, nonaqueous

liquid electrolyte (NaTf-TEGDME), the Na-BP-DME anolyte showed enhanced chemical and electrochemical stability with better cycling stability and cost-effectiveness.

2.1.5. Electrocatalyst: Oxygen Evolution Reaction and Oxygen Reduction Reaction

Charging and discharging a seawater battery combines the concurrence of sodium-ion reactions (much common to NIBs) at the anode and an electrocatalytic reaction involving seawater at the cathode/catholyte side.^[68,114] Due to the usually very open-structured design of the cathode in the seawater battery, this part is continuously exposed to the renewed inflow of oxygen from the environment. The battery cell takes advantage of this and uses this abundant gas directly to discharge as electricity. Due to the excess of (dissolved) oxygen, it actively participates in the redox reaction of the seawater catholyte, which leads to the well-known OER/ORR shown in Equations (1)–(3)



The facile reduction of oxygen dissolved in seawater carries the ORR process. During discharging, the stored chemical energy is converted to electricity, and charge-compensation is accomplished by transferring sodium ions from the anode compartment across the membrane (back) into the seawater. This two-electron reduction pathway process ($\text{O}_2 + \text{H}_2\text{O} + 2\text{e}^- \rightarrow \text{HO}_2^- + \text{OH}^-$) is kinetically advantageous but will cause a lower theoretical cell voltage of seawater batteries from 3.48 to 2.9 V with the pH of seawater at 8. This can be avoided by using the selective four-electron reduction pathway ($\text{O}_2 + 2\text{H}_2\text{O} + 4\text{e}^- \rightarrow 4\text{OH}^-$) electrocatalysts, which lead to a thermodynamically favored process (pH = 8) with more charge carriers.^[45] This reaction plays a crucial role in the process, strongly linked to the resulting cell performance. An electrocatalyst can be used as a critical component to enhance the reaction kinetics, and the cathode current collector can be carefully chosen.

To develop an optimal catalyst for this complex system, the following criteria must be fulfilled: 1) high catalytic activity, 2) high pore volume with a large specific surface area, balancing ion transport, and electrode kinetics, 3) high density of accessible, active sites with a homogenous distribution to enable a low OER and high ORR potential, 4) (electro)chemical and mechanical stability to enable device longevity, 5) high and volumetric activity, and 6) cost-efficiency associated with available resources.^[45] Electrocatalysts used in seawater batteries can be divided into nonprecious metal oxide-based electrocatalysts (Co_xMn_{3-x}O₄,^[68] Co₃V₂O₈^[115]), carbon-based electrocatalysts (mostly doped carbon black, nanotubes, porous carbon, graphene, and nanofibers),^[116–119] and hybrid or composite electrocatalysts (graphene-carbon nanotube-cobalt hybrid)^[112] as an alternative to the usual precious-metal-based electrocatalysts (iridium oxide, ruthenium oxide, and Pt/C). Catalysts such as

iridium oxide and ruthenium oxide are well-known for providing an attractive OER performance.^[120,121] Most commonly, Pt/C catalysts are being used as an accelerator for the ORR.^[113] However, using such noble metal catalysts does not align with the cost sensitivity intrinsic to large-scale applications.^[122]

2.1.6. Cell Design

Since operation with only one electrode compartment is not energy-efficient, operation in the aqueous medium for the anode and cathode sides is not promising. One of the reasons for this is that most high-capacity materials are not stable in aqueous media, and the potential window is limited to the stable range of water (1.2 V). The main seawater battery design can be divided into an organic anode compartment and a seawater cathode compartment. Larger systems are also being designed and successfully used for applications beyond energy storage. These systems are mostly built as dual-use systems; while water is desalinated during the charging process, the charge is stored during subsequent discharging. Therefore, at least one additional compartment is responsible for the desalination, besides the sodium collection compartment and another compartment. This extra compartment, which consists of the seawater and a current collector, is used in this additional application in the work of Bae et al. as a carbon capture compartment.^[123] In this hybrid system, silver was used to form AgCl particles during the charging of the system and the resulting oxidation on the Ag electrode. For this purpose, Na-ions are brought into the anode compartment in the same step as already done in the well-known seawater battery. In addition, the water is desalinated. In the subsequent discharge process, the Na metal in the Na-compartment is oxidized to ions and made available to the carbon capture side. At the same time, the ORR takes place, generating electrical energy. The presence of Ca²⁺ in the seawater and the relaxed OH⁻ leads to the formation of CaCO₃ from the CO₂ gas.^[123]

Seawater battery design also capitalizes on established concepts and components from other energy storage segments (lithium-ion and sodium-ion batteries). So far, a modified coin cell, shown in **Figure 5A**, has been used in most cases, mostly with a direct connection to a flow-type cell tester. The pouch cell is also being used more and more. Recently, new optimization attempts have emerged that employ a rectangular cell produces an improved charge–discharge performance (comparison illustrated in **Figure 5B**). With improved conductivity and efficiency in stacking, this cell should show enhanced competitive performance with other already published commercial battery systems.^[124]

2.2. Criteria Evaluating the Performance of Seawater Battery

The individual parts of the seawater battery are combined in a complex structure and are fully functional, which optimally results in an environmentally friendly battery cell with good performance. The following sections outline the criteria for seawater battery performance. An illustrative graph is given in **Figure 6** showing the actual performance of the seawater battery as well as the future design goals considering different key points

2.2.1. Capacity

The capacity describes the charge storage capacity of an electrochemical energy storage device. The capacity indicates the amount of electrical charge Q that a battery can supply or store. Capacity is usually expressed in ampere-hours (Ah), and it is commonly normalized to mass (Ah g⁻¹) or volume (Ah cm⁻³), thus forming the basis for the battery field naturalized nomenclature of mAh g⁻¹. This index is applied to describe the performance of alkaline metal batteries, as well as likewise for seawater batteries. The capacity also depends on the type/amount of active material, discharge current, discharge voltage, and temperature^[125] and can be used to calculate how long a given current or how long a specific current, or how much current can be extracted over a specific time. The limit of electrochemical charge storage is the theoretical capacity of a material given by Faraday's law of electrolysis.^[126] The theoretical capacity cannot be reached in practical applications due to polarization effects or losses due to side reactions or material defects. The overall capacity of the cell can only be as good as the weakest component of a battery. Hence, anode and cathode must provide the same capacity, resulting in a balanced and perfectly composed interaction. While a high capacity is desired, other criteria and parameters are also critical. Typical values of the capacities, which are reached in the state-of-the-art seawater batteries, range from 10 mAh g⁻¹ (β'' -Al₂O₃ membrane and hard carbon anode^[88]) to 900 mAh g⁻¹ (NASICON membrane and red phosphorus anode^[49]), depending on the used electrode material, based on the reaction mechanism and the applied current.

2.2.2. Efficiency

Efficiency is a critical evaluation criterion that describes a particular system's performance, especially for electrochemical systems. Three parameters (Coulombic efficiency, energy efficiency, and voltage efficiency) are typically used in this context.

The Coulombic efficiency (CE) is the ratio of the amount of charge (Q) flowing through the cell during discharging and charging and will be expressed as a percentage. Optimally, the standard potential of the cell at the start of charging should correspond to the lower end-of-charge voltage at the subsequent discharge. The Coulombic efficiency is based on losses such as SEI formation and aging effects. Past works show a Coulombic efficiency in the range of 76–98%,^[51,111,127] whereas commercial lithium-ion batteries typically show values above 99%.

Two more efficiency values are to be considered. First, the voltage efficiency (VE) represents the voltage ratio between charging and discharging, considering the internal resistance and different polarizations. Second, the energy efficiency (EE) is a derivative of the Coulombic efficiency and the voltage efficiency (EE = CE × VE).^[128] Several conditions, such as the temperature, electrolyte conductivity, specific current, and the selection of the membrane/separator, influence the values of the efficiencies. In general, the efficiency of the seawater battery can be evaluated with all these three factors. Commonly, the Coulomb efficiency is taken as a comparative value to determine the capacity loss cycle by cycle, which is an essential parameter for predicting the remaining battery life.

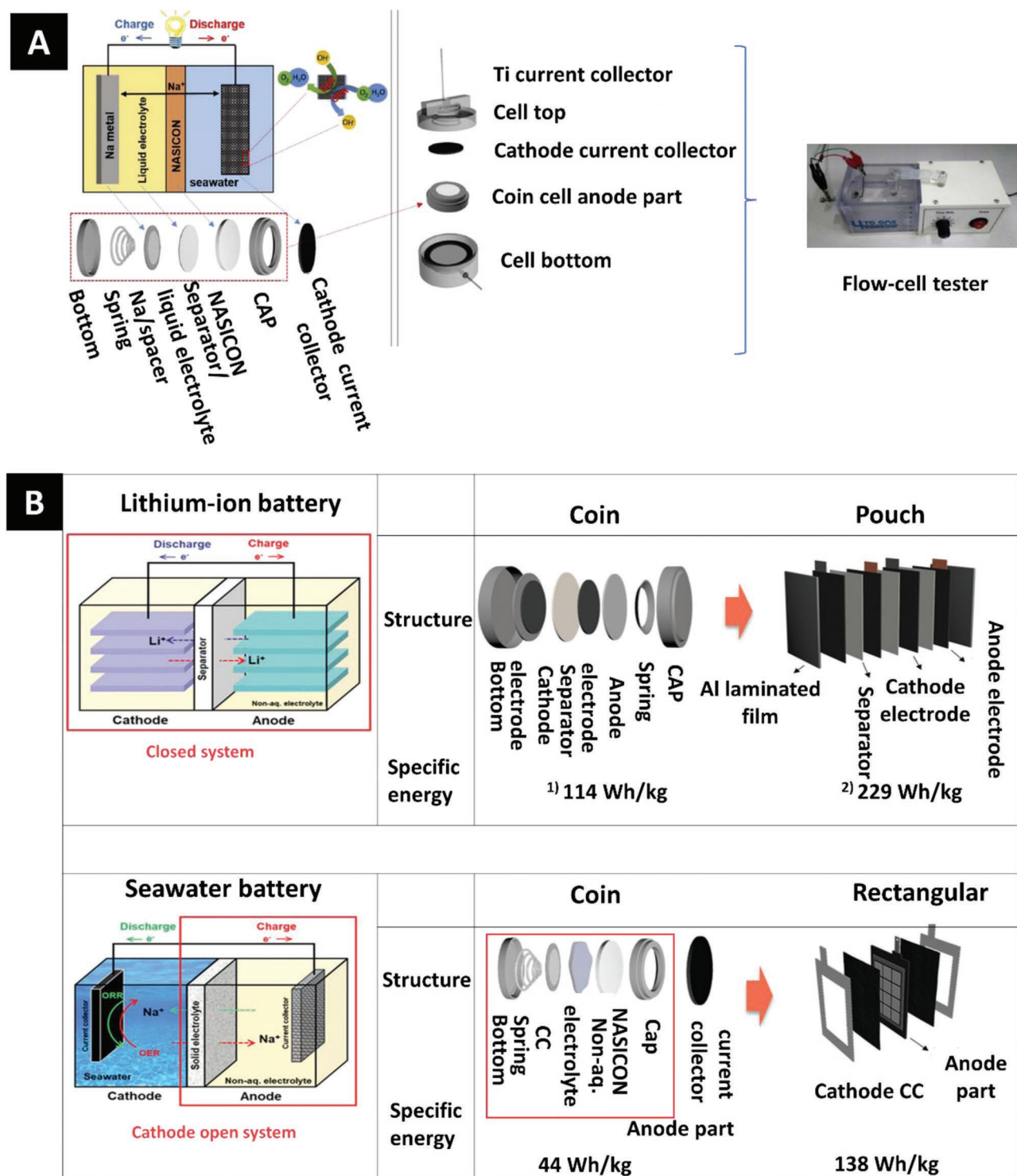


Figure 5. State-of-the-art seawater battery cell set up. A) Schematic diagram of the seawater battery (top) and the integrated cell components of the coin-type cell (bottom) and assembled coin-type cell with flow-cell tester adapted and modified with permission from.^[82] Copyright 2018, Elsevier Note: (1) PD2450 rechargeable Li-ion battery, Routejade. (2) LG325134115 Li-ion polymer battery, LG chem. B) Scheme of the operating mechanism of a lithium-ion battery compared to a seawater battery and the corresponding unit cell adapted and modified with permission from.^[124] Copyright 2020, John Wiley and Sons. CC = current collector.

2.2.3. Stability and Performance Longevity

In addition to the efficiency and capacity, which mainly characterize the instantaneous consumption of a state, the cell's

lifetime and stability are critical parameters for evaluating seawater batteries. In addition to all the other factors involved in the aging of battery cells and several side reactions, the stability of the solid electrolyte in the aqueous medium (NaCl solution)

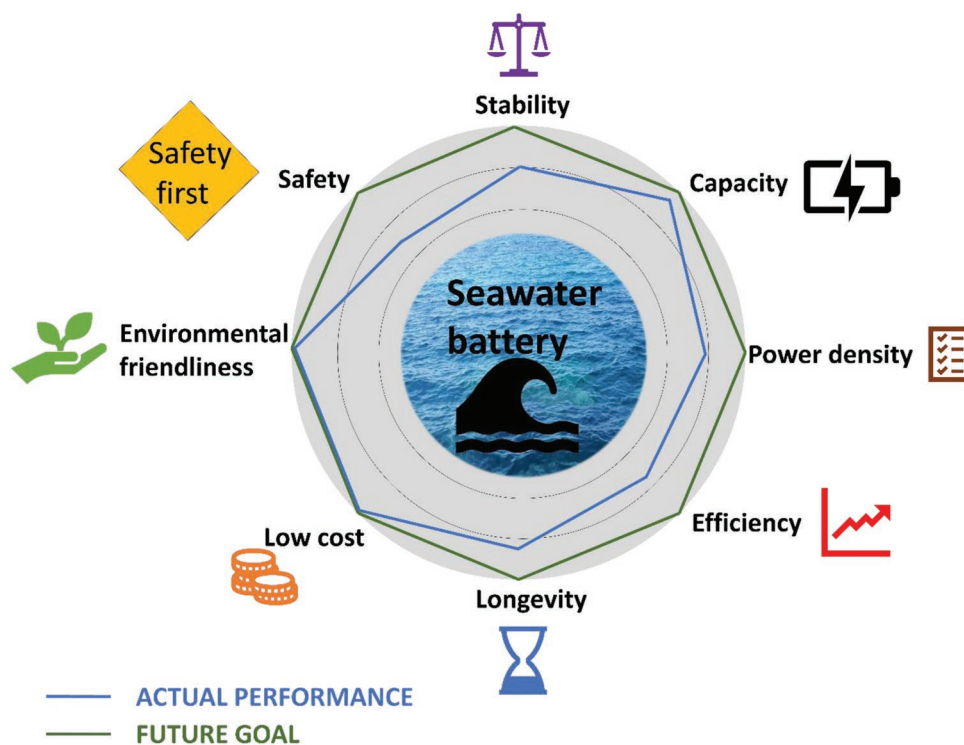


Figure 6. Parameters of designing a good performing seawater battery.

is a limiting factor. The cycle numbers typically reported for seawater batteries are 20–100 cycles^[52,55,56,87,129] with satisfying capacity retention. Therefore, the aim is to reduce these limiting factors as far as possible to create batteries that are as long-lasting and stable as possible.

2.2.4. Safety and Environmental Friendliness

Seawater batteries present a particular issue as many device types employ both metallic sodium and water. A dangerous and unsafe action can also happen, for example, by forming Na dendrites, which can then cause a short circuit in the cell and trigger a simple ignition of the battery.^[113]

An equally important aspect is the environmental friendliness of seawater batteries. There is the environmental hazard of some materials used as electrodes or even organic electrolytes. As common in the battery industry, polyvinylidene fluoride (PVdF) with *N*-methyl pyrrolidone (NMP) as its respective solvent is often used to prepare the electrode coating.^[55,130–132] The environmental concerns of NMP are aggravated by health concerns, such as cancerogeneity and the cause of respiratory difficulties, and excessive mortality mandate to explore safer and greener alternatives.^[133] As electrolytes are often adopted from the NIB community, the safety risks also apply to seawater batteries. So, the physical hazards associated with conventional NaClO_4 and carbonate-based electrolytes are well documented.^[134,135] Sometimes, this can result in elevated temperature, large combustion enthalpy, and high flammability.^[135]

It is also necessary to consider recycling after the cell has reached the end of its battery life. So far, no work proposes or

applies the recycling of seawater battery components. While the metallic components may be straightforward to recycle and repurpose, issues arise with ceramic ion-exchange membranes. However, the ceramic membranes may well be the most cost-intense component; therefore, their recyclability may be highly desirable.

2.3. Limitations and Advantages of Present-Day Seawater Batteries

Due to the growing electrification and increased demand for renewable energy storage systems, exploring alternatives and substitutes to existing primary power sources is necessary. These include, among other things, that the lithium-ion batteries must consider increased prices due to the exhausted resources of Li and the concerns about geopolitical and environmental aspects. Additionally, the typical metal-ions batteries, like lithium-ion and sodium-ion batteries, the cathode accounts for 30% to 35% of the total costs (Figure 7A).^[49]

Using natural seawater as the catholyte is highly cost attractive, abundantly available, and rich in sodium ions. Seawater can be circulated along the aqueous components to mitigate possible heat-buildup in large-scale modules.^[43] So far, it is not common in the seawater battery community to present the material's rate stability, and only a few works provide such data.^[51]

2.3.1. Issues at the Anode

On the anode side, if this is not an elementary anode, there are often simply degradation problems compared to those in

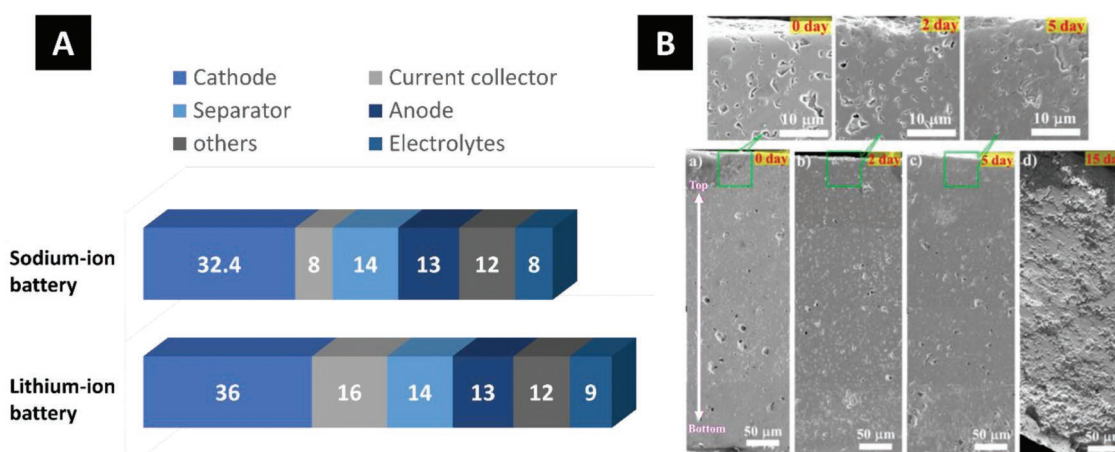


Figure 7. A) Comparison of cost contribution of each component for lithium- and sodium-ion battery system in percent. Reproduced with permission.^[49] Copyright 2014, John Wiley and Sons. B) Scanning electron images of the polished surfaces of the Hong-type NASICON ceramic samples immersed in seawater at 80 °C for 0 d, 2 d, 5 d, and 15 d. Reproduced with permission.^[45] Copyright 2017, American Chemical Society.

a NIB.^[136] One problem is the proper selection of the binder. Many systems have been adopted directly from the lithium-ion battery community without considering a seawater battery's unique (electro)chemical setting. The choice of the binder significantly influences the battery life, costs, and the avoidance of toxic organic solvents.^[137] PVdF is a standard binder in lithium-ion batteries. Due to the low number of functional groups, it has the advantage of low reactivity, good adhesion properties, and electrochemical stability.^[138] Still, PVdF binder can also cause system instability as other side reactions may occur. For example, using fluorinated binders leads to reductions that influence the cell reaction and reduce the capacity and performance of the cell.^[139] Sodium in the presence of the PVdF binder may also destabilize the cell.^[140] The decomposition of PVdF weakens the electrode, so individual particles may become detached and act as insulators. This results in lower efficiency and high capacitance loss.^[141,142] The formation of SEI also has a significant influence on the cell's performance. PVdF, for example, has a significantly lower cycle performance as it continuously reduces carbonate solvents, resulting in a (too) thick or unstable SEI layer.^[143]

A further problem known from sodium-ion batteries relates to using elemental sodium as an electrode. During electrochemical cycling, dendrites can occur, and uncontrolled growth of tree-like Na dendrites hinders safe battery operation and shortens lifetime while still exhibiting low Coulombic efficiency.^[57–61] Therefore, limiting or avoiding the growth of sodium dendrites is crucial. The future of seawater battery electrode materials may well be with anode systems that do not require binders or elemental sodium, such as the redox-mediated red-phosphorous semiliquid anode system.^[144]

2.3.2. Stability of the Membrane and Cathode in Saltwater

The selective sodium permeable membrane's stability is highly important for seawater batteries. Like the rarely used β' -Al₂O₃ membrane, NASICON also shows signs of aging after a certain period (Figure 7B), whereby different stresses build up inside the NASICON ceramic during the structural

degradation process and increased compressive stress can be observed. Likewise, investigations by Jung et al. have described the local compaction of NaCl at the surface, which can be related to a reaction of the chloride ions with the sodium species from the NASICON structure.^[145] These exposed sodium sites get occupied by H₃O⁺ ions in a subsequent reaction, which leads to volume changes and intense precipitation of NaCl.

Comparing the energy densities of different energy storage systems, the seawater battery with an energy density of mostly <150 Wh kg⁻¹^[65] has been relatively moderate. In comparison, considering a commercial lithium-ion battery, a conventional battery can deliver up to four times the energy density (250–590 Wh kg⁻¹).^[6,146] The reasons are complex but can be due to the low capacity, achieved mainly by limitations in the anode and cathode selection and the low working voltage. At least one compartment must continuously be operated in the aqueous medium. However, optimizing the cathode materials remains challenging since they have to be stable in the aqueous medium and resistant to side reactions concerning the OER and ORR.

Despite this knowledge and further studies on undesired side-reactions in OER/ORR on the cathode side, there is still a lack of a more profound understanding of performance failure, especially performance degradation. From the transfer from fuel cells, it could be assumed that the primary carbon material used as a cathode current collector can be oxidized by a corrosion reaction and thus rendered unusable/less efficient.^[147–154] Another issue is scaling via the possible precipitation of CaCO₃ in primary seawater batteries.^[155,156] This process may occur during the cell discharging via the ORR process in seawater.^[53]

Activated carbon can be an environmentally friendly and (electro)chemically stable choice for the current collector at the cathode side. Past works show that it provides an increased voltage gap (0.6 to 1.42 V) and limited energy efficiency (64–83%).^[53] The gradual increase in overvoltage and the recovery of voltage efficiency after replacement of the cathode suggests that the cathode is the leading cause of cell performance degradation and that there may be several degradation processes.^[53] On the one hand, oxidation of the carbon

current collector surface probably occurs, leading to a gradual build-up of the impedance. On the other hand, structural damage to the cathode occurs after a critical running time of the cell.

2.4. Approaches to Improve Present-Day Seawater Battery Technology

2.4.1. Voltage Efficiency: Enhancing the Kinetics of ORR/OER

Increasing Concentration of Dissolved Oxygen: Since seawater batteries use seawater as catholyte, fresh reactants (water and oxygen) must be continuously supplied to the cathode current collector during cell operation.^[45] If this is not the case, few to no reactants will be available, reactions will be slower and weaker, and the cell efficiency will be low. The concentration of dissolved oxygen in the catholyte can be increased to counteract this limiting factor by flowing seawater continuously through the cell compartment. Han et al. have compared the values of efficiency and overpotential with and without a continuous electrolyte flow. Without flowing the seawater, the charge and discharge voltage of the cell is slowly saturated with a voltage gap of 1.1 V between charging and discharging. By contrast, when the seawater is flowing, that difference decreases to 0.7 V. Thus, it also appears essential to have a continuous flow of seawater catholyte. This may partly be due to the facilitated diffusion of the reaction to the cathode current collector, resulting in reduced concentration polarization during the charge and discharge cycle.

Synthesis of a New Catalytical Electrode with High Catalytical Activity: To increase the efficiency, one can use a suitable bifunctional oxygen evolution reaction/oxygen reduction reaction electrocatalyst at the cathode. This approach could effectively reduce the side reactions (like other reactions of Cl_2 with the water) to OER/ORR at high overvoltages.^[68] These side reactions depend on the applied current, the pH, and the local Cl^- concentration at the air cathode.^[68] The large overpotentials that often occur in the charge and discharge cycles result from slow OER and ORR reaction kinetics. This yields a significant difference between the discharging and charging voltage profiles; the low voltage efficiency is accompanied by a low energy storage ability and insufficient cycling stability.^[157–159]

These problems can be (partially) overcome with effective electrocatalyst systems, which allow the reaction to proceed faster. Mainly elements taken from general catalyst research, such as Pt, Ru, Pd, Au, and Ir, are used. Due to their comparatively high costs and scarce availability, they have not yet established themselves in large-scale industrial use.^[147–154,157,159–161] Many studies have explored nonprecious metal oxides or heteroatom(s)-incorporated carbonaceous materials. Mixed spinel-type transition metal oxides based on Ni, Co, and/or Mn are promising. For example, Abirami et al. used cobalt manganese oxide with a spinel structure ($\text{Co}_x\text{Mn}_{3-x}\text{O}_4$, CMO) as a seawater battery electrocatalyst without noble elements.^[68] This catalyst accelerated the cathode reactions (OER/ORR) because of the large specific surface area with many electrocatalytically active sites by reducing the voltage gap and enhancing the voltage efficiency to a value of 85%.^[68]

Further approaches are proposed to eliminate the efficiency problems by synthesizing completely new catalytic electrodes with high catalytic activity. For example, Liu et al. showed Mg-ion-based seawater batteries.^[162] The porous heterostructure of the synthesized $\text{CoP}/\text{Co}_2\text{P}$ provided a large specific surface area, abundant active interfaces, and enhanced active sites with accelerated charge transfer.^[162] This enabled a high hydrogen evolution reaction activity, enhanced performance with good efficiency, and promising stability for Mg seawater batteries.^[162]

Shin et al. proposed a new electrocatalyst that optimizes the kinetic of the seawater cathode OER/ORR process.^[115] $\text{Co}_3\text{V}_2\text{O}_8$ with large active sites enabled an increased voltage efficiency of $\approx 76\%$ by lowering the charge voltage from 3.88 to 3.76 V and increasing the discharge voltage from 2.80 to 2.87 V (compared to a cell without catalyst).^[115] The resulting seawater battery provided promising cycling stability with voltage gaps of ≈ 0.95 V.^[115]

Modifying the Carbon Current Collector at the Cathode Side: Side effects of carbon corrosion and scaling via CaCO_3 plague the cathode during the charging process. Preventing irreversible carbon corrosion at the cathode enables a higher voltage efficiency and better cycling stability.^[53] This can be accomplished by using more corrosion-resistive carbons and catalyst materials.^[163,164] For example, Tao et al. reported that inducing various defects and the resulting shift of charge in the subsequent electrochemical characterization makes it possible to increase the activity for electrocatalytic reactions (ORR, OER, and HER).^[165]

The carbon current collector can also be modified by heteroatom doping. This can be explored to improve electrocatalytic activity. For example, Jeoung et al. fabricated PNCs (high surface area, nitrogen-doped carbon) and efficiently adjusted the porosity of PNCs by varying the transformation conditions.^[166] The mesoporosity was crucial for controlling the electrocatalytic activity and the seawater battery performance. This distinct improvement made it possible also to obtain improved electrochemical properties (stable voltage gaps of <0.53 V at 0.01 mA cm^{-2} over 20 cycles),^[166] thus highlighting the use of PNCs as a promising metal-free catalyst in the seawater battery.

Another effective method to improve the efficiency from several points of view was proposed by Suh et al., who used hydrophilic carbon electrodes on the one hand and a 3D hybrid (S-rGO-CNT-Co).^[112] The uniform distribution of Co/CoO_x nanoparticles on the porous 3D graphene creates many active sites, resulting in good cycling stability and rate properties. The additional CNTs, with their high conductivity and stability, prevent rapid cell degradation due to electrode decomposition.

Hybridizing Catalytic Reaction: The optimized performance can also be enabled by hybridizing the catalytic reaction with other electrochemical processes or using other electrochemical processes as a substitute. No less attractive and effective is an approach in which the catalytic reaction is combined with another electrochemical process. Park et al. combined ion electrosorption via the formation of an electrical double-layer with the OER/ORR electrolytic activities in activated carbon cloth seawater batteries.^[64] This lowered the voltage gap to 0.49 V, increased the voltage efficiency to 86%, and yielded increased power performance.^[64] Kim et al. introduced a silver foil as a chloride ion capturing.^[111] Silver's reversible Ag/AgCl reaction

with the Cl^- -ions released from the seawater catholyte at 2.93 V versus Na^+/Na (in the charge and discharge cycle, respectively) bypasses the typical OER/ORR reaction. This process significantly reduced the voltage gap and increased the voltage efficiency to about 90%.^[111]

2.4.2. Stability

Eliminating Side Reactions: The problem of side reactions with a particular binder system and sodium is known from present-day NIB research and occurs in seawater batteries.^[67] As a promising binder, sodium alginate is very stable, environmentally friendly, and supports the formation of a stable SEI.^[167] The carboxymethyl cellulose binder, for example, is an environmentally friendly and green material. It is soluble in water, which allows the processing of aqueous pastes. However, due to the solubility in water, only an application in the anode compartment is possible since the electrode on the seawater side would dissolve otherwise. It is mainly used in anodes that have a high capacity.^[137]

Using elemental sodium as electrode material leads to a high capacity. Still, the cell voltage is limited by the (electro)chemical stability window of water.^[129,168] Some approaches to overcome this problem have been proposed in past works. For example, Tu et al. proposed a method with enhanced ORR/OER activities of seawater batteries using a cathode made from nitrogen-doped carbon cloth.^[169] Abirami et al. presented work that used next to the CMO cathode catalyst also a hard carbon electrode as a sodium-free anode; their cell provided a discharge capacity of around $190 \text{ mAh g}^{-1}_{\text{hard carbon}}$ with an average voltage of about 2.7 V during 100 cycles (corresponding with an energy efficiency of 74–79%).^[68] Kim et al. proposed a hard carbon anode separated by a ceramic membrane from a carbon paper as a current collector for the seawater cathode side.^[88] The discharge capacity of the resulting seawater battery was 120 mAh g^{-1} after the first cycle, with a resulting Coulombic efficiency of 91% after 20 cycles.^[88]

Many attempts have been made to counteract the rapid and uncontrolled growth of the Na dendrites. For example, approaches from Li-ion battery chemistry have been adopted, such as adjusting the charge/discharge rate at the current collector, increasing surface tension to suppress the dendrite formation mechanically, or modifying the electrolyte concentration.^[14,61,84,170–177] Other works explored using a $\text{NaPF}_6/\text{glyme}$ electrolyte, an artificial Al_2O_3 SEI layer, various inorganic electrolytes, or sodiated carbon as a nucleation layer.^[178–186] Using a low current density may further delay dendrite formation and increase the critical nucleation radius.^[171,187–189] Kim et al. proposed controlling the growth of sodium dendrites rather than avoiding their occurrence altogether.^[189] Thereby, enhanced performance stability resulted from a low number of sodium dendrite cores formed on the homogenous surface of a graphene-coated copper current collector.^[189]

Optimizing of the Anode Compartment: The liquid electrolyte is of critical importance at the anode because it reduces the interfacial resistance between the anode and the ceramic membrane (which serves as the solid electrolyte); this is important to enabling stable cell performance and efficiency.^[111] An electrolyte adopted from the NIB was often used in the anode compartment. Still, some studies showed that an ethylene carbonate/propylene

carbonate(EC/PC) electrolyte could not provide sufficient cycling stability.^[49,67,124] For example, Kim et al. showed for the EC/PC-based electrolyte the formation of a poorly conductive, thick SEI layer and the degradation of the PVdF.^[67] Successful and high-performance electrolytes based on TEGDME have been developed, which show good cycle performance over 100 cycles and are successfully used in almost every present-day seawater battery.

The areal/absolute capacity of some anode electrode materials can be increased by employing a semisolid anolyte, which includes two redox mediators.^[190] One of these mentioned anolytes would be, for example, sodium biphenyl, which has been successfully used in combination with a semiliquid negative electrode of red phosphorus for the realization of metal-free Na-seawater batteries. Remarkably, using the semiliquid electrode as a static anode, high area capacities of about 11 mAh cm^{-2} in Na half cells and 15 mAh cm^{-2} in Na seawater cells could be achieved at room temperature.^[144] For sodium metal batteries, sodium biphenyl is an attractive and cost-efficient anolyte system, which prevents hydrogen evolution and suppresses sodium dendrite growth, thus increasing the capacity and providing performance stability.^[191] Ionic liquids (ILs) may be a future choice for high-performance seawater batteries. For example, NaFSI salt in two ionic liquids ($\text{Pyr}_{13}\text{FSI}$ and $\text{Pyr}_{13}\text{TFSI}$) showed a very high (electro)chemical and thermal stability in combination with the well-known low vapor pressure of IL.^[51] This was accomplished despite the small amount (5 mass%) of organic solvent (EC) added to facilitate and enable the formation of a stable SEI on the hard carbon anode. In contrast to the typical liquid electrolytes (i.e., organic solvents), ILs show a lower cell polarization resulting in higher energy efficiency.^[51] Kim et al. used this electrode and anolyte to obtain a capacity of $290 \text{ mAh g}^{-1}_{\text{hard carbon}}$ with a Coulombic efficiency of 98% during 600 charge/discharge cycles at rates up to 5.0C, and associated energy efficiency up to 80%.^[51]

3. Dual-Use Application: Seawater Batteries for Energy Storage and Desalination

3.1. Energy Storage

3.1.1. Wearable Devices

Marine wearable devices like life jackets and wetsuits are usually equipped with lights to illuminate and locate drowning persons. Since the seawater battery utilizes the seawater as the catholyte, it is very suitable for marine wearable devices' power supply. Cho et al. put forward a novel design for marine life jackets.^[192] It takes advantage of the properties of seawater batteries that generate electricity once the cathode current collector contacts the seawater. Therefore, when people fall into the water wearing the life jacket, the batteries will be activated and charge the in-built global positioning system.^[43]

3.1.2. Marine Fundamental Facilities

Marine primary public facilities on the ocean, such as light buoys and water-quality monitoring stations, are commonly

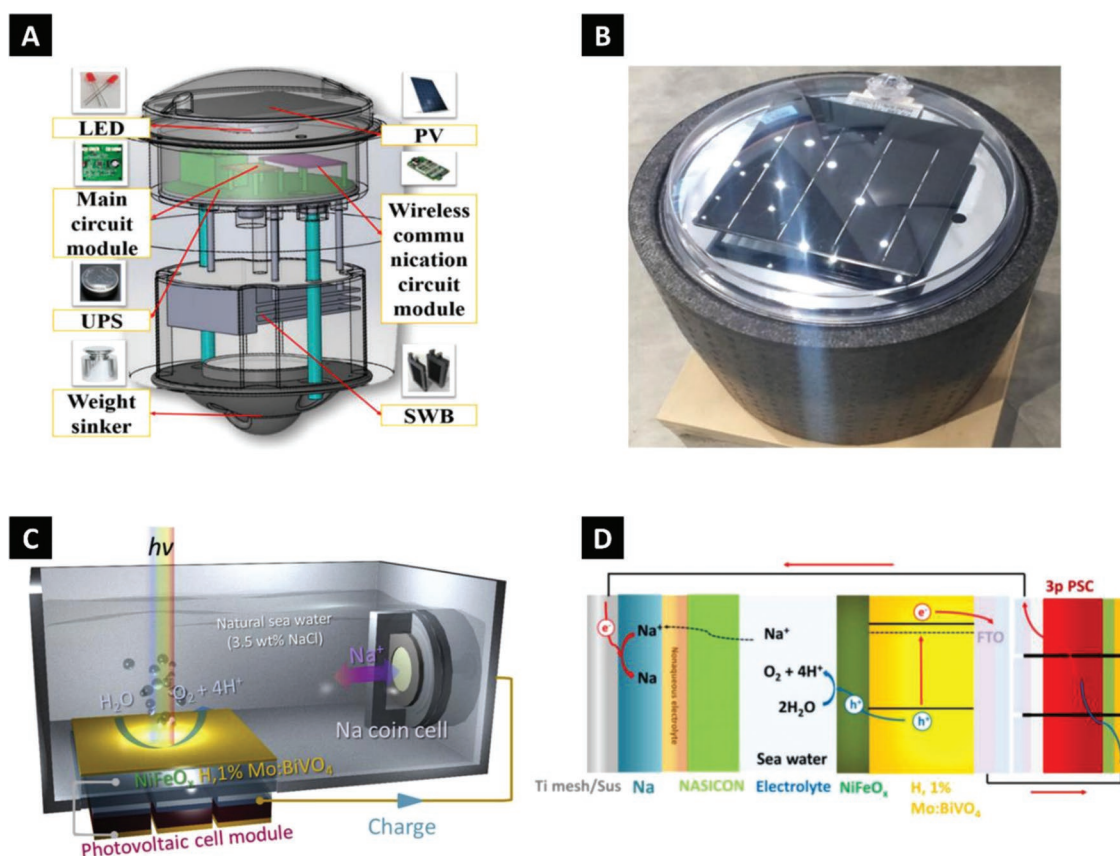


Figure 8. A) The conceptual diagram and B) optical photograph of seawater battery-based wireless buoy system. Reproduced under the terms of the Creative Commons Attribution 4.0 License.^[192] Copyright 2021, the Author(s), Published by IEEE. C) Scheme image of unassisted solar-charging rechargeable seawater battery with $\text{NiFeO}_x/\text{BiVO}_4$ PE combined with PSC or c-Si PVs and D) the mechanism image of it with three pieces of PSC as the example. Reproduced with permission.^[193] Copyright 2019, Elsevier.

powered by solar batteries assigned with energy storage systems like lithium-ion batteries or lead-acid batteries. Once these batteries have some leakage, the toxic component in the batteries will be released into the sea. Therefore, power with a long lifespan, low cost, and low/no environmental pollution are required. Recently, Kim et al. designed a wireless marine buoy system based on rechargeable seawater batteries.^[124] The system comprised seawater batteries (energy storage), light-emitting diodes light, the main circuit module, an uninterruptible power supply, a wireless communication circuit module, and photovoltaic batteries (self-powered energy resource), as shown in Figure 8A,B. The state-of-charge (SOC) is monitored by Coulomb counting, and variance measurements detect the state-of-health. Through wireless communication, the position of marine buoys and the SOC information of the batteries can be obtained on a mobile phone.

3.1.3. Large-Scale Energy Storage

Apart from the small devices, rechargeable seawater batteries are also expected to serve as the energy storage systems for the solar, wind, or tidal power station installed near the ocean. Recently, Kim et al. designed a combined photoelectrode (PE)– photovoltaic (PV) device to accomplish the solar energy-driven rechargeable seawater batteries.^[193] In the cell, NiFeO_x/H , 1% Mo:BiVO_4 , and

a series-connection of crystalline silicon solar cells or lead halide perovskite solar cells were applied as the cathode, and the other components were adopted from conventional rechargeable seawater batteries (Figure 8C). Oxygen and hydrogen are obtained during the charging process on the cathode side, while on the anode side, the sodium ions precipitate as metallic sodium, as shown in Figure 8D. This setup provides an avenue to apply rechargeable seawater batteries independently as marine facilities' power supply without extra power.

3.2. Desalination and Water Purification

3.2.1. Cell Configurations and Performance Metrics

Due to the unique structure, containing both aqueous (seawater) electrolyte and organic electrolyte, it is easy to implement simultaneous water desalination and energy storage if the system of rechargeable seawater batteries is modified.

In 2018, Zhang et al. proposed a rechargeable seawater battery desalination system.^[132] Unlike conventional seawater batteries, the system used still water as the catholyte and seawater as the feed water. Oxygen evolution reactions occur at the cathode part during the charging process, producing protons; sodium ions insert into the hard carbon anode. To keep the charge balance, Cl^- and Na^+ in the seawater (middle channel)

will migrate through the anion exchange membrane (AEM) and the NASICON membrane, respectively. Thereby, HCl and desalinated water are produced during the charging process, and during the discharging process, the sodium anode is regenerated, and NaOH is formed (Figure 9A). Due to the high resistance partially caused by the AEM, there is a high overpotential for OER, resulting in the competition between OER and chloride evolution reactions ($2\text{Cl}^- - 2\text{e}^- \rightarrow \text{Cl}_2$, $E^0 = -1.36$ V vs

SHE). Thereby, the partial migrated Cl^- could also be removed by CER.^[194] After 10 cycles, the total ion concentration decreases from 34.9 to 31.9 g L⁻¹, with an average Coulombic efficiency of 92% and an energy efficiency of 76%. The relatively low-efficiency values could be due to the irreversible intercalation of Na^+ in the hard carbon^[132] or the energy dissipation caused by sluggish ORR and OER reaction kinetics and the high resistance of the cell.^[194]

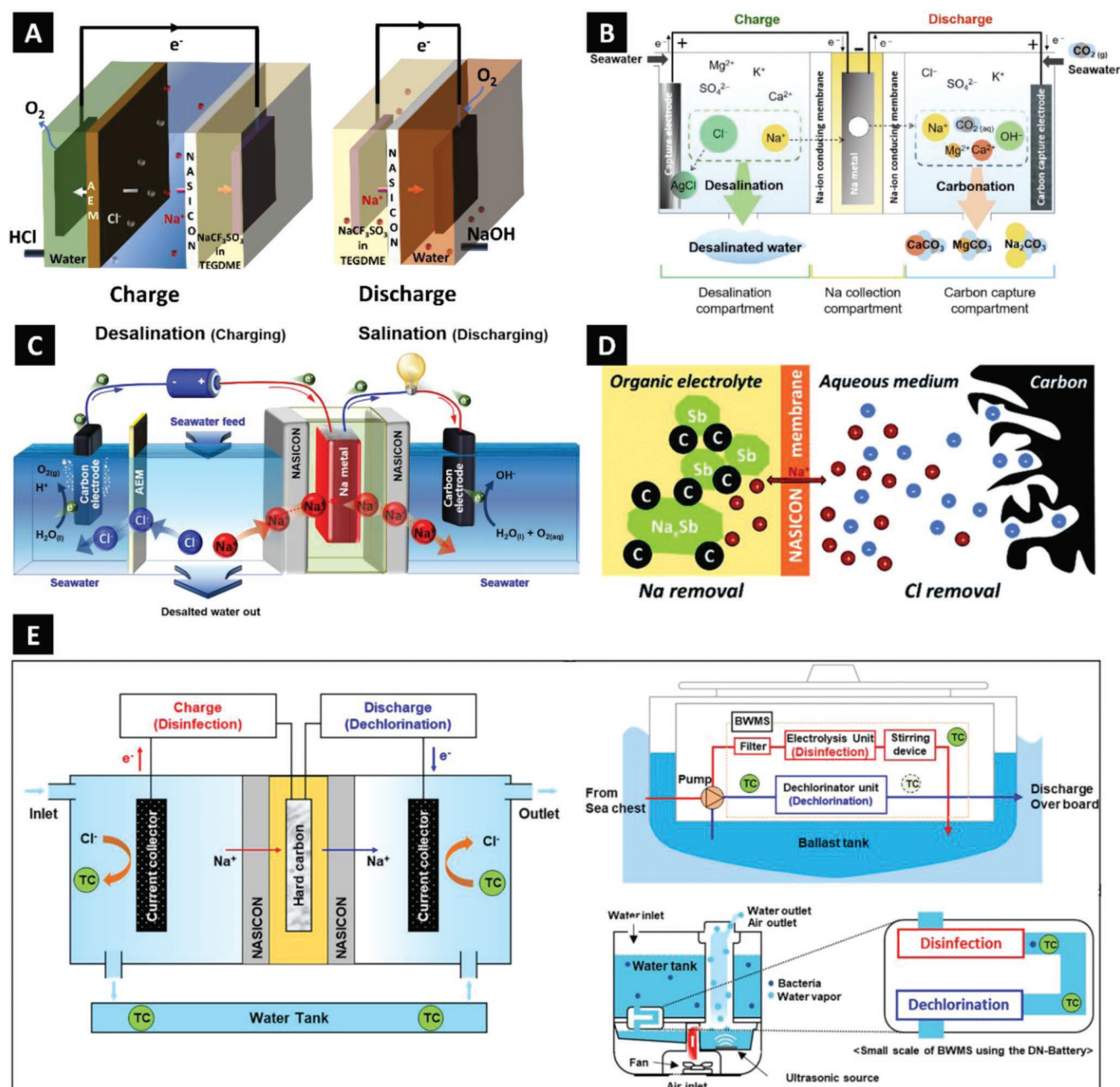
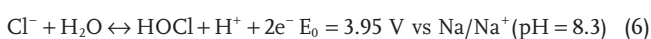
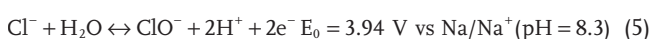


Figure 9. Schemes of different device technologies. A) Rechargeable seawater batteries desalination system with charging and discharging process, redesigned according to Figure 1 of ref. [132]. B) Hybrid of desalination and carbon capture system based on rechargeable seawater batteries. Reproduced with permission.^[123] Copyright 2019, Elsevier. C) Compartmentalized rechargeable seawater batteries desalination system. Reproduced with permission.^[194] Copyright 2020, Elsevier. D) Desalination mechanism in bielectrolyte desalination cell. Reproduced with permission.^[90] Copyright 2021, Royal Society of Chemistry. The schematic diagram E) of disinfection–dechlorination battery (left side), conventional electrochlorination and dechlorination of ballast water (right upper corner), and the disinfection–dechlorination battery used in a humidifier (right bottom corner). Reproduced with permission.^[195] Copyright 2021, American Chemical Society.

Following works modified the basic rechargeable seawater desalination system mentioned before to optimize the system or add more functionalities. For instance, Bae et al. combined the seawater battery system with a CO₂ capture system (Figure 9B).^[123] This system contains the desalination compartment and the carbon dioxide capture compartment. Silver was used as a Cl⁻ capture electrode instead of an OER catalytic electrode to compose the desalination parts with NASICON and Na metal, unlike the typical seawater battery system. This effectively reduces the overpotential and improves the voltage efficiency during the charging time caused by the sluggish kinetics of OER.^[45] After the desalination process (system charging), the system is discharged with Na metal and porous carbon paper as the electrodes, where OH⁻ is generated and CO₂ is captured by the metal hydroxides, like NaOH, Mg(OH)₂, and Ca(OH)₂. Consequently, CaCO₃ or MgCO₃ are simultaneously generated as a by-product.

Arnold et al. used carbon cloth as the alternative to OER, for its low price compared to Ag (Figure 9D).^[90] With antimony/C as the anode, the initial capacity of the cell was 714 mAh g⁻¹ and the average desalination capacity was 294 mg_{Na} g⁻¹_{Sb} with a charge efficiency of around 74%. In 2020, Kim et al. improved the previous architecture of seawater batteries.^[194] The cell contains independent desalination and salination parts (Figure 9C). This avoids disassembling cells between the charging and discharging process, which reduces the energy losses and enables a higher nominal cell potential of 3.46 V (pH 8.4) and a theoretical energy density of 4010 kWh kg⁻¹. After galvanostatic charging for 20 mAh, 77% of the salts are removed from the seawater.

Apart from desalinating water, rechargeable seawater batteries also can disinfect the water if a higher voltage is applied. Recently, Park et al. proposed a disinfection-dechlorination battery with a NASICON ceramic membrane, depicted on the left part of Figure 9E.^[195] During the charging process, the Na⁺ moves through the NASICON membrane and deposits on the anode; Cl⁻ or OH⁻ partake at a redox reaction at the cathode (Equations (4)–(7)). The produced HOCl, ClO⁻, and Cl₂ could kill microbes in the water. The residual chloride base product will be oxidized into Cl⁻ during the discharging process. After charging the cell for 3 h, the reduction rate of microorganism, *Escherichia coli* (MG1655), reaches 100%, while 8 h is required to 100% remove another microorganism, *Enterococcus aquimarinus* (DSM17690). This new system avoids the extra dechlorination process of standard disinfection technologies based on chloride disinfectant.^[196] However, the competitive OER reactions would reduce the energy efficiency of this system, which may be addressed by applying selective catalysts for chloride evolution reactions.^[197] In addition, the authors also put forward two typical applications; one is in the ballast water treatment, and the other is to disinfect microorganisms in humidifiers, which are illustrated in the upper right corner and bottom right corner of Figure 9E



3.2.2. Desalination Performance and Energy Consumption

Seawater batteries provide a high desalination capacity compared to other electrochemical desalination technologies. This beneficial performance results from the extended voltage window and the possibility of using materials with higher capacity as anodes, such as Na metal (theoretical capacity, 1165 mAh g⁻¹),^[47] red phosphorus (theoretical capacity, 2596 mAh g⁻¹).^[124] Therefore, seawater batteries could remove 70–80% of salts from seawater, among which Na⁺ and Cl⁻ dominate due to the selectivity of the NASICON membrane (Table 2).

Limited by the water-splitting voltage window, a relatively low voltage (generally <1.2 V) is applied in other electrochemical technologies, such as capacitive deionization,^[37] and desalination batteries.^[198] Consequently, materials with suitable potential range but relatively low capacity like carbon (5–30 mg_{NaCl} g⁻¹_{electrode}), some intercalation materials (50–100 mg g⁻¹), and some conversion materials (100–150 mg g⁻¹), are employed as the electrode, as shown in Table 2. Compared with the salt rejection rates of current seawater desalination technologies, such as reverse osmosis (RO) (≥99%),^[199] multiple-effect distillation (MED) (almost 100%),^[200] seawater batteries technology is not suitable to produce potable water, which requires the total dissolved solid lower than 500 mg L⁻¹,^[199] independently from the seawater. This is because seawater battery desalination generally removes sodium ions due to the selectivity of the NASICON membrane. However, it adapts desalinating the water with the salinity from low to hypersaline. Thereby, this technology could combine with some filtration technologies playing the role of pretreatment and the 2nd pass treatment to desalinate seawater; this technology could also replace some units or be added additionally in the current seawater desalination plants to reduce the energy consumption.

The energy consumption of seawater batteries must also be considered when assessing its application potential. The energy consumption of seawater batteries desalination depends on the amount of removed salt. The removal of 9% of all salt ions corresponded with an energy consumption of 4.7 kWh m⁻³.^[132] The energy consumption increased to 53.9 kWh m⁻³ when the salt removal increased to ≈75%.^[201] Table 3 shows the energy consumption of some industrial plants with various desalination technologies. As can be seen, the energy consumption of RO is ≈3–5 kWh m⁻³,^[202] varying from the operation parameters, which is less than that of MED (5–58 kWh m⁻³)^[203] and electrodialysis (ED; 3–20 kWh m⁻³). These industrial plants also employ energy recovery devices to reduce the total energy consumption. Considering the energy recovery of seawater batteries desalination technologies (i.e., discharging process), the energy consumption could reduce to around 5 kWh m⁻³ with the energy recovery reaching 90% by declining the voltage gap during the cycling.^[131]

Recently, Ligaray et al. used reverse osmosis models to evaluate the energy consumption of a new system where a seawater battery is applied to be the energy recovery component or the substitute of the first RO in the conventional RO design with the energy recovery devices after the first filtration for the energy recovery of 50% (Figure 10A).^[201] Their modeling assumed the Coulombic efficiency of seawater batteries to be 100%. Consequently, compared with the standard RO system

Table 2. Desalination performance of seawater-battery-based system, carbon materials, and Faradaic materials used for desalination.

	Electrodes	Feedwater salinity [mg L ⁻¹]	Feedwater volume [mL]	Desalination	Desalination capacity [mg g ⁻¹]	Charge efficiency [%]	Energy consumption	Refs.
Seawater- battery based system	Sodium metal//carbon felt	33 460	3.4	77%	–	≈70% for Cl ⁻ ≈80% for Na ⁺	37 kT ion ⁻¹	[194]
	Sodium metal//silver foil	34 000	–	97% for Na ⁺ 9% for Cl ⁻	–	–	–	[123]
	Hard carbon//Pt/C	34 910	10	9% after 10 cycles	–	–	4.7 Wh L ⁻¹	[132]
	Antimony/C//carbon cloth	35 100	–	–	294	74	16 kT ion ⁻¹	[90]
	Sodium metal coated on carbon cloth//carbon cloth	12 182.5	3.4	73%	–	–	–	[220]
Carbon materials	Carbon cloth//carbon cloth	58 400	–	–	30	≈90	20 kT ion ⁻¹	[221]
	Activated carbon// activated carbon	292.5	–	–	13	86	–	[222]
	Activated carbon//activated carbon	35 100	–	–	12	63	–	[223]

	Electrodes	Feed water salinity[mg L ⁻¹]	Volume of the feed water [mL]	Desalination	Desalination capacity [mg g ⁻¹]	Charge efficiency [%]	Energy consumption	Refs.
Faradaic materials	Na _{0.44} MnO ₂ //BiOCl	760	50	–	69	97.7	–	[224]
	Na _{2-x} Mn ₅ O ₁₀ //Ag/AgCl	34 800	≈0.3	25%	–	–	0.3 Wh L ⁻¹	[38]
	VS ₂ -CNT//carbon cloth	35 100	–	–	15	>85	29 kT ion ⁻¹	[225]
	NaNiHCF//NaFeHCF	34 465	0.6	40% for Na ⁺	60	–	0.3 Wh L ⁻¹	[226]
	Iodide// activated carbon	35 100	–	–	69	64	1.6 Wh L ⁻¹	[204]
	Bi/C// activated carbon	1000	50	–	113	–	–	[227]

for seawater desalination, which contains the ultrafiltration (UF), RO, and brackish water reverse osmosis (BWRO), using seawater batteries as the additional energy storage devices could save about 104 kWh m⁻³ energy by reducing the salt concentration from 61 200 mg L⁻¹ to less than 20 000 mg L⁻¹. Applying seawater batteries instead of the first RO step (UF-SWB system, UF + SWB + BWRO), the seawater batteries could save 49–50 kWh m⁻³; utilizing nanofiltration (NF) + seawater batteries (NF-SWB system, UF + NF + SWB + BWRO) together as the alternative of first RO, the seawater batteries can save 24 kWh m⁻³ and 1.1 kWh m⁻³ pump energy could be reduced. The net specific energy consumption (SEC) of the UF-SWB

system and NF-SWB system are 1.35 and 2.1 kWh m⁻³, respectively; these values are below what is needed for the net SEC of a standard 2nd-pass-RO system (2.8 kWh m⁻³).

The energy consumption of the seawater battery system is relatively high compared with desalination batteries based on the intercalation materials^[38] or redox electrolytes^[204] (Table 2); this could be due to the high overpotential of the seawater battery system and the high resistance of NASICON membrane.^[43] Another potential issue of the seawater battery system is the relatively low desalination rate (generally < 1 mg cm⁻² h⁻¹), compared with other electrochemical technologies, for instance, flow electrode capacitive deionization (2–40 mg cm⁻² h⁻¹)^[205–211]

Table 3. Comparison the performance of current industrial desalination technologies and seawater batteries.

	TDS ^{a)} of feed water [mg L ⁻¹]	TDS of product water [mg L ⁻¹]	Water recovery [%]	Specific energy consumption [kWh m ⁻³]	Scale	Refs.
Reverse osmosis	40 070	183	46	4.8	Industrial application 16 800 m ³ day ⁻¹	[228]
	35 000	174–214	30–50	1.89–2.04	Modeling	[229]
Electrodialysis	35 000	<500	50–60	16.21	Pilot test 30 m ³ day ⁻¹	[230]
	35 000	450	41	6.6	Laboratory-scale experiments	[231]
Multieffect distillation	–	–	–	<5	Industrial application (10 000 t day ⁻¹)	[200]
Seawater batteries ^{b)}	33 700	<200	–	1.35	Modeling	[201]

^{a)}TDS the abbreviation of total dissolved solid; ^{b)}The results are modeled by RO analysis software where seawater batteries replace RO in the typical RO system.

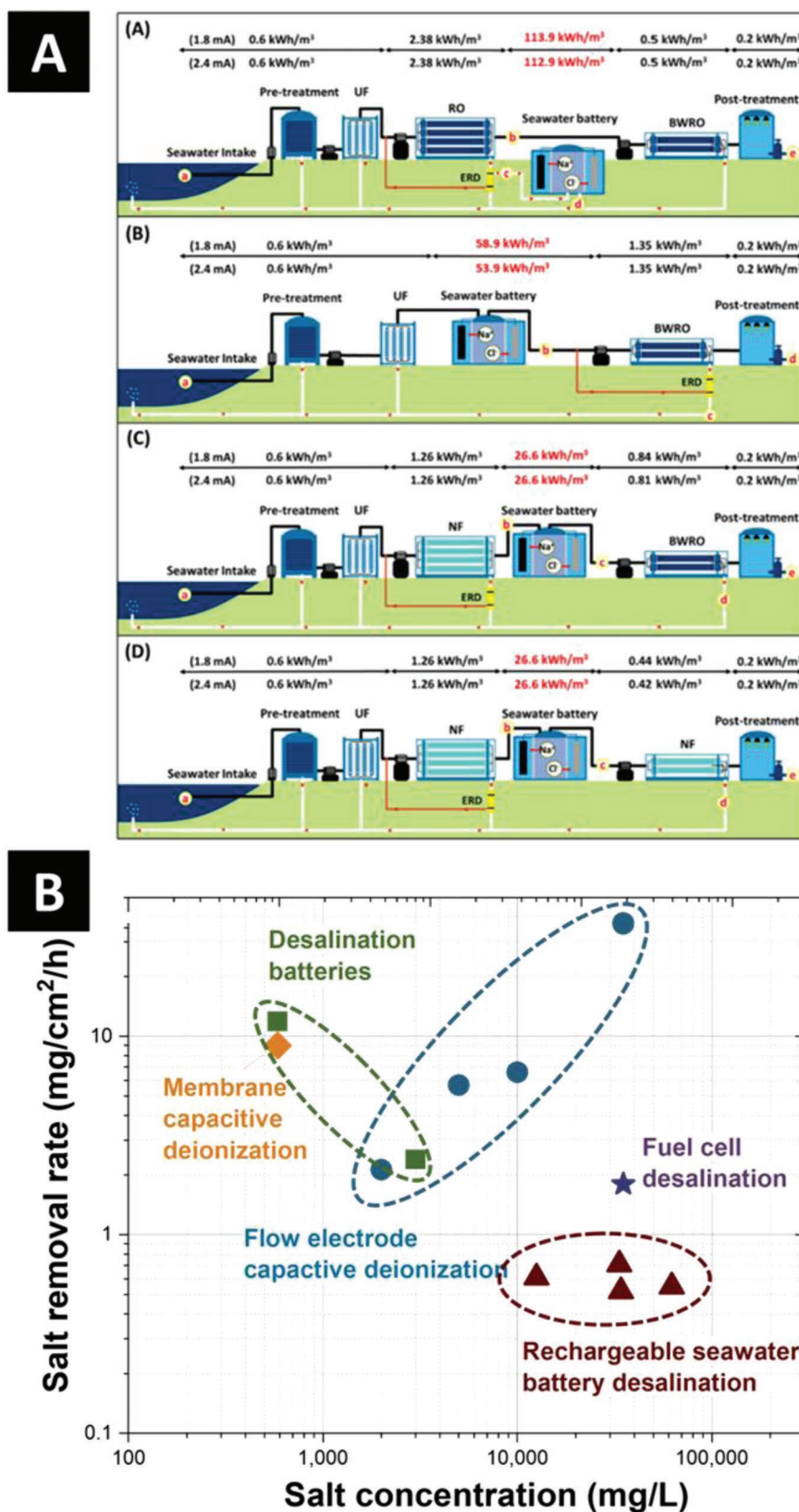


Figure 10. A) Proposed designs for rechargeable seawater battery desalination with various feed water. Reproduced with permission.^[201] Copyright 2020, Elsevier. B) Average salt removal rate of different electrochemical desalination technologies. Data adapted from refs. [40,194,201,205–210,212].

and desalination batteries ($1\text{--}10\text{ mg cm}^{-2}\text{ h}^{-1}$),^[204,212] as shown in Figure 10B. This could be due to the relatively low ion diffusion rate of the NASICON membrane^[94] and the sluggish kinetics rate of ORR and OER.^[45] However, it should note that the salt removal rate also has a strong relationship with the operation parameters, like the voltage, current, and concentration of the feed water.^[213]

4. Conclusions

Since expanding the rechargeable battery industry is indispensable when considering the growing demand for portable electronic devices and sizeable stationary energy storage systems, the seawater battery offers a promising alternative. So far, mainly used lithium-ion battery technology cannot be used as the sole power due to the exploitation of raw materials, the resulting prices increase, and other concerns about geopolitical and environmental aspects. Therefore, the seawater battery, which uses a very environmentally friendly and resource-saving raw material, namely natural seawater, as an almost inexhaustible ion source, provides the possibility of more environmentally friendly energy storage.

Simultaneously energy storage and desalination encourage seawater desalination batteries to be a good choice for replacing some seawater reverse osmosis components. Additionally, attributed to the high selectivity of the NASICON membrane, using seawater batteries to desalinate the water also means extracting sodium ions from seawater. In addition, using other ion-selective membranes would enable elemental harvesting within the context of lithium extraction. Alternatively, nonselective membranes would boost the performance in seawater because cations beyond sodium would be removed. Finally, the advantages of seawater batteries provide a perspective toward sustainable, environmentally friendly, performance-oriented, and cost-efficient applications at the energy/water nexus.

Seawater battery development has yet to overcome technological challenges. A shortened lifetime, prevented safe battery operation, low Coulombic/energy efficiency, and low stability result from the partial instability of the individual cell components such as the solid electrolyte membrane or the anode electrode, as well as side reactions and nonoptimized cell components. Extending seawater batteries for desalination from the laboratory scale to pilot plants also requires optimized system design and benchmarking in real-water applications. The low desalination rate and high voltage gap are significant obstacles. However, these challenges can be addressed by advances in materials science, battery chemistry, and process engineering. In addition, the successful use and application of present-day seawater batteries make us optimistic about the more widespread application of this technology and the positive impact on sustainable devices at the energy/water research nexus.

Acknowledgements

The authors thank Eduard Arzt (INM) for his continuing support. L.W. acknowledges funding from the China Scholarship Council (CSC) via Award No. 201906260277. The authors acknowledge support for the MERLIN project from the RAG-Stiftung; the RAG-Stiftung generates

long-term momentum for transforming the regions along the Ruhr and Saar Rivers and in Ibbenbüren. The authors thank Cansu Kök (INM) for helpful discussions.

Open access funding enabled and organized by Projekt DEAL.

Conflict of Interest

The authors declare no conflict of interest.

Keywords

desalination, energy storage, ion removal, seawater batteries, sodium-ion batteries

Received: December 20, 2021

Revised: July 17, 2022

Published online: August 31, 2022

- [1] K. G. Cassman, P. Grassini, *Nat. Sustain.* **2020**, *3*, 262.
- [2] S. Mitchell, R. Qin, N. Zheng, J. Pérez-Ramírez, *Nat. Nanotechnol.* **2021**, *16*, 129.
- [3] J. D. Hunt, E. Byers, Y. Wada, S. Parkinson, D. E. Gernaat, S. Langan, D. P. van Vuuren, K. Riahi, *Nat. Commun.* **2020**, *11*, 947.
- [4] C. S. Lai, G. Locatelli, *Energy* **2021**, *214*, 118954.
- [5] K. Turcheniuk, D. Bondarev, V. Singhal, G. Yushin, *Nature* **2018**, *559*, 467.
- [6] D. Larcher, J.-M. Tarascon, *Nat. Chem.* **2015**, *7*, 19.
- [7] L. Wang, K. Frisella, P. Srimuk, O. Janka, G. KICKelbick, V. Presser, *Sustainable Energy Fuels* **2021**, *5*, 3124.
- [8] M. Pasta, A. Battistel, F. La Mantia, *Energy Environ. Sci.* **2012**, *5*, 9487.
- [9] P. Srimuk, X. Su, J. Yoon, D. Aurbach, V. Presser, *Nat. Rev. Mater.* **2020**, *5*, 517.
- [10] K. Turcheniuk, D. Bondarev, G. G. Amatucci, G. Yushin, *Mater. Today* **2021**, *42*, 57.
- [11] B. E. Murdock, K. E. Toghil, N. Tapia-Ruiz, *Adv. Energy Mater.* **2021**, *11*, 2102028.
- [12] H. Pan, Y.-S. Hu, L. Chen, *Energy Environ. Sci.* **2013**, *6*, 2338.
- [13] J. B. Goodenough, K.-S. Park, *J. Am. Chem. Soc.* **2013**, *135*, 1167.
- [14] D. Lin, Y. Liu, Y. Cui, *Nat. Nanotechnol.* **2017**, *12*, 194.
- [15] M. Ko, S. Chae, J. Ma, N. Kim, H.-W. Lee, Y. Cui, J. Cho, *Nat. Energy* **2016**, *1*, 16113.
- [16] L. Lu, X. Han, J. Li, J. Hua, M. Ouyang, *J. Power Sources* **2013**, *226*, 272.
- [17] J.-M. Tarascon, *Nat. Chem.* **2010**, *2*, 510.
- [18] D. Kundu, E. Talaie, V. Duffort, L. F. Nazar, *Angew. Chem., Int. Ed.* **2015**, *54*, 3431.
- [19] C. Vaalma, D. Buchholz, S. Passerini, *Curr. Opin. Electrochem.* **2018**, *9*, 41.
- [20] T. Perveen, M. Siddiq, N. Shahzad, R. Ihsan, A. Ahmad, M. I. Shahzad, *Renewable Sustainable Energy Rev.* **2020**, *119*, 109549.
- [21] R. Rajagopalan, Y. Tang, X. Ji, C. Jia, H. Wang, *Adv. Funct. Mater.* **2020**, *30*, 1909486.
- [22] R. K. Guduru, J. C. Icaza, *Nanomaterials* **2016**, *6*, 41.
- [23] T. Liu, X. Cheng, H. Yu, H. Zhu, N. Peng, R. Zheng, J. Zhang, M. Shui, Y. Cui, J. Shu, *Energy Storage Mater.* **2019**, *18*, 68.
- [24] Y. Li, J. Fu, C. Zhong, T. Wu, Z. Chen, W. Hu, K. Amine, J. Lu, *Adv. Energy Mater.* **2019**, *9*, 1802605.
- [25] A. Ebensperger, P. Maxwell, C. Moscoso, *Resour. Policy* **2005**, *30*, 218.
- [26] S. Komaba, W. Murata, T. Ishikawa, N. Yabuuchi, T. N. Ozeki, *Adv. Funct. Mater.* **2011**, *21*, 3859.

- [27] N. Tapia-Ruiz, A. R. Armstrong, H. Alptekin, M. A. Amores, H. Au, J. Barker, R. Boston, W. R. Brant, J. M. Brittain, Y. Chen, M. Chhowalla, Y.-S. Choi, S. I. R. Costa, M. Crespo Ribadeneyra, S. A. Cussen, E. J. Cussen, W. I. F. David, A. V. Desai, S. A. M. Dickson, E. I. Eweka, J. D. Forero-Saboya, C. P. Grey, J. M. Griffin, P. Gross, X. Hua, J. T. S. Irvine, P. Johansson, M. O. Jones, M. Karlsmo, E. Kendrick, et al., *J. Phys.: Energy* **2021**, 3, 031503.
- [28] K. Chayambuka, G. Mulder, D. L. Danilov, P. H. Notten, *Adv. Energy Mater.* **2018**, 8, 1800079.
- [29] C. Yang, S. Xin, L. Mai, Y. You, *Adv. Energy Mater.* **2021**, 11, 2000974.
- [30] UN Water, *Sustainable Development Goal 6 Synthesis Report on Water and Sanitation*, United Nations, New York **2018**.
- [31] C. E. Cosgrove, W. J. Cosgrove, *The United Nations World Water Development Report No 4: The Dynamics of Global Water Futures: Driving Forces 2011–2050*, Vol. 2, UNESCO, Paris, France **2012**.
- [32] J. Mohammed-Ibrahim, H. Moussab, *Mater. Sci. Energy Technol.* **2020**, 3, 780.
- [33] M. A. Al-Obaidi, G. Filippini, F. Manenti, I. M. Mujtaba, *Desalination* **2019**, 456, 136.
- [34] O. A. Hamed, M. A. K. Al-Sofi, M. Imam, G. M. Mustafa, K. Ba Mardouf, H. Al-Washmi, *Desalination* **2000**, 128, 281.
- [35] Y. J. Lim, K. Goh, M. Kurihara, R. Wang, *J. Membr. Sci.* **2021**, 629, 119292.
- [36] M. Sadrzadeh, T. Mohammadi, *Desalination* **2008**, 221, 440.
- [37] M. E. Suss, S. Porada, X. Sun, P. M. Biesheuvel, J. Yoon, V. Presser, *Energy Environ. Sci.* **2015**, 8, 2296.
- [38] M. Pasta, C. D. Wessells, Y. Cui, F. La Mantia, *Nano Lett.* **2012**, 12, 839.
- [39] M. E. Suss, Y. Zhang, I. Atlas, Y. Gendel, E. B. Ruck, V. Presser, *Electrochem. Commun.* **2022**, 136, 107211.
- [40] Y. Zhang, L. Wang, V. Presser, *Cell Rep. Phys. Sci.* **2021**, 2, 100416.
- [41] F. A. AlMarzooqi, A. A. Al Ghaferi, I. Saadat, N. Hilal, *Desalination* **2014**, 342, 3.
- [42] H. Nassrullah, S. F. Anis, R. Hashaikheh, N. Hilal, *Desalination* **2020**, 491, 114569.
- [43] S. M. Hwang, J.-S. Park, Y. Kim, W. Go, J. Han, Y. Kim, Y. Kim, *Adv. Mater.* **2019**, 31, 1804936.
- [44] I. C. Blake, *J. Electrochem. Soc.* **1952**, 99, 202C.
- [45] S. T. Senthilkumar, W. Go, J. Han, L. Pham Thi Thuy, K. Kishor, Y. Kim, Y. Kim, *J. Mater. Chem. A* **2019**, 7, 22803.
- [46] J.-K. Kim, F. Mueller, H. Kim, D. Bresser, J.-S. Park, D.-H. Lim, G.-T. Kim, S. Passerini, Y. Kim, *NPG Asia Mater.* **2014**, 6, e144.
- [47] J. K. Kim, E. Lee, H. Kim, C. Johnson, J. Cho, Y. Kim, *ChemElectroChem* **2014**, 2, 328.
- [48] M. E. Suss, V. Presser, *Joule* **2018**, 2, 10.
- [49] Y. Kim, K.-H. Ha, S. M. Oh, K. T. Lee, *Chem.–Eur. J.* **2014**, 20, 11980.
- [50] Y. Kim, J.-K. Kim, C. Vaalma, G. H. Bae, G.-T. Kim, S. Passerini, Y. Kim, *Carbon* **2018**, 129, 564.
- [51] Y. Kim, G. T. Kim, S. Jeong, X. W. Dou, C. X. Geng, Y. Kim, S. Passerini, *Energy Storage Mater.* **2019**, 16, 56.
- [52] S. Lee, I. Y. Cho, D. Kim, N. K. Park, J. Park, Y. Kim, S. J. Kang, Y. Kim, S. Y. Hong, *ChemSusChem* **2020**, 13, 2220.
- [53] W. Lee, J. Park, J. Park, S. J. Kang, Y. Choi, Y. Kim, *J. Mater. Chem. A* **2020**, 8, 9185.
- [54] C. Lee, T.-U. Wi, W. Go, M. F. Rahman, M. T. McDowell, Y. Kim, H.-W. Lee, *J. Mater. Chem. A* **2020**, 8, 21804.
- [55] Z. Le, W. Li, Q. Dang, C. Jing, W. Zhang, J. Chu, L. Tang, M. Hu, *J. Mater. Chem. A* **2021**, 9, 8685.
- [56] T.-U. Wi, C. Lee, M. F. Rahman, W. Go, S. H. Kim, D. Y. Hwang, S. K. Kwak, Y. Kim, H.-W. Lee, *Chem. Mater.* **2021**, 33, 126.
- [57] C. Yang, K. Fu, Y. Zhang, E. Hitz, L. Hu, *Adv. Mater.* **2017**, 29, 1701169.
- [58] W. Luo, Y. Zhang, S. Xu, J. Dai, E. Hitz, Y. Li, C. Yang, C. Chen, B. Liu, L. Hu, *Nano Lett.* **2017**, 17, 3792.
- [59] L. Lutz, D. Alves Dalla Corte, M. Tang, E. Salager, M. Deschamps, A. Grimaud, L. Johnson, P. G. Bruce, J.-M. Tarascon, *Chem. Mater.* **2017**, 29, 6066.
- [60] X. B. Cheng, R. Zhang, C. Z. Zhao, F. Wei, J. G. Zhang, Q. Zhang, *Adv. Sci.* **2016**, 3, 1500213.
- [61] M. D. Tikekar, S. Choudhury, Z. Tu, L. A. Archer, *Nat. Energy* **2016**, 1, 16114.
- [62] J. M. Bergthorson, Y. Yavor, J. Palecka, W. Georges, M. Soo, J. Vickery, S. Goroshin, D. L. Frost, A. J. Higgins, *Appl. Energy* **2017**, 186, 13.
- [63] M. A. Rahman, X. Wang, C. Wen, *J. Electrochem. Soc.* **2013**, 160, A1759.
- [64] J. Park, J.-S. Park, S. T. Senthilkumar, Y. Kim, *J. Power Sources* **2020**, 450, 227600.
- [65] S. T. Senthilkumar, M. Abirami, J. Kim, W. Go, S. M. Hwang, Y. Kim, *J. Power Sources* **2017**, 341, 404.
- [66] P. Manikandan, K. Kishor, J. Han, Y. Kim, *J. Mater. Chem. A* **2018**, 6, 11012.
- [67] H. Kim, J.-S. Park, S. H. Sahgong, S. Park, J.-K. Kim, Y. Kim, *J. Mater. Chem. A* **2014**, 2, 19584.
- [68] M. Abirami, S. M. Hwang, J. Yang, S. T. Senthilkumar, J. Kim, W.-S. Go, B. Senthilkumar, H.-K. Song, Y. Kim, *ACS Appl. Mater. Interfaces* **2016**, 8, 32778.
- [69] H. Xiong, M. D. Slater, M. Balasubramanian, C. S. Johnson, T. Rajh, *J. Phys. Chem. Lett.* **2011**, 2, 2560.
- [70] L. Y. Yang, H. Z. Li, J. Liu, S. S. Tang, Y. K. Lu, S. T. Li, J. Min, N. Yan, M. Lei, *J. Mater. Chem. A* **2015**, 3, 24446.
- [71] C. Wu, W. Hua, Z. Zhang, B. Zhong, Z. Yang, G. Feng, W. Xiang, Z. Wu, X. Guo, *Adv. Sci.* **2018**, 5, 1800519.
- [72] C. Bommier, X. Ji, *Isr. J. Chem.* **2015**, 55, 486.
- [73] M.-S. Balogun, Y. Luo, W. Qiu, P. Liu, Y. Tong, *Carbon* **2016**, 98, 162.
- [74] V. L. Chevrier, G. Ceder, *J. Electrochem. Soc.* **2011**, 158, A1011.
- [75] J. K. Kim, F. Mueller, H. Kim, S. Jeong, J. S. Park, S. Passerini, Y. Kim, *ChemSusChem* **2016**, 9, 42.
- [76] A. Kraysberg, Y. Ein-Eli, *J. Solid State Electrochem.* **2017**, 21, 1907.
- [77] M. Fichtner, *Chem. Unserer Zeit* **2013**, 47, 230.
- [78] J. Wang, H. Tang, H. Wang, R. Yu, D. Wang, *Mater. Chem. Front.* **2017**, 1, 414.
- [79] H. Wang, S. Chen, C. Fu, Y. Ding, G. Liu, Y. Cao, Z. Chen, *ACS Mater. Lett.* **2021**, 3, 956.
- [80] H. Hou, M. Jing, Z. Huang, Y. Yang, Y. Zhang, J. Chen, Z. Wu, X. Ji, *ACS Appl. Mater. Interfaces* **2015**, 7, 19362.
- [81] S. M. Hwang, J. Kim, Y. Kim, Y. Kim, *J. Mater. Chem. A* **2016**, 4, 17946.
- [82] J. Han, S. M. Hwang, W. Go, S. T. Senthilkumar, D. Jeon, Y. Kim, *J. Power Sources* **2018**, 374, 24.
- [83] A. Cipollina, G. Micale, L. Rizzuti, *Seawater Desalination: Conventional And Renewable Energy Processes*, Springer-Verlag, Berlin, Heidelberg **2009**, Ch. 11, pp. 1–15.
- [84] Y. Zhang, J.-S. Park, S. T. Senthilkumar, Y. Kim, *J. Power Sources* **2018**, 400, 478.
- [85] C. Min, P. Nie, H.-J. Song, Z. Zhang, K. Zhao, *Tribol. Int.* **2014**, 80, 131.
- [86] J.-H. Huh, S. H. Kim, J. H. Chu, S. Y. Kim, J. H. Kim, S.-Y. Kwon, *Nanoscale* **2014**, 6, 4379.
- [87] S. T. Senthilkumar, S. O. Park, J. Kim, S. M. Hwang, S. K. Kwak, Y. Kim, *J. Mater. Chem. A* **2017**, 5, 14174.
- [88] Y. Kim, H. Kim, S. Park, I. Seo, Y. Kim, *Electrochim. Acta* **2016**, 191, 1.
- [89] C. Zhang, D. He, J. Ma, W. Tang, T. D. Waite, *Electrochim. Acta* **2019**, 299, 727.
- [90] S. Arnold, L. Wang, Ö. Budak, M. Aslan, P. Srimuk, V. Presser, *J. Mater. Chem. A* **2021**, 9, 585.
- [91] J.-J. Kim, K. Yoon, I. Park, K. Kang, *Small Methods* **2017**, 1, 1700219.
- [92] J.-K. Kim, Y. J. Lim, H. Kim, G.-B. Cho, Y. Kim, *Energy Environ. Sci.* **2015**, 8, 3589.

- [93] C. Zhao, L. Liu, X. Qi, Y. Lu, F. Wu, J. Zhao, Y. Yu, Y. S. Hu, L. Chen, *Adv. Energy Mater.* **2018**, *8*, 1703012.
- [94] Z. Zhang, Y. Shao, B. Lotsch, Y. Hu, H. Li, *Energy Environ. Sci.* **2018**, *11*, 1945.
- [95] M. L. Wolf, J. R. Walker, C. R. A. Catlow, *Solid State Ionics* **1984**, *13*, 33.
- [96] R. O. Fuentes, F. Figueiredo, F. M. B. Marques, J. I. Franco, *Ionics* **2002**, *8*, 383.
- [97] A. Ahmad, T. Wheat, A. Kuriakose, J. Canaday, A. McDonald, *Solid State Ionics* **1987**, *24*, 89.
- [98] J. Lee, P. Srimuk, R. L. Zornitta, M. Aslan, B. L. Mehdi, V. Presser, *ACS Sustainable Chem. Eng.* **2019**, *7*, 10132.
- [99] W. Go, J. Kim, J. Pyo, J. B. Wolfenstine, Y. Kim, *ACS Appl. Mater. Interfaces* **2021**, *13*, 52727.
- [100] J. B. Goodenough, H. Y. P. Hong, J. A. Kafalas, *Mater. Res. Bull.* **1976**, *11*, 203.
- [101] H.-P. Hong, *Mater. Res. Bull.* **1976**, *11*, 173.
- [102] N. Yabuuchi, K. Kubota, M. Dahbi, S. Komaba, *Chem. Rev.* **2014**, *114*, 11636.
- [103] R. O. Fuentes, F. Figueiredo, F. M. B. Marques, J. I. Franco, *Solid State Ionics* **2001**, *139*, 309.
- [104] P. Komorowski, S. Argyropoulos, R. Hancock, J. Gulens, P. Taylor, J. Canaday, A. Kuriakose, T. Wheat, A. Ahmad, *Solid State Ionics* **1991**, *48*, 295.
- [105] E. Peled, *J. Electrochem. Soc.* **1979**, *126*, 2047.
- [106] T. Famprikis, P. Canepa, J. A. Dawson, M. S. Islam, C. Masquelier, *Nat. Mater.* **2019**, *18*, 1278.
- [107] J. B. Goodenough, Y. Kim, *Chem. Mater.* **2010**, *22*, 587.
- [108] M. Widmaier, B. Krüner, N. Jäckel, M. Aslan, S. Fleischmann, C. Engel, V. Presser, *J. Electrochem. Soc.* **2016**, *163*, A2956.
- [109] K. Pfeifer, S. Arnold, Ö. Budak, X. Luo, V. Presser, H. Ehrenberg, S. Dsoke, *J. Mater. Chem. A* **2020**, *8*, 6092.
- [110] P. Verma, P. Maire, P. Novák, *Electrochim. Acta* **2010**, *55*, 6332.
- [111] K. Kim, S. M. Hwang, J.-S. Park, J. Han, J. Kim, Y. Kim, *J. Power Sources* **2016**, *313*, 46.
- [112] D. H. Suh, S. K. Park, P. Nakhanivej, Y. Kim, S. M. Hwang, H. S. Park, *J. Power Sources* **2017**, *372*, 31.
- [113] B. Lee, E. Paek, D. Mitlin, S. W. Lee, *Chem. Rev.* **2019**, *119*, 5416.
- [114] G. Kim, M. Oh, Y. Park, *Sci. Rep.* **2016**, *6*, 33400.
- [115] K. H. Shin, J. Park, S. K. Park, P. Nakhanivej, S. M. Hwang, Y. Kim, H. S. Park, *J. Ind. Eng. Chem.* **2019**, *72*, 250.
- [116] E. Yoo, H. Zhou, *ACS Nano* **2011**, *5*, 3020.
- [117] Z. Zhao, M. Li, L. Zhang, L. Dai, Z. Xia, *Adv. Mater.* **2015**, *27*, 6834.
- [118] S. Chen, J. Duan, M. Jaroniec, S. Z. Qiao, *Adv. Mater.* **2014**, *26*, 2925.
- [119] L. Tao, Q. Wang, S. Dou, Z. Ma, J. Huo, S. Wang, L. Dai, *Chem. Commun.* **2016**, *52*, 2764.
- [120] P. He, T. Zhang, J. Jiang, H. Zhou, *J. Phys. Chem. Lett.* **2016**, *7*, 1267.
- [121] Y. Lee, J. Suntivich, K. J. May, E. E. Perry, Y. Shao-Horn, *J. Phys. Chem. Lett.* **2012**, *3*, 399.
- [122] K. Kishor, S. Saha, M. K. Gupta, A. Bajpai, M. Chatterjee, S. Sivakumar, R. G. S. Pala, *ChemElectroChem* **2015**, *2*, 1839.
- [123] H. Bae, J.-S. Park, S. T. Senthilkumar, S. M. Hwang, Y. Kim, *J. Power Sources* **2019**, *410–411*, 99.
- [124] Y. Kim, A. M. Harzandi, J. Lee, Y. Choi, Y. Kim, *Adv. Sustainable Syst.* **2021**, *5*, 2000106.
- [125] R. Korthauer, *Handbuch Lithium-Ionen-Batterien*, Springer Vieweg, Berlin, Heidelberg **2013**, pp. 271–273.
- [126] M. Faraday, *Philos. Trans. R. Soc. London* **1834**, *124*, 77.
- [127] J. Jung, D. Y. Hwang, I. Kristanto, S. K. Kwak, S. J. Kang, *J. Mater. Chem. A* **2019**, *7*, 9773.
- [128] C. Menictas, M. Skyllas-Kazacos, T. M. Lim, *Advances in Batteries for Medium and Large-Scale Energy Storage: Types and Applications*, Elsevier, New York **2014**.
- [129] S. Park, B. Senthilkumar, K. Kim, S. M. Hwang, Y. Kim, *J. Mater. Chem. A* **2016**, *4*, 7207.
- [130] W. Wei, W. Zou, D. Yang, R. Zheng, R. Wang, H. Chen, *J. Mater. Chem. A* **2020**, *8*, 11811.
- [131] M. Son, S. Park, N. Kim, A. T. Angeles, Y. Kim, K. H. Cho, *Adv. Sci.* **2021**, *8*, 2101289.
- [132] Y. Zhang, S. T. Senthilkumar, J. Park, J. Park, Y. Kim, *Batteries Supercaps* **2018**, *1*, 6.
- [133] K. Lee, N. Chromey, R. Culik, J. Barnes, P. Schneider, *Fundam. Appl. Toxicol.* **1987**, *9*, 222.
- [134] Y. Yu, H. Che, X. Yang, Y. Deng, L. Li, Z.-F. Ma, *Electrochem. Commun.* **2020**, *110*, 106635.
- [135] E. P. Roth, C. J. Orendorff, *Electrochem. Soc. Interface* **2012**, *21*, 45.
- [136] Y. Fang, L. Xiao, Z. Chen, X. Ai, Y. Cao, H. Yang, *Electrochem. Energy Rev.* **2018**, *1*, 294.
- [137] S.-L. Chou, J.-Z. Wang, H.-K. Liu, S.-X. Dou, *J. Phys. Chem. C* **2011**, *115*, 16220.
- [138] D. Versaci, R. Nasi, U. Zubair, J. Amici, M. Sgroi, M. A. Dumitrescu, C. Francia, S. Bodoardo, N. Penazzi, *J. Solid State Electrochem.* **2017**, *21*, 3429.
- [139] L. Fransson, T. Eriksson, K. Edström, T. Gustafsson, J. O. Thomas, *J. Power Sources* **2001**, *101*, 1.
- [140] K. Pfeifer, S. Arnold, J. Becherer, C. Das, J. Maibach, H. Ehrenberg, S. Dsoke, *ChemSusChem* **2019**, *12*, 3312.
- [141] T. Nakajima, H. Groult, *Fluorinated Materials for Energy Conversion*, Elsevier, New York **2005**.
- [142] T. Nakajima, H. Groult, *Advanced Fluoride-Based Materials for Energy Conversion*, Elsevier, New York **2015**.
- [143] C. C. Nguyen, T. Yoon, D. M. Seo, P. Guduru, B. L. Lucht, *ACS Appl. Mater. Interfaces* **2016**, *8*, 12211.
- [144] Y. Kim, A. Varzi, A. Mariani, G.-T. Kim, Y. Kim, S. Passerini, *Adv. Energy Mater.* **2021**, *11*, 2102061.
- [145] J.-I. Jung, D. Kim, H. Kim, Y. N. Jo, J. S. Park, Y. Kim, *ACS Appl. Mater. Interfaces* **2017**, *9*, 304.
- [146] B. D. McCloskey, *J. Phys. Chem. Lett.* **2015**, *6*, 3592.
- [147] S. Maass, F. Finsterwalder, G. Frank, R. Hartmann, C. Merten, *J. Power Sources* **2008**, *176*, 444.
- [148] J. Park, H. Oh, T. Ha, Y. I. Lee, K. Min, *Appl. Energy* **2015**, *155*, 866.
- [149] H.-S. Oh, J.-G. Oh, S. Haam, K. Arunabha, B. Roh, I. Hwang, H. Kim, *Electrochem. Commun.* **2008**, *10*, 1048.
- [150] J. Wang, G. Yin, Y. Shao, S. Zhang, Z. Wang, Y. Gao, *J. Power Sources* **2007**, *171*, 331.
- [151] B. Avasarala, R. Moore, P. Haldar, *Electrochim. Acta* **2010**, *55*, 4765.
- [152] L. Roen, C. Paik, T. Jarvi, *Electrochem. Solid State Lett.* **2003**, *7*, A19.
- [153] H. Tang, Z. Qi, M. Ramani, J. F. Elter, *J. Power Sources* **2006**, *158*, 1306.
- [154] M. Cai, M. S. Ruthkosky, B. Merzougui, S. Swathirajan, M. P. Balogh, S. H. Oh, *J. Power Sources* **2006**, *160*, 977.
- [155] L. Eifert, R. Banerjee, Z. Jusys, R. Zeis, *J. Electrochem. Soc.* **2018**, *165*, A2577.
- [156] Ø. Hasvold, H. Henriksen, E. Melv, G. Citi, B. Ø. Johansen, T. Kjøningsten, R. Galetti, *J. Power Sources* **1997**, *65*, 253.
- [157] H. Wang, B.-H. Chen, D.-J. Liu, *Adv. Mater.* **2021**, *33*, 2008023.
- [158] A. K. Thakur, M. Majumder, S. P. Patole, K. Zaghbi, M. V. Reddy, *Mater. Adv.* **2021**, *2*, 2457.
- [159] B. Singh, A. Indra, *Mater. Today Energy* **2020**, *16*, 100404.
- [160] T. Hashimoto, K. Hayashi, *Electrochim. Acta* **2015**, *182*, 809.
- [161] S. Dong, X. Chen, S. Wang, L. Gu, L. Zhang, X. Wang, X. Zhou, Z. Liu, P. Han, Y. Duan, *ChemSusChem* **2012**, *5*, 1712.
- [162] G. Liu, M. Wang, Y. Xu, X. Wang, X. Li, J. Liu, X. Cui, L. Jiang, *J. Power Sources* **2021**, *486*, 229351.
- [163] S.-E. Jang, H. Kim, *J. Am. Chem. Soc.* **2010**, *132*, 14700.
- [164] J.-G. Oh, W. H. Lee, H. Kim, *Int. J. Hydrogen Energy* **2012**, *37*, 2455.
- [165] L. Tao, M. Qiao, R. Jin, Y. Li, Z. Xiao, Y. Wang, N. Zhang, C. Xie, Q. He, D. Jiang, *Angew. Chem., Int. Ed.* **2019**, *131*, 1031.

- [166] S. Jeoung, S. H. Sahgong, J. H. Kim, S. M. Hwang, Y. Kim, H. R. Moon, *J. Mater. Chem. A* **2016**, *4*, 13468.
- [167] B. Koo, H. Kim, Y. Cho, K. T. Lee, N. S. Choi, J. Cho, *Angew. Chem., Int. Ed.* **2012**, *124*, 8892.
- [168] C. Kim, P. Srimuk, J. Lee, V. Presser, *Desalination* **2018**, *443*, 56.
- [169] N. D. K. Tu, S. O. Park, J. Park, Y. Kim, S. K. Kwak, S. J. Kang, *ACS Appl. Energy Mater.* **2020**, *3*, 1602.
- [170] G.-y. Zheng, S. Lee, Z. Liang, H. Lee, K. Yan, H. Yao, H. Wang, W. Li, Y. Cui, *Nat. Nanotechnol.* **2014**, *9*, 618.
- [171] P. Bai, J. Li, F. R. Brushett, M. Z. Bazant, *Energy Environ. Sci.* **2016**, *9*, 3221.
- [172] W. Li, H. Yao, K. Yan, G. Zheng, Z. Liang, Y.-M. Chiang, Y. Cui, *Nat. Commun.* **2015**, *6*, 7436.
- [173] C.-P. Yang, Y.-X. Yin, S.-F. Zhang, N.-W. Li, Y.-G. Guo, *Nat. Commun.* **2015**, *6*, 8058.
- [174] S. Liu, A. Wang, Q. Li, J. Wu, K. Chiou, J. Huang, J. Luo, *Joule* **2018**, *2*, 184.
- [175] R. Zhang, X. R. Chen, X. Chen, X. B. Cheng, X. Q. Zhang, C. Yan, Q. Zhang, *Angew. Chem., Int. Ed.* **2017**, *129*, 7872.
- [176] R. Xu, X. Q. Zhang, X. B. Cheng, H. J. Peng, C. Z. Zhao, C. Yan, J. Q. Huang, *Adv. Funct. Mater.* **2018**, *28*, 1705838.
- [177] H. Lee, X. Ren, C. Niu, L. Yu, M. H. Engelhard, I. Cho, M. H. Ryou, H. S. Jin, H. T. Kim, J. Liu, *Adv. Funct. Mater.* **2017**, *27*, 1704391.
- [178] Z. W. Seh, J. Sun, Y. Sun, Y. Cui, *ACS Cent. Sci.* **2015**, *1*, 449.
- [179] Y. Zhao, L. V. Goncharova, A. Lushington, Q. Sun, H. Yadegari, B. Wang, W. Xiao, R. Li, X. Sun, *Adv. Mater.* **2017**, *29*, 1606663.
- [180] A. P. Cohn, N. Muralidharan, R. Carter, K. Share, C. L. Pint, *Nano Lett.* **2017**, *17*, 1296.
- [181] W. Zhou, Y. Li, S. Xin, J. B. Goodenough, *ACS Cent. Sci.* **2017**, *3*, 52.
- [182] J. Song, G. Jeong, A.-J. Lee, J. H. Park, H. Kim, Y.-J. Kim, *ACS Appl. Mater. Interfaces* **2015**, *7*, 27206.
- [183] D. Ruiz-Martinez, A. Kovacs, R. Gómez, *Energy Environ. Sci.* **2017**, *10*, 1936.
- [184] Y. Zhao, L. V. Goncharova, Q. Zhang, P. Kaghazchi, Q. Sun, A. Lushington, B. Wang, R. Li, X. Sun, *Nano Lett.* **2017**, *17*, 5653.
- [185] A. Wang, X. Hu, H. Tang, C. Zhang, S. Liu, Y. W. Yang, Q. H. Yang, J. Luo, *Angew. Chem., Int. Ed.* **2017**, *129*, 12083.
- [186] S. Liu, S. Tang, X. Zhang, A. Wang, Q.-H. Yang, J. Luo, *Nano Lett.* **2017**, *17*, 5862.
- [187] W. Xu, J. Wang, F. Ding, X. Chen, E. Nasybulin, Y. Zhang, J.-G. Zhang, *Energy Environ. Sci.* **2014**, *7*, 513.
- [188] Y. Guo, H. Li, T. Zhai, *Adv. Mater.* **2017**, *29*, 1700007.
- [189] D. H. Kim, H. Choi, D. Y. Hwang, J. Park, K. S. Kim, S. Ahn, Y. Kim, S. K. Kwak, Y.-J. Yu, S. J. Kang, *J. Mater. Chem. A* **2018**, *6*, 19672.
- [190] D. Kim, J.-S. Park, W.-G. Lee, Y. Choi, Y. Kim, *J. Electrochem. Soc.* **2022**, *169*, 040508.
- [191] Y. Kim, J. Jung, H. Yu, G.-T. Kim, D. Jeong, D. Bresser, S. J. Kang, Y. Kim, S. Passerini, *Adv. Funct. Mater.* **2020**, *30*, 2001249.
- [192] J. Cho, M. W. Kim, Y. Kim, J.-S. Park, D.-H. Lee, Y. Kim, J. J. Kim, *IEEE Access* **2021**, *9*, 104104.
- [193] J. H. Kim, S. M. Hwang, I. Hwang, J. Han, J. H. Kim, Y. H. Jo, K. Seo, Y. Kim, J. S. Lee, *iScience* **2019**, *19*, 232.
- [194] N. Kim, J.-S. Park, A. M. Harzandi, K. Kishor, M. Ligaray, K. H. Cho, Y. Kim, *Desalination* **2020**, *495*, 114666.
- [195] J.-S. Park, S. Kim, Y. Choi, A. M. Harzandi, Y. Kim, *ACS ES&T Water* **2021**, *1*, 2146.
- [196] *Wastewater Technology Fact Sheet: Dechlorination*, United States Environmental Protection Agency, Washington, DC **2000**, p. EPA 832-F-00-022.
- [197] T. Lim, G. Y. Jung, J. H. Kim, S. O. Park, J. Park, Y.-T. Kim, S. J. Kang, H. Y. Jeong, S. K. Kwak, S. H. Joo, *Nat. Commun.* **2020**, *11*, 412.
- [198] F. Yu, L. Wang, Y. Wang, X. Shen, Y. Cheng, J. Ma, *J. Mater. Chem. A* **2019**, *7*, 15999.
- [199] L. F. Greenlee, D. F. Lawler, B. D. Freeman, B. Marrot, P. Moulin, *Water Res.* **2009**, *43*, 2317.
- [200] A. Ophir, A. Gendel, *Desalination* **2007**, *205*, 224.
- [201] M. Ligaray, N. Kim, S. Park, J.-S. Park, J. Park, Y. Kim, K. H. Cho, *Chem. Eng. J.* **2020**, *395*, 125082.
- [202] J. Kim, K. Park, D. R. Yang, S. Hong, *Appl. Energy* **2019**, *254*, 113652.
- [203] R. Semiat, *Environ. Sci. Technol.* **2008**, *42*, 8193.
- [204] J. Lee, P. Srimuk, S. Carpiere, J. Choi, R. L. Zornitta, C. Kim, M. Aslan, V. Presser, *ChemSusChem* **2018**, *11*, 3460.
- [205] J. Ma, C. He, D. He, C. Zhang, T. D. Waite, *Water Res.* **2018**, *144*, 296.
- [206] K. B. Hatzell, M. C. Hatzell, K. M. Cook, M. Boota, G. M. Housel, A. McBride, E. C. Kumbur, Y. Gogotsi, *Environ. Sci. Technol.* **2015**, *49*, 3040.
- [207] S. Yang, J. Choi, J.-g. Yeo, S.-i. Jeon, H.-r. Park, D. K. Kim, *Environ. Sci. Technol.* **2016**, *50*, 5892.
- [208] F. Chen, J. Wang, C. Feng, J. Ma, T. David Waite, *Chem. Eng. J.* **2020**, *401*, 126111.
- [209] S. Yang, S.-i. Jeon, H. Kim, J. Choi, J.-g. Yeo, H.-r. Park, D. K. Kim, *ACS Sustainable Chem. Eng.* **2016**, *4*, 4174.
- [210] J. Chang, F. Duan, H. Cao, K. Tang, C. Su, Y. Li, *Desalination* **2019**, *468*, 114080.
- [211] H.-r. Park, J. Choi, S. Yang, S. J. Kwak, S.-i. Jeon, M. H. Han, D. K. Kim, *RSC Adv.* **2016**, *6*, 69720.
- [212] J. Lee, S. Kim, C. Kim, J. Yoon, *Energy Environ. Sci.* **2014**, *7*, 3683.
- [213] L. Wang, S. Lin, *Water Res.* **2018**, *129*, 394.
- [214] J.-Y. Hwang, S.-T. Myung, Y.-K. Sun, *Chem. Soc. Rev.* **2017**, *46*, 3529.
- [215] M. R. Palacin, *Chem. Soc. Rev.* **2009**, *38*, 2565.
- [216] S. Liang, Y. Yang, K. Li, X. Zhang, *J. Eur. Ceram. Soc.* **2020**, *40*, 4047.
- [217] H. Park, K. Jung, M. Nezaferi, C. S. Kim, B. Kang, *ACS Appl. Mater. Interfaces* **2016**, *8*, 27814.
- [218] W. Go, M.-H. Kim, J. Park, C. H. Lim, S. H. Joo, Y. Kim, H.-W. Lee, *Nano Lett.* **2019**, *19*, 1504.
- [219] H. Choi, D. Y. Hwang, J. Park, K. S. Kim, S. Ahn, Y. Kim, S. K. Kwak, Y.-J. Yu, S. J. Kang, *J. Mater. Chem. A* **2018**, *6*, 19672.
- [220] S. Park, M. Ligaray, Y. Kim, K. Chon, M. Son, K. H. Cho, *Desalination* **2021**, *506*, 115018.
- [221] C. Kim, J. Lee, P. Srimuk, M. Aslan, V. Presser, *ChemSusChem* **2017**, *10*, 4914.
- [222] M. Aslan, M. Zeiger, N. Jäckel, I. Grobelsek, D. Weingarth, V. Presser, *J. Phys.: Condens. Matter* **2016**, *28*, 114003.
- [223] Y. Zhang, P. Srimuk, M. Aslan, M. Gallei, V. Presser, *Desalination* **2020**, *479*, 114331.
- [224] F. Chen, Y. Huang, L. Guo, L. Sun, Y. Wang, H. Y. Yang, *Energy Environ. Sci.* **2017**, *10*, 2081.
- [225] P. Srimuk, J. Lee, A. Tolosa, C. Kim, M. Aslan, V. Presser, *Chem. Mater.* **2017**, *29*, 9964.
- [226] J. Lee, S. Kim, J. Yoon, *ACS Omega* **2017**, *2*, 1653.
- [227] W. Shi, X. Qian, M. Xue, W. Que, X. Gao, D. Zheng, W. Liu, F. Wu, J. Shen, X. Cao, *ACS Appl. Mater. Interfaces* **2021**, *13*, 21149.
- [228] F. Reverberi, A. Gorenflo, *Desalination* **2007**, *203*, 100.
- [229] J. Kim, K. Park, S. Hong, *J. Membr. Sci.* **2020**, *601*, 117889.
- [230] T. Seto, L. Ehara, R. Komori, A. Yamaguchi, T. Miwa, *Desalination* **1978**, *25*, 1.
- [231] M. Turek, *Desalination* **2003**, *153*, 371.



Stefanie Arnold is presently a Ph.D. student under the supervision of Prof. Volker Presser at the Department of Materials Science and Engineering, Saarland University, and the INM – Leibniz Institute for New Materials in Saarbrücken, Germany. A trained chemist, she received her bachelor's degree and her master's degree from the Karlsruhe Institute of Technology, Germany, in 2018 and 2020, respectively. Her research explores high-performance sodium-ion battery materials, novel technologies for battery recycling, and water remediation.



Lei Wang is a doctoral student under the supervision of Prof. Volker Presser at the Department of Materials Science and Engineering, Saarland University, and the INM – Leibniz Institute for New Materials in Saarbrücken, Germany. He received his bachelor's degree at Sun Yat-sen University, Guangzhou, China, in 2016 and his master's degree in Environmental Engineering at Tongji University, Shanghai, China, in 2019. His current research is related to ion separation and water desalination via electrochemical methods.



Volker Presser is professor for Energy Materials at Saarland University, Program Division Leader at the INM – Leibniz Institute for New Materials, and Managing Director of the Saarland Center for Energy Materials and Sustainability (saarene) in Saarbrücken (Germany). He obtained his Ph.D. from the Eberhard-Karls-University Tübingen (Germany) in 2009 and worked as a Humboldt Fellow and Research Assistant Professor in the team of Yury Gogotsi at Drexel University (2010–2012). His research focuses next-generation materials (incl. MXene and hybrid materials) for energy storage and water remediation (esp. lithium recovery and seawater desalination).

4.3 MXene/activated-carbon hybrid capacitive deionization for permselective ion removal at low and high salinity

Mohammad Torkamanzadeh,^{1,2} Lei Wang,^{1,2} Yuan Zhang,^{1,2}
Öznil Budak,^{1,2} Pattarachai Srimuk,^{1,2} and Volker Presser^{1,2}

¹ INM - Leibniz Institute for New Materials, 66123 Saarbrücken, Germany

² Department of Materials Science and Engineering, Saarland University, 66123 Saarbrücken, Germany

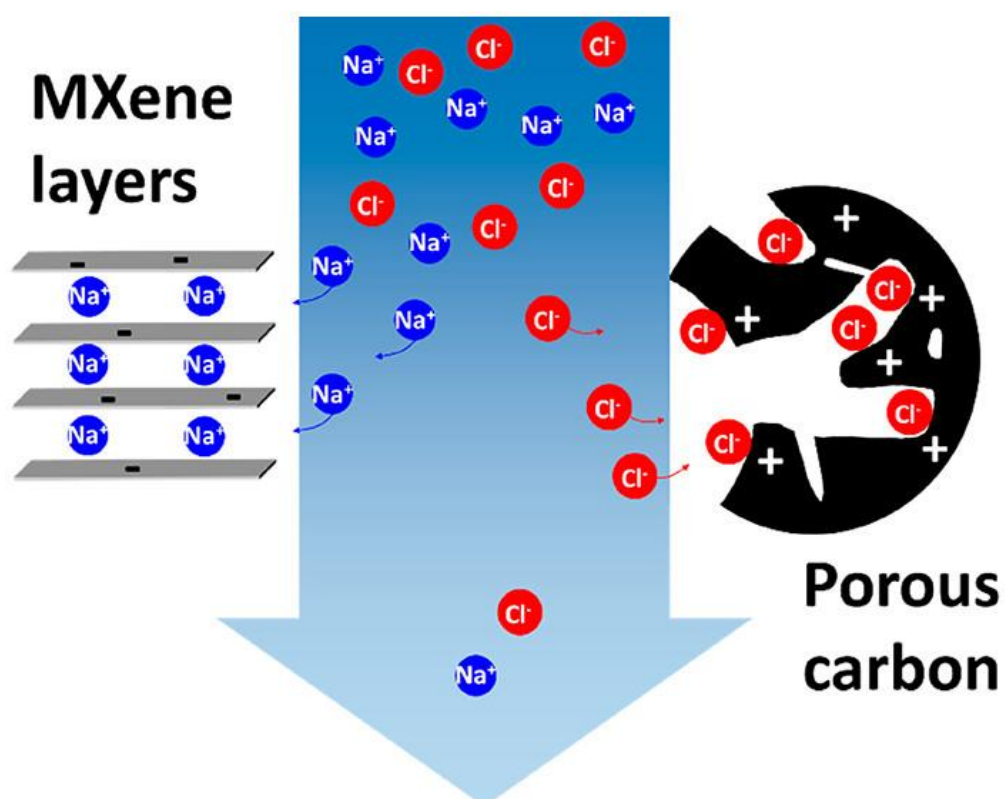
Citation:

M. Torkamanzadeh, L. Wang, Y. Zhang, Ö. Budak, P. Srimuk, V. Presser, MXENE/ACTIVATED-CARBON HYBRID CAPACITIVE DEIONIZATION FOR PERMSELECTIVE ION REMOVAL AT LOW AND HIGH SALINITY, **ACS Applied Materials & Interfaces**, 12 (2020) 26013-26025.

DOI: 10.1021/acsami.0c05975.

Own contribution:

Investigation, Formal analysis, data curation, Writing - Review & Editing



MXene/Activated-Carbon Hybrid Capacitive Deionization for Permselective Ion Removal at Low and High Salinity

Mohammad Torkamanzadeh, Lei Wang, Yuan Zhang, Öznil Budak, Pattarachai Srimuk, and Volker Presser*



Cite This: *ACS Appl. Mater. Interfaces* 2020, 12, 26013–26025



Read Online

ACCESS |



Metrics & More



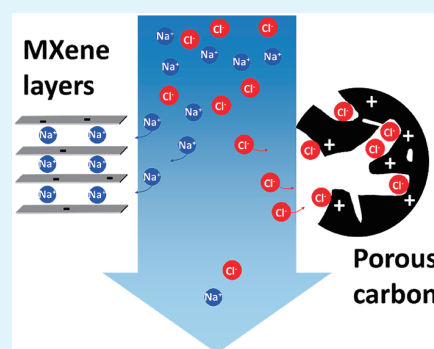
Article Recommendations



Supporting Information

ABSTRACT: Two-dimensional, layered transition metal carbides (MXenes) are an intriguing class of intercalation-type electrodes for electrochemical applications. The ability for preferred counterion uptake qualifies MXenes as an attractive material for electrochemical desalination. Our work explores $\text{Ti}_3\text{C}_2\text{T}_x$ -MXene paired with activated carbon in such a way that both electrodes operate in an optimized potential range. This is accomplished by electrode mass balancing and control over the cell voltage. Thereby, we enable effective remediation of saline media with low (brackish) and high (seawater-like) ionic strength by using 20 and 600 mM aqueous NaCl solutions. It is shown that MXene/activated-carbon asymmetric cell design capitalizes on the permselective behavior of MXene in sodium removal, which in turn forces carbon to mirror the same behavior in the removal of chloride ions. This has minimized the notorious co-ion desorption of carbon in highly saline media (600 mM NaCl) and boosted the charge efficiency from 4% in a symmetric activated-carbon/activated-carbon cell to 85% in a membrane-less asymmetric MXene/activated-carbon cell. Stable electrochemical performance for up to 100 cycles is demonstrated, yielding average desalination capacities of 8 and 12 mg/g, respectively, for membrane-less MXene/activated-carbon cells in NaCl solutions of 600 mM (seawater-level) and 20 mM (brackish-water-level). In the case of the 20 mM NaCl solutions, surprising charge efficiency values of over 100% have been obtained, which is attributed to the role of MXene interlayer surface charges.

KEYWORDS: MXene, intercalation, capacitive deionization, desalination, seawater, asymmetric



1. INTRODUCTION

The development of sustainable water desalination technologies is crucial as clean water shortage has become a global concern.¹ This challenge pertains to enhanced energy efficiency and performance durability at low operational costs. Capacitive deionization (CDI) is a promising water desalination technology that offers certain advantages over other widely employed alternatives such as reverse osmosis, and thermal desalination.² CDI devices operate at low pressure and have reduced energy consumption, especially at ultralow to low salinity levels.³ A CDI cell is conceptually a flow-through electrochemical capacitor.⁴ Upon charging the CDI cell, water-dissolved ions are removed from the saline water feed stream via electrosorption: Sodium ions are attracted to the negatively charged electrode, and chloride ions are attracted to the positively charged electrode. Upon discharging, the ions are released back to the stream, and, as a result, the regenerated electrodes can be used in the subsequent cycle. At the same time, the invested electrical charge is (mostly) recovered by which feature added energy efficiency of the CDI technology is afforded. In this context, there are two important, among other performance metrics: the desalination capacity (DC) measures the effective amount of salt removed per mass

of the electrode and the charge efficiency (CE) gives the ratio of invested total charge versus the charge corresponding to the removed ionic species.⁵

Until recently, CDI research had focused on carbon-based materials as electrodes.⁶ The large surface area of nanoporous carbon provides microporous channels for effective electrostatic immobilization of ions at the carbon/electrolyte interface.⁷ In the absence of intrinsic permselectivity, co-ion desorption of microporous carbon prevents bulk ion removal via ion electrosorption at high molar strength, such as that found in saline water or brine.⁷ This issue can, partially, be remedied by implementing ion-exchange membranes, giving rise to membrane CDI (MCDI).⁸ However, while the implementation of ion-exchange membranes also allows the design of multichannel desalination cells,⁹ it adds additional costs and cannot overcome the intrinsic charge-limitation of

Received: March 31, 2020

Accepted: May 13, 2020

Published: May 13, 2020



carbon material. Alternatively, permselective counterion adsorption via suppressed co-ion presence can be enhanced even at high molar strength when lowering the carbon pore size below 1 nm.¹⁰

In recent years, electrochemical desalination employing Faradaic (charge-transfer) materials has overcome the limitation to low molar regimes (<100–200 mM) and limited desalination capacity (ca. 20–30 mg_{NaCl}/g_{electrode}) of carbon-based CDI.¹¹ In 2012, Pasta et al. introduced a desalination battery by employing layered sodium manganese oxide to remove sodium ions from seawater without a need for ion-exchange membranes.¹² Lee et al. introduced the combination of a Faradaic and an electrosorption (carbon) electrode to enhance the CDI performance, but without accessing high molar strength regimes.¹³ Until now, a large and rapidly growing number of charge-transfer materials have already been explored, including intercalation compounds,¹⁴ conversion materials,¹⁵ electroactive polymers,¹⁶ redox-active electrolytes,¹⁷ and combinations of such materials. Even more advanced approaches utilize high-capacity processes, such as oxidant generation¹⁸ or metal–air processes.¹⁹

Of interest for any application involving the intercalation of cations and anions are two-dimensional (2D) materials. For example, Ti₃C₂T_x is a member of a large family of 2D materials called MXene.²⁰ MXene is derived via selective etching of A-site atoms from a M_{n+1}AX_n phase, where M stands for an early transition metal, A stands for group 13 or 14 elements (typically Al), X stands for carbon and/or nitrogen, and *n* = 1, 2, or 3.²¹ To carry the meaning of surface functional groups, T_x is added to the chemical formula of MXene, to describe fluorine-, chlorine-, and oxygen-containing functionalities.²² For instance, Ti₃C₂T_x is commonly obtained by removing Al from Ti₃AlC₂ through aqueous HF etching (but nonaqueous processing is also possible).²³ Upon etching, Al is replaced by a mixture of surface terminations (O, OH, and F), rendering a typical MXene hydrophilic with a negative surface charge.²⁰ The layered structure of MXene allows for ions to be inserted into the material (ion intercalation), a property that in addition to a high conductivity²⁴ and facile processability²⁵ makes MXene attractive for electrochemical energy storage and water remediation. MXenes have shown promise in numerous energy storage applications as lithium-ion battery²⁶ or supercapacitor²⁷ electrodes, as well as in environmental remediation applications such as ion-sieving membranes²⁸ or heavy metal ion removal.²⁹

Electrochemical desalination is a less widely explored domain of MXene research.³⁰ As the first, Srimuk et al. introduced Ti₃C₂T_x-MXene in a symmetric cell for desalination of low molar (5 mM NaCl) water.¹⁴ Using MXene as an intercalation type material for both electrodes, a desalination capacity of 13 mg_{NaCl}/g_{electrode} was obtained with stable performance for 30 cycles. Subsequent works on MXene electrochemical desalination have focused on postprocessing and modification of Ti₃C₂T_x MXene to enhance its salt removal capacity. The latter works include vacuum freeze-drying and (45 mg_{NaCl}/g_{electrode}),³¹ substituting HF-etching with LiF/HCl treatment (68 mg_{NaCl}/g_{electrode}),³² and nitrogen-doping (44 mg_{NaCl}/g_{electrode})³³ to prevent restacking of MXene layers and form electrochemically active porous structures. These promising works underline MXene as an aspiring material for water treatment applications.³⁴

However, Ti-based MXenes operated in aqueous environments are notoriously affected by aging via hydrolysis-aided

oxidation.³⁵ This issue particularly affects the usefulness of Ti₃C₂T_x as the positively polarized electrode for electrochemical desalination of water. To fully capitalize on the electrochemical performance of Ti-MXene in aqueous media, it is convenient to limit its application to the negatively polarized electrode where no oxidation will occur. Unlike operation as asymmetric supercapacitors,³⁶ asymmetric desalination cells with MXene as only one of the electrode pair has remained incompletely explored.³⁴ This includes the important aspect of mass balancing to optimize the operational cell voltage of each of the two electrodes, as recently shown by Dryfe's group for carbon-based CDI.³⁷ Mechanistically, the interesting aspect of addressing is the degree of permselectivity of the nanoporous carbon electrode when paired with a permselective intercalation-type electrode, such as MXene. We explore if the permselective behavior of the intercalation electrode will "force" the carbon electrode to prefer counterions rather than 1:1 exchange a co-ion with a counterion. This is of high importance for saline media with high salt concentration because using only one intercalation-type electrode paired with activated carbon as the other electrode would lower system cost because of the high abundance of carbon and eliminate the need for expensive ion-exchange membranes.

Our study investigates the desalination of seawater-level saline solutions (600 mM NaCl) and brackish water (20 mM NaCl). We paired Ti₃C₂T_x-MXene with activated carbon in an asymmetric cell so that we can capitalize on sodium-ion intercalation on the MXene side and chloride ion electrosorption within carbon nanopores. Our focus is not the optimization toward the highest possible desalination metrics; instead, our work focuses on the mechanistic aspect of the desalination process. Specifically, our work explores the ion permselectivity of the carbon electrode paired with that of MXene by comparing cell performance with and without adding a polymeric ion-exchange membrane in front of the activated carbon. Thereby, we can compare the electrochemical desalination performance of the cell when the carbon electrode is shielded (with an ion-exchange membrane) or directly exposed to the saline medium. Characterization of the MXene-CNT electrodes before and after use for over 100 cycles provides insights into performance stability and degradation mechanisms.

2. MATERIALS AND METHODS

2.1. Electrode Preparation and Electrochemical Measurements. The following materials were used as-received: activated carbon (type YP-80F, Kuraray), multiwalled carbon nanotubes (CNT, Graphene Supermarket), and Ti₃C₂T_x-MXene (Laizhou Kai Kai Ceramic Materials Co.). As seen from Figure S1, activated carbon has a large surface area of 1644 m²/g and is composed of internal porosity within the activated carbon particles. In contrast, carbon nanotubes have a very small surface area of just 71 m²/g (Figure S1) which relates to external porosity.³⁸

To prepare carbon electrodes, activated carbon and polytetrafluoroethylene binder (PTFE, 60 mass% solution in water from Sigma-Aldrich) in a 95:5 carbon/binder mass-ratio were mixed in ethanol to give a homogeneous carbon paste.³⁹ Afterward, the carbon paste was rolled (MTI HR01, MIT Corp.) to 600 μm thick freestanding electrode films, which was then dried in a vacuum oven at +120 °C overnight.

To prepare MXene-CNT electrodes, Ti₃C₂T_x-MXene and CNT in a 10:1 MXene/CNT mass ratio were tip-sonicated in ethanol for 30 min.⁴⁰ The solution was subsequently vacuum filtered through polyvinylidene fluoride (PVDF) membranes (0.22 μm, Durapore)

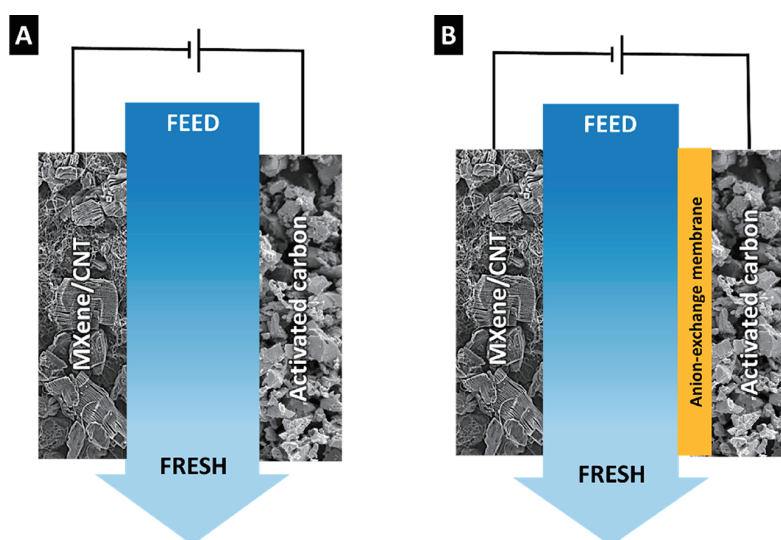


Figure 1. Schematic of an asymmetric electrochemical water desalination cell (A) without an ion-exchange membrane and (B) with an anion-exchange membrane.

and dried in an oven at +80 °C overnight. This electrode is labeled MXene-CNT in our work.

In a typical half-cell experiment, circular-shaped 12 mm diameter pieces were punched out of the MXene-CNT electrode and used as the working electrode. An oversized activated carbon electrode was used as counter electrode and glass fiber (GF/A, Whatman) was used as a separator. All components were placed in a custom-built cell between spring-loaded titanium pistons.⁴¹ A reference electrode (Ag/AgCl, 3 M NaCl) was mounted onto the side of the cell in a way that its porous frit was near the working and counter electrodes. The cell was filled with 600 mM NaCl aqueous electrolyte by vacuum backfilling using a syringe. Cyclic voltammetry (CV; scan rate: 1 mV/s) and galvanostatic charge/discharge tests were performed with a VSP300 potentiostat/galvanostat (Bio-Logic).

For full-cell electrochemical water desalination, a 30 mm diameter MXene-CNT electrode was punched out and used as the working electrode. On the basis of the mass of MXene-CNT, an activated carbon electrode with a suitable mass ratio (section 2.2) was cut and used as the counter electrode. The working and counter electrodes were stacked together and separated by glass fiber membranes. Thereby, the middle channel was formed and provided a pathway for 600 mM NaCl electrolyte to flow in between the electrodes (flow-by mode, Figure 1).⁴² A nonreinforced $31 \pm 2 \mu\text{m}$ thick anion-exchange membrane (Fumatech, FAS-30) was used on the side of the carbon electrode in certain cells. An Ag/AgCl spectator reference electrode was used to allow recording the electrode potentials of the activated carbon and MXene-CNT electrodes individually.

2.2. Electrode Mass Balancing. To determine the suitable mass ratio between MXene-CNT and activated carbon electrodes in a full desalination cell, cyclic voltammetric window-opening experiments⁴³ were performed at both negative and positive potentials. The results of this method reveal the ideal stable potential window for each of the electrode materials, as well as quantifying the amount of charge storable in each electrode at a certain potential. Using eq 1, one can balance the mass ratio of the electrodes based on cyclic voltammetric window-opening experiments:

$$\frac{m_{\text{MXene-CNT}}}{m_{\text{Activated_carbon}}} = \frac{Q_{\text{Activated_carbon}}}{Q_{\text{MXene-CNT}}} \quad (1)$$

where $Q_{\text{MXene-CNT}}$ (C/g) and $Q_{\text{Activated_carbon}}$ (C/g) are, respectively, the specific electric charge stored in MXene-CNT and activated carbon electrodes at a certain potential. The value of $m_{\text{MXene-CNT}}/m_{\text{Activated_carbon}}$ then gives the mass ratio between the two electrodes,

based on which a full cell with maximum desalination performance can be fabricated.

2.3. Desalination Experiments. All desalination experiments were performed using galvanostatic cycling with potential limitation (GCPL) technique via VSP300 potentiostat/galvanostat (Bio-Logic) electrochemical workstation at +25 °C. Each cycle duration was 2 h and consisted of two half-cycles. In the first half-cycle, the cell was charged to 1.2 V and held at that voltage for 1 h. In the second half-cycle, the cell was discharged to 0.3 V and at that voltage for another 1 h. Both charging and discharging steps were accomplished at 0.1 A/g current density (normalized to the combined mass of both activated carbon and MXene-CNT electrodes). A stream of saline was pumped into the cell at a 2 mL/min rate from a reservoir tank, which contained 10 L of electrolyte and was constantly bubbled with nitrogen prior to and during the experiments to deaerate the fluid. The effluent stream flowed out of the cell into a conductivity meter (Metrohm PT1000) and pH meter (WTW SensoLyt 900P) and flowed back into the tank to complete the loop. The pH and conductivity data were recorded every second online by computer. Calculations regarding the correlation of pH and conductivity data to concentration may be found in our previous work.⁴⁴ The desalination capacity ($\text{mg}_{\text{NaCl}}/\text{g}_{\text{electrode}}$) was calculated according to eq 2:

$$\text{desalination capacity (DC)} = \frac{\nu M_{\text{NaCl}}}{m_{\text{total}}} \int \Delta C \, dt \quad (2)$$

where ν is the flow rate (mL/min), M_{NaCl} is the molecular weight of NaCl (58.44 g/mol), m_{total} is the total mass of electrodes (g), t is the time over the adsorption or desorption step (min), and ΔC is the concentration change of NaCl (mM) in the effluent stream of the cell. The charge efficiency (%) was calculated following

$$\text{charge efficiency (CE)} = \frac{\frac{\text{DC}}{M_{\text{NaCl}}}}{\frac{Q}{F}} \times 100\% \quad (3)$$

where F is the Faraday constant (26 801 mAh/mol) and Q is the average of total charge stored in the two electrodes normalized to the total electrode mass (mAh/g).

2.4. Material Characterization. X-ray diffraction (XRD) analysis was conducted using a D8 Advance diffractometer (Bruker AXS) with a Ni-filtered copper X-ray source (Cu $K\alpha$, 40 kV, 40 mA) and a 2D detector (VANTEC-500). A JEOL JSM 7500F field-emission scanning electron microscope (JEOL) was used to record scanning electron microscopy (SEM) images. Energy-dispersive X-ray spec-

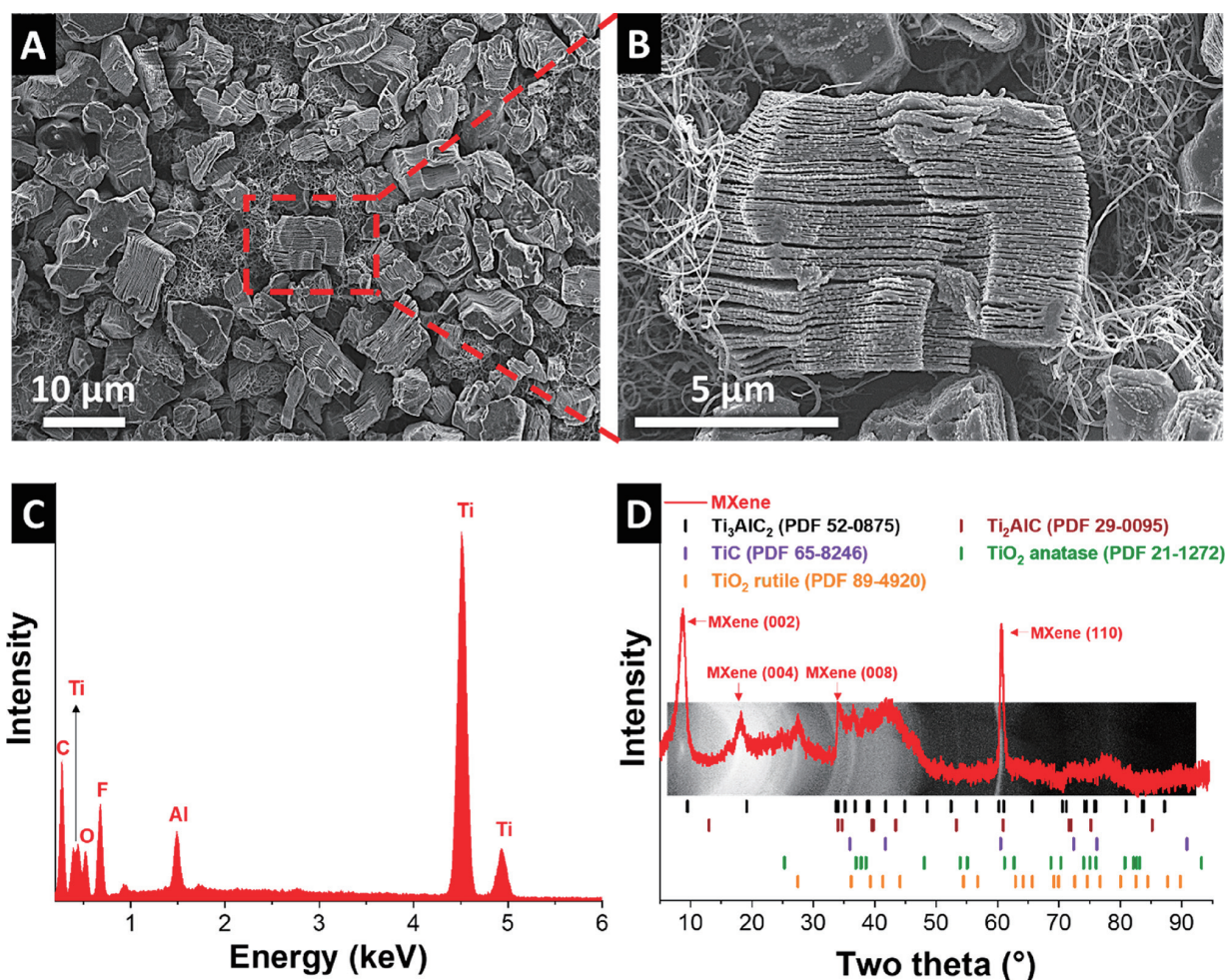


Figure 2. Characterization of the MXene-CNT electrode. (A, B) Scanning electron micrographs, (C) energy-dispersive X-ray spectrum (EDX), and (D) X-ray diffractogram and overlaid 2D diffraction pattern of $\text{Ti}_3\text{C}_2\text{T}_x$ -MXene alongside ideal pattern of different phases [Powder Diffraction File (PDF) nos. 21-1272, 29-0095, 52-0875, 65-8246, and 89-4920 are Joint Committee on Powder Diffraction Standards, 2004].

troscopy (EDX) was carried out at 12 kV with an X-Max Silicon Detector from Oxford Instruments using the AZtec software. Transmission electron microscopy (TEM) was conducted using a JEOL JEM-2100F system at an operating voltage of 200 kV. The samples were dispersed in ethanol and tip-sonicated briefly. The dispersion was then drop casted on a TEM copper grid with a lacy carbon film.

We used an Autosorb iQ system (Quantachrome) for nitrogen sorption at $-196\text{ }^\circ\text{C}$. The samples were degassed at 100 Pa and $200\text{ }^\circ\text{C}$ for 1 h and then at $300\text{ }^\circ\text{C}$ for 20 h. Alongside the isotherm of activated carbon, carbon nanotubes, MXene powder, and MXene-CNT electrodes, the specific surface area (SSA) was obtained via Brunauer–Emmett–Teller (BET) theory and by applying the quenched-solid density functional theory (QSDFT), assuming a slit-shaped pore model as provided in Figure S1.

The streaming potential was measured using a Müttek PCD-T3 instrument with the particle charge detection method. In a typical experiment, 50 mg of MXene or YP-80F carbon was dispersed in 30 mL of water. The mixture was then poured into a cylindrical PTFE container of the instrument with a PTFE piston inside. The automatic titration was conducted by gradual injection of HCl or NH_3 solutions into the mixture while the potential recorded online.

3. RESULTS AND DISCUSSION

3.1. Material Characterization. The SEM images depicted in Figure 2A show the morphology of pristine MXene-CNT electrodes. $\text{Ti}_3\text{C}_2\text{T}_x$ -MXene structures are observed with their typical layered accordion-like morphologies, entangled by CNTs. TEM images of the CNTs are provided in Figure S2. The incorporation of CNTs improves the mechanical stability of the electrode, as well as enhancing the electrical conductivity.⁴⁰ CNTs themselves have a specific surface area of $71\text{ m}^2/\text{g}$, which is predominately on the outer surface. $\text{Ti}_3\text{C}_2\text{T}_x$ -MXene exhibits an external surface area of $3\text{ m}^2/\text{g}$, and the mechanical mixture of 10 mass % CNTs and 90 mass % of MXene yields a surface area of $12\text{ m}^2/\text{g}$. The latter value is very close to the theoretical value of such a mixture (i.e., $10\text{ m}^2/\text{g}$), and the same goes for the corresponding pore volume ($0.04\text{ cm}^3/\text{g}$ measured for the composite electrode; Figure S1). The low values of surface area and pore volume originate from the porous space between the MXene bundles (Figure 2A) and not from within the interlayers of MXenes. There is no detriment to such a low level of porosity since electrochemical desalination via MXene is not based on ion electroadsorption but on the ion intercalation between the layers of the electrode material. In addition to providing electronic

Table 1. EDX Elemental Analysis of the Pristine MXene-CNT and Post-Mortem Electrodes of Different Cells after Long-Term Cycling^a

	C	Ti	O	Al	F	Na	Cl
pristine	13 ± 9	57 ± 13	9 ± 3	3 ± 3	17 ± 6		
post-mortem (600 mM + AEM)	12 ± 2	53 ± 5	22 ± 3	1 ± 0	6 ± 1	3 ± 0	3 ± 1
post-mortem (600 mM)	15 ± 3	58 ± 8	16 ± 4	0 ± 0	8 ± 2	2 ± 1	1 ± 0
post-mortem (20 mM + AEM)	10 ± 2	67 ± 8	15 ± 4	0 ± 0	5 ± 2	2 ± 0	1 ± 0
post-mortem (20 mM)	10 ± 2	61 ± 7	22 ± 4	1 ± 0	6 ± 2	1 ± 0	0 ± 0

^aAll values in mass %.

pathways and entangling MXene flakes, the CNTs also likely provide facile ion-transport pathways by preventing too tight packing of MXene particles.

At a higher resolution, we also see from the SEM image in Figure 2B, the presence of cuboid particles spread over the MXene surface. The latter particles are consistent with titanium oxide, and the presence of oxygen is confirmed by the EDX spectrum displayed in Figure 2C (EDX results are listed in Table 1). Ti-based MXene is known to oxidize in air, especially in the presence of humidity.³⁵ The EDX results also show a low amount (around 3 mass%) of residual aluminum, which stems from nonetched MAX phases or traces of aluminum fluoride from the etching products of the MAX phases.

XRD analysis confirms the presence of Ti₃C₂T_x-MXene. The XRD pattern in Figure 2D shows a strong (002) peak at 8.59° 2θ of Ti₃C₂T_x, compared to the initial value of (002)-Ti₃AlC₂ of the parent MAX phase at 9.52° 2θ. This corresponds with an 11% increase in the *d*-spacing along the *c*-axis. In addition to higher-order (00*l*)-type MXene reflections, we also see the characteristic MXene-peak related to (110)-Ti₃C₂T_x at about 61° 2θ.⁴⁵ No significant amounts of either Ti₂AlC or TiC are found from the diffraction pattern analysis. We also see the presence of minor amounts of titanium oxide (possibly rutile) from the diffraction signal generate at about 27° 2θ. Figure S3 provides the XRD pattern of the corresponding phases with their relative intensities.

3.2. Electrochemical Behavior. In the first step to determining the stable electrochemical potential window of the MXene-CNT and activated carbon electrodes, half-cell cyclic voltammetric window-opening measurements at a scan rate of 1 mV/s were carried out with 100 mV increments (Figure 3A,B). These experiments were carried out in aqueous 600 mM NaCl to avoid issues of ion starvation and to provide a baseline for later desalination experiments at seawater-like ionic strength.⁴⁶

The cyclic voltammograms of activated carbon are rectangular-shaped, showing a near-ideal capacitive behavior (Figure 3A). As the potential difference is increased, there is a notable increase in the capacitance during positive and negative polarization when comparing identical potential window widths. This effect is linked to the quantum capacitance effect induced by the increased number of charge carriers in carbon, as the latter is not a perfect metallic conductor.^{41,47} At very high positive potentials, starting at around +0.6 V vs Ag/AgCl, we also see an irreversible increase in transferred charge linked to water splitting.³⁸ We note a similar capacitance during positive and negative polarization, which would indicate a similar ability to serve as an electrode for sodium and chloride removal (under the condition of permselectivity).^{48,49} These features make activated carbon

electrodes suitable for positive and negative polarization regimes in the context of capacitive deionization.

For MXene-CNT electrodes, an onset of the oxygen evolution peak is seen at positive potentials as early as +0.3 V vs Ag/AgCl (Figure 3B). This makes the chosen MXene-CNT electrodes unsuitable to serve as the positive electrode in our setup. During negative polarization, there is a continued increase in the corresponding capacitance when increasing the voltage bias. This process aligns with the conditioning of the MXene interlayer space and is irreversible. The latter is obvious when comparing the low capacitance found during the initial cycles at low potential bias, seeing the increased area under the cyclic voltammogram as the lower scan limit transitions toward more negative polarization, and the significantly increased capacitance for small voltage windows during repeat measurements (solid line graphs in Figure 3C). Electrochemical dilatometry also shows the increased strain of the MXene-CNT electrode when the polarization bias is increased (Figure 3D). The electrode shrinking follows the same pattern observed during negative polarization in Na₂SO₄ reported before and is aligned with the stronger MXene layer attraction in the sodiated state.⁵⁰ This process is likely to be accompanied by a change in the number of solvent molecules within the interlayer space.⁵¹ We also note the prominent current-peak at −0.5 V (cathodic scan) and −0.3 V (anodic scan), which may be related to interlayer proton-redox processes and ion arrangement effects.⁵² In past works, this peak was mostly reported and analyzed in aqueous H₂SO₄ electrolytes.⁵²

Half-cell cyclic voltammograms of CNTs are provided in Figure S4. Cyclic voltammograms show a rectangular-shaped profile typical for ion electrosorption. The low surface area of CNTs explains the low capacitance of about 20–30 F/g (depending on the potential range). Given that CNTs account for only 10 mass % of the MXene-CNT electrodes, the electrochemical contribution arising from CNTs to the total capacitance of about 120 F/g of the electrode is negligible. Specifically, at a polarization potential of −0.8 V vs Ag/AgCl, for instance, the charge stored in CNT electrodes is only 6% that of MXene-CNT (Figure 3B).

Galvanostatic charge/discharge cycling was employed to quantify the specific capacitance (Figure 3E) and specific capacity (Figure 3F) of the electrodes. Galvanostatic charge/discharge cycling at 0.1 A/g gave a capacitance of 123 F/g for MXene-CNT at the potential window between −1 and 0 V vs Ag/AgCl and 95 F/g for activated at the potential window from 0 to +0.4 V vs Ag/AgCl. For the two materials, the capacitance originates from different electrochemical processes. While the large surface area of activated carbon (1644 m²/g; Figure S1A) enables ion electrosorption, we see pseudocapacitive ion intercalation of sodium for MXene-CNT considering the low surface area (3 m²/g for MXene and 12 m²/g for

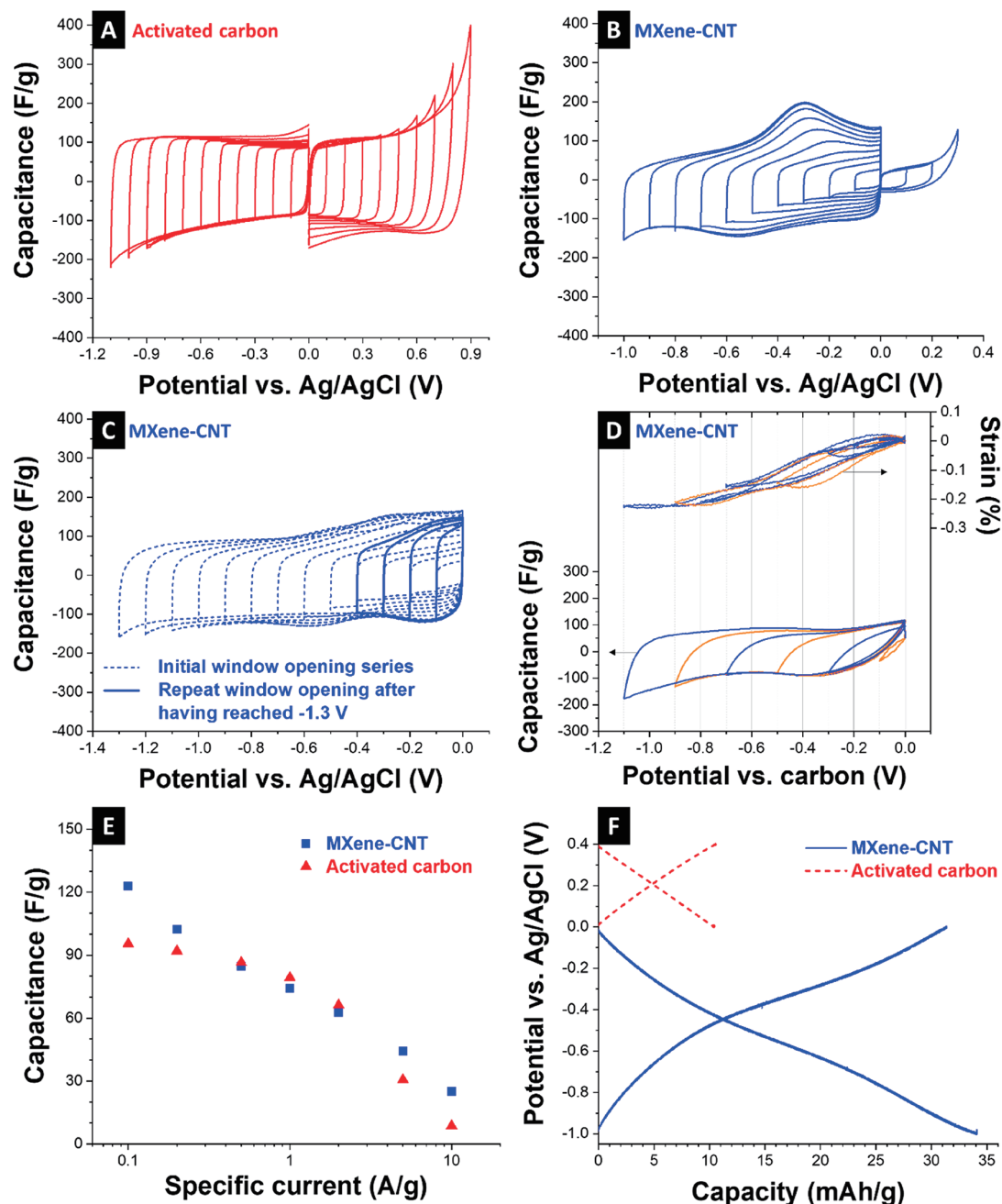


Figure 3. Half-cell electrochemical characterizations: window-opening cyclic voltammograms of (A) activated carbon and (B) MXene-CNT; (C) initial and repeated cyclic voltammetric window opening. (D) Cyclic voltammograms and corresponding dilatograms (electrode height change/initial height = strain; the different colors help to differentiate between individual scans). (E) Gravimetric capacitance of MXene-CNT (-1 to 0 V vs Ag/AgCl) and activated carbon (0 to $+0.4$ V vs Ag/AgCl), and (F) corresponding capacities. All measurements were carried out in aqueous 600 mM NaCl.

MXene-CNT; Figure S1C,D). At a rate of 2 A/g, both electrodes yield a comparable capacitance of 63 – 66 F/g, and we see a lower rate handling ability of the activated carbon electrode compared to MXene-CNT. Characteristic galvanostatic charge/discharge profiles are displayed in Figure 3F, and we chose capacity as the displayed unit to correctly quantify the charge and to compensate for any deviation from a perfectly rectangular cyclic voltammogram found for MXene-CNT. The capacity of about 10 mAh/g for activated carbon

and 34 mAh/g for MXene-CNT informed the mass balancing, which will be used in section 3.3.

3.3. Desalination Performance. On the basis of the electrochemical results obtained by half-cell measurements, asymmetric full-cells comprising of MXene-CNT and activated carbon electrodes were fabricated. For the desalination cell, we chose the mass ratio between the two electrodes that was optimized according to the method explained in section 2.2. We also carefully adjusted the potential window to cycle between cell voltages 1.2 and 0.3 V instead of discharging to 0

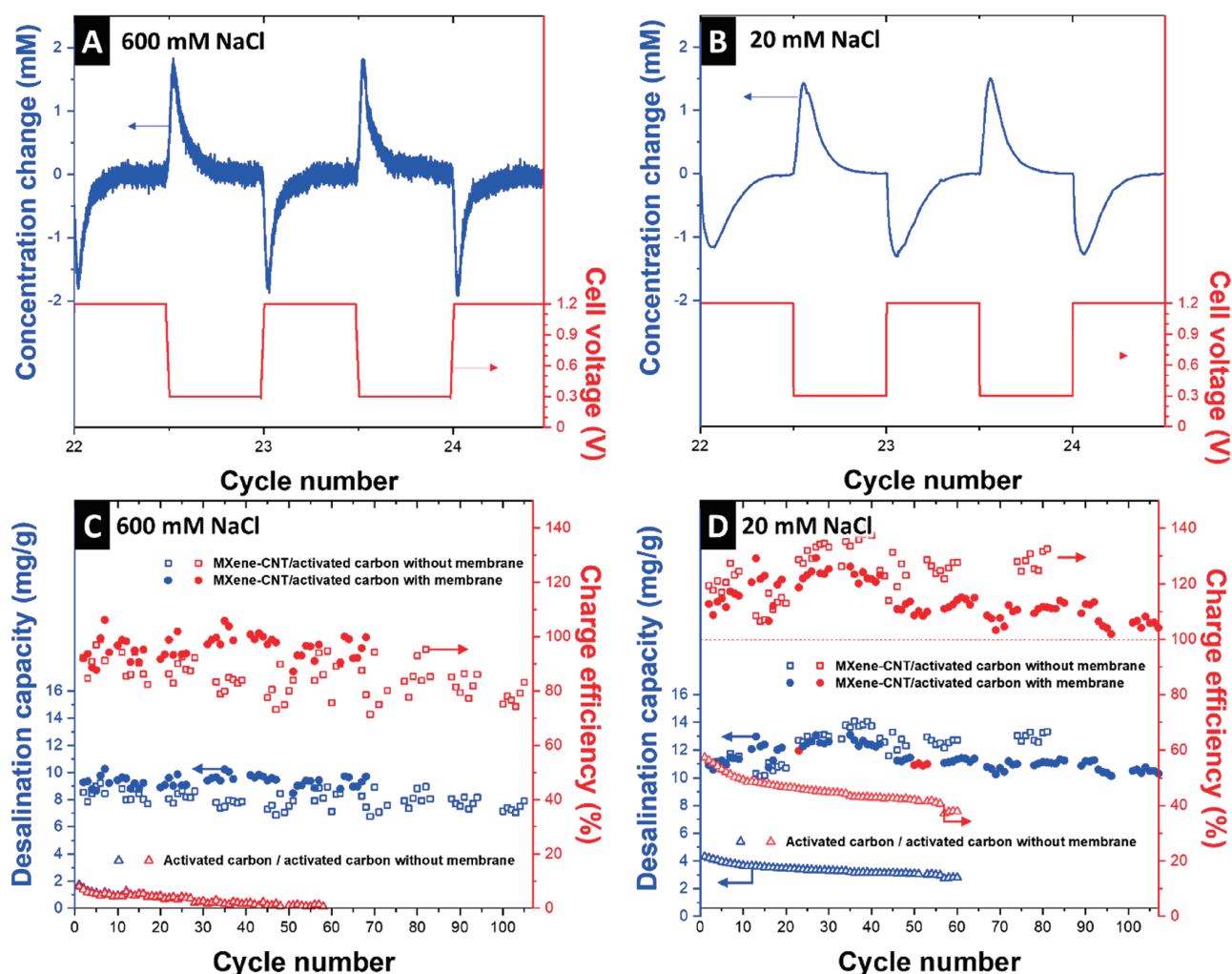


Figure 4. Effluent concentration change and cell voltage profiles of MXene/activated-carbon cell for two full cycles in (A) 600 mM NaCl and (B) 20 mM NaCl, both without membrane. Salt removal capacity stability and charge efficiency for cells with and without membrane in (C) 600 mM NaCl and (D) 20 mM NaCl, alongside membrane-less symmetric activated-carbon cells (the latter includes 60 cycles).

V to ensure activated carbon remains within the positive polarization regime (and, in return, MXene-CNT remains negatively polarized). The potential profiles of the individual MXene-CNT and activated carbon electrodes are provided in Figure S5. To ensure stable performance and to avoid first-cycle effects, all cells were initially cycled for around 30 cycles before the desalination experiments. As was seen from the electrochemical characterization data, the low amount of low-surface area carbon nanotubes aligns with a small contribution to the charge capacity of the MXene-CNT electrode, and as a consequence, the contribution of desalination via ion electro-sorption by the CNTs is negligible (based on 2–3 F/g via 10 mass% of pure CNTs, the corresponding desalination capacity is expected to be below 1 mg_{NaCl}/g_{electrode}).⁵³

Figure 4A,B shows the effluent salt concentrations (alternating peaks and troughs) alongside the voltage profile applied (without the use of an anion-exchange membrane). Upon charging the cell to 1.2 V, ions are attracted to the electrodes, causing a sudden drop in the concentration of the effluent stream. The concentration then levels off to the previous level before discharging, indicating that the system is approaching equilibrium and that the electrodes are saturating

with salt ions. Likewise, a similar process occurs upon discharging the cell to 0.3 V, where electrodes are depleted from ions and are regenerated for the next cycle.

The potential distribution between MXene-CNT and activated-carbon electrodes in different cells are shown in Figure S5. At 600 mM NaCl in the absence of an ion-exchange membrane (Figure S5A), we see the highly linear slope of charge/discharge profiles of each monitored electrode potential. The potential range of activated carbon remains fully in the positive polarization regime and has a lower amplitude compared to the MXene-CNT electrode. This is because of the different charge storage capacities of the two electrode materials and the chosen mass ratio. At low molar strength (20 mM NaCl), we note the presence of short-lived spikes in the potential curves of MXene-CNT at vertex potentials (Figure S5C). This is because of the lowered ion mobility at low molar strength; since we only control the cell voltage and just monitor the individual electrode potentials, we see a quicker charging behavior of the activated carbon electrode because the latter capitalizes on interfacial charge storage via ion electro-sorption. In contrast, charge transfer is slightly slower in the case of ion intercalation in MXene-CNT,

whereby, upon charging and discharging, the slower electrode is briefly forced to higher potentials. Each small spike in the profile of MXene-CNT is accompanied by a small notch in the profile of the activated carbon electrode.

Figure 4C,D shows the desalination capacity and charge efficiency of up to 100 cycles in aqueous 600 mM NaCl and 20 mM NaCl. In the absence of an ion-exchange membrane, we see at 600 mM a desalination capacity of $8 \pm 1 \text{ mg}_{\text{NaCl}}/\text{g}_{\text{electrode}}$ at a charge efficiency of $85 \pm 6\%$; at 20 mM, we find a desalination capacity of $12 \pm 1 \text{ mg}_{\text{NaCl}}/\text{g}_{\text{electrode}}$ at a charge efficiency of $125 \pm 8\%$ (we comment on exceeding 100% charge efficiency and its importance later in this section).

For comparison: In a membrane-free configuration, activated carbon only affords at 600 mM a desalination capacity of $0.8 \pm 0.3 \text{ mg}_{\text{NaCl}}/\text{g}_{\text{electrode}}$ at a charge efficiency of $4 \pm 2\%$; at 20 mM, we find a desalination capacity of $3 \pm 1 \text{ mg}_{\text{NaCl}}/\text{g}_{\text{electrode}}$ at a charge efficiency of $41 \pm 9\%$. The data for using only activated carbon for both electrodes is from a previous study where a cell voltage of 1.0 V and discharging to 0 V was employed.⁵⁴ Higher desalination capacities for this type of activated carbon are found for membrane-free desalination only at lower molar strength; for example, we found at 5 mM a desalination capacity of about $10 \text{ mg}_{\text{NaCl}}/\text{g}_{\text{electrode}}$ at a corresponding charge efficiency of 75–79%.⁴⁶

Figure 4C,D displays the desalination capacity and charge efficiency for the cell modified by placing an anion-exchange membrane in front of the activated-carbon electrode. This means that the positively polarized carbon electrode allows (almost exclusively) only the uptake of counterions because of the permselective feature of the ion-exchange membrane.^{8,54} For this case, we find at 600 mM a desalination capacity of $9 \pm 0 \text{ mg}_{\text{NaCl}}/\text{g}_{\text{electrode}}$ at a charge efficiency of $96 \pm 4\%$; at 20 mM, we find barely statistically differentiable values, namely, a desalination capacity of $11 \pm 1 \text{ mg}_{\text{NaCl}}/\text{g}_{\text{electrode}}$ at a charge efficiency of $114 \pm 7\%$. The corresponding electrode potentials are found in Figure S5B,D. While the potential profiles with or without the anion-exchange membrane are highly comparable at aqueous 600 mM NaCl (Figure S5A-B), there is a notable difference at 20 mM. As seen from Figure 4C,D, the spikes in the potential profiles of MXene-CNT in the configuration without the ion-exchange membrane are absent after adapting the anion-exchange membrane in front of the activated-carbon electrode. This caused in return a more sluggish ion transport toward the nanoporous carbon electrode through the ion-exchange membrane, which kinetically resulted in a slower process compared to ion intercalation within the MXene interlayers. Accordingly, there are visible spikes in the potential distribution of the activated-carbon electrode and corresponding notches in the MXene-CNT profiles.

3.4. Why Is the Asymmetric Cell Accomplishing Desalination Even at High Molar Strength? As seen from our data (and previous works), it is well-known that activated carbon with pores larger than 1 nm fails to provide any significant permselectivity in the context of counterion electroadsorption during capacitive deionization.^{10,55} The activated carbon used in this study has a rather wide pore size of 1.3 nm (Figure S1A), which is much larger than the hydrated sodium or chloride ions ($\sim 4 \text{ \AA}$).^{56,57} Since the pristine activated carbon used in this study is neither oxidized nor reduced, few surface groups must exist on the carbon surface, rendering it nonstereoselective and nonmolecular sieving without discrimination toward cations or anions. In other words, in an uncharged state, both sodium and chloride

ions coexist within carbon micropores, as previously shown in our work, by use of in situ small-angle X-ray scattering⁵⁸ and via modeling.¹⁰ Therefore, when two activated-carbon electrodes are paired in a symmetrical desalination cell, carbon micropores will both desorb co-ions (undesired) and attract counterions (desired). At a high molar strength, the co-ion expulsion dominates to such a great extent that effectively no desalination is accomplished (Figure 4C).

When MXene is paired with activated carbon, a charge efficiency of above 80% is maintained in the case of 600 mM without any ion-exchange membrane. This high charge efficiency implies that minimal co-ion expulsion takes place at both MXene and activated-carbon electrodes in an asymmetric configuration. On the side of the MXene-CNT electrode, the negative surface charges repel chloride ions that approach the surface, and as a result, no electric charge is wasted repelling the chloride ions but rather is exclusively invested to intercalating of sodium ions in between the MXene sheets. Given that the bulk solution must be electroneutral, chloride ions are then forced to be electrosorbed onto the otherwise nonpermselective activated carbon. MXene itself has the intrinsic ability to intercalate cations and anions; however, it does so in a nearly perfectly permselective manner, that is, the screened environment within the MXene interlayers allows for counterion intercalation at low and high molar strength of the bulk electrolyte.^{14,40}

The permselectivity forced upon the activated carbon by the MXene-CNT electrode can also be aided by the asymmetric electrode potential distribution. In regular CDI with symmetric cells and two electrodes composed of activated carbon, the cell is usually discharged to 0 V. The potential range around 0 V, however, is the regime in which the electroneutrality within the carbon nanopores is re-established by replenishing the initial population of co- and counterions (ideally in the same ratio as that found in bulk).^{48,49,59} Keeping the carbon electrode at all times outside that potential regime aids in avoiding the regime of permselectivity failure.⁶⁰ For example, Kim et al. demonstrated for a symmetric CDI system based on a similar activated carbon (Kuraray YP-50F) cycled between 0.3 and 1.2 V cell voltage a maximum desalination capacity of about $9 \text{ mg}_{\text{NaCl}}/\text{g}_{\text{electrode}}$ at a corresponding charge efficiency of 60–90% (depending on the half-cycle time) at a molar strength of 20 mM NaCl.⁶¹ However, it is not realistic to assume that the permselective regime can be accessed by activated carbon within the range of +0.2 V to +0.5 V vs Ag/AgCl at high molar strength, such as studied by us when using 600 mM NaCl. At such a high ion concentration, the entire potential range is dominated by nonpermselective ion-exchange.⁵⁸

When we now compare the performance at low and high molar strength with or without the added ion-exchange membrane to screen ions moving toward the carbon electrode, we see only small effective differences in the desalination performance. At 20 mM NaCl, the desalination capacity is virtually indistinguishable, while at 600 mM, there is a small increase when using the anion-exchange membrane. For the system at 20 mM, it is reasonable to assume that the potential range control of activated carbon and the intrinsic uptake of counterions of MXene-CNT alone allow for permselective ion removal. Adding an ion-exchange membrane has little effect in that case. However, for 600 mM, the carbon electrode is forced by the permselectivity of MXene-CNT to also behave permselectively: This is not a perfect state, and we see an improvement in desalination performance in case of enhancing

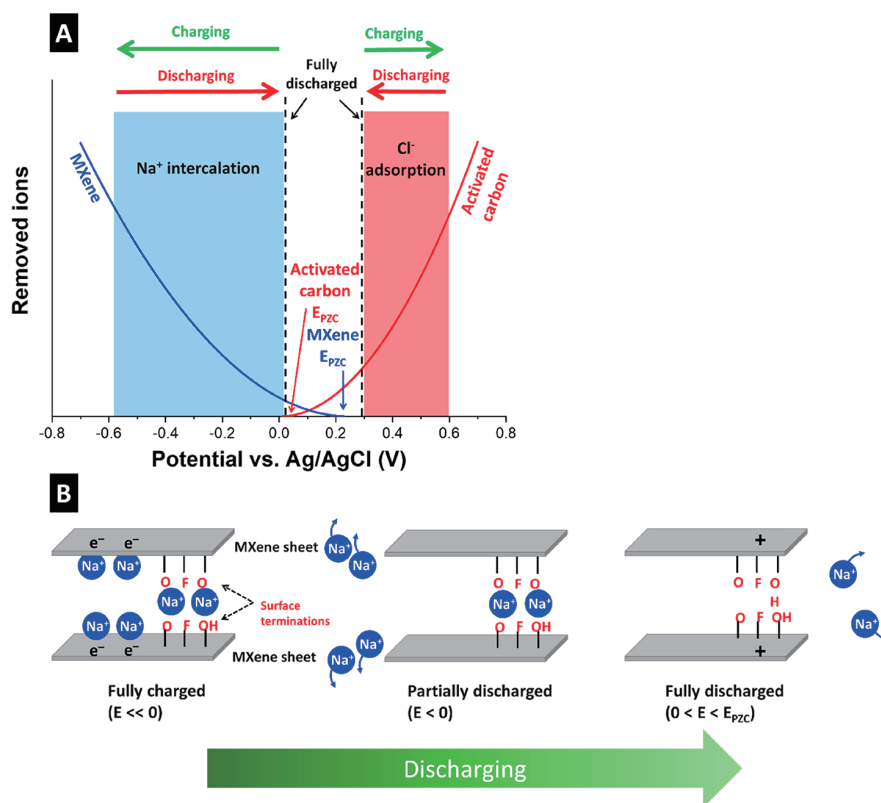


Figure 5. (A) Illustration of (approximate) location of potential at zero charge and the population of adsorbed ions upon charge/discharge. The E_{PZC} values of MXene and carbon electrodes are meant to schematically show the relative positions of these values with respect to each other. (B) Schematic representation of sodium ions interaction with MXene surface terminations during discharge half-cycle.

the carbon electrode's permselectivity further with an added ion-exchange membrane allowing only the removal of anions.

The enhanced permselectivity of the asymmetric MXene-CNT/activated-carbon system over that of the symmetric activated-carbon/activated-carbon system is seen from the corresponding energy consumptions (Figure S6). In all MXene/activated-carbon cells, the energy consumed per removed salt ion is around 40 kT, and it barely changes across the two concentrations tested. However, activated-carbon/activated-carbon cells show an energy consumption of 82 kT at 20 mM and 670 kT at 600 mM, showing ineffective desalination in case of the latter salt concentration. The energy consumed to accomplish desalination could be an important metric to take into consideration when comparing various CDI systems with each other, as well as comparisons across available desalination technologies.

3.5. Why Is the Asymmetric System Exceeding a Charge Efficiency of 100% at 20 mM? In the 20 mM system, the charge efficiency repeatedly exceeds 100% and stays there persistently for the whole duration of measurements. This effect, at low molar strength, is not limited to the presence of an ion-exchange membrane, so we cannot explain the charge efficiency in terms of an additional ion-removal capacity of the (mass-wise not accounted) anion-exchange membrane (as shown, for example, by Zhang et al.⁵⁴ and Tang et al.).⁶² This effect also enhanced the average desalination capacity at 20 mM system (12 mg/g for the cell without membrane) compared to that in the 600 mM system (8 mg/g for the cell without membrane). In the system operated at aqueous 20 mM NaCl, we do not see much of a statistically

significant difference between operation with or without the anion-exchange membrane regarding the charge efficiency. A charge efficiency above 100% means that per 1 mole of electric charge invested upon charging, more than 1 mole of salt ions is removed (or released upon discharging). This surprising effect might be explained in the context of MXene surface charges and the concept of potential at zero charge (E_{PZC}), which follows herein.

$Ti_3C_2T_x$ -MXene has negatively charged surface functionalities such as $-O$, $-OH$, or $-F$,⁶³ and as a result has a strong affinity toward positive ionic species such as metal cations^{64,65} in aqueous media even under no applied potential (MXene as an adsorbent powder, not as an electrode). These negative surface charges shift the E_{PZC} toward positive potentials. This is evidenced by the streaming potential measurements (Figure S7) on MXene that show a point of zero charge at a pH of 1.5. This means that MXene is negatively charged all the way down to this highly acidic pH, at which point it exhibits a neutral net electric charge, possibly due to protonation of the hydroxyl terminal groups of MXene.⁶⁵ Zeta potential measurements on $Ti_3C_2T_x$ -MXene in other studies has also shown a point of zero charge at pH values between 2 and 3.^{64,65} For comparison, the activated carbon reaches charge neutrality at a pH value of about 3.5 but with a much steeper streaming potential profile as a function of the pH value (in agreement with previous work).⁴⁶

The applied potential range has an important effect on the charge efficiency of a desalination cell.^{42,66,67} Systematic studies on symmetric activated-carbon CDI cells^{48,49} have shown that highest charge efficiencies (i.e., low co-ion

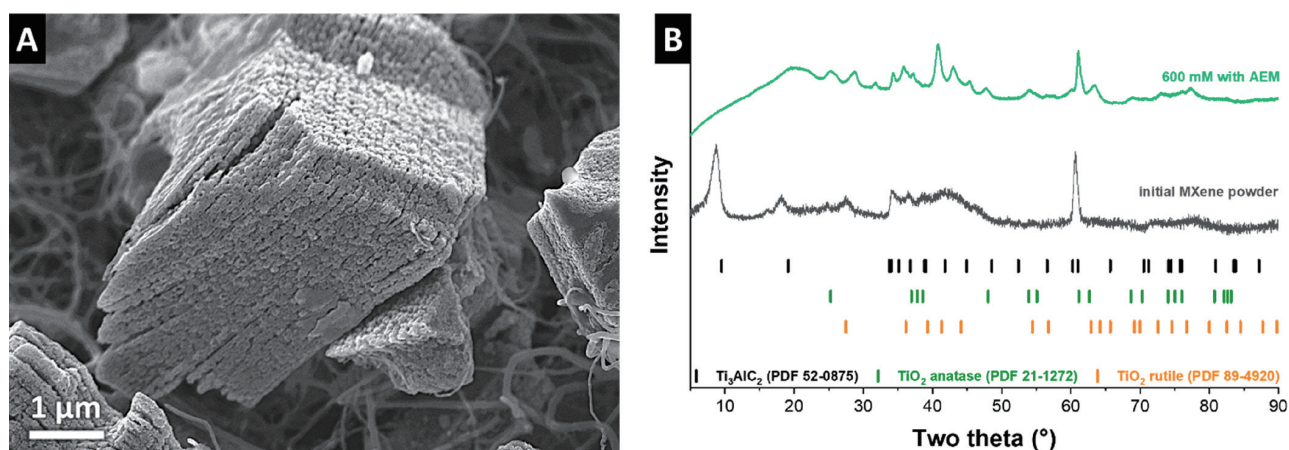


Figure 6. (A) SEM image of post mortem MXene-CNT electrode after long-term cycling and (B) its corresponding X-ray diffractograms, compared to those of pristine MXene-CNT and a number of different titanium oxide species [Powder Diffraction File (PDF) nos. 21-1272, 52-0875, and 89-4920, Joint Committee on Powder Diffraction Standards, 2004].

expulsion/high counterion uptake) are obtained when the cell is not fully discharged to E_{PZC} , but rather to a potential far enough thereof.⁶¹ This condition has apparently been met in our work by cycling within 0.3–1.2 V, as shown schematically in Figure 5A. Discharging to a lower potential limit of 0.3 V prevents MXene and activated carbon to cross their respective E_{PZC} and minimizes parasitic co-ion expulsion phenomenon, resulting in a high charge efficiency. This effect, however, does not explain why the system at low molar strength would be able to exceed charge efficiency values of 100%.

The additional gain in charge efficiency above 100% should then be attributed to the negative surface charges of MXene, which serve as an additional chemical charge.⁶⁹ When MXene is negatively polarized, sodium ions intercalate between MXene sheets due to the attraction they feel from both negative applied electric charge and negative surface dipole of functional groups, as schematically illustrated in Figure 5B. Upon discharging the MXene-CNT electrode to 0 V vs Ag/AgCl (Figure S5), all the said applied negative electric charge are retracted, resulting in the release of the corresponding sodium ions adsorbed, while the surface charges still cling to their corresponding sodium ions. Upon further discharging to potentials slightly higher than zero (but still away from E_{PZC}), a positive charge is induced in MXene sheets, which helps to overcome the negative charge of surface charges and thereby releasing the remaining sodium ions and regenerating the surface groups. At this point, sodium ions are again in part spontaneously adsorbed to the surface charges in addition to the attraction arising from electric charges. The former is similar to the inverted CDI system at a lower voltage limit, that is, ion adsorption upon discharge due to electrode surface charges.⁶⁸ The spontaneous chemisorption of sodium ions onto the negative surface functionalities of MXene could explain the additional gain in charge efficiency. That is, no electric charge is invested for those fractions of ions desalinated via interaction with MXene surface terminations. Consequently, the system capitalizes on MXene surface charges and can remove more than one ion per one electron charge invested; hence, a charge efficiency of above 100% is obtained.

3.6. Post-Mortem Analysis of MXene-CNT Electrodes after Desalination Operation.

Post-mortem data of the

MXene-CNT electrodes after long-term cycling, including electron microscopy, EDX analysis, and X-ray diffraction, are shown in Figure 6 and Table 1. The data shown in Figure 6 originate from the cell with an anion-exchange membrane at a discharged state cycled in 600 mM solution; SEM images and X-ray diffraction data for post-mortem samples after the operation at 20 mM (with and without ion-exchange membrane) and at 600 mM without the anion-exchange membrane are found in Figures S8 and S9.

As seen in Figure 2, the pristine MXene surface is already slightly oxidized, covered with cuboid-like titanate particles. A comparison of SEM images of pristine MXene-CNT (Figure 2A) and post-mortem electrodes (Figure 6A) reveals a much larger degree of coverage of MXene layers with titanium oxide particles. The increase in oxygen (found for all samples) is mostly accomplished by a decrease in the content of fluorine (Table 1).

The X-ray diffraction pattern of the post-mortem electrode is consistent with previous works on oxidized $Ti_3C_2T_x$;⁶⁹ specifically, we note the absence of the characteristic (002)-MXene peak due to oxidation-related disruption in the stacking periodicity and the development of a broad peak at around $20^\circ 2\theta$. The disappearance of the (002) peak can also relate to the insertion/deinsertion of sodium ions between the MXene layers during the electrochemical process and the formation of TiO_2 crystals; both effects disrupt the initial MXene-layer stacking order. The low temperature of the oxidation process and the small length-scale of the formed titanium oxide domains are mostly consistent with the formation of nanorutile, but further TiO_2 phases (such as anatase) cannot be excluded.

4. CONCLUSIONS

Our work explores the electrochemical desalination of asymmetric hybrid CDI using MXene-CNT paired with activated carbon for electrochemical desalination of brackish- and seawater-level NaCl concentrations in aqueous media. Using $Ti_3C_2T_x$ -MXene as the negative electrode and nanoporous activated carbon as the positive electrode, stable desalination performance for up to 100 cycles has been accomplished with desalination capacities up to 12 mg/g and charge efficiencies over 80%. It was shown that in the case of

asymmetric configuration permselective behavior is observed without the use of an ion-exchange membrane. While at 20 mM NaCl, the attained permselectivity of the system's response can be rationalized by the selected potential range (avoiding 0 V), it cannot explain the near-100% charge efficiency when using 600 mM NaCl. In addition, we see an excess of the charge efficiency beyond 100% at low molar strength, which can only be explained by the active role played by interlayer surface termination of MXene during the electrochemical desalination cycling. Our data show that at slightly reduced charge efficiency and desalination capacity MXene-CNT paired with activated carbon does not require an ion-exchange membrane for remediation of aqueous 600 mM NaCl. The omission of the ion-exchange membrane from the cell components can thus significantly reduce the overall costs in light of industrial applications.

■ ASSOCIATED CONTENT

SI Supporting Information

The Supporting Information is available free of charge at <https://pubs.acs.org/doi/10.1021/acsami.0c05975>.

Nitrogen gas sorption isotherms, transmission electron micrograph images of CNT, cyclic voltammetry of CNT, potential distribution profiles of MXene-CNT/AC cells, energy consumption, streaming potential response of MXene and AC, SEM and XRD of post-mortem MXene-CNT electrodes(PDF)

■ AUTHOR INFORMATION

Corresponding Author

Volker Presser – INM - Leibniz Institute for New Materials, 66123 Saarbrücken, Germany; Department of Materials Science & Engineering, Saarland University, 66123 Saarbrücken, Germany; orcid.org/0000-0003-2181-0590; Email: presser@presser-group.com

Authors

Mohammad Torkamanzadeh – INM - Leibniz Institute for New Materials, 66123 Saarbrücken, Germany; Department of Materials Science & Engineering, Saarland University, 66123 Saarbrücken, Germany

Lei Wang – INM - Leibniz Institute for New Materials, 66123 Saarbrücken, Germany; Department of Materials Science & Engineering, Saarland University, 66123 Saarbrücken, Germany

Yuan Zhang – INM - Leibniz Institute for New Materials, 66123 Saarbrücken, Germany; Department of Materials Science & Engineering, Saarland University, 66123 Saarbrücken, Germany

Öznil Budak – INM - Leibniz Institute for New Materials, 66123 Saarbrücken, Germany; Department of Materials Science & Engineering, Saarland University, 66123 Saarbrücken, Germany

Pattarachai Srimuk – INM - Leibniz Institute for New Materials, 66123 Saarbrücken, Germany

Complete contact information is available at: <https://pubs.acs.org/doi/10.1021/acsami.0c05975>

Notes

The authors declare no competing financial interest.

■ ACKNOWLEDGMENTS

We acknowledge funding of the MXene-CDI project (PR-1173/11) by the German Research Foundation (DFG, Deutsche Forschungsgemeinschaft). L.W. acknowledges funding from the Chinese Scholarship Council (CSC) via award number 201906260277. We thank Eduard Arzt (INM) for his continuing support.

■ REFERENCES

- (1) Elimelech, M.; Phillip, W. A. The Future Of Seawater Desalination: Energy, Technology, And The Environment. *Science* **2011**, *333* (6043), 712–717.
- (2) Suss, M. E.; Porada, S.; Sun, X.; Biesheuvel, P. M.; Yoon, J.; Presser, V. Water Desalination Via Capacitive Deionization: What Is It And What Can We Expect From It? *Energy Environ. Sci.* **2015**, *8* (8), 2296–2319.
- (3) Porada, S.; Zhao, R.; Van Der Wal, A.; Presser, V.; Biesheuvel, P. Review On The Science And Technology Of Water Desalination By Capacitive Deionization. *Prog. Mater. Sci.* **2013**, *58* (8), 1388–1442.
- (4) Andelman, M. D. The Flow Through Capacitor: A New Tool In Wastewater Purification. *Filtr. Sep.* **1998**, *May*, 345–347.
- (5) Porada, S.; Weinstein, L.; Dash, R.; Van Der Wal, A.; Bryjak, M.; Gogotsi, Y.; Biesheuvel, P. Water Desalination Using Capacitive Deionization With Microporous Carbon Electrodes. *ACS Appl. Mater. Interfaces* **2012**, *4* (3), 1194–1199.
- (6) Srimuk, P.; Su, X.; Yoon, J.; Aurbach, D.; Presser, V. Charge-Transfer Materials For Electrochemical Water Desalination, Ion Separation and The Recovery Of Elements. *Nat. Rev. Mater.* **2020**, DOI: 10.1038/s41578-020-0193-1.
- (7) Zhao, R.; Biesheuvel, P.; Van der Wal, A. Energy Consumption And Constant Current Operation In Membrane Capacitive Deionization. *Energy Environ. Sci.* **2012**, *5* (11), 9520–9527.
- (8) Biesheuvel, P. M.; van der Wal, A. Membrane Capacitive Deionization. *J. Membr. Sci.* **2010**, *346* (2), 256–262.
- (9) Kim, N.; Lee, J.; Kim, S.; Hong, P. S.; Lee, C.; Yoon, J.; Kim, C. Short Review Of Multichannel Membrane Capacitive Deionization: Principle, Current Status, And Future Prospect. *Appl. Sci.* **2020**, *10* (2), 683.
- (10) Bi, S.; Zhang, Y.; Cervini, L.; Mo, T.; Griffin, J. M.; Presser, V.; Feng, G. Permselective Ion Electrosorption Of Subnanometer Pores At High Molar Strength Enables Capacitive Deionization Of Saline Water. *Sustainable Energy Fuels* **2020**, *4* (3), 1285–1295.
- (11) Singh, K.; Porada, S.; de Gier, H. D.; Biesheuvel, P. M.; de Smet, L. C. P. M. Timeline On The Application Of Intercalation Materials In Capacitive Deionization. *Desalination* **2019**, *455*, 115–134.
- (12) Pasta, M.; Wessells, C. D.; Cui, Y.; La Mantia, F. A Desalination Battery. *Nano Lett.* **2012**, *12* (2), 839–843.
- (13) Lee, J.; Kim, S.; Kim, C.; Yoon, J. Hybrid Capacitive Deionization To Enhance The Desalination Performance Of Capacitive Techniques. *Energy Environ. Sci.* **2014**, *7* (11), 3683–3689.
- (14) Srimuk, P.; Kaasik, F.; Krüner, B.; Tolosa, A.; Fleischmann, S.; Jäckel, N.; Tekeli, M. C.; Aslan, M.; Suss, M. E.; Presser, V. MXene As A Novel Intercalation-Type Pseudocapacitive Cathode And Anode For Capacitive Deionization. *J. Mater. Chem. A* **2016**, *4* (47), 18265–18271.
- (15) Srimuk, P.; Husmann, S.; Presser, V. Low Voltage Operation Of A Silver/Silver Chloride Battery With High Desalination Capacity In Seawater. *RSC Adv.* **2019**, *9* (26), 14849–14858.
- (16) Su, X.; Hatton, T. A. Redox-Electrodes For Selective Electrochemical Separations. *Adv. Colloid Interface Sci.* **2017**, *244*, 6–20.
- (17) Lee, J.; Srimuk, P.; Zornitta, R. L.; Aslan, M.; Mehdi, B. L.; Presser, V. High Electrochemical Seawater Desalination Performance Enabled By An Iodide Redox Electrolyte Paired With A Sodium Superionic Conductor. *ACS Sustainable Chem. Eng.* **2019**, *7* (11), 10132–10142.

- (18) Kim, S.; Kim, C.; Lee, J.; Kim, S.; Lee, J.; Kim, J.; Yoon, J. Hybrid Electrochemical Desalination System Combined With An Oxidation Process. *ACS Sustainable Chem. Eng.* **2018**, *6* (2), 1620–1626.
- (19) Srimuk, P.; Wang, L.; Budak, Ö.; Presser, V. High-Performance Ion Removal Via Zinc-Air Desalination. *Electrochem. Commun.* **2020**, *115*, 106713.
- (20) Naguib, M.; Mashtalir, O.; Carle, J.; Presser, V.; Lu, J.; Hultman, L.; Gogotsi, Y.; Barsoum, M. W. Two-Dimensional Transition Metal Carbides. *ACS Nano* **2012**, *6* (2), 1322–1331.
- (21) Gogotsi, Y.; Anasori, B. The Rise of MXenes. *ACS Nano* **2019**, *13* (8), 8491–8494.
- (22) Anasori, B.; Lukatskaya, M. R.; Gogotsi, Y. 2D Metal Carbides And Nitrides (MXenes) For Energy Storage. *Nat. Rev. Mater.* **2017**, *2*, 16098.
- (23) Natu, V.; Pai, R.; Sokol, M.; Carey, M.; Kalra, V.; Barsoum, M. W. 2D $Ti_3C_2T_x$ Mxene Synthesized By Water-Free Etching Of Ti_3AlC_2 In Polar Organic Solvents. *Chem.* **2020**, *6* (3), 616–630.
- (24) Shahzad, F.; Alhabeab, M.; Hatter, C. B.; Anasori, B.; Man Hong, S.; Koo, C. M.; Gogotsi, Y. Electromagnetic Interference Shielding With 2D Transition Metal Carbides (MXenes). *Science* **2016**, *353* (6304), 1137–1140.
- (25) Orangi, J.; Hamade, F.; Davis, V. A.; Beidaghi, M. 3D Printing Of Additive-Free 2D $Ti_3C_2T_x$ (MXene) Ink For Fabrication Of Micro-Supercapacitors With Ultra-High Energy Densities. *ACS Nano* **2020**, *14* (1), 640–650.
- (26) Sun, D.; Wang, M.; Li, Z.; Fan, G.; Fan, L.-Z.; Zhou, A. Two-Dimensional Ti_3C_2 As Anode Material For Li-Ion Batteries. *Electrochem. Commun.* **2014**, *47*, 80–83.
- (27) Lukatskaya, M. R.; Mashtalir, O.; Ren, C. E.; Dall'Agnese, Y.; Rozier, P.; Taberna, P. L.; Naguib, M.; Simon, P.; Barsoum, M. W.; Gogotsi, Y. Cation Intercalation And High Volumetric Capacitance Of Two-Dimensional Titanium Carbide. *Science* **2013**, *341* (6153), 1502–1505.
- (28) Ren, C. E.; Hatzell, K. B.; Alhabeab, M.; Ling, Z.; Mahmoud, K. A.; Gogotsi, Y. Charge-And Size-Selective Ion Sieving Through $Ti_3C_2T_x$ MXene Membranes. *J. Phys. Chem. Lett.* **2015**, *6* (20), 4026–4031.
- (29) Peng, Q.; Guo, J.; Zhang, Q.; Xiang, J.; Liu, B.; Zhou, A.; Liu, R.; Tian, Y. Unique Lead Adsorption Behavior Of Activated Hydroxyl Group In Two-Dimensional Titanium Carbide. *J. Am. Chem. Soc.* **2014**, *136* (11), 4113–4116.
- (30) Rasool, K.; Pandey, R. P.; Rasheed, P. A.; Buczek, S.; Gogotsi, Y.; Mahmoud, K. A. Water Treatment And Environmental Remediation Applications Of Two-Dimensional Metal Carbides (MXenes). *Mater. Today* **2019**, *30*, 80–102.
- (31) Bao, W.; Tang, X.; Guo, X.; Choi, S.; Wang, C.; Gogotsi, Y.; Wang, G. Porous Cryo-Dried MXene For Efficient Capacitive Deionization. *Joule* **2018**, *2* (4), 778–787.
- (32) Ma, J.; Cheng, Y.; Wang, L.; Dai, X.; Yu, F. Free-Standing $Ti_3C_2T_x$ MXene Film As Binder-Free Electrode In Capacitive Deionization With An Ultrahigh Desalination Capacity. *Chem. Eng. J.* **2020**, *384*, 123329.
- (33) Amiri, A.; Chen, Y.; Bee Teng, C.; Naraghi, M. Porous Nitrogen-Doped MXene-Based Electrodes For Capacitive Deionization. *Energy Storage Materials* **2020**, *25*, 731–739.
- (34) Chen, B.; Feng, A.; Deng, R.; Liu, K.; Yu, Y.; Song, L. MXene as a Cation-Selective Cathode Material for Asymmetric Capacitive Deionization. *ACS Appl. Mater. Interfaces* **2020**, *12* (12), 13750–13758.
- (35) Huang, S.; Mochalin, V. N. Hydrolysis Of 2D Transition-Metal Carbides (MXenes) In Colloidal Solutions. *Inorg. Chem.* **2019**, *58* (3), 1958–1966.
- (36) Tian, Y.; Yang, C.; Tang, Y.; Luo, Y.; Lou, X.; Que, W. $Ti_3C_2T_x$ //AC Dual-Ions Hybrid Aqueous Supercapacitors With High Volumetric Energy Density. *Chem. Eng. J.* **2020**, *393*, 124790.
- (37) Carmona-Orbezo, A.; Le Fevre, L. W.; Dryfe, R. A. W. Performance Optimization Of Carbon Electrodes For Capacitive Deionization By Potentiostatic Analysis. *Electrochim. Acta* **2019**, *325*, 134898.
- (38) Zhang, Y.; Srimuk, P.; Husmann, S.; Chen, M.; Feng, G.; Presser, V. Effect Of Pore Size On The Ion Electrosorption And Hydrogen/Deuterium Electrosorption Using Sodium Chloride In H_2O And D_2O . *J. Electrochem. Soc.* **2019**, *166* (16), A4158–A4167.
- (39) Jäckel, N.; Weingarh, D.; Zeiger, M.; Aslan, M.; Grobelsek, I.; Presser, V. Comparison Of Carbon Onions And Carbon Blacks As Conductive Additives For Carbon Supercapacitors In Organic Electrolytes. *J. Power Sources* **2014**, *272* (1), 1122–1133.
- (40) Srimuk, P.; Halim, J.; Lee, J.; Tao, Q.; Rosen, J.; Presser, V. Two-Dimensional Molybdenum Carbide (MXene) With Divacancy Ordering For Brackish And Seawater Desalination Via Cation And Anion Intercalation. *ACS Sustainable Chem. Eng.* **2018**, *6* (3), 3739–3747.
- (41) Weingarh, D.; Zeiger, M.; Jäckel, N.; Aslan, M.; Feng, G.; Presser, V. Graphitization As A Universal Tool To Tailor The Potential-Dependent Capacitance Of Carbon Supercapacitors. *Adv. Energy Mater.* **2014**, *4* (13), 1400316.
- (42) Zornitta, R. L.; Srimuk, P.; Lee, J.; Krüner, B.; Aslan, M.; Ruotolo, L. A. M.; Presser, V. Charge And Potential Balancing For Optimized Capacitive Deionization Using Lignin-Derived, Low-Cost Activated Carbon Electrodes. *ChemSusChem* **2018**, *11* (13), 2101–2113.
- (43) Weingarh, D.; Noh, H.; Foelske-Schmitz, A.; Wokaun, A.; Kötz, R. A Reliable Determination Method Of Stability Limits For Electrochemical Double Layer Capacitors. *Electrochim. Acta* **2013**, *103*, 119–124.
- (44) Srimuk, P.; Lee, J.; Fleischmann, S.; Choudhury, S.; Jäckel, N.; Zeiger, M.; Kim, C.; Aslan, M.; Presser, V. Faradaic Deionization Of Brackish And Sea Water Via Pseudocapacitive Cation And Anion Intercalation Into Few-Layered Molybdenum Disulfide. *J. Mater. Chem. A* **2017**, *5* (30), 15640–15649.
- (45) Ghidui, M.; Barsoum, M. W. The {110} Reflection In X-Ray Diffraction Of Mxene Films: Misinterpretation And Measurement Via Non-Standard Orientation. *J. Am. Ceram. Soc.* **2017**, *100* (12), 5395–5399.
- (46) Aslan, M.; Zeiger, M.; Jäckel, N.; Grobelsek, I.; Weingarh, D.; Presser, V. Improved Capacitive Deionization Performance Of Mixed Hydrophobic/Hydrophilic Activated Carbon Electrodes. *J. Phys.: Condens. Matter* **2016**, *28* (11), 114003.
- (47) Gerischer, H.; McIntyre, R.; Scherson, D.; Storck, W. Density Of The Electronic States Of Graphite: Derivation From Differential Capacitance Measurements. *J. Phys. Chem.* **1987**, *91* (7), 1930–1935.
- (48) Avraham, E.; Noked, M.; Bouhadana, Y.; Soffer, A.; Aurbach, D. Limitations Of Charge Efficiency In Capacitive Deionization II. On The Behavior Of CDI Cells Comprising Two Activated Carbon Electrodes. *J. Electrochem. Soc.* **2009**, *156* (10), P157–P162.
- (49) Avraham, E.; Noked, M.; Bouhadana, Y.; Soffer, A.; Aurbach, D. Limitations Of Charge Efficiency In Capacitive Deionization Processes III: The Behavior Of Surface Oxidized Activated Carbon Electrodes. *Electrochim. Acta* **2010**, *56* (1), 441–447.
- (50) Come, J.; Black, J. M.; Lukatskaya, M. R.; Naguib, M.; Beidaghi, M.; Rondinone, A. J.; Kalinin, S. V.; Wesolowski, D. J.; Gogotsi, Y.; Balke, N. Controlling The Actuation Properties Of MXene Paper Electrodes Upon Cation Intercalation. *Nano Energy* **2015**, *17*, 27–35.
- (51) Srimuk, P.; Lee, J.; Budak, Ö.; Choi, J.; Chen, M.; Feng, G.; Prehal, C.; Presser, V. In Situ Tracking Of Partial Sodium Desolvation Of Materials With Capacitive, Pseudocapacitive, And Battery-Like Charge/Discharge Behavior In Aqueous Electrolytes. *Langmuir* **2018**, *34* (44), 13132–13143.
- (52) Sun, Y.; Zhan, C.; Kent, P. R. C.; Naguib, M.; Gogotsi, Y.; Jiang, D. E. Proton Redox And Transport In Mxene-Confined Water. *ACS Appl. Mater. Interfaces* **2020**, *12* (1), 763–770.
- (53) Porada, S.; Borchardt, L.; Oschatz, M.; Bryjak, M.; Atchison, J. S.; Keesman, K. J.; Kaskel, S.; Biesheuvel, P. M.; Presser, V. Direct Prediction Of The Desalination Performance Of Porous Carbon Electrodes For Capacitive Deionization. *Energy Environ. Sci.* **2013**, *6* (12), 3700–3712.

- (54) Zhang, Y.; Srimuk, P.; Aslan, M.; Gallei, M.; Presser, V. Polymer Ion-Exchange Membranes For Capacitive Deionization Of Aqueous Media With Low And High Salt Concentration. *Desalination* **2020**, *479*, 114331.
- (55) Biesheuvel, P. M.; Porada, S.; Levi, M.; Bazant, M. Z. Attractive Forces In Microporous Carbon Electrodes For Capacitive Deionization. *J. Solid State Electrochem.* **2014**, *18* (5), 1365–1376.
- (56) Salitra, G.; Soffer, A.; Eliad, L.; Cohen, Y.; Aurbach, D. Carbon Electrodes For Double-Layer Capacitors I. Relations Between Ion And Pore Dimensions. *J. Electrochem. Soc.* **2000**, *147* (7), 2486.
- (57) Avraham, E.; Yaniv, B.; Soffer, A.; Aurbach, D. Developing Ion Electroadsorption Stereoselectivity, By Pore Size Adjustment With Chemical Vapor Deposition Onto Active Carbon Fiber Electrodes. Case of $\text{Ca}^{2+}/\text{Na}^+$ Separation In Water Capacitive Desalination. *J. Phys. Chem. C* **2008**, *112* (19), 7385–7389.
- (58) Prehal, C.; Koczwar, C.; Amenitsch, H.; Presser, V.; Paris, O. Salt Concentration And Charging Velocity Determine Ion Charge Storage Mechanism In Nanoporous Supercapacitors. *Nat. Commun.* **2018**, *9* (1), 4145.
- (59) Gao, X.; Omosebi, A.; Ma, Z.; Zhu, F.; Landon, J.; Ghorbanian, M.; Kern, N.; Liu, K. Capacitive Deionization Using Symmetric Carbon Electrode Pairs. *Environ. Sci.: Water Res. Technol.* **2019**, *5* (4), 660–671.
- (60) Shpigel, N.; Levi, M. D.; Sigalov, S.; Aurbach, D.; Daikhin, L.; Presser, V. Novel In Situ Multiharmonic EQCM-D Approach To Characterize Complex Carbon Pore Architectures For Capacitive Deionization Of Brackish Water. *J. Phys.: Condens. Matter* **2016**, *28* (11), 114001.
- (61) Kim, T.; Dykstra, J. E.; Porada, S.; van der Wal, A.; Yoon, J.; Biesheuvel, P. M. Enhanced Charge Efficiency And Reduced Energy Use In Capacitive Deionization By Increasing The Discharge Voltage. *J. Colloid Interface Sci.* **2015**, *446*, 317–326.
- (62) Tang, K.; Kim, Y.-h.; Chang, J.; Mayes, R. T.; Gabitto, J.; Yiacoymi, S.; Tsouris, C. Seawater Desalination By Over-Potential Membrane Capacitive Deionization: Opportunities And Hurdles. *Chem. Eng. J.* **2019**, *357* (1), 103–111.
- (63) Alhabeib, M.; Maleski, K.; Anasori, B.; Lelyukh, P.; Clark, L.; Sin, S.; Gogotsi, Y. Guidelines For Synthesis And Processing Of Two-Dimensional Titanium Carbide ($\text{Ti}_3\text{C}_2\text{T}_x$ MXene). *Chem. Mater.* **2017**, *29* (18), 7633–7644.
- (64) Fard, A. K.; Mckay, G.; Chamoun, R.; Rhadfi, T.; Preud'Homme, H.; Atieh, M. A. Barium Removal From Synthetic Natural And Produced Water Using MXene As Two Dimensional (2-D) Nanosheet Adsorbent. *Chem. Eng. J.* **2017**, *317*, 331–342.
- (65) Shahzad, A.; Rasool, K.; Miran, W.; Nawaz, M.; Jang, J.; Mahmoud, K. A.; Lee, D. S. Two-Dimensional $\text{Ti}_3\text{C}_2\text{T}_x$ MXene Nanosheets For Efficient Copper Removal From Water. *ACS Sustainable Chem. Eng.* **2017**, *5* (12), 11481–11488.
- (66) Abu Khalla, S.; Suss, M. E. Desalination Via Chemical Energy: An Electrodialysis Cell Driven By Spontaneous Electrode Reactions. *Desalination* **2019**, *467*, 257–262.
- (67) Porada, S.; Schipper, F.; Aslan, M.; Antonietti, M.; Presser, V.; Fellingner, T.-P. Capacitive Deionization Using Biomass-Based Microporous Salt-Templated Heteroatom-Doped Carbons. *ChemSusChem* **2015**, *8* (11), 1867–1874.
- (68) Gao, X.; Omosebi, A.; Landon, J.; Liu, K. Surface Charge Enhanced Carbon Electrodes For Stable And Efficient Capacitive Deionization Using Inverted Adsorption–Desorption Behavior. *Energy Environ. Sci.* **2015**, *8* (3), 897–909.
- (69) Zhang, M.; Chen, X.; Sui, J.; Abrah, B. S.; Li, Y.; Peng, W.; Zhang, G.; Zhang, F.; Fan, X. Improving the Performance of Titanium Carbide MXene in Supercapacitor by Partial Oxidation Treatment. *Inorg. Chem. Front.* **2020**, *7* (5), 1205–1211.

Supporting Information

MXene/activated carbon hybrid capacitive deionization for permselective ion removal at low and high salinity

Mohammad Torkamanzadeh,^{1,2} Lei Wang,^{1,2} Yuan Zhang,^{1,2}
Öznil Budak,^{1,2} Pattarachai Srimuk,¹ Volker Presser,^{1,2,*}

¹ *INM - Leibniz Institute for New Materials, D2 2, 66123, Saarbrücken, Germany*

² *Department of Materials Science & Engineering, Saarland University, Campus D2 2, 66123, Saarbrücken, Germany*

* Corresponding author's email: presser@presser-group.com

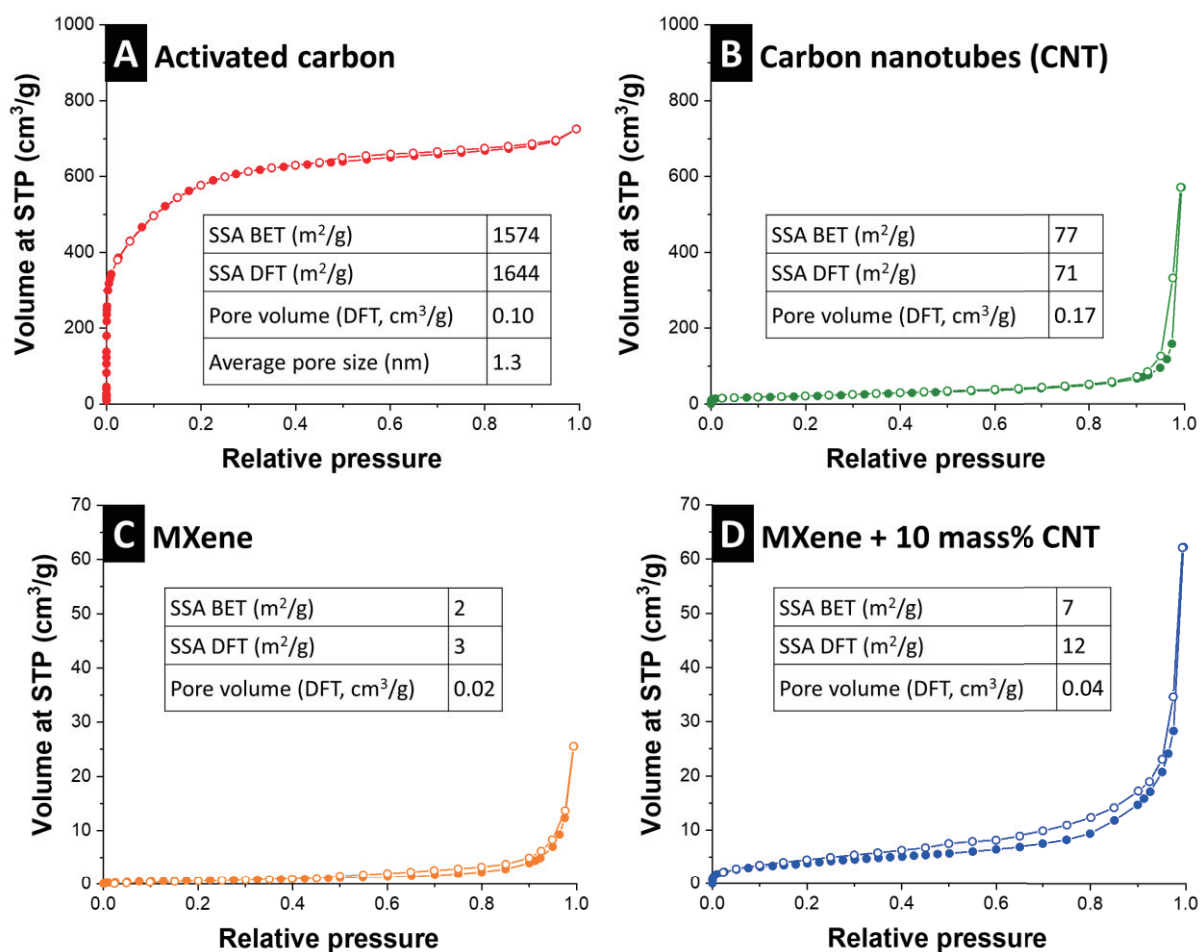


Figure S1: Nitrogen gas sorption isotherm of (A) activated carbon, (B) carbon nanotubes, (C) MXene powder, and (D) MXene/carbon nanotube electrodes recorded at a temperature of -196 °C. STP: standard temperature and pressure.

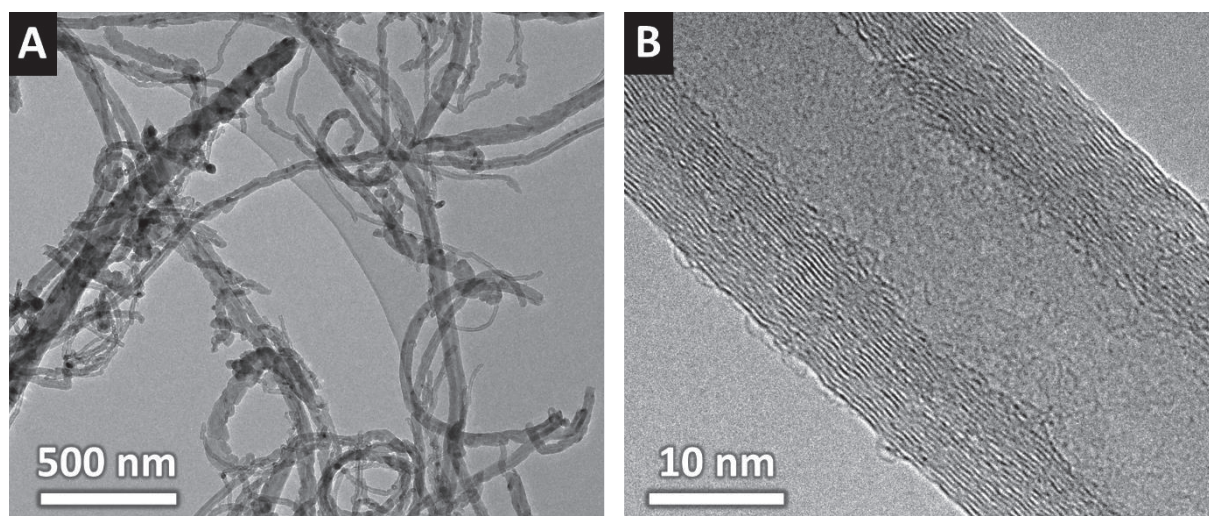


Figure S2: Transmission electron micrographs of the carbon nanotubes.

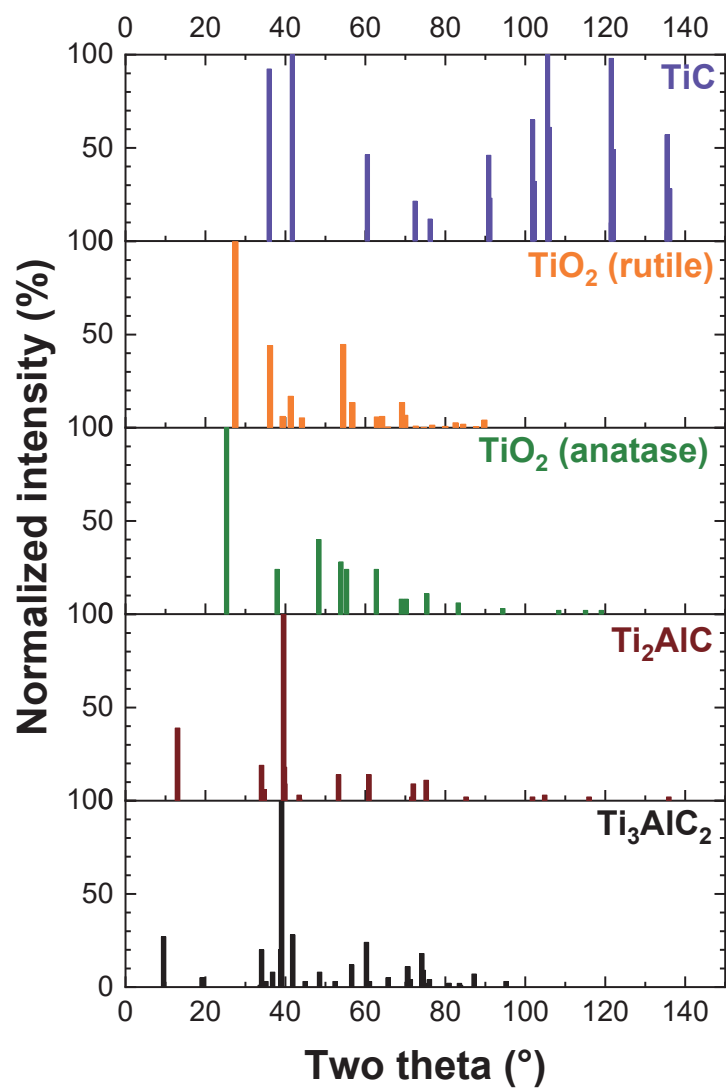


Figure S3: Relative intensities of the reference phases provided in Figure 2D.

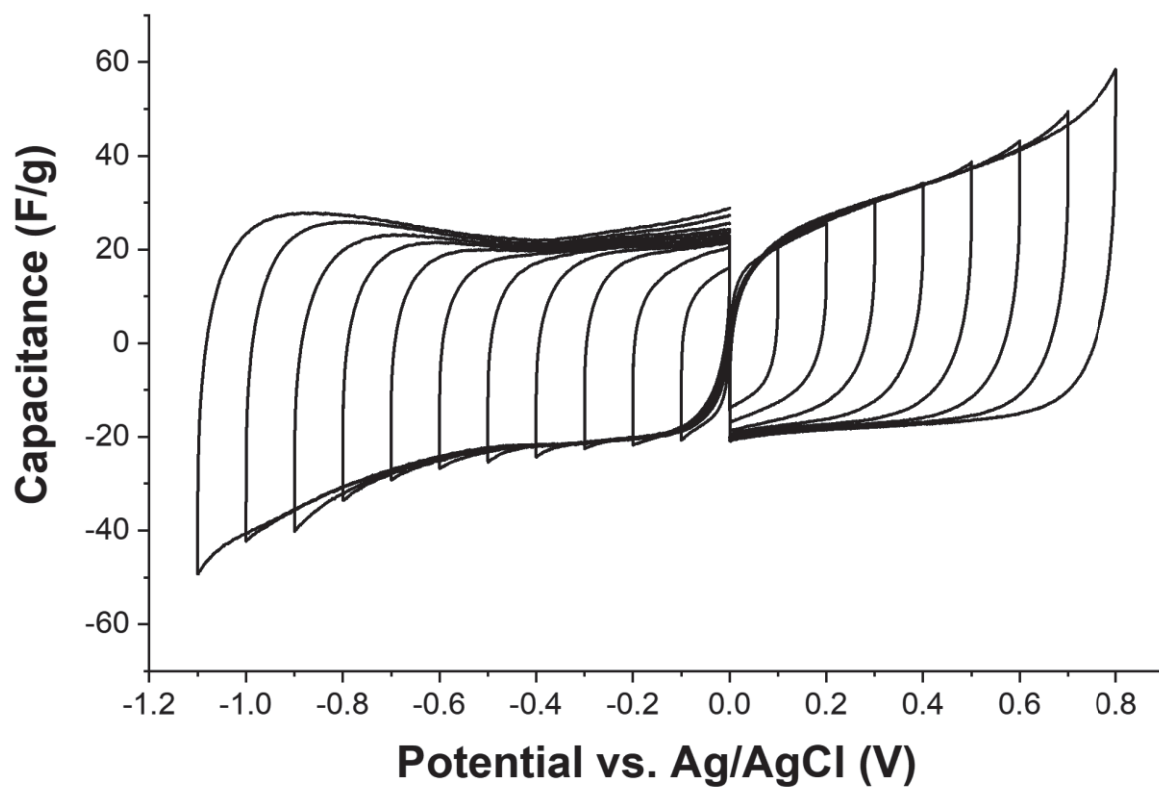


Figure S4: Half-cell window opening cyclic voltammograms of electrodes just composed of CNTs in aqueous 1 M NaCl electrolyte.

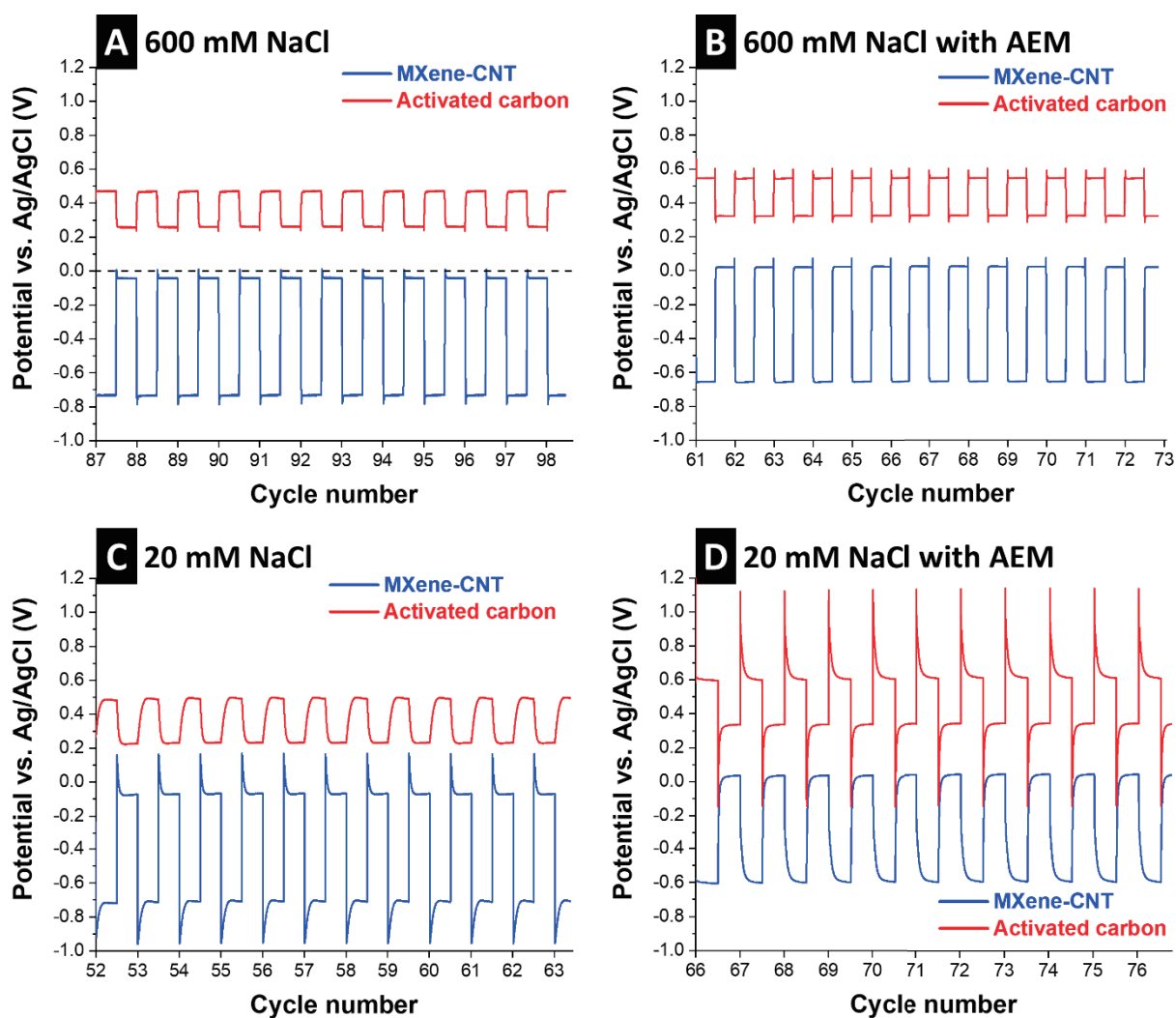


Figure S5: Potential development of individual electrodes upon charging the MXene/AC cell to a cell voltage of 1.2 V and discharging to a cell voltage of 0.3 V. (A-B) aqueous 600 mM NaCl; (C-D) aqueous 20 mM NaCl; (A,C) without an anion-exchange membrane (AEM) placed in front of the activated carbon electrode; (B,D) experiments with an AEM at the activated carbon electrode.

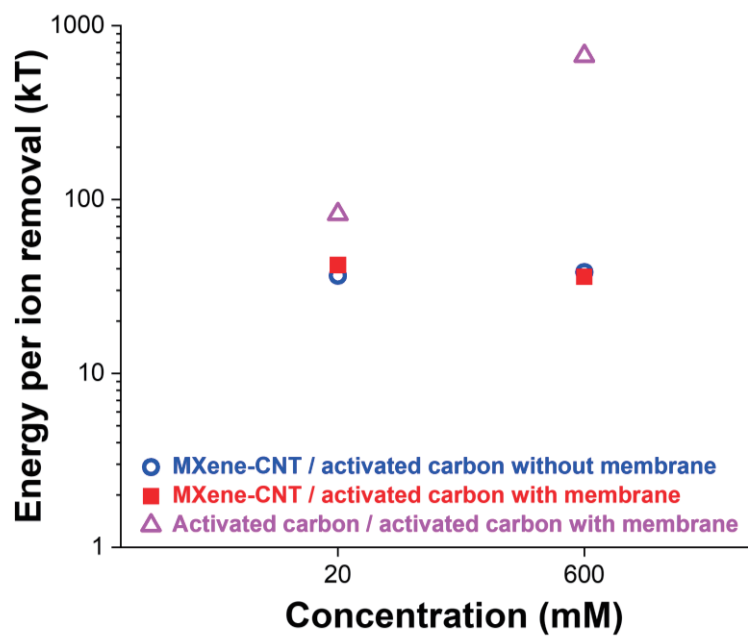


Figure S6: Energy consumption per ion removal.

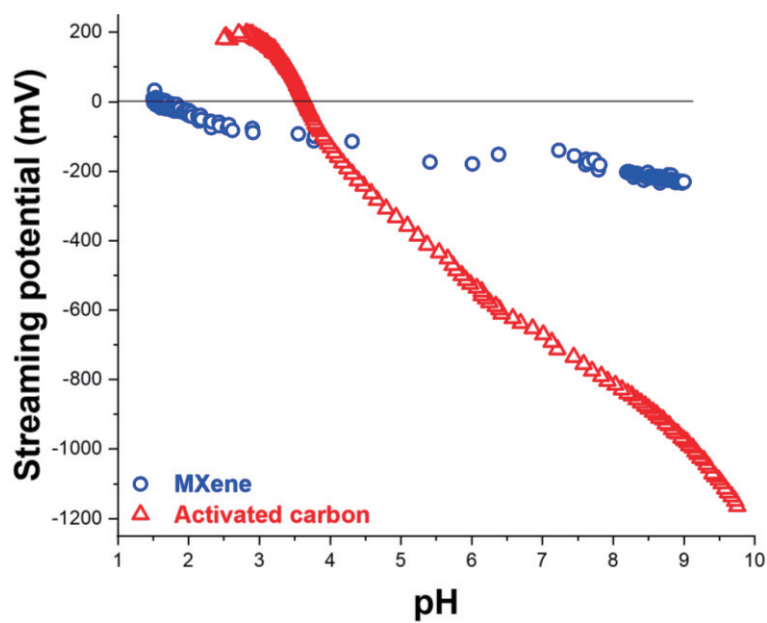


Figure S7: Streaming potential response of MXene and activated carbon in water.

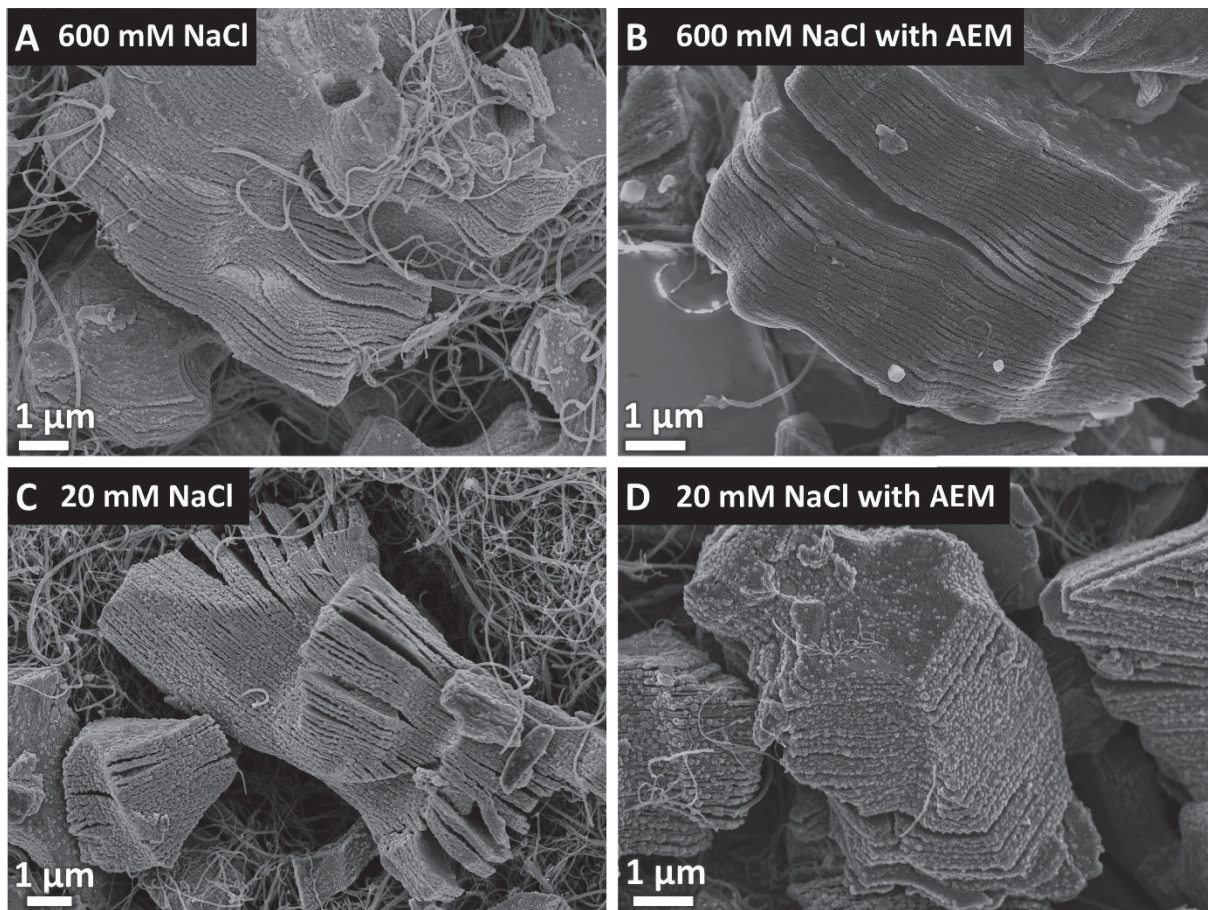


Figure S8: Post mortem scanning electron micrographs of MXene-CNT electrodes.

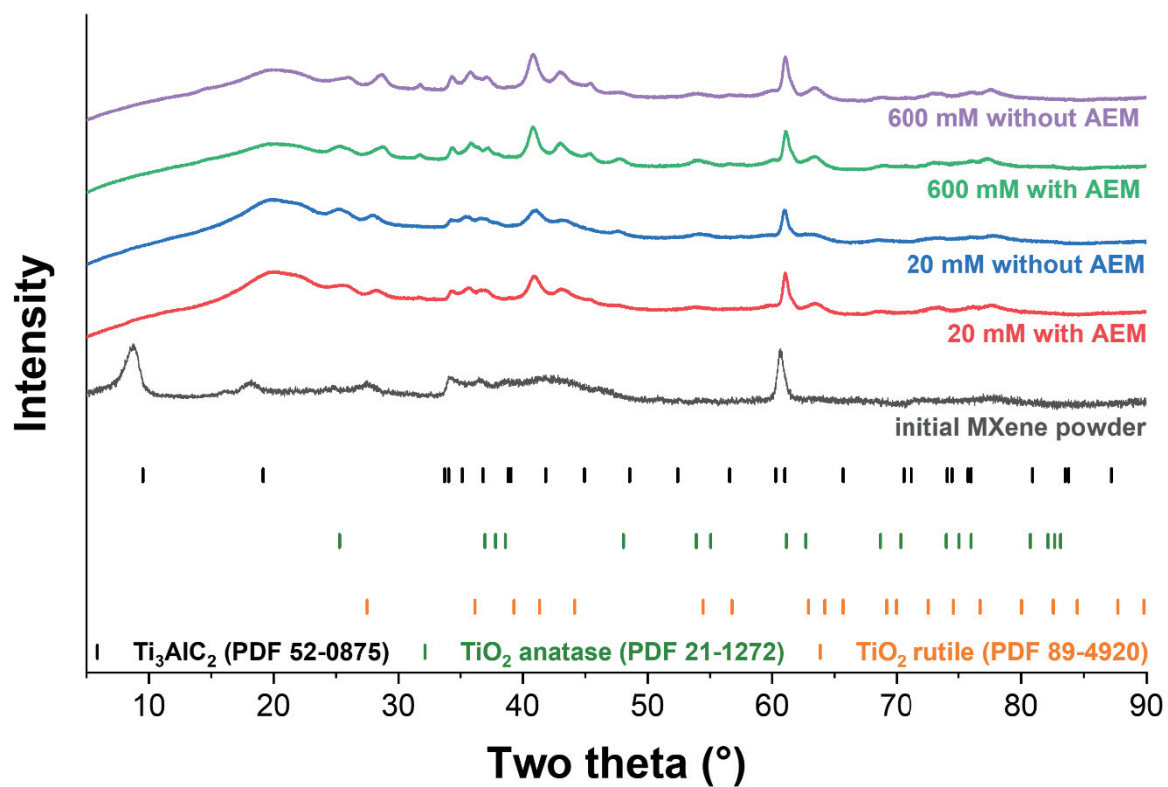


Figure S9: X-ray powder diffraction pattern of the initial MXene powder and after electrochemical operation for desalination (post mortem).

4.4 Antimony alloying electrode for high-performance sodium removal: how to use a battery material not stable in aqueous media for saline water remediation

Stefanie Arnold,^{1,2} Lei Wang,^{1,2} Öznil Budak,^{1,2}
Mesut Aslan,¹ Pattarachai Srimuk,¹ Volker Presser^{1,2}

¹ INM - Leibniz Institute for New Materials, 66123 Saarbrücken, Germany

² Department of Materials Science and Engineering, Saarland University, 66123 Saarbrücken, Germany

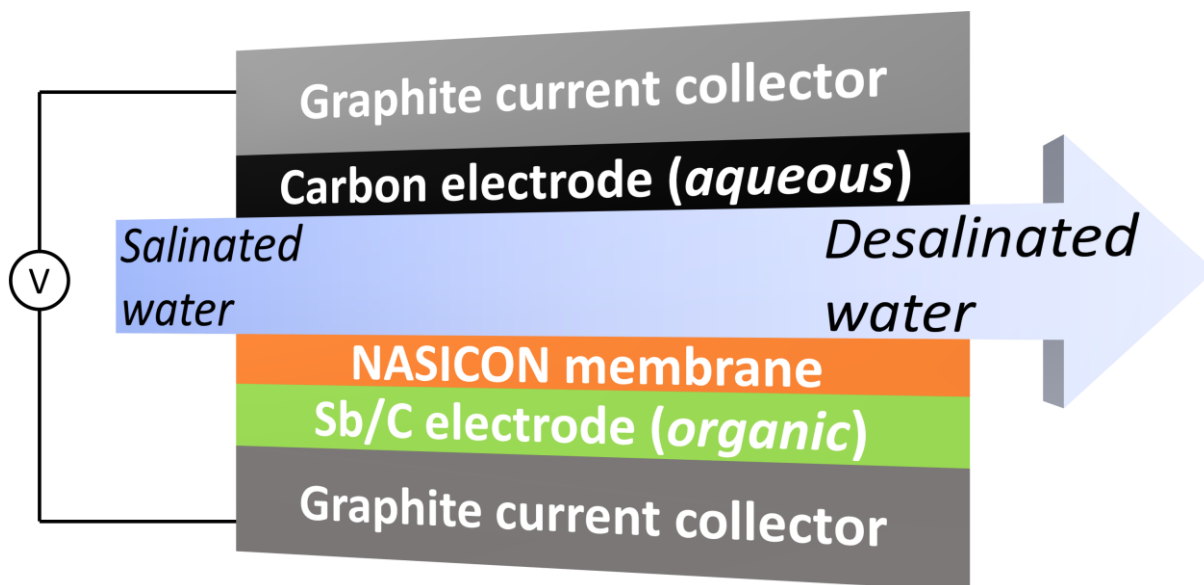
Citation:

S. Arnold, L. Wang, Ö. Budak, M. Aslan, P. Srimuk, V. Presser, ANTIMONY ALLOYING ELECTRODE FOR HIGH-PERFORMANCE SODIUM REMOVAL: HOW TO USE A BATTERY MATERIAL NOT STABLE IN AQUEOUS MEDIA FOR SALINE WATER REMEDIATION, **Journal of Materials Chemistry A**, 9 (2021) 585-596.

DOI: 10.1039/D0TA09806J.

Own contribution:

Validation, Investigation, Formal analysis, Writing - Review & Editing



Cite this: *J. Mater. Chem. A*, 2021, **9**, 585

Antimony alloying electrode for high-performance sodium removal: how to use a battery material not stable in aqueous media for saline water remediation†

Stefanie Arnold, ^{ab} Lei Wang, ^{ab} Öznil Budak, ^{ab} Mesut Aslan,^a Pattarachai Srimuk ^a and Volker Presser ^{*ab}

Capacitive deionization (CDI) is based on ion electrosorption and has emerged as a promising desalination technology, for example, to obtain drinking water from brackish water. As a next-generation technology, battery desalination uses faradaic processes and, thereby, enables higher desalination capacities and remediation of feed water with high molar strength such as seawater. However, the full use of a large capacity of charge transfer processes is limited by the voltage window of water and the need to use electrode materials non-reactive towards the water. Using our multi-channel bi-electrolyte cell, we now introduce for the first time an alloying electrode for sodium removal in the context of water desalination. Separated by a ceramic sodium superionic conductor (NASICON) membrane, the antimony/carbon composite electrode accomplished sodium removal while chlorine removal is enabled via ion electrosorption with nanoporous carbon (activated carbon cloth). In a sodium-ion battery half-cell setup, the antimony/carbon composite electrode reaches an initial capacity of 714 mA h g⁻¹ at a specific current of 200 mA g⁻¹, which shows a slow but continuous degrading over the course of 80 cycles (426 mA h g⁻¹ in 80th cycle). Our hybrid CDI cell provides a desalination capacity of an average of 294 mg_{Na} g_{Sb}⁻¹ (748 mg_{NaCl} g_{Sb}⁻¹) with a charge efficiency of ca. 74% in a 600 mM NaCl at a specific current of 200 mA g⁻¹ and a voltage range of -2.0 V to +2.0 V.

Received 7th October 2020
Accepted 24th November 2020

DOI: 10.1039/d0ta09806j

rsc.li/materials-a

1 Introduction

In the 21st century, due to the ever-increasing population and correspondingly the deterioration of the environment, obtaining clean potable water becomes a serious issue for sustaining livelihood, especially in arid regions.¹ Large-scale efforts have been invested in developing desalination technology to address this issue. From simple distillation, multi-stage flash distillation,² to reverse osmosis,^{3,4} many methods have been studied. However, many of these methods are expensive and require high energy input. Among them, capacitive deionization (CDI) is considered as an energy-efficient technology, compared to the pressure or filtration-based desalination technology.⁵ In CDI, ions are immobilized at the fluid/solid interface of nanoporous carbon by reversible ion-electrosorption.⁶ A typical CDI cell

employs a pair of nanoporous carbon electrodes and a separator (open channel or porous dielectric material), to prevent short-circuiting.⁷ By applying a constant voltage or current, the salt ions present in feedwater migrate into the electrical double-layer (EDL) and, thus, remove salt from the water (ion-electrosorption). When the cell is discharged, the ions are released again, and the invested charge is recovered. The voltage applied to each electrode pair is typically around (slightly above) 1 V, depending on the overpotential of water splitting. Because of the low voltage, and because there is no need for other energy input such as high pressure or high temperature, CDI holds the promise of being a more energy-efficient method of desalinating water on a larger scale.⁷

However, uncharged carbon nanopores are populated by both co-ions and counter-ions, that is, ions with the same or opposite charge compared to the electrode.^{8,9} Once the electrodes are polarized, co-ions will be released from the EDL at the same extent as counter-ion attraction takes place; only once the co-ion population has been depleted (at higher states-of-charge), permselective ion removal will be possible.¹⁰ Thereby, CDI remains limited to low molar concentrations (with an initially low number of co-ions present in carbon nanopores).¹¹ This condition is only (partially) remedied when the pore

^aINM – Leibniz Institute for New Materials, 66123 Saarbrücken, Germany. E-mail: volker.presser@leibniz-inm.de

^bDepartment of Materials Science and Engineering, Saarland University, 66123 Saarbrücken, Germany

† Electronic supplementary information (ESI) available: chemical analysis data, supporting electrochemical characterization, schematic illustration of the cell operation, post mortem material characterization (SEM, XRD). See DOI: 10.1039/d0ta09806j

diameter significantly falls below 1 nm.¹² Also, the charge storage capacity intrinsically linked to EDL carbon electrodes is limited to about 0.1 F m⁻² (typical values for the gravimetric capacitance of activated carbon is about 100–150 F g⁻¹).^{13–15} Therefore, the desalination capacity of low-concentration brackish water with carbon electrodes is typically in the range of 10–30 mg_{NaCl} g_{electrode}⁻¹ (~4–12 mg_{Na} g_{electrode}⁻¹).¹⁶

To overcome the desalination limitations of carbon-based CDI, Pasta *et al.* introduced the concept of the desalination battery built of sodium manganese oxide and silver electrodes to deionize seawater.¹⁷ Instead of using two faradaic electrodes, it is also possible to pair carbon with a charge-transfer electrode. For example, Lee *et al.* used sodium manganese oxide to capture sodium and carbon to electrosorb chloride.¹⁸ By doing so, the authors achieved a desalination capacity of 31 mg_{NaCl} g_{electrode}⁻¹ (~12 mg_{Na} g_{electrode}⁻¹), while the carbon itself only provided 14 mg_{NaCl} g_{electrode}⁻¹ (~6 mg_{Na} g_{electrode}⁻¹).¹⁸ Until now, mostly two kinds of faradaic materials have been applied for desalination: intercalation-type materials (*e.g.*, sodium manganese oxides,¹⁹ nickel hexacyanoferrate,²⁰ titanium disulfide²¹) and conversion-type materials (*e.g.*, silver²²), which show a desalination capacity of 85–115 mg_{NaCl} g_{electrode}⁻¹ (up to about 22 mg_{Na} g_{electrode}⁻¹).^{23–27}

The selection of suitable sodium-removal electrode for electrochemical desalination is limited by their compatibility with water. Many new materials could be used for desalination, especially anode materials of sodium-ion batteries if the requirement to expose the electrode to the feedwater stream would be lifted. As a first step towards this goal, we introduced the use of organic solvent CDI in 2016 (ref. 28) and aqueous/organic bi-electrolyte CDI in 2018 (ref. 29). In the latter concept, a multi-channel system is used, and one of the electrodes, covered by an ion-exchange membrane, is operated in an organic electrolyte instead of an aqueous solution. Ion transfer into and out from the organic compartment is ensured by the ion-exchange membrane. Our initial design used a polymer-based ion-exchange membrane, so water cross-over was not fully eliminated. Still, the system allowed stable cell operation at voltages significantly above 1.2 V and resulting desalination capacities of up to 60 mg_{NaCl} g_{electrode}⁻¹ (~24 mg_{Na} g_{electrode}⁻¹; at 2.4 V cell voltage).

Research at the water/energy nexus between battery desalination and seawater batteries is a rapidly growing field for stationary applications.^{30–33} Our present proof-of-concept now uses the bi-electrolyte concept and demonstrates the highly promising concept of combining a ceramic ion-exchange membrane (sodium superionic conductor: NASICON)³⁴ with antimony (Sb) as a high-performance sodium-alloy electrode material. Antimony offers a very high theoretical capacity of 660 mA h g⁻¹ when assuming the formation of Na₃Sb.³⁵ However, it readily reacts with water and the electrode potential for the alloying reactions is far outside of the stability window of aqueous electrolytes. Therefore, one would never consider it for use in conventional desalination batteries. In previous work by Pfeifer *et al.*, the influence of different carbon additives in the antimony electrode on the electrical performance in sodium-ion batteries was investigated.³⁶ The highest capacity (620 mA h g⁻¹)

and stability (capacity loss of 19% after 100 cycles) were shown by a composite mixture of 70 mass% nanoscale antimony with 20 mass% of carbon onions and 10% carboxymethyl cellulose binder.³⁶ The low alloying reaction potential, generally lower than 1.0 V vs. Na⁺/Na, make alloy materials impossible to be adopted to conventional cells for electrochemical desalination because of the exposure to water.³⁷ Due to that reason, we chose this promising electrode material for use in the bi-electrolyte desalination concept. In this multi-channel cell, Sb and carbon electrodes were in organic and aqueous electrolyte, respectively. The two electrodes were separated by a Na⁺ permeable membrane (NASICON). During the charging process, Na⁺ in the organic electrolyte was captured by the alloying reaction between Sb and Na⁺ in the organic compartment. To keep the charge neutrality in the organic compartment, Na⁺ from feed water would diffuse into organic electrolytes resulting in desalination. The initial performance of this cell in 600 mM NaCl is about 495 mg_{Na} g_{Sb}⁻¹ (excluding the first two pre-conditioning cycles), and the performance stabilizes at around 294 mg_{Na} g_{Sb}⁻¹ with a charge efficiency of about 74% in aqueous 600 mM NaCl for 40 operating cycles.

2 Experimental

2.1 Materials synthesis

The synthesis of antimony nanopowder was carried out by optimizing a synthesis route given in the literature.³⁸ To obtain a high purity of antimony, an excess of sodium borohydride (NaBH₄, 1.216 g, ≥98.0% purity, Sigma Aldrich) was suspended in 400 mL technical ethanol (>99.0% purity, Merck). Antimony chloride (SbCl₃, 2.244 g, ≥99.0% purity, Sigma Aldrich) was dissolved in 100 mL absolute ethanol (>99.8% purity, Honeywell). The antimony chloride solution was added dropwise into the stirring solution of sodium borohydride in ethanol at room temperature within one hour. The resultant mixture was stirred for another hour at room temperature. To break up agglomerates, the reaction mixture was sonicated for 10 min after stirring (P120H, Elmasonic). After sedimentation of the antimony particles, they were filtered under vacuum, washed three times with ethanol and three times with deionized water. Antimony particles were dried in an oven at +80 °C for 4 h. NASICON powder with excess Na was synthesized in analogy to literature (*via* Na_{3.3}Zr₂Si₂PO₁₂)³⁹ by using a solid-state reaction. As the precursor, 26.80 g NH₄H₂PO₄ (98.0% purity, Alfa Aesar), 40.35 g Na₂CO₃ (100.0% purity, Alfa Aesar), 27.45 g SiO₂ (particle size <50 nm, Aerosil O × 50) and 56.00 g ZrO₂ (particle size 40 nm, Tosoh) were applied. They were homogenized in a tumbler mixer for first step dry with 10 mm zirconia balls for 1 h, and then for another 24 h as an ethanolic slurry (absolute ethanol) with 15 mass% solid content (without balls to avoid contamination). After evaporation of ethanol, the dry powder was calcinated in two steps: first, at +600 °C in the air for 4 h, followed by a second calcination step at +1150 °C in the air for 4 h. The calcinated powder was crushed by hand and dry milled with 10 mm diameter zirconia balls for 1 h in a tumbler mixer. After sieving, the powder was cold-isostatically pressed at 400 MPa in a cylindrical rubber mold to obtain a green body.

The pressed body with a relative density of around 74% was sintered at +1100 °C for 10 h in an air atmosphere to obtain a NASICON cylinder with a relative density of 78%. Membrane discs of 0.5 ± 0.05 mm thickness and a diameter of 40 mm were cut using a saw with a diamond blade. The open pores in the membrane were filled with epoxy resin. More details about this synthesis procedure are given in previous work.³⁴

2.2 Structural and chemical characterization

X-ray diffraction (XRD) measurements of the antimony and NASICON powder were performed with a D8 Discover diffractometer (Bruker AXS) with a copper X-ray source (Cu-K α ($\lambda = 1.5406$ Å), 40 kV, 40 mA) and a Göbel mirror and a 1 mm point focus as optics. With a VANTEC-500 (Bruker AXS) two-dimensional X-ray detector positioned at $17^\circ 2\theta$, $37^\circ 2\theta$, $57^\circ 2\theta$, and $97^\circ 2\theta$ with a measurement time of 1000 s per step, five frames were recorded.

Scanning electron microscope (SEM) images were recorded with a field emission scanning electron microscope (JEOL JSM-7500F) operating at an acceleration voltage of 3 kV. The samples were dispersed in ethanol, drop casted multiple times on the carbon film sticky tape on the steel sample holder. The samples were dried under vacuum for 30 min and analyzed without the aid of an additional, conductive sputter coating.

Raman spectroscopy was carried out with a Renishaw inVia Microscope equipped with a neodymium-doped yttrium aluminum garnet laser with an excitation wavelength of 532 nm and a laser power of approximately 0.05 mW, a 2400 mm^{-1} grating, and a $50\times$ objective lens with a numeric aperture of 0.75. Three to four different spots of each sample were recorded with five accumulations and 30 s exposure time.

Elemental analysis (CHNS) was performed with a Vario Micro Cube system from Elementar. The samples were each weighed in tin boats with the same amount of WO_3 and pressed under air exclusion. The reduction temperature in the pipe represented +850 °C (combustion tube temperature: +1150 °C), and the device was calibrated through repeated measurements of sulfanilamide.

Quantitative analysis of elemental oxygen was performed by using a rapid OXY cube oxygen analyzer from Elementar at a pyrolysis temperature of +1450 °C. The samples were weight in silver boats and pressed under air exclusion. The system was calibrated by measurements of benzoic acid.

2.3 Electrode materials and preparation

The Sb/C electrodes were manufactured by mixing the active material of 70 mass% synthesized antimony nanopowder with 20 mass% carbon onions, produced from nanodiamond powder at a temperature of 1300 °C under vacuum (OLC1300-Va),⁴⁰ and 10 mass% carboxymethyl cellulose as binder from a 3 mass% aqueous solution (CMC, degree of substitution = 0.7, molecular weight = $250\,000\text{ g mol}^{-1}$, Sigma Aldrich), by hand mixing for 40 min. First, the active material and the carbon were mixed and ground dry in a mortar. After adding isopropanol, the suspension was kept grinding until the isopropanol is completely vaporized. In the next step, this was repeated with

ethanol. After that, the electrode material with a small amount of ethanol and water (ratio 1 : 1) kept stirring for 30 min. Finally, the CMC binder solution was added, and the electrode past kept stirring for another 1 hour. The suspension was stirred for several hours on a magnetic stirrer to obtain a homogeneous slurry. The obtained electrode slurries were doctor bladed on aluminum foil (Ranafoil, Toyo Aluminium), used as a current collector, with a thickness of 15 μm . The electrodes were initially dried at ambient conditions overnight. Then, they were dried further in a vacuum oven at +120 °C for 12 h. Subsequently, the electrodes were punched out with a 12 mm diameter and transferred into a vacuum oven. Finally, a vacuum drying step at +80 °C for 12 h was conducted to remove the remaining solvent. The resulting electrode thickness of the dried electrodes was 40–60 μm with a material loading of $1.4 \pm 0.2\text{ mg cm}^{-2}$.

To evaluate the performance of the carbon on the aqueous side, commercially available microporous activated carbon cloth (Kynol ACC-507-20) was investigated as a working electrode. These electrodes, showing thickness of 250 μm , were punched in 12 mm discs and can be operated as free-standing, binder-free electrodes. In aqueous half-cell setups, a free-standing oversized activated carbon powder electrode (YP-80F, Kuraray) function as a counter electrode. These electrodes were prepared by mixing 90 mass% of activated carbon and 10 mass% polytetrafluoroethylene (60 mass% dispersion in water, Sigma Aldrich) together with ethanol. The mixture was ground until a dough-like slurry was obtained, and then rolled to a thickness of about 600 μm . These electrodes were dried under vacuum at +80 °C and punched into circular plates with a diameter of 12 mm.

2.4 Cell preparation and electrochemical characterization

2.4.1 Electrochemical half-cells. For electrochemical testing in an aqueous or organic electrolyte, custom-built polyether ether ketone (PEEK) cells with spring-loaded titanium pistons were used.⁴¹ The cells were arranged in a three-electrode configuration for electrochemical measurements. The electrode discs were punched out of the electrode films with a diameter of 12 mm (1.13 cm^2). In sodium-ion-batteries, an elemental sodium electrode is commonly used as a reference and counter electrode.

All cell parts were dried overnight at +80 °C and introduced into an argon-filled glovebox (MBraun Labmaster 130; O_2 and $\text{H}_2\text{O} < 0.1\text{ ppm}$). First, the 12 mm diameter working electrode was placed in the cell, followed by a 13 mm diameter vacuum dried compressed glass-fiber separator (GF/D, Whatman). The counter electrode was punched into circular plates with a diameter of 10 mm and placed on top of the separator. Before using sodium metal, the oxidized surface of sodium was removed to obtain a smooth surface to avoid inhomogeneity and impurities. The counter electrodes were pressed to a uniform thickness of approximately 1 mm. A copper foil current collector was placed on the backside of each counter electrode. The sodium reference electrode was placed on a 2 mm diameter compressed glass-fiber separator (GF/D,

Whatman) in a cavity close to the working electrode/counter electrode stack and contacted with titanium wire. The other three holes were closed with PEEK-screws.

The cells were vacuum filled with the electrolyte. The preparation and handling of the electrolyte solvent and salt were conducted in an argon-filled glovebox (MBraun Labmaster 130, O₂, H₂O < 0.1 ppm). A 1 M sodium perchlorate (NaClO₄, >99% purity, Alfa Aesar) solution in a solvent mixture of ethylene carbonate (EC, ≥99% purity, Sigma Aldrich) and dimethyl carbonate (DMC, ≥99% purity, Sigma Aldrich) in a 1 : 1 mass ratio with the addition of 5 mass% fluoroethylene carbonate (FEC, 99% purity, Sigma Aldrich) was used as an electrolyte. FEC is an additive for sodium-ion batteries used to improve the stability by increasing the solid electrolyte interface (SEI) stability, modifying the composition of the SEI layer, and preventing the decomposition of EC and DMC because the oxidation potential of FEC is higher than those of EC and DMC.^{42–46} The sodium salt for the electrolyte was dried under vacuum at +80 °C for 48 h. The electrolyte was examined *via* Karl-Fischer titration and was found to contain less than 25 ppm water.

For measurements in aqueous electrolyte, half-cells were prepared by using Kynol ACC-507-20 as a working electrode and YP-80F as the counter electrode, the electrodes were separated by a 13 mm diameter vacuum dried glass-fiber disc (GF/A, 210 μm thickness, Whatman) to avoid short-circuiting. We used aqueous 600 mM NaCl as the electrolyte. Graphite foil was used as a current collector, and the Ag/AgCl (3 M KCl E_0 Ag/AgCl = 0.210 V *vs.* normal hydrogen electrode) electrode was employed as a reference electrode.

To determine the electrochemical behavior and electrochemical stability window of aqueous electrolyte, an *S*-value test, according to Xu *et al.*⁴⁷ was conducted. The vertex potential started at 0 V and was increased with an incremental of 50 mV steps until the final potential of 1.2 V *vs.* Ag/AgCl was reached. These measurements were done with a scan rate of 1 mV s⁻¹. For *S*-value calculation, the data at the 4th cycle is selected so that the electrode is conditioned at every vertex potential. For positive potential window opening, the *S*-values obtained from cyclic voltammetry were calculated by applying the eqn (1):

$$S = \frac{Q_{\text{pos}}}{Q_{\text{neg}}} - 1 \quad (1)$$

By integrating the positive and negative current *vs.* time of each cycle, the values for Q_{neg} and Q_{pos} are calculated.

Galvanostatic cycling with potential limitation (GCPL), cyclic voltammetry (CV), and performance measurements were carried out using a VMP3 multi-channel potentiostat/galvanostat from Bio-Logic. All obtained values for the capacity in Sb/C *vs.* sodium cells relate to the respective active mass (*i.e.*, the total mass of antimony). All electrochemical measurements were carried out at a climate chamber (Binder) with a constant temperature of +25 ± 1 °C. The galvanostatic charge/discharge cycling with potential limitation (GCPL) experiments was recorded at voltages in the range of 0.1–2.0 V *vs.* Na⁺/Na. For all GCPLs in this work, a specific current of

200 mA g⁻¹ was used. Rate performance measurements were conducted at different currents to get more information about the half-cell rate capability and stability at higher currents. The applied specific currents were 0.1 A g⁻¹, 0.2 A g⁻¹, 0.5 A g⁻¹, 1.0 A g⁻¹, 2.0 A g⁻¹, 4.0 A g⁻¹, 8.0 A g⁻¹, and (again) 0.1 A g⁻¹. All CV measurements were carried out with a scan rate of 0.1 mV s⁻¹ in a potential window of 0.1–2.0 V *vs.* Na⁺/Na.

2.4.2 Electrochemical desalination. For electrochemical desalination, a custom-built multi-channel concentration bi-electrolyte cell was used, following the design described by Lee *et al.*⁴⁸ This cell persists of two side channels out of acrylic glass and one middle channel through which the aqueous electrolyte can flow. The tightness of the cell is guaranteed by various silicon gaskets (600 μm thickness). Graphite blocks (5 × 5 cm², thickness: 10 mm) served as the current collector. First the 20 mm diameter Sb/C electrode (preparation see above; 7 ± 0.5 mg active material) was placed in the cell between the silicon gasket, followed by a 24 mm vacuum dried glass-fiber separator (GF/D from Whatman), on which 2 mL of the organic electrolyte (1 M NaClO₄ in EC/DMC + 5% FEC) was dropped. After that, the NASICON membrane (Ø = 40 mm, 300 μm thickness) was inserted, surrounded by the gasket, to separate the aqueous side from the organic side. After placing the flow channel, a porous separator (Ø = 24 mm, glass-fiber pre-filler, Millipore, 380 μm thickness), the activated carbon cloth electrodes (Ø = 24 mm; 160 ± 20 mg), followed by graphite current-collector, complete the cell setup. A picture of our desalination cell and the generalized operation process are depicted in Fig. 1.

Mass balancing between a carbon electrode and Sb/C electrode followed eqn (2):

$$m_{\text{Sb/C}} Q_{\text{Sb/C}} = m_{\text{C}} Q_{\text{C}} \quad (2)$$

The feed solution with 600 mM NaCl was prepared by dissolving NaCl (≥99.5% purity, Sigma Aldrich) in deionized water (Milli-Q). Using a 10 L reservoir, this aqueous electrolyte was pumped at an average of 1.1 mL min⁻¹ into one side channel of the cell by a peristaltic pump (Masterflex, L/S Series). The electrolyte tank was continuously flushed with nitrogen gas to remove dissolved oxygen. The electrochemical test was carried out using a VSP3 multi-channel potentiostat/galvanostat from Bio-Logic. The conductivity- and pH-modules (Metrohm) are controlled by the Tiamo software. All electrochemical measurements were carried out in a climate chamber (Binder) with a constant temperature of +25 ± 1 °C. The GCPL experiments were recorded in the range of ±2.0 V *vs.* antimony.

The desalination capacity is calculated with eqn (3):

$$\text{Desalination capacity} = \frac{\nu M_{\text{NaCl}}}{m_{\text{total}}} \int \Delta c dt \quad (3)$$

where ν stands for the flow rate (mL min⁻¹), M_{NaCl} is the molecular mass of NaCl (58.44 g mol⁻¹), m_{total} is the mass of the electrodes (g), Δc is the change of concentration of NaCl (mM), and t is the time over the adsorption step (min). Note: we also normalized the desalination performance just normalized to the mass of the Sb/C electrode and when only considering sodium to yield a value for the sodium-removal capacity.

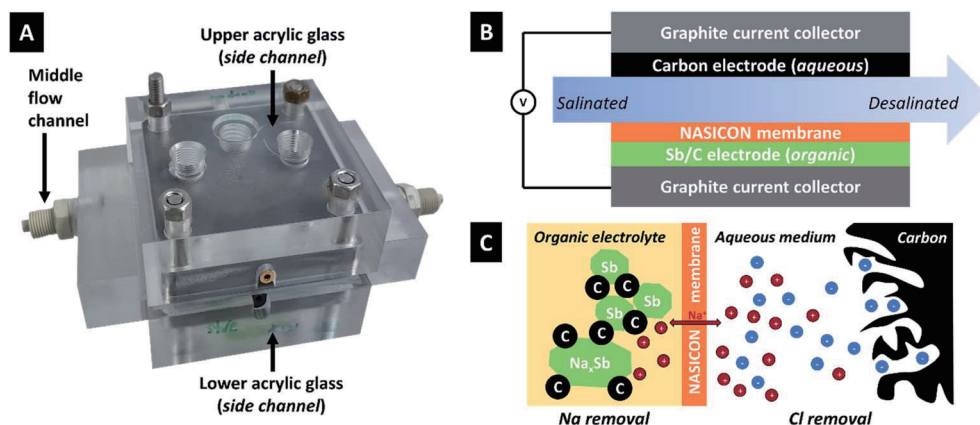


Fig. 1 (A) Photograph and (B) schematic drawing of the desalination cell used for this work. (C) Schematic drawing of the desalination mechanism.

3 Results and discussion

3.1 Working principle of the Sb/C vs. activated carbon cloth cell

We chose an optimized Sb/C composite electrode material based on our previous work which surveyed an array of different carbon additives; a detailed report on the structural, chemical, and porosity-related properties of the used carbon onion/antimony composite electrodes is found in ref. 36.

In this work, an Sb/C electrode is surrounded by an organic electrolyte and separated from the feedwater (aqueous 600 mM NaCl) by a ceramic cation-exchange membrane. During charging, 1 Sb atom reacts with (up to) 3 Na⁺ ions in a multi-stage alloying process. Na⁺ originates from the electrolyte solution on this side of the cell. This creates a concentration gradient of Na⁺ during charging and a lack of these ions in the electrolyte. The saltwater on the other side of the cell is rich in Na⁺ and the concentration gradient allows Na⁺ to move through

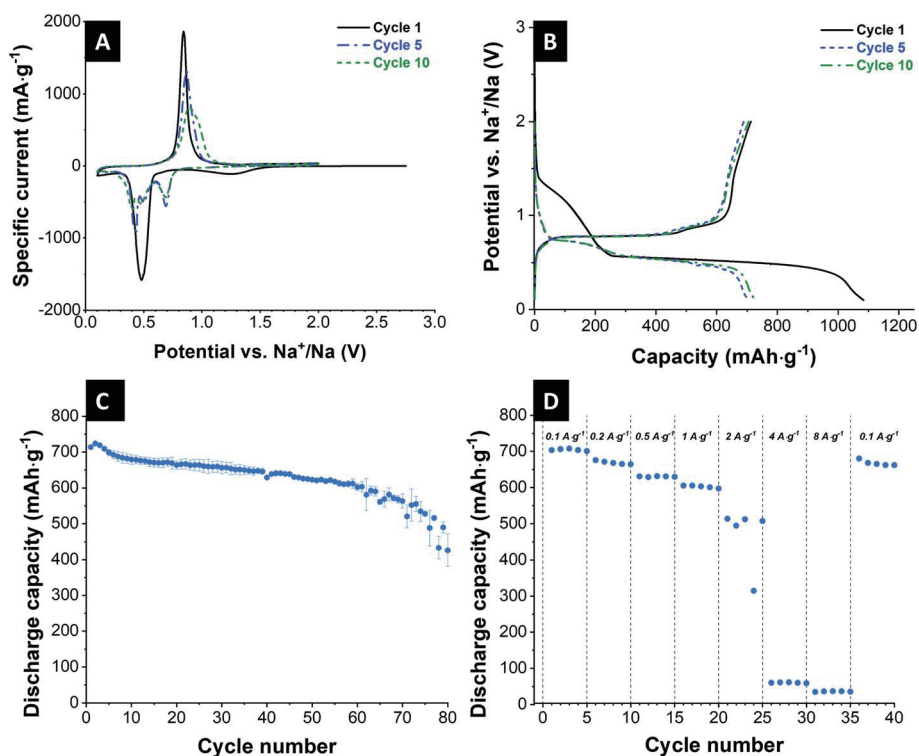


Fig. 2 Electrochemical performance of the Sb/C electrode. (A) 1st, 5th, and 10th cyclic voltammogram at a scanning rate of 0.1 mV s⁻¹ from 0.1 V up to 2.0 V vs. Na⁺/Na. (B) Galvanostatic charge and discharge profiles of the 1st, 5th, and 10th cycle at 200 mA g⁻¹ between 0.1 V and 2.0 V vs. Na⁺/Na. (C) Galvanostatic charge/discharge cycling performance electrochemical stability at a specific current of 200 mA g⁻¹. (D) Rate performance using galvanostatic charge/discharge cycling at different values for the specific current.

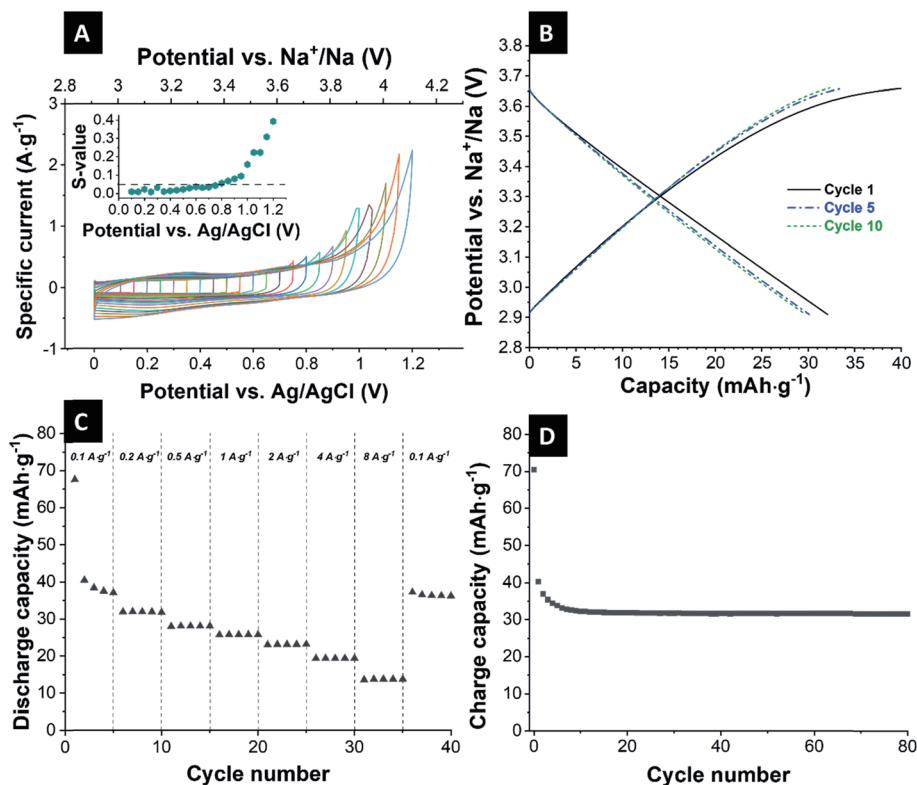


Fig. 3 Characterization of the activated carbon cloth electrode in 600 mM NaCl with an oversized activated carbon counter-electrode. (A) Voltammetric potential window opening experiments were recorded at a scan rate of 0.1 mV s^{-1} (inset: S-value vs. vertex voltage plot). (B) Galvanostatic charge-discharge profiles of the 1st, 5th, and 10th cycle at 200 mA g^{-1} of the activated carbon cloth electrode between 0 V and 0.75 V vs. Ag/AgCl, which corresponds with 2.91 V and 3.66 V vs. Na⁺/Na. (C) Rate performance of the activated carbon cloth electrode from galvanostatic charge/discharge cycling at different values for the specific current. (D) Galvanostatic charge/discharge cycling performance electrochemical stability at a specific current of 200 mA g^{-1} .

the NASICON membrane, whereby sodium removal of the feedwater stream is accomplished. On the other side of the electrochemical desalination cell, chloride is removed from the saline solution *via* ion electrosorption at the fluid/solid interface. When discharging, the process would be reversed, and an increased amount of NaCl is released back into the effluent stream. Thereby, both the Sb and the carbon electrodes are both regenerated and ready for the next desalination cycle.

Data on the material characterization of antimony nanopowder and NASICON powder and membrane are given in ESI, Fig. S1 and S2.†

3.2 Electrochemical characterization

3.2.1 Electrochemical characterization of the Sb/C electrodes. Prior to desalination testing, we established the general electrochemical performance of the Sb/C electrodes in the organic electrolyte. Based on the investigations of Pfeifer *et al.*,³⁶ an electrode consisting of 70 mass% antimony and 20 mass% carbon onions were used as a working electrode. In the latter work, we compared different carbon additives, and we employ carbon onions because they showed the most promising electrochemical performance metrics.³⁶

Cyclic voltammetry was carried out to characterize the redox behavior of the electrode material. Fig. 2A shows the typical CV

of the first, fifth, and tenth cycle at a scan rate of 0.1 mV s^{-1} between 0.1 V and 2.0 V vs. Na⁺/Na. The redox peaks at around 1.2 V and 0.5 V vs. Na⁺/Na in the first cycle correspond to the SEI formation and conversion of crystalline Sb to Na_xSb, respectively.⁴⁹ The oxidation peak in the subsequent sodiation scan at a potential of 0.8 V vs. Na⁺/Na characterize the de-sodiation reaction of Na_xSb alloy back to elemental amorphous antimony. In the 5th and 10th cycles, there are additional reduction peaks at the potential of 0.7 V and 0.45 V vs. Na⁺/Na. This is related to the reaction mechanism of the crystalline antimony, which reacts with the sodium to form amorphous compounds. NaSb further reacts with additional sodium to form crystalline Na₃Sb. Between the first and the following cycle, we can see key differences. The oxidation peak, resulting from the de-sodiation reaction of the alloy, is shifting from 0.74 V vs. Na⁺/Na (1st cycle) over 0.87 V vs. Na⁺/Na (5th cycle) to 0.91 V vs. Na⁺/Na (10th cycle). These differences and the significant decrease in the current intensity after cycling can be attributed to the decomposition of the electrolyte, a change of reaction mechanism, and several changes in the involved structures.

The cycling stability of the Sb/C electrode was tested for 80 cycles at a specific current of 200 mA h g^{-1} in a voltage range between 0.1–2.0 V vs. Na⁺/Na. The corresponding galvanostatic charge and discharge curves are displayed in Fig. 2B, which

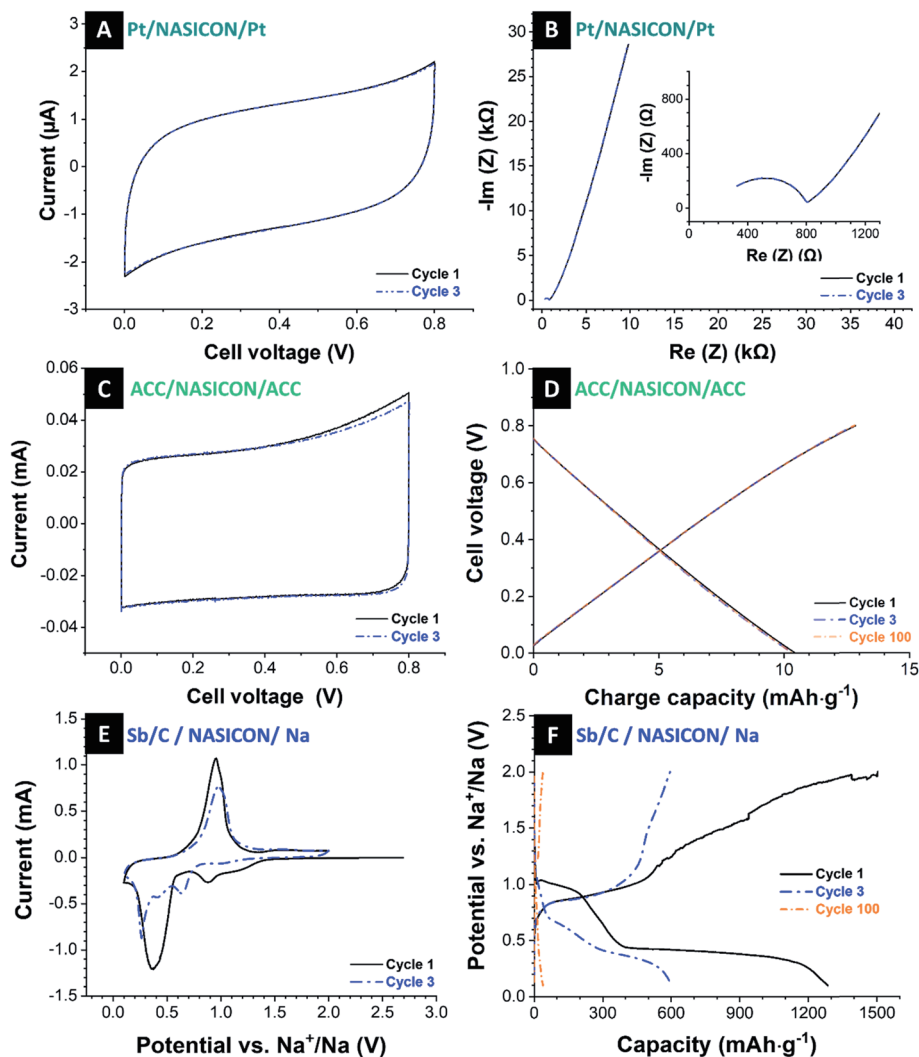


Fig. 4 (A and B) Electrochemical characterization of the platinum-sputtered NASICON membrane: (A) cyclic voltammograms recorded at 5 mV s^{-1} in the potential range of $0.0\text{--}0.8 \text{ V}$, (B) Nyquist plots. (C and D) Electrochemical characterization of activated carbon cloth with a NASICON separator: (C) cyclic voltammograms recorded at 0.1 mV s^{-1} in the potential range of $0.0\text{--}0.8 \text{ V}$, (D) galvanostatic charge and discharge curves of the 1st, 3rd, and 100th cycle. (E and F) Electrochemical characterization of the Sb/C electrode with a NASICON separator paired with a Na-disk counter electrode: (E) first and third cyclic voltammogram recorded with 0.1 mV s^{-1} within the potential range from 0.1 V up to 2.0 V vs. Na^+/Na , (F) galvanostatic charge and discharge curves of the 1st, 3rd, and 100th cycle.

show typical characteristics of the antimony electrodes.^{38,49,50} The different plateaus correspond to the redox reactions associated with Na^+ alloying/de-alloying. The initial sodiation curve exhibits a long plateau at 0.4 V vs. Na^+/Na , which can, besides the alloying products, be assigned to the formation of SEI films on the electrode.⁵¹ In the following cycles, it continuously shows the plateaus according to the alloying reaction from Sb to amorphous Na_xSb to cubic and hexagonal Na_3Sb mixture to hexagonal Na_3Sb .⁵² Subsequent to the 2nd cycle, there are no significant changes in the shape of the curves. Only a small loss of capacity is visible in the discharge curves. The results of these galvanostatic curves confirm the findings received from cyclic voltammetry.

The galvanostatic curves display a potential drift during the electrochemical measurements of the cell. The plateau of the charge curve shifts in the direction of lower capacity, while the

plateau of the discharge curve shifts partially in the direction of higher capacity. This characterizes an overvoltage in the cell, and the capacity is less affected compared to the plateau position (ESI, Fig. S3A[†]). The reasons for this shift may include low kinetics, inhomogeneities of the electrode, and undesired side reactions to a change in the reaction mechanism according to previous works on alloying electrodes.^{38,53–55}

The cycling stability is depicted in Fig. 2C. The initial capacity has a value of 714 mA h g^{-1} . As usual for sodium-ion batteries, there is a small increase of the capacity over the course of the first cycles. The cells slowly degrade continuously over the course of the 80 cycles, especially toward the higher cycle numbers. The degradation occurred in all cells, but at different rates, which resulted in an increased error bar seen at higher cycle numbers in Fig. 2C. After 80 cycles, Sb/carbon

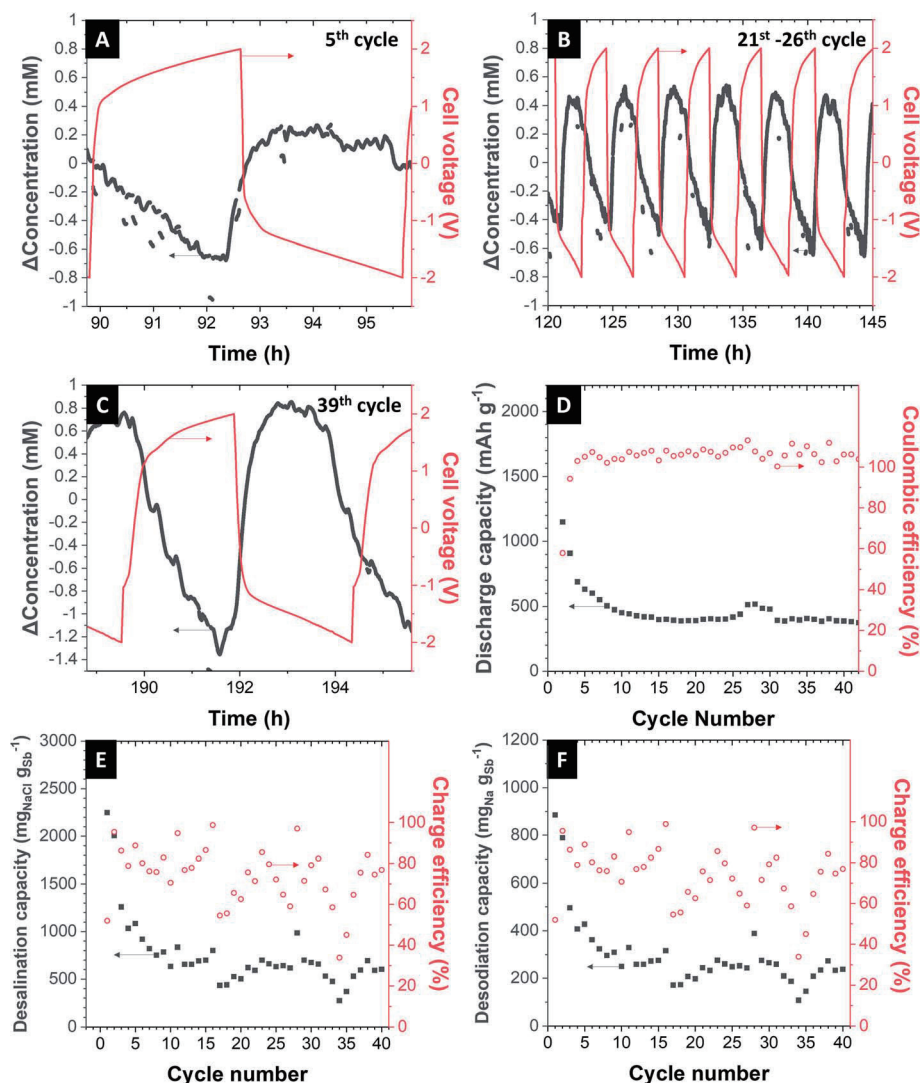


Fig. 5 Performance of the electrochemical desalination cell. (A–C) The change of concentration and voltage profile at the 5th cycle, 21st to 26th cycles and the 39th cycle. (D) The charge capacity and the corresponding values of the coulombic efficiency. (E) The desalination capacity ($\text{mg}_{\text{NaCl}} \text{g}_{\text{Sb}}^{-1}$) and charge efficiency. (F) The desalination capacity ($\text{mg}_{\text{Na}} \text{g}_{\text{Sb}}^{-1}$) and charge efficiency.

electrode reaches a capacity of 426 mA h g^{-1} , which corresponds to a value of 60% of the initial capacity.

The rate capability of these Sb/C electrodes is evaluated at a varying specific current from 0.1 A g^{-1} to 8 A g^{-1} (Fig. 2D). Up to a specific current of 1 A g^{-1} , the electrodes show stable electrochemical behavior with a capacity of higher than 600 mA h g^{-1} (0.1 A g^{-1} : 708 mA h g^{-1} ; 0.2 A g^{-1} : 668 mA h g^{-1} ; 0.5 A g^{-1} : 632 mA h g^{-1} ; 1 A g^{-1} : 603 mA h g^{-1}). At a specific current of 2 A g^{-1} and higher, the cells lost most of their charge storage capacity. When the specific current is again reduced to 0.1 A g^{-1} , the cell nearly reaches its initial capacity but degrades toward the 5th cycle.

3.2.2 Electrochemical characterization of the activated carbon cloth electrodes. As a next step, we characterized the electrochemical behavior of the activated carbon cloth, which will be used on the aqueous side of our desalination cell. Using 600 mM NaCl electrolyte, we carried out *S*-value tests, cyclic voltammetry, galvanostatic cycling, cycling stability, and rate

capability benchmarking (Fig. 3). The electrochemical stability of aqueous electrolyte in the range of 2.9 V up to 4.1 V vs. Na^+/Na was identified *via* the *S*-value test, where the criterion of $dS/dV < 0.05$ (5%) were applied.^{47,56,57} The stable potential window for the activated carbon cloth is between 0 V and 0.75 V vs. Ag/AgCl ; this potential window corresponds to values of 2.9 V and 3.7 V vs. Na^+/Na . The measured cyclic voltammograms (Fig. 3A) at a scan rate of 0.1 mV s^{-1} show the typical ion-electrosorption behavior of carbon without any reduction and oxidation peaks within the identified stable potential region.

The obtained galvanostatic charge and discharge data (Fig. 3B) agree with the data from cyclic voltammetry. As expected for a nearly perfect electrical double-layer capacitor, the galvanostatic profiles show no plateaus, and the electrode delivers an initial capacity of 40 mA h g^{-1} . Over the next cycles, the capacity is stabilized at 32 mA h g^{-1} ($\approx 146 \text{ F g}^{-1}$) for 80 cycles (Fig. 3C).

Table 1 Overview of desalination capacities and charge efficiencies reported for different desalination systems and electrode materials. Not available data from literature references are denoted as "n.a."

System	Electrode	Desalination capacity $\text{mg}_{\text{NaCl}} \text{g}_{\text{electrode}}^{-1} / \text{mg}_{\text{Na}} \text{g}_{\text{electrode}}^{-1}$	Charge efficiency (%)	Energy consumption W h L^{-1}	Cell voltage (V)	Electrolyte	Reference
Faradaic deionization	$\text{Na}_{2-x}\text{Mn}_5\text{O}_{10}/\text{Ag}/\text{AgCl}$	n.a.	n.a.	0.29 W h L^{-1}	$\sim 0.55/0.19$	600 mM NaCl	17
Capacitive deionization	Nanoporous carbon	7/3	$\sim 85\%$	n.a.	1.4/1.2 V	5 mM	69
Capacitive deionization	Nanoporous carbon	13/	86%	n.a.	1.2 V	1000 M NaCl	70
Faradaic deionization	$\text{Ti}_3\text{C}_2\text{-MXene}$	$13 \pm 2/5$	n.a.	n.a.	1.2 V	5 mM NaCl	71
Faradaic deionization	$\text{Bi}/\text{NaTi}_2(\text{PO}_4)_3$	83/	n.a.	n.a.	0.75/0.55 V	600 M NaCl	25
Multi-channel membrane capacitive deionization	Activated carbon cloth	56/33	$\sim 82\%$	$\sim 20 \text{ kT}$	0.0/−1.2 V	Side channel: 1000 M, middle channel: 5 mM	64
Membrane capacitive deionization (aqueous/organic bi-electrolyte)	Nanoporous carbon	$64 \pm 4/25 \pm 2$	95%	14–27 kT	2.4 V	5 mM NaCl	29
Faradaic deionization	$\text{MoS}_2\text{-CNT}$	25/10	80%	24.6 kT	0.8/0.0 V	500 M NaCl	72
Hybrid capacitive deionization	$\text{Na}_4\text{Mn}_9\text{O}_{18}/\text{nanoporous carbon}$	31/12	n.a.	n.a.	0.8/0.0 V	1000 M NaCl	18
Hybrid capacitive deionization (aqueous/organic bi-electrolyte)	Sb-C/nanoporous carbon	$748 \text{ mg}_{\text{NaCl}} \text{g}_{\text{Sb}}^{-1}, 294 \text{ mg}_{\text{Na}} \text{g}_{\text{Sb}}^{-1}$	74%	16 kT ($0.0005 \text{ W h L}^{-1}$)	+2.0/−2.0 V	600 M NaCl	This work

Fig. 3D shows the reversible capacities at various discharge/charge rates. The system retained a capacity of 36/32/27/24/23/19/14 mA h g^{−1} at a specific current of 0.1/0.2/0.5/1.0/2.0/4.0/8.0 A g^{−1}. During running different values of specific current, stable values for the capacities can be obtained, even for high currents of 8 A g^{−1}, which is the advantage of the ion-electrosorption. Only at the very first cycle, one can see that the cell needs one cycle for stabilization. When the specific current is returned to 0.1 A g^{−1}, the cell nearly reaches its initial capacity and shows good stability.

3.2.3 Electrochemical characterization of the NASICON membranes. As a next step, we only characterized the electrochemical behavior of ceramic NASICON membrane with a thickness of 950 μm. To this end, we assembled a solid-state cell by use of a platinum-sputtered NASICON electrode. The NASICON discs were sputtered with platinum to create blocking electrodes and then clamped well between the titanium pistons of the electrochemical cell, to ensure good surface contact and electrical conductivity. Cyclic voltammetry was conducted in a cell voltage range of 0.0–0.8 V. Fig. 4A presents the first and the third voltammetric cycle at a scan rate of 5 mV s^{−1}. Cyclic voltammograms at higher rates are provided in ESI, Fig. S4A.† These two cycles did not differ from each other. In the current vs. voltage profile, we see no anodic (oxidation) and cathodic (reduction) peaks. This means that there are no redox-active species, and no electrochemically reversible reactions are taking place.

Electrochemical impedance spectroscopy (EIS) at a voltage amplitude of 100 mV was conducted using a frequency sweep of 100 mHz to 1 MHz to characterize the NASICON membrane

conductivity. Fig. 4B shows the Nyquist plot with a semicircle in the medium-to-high frequency region. In the impedance spectra at high frequencies, the semicircle indicates the grain resistance of the membrane, whereas, at medium to low frequencies, the semicircle represents the grain boundary resistance. These resistors are characterized by a single semicircle as the total resistance of the membrane.^{39,58} At low frequencies, the diffusion phenomena can be observed. Here, the near-straight line in the low-frequency range corresponds with the interface components (electrode polarization).⁵⁹

Using these data, we can calculate the effective ionic conductivity. The latter is given by the theoretical intersections of the low-frequency ends of the semicircle with the Z' axis.

$$\kappa_{\text{total}} = \frac{1}{R} \frac{A}{d} \quad (4)$$

where κ indicates the total ion conductivity in Siemens per meter, R is the obtained resistance out of the EIS in Ω , d is the thickness of the electrode in cm, and A is the cross-sectional area of the sample in cm². The resulting effective ionic conductivity for our NASICON sample was 0.17 mS cm^{−1}. The value is lower compared to the literature (10^{−5} to 10^{−3} mS cm^{−1}),^{30,60,61} but usually higher sintering temperatures and thinner membranes are being used in other works. Thus, electrodes with sufficient conductivity for desalination were produced.

To characterize sodium transport across the ceramic NASICON membrane in an aqueous electrolyte, we paired the

NASICON disc with two activated carbon cloth electrodes in 600 mM NaCl electrolyte and sandwich on the NASICON membrane. The first and third cyclic voltammograms at a scan rate of 0.1 mV s^{-1} are given in Fig. 4C within a cell voltage of 0.0 V to 0.8 V. Cyclic voltammograms at higher rates are provided in ESI, Fig. S4B.† We see highly rectangular profiles, which are typical for an ideal electrical double-layer capacitor.⁶² Additionally, the cell voltage of carbon cloth in the semi-solid cell is significantly lower than in a traditional cell. This is possibly due to the high contact resistance between carbon and NASICON interface as well as low ionic conductivity of the membrane.

The galvanostatic charge and discharge profiles of activated carbon cloth are shown in Fig. 4D. At a specific current of 200 mA g^{-1} within a voltage range of 0.0–0.8 V, there is a typical linear relation between charge and cell voltage in alignment with a nearly perfect capacitive behavior. There are no significant changes in charge/discharge capacity for 100 cycles (ESI, Fig. S5A and C†). However, considering the rate handling of carbon cloth (ESI, Fig. S5E†), the cell cannot provide fast charge/discharge as compared to the conventional cell with a glass fiber separator due to the fact that the sodium transport kinetics are much slower than that in glass fiber separator; a comparison thereof is shown in ESI, Fig. S3B.†

As in the next step, we used the Sb/C electrode as the working electrode and the pure sodium electrode as a counter electrode with the NASICON membrane as a separator. We used an organic electrolyte of 1 M NaClO₄ in EC/DMC + 5% FEC and a scan rate of 0.1 mV s^{-1} within the range from 0.1–2.0 V vs. Na⁺/Na. The obtained cyclic voltammograms with the NASICON membrane (Fig. 4E) are similar to those with just a porous separator (Fig. 2A) with the characteristic peaks for the alloy reactions of antimony with sodium. This indicates that the comparatively thick NASICON electrode can transport Na⁺ to the extent or at speed required for the alloy reactions to take place. Cyclic voltammograms at higher rates are provided in ESI, Fig. S4C.† Conspicuous is the broader shape of the obtained cyclic voltammograms with the NASICON membrane compared with the same cell setup with glass fiber separator. In general, the breadth of peaks depends on the limiting stage of processes like the velocity of mass or electron transfer and diffusion and chemical processes before or after electron transfer. So, in this current case, the broader peaks may be an indicator of lower transport rates of the ions in the cell because of the thick NASICON membrane.

Fig. 4F presents the galvanostatic charge and discharge profiles of Sb/C electrode vs. Na⁺/Na with a NASICON membrane as the separator, at a specific current of 200 mA g^{-1} and a voltage range of 0.1–2.0 V. The initial charge curve exhibits the similar a long plateau at 0.4 V which represents the SEI formation. In addition, the discharge curve reaches beyond 1285 mA h g^{-1} of the corresponding charge curve. It seems that the sodium ions in the NASICON block the channels at times, and the cell cannot be discharged as easily. After the first cycle, this phenomenon is vanishing. During the next cycles, one sees the plateaus at 0.7–1.0 V during sodium-ion removal, which can be related to the reaction of Na₃Sb alloys back to crystalline

antimony. The observations from the galvanostatic charge and discharge curves are consistent with the information obtained from cyclic voltammetry.

The cycling stability is presented in ESI, Fig. S5B.† The performance is characterized by a continuous loss of capacity in each cycle. The cells exhibit a capacity of 643 mA h g^{-1} in the second cycle and show a capacity of about 453 mA h g^{-1} after only 10 cycles, which correspond to a loss of capacity of 30%. In the 50th cycle, the cells still reach a capacity of approximately 100 mA h g^{-1} , and after the 80 cycles, only a low capacity of 44 mA h g^{-1} is delivered, which corresponds to a total capacity loss of 93% over 80 cycles. The coulombic efficiency, shown in ESI, Fig. S5D,† shows constant values of 96–97%. Compared to the cell with porous separator, the rate capability shows a lower capacity and stability at all rates (ESI, Fig. S5F†) as the sodium ion diffusion through the element-specific channels of the NASICON membrane is limited by the thick membrane. Yet, the ceramic NASICON membrane works sufficiently well to provide the antimony electrode with a sufficient supply of sodium for the alloying reaction.

3.3 Desalination performance

Electrochemical desalination was performed in a desalination cell described elsewhere.^{29,34} The Sb/C electrode was surrounded by 1 M NaClO₄ in EC/DMC + 5% FEC electrolyte and separated from the feedwater stream by a ceramic NASICON membrane with 300 μm thickness. Oversized activated carbon cloth is used as a counter electrode. As feedwater, aqueous 600 mM NaCl is fed to the cell with a peristaltic pump. To be sure that the electrolyte is oxygen-free, we constantly flushed the electrolyte with N₂ gas throughout the desalination experiment. As a specific current of 200 mA g^{-1} was applied to the cell with the cut-off cell voltage of $\pm 2.0 \text{ V}$, the concentration profile behaves like in a regular capacitive deionization cell. In the first cycle, the concentration of NaCl has decreased with the amplitude of about 5 mM when the cell is charged. After 80 min of charging, the cell is rested for 2 min and discharged, one can see the increasing of NaCl concentration, indicating the de-sodiation of Sb/C electrode (Fig. 5A). After 40 cycles of operation, the amplitude of decreased NaCl concentration is significantly lower than that of the first cycle (Fig. 5B). This is due to the intrinsic mechanism of sodium-alloying in the Sb electrode. The charge capacity of our desalination cell is about $669 \text{ mA h g}_{\text{Sb}}^{-1}$ at the first cycle after conditioning cycles and decays to $360 \text{ mA h g}_{\text{Sb}}^{-1}$ after 40 cycles (Fig. 5C). The corresponding desalination capacity of the first cycle is $495 \text{ mg}_{\text{Na}} \text{ g}_{\text{Sb}}^{-1}$ and stabilizes at around $250 \text{ mg}_{\text{Na}} \text{ g}_{\text{Sb}}^{-1}$ (corresponds to $635 \text{ mg}_{\text{NaCl}} \text{ g}_{\text{Sb}}^{-1}$ and $1116 \text{ mg}_{\text{Na}} \text{ m}_{\text{membrane}}^{-2}$) with the charge efficiency of about 74% for 40 cycles (Fig. 5D).

Reasons for the low charge efficiency could be, among others, the side reactions (like oxidation of carbon or splitting of water), the imperfect shape, and properties of the NASICON membrane, which prevents the ions from being transported in the fastest and easiest way, which also results in poorer kinetics. These factors also will contribute towards the decay of performance seen during continued cell operation.

In comparison to other systems (charge-transfer materials),³³ which successfully desalinate with different mechanisms like an ion electrosorption ($3\text{--}27 \text{ mg}_{\text{NaCl}} \text{ g}_{\text{electrode}}^{-1}$; $1\text{--}11 \text{ mg}_{\text{Na}} \text{ g}_{\text{electrode}}^{-1}$),⁶³ insertion of different materials and redox couples ($6\text{--}140 \text{ mg}_{\text{NaCl}} \text{ g}_{\text{electrode}}^{-1}$; $2\text{--}55 \text{ mg}_{\text{Na}} \text{ g}_{\text{electrode}}^{-1}$),²⁷ or conversion type ($17\text{--}115 \text{ mg}_{\text{NaCl}} \text{ g}_{\text{electrode}}^{-1}$; $7\text{--}22 \text{ mg}_{\text{Na}} \text{ g}_{\text{electrode}}^{-1}$),^{23,24} the system described in this work shows very promising values (Table 1).

For membrane capacitive deionization (MCDI), a value of 22 kT is often reported.^{8,29} The first desalination battery achieved a value of 0.29 W h L^{-1} for energy consumption.¹⁷ Kim *et al.* report for a multi-channel membrane capacitive deionization an energy consumption of 20 kT.⁶⁴ The energy consumption of the cell configuration in this work is calculated to be 16 kT or $39 \text{ kJ mol}^{-1}_{\text{NaCl}}$ after the first cycles. This value corresponds to the energy per processed water of $0.0005 \text{ W h L}^{-1}$, which is also comparable to traditional methods like reverse osmosis ($0.5\text{--}2 \text{ W h L}^{-1}$),⁶⁵ multistage flash distillation ($20\text{--}30 \text{ W h L}^{-1}$),⁶⁶ multi-effect distillation ($15\text{--}20 \text{ W h L}^{-1}$),⁶⁷ freezing methods ($6\text{--}8 \text{ W h L}^{-1}$).⁶⁸ Compared to other faradaic materials (including intercalation materials), conversion materials, redox electrolytes, and zinc-air desalination, alloying with the aid of NASICON deliver energy consumption lower than others. A direct comparison, however, is complicated by different experimental settings, such as flow rate, cell volume, and the extent of salt reduction.²⁷

4 Conclusion

This study demonstrates a desalination cell by using antimony as a sodium-alloying material, which is a promising and high-performing electrode in sodium-ion batteries. By applying a bi-electrolyte system (organic and aqueous part), the cell can provide stable desalination performance at higher maximum cell voltage than the conventional capacitive deionization technology allows (1.0–1.2 V). In an optimized desalination cell configuration with a middle channel for the inflowing feed stream and a selective sodium permeable membrane (NASICON), the Sb/C electrodes exhibit an improved electrochemical performance with a discharge capacity of initially 669 mA h g^{-1} (395 mA h g^{-1} after 40 cycles) at a specific current of 200 mA g^{-1} and a voltage range of -2.0 V to $+2.0 \text{ V}$, which results in a desalination capacity on the average of $294 \text{ mg}_{\text{Na}} \text{ g}_{\text{Sb}}^{-1}$ with a charge efficiency of about 74% in aqueous 600 mM NaCl. Future work will have to further optimize the cell design, and further reduction of the ceramic membrane thickness will allow the faster operation of the desalination battery.

Conflicts of interest

There are no conflicts to declare.

Acknowledgements

L. W. acknowledges funding from the Chinese Scholarship Council (CSC) via award number 201906260277. We thank Eduard Arzt (INM) for his continuing support. Further, we thank the INM Service Group Chemical Analytics for chemical

analysis and Samantha Husmann (INM) for technical support and discussions.

References

- 1 N. C. Darre and G. S. Toor, *Curr. Pollut. Rep.*, 2018, **4**, 104–111.
- 2 A. D. Khawaji, I. K. Kutubkhanah and J.-M. Wie, *Desalination*, 2008, **221**, 47–69.
- 3 A. Matin, Z. Khan, S. M. J. Zaidi and M. C. Boyce, *Desalination*, 2011, **281**, 1–16.
- 4 Y.-y. Lu, Y.-d. Hu, D.-m. Xu and L.-y. Wu, *J. Membr. Sci.*, 2006, **282**, 7–13.
- 5 A. Rich, Y. Mandri, N. Bendaoud, D. Mangin, S. Abderafi, C. Bebon, N. Semlali, J.-P. Klein, T. Bounahmidi, A. Bouhaouss and S. Veesler, *Desalin. Water Treat.*, 2010, **13**, 120–127.
- 6 S. Porada, R. Zhao, A. van der Wal, V. Presser and P. M. Biesheuvel, *Prog. Mater. Sci.*, 2013, **58**, 1388–1442.
- 7 M. E. Suss, S. Porada, X. Sun, P. M. Biesheuvel, J. Yoon and V. Presser, *Energy Environ. Sci.*, 2015, **8**, 2296–2319.
- 8 R. Zhao, S. Porada, P. M. Biesheuvel and A. van der Wal, *Desalination*, 2013, **330**, 35–41.
- 9 S. Porada, L. Zhang and J. E. Dykstra, *Desalination*, 2020, **488**, 114383.
- 10 P. M. Biesheuvel, S. Porada, M. Levi and M. Z. Bazant, *J. Solid State Electrochem.*, 2014, **18**, 1365–1376.
- 11 C. Prehal, C. Koczwara, H. Amenitsch, V. Presser and O. Paris, *Nat. Commun.*, 2018, **9**, 4145.
- 12 S. Bi, Y. Zhang, L. Cervini, T. Mo, J. M. Griffin, V. Presser and G. Feng, *Sustainable Energy Fuels*, 2020, **4**, 1285–1295.
- 13 N. Jäckel, P. Simon, Y. Gogotsi and V. Presser, *ACS Energy Lett.*, 2016, **1**, 1262–1265.
- 14 F. Stoeckli and T. A. Centeno, *Phys. Chem. Chem. Phys.*, 2012, **14**, 11589–11591.
- 15 H. Ji, X. Zhao, Z. Qiao, J. Jung, Y. Zhu, Y. Lu, L. L. Zhang, A. H. MacDonald and R. S. Ruoff, *Nat. Commun.*, 2014, **5**, 3317.
- 16 Z.-H. Huang, Z. Yang, F. Kang and M. Inagaki, *J. Mater. Chem. A*, 2017, **5**, 470–496.
- 17 M. Pasta, C. D. Wessells, Y. Cui and F. La Mantia, *Nano Lett.*, 2012, **12**, 839–843.
- 18 J. Lee, S. Kim, C. Kim and J. Yoon, *Energy Environ. Sci.*, 2014, **7**, 3683–3689.
- 19 P. Srimuk, J. Lee, Ö. Budak, J. Choi, M. Chen, G. Feng, C. Prehal and V. Presser, *Langmuir*, 2018, **34**, 13132–13143.
- 20 S. Porada, A. Shrivastava, P. Bukowska, P. M. Biesheuvel and K. C. Smith, *Electrochim. Acta*, 2017, **255**, 369–378.
- 21 P. Srimuk, J. Lee, A. Tolosa, C. Kim, M. Aslan and V. Presser, *Chem. Mater.*, 2017, **29**, 9964–9973.
- 22 E. Grygolowicz-Pawlak, M. Sohail, M. Pawlak, B. Neel, A. Shvarev, R. de Marco and E. Bakker, *Anal. Chem.*, 2012, **84**, 6158–6165.
- 23 P. Srimuk, S. Husmann and V. Presser, *RSC Adv.*, 2019, **9**, 14849–14858.
- 24 J. Ahn, J. Lee, S. Kim, C. Kim, J. Lee, P. M. Biesheuvel and J. Yoon, *Desalination*, 2020, **476**, 114216.

- 25 D.-H. Nam and K.-S. Choi, *J. Am. Chem. Soc.*, 2017, **139**, 11055–11063.
- 26 F. Yu, L. Wang, Y. Wang, X. Shen, Y. Cheng and J. Ma, *J. Mater. Chem. A*, 2019, **7**, 15999–16027.
- 27 P. Srimuk, X. Su, J. Yoon, D. Aurbach and V. Presser, *Nat. Rev. Mater.*, 2020, **5**, 517–538.
- 28 S. Porada, G. Feng, M. E. Suss and V. Presser, *RSC Adv.*, 2016, **6**, 5865–5870.
- 29 C. Kim, P. Srimuk, J. Lee and V. Presser, *Desalination*, 2018, **443**, 56–61.
- 30 Y. Kim, H. Kim, S. Park, I. Seo and Y. Kim, *Electrochim. Acta*, 2016, **191**, 1–7.
- 31 Y. Kim, G.-T. Kim, S. Jeong, X. Dou, C. Geng, Y. Kim and S. Passerini, *Energy Storage Materials*, 2019, **16**, 56–64.
- 32 N. Kim, J.-S. Park, A. M. Harzandi, K. Kishor, M. Ligaray, K. H. Cho and Y. Kim, *Desalination*, 2020, **495**, 114666.
- 33 M. E. Suss and V. Presser, *Joule*, 2018, **2**, 10–15.
- 34 J. Lee, P. Srimuk, R. L. Zornitta, M. Aslan, B. L. Mehdi and V. Presser, *ACS Sustainable Chem. Eng.*, 2019, **7**, 10132–10142.
- 35 S. Z. Liang, Y. J. Cheng, J. Zhu, Y. G. Xia and P. Müller-Buschbaum, *Small Methods*, 2020, **4**, 2000218.
- 36 K. Pfeifer, S. Arnold, Ö. Budak, X. Luo, V. Presser, H. Ehrenberg and S. Dsoke, *J. Mater. Chem. A*, 2020, **8**, 6092–6104.
- 37 H. Tan, D. Chen, X. Rui and Y. Yu, *Adv. Funct. Mater.*, 2019, **29**, 1808745.
- 38 H. Hou, Y. Yang, Y. Zhu, M. Jing, C. Pan, L. Fang, W. Song, X. Yang and X. Ji, *Electrochim. Acta*, 2014, **146**, 328–334.
- 39 H. Park, K. Jung, M. Nezafati, C.-S. Kim and B. Kang, *ACS Appl. Mater. Interfaces*, 2016, **8**, 27814–27824.
- 40 M. Zeiger, N. Jäckel, M. Aslan, D. Weingarth and V. Presser, *Carbon*, 2015, **84**, 584–598.
- 41 D. Weingarth, M. Zeiger, N. Jäckel, M. Aslan, G. Feng and V. Presser, *Adv. Energy Mater.*, 2014, **4**, 1400316.
- 42 J. Qian, Y. Chen, L. Wu, Y. Cao, X. Ai and H. Yang, *Chem. Commun.*, 2012, **48**, 7070–7072.
- 43 Y.-X. Wang, Y.-G. Lim, M.-S. Park, S.-L. Chou, J. H. Kim, H.-K. Liu, S.-X. Dou and Y.-J. Kim, *J. Mater. Chem. A*, 2014, **2**, 529–534.
- 44 A. Ponrouch, D. Monti, A. Boschini, B. Steen, P. Johansson and M. R. Palacin, *J. Mater. Chem. A*, 2015, **3**, 22–42.
- 45 A. Ponrouch, A. R. Goñi and M. R. Palacín, *Electrochem. Commun.*, 2013, **27**, 85–88.
- 46 V. Simone, L. Lecarme, L. Simonin and S. Martinet, *J. Electrochem. Soc.*, 2016, **164**, A145–A150.
- 47 K. Xu, S. P. Ding and T. R. Jow, *J. Electrochem. Soc.*, 1999, **146**, 4172–4178.
- 48 J. Lee, P. Srimuk, S. Carpier, J. Choi, R. L. Zornitta, C. Kim, M. Aslan and V. Presser, *ChemSusChem*, 2018, **11**, 3460–3472.
- 49 S. Liu, J. Feng, X. Bian, J. Liu and H. Xu, *Energy Environ. Sci.*, 2016, **9**, 1229–1236.
- 50 L. Wu, X. Hu, J. Qian, F. Pei, F. Wu, R. Mao, X. Ai, H. Yang and Y. Cao, *Energy Environ. Sci.*, 2014, **7**, 323–328.
- 51 X. Zhou, Z. Dai, J. Bao and Y.-G. Guo, *J. Mater. Chem. A*, 2013, **1**, 13727–13731.
- 52 A. Darwiche, C. Marino, M. T. Sougrati, B. Fraisse, L. Stievano and L. Monconduit, *J. Am. Chem. Soc.*, 2012, **134**, 20805–20811.
- 53 P. R. Abel, Y.-M. Lin, T. de Souza, C.-Y. Chou, A. Gupta, J. B. Goodenough, G. S. Hwang, A. Heller and C. B. Mullins, *J. Phys. Chem. C*, 2013, **117**, 18885–18890.
- 54 M.-S. Balogun, Y. Luo, W. Qiu, P. Liu and Y. Tong, *Carbon*, 2016, **98**, 162–178.
- 55 Y. Kim, Y. Park, A. Choi, N.-S. Choi, J. Kim, J. Lee, J. H. Ryu, S. M. Oh and K. T. Lee, *Adv. Mater.*, 2013, **25**, 3045–3049.
- 56 M. Bahdanchyk, M. Hashempour and A. Vicenzo, *Electrochim. Acta*, 2020, **332**, 135503.
- 57 D. Weingarth, H. Noh, A. Foelske-Schmitz, A. Wokaun and R. Kötz, *Electrochim. Acta*, 2013, **103**, 119–124.
- 58 S. Narayanan, S. Reid, S. Butler and V. Thangadurai, *Solid State Ionics*, 2019, **331**, 22–29.
- 59 A. Jalalian-Khakshour, C. O. Phillips, L. Jackson, T. O. Dunlop, S. Margadonna and D. Deganello, *J. Mater. Sci.*, 2020, **55**, 2291–2302.
- 60 S. Naqash, D. Sebold, F. Tietz and O. Guillon, *J. Am. Ceram. Soc.*, 2019, **102**, 1057–1070.
- 61 S.-M. Lee, S.-T. Lee, D.-H. Lee, S.-H. Lee, S.-S. Han and S.-K. Lim, *Journal of Ceramic Processing Research*, 2015, **16**, 49–53.
- 62 H. Shao, Y. C. Wu, Z. Lin, P. L. Taberna and P. Simon, *Chem. Soc. Rev.*, 2020, **49**, 3005–3039.
- 63 Y. Liu, C. Y. Nie, X. J. Liu, X. T. Xu, Z. Sun and L. K. Pan, *RSC Adv.*, 2015, **5**, 15205–15225.
- 64 C. Kim, J. Lee, P. Srimuk, M. Aslan and V. Presser, *ChemSusChem*, 2017, **10**, 4914–4920.
- 65 A. Shrivastava, S. Rosenberg and M. Peery, *Desalination*, 2015, **368**, 181–192.
- 66 R. Semiat, *Environ. Sci. Technol.*, 2008, **42**, 8193–8201.
- 67 A. Al-Karaghouli and L. L. Kazmerski, *Renewable Sustainable Energy Rev.*, 2013, **24**, 343–356.
- 68 T. Mtombeni, J. Maree, C. Zvinowanda, J. Asante, F. Oosthuizen and W. Louw, *Int. J. Environ. Sci. Technol.*, 2013, **10**, 545–550.
- 69 S. Porada, L. Weinstein, R. Dash, A. van der Wal, M. Bryjak, Y. Gogotsi and P. M. Biesheuvel, *ACS Appl. Mater. Interfaces*, 2012, **4**, 1194–1199.
- 70 M. Aslan, M. Zeiger, N. Jäckel, I. Grobelsek, D. Weingarth and V. Presser, *J. Phys.: Condens. Matter*, 2016, **28**, 114003.
- 71 P. Srimuk, F. Kaasik, B. Krüner, A. Tolosa, S. Fleischmann, N. Jäckel, M. C. Tekeli, M. Aslan, M. E. Suss and V. Presser, *J. Mater. Chem. A*, 2016, **4**, 18265–18271.
- 72 P. Srimuk, J. Lee, S. Fleischmann, S. Choudhury, N. Jäckel, M. Zeiger, C. Kim, M. Aslan and V. Presser, *J. Mater. Chem. A*, 2017, **5**, 15640–15649.

Supporting Information

Antimony alloying electrode for high-performance sodium removal: how to use a battery material not stable in aqueous media for saline water remediation

Stefanie Arnold,^{1,2} Lei Wang,^{1,2} Öznil Budak,^{1,2}

Mesut Aslan,¹ Pattarachai Srimuk,¹ Volker Presser^{1,2,*}

¹ INM - Leibniz Institute for New Materials, 66123 Saarbrücken, Germany

² Department of Materials Science and Engineering, Saarland University, 66123 Saarbrücken, Germany

* Corresponding author's E-Mail: volker.presser@leibniz-inm.de

Supporting Table

Table S1: Results of the elemental analysis (CHNS/O).

	CHNS/O elemental analysis (mass%)				
	Carbon	Hydrogen	Nitrogen	Sulfur	Oxygen
Antimony powder	0.18±0.11	Not detected			5.66±0.04

Supporting Material Characterization

We used a co-precipitation method to obtain the antimony nanopowder. Scanning electron micrographs, X-ray diffraction data, and Raman data are given in **Figure S1**. **Figure S1A**, the scanning electron micrograph shows partially agglomerated particles with a primary size of about 10-40 nm. The X-ray diffractogram (**Figure S1C**) is consistent with elemental antimony (space group of $R\bar{3}m$, ICSD: #55402, $a=4.307$ Å). Rietveld analysis yields an Sb phase content of about 97-98 mass% with a small amount of Sb_2O_3 . This aligns with the small amount of oxygen found from chemical CHNS/O elemental analysis (*Supporting Information, Table S1*). The Raman spectra of antimony at ambient conditions (**Figure S1D**) shows two peaks at 113 cm^{-1} and 150 cm^{-1} , which agrees with previous works on antimony.¹⁻³ Trigonal antimony forms stacked layers of atoms along the hexagonal axis. This structure results in two Raman active modes, the A_{1g} mode at 150 cm^{-1} and a two-fold degenerated E_g mode at 115 cm^{-1} , whereby the A_{1g} mode corresponds to the longitudinal motion of the atom planes and the E_g mode the transverse motion.² The Raman spectra also shows the presence of small amounts of Sb_2O_3 from the broad and low-intensity peak at around 270 cm^{-1} (Sb-O-Sb). The antimony oxide is most likely present in the form of thin skin around the antimony particles, which would act as an insulative layer between the antimony particle. This would result in high resistance of the electrode and poor electrochemical performance with a capacity close to zero. Therefore, the use (and choice) of the conductive additive plays a central role.

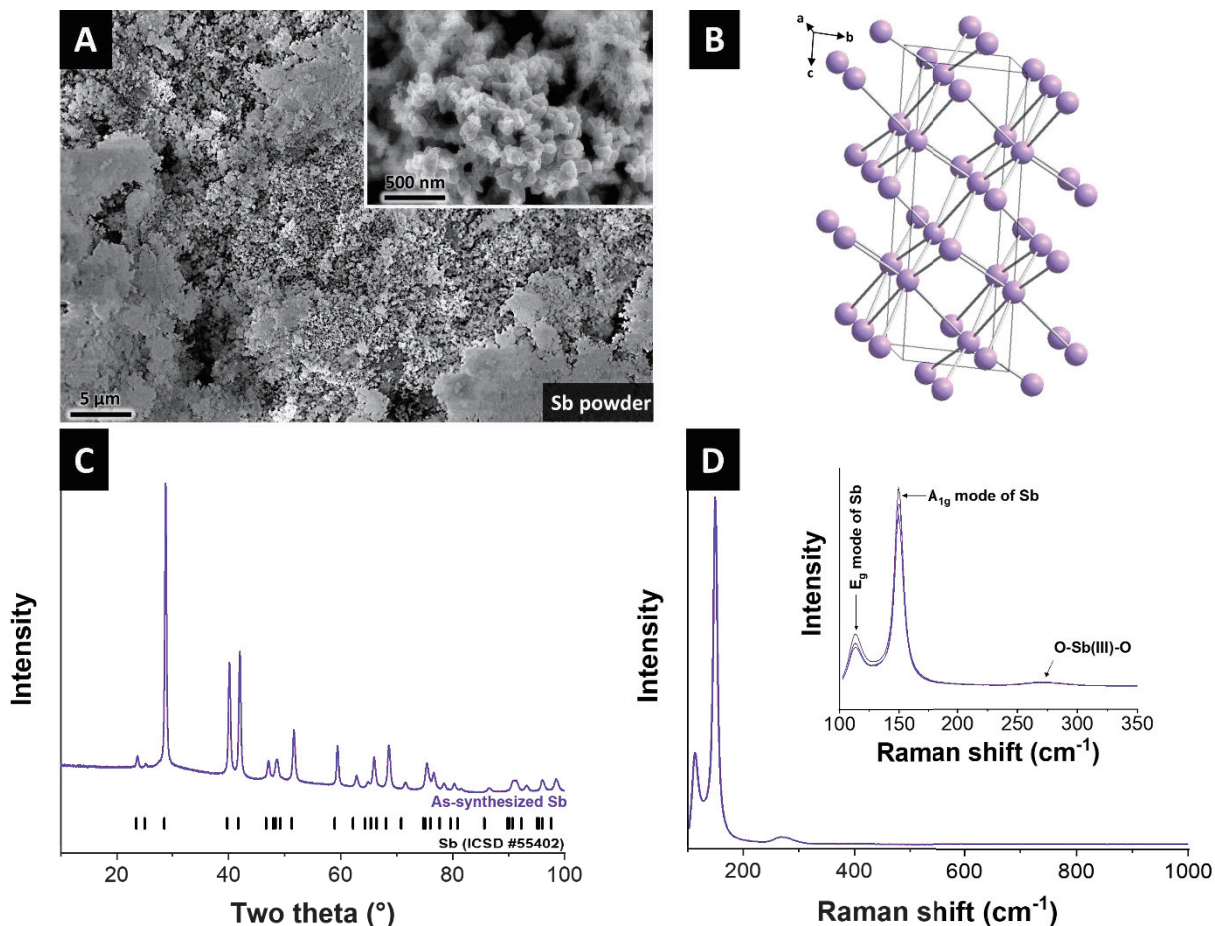


Figure S1: Material characterization of the as-synthesized antimony. (A) Scanning electron micrographs. (B) Crystal structure. (C) X-ray diffraction pattern. (D) Raman spectra (the inset shows the Raman mode assignment and three characteristic individual spectra).

We also analyzed the ceramic NASICON membrane. The XRD pattern in **Figure S2A** shows the characteristic peaks of low-NASICON (powder diffraction file, PDF 84-1184, space group C2/c; $a=15.674$ Å). Rietveld analysis yields a NASICON phase content of about 97-98%. There is also a second phase present, namely 2-3 mass% baddeleyite-type ZrO₂ (PDF 89-9066). The presence of ZrO₂ can potentially be due to both unreacted precursor and abrasion of the grinding balls.

The sintered material exhibits a theoretical density of 78%. This means the material still has open pores which are accessible to the electrolyte. For this reason, the pores are sealed by a post epoxy infiltration to close the pores of the membrane. The tightness of epoxy filled membranes was provided by checking the water uptake to be <1 mass%. Membranes with a diameter of 4 cm and a thickness of 300 μm were prepared for use as a membrane between the organic and the aqueous side in the desalination cell.

Photographs of the NASICON discs with a thickness of 950 μm for electrochemical testing and NASICON discs with a thickness of 300 μm for desalination testing are shown in **Figure S2B**. For the electrochemical testing of the NASICON electrode, both sides of the electrode were sputtered with platinum. **Figure S2C-D** shows scanning electron micrographs of NASICON powder and NASICON membrane. The ceramic matrix is composed of sub-micrometer particles, and the interparticle pore space in the NASICON membrane is effectively filled with epoxy resin.

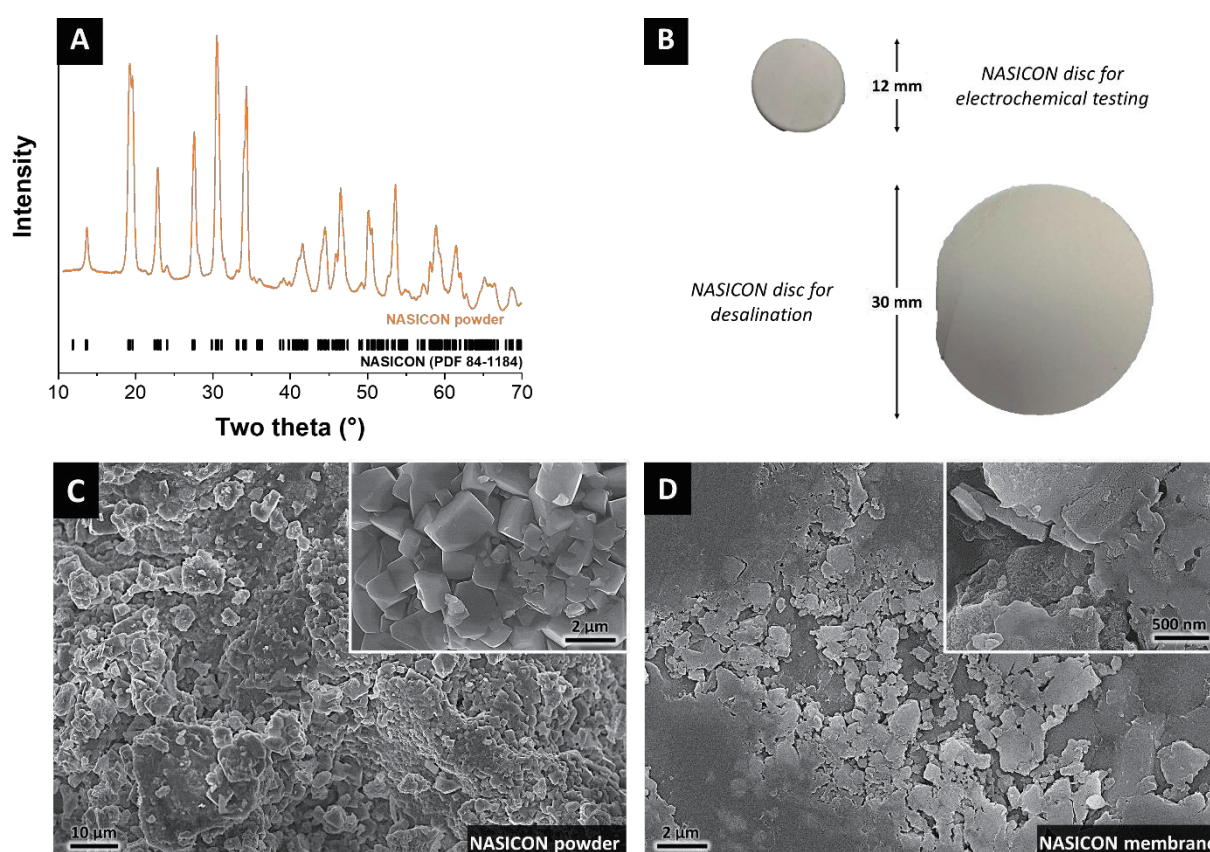


Figure S2: Material characterization of NASICON. (A) Diffractogram of the final NASICON powder, (B) photograph of NASICON discs for electrochemical characterization and desalination. (C) scanning electron micrographs of NASICON powder. (D) scanning electron micrographs of epoxy infiltrated NASICON membrane.

Supporting Electrochemical Characterization

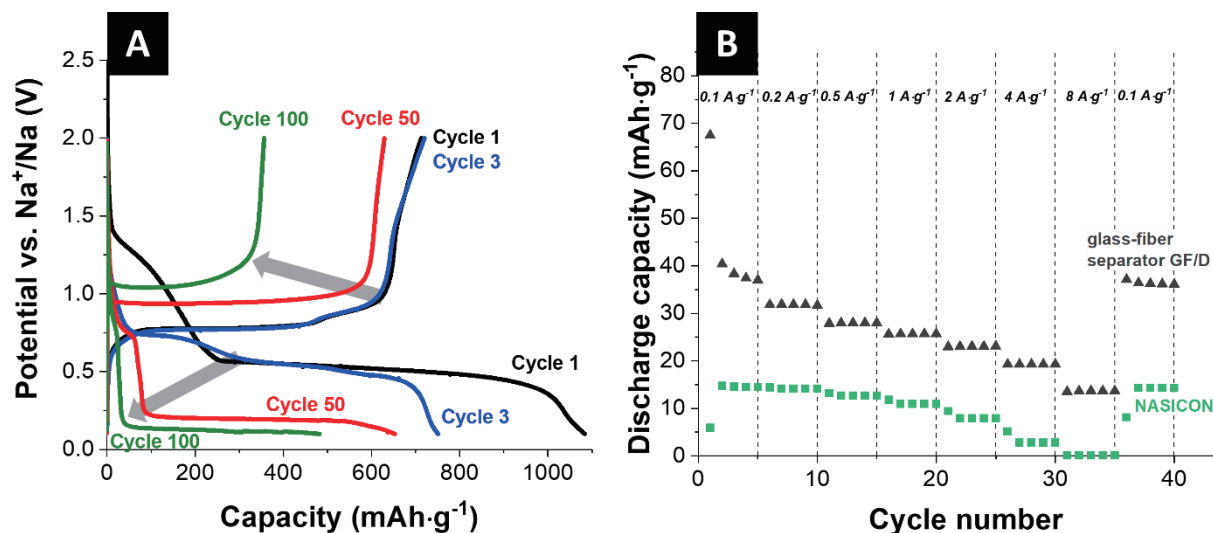


Figure S3: (A) Galvanostatic charge and discharge profiles of Sb/C electrode of the 1st, 3rd, 50th and 100th cycle at 200 mA·g⁻¹ between 0.1 V and 2.0 V vs. Na⁺. (B) Rate performance of the activated carbon cloth full-cell from galvanostatic charge/discharge cycling at different specific currents.

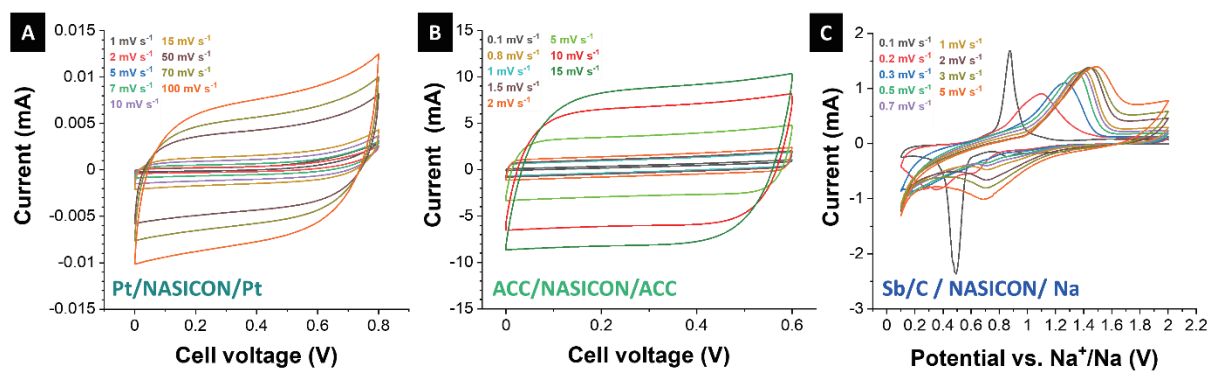


Figure S4: Cyclic voltammograms at different scan rates of (A) just the NASICON membrane contacted with platinum, (B) two activated carbon cloth electrodes separated by the NASICON membrane, and (C) Sb/C vs. Na separated by the NASICON membrane.

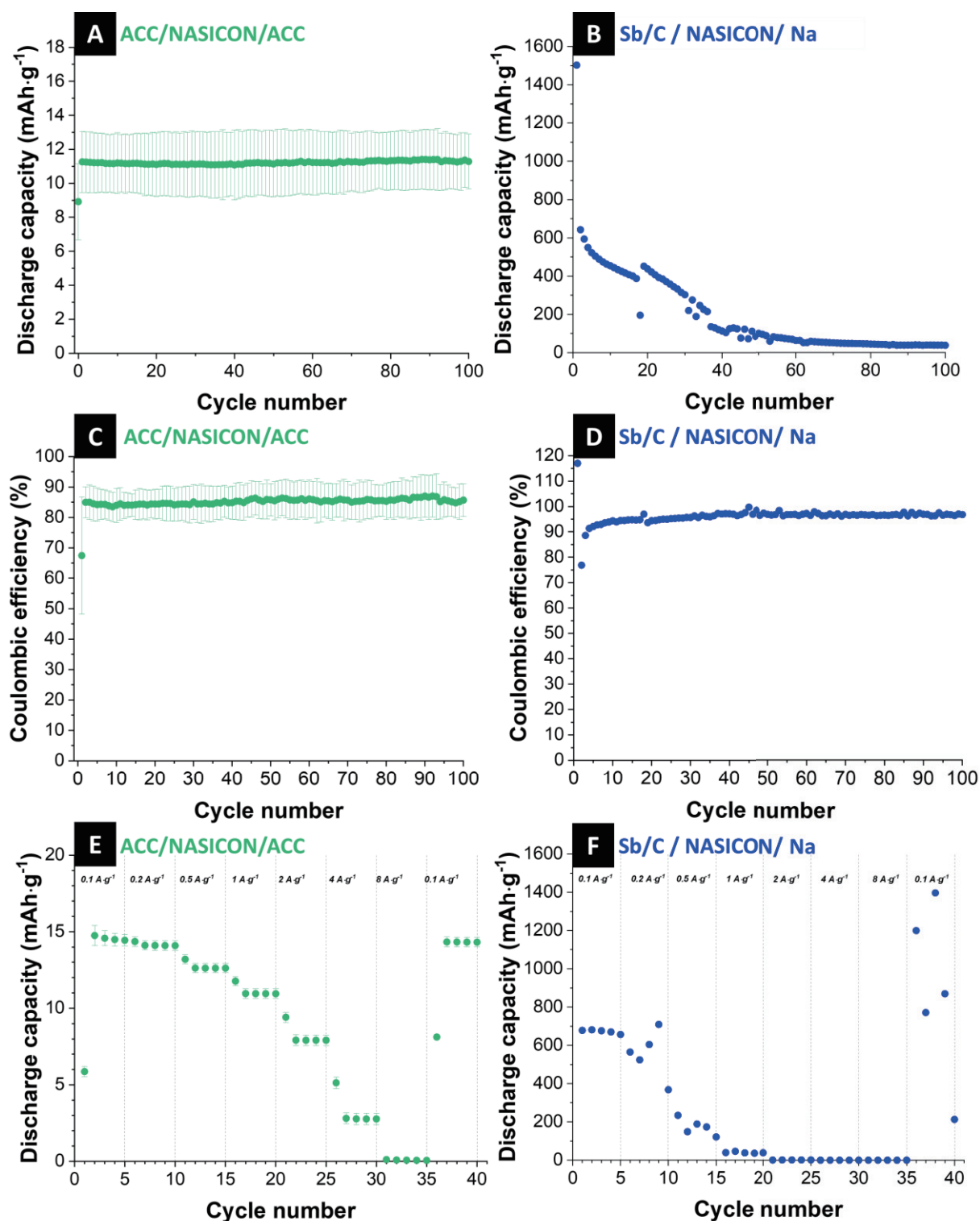


Figure S5: Electrochemical performance with NASICON as separator. (A) Electrochemical cycling stability at specific current of 200 mA g⁻¹ of activated carbon cloth full-cell with NASICON membrane. (B) Electrochemical cycling stability at specific current of 200 mA g⁻¹ of Sb/C vs. Na. (C) Coulombic efficiency at charging/discharging rates of the activated carbon cloth full-cell. (D) Coulombic efficiency of Sb/C electrode. (E) Rate performance of the activated carbon cloth full-cell from galvanostatic charge/discharge cycling at different specific currents. (F) Rate performance of the Sb/C electrode from galvanostatic charge/discharge cycling at different specific currents between 0.1-2.0 V vs. Na/Na⁺.

Supporting References

1. A. Roy, M. Komatsu, K. Matsuishi and S. Onari, *Journal of Physics and Chemistry of Solids*, 1997, **58**, 741-747.
2. O. Degtyareva, V. V. Struzhkin and R. J. Hemley, *Solid State Communications*, 2007, **141**, 164-167.
3. M. L. Bansal and A. P. Roy, *Physical Review B*, 1986, **33**, 1526-1528.

4.5 Time-dependent cation selectivity of titanium carbide MXene in aqueous solution

Lei Wang,^{1,2} Mohammad Torkamanzadeh,^{1,2} Ahmad Majed,³ Yuan Zhang,^{1,2}
Qingsong Wang,^{1,4} Ben Breitung,⁴ Guang Feng,^{5,6} Michael Naguib,³ Volker Presser,^{1,2,7}

¹ INM - Leibniz Institute for New Materials, D2 2, 66123, Saarbrücken, Germany

² Department of Materials Science & Engineering, Saarland University, Campus D2 2, 66123, Saarbrücken, Germany

³ Department of Physics and Engineering Physics, Tulane University, New Orleans, Louisiana 70118, United States of America

⁴ Institute of Nanotechnology, Karlsruhe Institute of Technology, Hermann-von-Helmholtz-Platz 1, 76344, Eggenstein-Leopoldshafen, Germany

⁵ State Key Laboratory of Coal Combustion, School of Energy and Power Engineering, Huazhong University of Science and Technology, Wuhan 430074, Hubei, China

⁶ Nano Interface Centre for Energy, School of Energy and Power Engineering, HUST, Hubei, 430074 China

⁷ Saarene, Saarland Center for Energy Materials and Sustainability, Campus C4 2, 66123 Saarbrücken, Germany

Citation:

L. Wang, M. Torkamanzadeh, A. Majed, Y. Zhang, Q. Wang, B. Breitung, G. Feng, M. Naguib, V. Presser, TIME-DEPENDENT CATION SELECTIVITY OF TITANIUM CARBIDE MXENE IN AQUEOUS SOLUTION, **Advanced Sustainable Systems**, 6 (2022) 2100383.

DOI: <https://doi.org/10.1002/adsu.202100383>

Own contribution:

Conceptualization, Investigation, Formal analysis, Data curation, Visualization, Writing-Original Draft, Writing - Review & Editing



RESEARCH ARTICLE

Time-Dependent Cation Selectivity of Titanium Carbide MXene in Aqueous Solution

Lei Wang, Mohammad Torkamanzadeh, Ahmad Majed, Yuan Zhang, Qingsong Wang, Ben Breitung, Guang Feng, Michael Naguib, and Volker Presser*

Electrochemical ion separation is a promising technology to recover valuable ionic species from water. Pseudocapacitive materials, especially 2D materials, are up-and-coming electrodes for electrochemical ion separation. For implementation, it is essential to understand the interplay of the intrinsic preference of a specific ion (by charge/size), kinetic ion preference (by mobility), and crystal structure changes. $Ti_3C_2T_z$ MXene is chosen here to investigate its selective behavior toward alkali and alkaline earth cations. Utilizing an online inductively coupled plasma system, it is found that $Ti_3C_2T_z$ shows a time-dependent selectivity feature. In the early stage of charging (up to about 50 min), K^+ is preferred, while ultimately Ca^{2+} and Mg^{2+} uptake dominate; this unique phenomenon is related to dehydration energy barriers and the ion exchange effect between divalent and monovalent cations. Given the wide variety of MXenes, this work opens the door to a new avenue where selective ion-separation with MXene can be further engineered and optimized.

has emerged as a promising alternative to traditional separation processes due to its high selectivity metrics and energy efficiency.^[7]

Depending on the nature of electroactive material, the ion immobilization and separation process mechanisms are different. For example, nanoporous carbons immobilize ions via electrosorption. Sub-nanometer pores may cause ion sieving or require ions to (partially) shed their solvation shell; this effect enables further tunability of the ion selectivity.^[8] Even more confined sites for ion uptake are found in Faradaic materials.^[9] Thereby, processes such as ion intercalation or other redox processes enable selectivity toward certain cations or anions.^[9,10] For example, $LiMn_2O_4$ provides facile intercalation into its crystal structure

only for specific ions with matched size and valence, aligning with intrinsic ion selectivity.^[11] Other materials like TiS_2 ^[12] show potential-dependent (tunable) ion selectivity according to the hydration energy of ions. This mechanism is linked with the specific onset potential for ion intercalation (or other redox processes), which gives rise to the unique battery-like feature in electrochemical measurements.^[13] Yet, the ion selectivity of pseudocapacitive materials has remained largely unexplored.^[14]

MXene is a promising, quickly growing, and novel family of 2D metal carbides or nitrides.^[15] The ability to reversibly

1. Introduction

Ion separation is an essential process to extract valuable metal from natural water^[1] and achieve sustainable development.^[2] Most commonly, ion separation is studied through adsorption^[3] or membrane-based sieving processes^[4] and is extended to organic compounds.^[5] In addition to seeking reduced cost and energy consumption approaches, there is also a strong motivation to explore and implement more sustainable ion separation technologies.^[6] Recently, electrochemical ion separation

L. Wang, M. Torkamanzadeh, Y. Zhang, Q. Wang, V. Presser
INM – Leibniz Institute for New Materials
D2 2, 66123 Saarbrücken, Germany
E-mail: volker.presser@leibniz-inm.de

L. Wang, M. Torkamanzadeh, Y. Zhang, V. Presser
Department of Materials Science and Engineering
Saarland University
Campus D2 2, 66123 Saarbrücken, Germany

A. Majed, M. Naguib
Department of Physics and Engineering Physics
Tulane University
New Orleans, LA 70118, USA

Q. Wang, B. Breitung
Institute of Nanotechnology
Karlsruhe Institute of Technology
Hermann-von-Helmholtz-Platz 1, 76344 Eggenstein-Leopoldshafen, Germany

G. Feng
State Key Laboratory of Coal Combustion
School of Energy and Power Engineering
Huazhong University of Science and Technology
Wuhan, Hubei 430074, China

G. Feng
Nano Interface Centre for Energy
School of Energy and Power Engineering
HUST
Wuhan, Hubei 430074, China

V. Presser
Saarene
Saarland Center for Energy Materials and Sustainability
Campus C4 2, 66123 Saarbrücken, Germany

 The ORCID identification number(s) for the author(s) of this article can be found under <https://doi.org/10.1002/advs.202100383>.

© 2022 The Authors. Advanced Sustainable Systems published by Wiley-VCH GmbH. This is an open access article under the terms of the Creative Commons Attribution License, which permits use, distribution and reproduction in any medium, provided the original work is properly cited.

DOI: 10.1002/advs.202100383

intercalate cations and anions between the MXene-layers^[16] yields a pseudocapacitive response, while the carbide/nitride core provides rapid charge transport.^[17] Moreover, the surface functional groups such as $-F$, $-OH$, and $-O$ on the transition metal atoms formed during the etching process facilitate easier cation intercalation.^[18] Thereby, MXenes are widely studied in electrochemical energy storage,^[19] water purification,^[20] and sensing,^[21] among other applications. Regarding aqueous media, Gao et al. used computational simulations to study the positionings of the cations within the MXene slit pores and found that Li^+ , Na^+ , and K^+ display specific adsorption on the pore surface while Cs^+ and Mg^{2+} are located in the pore center.^[22] Recently, Sun et al. reported that titanium carbide-based MXene showed selectivity toward Ca^{2+} compared with Na^+ and Mg^{2+} .^[23] The latter work limited its scope to three cations (Ca^{2+} , Mg^{2+} , and Na^+) and the influence of the anode on the selectivity performance of the MXene cathode.

Our work investigates the intercalation process of $Ti_3C_2T_z$ in a multi-cation aqueous electrolyte and the competition for intrinsic and time-dependent preferences between different cations. Using online chemical monitoring with inductively coupled plasma optical emission spectroscopy (ICP-OES), we find that the $Ti_3C_2T_z$ exhibits a time-dependent selectivity between Li^+ , Na^+ , K^+ , Ca^{2+} , and Mg^{2+} . At the same time, there is an ion-exchange phenomenon between the divalent cations and monovalent cations (except Li^+) during the late ion-intercalation process. The variation of the crystal structure of $Ti_3C_2T_z$ during the electrochemical process is explored by in situ X-ray diffraction (XRD).

2. Results and Discussion

The scanning electron images show that $Ti_3C_2T_z$ has common accordion-like multilayers of MXene (Figure S1A,B, Supporting Information), implying a successful exfoliation. The MXene-carbon nanotube ($Ti_3C_2T_z$ -CNT) electrode also shows the same morphology as the $Ti_3C_2T_z$ powder except that CNTs are distributed on the surface of $Ti_3C_2T_z$ particle (Figure S2, Supporting Information). CNTs entangle the MXene flakes and enhance the electrode's mechanical stability to avoid MXene loss during the desalination experiments. The removal of aluminum from the parent Ti_3AlC_2 MAX phase is confirmed by energy-dispersive X-ray (EDX) spectra of $Ti_3C_2T_z$ (Figure S3, Supporting Information). The XRD patterns (Figure S1C, Supporting Information) also confirm the presence of $Ti_3C_2T_z$ -type MXene with repeating (00 l) diffraction peaks. The (002) reflection of $Ti_3C_2T_z$ splits into two peaks (Figure S1D, Supporting Information), at 6.9° 2θ (d -spacing, 1.28 nm) and 8.2° 2θ (d -spacing, 1.08 nm). After heating at $80^\circ C$ under vacuum overnight, only one peak is seen at 8.5° 2θ (d -spacing, 1.04 nm), indicating that the split (002) peak is caused by the residual water in between the layers. Compared with the powder sample, the $Ti_3C_2T_z$ electrode shows almost the same (002) peak, demonstrating that the probe ultrasonication does not affect the inherent characteristics of $Ti_3C_2T_z$.

To investigate the ion selectivity of $Ti_3C_2T_z$ electrodes, we used a low concentration aqueous electrolyte of Li^+ , Na^+ , K^+ , Ca^{2+} , and Mg^{2+} , with a concentration of 10 nM for each cation; and each charging and discharging process of 3 h. As shown in Figure S4 in the Supporting Information, the potential holding

of the $Ti_3C_2T_z$ remains below 0 V versus Ag/AgCl, ensuring that the $Ti_3C_2T_z$ electrode only uptakes cations.^[24] Figure 1 shows the cation concentration changes over time in the 2nd, 6th, 10th, and 17th cycles obtained by subtracting the baseline from the initial concentration curve. The 14th cycle is shown in Figure S5 in the Supporting Information. The baseline of each cycle is established by connecting the start and endpoint of each half-cycle (Figure S6, Supporting Information). During the charging process, in the beginning, the concentration of all the cations decreases over time. Moreover, the concentration changes of these five cations reach the maximum simultaneously, meaning that the intercalation of these cations is synchronous. This phenomenon is different from obvious dynamics-dependent electrosorption (e.g., monovalent cations are up-taken faster than divalent cations) in subnanometer pores of carbon materials.^[8] The difference is attributed to the flexible interlayer spacing of $Ti_3C_2T_z$, which will increase (breathe) as the cations intercalate into $Ti_3C_2T_z$.^[25] The maximum concentration change during the charging process follows $K^+ > Na^+ > Ca^{2+} \approx Mg^{2+} > Li^+$, implying that K^+ is preferred during this process. After around 50 min, the concentration change of monovalent cations is positive, while that of divalent cations is still negative. This phenomenon can be explained by ion exchange between monovalent and divalent cations, which is because Mg^{2+} and Ca^{2+} carry twice the amount of the charge as Li^+ , Na^+ , and K^+ .^[26]

Having a certain amount of negative electric charge applied to the MXene electrode, the required number of divalent cations would be less than (half) that of monovalent cations to compensate the same electric charge. Therefore, divalent cations have higher competitiveness for intercalation in a confined space between $Ti_3C_2T_z$ layers. A similar ion exchange between monovalent and divalent cations is also observed in the case of porous carbon electrodes, where ions are stored based on electrical double layers (EDLs). In EDLs, as long as the dilute-theory works, in the beginning, the majority of ions in the solution are preferred while subsequently they will be replaced by ions with higher valence.^[27] After the 10th cycle, the cation exchange between divalent and Li^+ is very weak, concluded from no net concentration increase in the course of charging.

Figure 2 shows ion uptake capacities (calculated according to Equation (1)) versus charging time in different cycles. In the 2nd cycle (Figure 2A), before around 64 min, the Li^+ , Na^+ , and K^+ ion removal capacities steadily increase, representing the continuous uptake of these three cations. The maximum removal capacities are $0.041 \text{ mmol g}^{-1}$ for Li^+ , $0.083 \text{ mmol g}^{-1}$ for Na^+ , and $0.095 \text{ mmol g}^{-1}$ for K^+ . The removal capacities decrease from 64 to 180 min, caused by the ion exchange between monovalent and divalent cations. In contrast to the behavior of monovalent cations, Mg^{2+} and Ca^{2+} removal capacities constantly increase before reaching a plateau, with the maximum capacity of 0.12 and $0.086 \text{ mmol g}^{-1}$, respectively. The selectivity factors, M^{x+}/Li^+ ($M = Na^+, K^+, Ca^{2+},$ and Mg^{2+}), are calculated every 10 min (according to Equation (2)), illustrating the selectivity behavior of $Ti_3C_2T_z$ at different charging times (Figure 2A). From the studied ions, Li^+ is least preferred by $Ti_3C_2T_z$. Before 90 min of charging, $Ti_3C_2T_z$ preferably uptakes K^+ with a maximum selectivity factor of 2.5 (at 30 min), which will be interpreted by the intercalation process of the cations later herein. After 90 min, Mg^{2+} dominates and reaches the

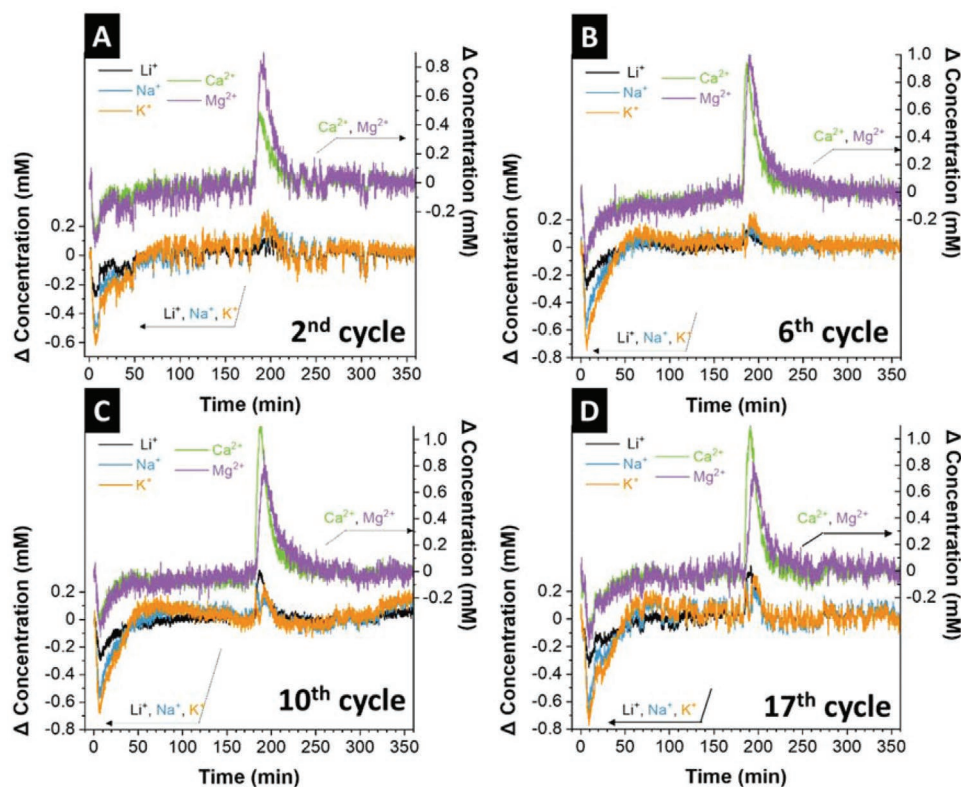


Figure 1. The concentration changes of Li^+ , Na^+ , K^+ , Ca^{2+} , and Mg^{2+} during the A) 2nd, B) 6th, C) 10th, and D) 17th cycle with a flow rate of 1.1 mL min^{-1} .

highest selectivity factor of 3.9 at 180 min, attributed to the ion exchange between monovalent and divalent cations.

To investigate the material structural changes during the electrochemical process, we conducted in situ XRD measurements. This was done in a coin cell instead of the desalination flow cell while using the same electrolyte and same mass ratio between cathode and anode. The (002) peak shift is illustrated for five X-ray diffractograms for each charging/discharging process (Figure S7, Supporting Information). Without an external circuit, the intercalation distance (the distance between two Ti atoms) is about 0.57 nm (without considering any surface functional groups), calculated by subtracting the theoretical thickness of the MX-layer (Ti-C-Ti-C-Ti)^[28] from the d -spacing obtained from XRD measurement (Figure S8, Supporting Information). This value is slightly larger than that of the pristine $\text{Ti}_3\text{C}_2\text{T}_z$ electrode (0.51 nm). The intercalation distance of the electrode soaked in deionized water (0.51 nm) suggests that the water and cations cannot spontaneously co-intercalate into the hydrofluoric acid (HF)-etched $\text{Ti}_3\text{C}_2\text{T}_z$, in agreement with the previous study.^[29] After charging, the (002) reflection shifts to $5.78^\circ 2\theta$, corresponding to a d -spacing of 1.53 nm, that is, 1.05 nm of intercalation distance (Figure 4A). Considering that the initial intercalation distance is less than the smallest hydrated diameters of these five cations in the bulk water (K^+ , 0.662 nm; Figure S9, Supporting Information), all cations must (partially) dehydrate to intercalate into the $\text{Ti}_3\text{C}_2\text{T}_z$ layers. The dehydration energy (normalized by the charge) of K^+ is the lowest while that of Li^+ is the highest.^[22] As a result, K^+ is

most preferred, whereas Li^+ is least preferred in the beginning. However, in the late charging stages, Mg^{2+} is most preferred instead of K^+ , and Ca^{2+} becomes the second preferred cation (Figure 3A) due to the ion exchange effect.

The other cycles resemble the 2nd cycle and the difference lies only in the slightly different magnitude of removal capacities (Figure 2B–D; Figure S5B, Supporting Information). However, selectivity factors exhibit different trends from the 10th cycle. In the 2nd and 6th cycle, the selectivity factors of K^+/Li^+ and Na^+/Li^+ decrease gradually over time (Figure 3A,B), while from the 10th cycle, they drop steeply from 50 min (charging time); and at the end of the charging period, the amount of removed Na^+ and K^+ ions is less than that of Li^+ (Figure 3C,D and Figure S5C, Supporting Information). For example, the selectivity factors of K^+/Li^+ and Na^+/Li^+ at 180 min in the 14th cycle are 0.7 and 0.5, respectively. This indicates that Li^+ barely participates in the ion exchange after the 10th cycle. Additionally, the maximal selectivity factors of Na^+ , K^+ , Ca^{2+} , and Mg^{2+} all decrease from the 6th cycle to the 17th cycle. This may be due to the growth of amorphous TiO_2 on the surface of $\text{Ti}_3\text{C}_2\text{T}_z$ (Figure S10, Supporting Information), which has a lower Li diffusion barrier.^[30]

In situ XRD (Figure 4) indicates that from the 10th cycle, one more (002) reflection appears at about $6.5^\circ 2\theta$ (d -spacing, $\approx 1.34 \text{ nm}$) apart from that initially at $\approx 5.8^\circ 2\theta$ (corresponding to a d -spacing of 1.53 nm). In the 6th cycle, (002) at $6.5^\circ 2\theta$ already appears with low intensity and broad shape. Among the two latter layer spacings, 1.53 nm is a value similar to the reported

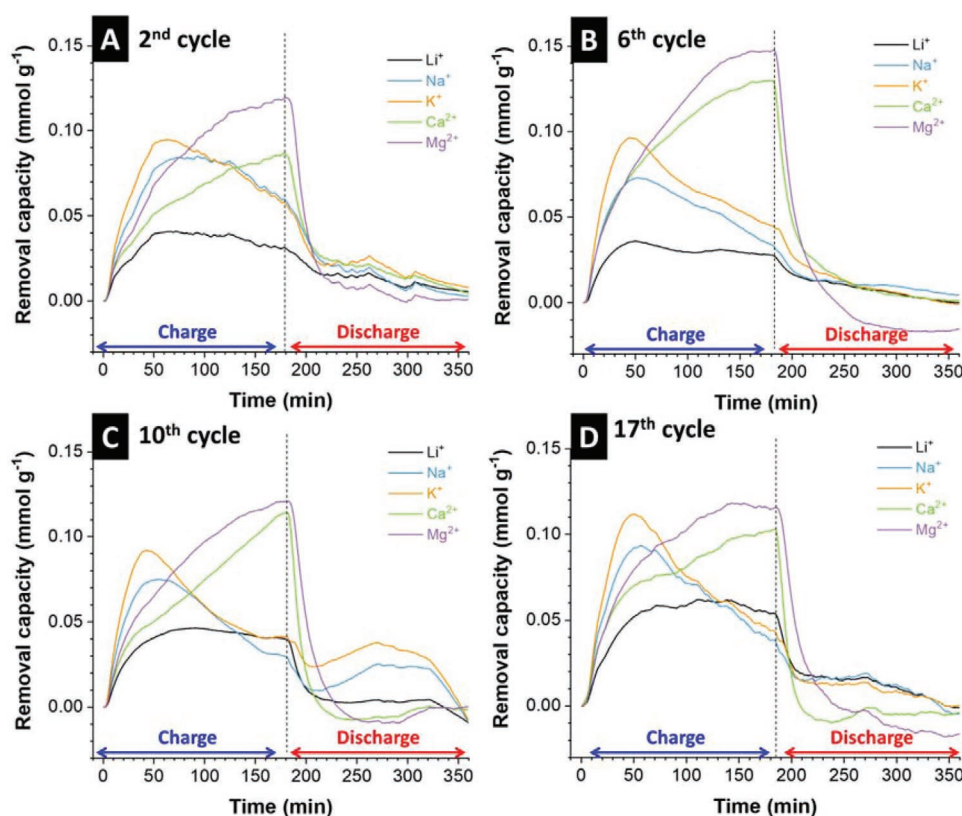


Figure 2. The ion removal capacity of Li^+ , Na^+ , K^+ , Ca^{2+} , and Mg^{2+} during the A) 2nd, B) 6th, C) 10th, and D) 17th cycle with a flow rate of 1.1 mL min^{-1} .

results of kosmotropic cations (Li^+ , Na^+ , Mg^{2+} , and Ca^{2+}) intercalated $\text{Ti}_3\text{C}_2\text{T}_z$ at high relative humidity. In comparison, 1.34 nm is a value close to chaotropic cations found for K^+ -intercalated $\text{Ti}_3\text{C}_2\text{T}_z$ at high relative humidity.^[29] This indicates that the kosmotropic cations dictate the d -spacing of $\text{Ti}_3\text{C}_2\text{T}_z$ in the 2nd cycle. The second reflection, occurring after the 10th cycle, may result from partially desolvated, kosmotropic cations intercalating $\text{Ti}_3\text{C}_2\text{T}_z$.^[31] This may relate to changes in the surface functional groups. In addition, during charging, the reflection shifts toward larger diffraction angles. The associated shrinkage of the d -spacing may be related to decreased electrostatic repulsions between negatively charged $\text{Ti}_3\text{C}_2\text{T}_z$ sheets due to cation intercalation.^[32] During discharging, the $\text{Ti}_3\text{C}_2\text{T}_z$ sheets expand. While shrinking lasts over the whole charging process (180 min), the expansion is observed only for about an initial 45 min into the discharge process. This can be explained by continued cation intercalation during the whole charging time, caused by the ion exchange. Whereas, there is almost no cation deintercalation after about 45 min during the discharging process (Figure 4B–E).

We additionally studied the selective behavior of $\text{Ti}_3\text{C}_2\text{T}_z$ at a higher flow rate of feed water. In case of a flow rate double as much as before, the ion exchange phenomenon still occurs. However, before the ion exchange occurs, the removal capacities of Ca^{2+} and Mg^{2+} are much higher (Figures S11 and S12, Supporting Information), signaling that the divalent cations are more preferred at a higher flow rate. This is because the higher flow rate reduces the residence time that each cation in the feed

water spends near the electrode surface. As a result, divalent ions, with a higher charge and diffusion rate in the electrolyte,^[33] enter the electrodes more readily than monovalent ones.

Development of a selective separation system, such as the one introduced in the present study, is well in alignment with UN's Sustainable Development Goals (SDGs) on a number of different levels. Such a system can specifically remove undesired ions (for example, ions responsible for scaling/fouling such as Ca^{2+}) or recover valuable ions like Li^+ from industrial wastewater or seawater. Recovery of lithium, particularly, is of great economical interest for the decades to come, as it serves as a key element in construction of Li-ion batteries for electric vehicles and portable electronics. As such, we can envision that the findings presented in this work can contribute to SDGs number 2, 6, 9, and 11–15, encompassing: sustainable management of water and industrialization, sustainable consumption and production patterns, climate change mitigation, sustainable use of the oceans and terrestrial ecosystems, sustainable agriculture, and the development of sustainable cities and human settlements.

3. Conclusions

In summary, our work investigates the selectivity of $\text{Ti}_3\text{C}_2\text{T}_z$ toward common alkali and alkaline earth cations. By online monitoring via ICP, we find that the ion-selective behavior of $\text{Ti}_3\text{C}_2\text{T}_z$ depends on the charging time. In the early charging

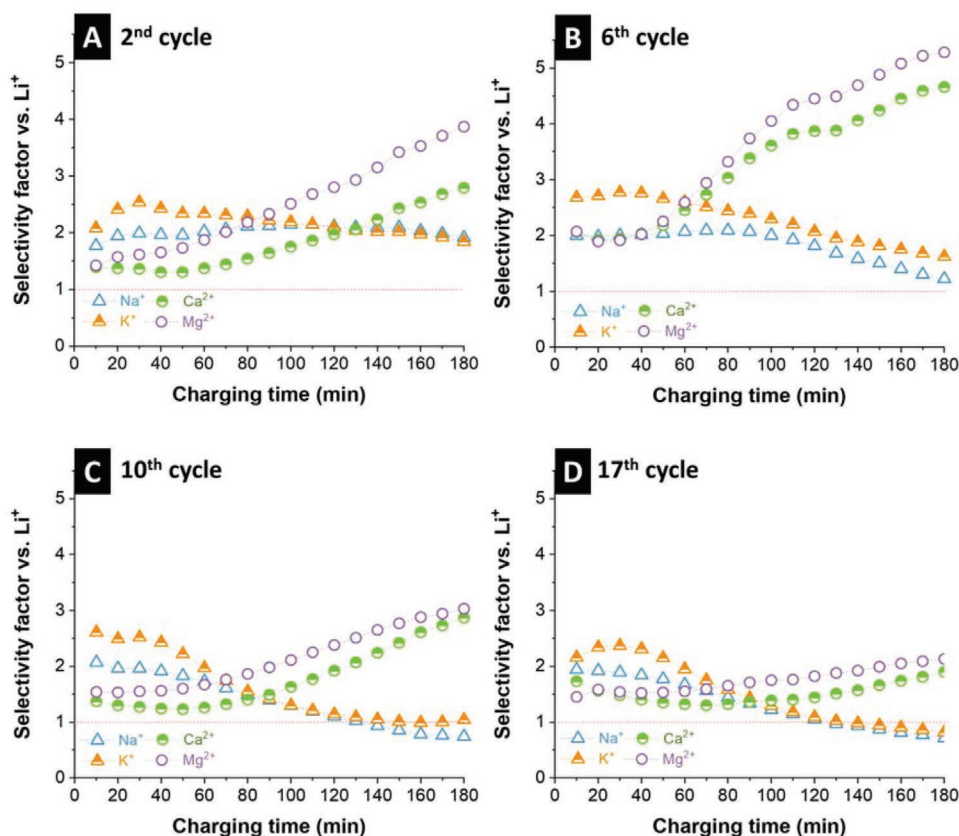


Figure 3. The selectivity factor versus Li^+ of Na^+ , K^+ , Ca^{2+} , and Mg^{2+} during the A) 2nd, B) 6th, C) 10th, and D) 17th cycle with a flow rate of 1.1 mL min^{-1} .

stages (before about 50 min), benefiting from the least dehydration energy, K^+ is preferred, with the maximum selectivity factor of 2.5 ± 0.2 . Subsequently (70–90 min), due to the ion exchange effect between monovalent and divalent cations, the removal capacities of Ca^{2+} and Mg^{2+} (highest value about 0.12 mmol g^{-1}) increase and exceed that of K^+ at the end of charging time. Meanwhile, fewer Na^+ and K^+ compared with Li^+ are immobilized in $\text{Ti}_3\text{C}_2\text{T}_z$ (from the 10th cycle). In situ XRD data shows a symmetric (002) reflection of $\text{Ti}_3\text{C}_2\text{T}_z$ in the 2nd cycle. In contrast, after the 10th cycle, the asymmetry of the (002) reflection aligns with the emergence of two individual and overlapping peaks associated with the coexistence of cations with a different coordination number of water molecules. This could be an interesting preprocessing step for lithium recovery techniques. Meanwhile, we see potential to extend this approach to other MXene types and other ionic systems such as trivalent cations or metal-organic complexes.

4. Experimental Section

Materials and Material Synthesis: The parent Ti_3AlC_2 MAX phase was synthesized by mixing titanium (Ti, –325 mesh, 99%, Alfa Aesar), aluminum (Al, –325 mesh, 99.5%, Alfa Aesar), and graphite (C, 7–11 μm , 99%, Alfa Aesar) with atomic ratio of $\text{Ti}:\text{Al}:\text{C} = 3:1.2:1.88$ in a Turbula T2F mixer for 3 h using zirconia balls, followed by sintering inside a Sentro Tech induction furnace (STT-1700C-2.5-12, SN: 1052217) an alumina tube at $1600 \text{ }^\circ\text{C}$ for 2 h. A heating rate of $10 \text{ }^\circ\text{C min}^{-1}$ was used to reach the maximum temperature. After the holding time, the sample was left

to cool to room temperature. The sintering process was done under flowing argon.

To prepare $\text{Ti}_3\text{C}_2\text{T}_z$, Ti_3AlC_2 was ground to less than $45 \mu\text{m}$ and slowly added to 10 mass% aqueous HF (Acros Organics, 47–51 mass%). For each 1 g of MAX powder, 10 mL of the acidic solution was used. The mixture was stirred at $27 \text{ }^\circ\text{C}$ for 24 h. To remove HF and other unwanted products, the mixture was divided equally and distributed to 50 mL centrifuge tubes to have 0.5 g of MAX phase per tube. Deionized (DI) water was added to fill up the tubes to 50 mL. The tubes were centrifuged at 3500 rpm for 5 min to sediment the powders, the supernatant was discarded as hazardous waste. DI water was then added and the sediment was fully redispersed using a vortex machine. The washing step was repeated several times until a $\text{pH} > 6$ was obtained. At that point, the powders were collected and dried using vacuum-assisted filtration at room temperature overnight.

Electrode Preparation: Activated carbon (YP-80F, Kuraray) was mixed with polytetrafluoroethylene binder (60 mass% solution in water from Sigma-Aldrich) in 95:5 carbon: binder mass ratio. After adding ethanol, a sticky paste was obtained, which was subsequently cold-rolled (MTI HR01, MTI Corp.) to give $600 \mu\text{m}$ thick free-standing films and then dried in a vacuum oven at $120 \text{ }^\circ\text{C}$ overnight. These activated carbon film electrodes are labeled AC herein.

To fabricate MXene electrodes, $\text{Ti}_3\text{C}_2\text{T}_z$ was first mixed with multiwalled CNT (Graphene Supermarket) with a 90:10 MXene:CNT mass ratio. Then the mixture was stirred while being tip-sonicated in ethanol in an ice bath for 30 min using BRANSON Sonifier 450 (maximum power of 400 W) with 30% duty cycle and 30% power. The dispersed MXene-CNT in ethanol mixture was then vacuum filtered through polyvinylidene fluoride (PVDF) membranes ($0.22 \mu\text{m}$, Durapore), followed by excessive DI water filtration to remove residual salts or acids from the synthesis steps. The electrodes were then dried in a vacuum oven at $80 \text{ }^\circ\text{C}$ overnight.

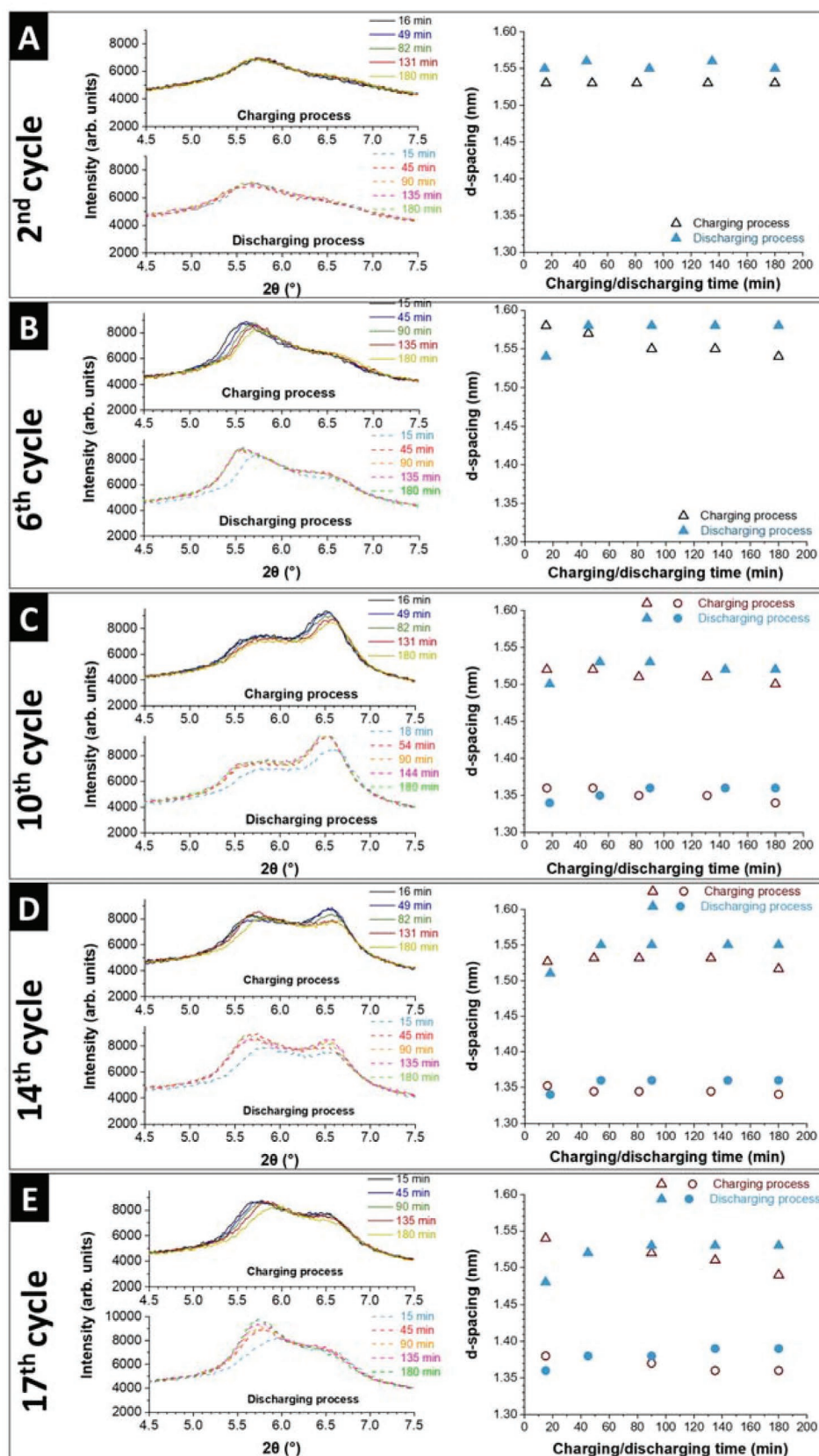


Figure 4. In situ X-ray diffractograms from 4.5° 2θ to 7.5° 2θ of $\text{Ti}_3\text{C}_2\text{T}_x$ electrode and corresponding d -spacing, in different cycles: A) 2nd, B) 6th, C) 10th, D) 14th, and E) 17th cycle. Five X-ray diffractograms are shown for the charging/discharging process of each cycle.

Electrochemical Ion Separation Experiments: The electrochemical ion separation experiments were performed in a single-pass channel cell. Following the vacuum filtration of $\text{Ti}_3\text{C}_2\text{T}_z$ material (with 10 mass% CNT), a 30 mm diameter electrode (around 120 mg mass loading, 17 mg cm^{-2} , on a 30 mm diameter PVDF support) was punched and used as the working electrode. As the counter electrode, free-standing AC films were used, whose mass was adjusted according to the MXene electrode, as described in the previous work.^[24] Based on the half-cell cyclic voltammograms of the $\text{Ti}_3\text{C}_2\text{T}_z$ electrode (Figure S13, Supporting Information), $\text{Ti}_3\text{C}_2\text{T}_z$:AC mass ratio of 1:1.7 was maintained for all full-cell experiments throughout this study. The $\text{Ti}_3\text{C}_2\text{T}_z$ and AC electrodes were separated by a central water channel filled with a glass fiber mat (GF/A, Whatman). A Ag/AgCl reference electrode was used as a spectator to measure the potential of the electrodes individually.

To prepare the electrolyte, LiCl, NaCl, KCl, CaCl_2 , and MgCl_2 salts (Sigma-Aldrich) were dissolved in DI water. A 10 L tank containing Li^+ , Na^+ , K^+ , Ca^{2+} , and Mg^{2+} with 10 mM concentration for each cation was used as the electrolyte reservoir. The reservoir was constantly flushed with nitrogen gas throughout the experiment to remove the oxygen from the solution to prolong the life of $\text{Ti}_3\text{C}_2\text{T}_z$ electrode, as was done in the previous work.^[24,33] Before the cell undergoes charging or discharging, the cell rested overnight to eliminate the influence of adsorption. The cell was charged and discharged with a constant specific current of 0.1 A g^{-1} . The upper voltage limit was set to 1.2 V, where the voltage was held for 3 h, and the lower voltage limit was 0.3 V, where the voltage was held for 3 h.

The cell was operated for 20 cycles; each cycle consists out of a charging and discharging process. The outlet of the middle water channel was connected to an ICP-OES (ARCOS FH22, SPECTRO Analytical Instruments) through a peristaltic pump (at the flow rate of 1.1 mL min^{-1}), where the changes of the ions' concentration were recorded online. The extracted solution fed into the ICP-OES system was consumed by the measurement. The measured intensity of the ICP-OES signal was transformed into the concentration according to the calibrated intensity-concentration curves. Finally, the cation removal capacity (mmol g^{-1}) was calculated according to Equation (1), and selectivity factors for lithium were calculated following Equation (2).

$$\text{Removal capacity (mmol/g}_{\text{electrode}}) = \frac{\nu}{1000 \cdot m} \int \Delta c dt \quad (1)$$

where ν is the flow rate (mL min^{-1}), m is the mass of $\text{Ti}_3\text{C}_2\text{T}_z$ electrode, t is the selected time of the cation uptake step (min), and Δc is the concentration change of the cations (mM).

$$\text{Selectivity factor} = \frac{\text{Removal capacity of a certain cation}}{\text{Removal capacity of lithium ions}} \quad (2)$$

Material Characterization: XRD analysis was conducted using a D8 Discover diffractometer (Bruker AXS) with a copper X-ray source (40 kV, 40 mA) and a 1D detector. Scanning electron microscopy (SEM) images were obtained using ZEISS (Gemini 500) at acceleration voltages of 1–3 kV. EDX spectroscopy was carried out at 15 kV with X-Max Silicon Detector from Oxford Instruments attached as a column to the SEM instrument. The EDX spectra were recorded and analyzed via AZtec software.

In Situ X-Ray Diffraction: In situ XRD measurements were carried out using a customized CR2032 coin cell with Kapton windows on STOE Stadi P diffractometer equipped with a Ga-jet X-ray source ($\text{Ga-K}\beta$ radiation, $\lambda = 1.20793 \text{ \AA}$). The XRD patterns were collected in the transmission mode in the range of 2θ from 3.5° to 10.3° , with a step of $0.04^\circ 2\theta$ and 5 s per step with the equivalent counting time of around 15 min. A 13 mm diameter $\text{Ti}_3\text{C}_2\text{T}_z$ electrode with the mass loading of 8.5 mg cm^{-2} was used for the electrochemical testing to ensure the successful collection of the XRD diffraction signal. The mass ratio between $\text{Ti}_3\text{C}_2\text{T}_z$ electrode (cathode) and AC electrodes (anode) is also 1.7, the same as in the ICP experiments. The same charging and discharging processes as the above-mentioned electrochemical ion separation experiments were performed via potentiostat/galvanostat

(SP-150, BioLogic). The resulted patterns were converted based on the wavelength of $\text{Cu-K}\alpha$ for easier comparison with the literature and ex situ XRD results.

Supporting Information

Supporting Information is available from the Wiley Online Library or from the author.

Acknowledgements

L.W. and M.T. contributed equally to this work. The authors acknowledge funding of the MXene-CDI project (PR-1173/11) by the German Research Foundation (DFG, Deutsche Forschungsgemeinschaft). The authors thank Eduard Arzt (INM) for his continuing support. L.W. acknowledges funding from the China Scholarship Council (CSC) via award number 201906260277. Materials synthesis at Tulane University was supported as part of the Fluid Interface Reactions, Structures and Transport (FIRST) Center, an Energy Frontier Research Center funded by the U.S. Department of Energy, Office of Science, Office of Basic Energy Sciences. Open access funding enabled and organized by Projekt DEAL.

Conflict of Interest

The authors declare no conflict of interest.

Data Availability Statement

The data that support the findings of this study are available from the corresponding author upon reasonable request.

Keywords

electrochemistry, ion selectivity, ion-exchange, MXene

Received: October 10, 2021

Revised: December 7, 2021

Published online: January 18, 2022

- [1] S. Yang, F. Zhang, H. Ding, P. He, H. Zhou, *Joule* **2018**, 2, 1648.
- [2] H. Yoon, J. Lee, S. Kim, J. Yoon, *Sep. Purif. Technol.* **2019**, 215, 190.
- [3] L. Tian, W. Ma, M. Han, *Chem. Eng. J.* **2010**, 156, 134.
- [4] J. Zhou, Z. Jiao, Q. Zhu, Y. Li, L. Ge, L. Wu, Z. Yang, T. Xu, *J. Membr. Sci.* **2021**, 627, 119246.
- [5] J. Zhou, Y. Zhang, M. Balda, V. Presser, F.-D. Kopinke, A. Georgi, *Chem. Eng. J.*, <https://doi.org/10.1016/j.cej.2021.133544>.
- [6] K.-J. Tan, X. Su, T. A. Hatton, *Adv. Funct. Mater.* **2020**, 30, 1910363.
- [7] F. Yu, L. Wang, Y. Wang, X. Shen, Y. Cheng, J. Ma, *J. Mater. Chem. A* **2019**, 7, 15999.
- [8] Y. Zhang, J. Peng, G. Feng, V. Presser, *Chem. Eng. J.* **2021**, 419, 129438.
- [9] P. Srimuk, X. Su, J. Yoon, D. Aurbach, V. Presser, *Nat. Rev. Mater.* **2020**, 5, 517.
- [10] C. Zhan, F. Aydin, E. Schwegler, A. Noy, T. A. Pham, *ACS Appl. Nano Mater.* **2020**, 3, 9740.
- [11] J. G. Gamaethiralalage, K. Singh, S. Sahin, J. Yoon, M. Elimelech, M. E. Suss, P. Liang, P. M. Biesheuvel, R. L. Zornitta, L. C. P. M. de Smet, *Energy Environ. Sci.* **2021**, 14, 1095.

- [12] P. Srimuk, J. Lee, S. Fleischmann, M. Aslan, C. Kim, V. Presser, *ChemSusChem* **2018**, *11*, 2091.
- [13] S. Fleischmann, J. B. Mitchell, R. Wang, C. Zhan, D. E. Jiang, V. Presser, V. Augustyn, *Chem. Rev.* **2020**, *120*, 6738.
- [14] C. Choi, D. S. Ashby, D. M. Butts, R. H. DeBlock, Q. Wei, J. Lau, B. Dunn, *Nat. Rev. Mater.* **2019**, *5*, 5.
- [15] M. Naguib, V. N. Mochalin, M. W. Barsoum, Y. Gogotsi, *Adv. Mater.* **2014**, *26*, 992.
- [16] P. Srimuk, J. Halim, J. Lee, Q. Tao, J. Rosen, V. Presser, *ACS Sustainable Chem. Eng.* **2018**, *6*, 3739.
- [17] M. R. Lukatskaya, S. Kota, Z. Lin, M.-Q. Zhao, N. Shpigel, M. D. Levi, J. Halim, P.-L. Taberna, M. W. Barsoum, P. Simon, Y. Gogotsi, *Nat. Energy* **2017**, *2*, 17105.
- [18] P. Srimuk, F. Kaasik, B. Krüner, A. Tolosa, S. Fleischmann, N. Jäckel, M. C. Tekeli, M. Aslan, M. E. Suss, V. Presser, *J. Mater. Chem. A* **2016**, *4*, 18265.
- [19] X. Zhang, Z. Zhang, Z. Zhou, *J. Energy Chem.* **2018**, *27*, 73.
- [20] I. Ihsanullah, *Chem. Eng. J.* **2020**, *388*, 124340.
- [21] A. Sinha, Dhanjai, H. Zhao, Y. Huang, X. Lu, J. Chen, R. Jain, *TrAC, Trends Anal. Chem.* **2018**, *105*, 424.
- [22] Q. Gao, W. Sun, P. Ilani-Kashkouli, A. Tselev, P. R. C. Kent, N. Kabengi, M. Naguib, M. Alhabeb, W.-Y. Tsai, A. P. Baddorf, J. Huang, S. Jesse, Y. Gogotsi, N. Balke, *Energy Environ. Sci.* **2020**, *13*, 2549.
- [23] J. Sun, Q. Mu, T. Wang, J. Qi, C. Hu, *J. Colloid Interface Sci.* **2021**, *590*, 539.
- [24] M. Torkamanzadeh, L. Wang, Y. Zhang, Ö. Budak, P. Srimuk, V. Presser, *ACS Appl. Mater. Interfaces* **2020**, *12*, 26013.
- [25] J. Li, X. Yuan, C. Lin, Y. Yang, L. Xu, X. Du, J. Xie, J. Lin, J. Sun, *Adv. Energy Mater.* **2017**, *7*, 1602725.
- [26] C.-H. Hou, P. Taboada-Serrano, S. Yiacoumi, C. Tsouris, *J. Chem. Phys.* **2008**, *129*, 224703.
- [27] R. Zhao, M. van Soestbergen, H. H. M. Rijnaarts, A. van der Wal, M. Z. Bazant, P. M. Biesheuvel, *J. Colloid Interface Sci.* **2012**, *384*, 38.
- [28] M. Shekhirev, C. E. Shuck, A. Sarycheva, Y. Gogotsi, *Prog. Mater. Sci.* **2021**, *120*, 100757.
- [29] M. Ghidui, J. Halim, S. Kota, D. Bish, Y. Gogotsi, M. W. Barsoum, *Chem. Mater.* **2016**, *28*, 3507.
- [30] C. Liu, Y. Li, D. Lin, P.-C. Hsu, B. Liu, G. Yan, T. Wu, Y. Cui, S. Chu, *Joule* **2020**, *4*, 1459.
- [31] E. S. Muckley, M. Naguib, H.-W. Wang, L. Vlcek, N. C. Osti, R. L. Sacci, X. Sang, R. R. Unocic, Y. Xie, M. Tyagi, E. Mamontov, K. L. Page, P. R. C. Kent, J. Nanda, I. N. Ivanov, *ACS Nano* **2017**, *11*, 11118.
- [32] J. Come, J. M. Black, M. R. Lukatskaya, M. Naguib, M. Beidaghi, A. J. Rondinone, S. V. Kalinin, D. J. Wesolowski, Y. Gogotsi, N. Balke, *Nano Energy* **2015**, *17*, 27.
- [33] L. Wang, K. Frisella, P. Srimuk, O. Janka, G. Kickelbick, V. Presser, *Sustainable Energy Fuels* **2021**, *5*, 3124.

ADVANCED SUSTAINABLE SYSTEMS

Supporting Information

for *Adv. Sustainable Syst.*, DOI: 10.1002/adsu.202100383

Time-Dependent Cation Selectivity of Titanium Carbide
MXene in Aqueous Solution

*Lei Wang, Mohammad Torkamanzadeh, Ahmad Majed,
Yuan Zhang, Qingsong Wang, Ben Breitung, Guang
Feng, Michael Naguib, and Volker Presser**

Supporting Information

Time-dependent cation selectivity of titanium carbide MXene in aqueous solution

Lei Wang,^{‡a,b} Mohammad Torkamanzadeh,^{‡a,b} Ahmad Majed,^c Yuan Zhang,^{a,b}
Qingsong Wang,^{a,d} Ben Breitung,^d Guang Feng,^{e,f} Michael Naguib,^c Volker Presser,^{*a,b,g}

^a *INM - Leibniz Institute for New Materials, D2 2, 66123, Saarbrücken, Germany*

^b *Department of Materials Science & Engineering, Saarland University, Campus D2 2, 66123, Saarbrücken, Germany*

^c *Department of Physics and Engineering Physics, Tulane University, New Orleans, Louisiana 70118, United States of America*

^d *Institute of Nanotechnology, Karlsruhe Institute of Technology, Hermann-von-Helmholtz-Platz 1, 76344, Eggenstein-Leopoldshafen, Germany*

^e *State Key Laboratory of Coal Combustion, School of Energy and Power Engineering, Huazhong University of Science and Technology, Wuhan 430074, Hubei, China*

^f *Nano Interface Centre for Energy, School of Energy and Power Engineering, HUST, Hubei, 430074 China*

^g *Saarene, Saarland Center for Energy Materials and Sustainability, Campus C4 2, 66123 Saarbrücken, Germany*

[‡] Equal contributions

^{*} Corresponding author's email: volker.presser@leibniz-inm.de

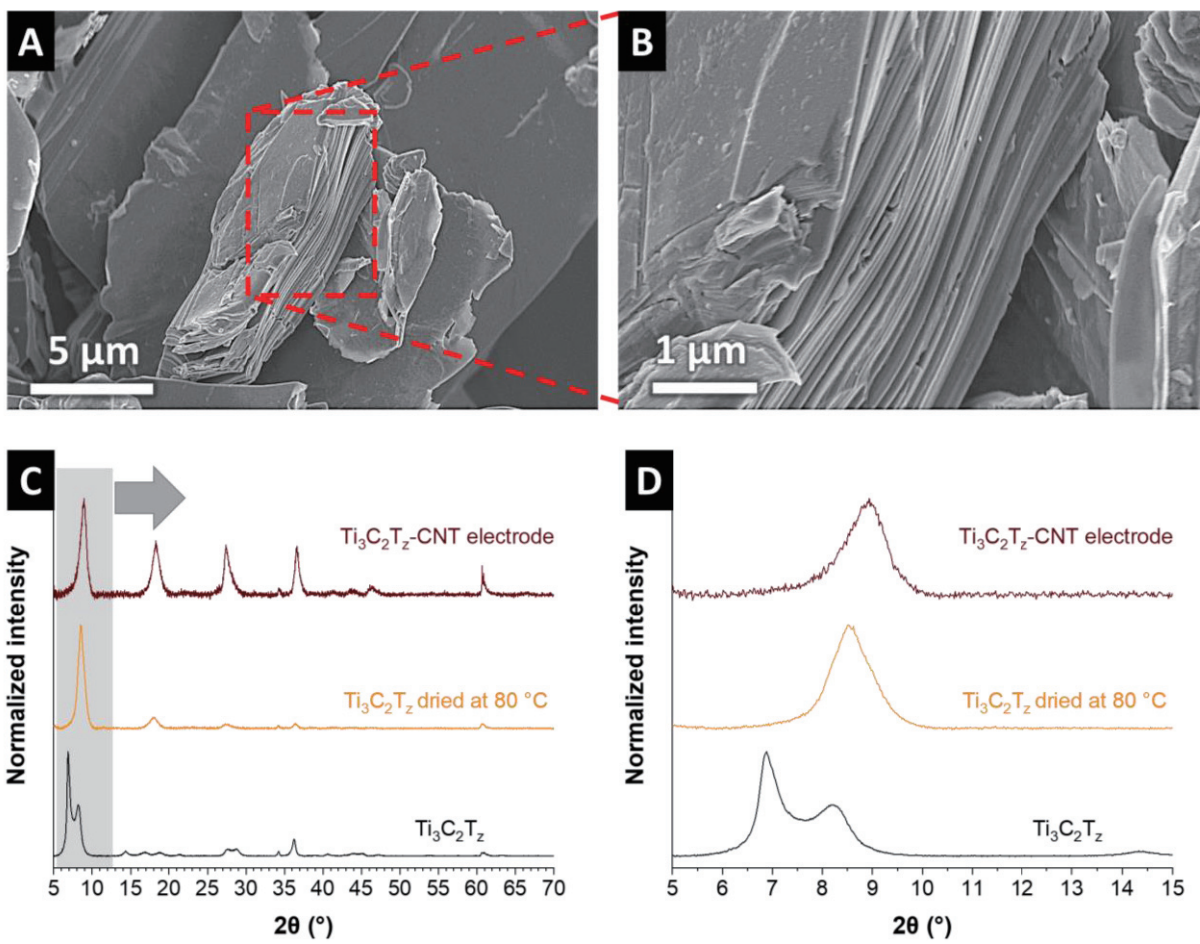


Figure S1: (A-B) Scanning electron micrographs of $\text{Ti}_3\text{C}_2\text{T}_z$. (C-D) X-ray diffractograms of $\text{Ti}_3\text{C}_2\text{T}_z$, dried $\text{Ti}_3\text{C}_2\text{T}_z$, and the $\text{Ti}_3\text{C}_2\text{T}_z$ -CNT electrode.

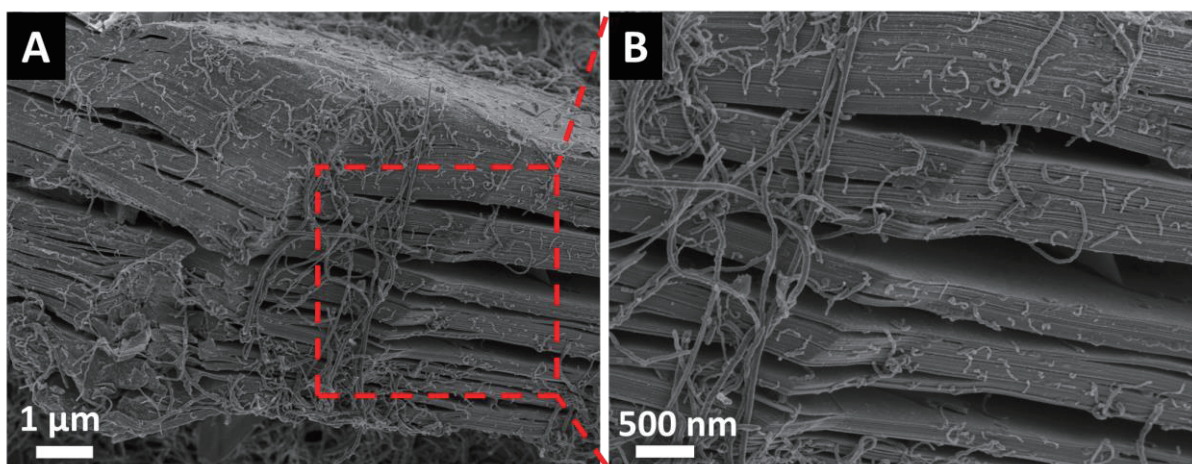


Figure S2: Scanning electron micrographs of the $\text{Ti}_3\text{C}_2\text{T}_z$ electrode.

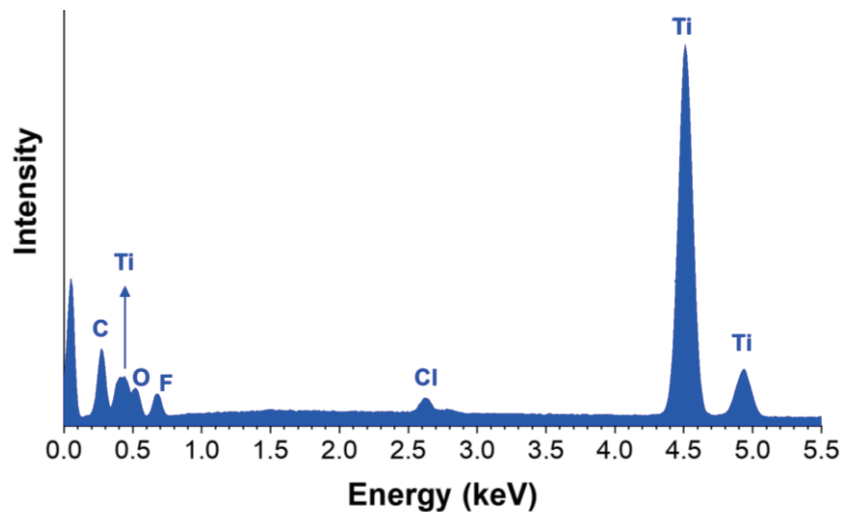


Figure S3: Energy-dispersive X-ray (EDX) spectrum of $\text{Ti}_3\text{C}_2\text{T}_z$.

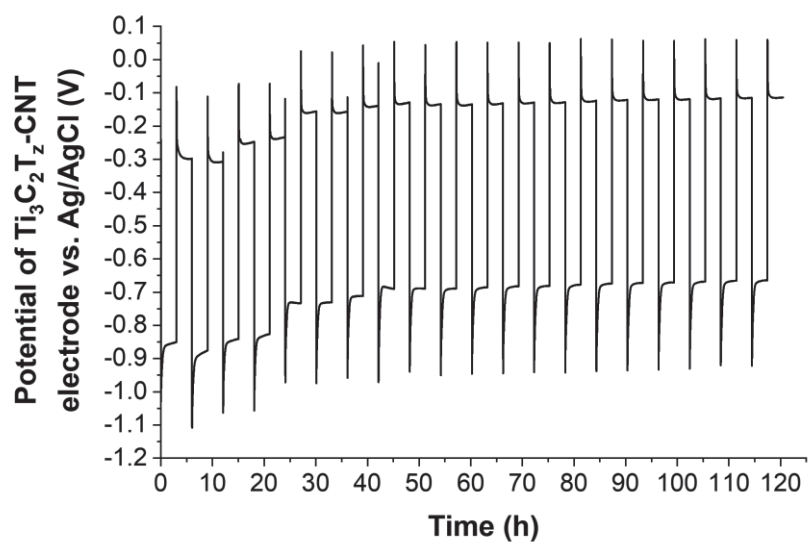


Figure S4: The potential of the $\text{Ti}_3\text{C}_2\text{T}_z$ electrode in 20 cycles.

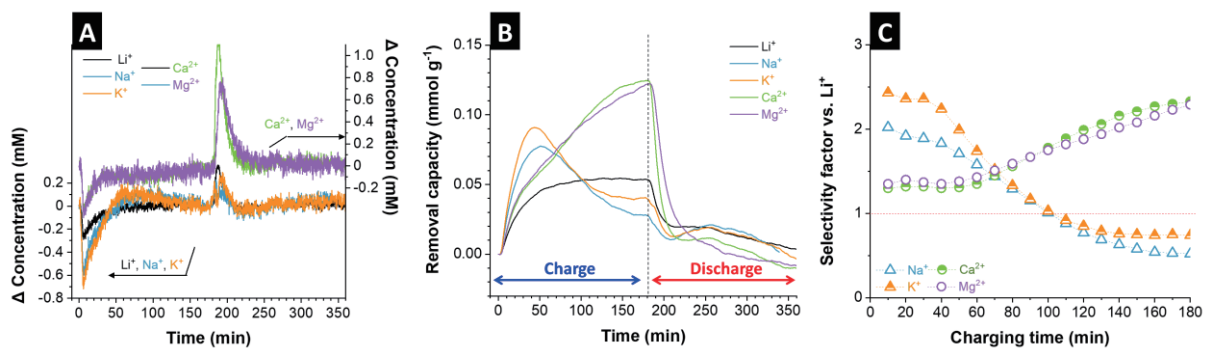


Figure S5: The time-dependent concentration change (A), ion removal capacity (B), and selectivity factor vs. Li^+ (C) of Li^+ , Na^+ , K^+ , Ca^{2+} and Mg^{2+} during the 14th cycle.

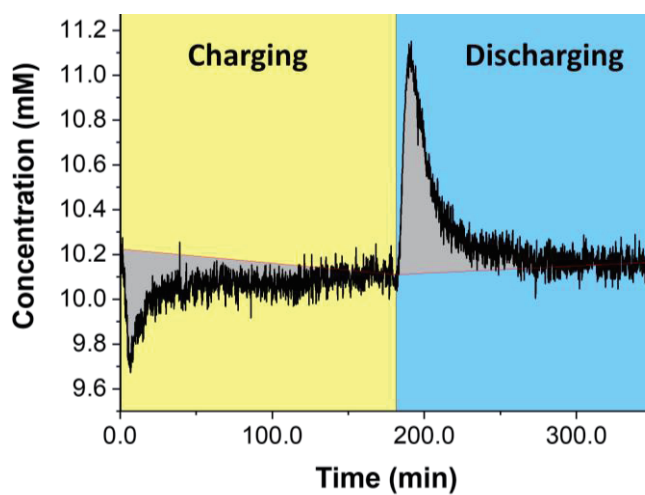


Fig. S6: The approach of the baseline establishment, taking Mg^+ in the 6th cycle as the example.

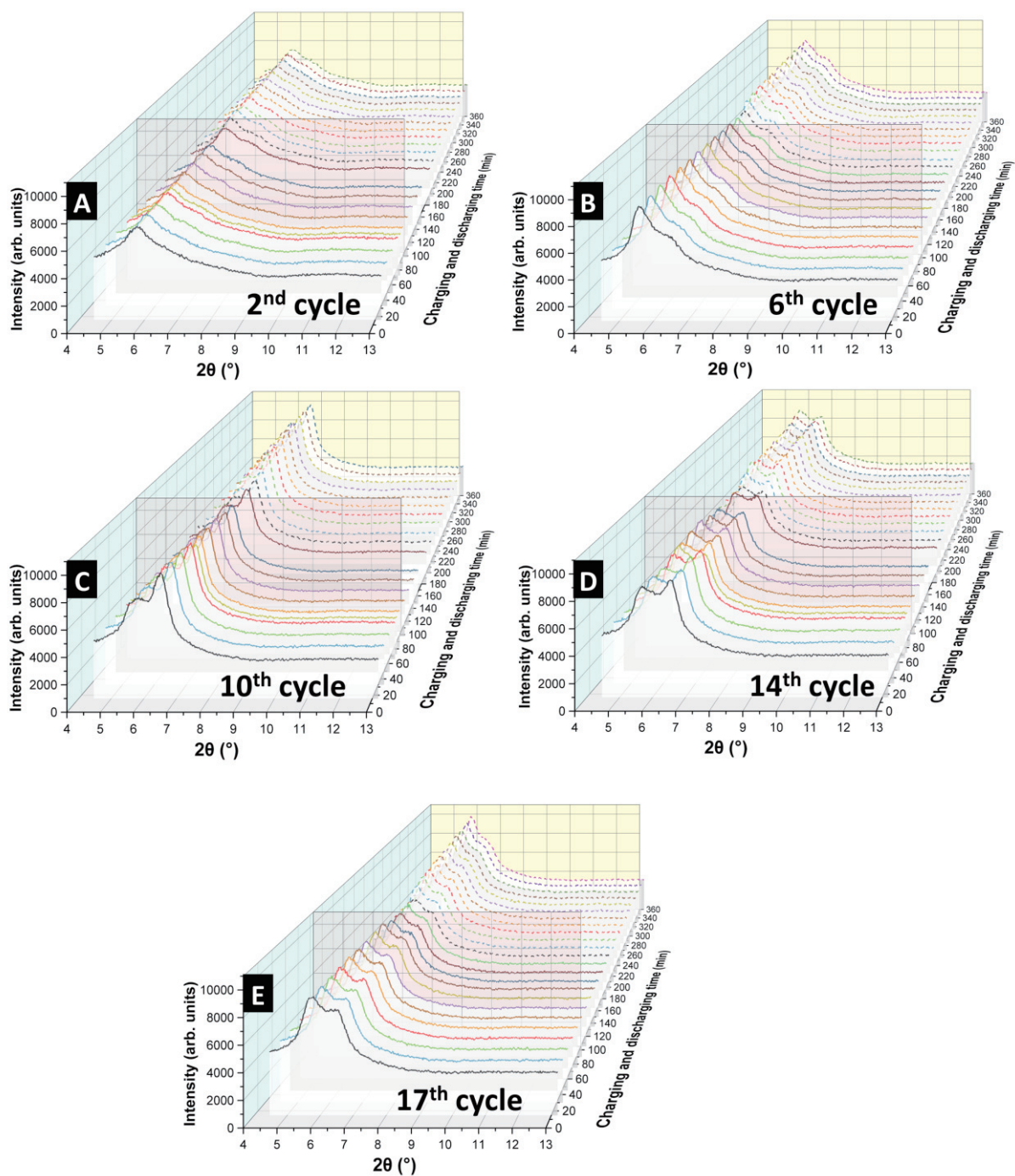


Fig. S7: In situ X-ray diffractograms of the $\text{Ti}_3\text{C}_2\text{T}_z\text{-CNT}$ electrode in different cycles: (A) 2nd, (B) 6th, (C) 10th, (D) 14th, and (E) 17th cycle. The red plane is the dividing plane of the charging and discharging process, and the discharging time is continuously counted after charging time.

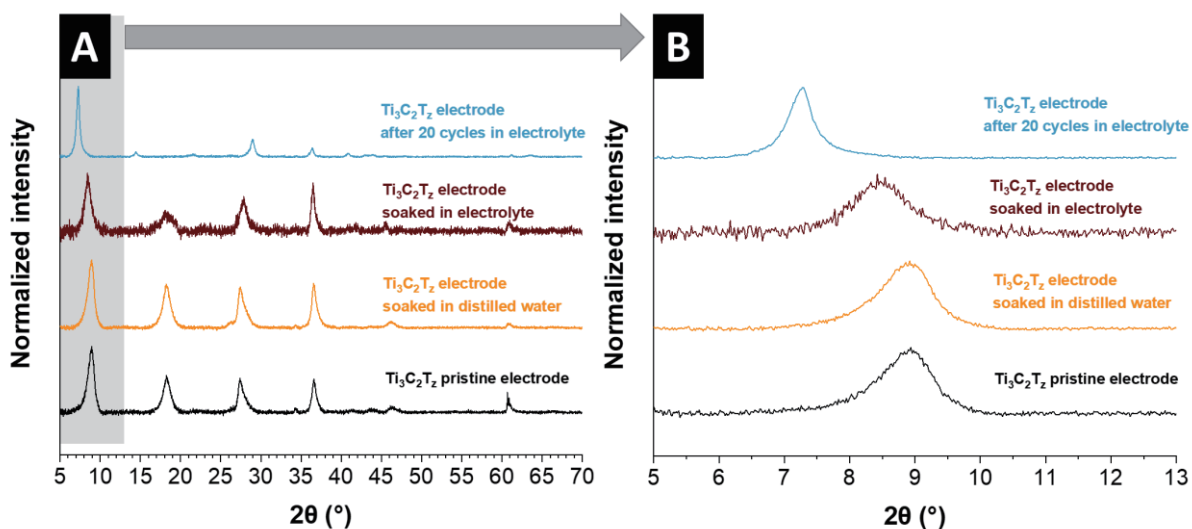


Fig. S8: (A-B) X-ray diffractograms (at different angular ranges) of the pristine $\text{Ti}_3\text{C}_2\text{T}_x$ electrode, the electrode soaked in DI water for 3 h, the electrode soaked in electrolyte overnight, and the electrode after ion selectivity experiment.

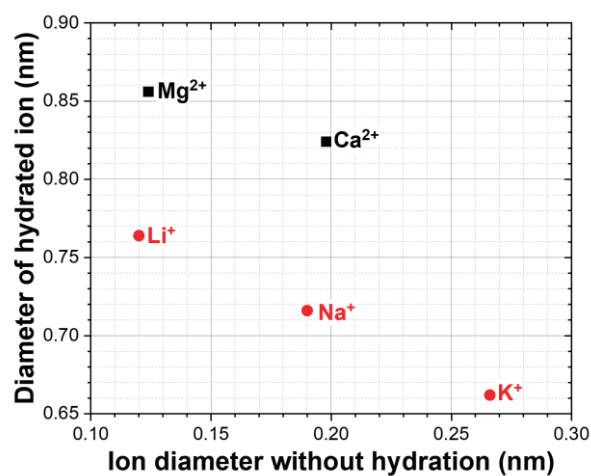


Fig. S9: Hydrated and ionic diameters of different cations studied in this work. Data adapted from Ref. [1].

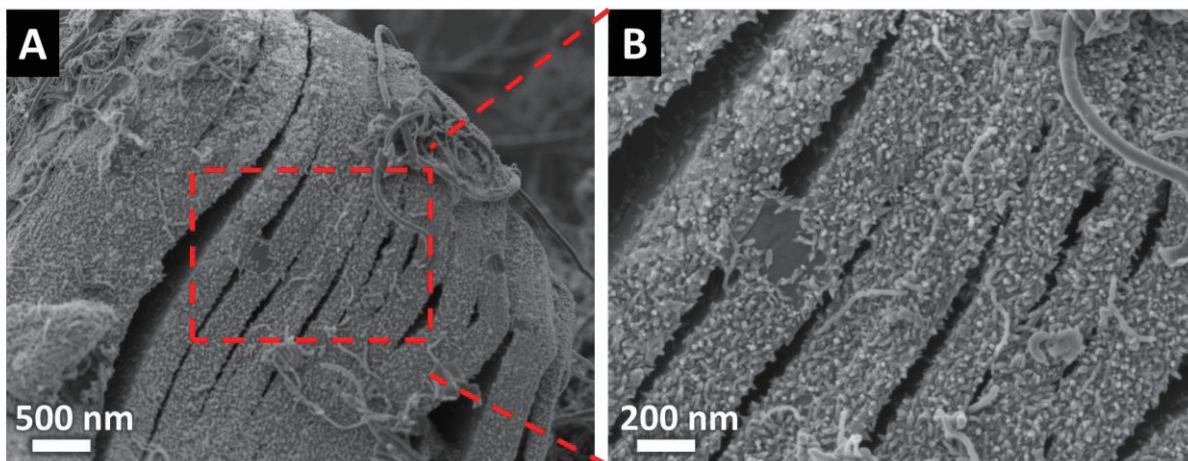


Fig. S10: SEM images of (A, B) postmortem $\text{Ti}_3\text{C}_2\text{T}_x$ electrode of after 20 cycles.

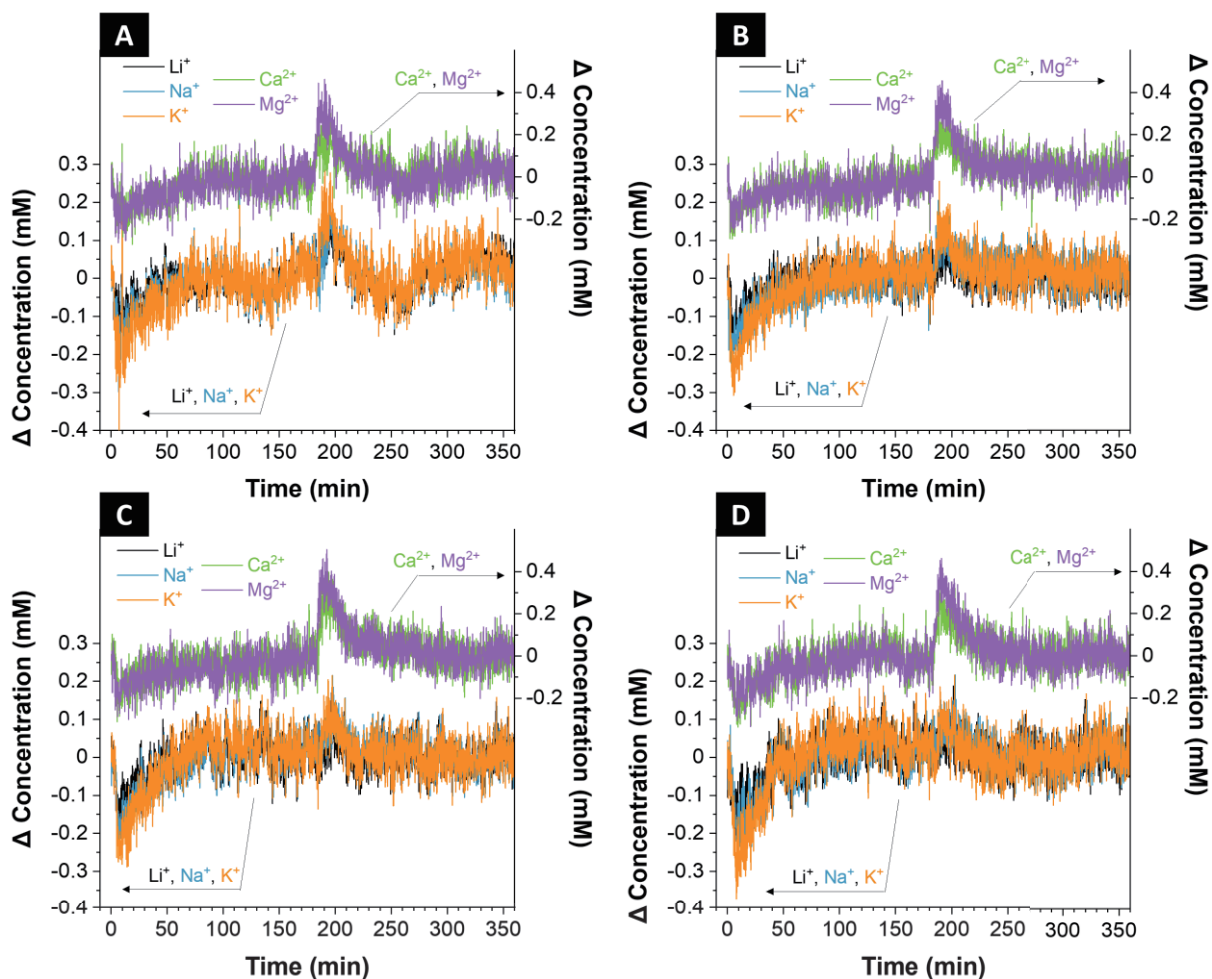


Fig. S11: The concentration change of Li^+ , Na^+ , K^+ , Ca^{2+} , and Mg^{2+} during the (A) 2nd, (B) 6th, (C) 10th, and (D) 14th cycle with the flow rate of 2.2 mL/min.

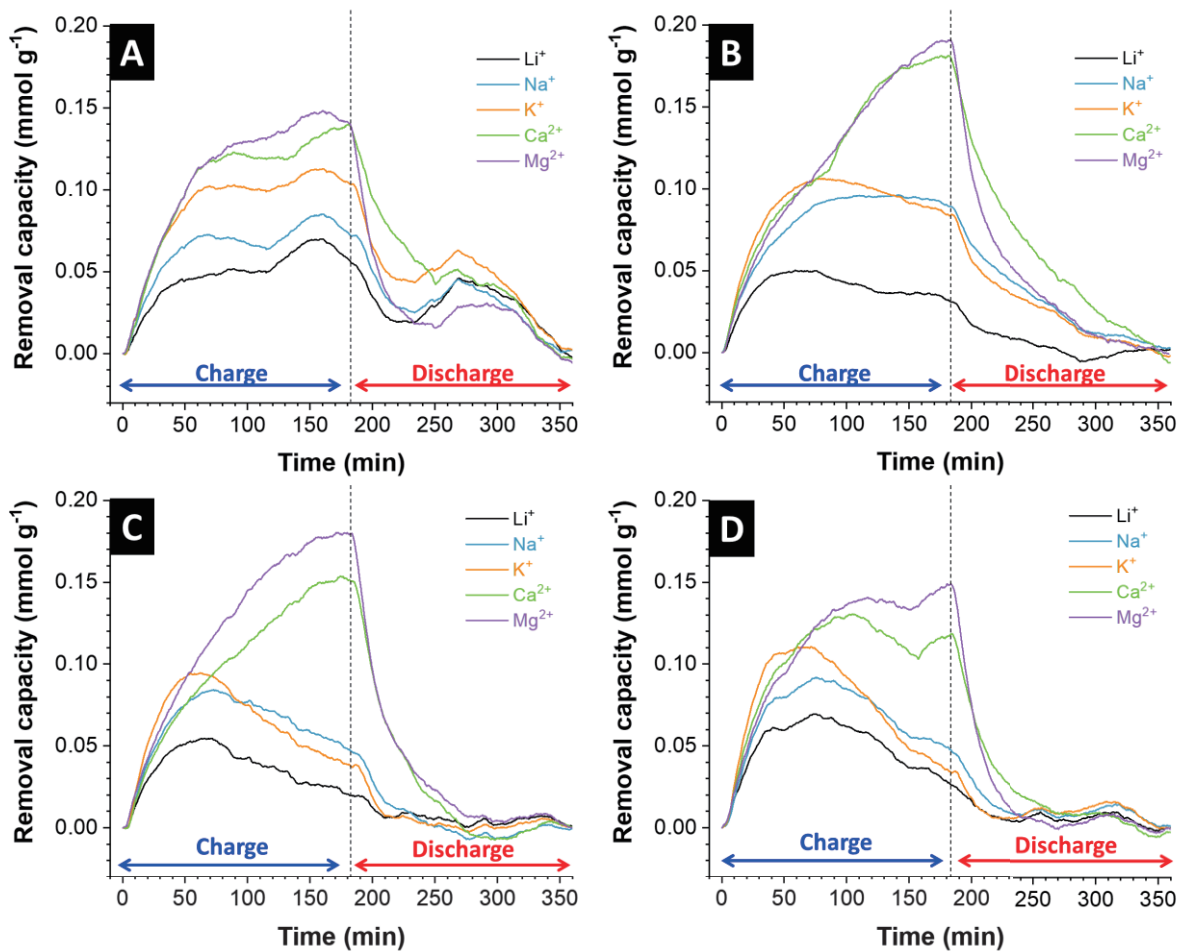


Fig. S12: The time-dependent ion removal capacity of Li^+ , Na^+ , K^+ , Ca^{2+} and Mg^{2+} during the (A) 2nd, (B) 6th, (C) 10th, (D) 14th cycle with the flow rate of 2.2 mL/min.

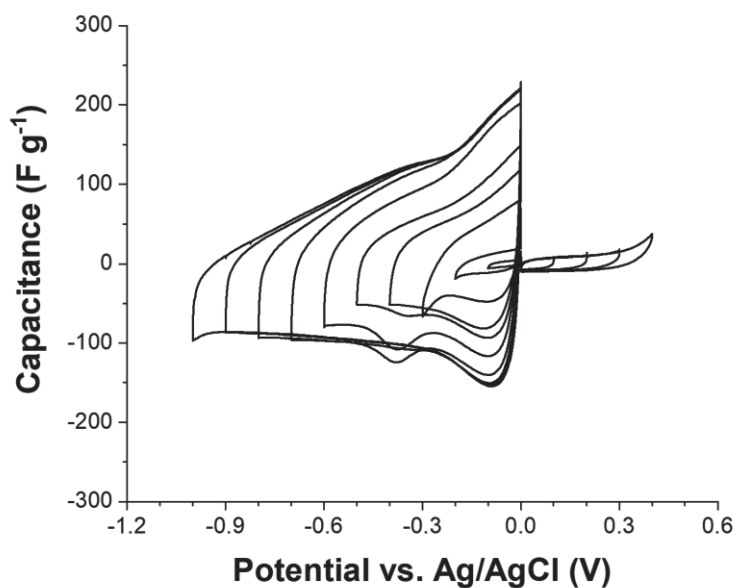


Fig. S13: Half-cell window opening cyclic voltammograms of $\text{Ti}_3\text{C}_2\text{T}_z$ in aqueous 1 M NaCl, with the scan rate of 1 mV/s.

Supporting References

[1] R. D. Shannon, *Acta Crystallographica A* **1976**, 32, 751; E. R. Nightingale, *The Journal of Physical Chemistry* **1959**, 63, 1381.

4.6 Electrochemical lithium recovery with lithium iron phosphate: what causes performance degradation and how can we improve the stability?

Lei Wang,^{1,2} Kathleen Frisella,^{1,2} Pattarachai Srimuk,^{1,2}
Oliver Janka,³ Guido Kickelbick,³ Volker Presser,^{1,2}

¹ INM - Leibniz Institute for New Materials, D2 2, 66123, Saarbrücken, Germany

² Department of Materials Science & Engineering, Saarland University, Campus D2 2, 66123, Saarbrücken, Germany

³ Inorganic Solid State Chemistry, Saarland University, Campus C4 1, 66123 Saarbrücken, Germany

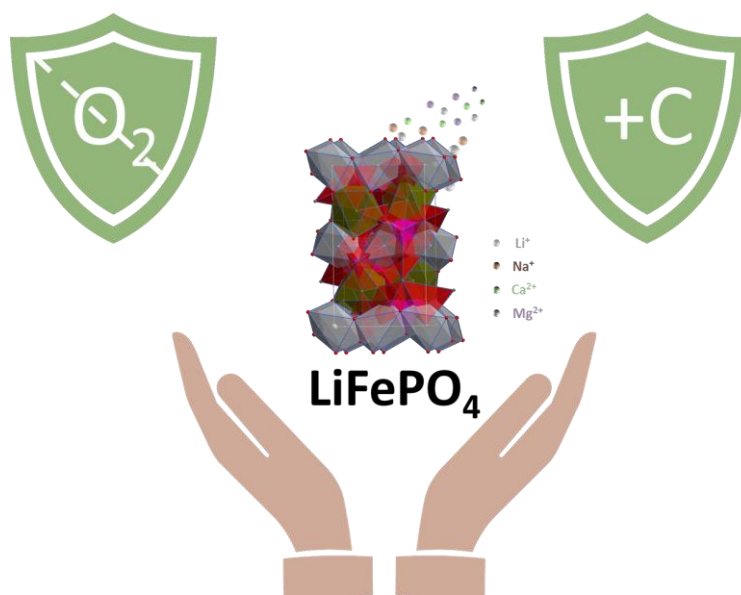
Citation:

L. Wang, K. Frisella, P. Srimuk, O. Janka, G. Kickelbick, V. Presser, ELECTROCHEMICAL LITHIUM RECOVERY WITH LITHIUM IRON PHOSPHATE: WHAT CAUSES PERFORMANCE DEGRADATION AND HOW CAN WE IMPROVE THE STABILITY?, **Sustainable Energy & Fuels**, 5 (2021) 3124-3133.

DOI: 10.1039/D1SE00450F.

Own contribution:

Investigation, Formal analysis, Data curation, Visualization, Writing-Original Draft, Writing - Review & Editing



Cite this: *Sustainable Energy Fuels*,
2021, 5, 3124

Electrochemical lithium recovery with lithium iron phosphate: what causes performance degradation and how can we improve the stability?[†]

Lei Wang,^{ab} Kathleen Frisella,^{ab} Pattarachai Srimuk,^{ab} Oliver Janka,^c
Guido Kickelbick,^c and Volker Presser^{id}*^{ab}

Electrochemical processes enable fast lithium extraction, for example, from brines, with high energy efficiency and stability. Lithium iron phosphate (LiFePO₄) and manganese oxide (λ -MnO₂) have usually been employed as the lithium gathering electrode material. Compared with λ -MnO₂, LiFePO₄ has a higher theoretical capacity and lower lithium insertion potential but suffers from low performance stability. Therefore, exploring the reason for capacity fading and putting forward an effective approach to address this issue is important. In this work, we studied the effect of additional present cations and dissolved oxygen on the stability of LiFePO₄, using a rocking chair cell configuration to eliminate the effect of the other electrode. We found that adding Ca²⁺ to the solution and dissolved oxygen aggravate the capacity fading of LiFePO₄, whereas Na⁺ and Mg²⁺ do not show an obvious influence on the stability of LiFePO₄. By continuous nitrogen-flushing of the electrolyte and carbon coating of the electrode material, the stability of LiFePO₄ was significantly enhanced. The lithium extraction capacity of LiFePO₄/C is 21 mg_{Li} g_{electrode}⁻¹ with an energy consumption of 3.03 ± 0.5 W h mol_{Li}⁻¹ and capacity retention of 82% in 10 cycles in 5 mM LiCl + 50 mM NaCl solution at a cell voltage range of -0.5 V to +0.5 V.

Received 25th March 2021
Accepted 6th May 2021

DOI: 10.1039/d1se00450f

rsc.li/sustainable-energy

1. Introduction

The demand for lithium ion-based rechargeable energy storage devices has grown dramatically due to the expected steep increase in the use of mobile electronics and electric vehicles powered by lithium-ion batteries.¹ It is forecasted that five million tons of lithium, more than one-third of the total lithium reserve available on land, will be consumed from 2015 to 2050. The lithium reserve may become depleted by 2080.² Currently, most lithium is extracted from brines because of its relatively low cost and richer reserves than mineral resources.^{3,4} There is a high demand for low-cost, environmentally friendly methods capable of extracting lithium rapidly and in large quantities. Several methods, such as solar evaporation,⁵ adsorption,^{6,7} and electrolysis,⁸ are suitable to extract lithium from brines. Recently, Kim *et al.* introduced a method that combines the adsorption and electrochemical desalination technologies, which could simultaneously achieve desalination and lithium

recovery.⁹ While the solar evaporation method is most widely used, it is time- and space-consuming.¹⁰ Adsorption methods require ample amounts of acids to regenerate,^{11,12} and electrolysis methods suffer from relatively low lithium recovery efficiency and membrane fouling.¹⁰ Consequently, there is a need to develop advanced, sustainable and effective technologies for lithium recovery.

Electrochemical processes are particularly promising for lithium extraction due to the easy process, energy efficiency, and high lithium selectivity.^{13–16} The 1993 work of Kanoh *et al.* introduced λ -MnO₂ (extracting lithium) and Pt (producing O₂) as electrodes for lithium extraction.¹⁷ In 2012, Pasta *et al.* introduced a new concept of the cell, where lithium iron phosphate (LiFePO₄) and silver served as cathode and anode, respectively.¹⁸ In this cell, one cycle includes two half-cycle processes of capture and release. During charging, the lithium and chloride ions are captured by iron phosphate and silver, respectively; during discharging, the ions are released into the solution from the electrodes. Over the years, studies have explored lithium extraction from brines; many were based on LiFePO₄ due to the high selectivity. For instance, Trócoli *et al.*¹⁹ reported using a cell with LiFePO₄ and NiHCFe as the electrodes to extract lithium from the Atacama brines; lithium concentration in the feed water increased from 4% to 11%, with energy consumption of 8.7 W h mol⁻¹. Kim *et al.* used polydopamine-coated LiFePO₄ and Pt immersed in I⁻/I₃⁻ as the electrodes; this cell achieved >4000-times amplification relative to Li/Na ion

^aINM – Leibniz Institute for New Materials, D2 2, 66123, Saarbrücken, Germany.
E-mail: volker.presser@leibniz-inm.de

^bDepartment of Materials Science & Engineering, Saarland University, Campus D2 2, 66123, Saarbrücken, Germany

^cInorganic Solid State Chemistry, Saarland University, Campus C4 1, 66123 Saarbrücken, Germany

[†] Electronic supplementary information (ESI) available. See DOI: 10.1039/d1se00450f

selectivity.²⁰ Previous works have focused on the selectivity and energy consumption of LiFePO₄, but few have investigated the stability of LiFePO₄, which is also a critical evaluation index for practical application. Also, only a few of the previous investigations addressed whether cations other than lithium, such as Na⁺, Ca²⁺, and Mg²⁺, harm the stability of LiFePO₄.

Here, we systematically studied the performance and stability of a pair of symmetric LiFePO₄ electrodes in extracting lithium from simulated brines. Unlike asymmetric electrodes, when using a system with symmetric electrodes, lithium is captured by one electrode and is released into the water by the other electrode during the charging process. Therefore, the performance of LiFePO₄ will not be limited by a separate chloride-capture electrode. By electrochemical testing and post-mortem analysis, we explore influencing factors for the performance degradation of LiFePO₄. We also demonstrate the ability to improve the performance stability by carbon coating of the faradaic electrode materials and reducing the saline medium's oxygen content. Our work, thereby, shows the ability to significantly improve the stability of LiFePO₄, making it a promising electrode for extraction of lithium from brines.

2. Materials and methods

2.1. Synthesis of LiFePO₄, LiFePO₄/C, and electrode preparation

We used commercially available LiFePO₄ (SÜD-CHEMIE) with a specific surface area of 16 m² g⁻¹. LiFePO₄/C was synthesized by a two-step method similar to the previous work.²¹ First, the as-received LiFePO₄ (0.4 g) and 0.21 g ethylene glycol (Sigma-Aldrich, 99.8%) were dispersed in 10 mL citric acid (0.18 g, Sigma-Aldrich, ≥99.5%) solution under stirring. The solution was heated at +80 °C to obtain the LiFePO₄ wrapped with the alkyl ester. After that, the alkyl-ester-coated LiFePO₄ was carbonized in argon *via* two heating steps. At first, the sample was heated to +200 °C for 2 h to remove the water in the materials, and then the sample was heated at +700 °C and held for 6 h to obtain the hybrid LiFePO₄/carbon material.

Electrodes were prepared by mixing and grinding the active material (LiFePO₄ or LiFePO₄/C), acetylene black (Alfa Aesar, 99.5%), and polyvinylidene fluoride (Alfa Aesar) with a mass ratio of 8 : 1 : 1 in 1-methyl-2-pyrrolidinone (Sigma-Aldrich, 99.5%) to form a slurry. The slurry was coated on graphite paper (300 μm in thickness, SGL) with a doctor blade (200 μm in thickness), then rested in the fume hood at room temperature in air overnight. The electrode was then dried at +80 °C in the vacuum oven for 24 h.

2.2. Electrochemical measurements

The electrochemical behavior of LiFePO₄ and LiFePO₄/C was studied with a custom-built cell in a three-electrode system.²² Electrodes of LiFePO₄, LiFePO₄/C, or activated carbon (YP-80F, Kuraray) were used with a diameter of 12 mm as a working electrode (LiFePO₄, LiFePO₄/C) or counter electrode (activated carbon). The electrodes were sandwiched and separated by a glass fiber mat (diameter 13 mm, GF/A, Whatman) in the cell

body. An Ag/AgCl reference electrode (3 M KCl, BASi) was mounted on the cell side. Before testing, the as-assembled cells were filled with various electrolytes. For single salt electrolytes, 1 M LiCl, 1 M MgCl₂, 1 M CaCl₂, and 1 M NaCl were used. For the mixed-salt electrolyte, we used a mixture of 5 mM of LiCl and 50 mM of MCl_x (M = Na, Ca, Mg).

The cell was connected to the VSP300 potentiostat/galvanostat (Bio-Logic), and the cyclic voltammogram with the scan rate of 0.1 mV s⁻¹ and cutoff potential of -0.4 V to +0.8 V vs. Ag/AgCl was applied. To test the performance stability of LiFePO₄ and LiFePO₄/C, galvanostatic charge/discharge measurements with potential limitation were conducted. Before the electrochemical operation, the electrolyte was continuously flushed with nitrogen gas for 1 h to remove the dissolved oxygen in the electrolyte (only in the study of the effect of oxygen). The concentration of dissolved oxygen after gas flushing is shown in the ESI, Table S1.†

Also, the electrodes were delithiated before electrochemical testing to avoid an increase of lithium concentration in the electrolyte caused by the charging process of LiFePO₄ and LiFePO₄/C. To delithiate the electrode, the electrodes were charged with a current of 0.1 A g⁻¹ with a limit voltage of +0.4 V vs. Ag/AgCl in a three-electrode system in 1 M LiCl electrolyte. The electrochemical impedance spectroscopy (EIS) was measured at the formal potential in the frequency range of 1 MHz to 10 mHz and with an excitation potential of 5 mV vs. Ag/AgCl.

Conductivities of solutions of LiCl, MgCl₂, CaCl₂, and NaCl with various concentrations were tested using a Microcell HC electrochemical cell with Pt electrodes (RHD Instruments) and a Modulab electrochemical workstation (Solartron Analytical) with a method similar to our previous research.²³ The Pt electrode crucible was closed after 0.9 mL of each electrolyte was placed into the measuring cup with a syringe. A heat sink paste was used in the middle of the closed-cell and base unit (Eurotherm 2000) to enhance the heat transfer. Potentiostatic impedance at each temperature was measured after the temperature had stabilized for 10 minutes. The impedance was measured from 1 Hz to 3 MHz at open circuit potential (OCV) at various temperatures from +10 °C to +60 °C in steps of Δ10 °C and at +25 °C. The conductivity and activation energy values were calculated according to eqn (1) and (2).

$$\sigma = \frac{l}{AR} \quad (1)$$

where σ is the conductivity (S cm⁻¹), R is the resistance (Ω), A pre-exponential factor is the area (cm²), and l is the length (cm).

The value of $\frac{l}{A}$ was obtained from 0.1 M KCl aqueous standard (VWR) with a conductivity of 12.880 mS cm⁻¹ at +25 °C.

$$\sigma = \frac{A}{T} e^{\left(\frac{-E_a}{kT}\right)} \quad (2)$$

where σ is the conductivity, T is the temperature (K), A is obtained from the experiment, k is the Boltzmann constant (1.380649 10⁻²³ J K⁻¹), and E_a is the activation energy (kJ mol⁻¹).

2.3. Lithium selectivity experiments

Lithium extraction experiments were performed in a multi-channel cell. Two water channels were provided by the gasket (area = 6.76 cm², thickness = 500 μm), filled with glass fiber mat (GF/A, Whatman), and were separated by an anion exchange membrane (FAS-PET-130, Fumatech). The LiFePO₄ or LiFePO₄/C electrodes were contacted with the graphite current collector. Before the experiment, one electrode was delithiated using the method mentioned in Section 2.2. In this work, the channel with a pretreated electrode is called “channel 1”, and the other is called “channel 2”. During the charging process, the cations in channel 1 will intercalate into the structure of the pretreated LiFePO₄ electrode while the lithium in the LiFePO₄ will be released into channel 2. Driven by the electronic neutralization, the Cl⁻ in channel 1 will migrate into channel 2. The discharging process is the opposite (ESI, Fig. S1†).

To investigate the selectivity and stability of LiFePO₄ and LiFePO₄/C, we used an electrolyte containing 5 mM LiCl and 50 mM NaCl with a volume of 10 L. The outlet of channel 2 was connected to an inductively coupled plasma optical emission spectrometer (ICP-OES, ARCOS FHX22, SPECTRO Analytical Instruments) to quantify the concentration change of cations. The mass of the electrodes was about 18 mg; a low specific current of 30 mA g⁻¹ and a flow rate of 1.2 mL min⁻¹ were used to enhance the ICP-OES signal. The calibration curve was made according to the correlation between the intensity of individual wavelength and the concentration of the solution (ESI, Fig. S2†). The measured intensities from the extracted sample were converted into concentration profiles. The charging and discharging processes were opposite, and the potential for energy recovery was negligible;²⁴ therefore, we used the lithium extraction amount and energy consumption in a half cycle calculated according to eqn (3) and (4) to evaluate the performance of LiFePO₄ and LiFePO₄/C.

$$\begin{aligned} \text{Lithium extraction capacity (mg}_{\text{Li}} \text{ g}_{\text{electrode}}^{-1}) \\ = \frac{v \cdot M_{\text{Li}}}{1000 m_{\text{total}}} \int \Delta c_{\text{channel 2}} dt \end{aligned} \quad (3)$$

where v is the flow rate (mL min⁻¹), M_{Li} is the molecular weight of Li (6.99 g mol⁻¹), m_{total} is the mass of the electrode (g), t is the time over the lithium-extraction step (min), and $\Delta c_{\text{channel 2}}$ is the concentration change of Li⁺ (mM) in channel 2.

$$\text{Energy consumption (W h mol}_{\text{Li}}^{-1}) = \frac{-\int \Delta E dq \cdot 1000}{3.6 \cdot v \cdot \int c_{\text{channel 2}} dt} \quad (4)$$

where ΔE is the cell voltage (V), q is the charge (A s), v is the flow rate (mL min⁻¹), t is the time over the lithium-extraction step (min), and $c_{\text{channel 2}}$ is the concentration of Li (mM) in channel 2.

2.4. Material characterization

The surface morphology of LiFePO₄ and LiFePO₄/C was investigated by scanning electron microscopy (JEOL JSM 7500F) at 1 kV acceleration voltage. X-ray diffraction experiments were conducted on a D8 Advance diffractometer (Bruker AXS) with a copper X-ray source (Cu K_α, 40 kV, 40 mA) and a Goebel mirror

in point focus (0.5 mm). With a VANTEC-500 two-dimensional X-ray detector, positioned at 20° 2θ, 40° 2θ, 60° 2θ, 80° 2θ with a measurement time of 1000 s per step, four frames were recorded.

Further XRD data were collected at room temperature on a D8-A25-Advance diffractometer (Bruker AXS) in Bragg-Brentano θ - θ -geometry (goniometer radius 280 mm) with Cu K_α radiation (40 kV, 40 mA). A 12 μm Ni foil working as K_β filter and a variable divergence slit were mounted at the primary beam side. A LYNXEYE detector with 192 channels was used at the secondary beam side. Experiments were carried out in a 2θ range of 7° to 120° with a step size of 0.013° and a total scan time of 1 h.

Raman spectra were recorded with a Renishaw in Via system using an Nd:YAG laser with an excitation wavelength of 532 nm. The spectral resolution was 1.2 cm⁻¹, and the diameter of the laser spot on the sample was around 2 μm with a total power exposure of 0.5 mW. The carbon contents (mass%) of LiFePO₄ and LiFePO₄/C were tested using a Vario Micro Cube system from Elementar.

3. Results and discussion

3.1. Material characterization

Fig. 1A shows the transmission electron micrographs of LiFePO₄. LiFePO₄ particles are typically about 300 nm long and about 150 nm wide. At higher resolution (Fig. 1B), we see lattice fringes with the typical spacing of 0.34–0.35 nm in alignment with the (111) and (021) planes of LiFePO₄. LiFePO₄/C shows the ubiquitous presence of carbon engulfing the LiFePO₄ particles (Fig. 1C and D).

Fig. 1E shows the X-ray diffractograms of LiFePO₄ and LiFePO₄/C. The diffraction pattern of LiFePO₄/C matches the one of pristine orthorhombic LiFePO₄ (CaMgSiO₄ type, *Pnma*, PDF 81-1173), which indicates the carbon coating process does not affect the inherent structure of LiFePO₄. Fig. 1F displays the Raman spectra of LiFePO₄ and LiFePO₄/C. The band at 952 cm⁻¹ can be attributed to the symmetric stretching of P–O bonds of LiFePO₄,²⁵ and the peaks at 1338 cm⁻¹ and 1598 cm⁻¹ correspond to the D-band and G-band of carbon, respectively. The D-band (disorder peak) is due to the A_{1g} vibrational mode, and the G-band (graphitic peak) is due to the E_{2g} vibrational mode of the C–C bond stretching.²⁶ Therefore, both commercial LiFePO₄ and LiFePO₄/C exhibit the presence of incompletely graphitic carbon; in the case of the former, carbon is a minority phase (2.4 ± 0.6 mass%), while for the latter, we have determined 4.4 ± 0.7 mass% *via* CHNS test (ESI, Table S2†).

3.2. Electrochemical measurements

We carried out cyclic voltammetry to investigate the selectivity behavior of LiFePO₄ towards Li⁺ compared to other cations. To this end, we compared the electrochemical performance in different single-cation electrolytes. As shown in Fig. 2A–C, a pair of redox peaks occurs in all kinds of electrolytes. Using an aqueous 1 M CaCl₂ electrolyte, we see the lowest peak current. In 1 M LiCl, the redox peak currents are the highest, and the

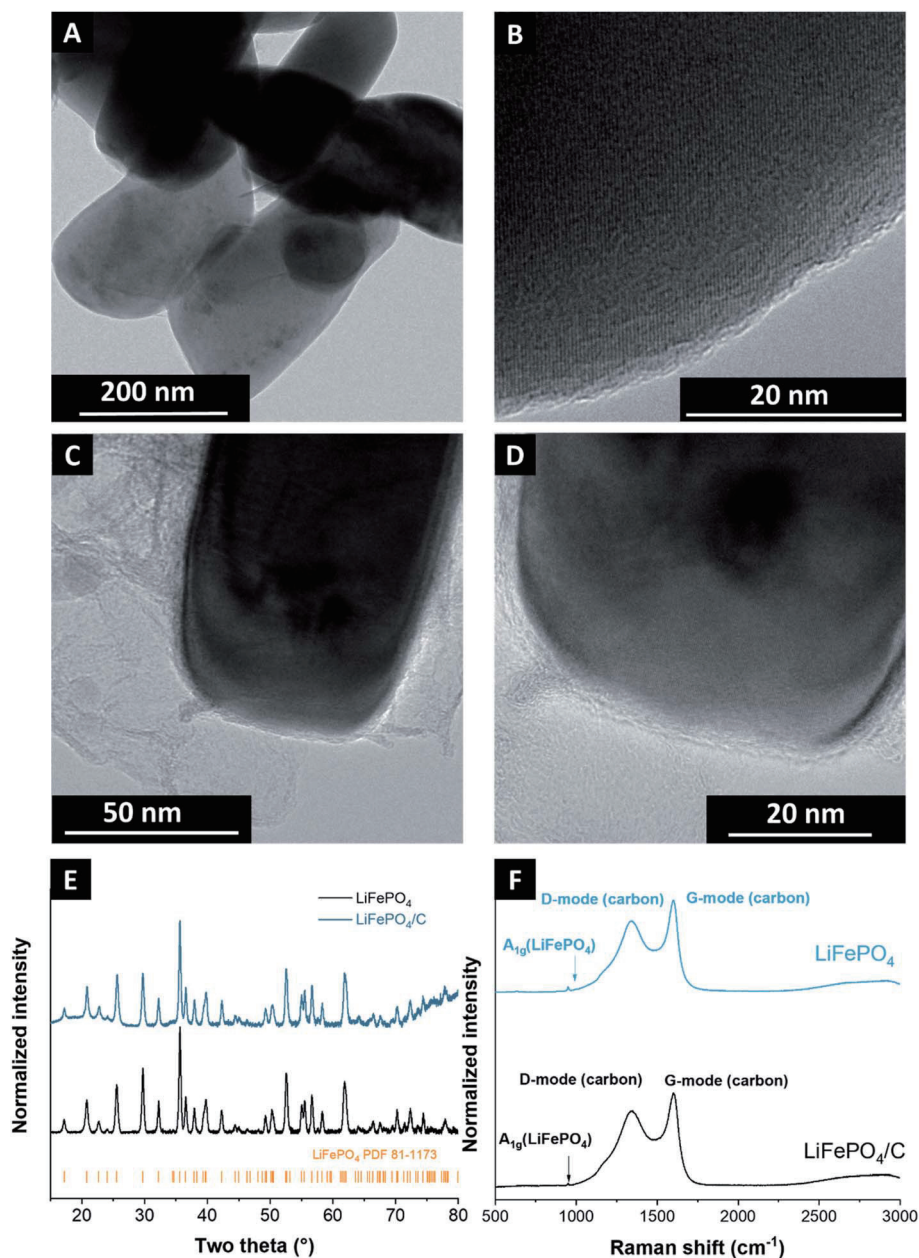


Fig. 1 Transmission electron micrographs of LiFePO₄ (A) and (B) and LiFePO₄/C (C) and (D). (E) X-ray diffraction patterns and (F) Raman spectra of LiFePO₄ and LiFePO₄/C.

peak potentials are shifted to a more positive region than the other electrolytes, which could be due to the contribution of additional lithium in the solution leached from the electrode.

To further quantify the potential shift, we investigated the formal potential ($E_{1/2}$).²⁷ As shown in ESI, Table S3,[†] the formal potential in LiCl solution is decreased as the concentration is decreased. During the charging process (the first electrochemical process during cyclic voltammetry), the Li⁺ in LiFePO₄ will be released into the electrolyte. Therefore, when tested in electrolytes with other cations, such as NaCl, MgCl₂, or CaCl₂, the cyclic voltammograms and the formal potential are almost identical.

To reduce the loss of additional lithium ions from the electrode to the electrolyte and compare the electrolyte of different concentrations, the LiFePO₄ electrodes were delithiated before the galvanostatic charge/discharge testing. We observed a significant decay of the initial capacity of LiFePO₄ in all electrolytes (Fig. 2D and E). The capacity decreases slowest in the mixed solution of Li⁺ and Na⁺ and the fastest in the electrolyte containing Ca²⁺, with retention of 60% and 46%, respectively, after 100 cycles. First, the capacity increases and then decreases in 5 mM LiCl + 50 mM MgCl₂ solution; the increase may be due to the intercalation of trace amounts of Mg²⁺. Compared with other cations, Mg²⁺ intercalates more easily into the structure of LiFePO₄.²⁸ However,

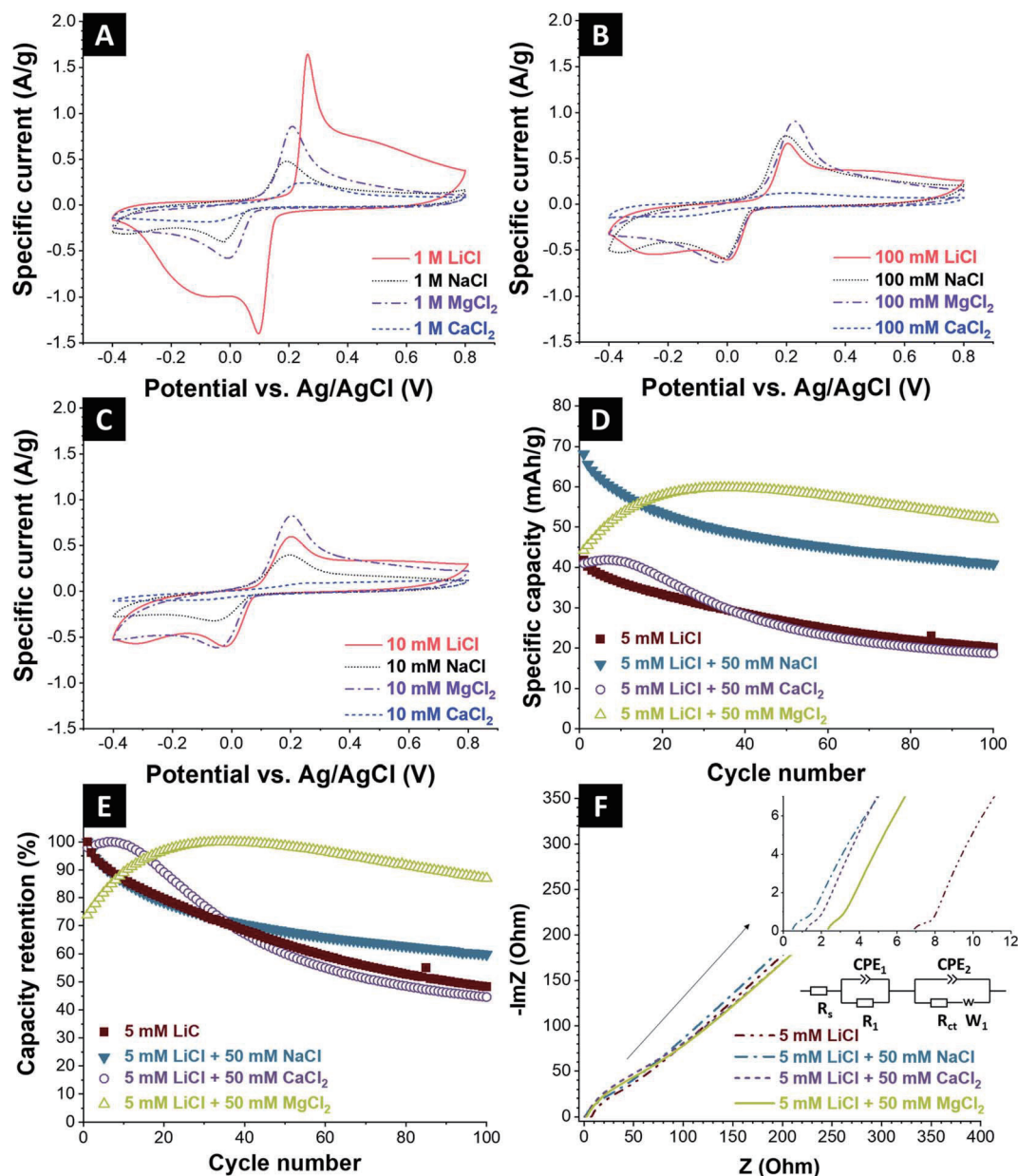


Fig. 2 Cyclic voltammograms (1 mV s⁻¹) of LiFePO₄ in aqueous electrolytes with concentration of LiCl, NaCl, MgCl₂, and CaCl₂ at (A) 1 M, (B) 100 mM, and (C) 10 mM. (D) and (E) Specific capacity of LiFePO₄ for selected LiCl mixtures recorded at 0.1 A g⁻¹ (D: absolute value; E: relative value). (F) Nyquist plot and equivalent circuit for the system of the mixed electrolyte system.

the intercalation of both Mg²⁺ and Li⁺ is not fully reversible, so the capacity still declines. To study why the capacity of LiFePO₄ electrodes fades during the cycles, we measured the post-mortem X-ray diffractograms of the delithiated LiFePO₄,

which was charged and discharged for 100 cycles in various electrolytes.

Besides the effect on stability, cations other than Li⁺ also influence the kinetics obtained from electrochemical

Table 1 Fitted values for delithiated LiFePO₄ in various electrolytes according to the equivalent circuit. See text and Fig. 2F

Electrolyte	R _s (Ω)	R ₁ (Ω)	R _{ct} (Ω)	W ₁ (Ω s ^{-1/2})	χ ²	χ ² / Z
5 mM LiCl	6.8	1.1	40.0	63.4	315.2	1.67 × 10 ⁻²
5 mM LiCl + 50 mM NaCl	0.4	1.0	38.7	51.8	210.5	1.36 × 10 ⁻²
5 mM LiCl + 50 mM MgCl ₂	2.2	0.9	74.2	76.2	265.7	5.98 × 10 ⁻³
5 mM LiCl + 50 mM CaCl ₂	1.1	0.8	77.0	71.4	669.4	7.24 × 10 ⁻³

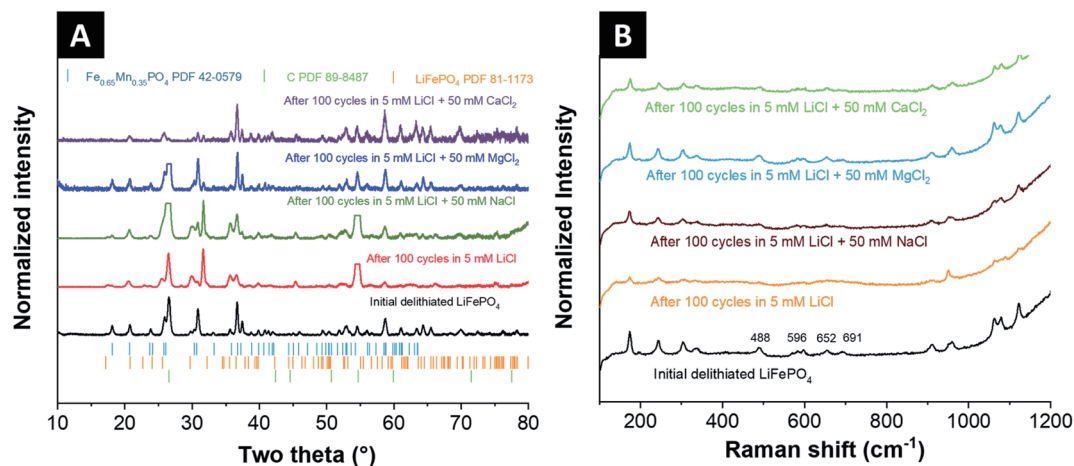


Fig. 3 (A) The post-mortem X-ray diffraction patterns and (B) Raman spectra of delithiated LiFePO₄ after 100 cycles in different electrolytes. The diffraction pattern in panel (A) were normalized to the reflections not associated with the graphite foil.

impedance measurements. The Nyquist plots are composed of two semi-circles and a line (Fig. 2F). The semi-circle at high frequency represents the electrolytes capacitance response; accordingly, we see it only in a significant amplitude when exploring the low concentration electrolyte.²⁹ The semi-circle at medium frequency indicates the charge transfer resistance (R_{ct}).³⁰ The inclined line in the low frequency represented the Warburg impedance (W_1), which corresponds to lithium-ion diffusion.^{31,32} The value of R_{ct} and W_1 is calculated according to the simulated circuit, as shown in Table 1. Ca²⁺ and Mg²⁺ harm the charge transfer process, with R_{ct} values of 38.7 Ω cm² and 37.3 Ω cm², respectively, which are nearly double the R_{ct} value in pure 5 mM LiCl (20.1 Ω cm²). The R_{ct} values in 5 mM LiCl and 50 mM NaCl are similar to those in pure LiCl electrolyte. The effect of other cations on the Warburg impedance follows the pattern seen for the R_{ct} , and the Warburg impedances in Mg²⁺- and Ca²⁺-containing electrolytes are higher than those in Na⁺-containing and pure LiCl. This finding suggests that lithium ions are more difficult to diffuse in the liquid side in the former electrolytes than the latter. The different effects originate from the different conductivities of cations (ESI, Fig. S4†).

As shown in Fig. 3A, the delithiated LiFePO₄ is composed of heterosite FePO₄ and LiFePO₄ because the LiFePO₄ is not fully delithiated. This result is consistent with the Raman data (ESI, Fig. S3†). When Raman measurements are carried out at two randomly selected points, there may be only one peak (952 cm⁻¹) which is associated with LiFePO₄ (Fig. 1F). At other locations, the observed peaks align with FePO₄.²⁵ After 100 cycles in 5 mM LiCl, diffraction patterns assigned to FePO₄, such as 37.4° 2 θ ((211) of FePO₄), disappear, which indicates a partial degeneration of FePO₄. Differently, after 100 cycles in Ca²⁺ containing electrolytes, the reflections at 18.13° 2 θ , corresponding to the (020) of FePO₄, disappear, which leads to the considerable capacity fading. Fig. 3B shows the Raman spectra of the electrodes after 100 cycles in different electrolytes. After charge/discharge in NaCl, LiCl and CaCl₂ electrolyte, the peaks

at 488 cm⁻¹ (Li cage/asymmetric bend PO₄³⁻), 596 cm⁻¹ (asymmetric bend PO₄³⁻, ν_4), 652 cm⁻¹ (symmetric bend PO₄³⁻, ν_2), and 691 cm⁻¹ are not pronounced, which indicates the breaking of P–O bond; this is to say another reason for the fading of the LiFePO₄ performance is the loss of oxygen species.³³

3.3. Lithium selectivity: effect of dissolved oxygen

We used a mixed electrolyte containing 5 mM LiCl and 50 mM NaCl as the feed water to investigate the effect of oxygen content on the stability of LiFePO₄. This choice was motivated by the observation that sodium ions have the smallest effect on the stability of LiFePO₄. First, we tested the stability of LiFePO₄ at 100 mA g⁻¹, with the potential range of -0.4 V to +0.5 V vs. Ag/AgCl, in 5 mM LiCl + 50 mM NaCl solution flushed with O₂ or N₂ for 1 h before the electrochemical operation. After 100 cycles, LiFePO₄ retains 69% of the initial capacity in the N₂-flushed electrolyte, while the capacity retention values in O₂-flushed electrolyte and non-treated electrolytes are 43% and 52%, respectively (Fig. 4A). This indicates that dissolved O₂ in the electrolyte accelerates the performance degradation of LiFePO₄ significantly.

The effluent solution was constantly analyzed by online monitoring with inductively coupled plasma optical emission spectroscopy (ICP-OES). As shown in Fig. 4B–D, LiFePO₄ always keeps a good selectivity towards lithium regardless of the oxygen content. Similar to the trend seen for the specific capacity (Fig. 4A), LiFePO₄ tested in the feed water with continuous N₂-flushing is most stable with the capacity retention of 70% after 10 cycles (Fig. 4E). The lithium extraction capacity is only about half of the initial value in the feed water without any treatment, which is slightly higher than in the feed water with continuous O₂-flushing. With higher oxygen content, the capacity fades at a larger amplitude. Unlike the Li⁺ extraction/recovery capacity, the energy consumption is stable during the 10 cycles, as shown in Fig. 4F. This result suggests that the content of oxygen has a small effect on the system's

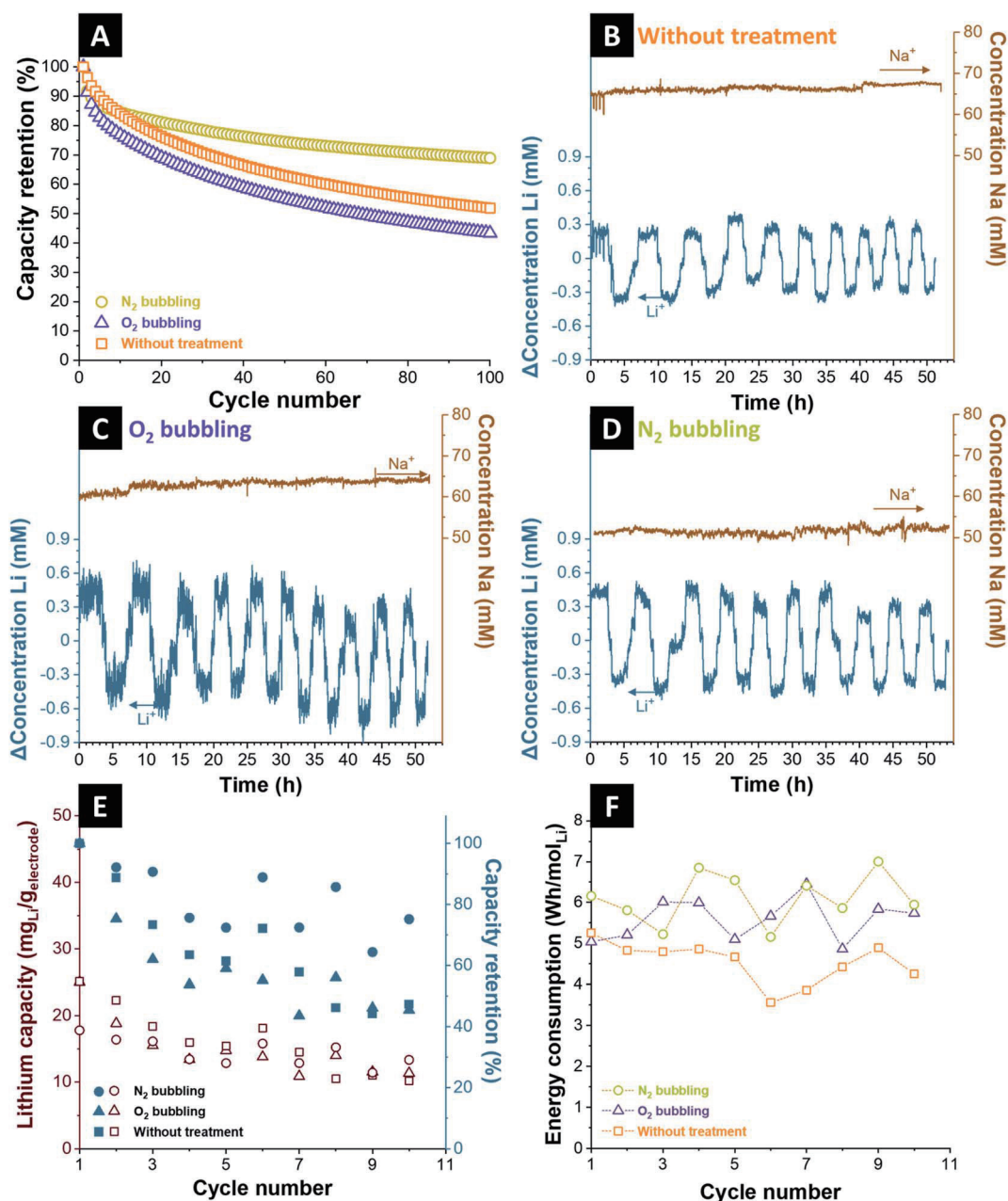


Fig. 4 (A) The comparison of the stability of LiFePO_4 in 5 mM LiCl + 50 mM NaCl with N_2 -flushing, O_2 -flushing, or no pre-treatment operated in a three-electrode setup at 0.1 A g^{-1} (B)–(D) The effluent concentration of lithium and sodium using LiFePO_4 electrodes in 5 mM LiCl + 50 mM NaCl (B) without treatment, (C) with O_2 -flushing, or (D) with N_2 -flushing. (E) Comparison of lithium extraction capacity and corresponding capacity retention of LiFePO_4 in 5 mM LiCl + 50 mM NaCl without treatment, with O_2 -flushing, or N_2 -flushing. (F) Energy consumption of LiFePO_4 in 5 mM LiCl + 50 mM NaCl without treatment with O_2 -flushing and N_2 -flushing.

energy consumption but a large effect on the structural and chemical stability of LiFePO_4 itself.

To explore how dissolved oxygen within the electrolyte influences the stability of LiFePO_4 , we used X-ray diffraction. Thereby, we characterized the structural changes of the electrode material after 100 cycles in the electrolyte composed of 5 mM LiCl and 50 mM NaCl (ESI, Fig. S5†). Unlike when measuring just the plain powder, we see strong reflections of the graphite paper ($26.5^\circ 2\theta$ (002)/(003) and $54.6^\circ 2\theta$ (004)/(006)) for the casted electrodes; therefore, the diffraction patterns

were normalized to the reflections not associated with the graphite foil. Compared with the initial LiFePO_4 powder and the initial LiFePO_4 electrode, for all the electrodes after 100 cycles, there are two further reflections at 31.7° and $45.5^\circ 2\theta$, originating from residual salt (NaCl).

Rietveld refinement (as shown in ESI, Fig. S6†) was used to obtain the unit cell parameters of LiFePO_4 electrode after 100-cycle charging and discharging in O_2 -flushing, N_2 -flushing, and common electrolyte (Table 2). As can be seen, after cycled on all measurement conditions, the unit cell parameters a and

Table 2 Unit cell parameters of LiFePO₄ and LiFePO₄/C tested in various electrolytes according to the Rietveld refinement

Electrolyte	<i>a</i> (Å)	<i>b</i> (Å)	<i>c</i> (Å)	Δ <i>a</i> (Å)	Δ <i>b</i> (Å)	Δ <i>c</i> (Å)
LiFePO ₄ electrode	10.324(1)	6.004(1)	4.691(1)	—	—	—
LiFePO ₄ tested in 5 mM LiCl + 50 mM NaCl	10.266(2)	5.978(1)	4.767(1)	−0.058	−0.026	+0.076
LiFePO ₄ tested in 5 mM LiCl + 50 mM NaCl O ₂ bubbling	10.263(4)	5.961(2)	4.777(2)	−0.061	−0.043	+0.086
LiFePO ₄ tested in 5 mM LiCl + 50 mM NaCl N ₂ bubbling	10.277(2)	5.979(1)	4.730(1)	−0.047	−0.025	+0.039
LiFePO ₄ /C electrode	10.324(1)	6.004(1)	4.691(1)	—	—	—
LiFePO ₄ /C tested in 5 mM LiCl + 50 mM NaCl	10.286(3)	5.977(2)	4.750(2)	−0.038	−0.027	0.059

b decrease while *c* increases. Compared with those of the initial LiFePO₄ electrode, this indicates that the Li content in LiFePO₄ is below 1 according to Li_{1-x}FePO₄.^{34,35} When LiFePO₄ is fully converted to FePO₄, the unit cell parameters change; however, the resulting structure remains orthorhombic with space group *Pnma*.³⁶ After 100 cycles, the absolute value of Δ*a*, Δ*b*, and Δ*c* increases as the O₂ concentration rises; that means the amount of Fe(n), which is irreversibly oxidized and loses the

electrochemical activity, is the largest in the LiFePO₄ tested in O₂-flushed electrolyte. Therefore, the higher amount of dissolved oxygen leads to a more substantial deterioration of the LiFePO₄ material.

3.4. Lithium selectivity: effect of carbon coating of LiFePO₄

To enhance the stability of LiFePO₄, we coated LiFePO₄ with carbon layers to prevent the attack of oxygen. Fig. 5A shows the

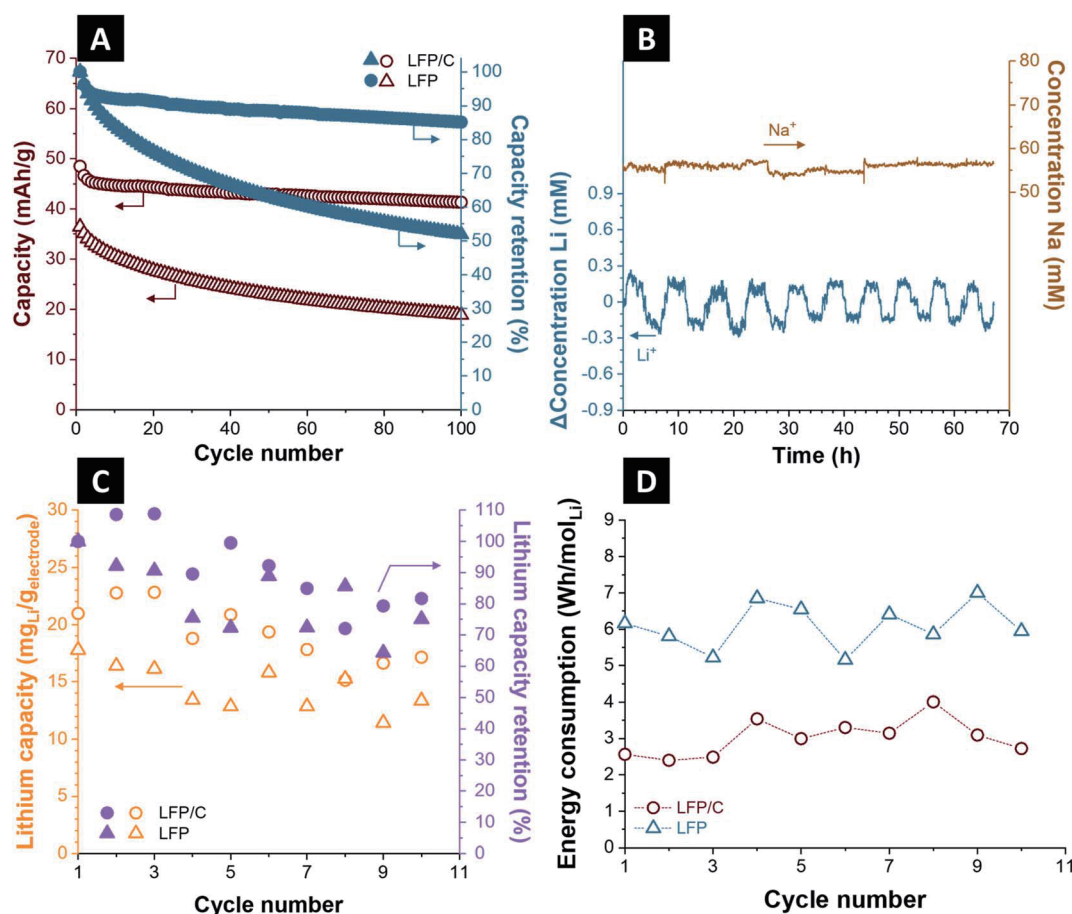


Fig. 5 The comparison of stability of LiFePO₄ and LiFePO₄/C in 5 mM LiCl + 50 mM NaCl solution in three-electrode system at 0.1 A g⁻¹ (A). (B) The effluent concentration of lithium and sodium using LiFePO₄/C electrodes in 5 mM LiCl + 50 mM NaCl with N₂-flushing. (C) Lithium removal capacity and retention in 5 mM LiCl + 50 mM NaCl of LiFePO₄/C or LiFePO₄. (D) Energy consumption in 5 mM LiCl + 50 mM NaCl of LiFePO₄/C or LiFePO₄.

difference between LiFePO_4 and LiFePO_4/C in 5 mM LiCl + 50 mM NaCl . As can be seen, the capacity of LiFePO_4/C declines slightly from 48.5 mA h g^{-1} to 40.7 mA h g^{-1} , with a retention of 85% of the initial capacity after 100 cycles. For comparison, LiFePO_4 without carbon coating maintains only 52% of the initial capacity, decreasing from 36.4 mA h g^{-1} to 18.9 mA h g^{-1} after 100 cycles.

To investigate why the LiFePO_4/C electrodes are more stable than plain LiFePO_4 , we carried out post-mortem XRD measurement and Rietveld fitting (ESI, Fig. S7†) of samples that have been subject to Li-intercalation reactions in the last step. The obtained unit cell parameters are shown in Table 2. Compared with the initial LiFePO_4/C electrode, after 100 cycles in 5 mM LiCl + 50 mM NaCl , the unit cell parameter decreased by 0.4% (*a*) and 0.4% (*b*), and *c* increased by 1.3%. Without carbon coating, after 100 cycles in the same electrolyte, the variation of *a*, *b*, and *c* are -0.6% , -0.4% , and $+1.6\%$, respectively (Table 2). Similar to the explanation in Section 3.3, after 100 cycles, in LiFePO_4/C , there is more electrochemically active LiFePO_4 . This phenomenon is because the carbon on the surface of the LiFePO_4 could reduce the contact between the LiFePO_4 particles and dissolved oxygen.³⁷

To further explore whether carbon coating can improve the stability of LiFePO_4 in lithium extraction, we tested the performance of LiFePO_4/C in 10 mM LiCl and 5 mM LiCl + 50 mM NaCl solution (continuous N_2 -flushing) using the rocking-chair cell. Analogous to LiFePO_4 , LiFePO_4/C also exhibits good selectivity towards lithium (Fig. 5B). However, LiFePO_4/C has a higher lithium extraction capacity ($21.0 \text{ mg}_{\text{Li}} \text{ g}_{\text{electrode}}^{-1}$ vs. $17.8 \text{ mg}_{\text{Li}} \text{ g}_{\text{electrode}}^{-1}$ in the first cycle) and better stability retention of 82% after carbon coating, as shown in Fig. 5C. The higher capacity of LiFePO_4/C could be due to the carbon coating improving the electronic conductivity of the LiFePO_4 ,³⁸ that is to say, the active materials can be fully utilized at high current. Also, the carbon layer can block the attack of oxygen and OH^- and increase the stability of LiFePO_4 .³⁹ Also, the extra carbon present in a nanohybridized form in LiFePO_4/C could effectively decrease the resistance of LiFePO_4 , which could reduce the energy consumption (Fig. 5D). The average energy consumption of LiFePO_4/C in 10 cycles is $3.0 \pm 0.5 \text{ W h mol}_{\text{Li}}^{-1}$.

4. Conclusions

In conclusion, we explored the influence of various cations and dissolved oxygen in the brines on the stability of LiFePO_4 in a symmetric cell (*i.e.*, LiFePO_4 paired with LiFePO_4). Cations other than Li^+ , like Na^+ , Mg^{2+} , and Ca^{2+} , affect the stability and electrochemical properties of LiFePO_4 . Ca^{2+} has the most adverse effect, and Na^+ does not show apparent influence at the potential range of -0.4 V to $+0.8 \text{ V}$. Dissolved oxygen also exacerbates the fading of LiFePO_4 by oxidizing LiFePO_4 particles irreversibly, which is demonstrated by the post-mortem XRD and Rietveld refinement. We put forward two approaches to address this issue. By decreasing dissolved oxygen (N_2 -flushing) concentration, the capacity retention is dramatically increased from 47% to 70% in 10 cycles in 5 mM LiCl + 50 mM NaCl . After carbon coating, the retention further increases to 82%, and the

energy consumption decreases to $3.0 \pm 0.5 \text{ W h mol}_{\text{Li}}^{-1}$. These two methods improve the performance stability of LiFePO_4 as a potential material for lithium extraction. While decreasing dissolved oxygen may not be practical to implement in scaled applications, the carbon coating of LiFePO_4 is a straightforward and promising approach.

Conflicts of interest

There are no conflicts to declare.

Acknowledgements

We acknowledge support for the MERLIN project from the RAG-Stiftung; the RAG-Stiftung generates long-term momentum for transforming the regions along the Ruhr and Saar Rivers and in Ibbenbüren. L. W. acknowledges funding from the China Scholarship Council (CSC) *via* award number 201906260277. The INM authors thank Eduard Arzt (INM) for his continuing support. Instrumentation and technical assistance for this work were provided by the Service Center X-ray Diffraction, with financial support from Saarland University and German Research Foundation (project number INST 256/349-1).

References

- 1 M. Li, J. Lu, Z. W. Chen and K. Amine, *Adv. Mater.*, 2018, **30**, 1800561.
- 2 S. Yang, F. Zhang, H. Ding, P. He and H. Zhou, *Joule*, 2018, **2**, 1648–1651.
- 3 T. G. Goonan, *Lithium use in batteries*, 2012.
- 4 P. Meshram, B. D. Pandey and T. R. Mankhand, *Hydrometallurgy*, 2014, **150**, 192–208.
- 5 J. A. Epstein, E. M. Feist, J. Zmora and Y. Marcus, *Hydrometallurgy*, 1981, **6**, 269–275.
- 6 L. Tian, W. Ma and M. Han, *Chem. Eng. J.*, 2010, **156**, 134–140.
- 7 S. Zandevakili, M. Ranjbar and M. Ehteshamzadeh, *Hydrometallurgy*, 2014, **149**, 148–152.
- 8 X. Liu, X. Chen, L. He and Z. Zhao, *Desalination*, 2015, **376**, 35–40.
- 9 N. Kim, X. Su and C. Kim, *Chem. Eng. J.*, 2020, 127715, DOI: 10.1016/j.cej.2020.127715.
- 10 X. Xu, Y. Chen, P. Wan, K. Gasem, K. Wang, T. He, H. Adidharma and M. Fan, *Prog. Mater. Sci.*, 2016, **84**, 276–313.
- 11 H.-J. Hong, I.-S. Park, J. Ryu, T. Ryu, B.-G. Kim and K.-S. Chung, *Chem. Eng. J.*, 2015, **271**, 71–78.
- 12 T. Ryu, J. Shin, D.-H. Lee, J. Ryu, I. Park, H. Hong, B.-G. Kim, J. B. Lee, Y. S. Huh and K.-S. Chung, *Mater. Chem. Phys.*, 2015, **167**, 225–230.
- 13 R. Trócoli, A. Battistel and F. L. Mantia, *Chem.–Eur. J.*, 2014, **20**, 9888–9891.
- 14 H. Yoon, J. Lee, S. Kim and J. Yoon, *Sep. Purif. Technol.*, 2019, **215**, 190–207.
- 15 S. Kim, H. Joo, T. Moon, S.-H. Kim and J. Yoon, *Environ. Sci.: Processes Impacts*, 2019, **21**, 667–676.

- 16 E. Guyot, S. Seghir, S. Diliberto, J.-M. Lecuire and C. Boulanger, *Electrochem. Commun.*, 2012, **23**, 29–32.
- 17 H. Kanoh, K. Ooi, Y. Miyai and S. Katoh, *Sep. Sci. Technol.*, 1993, **28**, 643–651.
- 18 M. Pasta, A. Battistel and F. La Mantia, *Energy Environ. Sci.*, 2012, **5**, 9487.
- 19 R. Trócoli, A. Battistel and F. La Mantia, *ChemSusChem*, 2015, **8**, 2514–2519.
- 20 J.-S. Kim, Y.-H. Lee, S. Choi, J. Shin, H.-C. Dinh and J. W. Choi, *Environ. Sci. Technol.*, 2015, **49**, 9415–9422.
- 21 Z. Ma, Y. Fan, G. Shao, G. Wang, J. Song and T. Liu, *ACS Appl. Mater. Interfaces*, 2015, **7**, 2937–2943.
- 22 M. Aslan, M. Zeiger, N. Jäckel, I. Grobelsek, D. Weingarth and V. Presser, *J. Phys.: Condens. Matter*, 2016, **28**, 114003.
- 23 H. Shim, Ö. Budak, V. Haug, M. Widmaier and V. Presser, *Electrochim. Acta*, 2020, 135760.
- 24 S. Porada, A. Shrivastava, P. Bukowska, P. Biesheuvel and K. C. Smith, *Electrochim. Acta*, 2017, **255**, 369–378.
- 25 J. Wu, G. K. P. Dathar, C. Sun, M. G. Theivanayagam, D. Applestone, A. G. Dylla, A. Manthiram, G. Henkelman, J. B. Goodenough and K. J. Stevenson, *Nanotechnology*, 2013, **24**, 424009.
- 26 T. Palaniselvam, H. B. Aiyappa and S. Kurungot, *J. Mater. Chem.*, 2012, **22**, 23799–23805.
- 27 N. Elgrishi, K. J. Rountree, B. D. McCarthy, E. S. Rountree, T. T. Eisenhart and J. L. Dempsey, *J. Chem. Educ.*, 2018, **95**, 197–206.
- 28 Z. Zhao, X. Si, X. Liu, L. He and X. Liang, *Hydrometallurgy*, 2013, **133**, 75–83.
- 29 Q. Huang, Q. Luo, Z. Chen, L. Yao, P. Fu and Z. Lin, *Environ. Sci.: Water Res. Technol.*, 2018, **4**, 1145–1151.
- 30 F. Gao and Z. Tang, *Electrochim. Acta*, 2008, **53**, 5071–5075.
- 31 T. Jacobsen and K. West, *Electrochim. Acta*, 1995, **40**, 255–262.
- 32 J. Huang, *Electrochim. Acta*, 2018, **281**, 170–188.
- 33 M. Gu, W. Shi, J. Zheng, P. Yan, J.-g. Zhang and C. Wang, *Appl. Phys. Lett.*, 2015, **106**, 203902.
- 34 C. Delacourt, P. Poizot, J.-M. Tarascon and C. Masquelier, *Nat. Mater.*, 2005, **4**, 254–260.
- 35 P. Gibot, M. Casas-Cabanas, L. Laffont, S. Levasseur, P. Carlach, S. Hamelet, J.-M. Tarascon and C. Masquelier, *Nat. Mater.*, 2008, **7**, 741–747.
- 36 H. Gabrisch, J. Wilcox and M. M. Doeff, *ECS Trans.*, 2019, **3**, 29–36.
- 37 J. Wang and X. Sun, *Energy Environ. Sci.*, 2012, **5**, 5163–5185.
- 38 J. Li, Q. Qu, L. Zhang, L. Zhang and H. Zheng, *J. Alloys Compd.*, 2013, **579**, 377–383.
- 39 P. He, J.-L. Liu, W.-J. Cui, J.-Y. Luo and Y.-Y. Xia, *Electrochim. Acta*, 2011, **56**, 2351–2357.

Supporting Information

Electrochemical lithium recovery with lithium iron phosphate: What causes performance degradation and how can we improve the stability?

Lei Wang,^{1,2} Kathleen Frisella,^{1,2} Pattarachai Srimuk,^{1,2}
Oliver Janka,³ Guido Kickelbick,³ Volker Presser,^{1,2,*}

¹ *INM - Leibniz Institute for New Materials, D2 2, 66123, Saarbrücken, Germany*

² *Department of Materials Science & Engineering, Saarland University, Campus D2 2, 66123, Saarbrücken, Germany*

³ *Inorganic Solid State Chemistry, Saarland University, Campus C4 1, 66123 Saarbrücken, Germany*

* Corresponding author's email: volker.presser@leibniz-inm.de

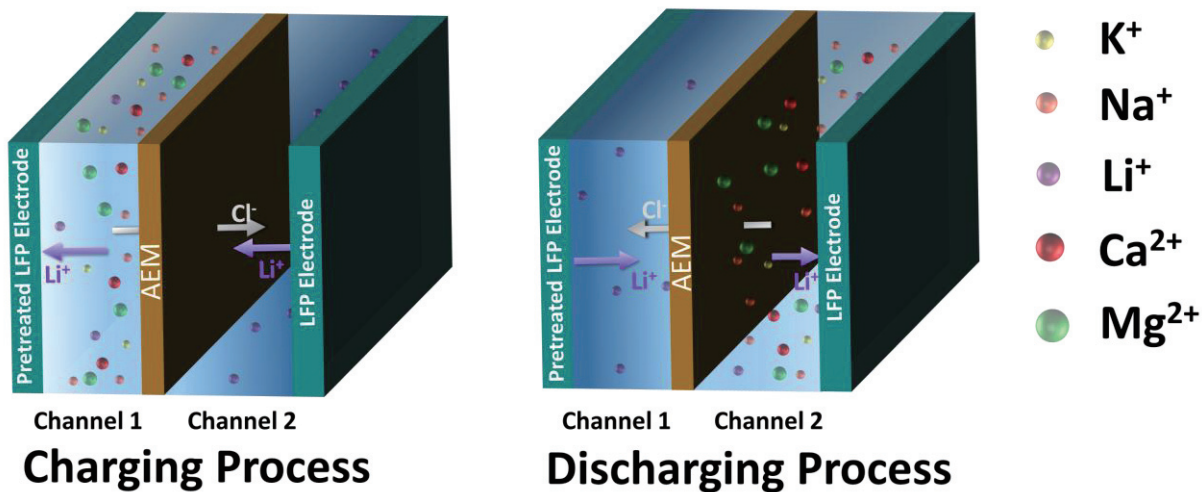


Figure S1. Schematic diagram of the principle of symmetric LiFePO₄ electrode during the charging and discharging process

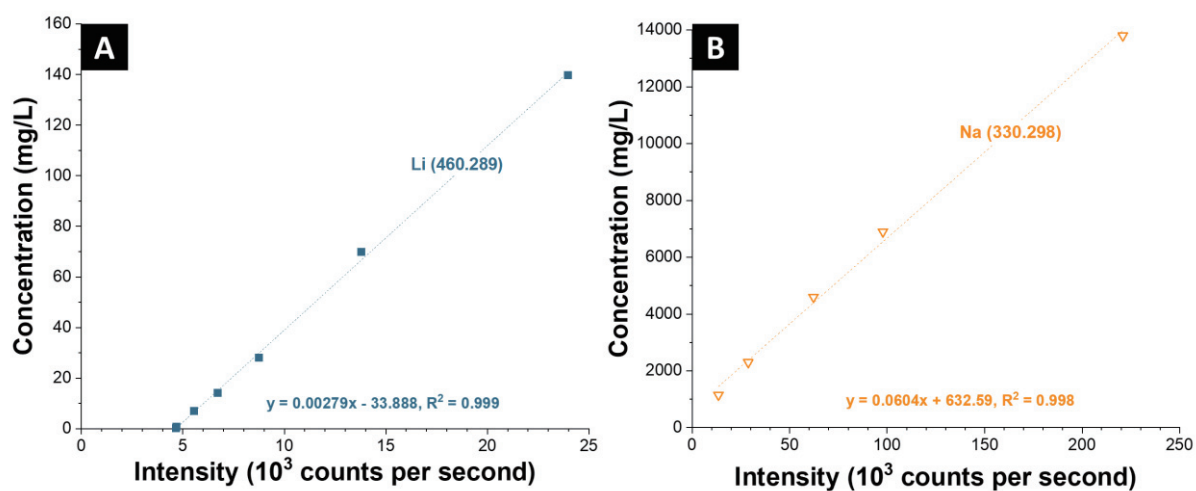


Figure S2. Calibration curves (i.e., the relation of ion concentration and characteristic peak intensity) of lithium (A) and sodium (B).

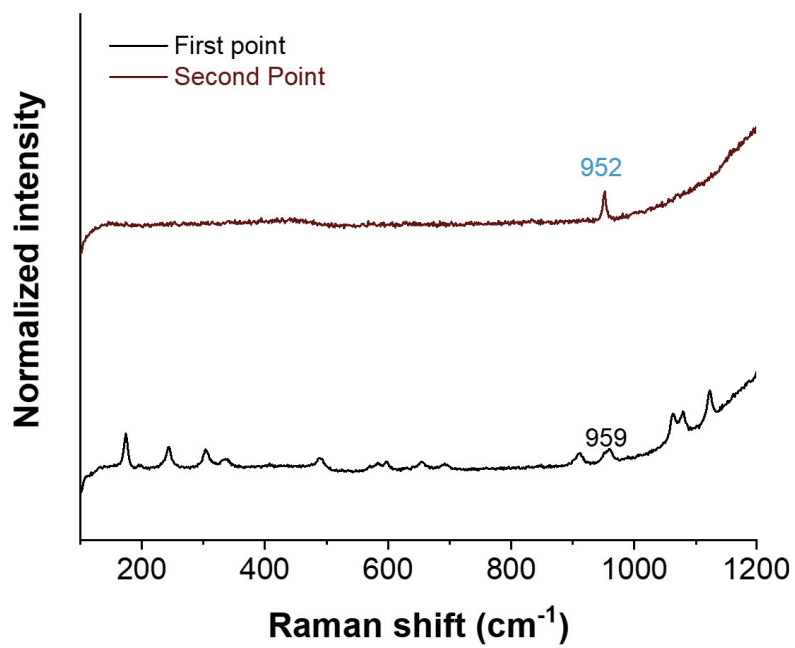


Figure S3. Raman spectra of delithiated LiFePO_4 recorded at different point on the sample.

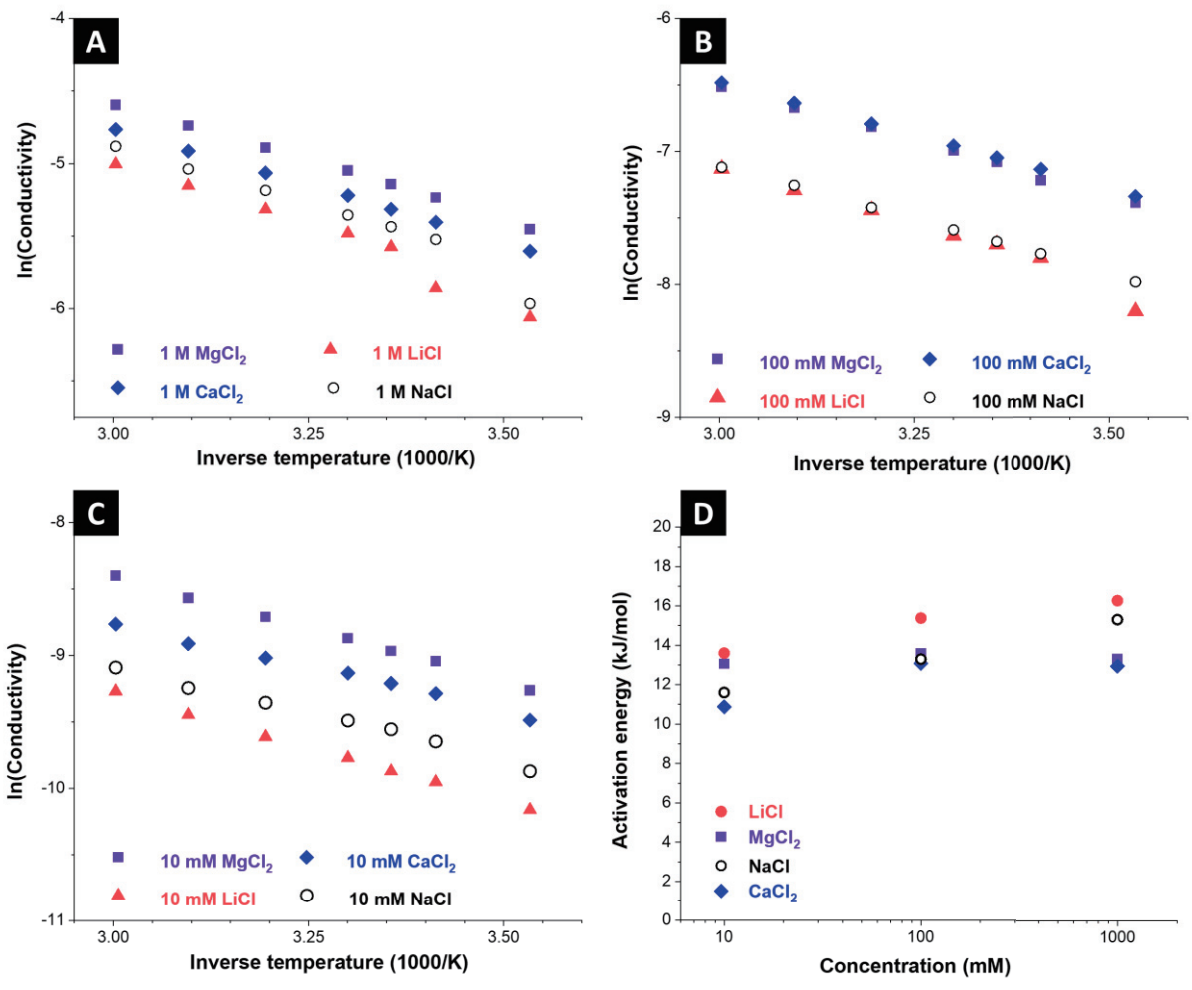


Figure S4. Plot of the electrolyte conductivity as a function of the reciprocal of the temperature (T^{-1}) in 1 mM (A), 100 mM (B), and 10 mM (C) LiCl, NaCl, MgCl_2 and CaCl_2 electrolyte and the activation energy of Na^+ , Li^+ , Mg^{2+} , and Ca^{2+} at various concentration (D).

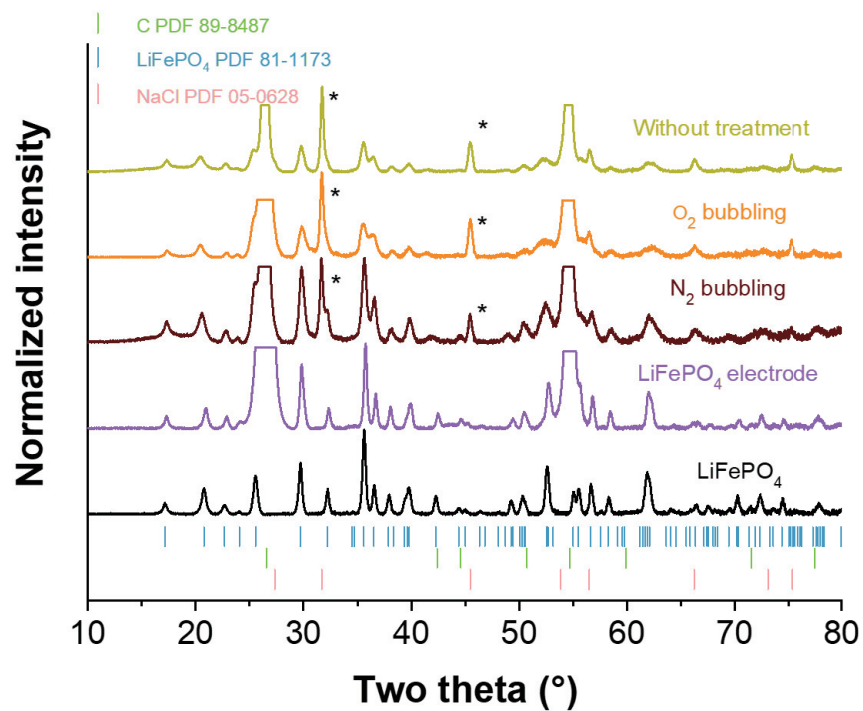


Figure S5. The post-mortem X-ray diffractograms of LiFePO₄ after 100 cycles in 5 mM LiCl + 50 mM NaCl with N₂-flushing, O₂-flushing, and without pre-treatment. The diffraction pattern were normalized to the reflections not associated with the graphite foil.

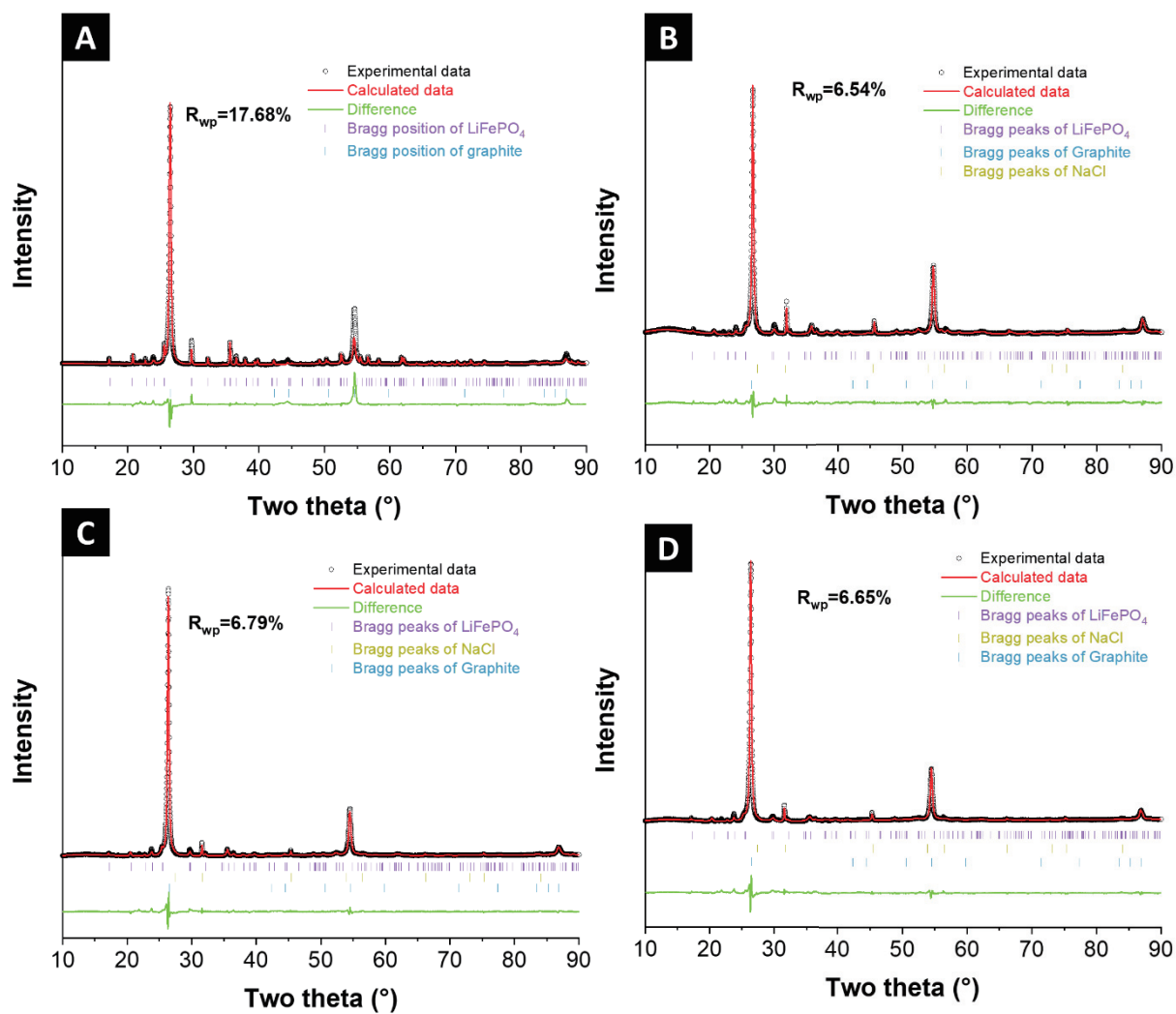


Figure S6. The X-ray Rietveld refinement fitting of initial LiFePO₄ electrode (A) and LiFePO₄ electrode after 100 cycles in 5 mM LiCl + 50 mM NaCl with without pre-treatment (B), N₂-flushing (C), and O₂-flushing (D).

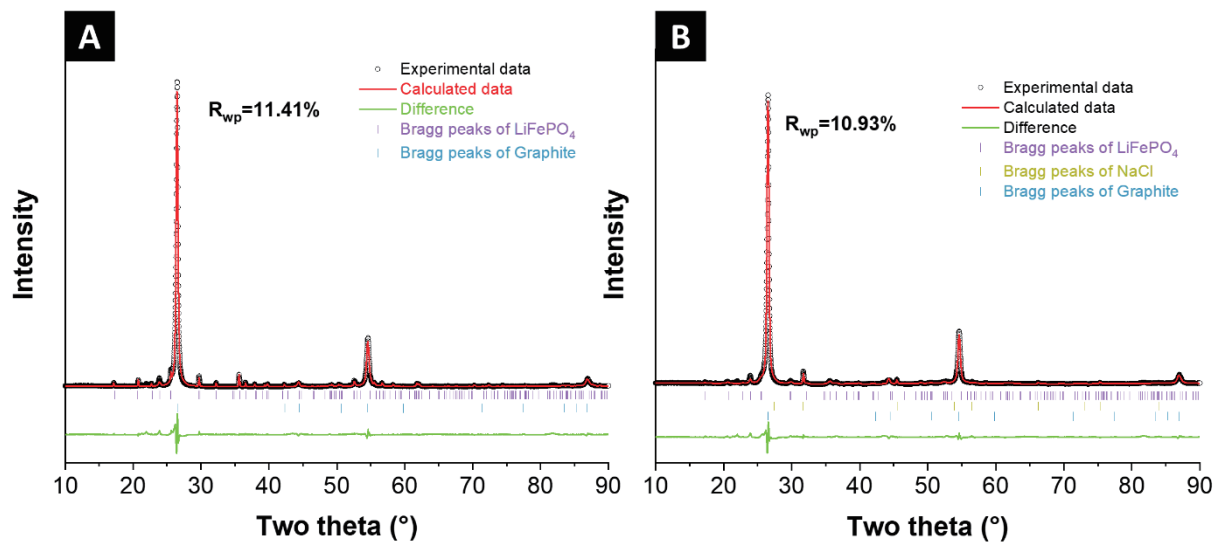


Figure S7. X-ray Rietveld refinement fitting of the initial LiFePO_4/C electrode (A), and the LiFePO_4/C electrode after 100 cycles in aqueous 5 mM LiCl + 50 mM NaCl .

Table S1: The concentration of dissolved oxygen after O₂-flushing and N₂-flushing.

Condition	Concentration of O ₂ (ppm)
Initial	8.8
O ₂ bubbling for 24 h	12.5
N ₂ bubbling for 24 h	4.0

Table S2: Results of the elemental analysis (CHNS).

Sample	Carbon content (mass%)
LiFePO ₄	2.4±0.6
LiFePO ₄ /C	4.4±0.7

Table S3: The formal potential of LiFePO₄ in LiCl, NaCl, MgCl₂ and CaCl₂ with the concentration of 1 M, 100 mM, and 10 mM.

Electrolyte	Average potential E _f (V vs. Ag/AgCl)
1 M LiCl	0.18
1 M NaCl	0.08
1 M MgCl ₂	0.1
1 M CaCl ₂	0.07
100 mM LiCl	0.12
100 mM NaCl	0.09
100 mM MgCl ₂	0.10
100 mM CaCl ₂	0.03
10 mM LiCl	0.09
10 mM NaCl	0.07
10 mM MgCl ₂	0.08
10 mM CaCl ₂	0.06

4.7 Redox flow battery for continuous and energy-effective lithium recovery from aqueous solution

Lei Wang,^{1,2} Stefanie Arnold,^{1,2} Panyu Ren,^{1,2}

Qingsong Wang,¹ Jun Jin,³ Zhaoyin Wen,^{3,4} and Volker Presser^{1,2,5}

¹ INM - Leibniz Institute for New Materials, 66123, Saarbrücken, Germany

² Department of Materials Science & Engineering, Saarland University, 66123, Saarbrücken, Germany

³ CAS Key Laboratory of Materials for Energy Conversion Shanghai Institute of Ceramics, Chinese Academy of Sciences, Shanghai, 200050 P. R. China

⁴ State Key Lab of High Performance Ceramics and Superfine Microstructure, Shanghai Institute of Ceramics, Chinese Academy of Sciences, Shanghai, 200050 P. R. China

⁵ Saarene, Saarland Center for Energy Materials and Sustainability, 66123 Saarbrücken, Germany

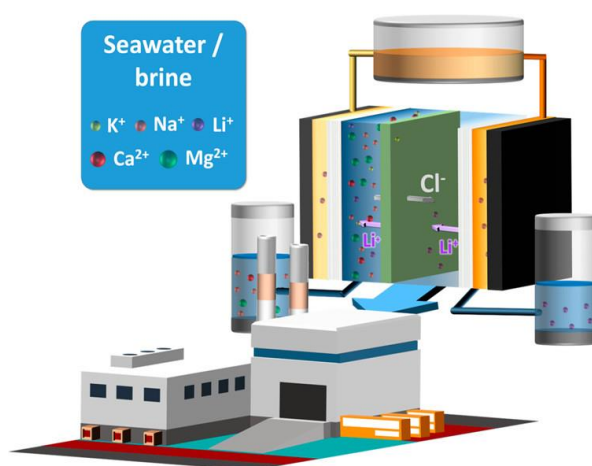
Citation:

L. Wang, S. Arnold, P. Ren, Q. Wang, J. Jin, Z. Wen, V. Presser, REDOX FLOW BATTERY FOR CONTINUOUS AND ENERGY-EFFECTIVE LITHIUM RECOVERY FROM AQUEOUS SOLUTION, **ACS Energy Letters**, 7 (2022) 3539-3544.

DOI: 10.1021/acsenergylett.2c01746.

Own contribution:

Conceptualization, Formal Analysis, Investigation, Visualization, Writing-Original Draft, Writing - Review & Editing



Redox Flow Battery for Continuous and Energy-Effective Lithium Recovery from Aqueous Solution

Lei Wang, Stefanie Arnold, Panyu Ren, Qingsong Wang, Jun Jin, Zhaoyin Wen,* and Volker Presser*

Cite This: *ACS Energy Lett.* 2022, 7, 3539–3544

Read Online

ACCESS |



Metrics & More

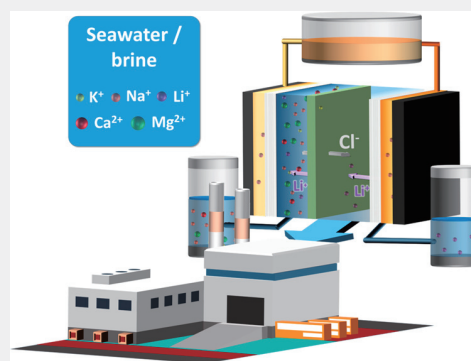


Article Recommendations



Supporting Information

ABSTRACT: Lithium-ion batteries are the primary power source for electric vehicles and portable electronic devices, creating a massive demand to mine and extract lithium. So far, lithium extraction has focused on brine and geological deposits. Yet, access to the enormous amount of lithium (at low concentration) in the earth's oceans and other aqueous media remains challenging. Electrodialysis with Li-selective ceramic membranes could effectively separate lithium from seawater but at a high energy cost. Reversible electrochemical processes, like redox flow batteries, can overcome the limitation of electrodialysis-based systems. Herein we propose a system combining Li-selective ceramic membranes and a simple redox flow electrolyte to accomplish continuous lithium recovery from seawater. The lithium-extraction redox flow battery (LE-RFB) extracts dissolved lithium with a purity of 93.5% from simulated seawater, corresponding to a high Li/Mg selectivity factor of about 500,000:1. Benefiting from a low operating voltage, 1 g of lithium is extracted with only 2.5 Wh of energy consumption.



With the universal usage of portable electronic equipment and electric vehicles, the demand for lithium-ion batteries has increased tremendously.¹ This sharply increasing consumption would result in a complete depletion of terrestrial lithium before this century is over.² Thereby, it is crucial to find alternative lithium reservoirs and environmentally friendly ways for lithium extraction. Apart from recycling lithium from abandoned lithium-ion batteries, seawater is another available lithium reserve containing 230 billion tons of lithium.³ However, the low lithium concentration (around 0.17 mg_{Li}/L on average) and high concentration of other competing cations, like Na⁺ and Mg²⁺, bring tremendous challenges to extracting lithium from seawater.^{3,4} So far, several approaches, such as coprecipitation,⁵ sorption,⁶ liquid–liquid extraction,⁷ membrane processes,⁸ and electrochemical methods,^{9,10} have been adapted to recover lithium from seawater.¹¹ However, coprecipitation, liquid–liquid extraction, and sorbent regeneration require many chemicals and are energy-costly and time-consuming.¹² In addition, while membrane-based processes can continuously extract lithium, this technology suffers from the low selectivity factor of the commercial membranes.¹³

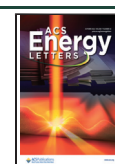
Electrochemical methods are an energy-efficient approach with relatively high selectivity toward Li⁺, as recent studies show. For example, Joo et al. used an electrode pair of λ-MnO₂

and AgCl to treat the actual desalination of concentrated seawater on a pilot scale.¹⁴ After the enrichment, the purity of Li⁺ increased from 0.0048 to 88%.¹⁴ In another example, an electrolysis-based technique was proposed to extract lithium from seawater utilizing a solid-state lithium superionic conductor membrane (LISICON membrane).² On the cathode side, elemental lithium metal was formed, while the Cl₂ or O₂ was produced in the anode area. However, the electrochemical methods have not yet been able to perform continuous lithium recovery with the typical cell configuration (i.e., a lithium-capture electrode + a chloride-capture electrode or a cation-release electrode).^{15,16} Kim et al. proposed a hybrid system with a redox flow battery system and lithium-selective adsorbent.¹⁷ In this system, the water can be continuously desalinated, while the lithium recovery process is not continuous. Meanwhile, the regeneration of adsorbents consumes acid. Recently, Li et al.¹⁸ put forward a continuous electrical pump membrane process, where a Li_{0.33}La_{0.56}TiO₃

Received: August 2, 2022

Accepted: September 14, 2022

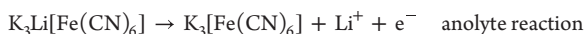
Published: September 23, 2022



membrane accomplished the selective extraction of lithium; the catalytic reactions occurred on the cathode and anode sides formed the driven force for lithium migration. After the treatment, the lithium concentration increased from 0.2 mg/L to 9 g/L. However, due to the high voltage, the energy consumption to enrich 1 kg of lithium is about 76 kWh. With humankind striving for more sustainable technologies, there is a high demand for an economical approach with continuous operation, a high selectivity factor, and low energy consumption for the large-scale lithium extraction from the seawater.

This work reports an innovative electrochemical cell configuration for continuously recovering lithium from seawater. Our system strives toward low-cost materials and environmental friendliness. The lithium-extraction redox flow battery (LE-RFB) uses a redox pair electrolyte ($\text{Fe}[\text{CN}]_6^{4-}/\text{Fe}[\text{CN}]_6^{3-}$) and operates at a low applied voltage of just 600 mV for continuous lithium extraction. The LE-RFB shows an excellent selectivity toward Li^+ with a low energy consumption of 2.5 Wh/g $_{\text{Li-extraction}}$. We also demonstrate the universal usage of this system with various lithium concentrations from seawater (ca. 0.17 mg/L) to lithium-rich brines (>1000 mg/L).

The LE-RFB cell contains four channels: one recovery-solution channel, one feedwater channel, and two redox-electrolyte channels (Figure 1A; Experimental Methods, Table S1, and Figure S1 in Supporting Information). The recovery-solution channel and the feedwater channel are each separated from the redox-electrolyte channels by a LISICON membrane. A polymer anion exchange membrane localized between the recovery-solution and feedwater channels serves to separate different compartments. During operation, the charging process results in the enrichment of lithium in the recovery-solution channel and the uptake of lithium from the feedwater channel. The ferricyanide is reduced to the ferrocyanide in the cathode area, drawing one cation (i.e., Li^+), on the basis of the selectivity of LISICON membrane from the feedwater channel into the redox-electrolyte reservoir. At the other end, the ferrocyanide in the anode area is oxidized into ferricyanide, releasing lithium into the recovery solution through the LISICON membrane. Simultaneously, the Cl^- will migrate through the anion exchange membrane to keep the charge balanced. The reactions in the anolyte and catholyte are shown as follows. These reactions are continuously ongoing because the initial redox electrolyte contains equimolar ferricyanide and ferrocyanide, and with this continuous circulation, the uptaken Li^+ is continuously brought from the catholyte through the redox-electrolyte reservoir to the anolyte.



As the core component of the LE-RFB system, the LISICON membrane plays the role of selectively uptaking and releasing Li^+ . The LISICON membrane used in this work consists of $\text{Li}_{1+x}\text{Al}_x\text{Ge}_{2-x}(\text{PO}_4)_3$ ($x = 0.5$, LAGP), prepared by a solid-state-reaction method as reported previously^{19,20} and as described in the Experimental Methods in the Supporting Information. Cross-sectional scanning electron micrographs confirm the presence of a dense membrane, having a thickness of about 500 μm without cracks (Figure 1B). The grain size of the particles ranges from 100 nanometers to several micro-

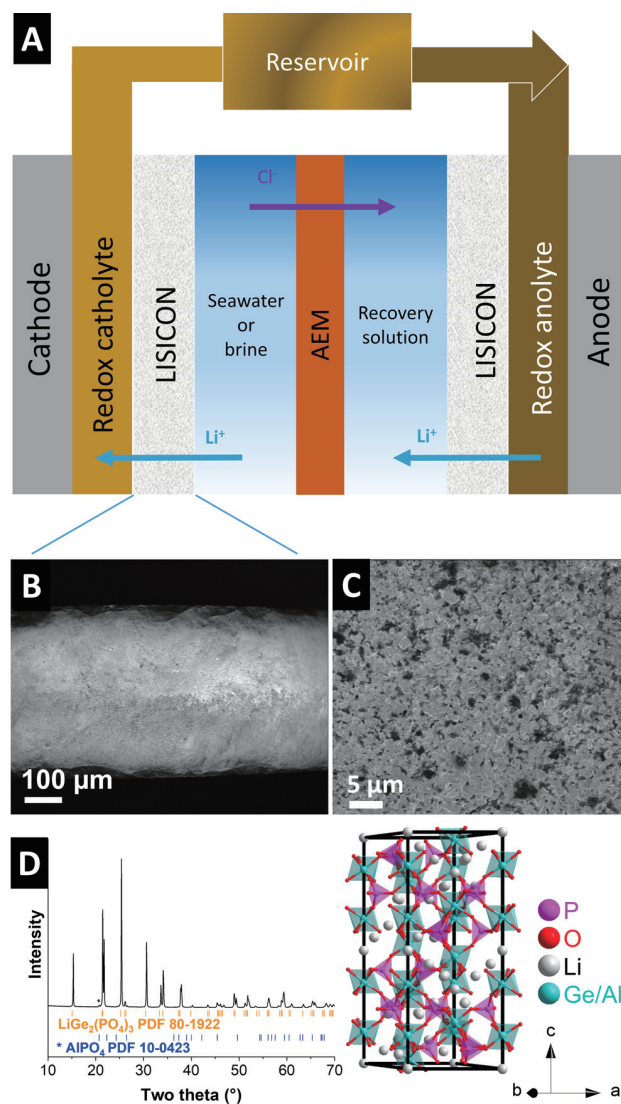


Figure 1. (A) The schematic images of a lithium-extraction redox flow battery. Cross-sectional scanning electron micrograph of the LISICON membrane at (B) low and (C) high magnification. (D) X-ray diffraction patterns of the LISICON membrane and the structure of $\text{Li}_{1+x}\text{Al}_x\text{Ge}_{2-x}(\text{PO}_4)_3$; the crystal structure is based on ref 40.

meters (Figure 1C), similar to that in the reported work.²¹ The energy-dispersive X-ray mapping results (Supporting Information, Figure S2) also suggest that the distribution of elements is uniform, indicating the membrane is very homogeneous. LAGP is a superionic conductor with lower energy barriers for the migration of Li^+ compared to other cations²¹ and superior stability in aqueous media^{22,23} (Figure 1D). The crystal structure of the membrane was verified using the XRD pattern of the LISICON membrane, which is consistent with the standard pattern of $\text{LiGe}_2(\text{PO}_4)_3$ (Figure 1D). There is a small reflection at $20.7^\circ 2\theta$, which aligns with trace amounts of AlPO_4 , the common impurity of the LAGP ceramic membrane.²⁴ The Li^+ conductivity of the LAGP membrane is around $1.2 \times 10^{-4} \text{ S cm}^{-1}$, calculated according to the impedance results in the Supporting Information, Figure S3.

To demonstrate the feasibility and investigate the performance of the LE-RFB system, we first explored LE-RFB for Li^+

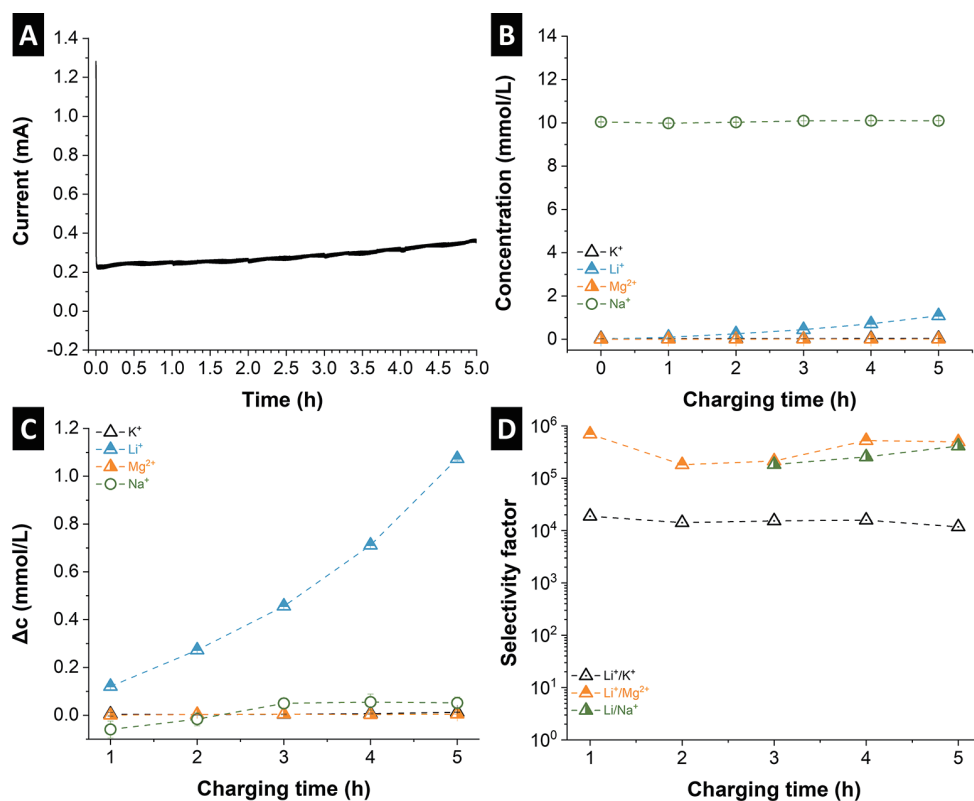


Figure 2. Lithium extraction from seawater by a lithium-extraction redox flow battery: (A) current curve, (B) concentration, (C) concentration change of cations in the recovery solution, and (D) selectivity factors between Li^+ and other cations at different times.

extraction in simulated seawater ($24 \mu\text{M Li}^+$; see Tables S1 and S2 in the Supporting Information). Figure 2A shows the trend of current change with increasing charging time. When the cell is charged at 0.6 V, the current increases from 0.22 to 0.36 mA. This is linked to the rise of the lithium-ion concentration in the recovery solution (Figure 2B), which also lowers the system resistance. In contrast to the Li^+ concentration, the other cations only change slightly. The concentration of Ca^{2+} is below the detection limit and is, therefore, not displayed. For better visualization of the cation concentration changes, we calculated the differences between the concentration at different charging times and the initial concentration of the recovery solution, as shown in Figure 2C. As it can be seen, the concentration of Li^+ increases by $1.07 \pm 0.06 \text{ mM}$ after a 5 h enrichment, while the concentrations of K^+ , Na^+ , and Mg^{2+} are $1.3 \times 10^{-2} \pm 1.1 \times 10^{-3} \text{ mM}$, $5.1 \times 10^{-2} \pm 2.4 \times 10^{-2} \text{ mM}$, and $5.0 \times 10^{-3} \pm 6.2 \times 10^{-5} \text{ mM}$, respectively.

To confirm that the enriched Li^+ originated from the feedwater and not from the Li^+ in the redox electrolyte, we measured the concentration of all the cations in the redox electrolyte (Supporting Information, Table S1). The Li^+ concentration in the redox electrolyte remains stable at a concentration of 9.35–9.37 mM, concluding that Li^+ in the recovery solution comes, indeed, just from the feedwater. Additionally, pH values of the redox electrolyte were continuously controlled to stay between 6 and 7 before and after the lithium recovery experiment. This is a crucial benefit for redox couples that can achieve better functioning with outstanding electrochemical stability.²⁵

The LE-RFB system shows excellent selectivity of Li^+ toward other cations. The selectivity factors of $K_{\text{Li}/\text{K}}$, $K_{\text{Li}/\text{Na}}$, and $K_{\text{Li}/\text{Mg}}$

after the 5 h enrichment are 1.2×10^4 , 4.1×10^5 , and 5.0×10^5 , respectively (Figure 2D). These extremely high selectivities yield a Li^+ purity of 93.5% in the extract. Mg^{2+} , which strongly influences the chemical precipitation of Li^+ , is present at a ratio of 0.43% (Supporting Information, Figure S4). The absence of $K_{\text{Li}/\text{Na}}$ at 1 and 2 h is due to the concentration change at these two data points being less than the standard error.

Much higher Li^+ concentrations than in seawater can be found, for example, in brines. Subsequently, we used brine with a Li^+ concentration of 210 mM (see Table S2 in Supporting Information) to demonstrate that the LE-RFB system is suitable for lithium extraction from a low to a high concentration. When brine is used as the feedwater, the amount of Mg^{2+} (0.21%) in the extracts is similar. In contrast, more K^+ and Na^+ (accounting for 4.48 and 30.7%, respectively) migrate into the recovery solution (Supporting Information, Figure S5). This may indicate a gradual reduction in membrane selectivity over time due to the changes in structure, composition, and inhomogeneous mechanical stress.^{26,27}

The lithium-extraction rate and energy consumption are other important parameters to evaluate the system's performance. The average lithium-extraction rate of LE-RFB is $0.04 \text{ mg/cm}^2/\text{h}$, which is comparable to other technologies for Li^+ extraction from seawater (Figure 3).^{18,28–30} However, only 2.5 Wh is consumed for extracting 1 g of Li^+ , which is at least 7 times lower than the electro dialysis-based technologies, which show a similar lithium purification effect (Figure 3). Considering the global average cost of the electricity fee (0.13 US\$ per kWh), the energy cost of this system would at least save 2.2 US\$ to extract 1 kg of lithium ions from seawater.

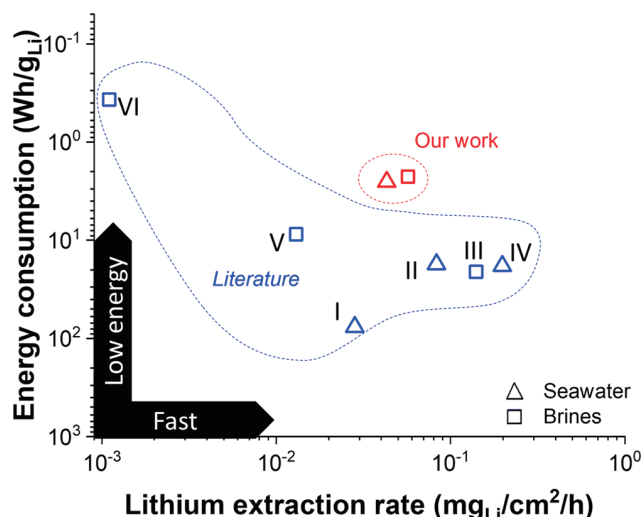


Figure 3. Comparison of lithium-extraction energy consumption and lithium-extraction rate for different extraction technologies. Data I, II, III, IV, V, and VI from refs 18, 29, 30, 28, 41, and 15, respectively.

This phenomenon is due to the low voltage of the system. Concerning lithium extraction from brines, our LE-RFB system is also energy efficient with the consumption of 2.3 Wh/g_{Li}, compared with nanofiltration (30–50 Wh/g_{Li})¹³ or an electro dialysis system (2–50 Wh/g_{Li}).^{31–33} The electrochemical ion pumping system is another popular electrochemical lithium-extraction system, generally utilizing LiFePO₄ or LiMn₂O₄ as the lithium-selective electrodes.³⁴ The energy consumption of this technology (0.1–3.0 Wh/g_{Li})³⁵ is lower than the LE-RFB system due to the energy recovery process. However, the ion pumping system could not accomplish continuous lithium extraction and suffers from switching between feedwater and recovery solution, which is time-consuming.

Herein, we present a brief technoeconomic analysis exploring the feasibility of LE-RFB for the industrial application (key economic price assumption shown in the Supporting Information, Table S3). Assuming an LE-RFB system with an effective area of 1 m², 18.4 kg of Li₂CO₃ could be produced per year (with a lithium-extraction rate of 0.04 mg/cm²/h), valued at 1256 US\$. That means the system requires about 6 years to compensate for the initial investment cost and energy consumption (excluding the cost of the pump and electricity consumed by the pump). The key costs relate to pumping energy (1130 US\$), which could be addressed by enhancing the lithium recovery rate by using thinner membranes/membranes with more rapid Li⁺ transport.

Further improvements to the LE-RFB system will leverage synergetic advances in ceramic solid electrolyte technology. For example, very thin ceramic membranes of just 55 μm have been reported (meaning a higher lithium-ion extraction rate), although such thin membranes bring further requirements for an improved cell design to avoid mechanical failure.¹⁸ Flexible hybrid organic–inorganic LAGP membranes have been synthesized, which could address the mechanical drawback of ceramic membranes, though the ion selectivity of hybrid membranes should be investigated.³⁶ The possible approaches for the improvement of our system could be but are not limited to optimizing the operation parameters,³⁷ using a LISICON membrane with higher Li⁺ permeance and ionic

conductivity, optimized electrodes with high specific surface area and fluid permeability, and improved flow fields for uniform distribution of redox chemicals across the electrode surface.

In summary, we have demonstrated a continuous electrochemical lithium-extraction battery that utilizes flow redox electrolytes and LISICON membranes to mine lithium from aqueous solutions. Among the extracted ions from seawater, Li⁺ predominates with a content of 93.5%. Using the redox pairs of Fe[CN]₆³⁻/Fe[CN]₆⁴⁻, the battery runs greenly, with no toxic byproducts, no safety concerns, and low energy consumption of 2.5 Wh/g_{Li}, which means less emission of CO₂. Furthermore, a LE-RFB system can utilize feedwater with varying chemical compositions. We see the potential of the LE-RFB system for lithium extraction from acidic leaching solution of spent lithium-ion batteries via hydrometallurgical processing.^{38,39}

ASSOCIATED CONTENT

Supporting Information

The Supporting Information is available free of charge at <https://pubs.acs.org/doi/10.1021/acseenergylett.2c01746>.

Full description of the experimental methods, calculation methods, photographs, results from energy-dispersive X-ray spectroscopy, and supplemental lithium-extraction performance (PDF)

AUTHOR INFORMATION

Corresponding Authors

Zhaoyin Wen – CAS Key Laboratory of Materials for Energy Conversion, Shanghai Institute of Ceramics, Chinese Academy of Sciences, Shanghai 200050, P. R. China; State Key Lab of High Performance Ceramics and Superfine Microstructure, Shanghai Institute of Ceramics, Chinese Academy of Sciences, Shanghai 200050, P. R. China; orcid.org/0000-0003-1698-7420; Email: zywen@mail.sic.ac.cn

Volker Presser – INM - Leibniz Institute for New Materials, 66123 Saarbrücken, Germany; Department of Materials Science & Engineering, Saarland University, 66123 Saarbrücken, Germany; Saarene, Saarland Center for Energy Materials and Sustainability, 66123 Saarbrücken, Germany; orcid.org/0000-0003-2181-0590; Email: volker.presser@leibniz-inm.de

Authors

Lei Wang – INM - Leibniz Institute for New Materials, 66123 Saarbrücken, Germany; Department of Materials Science & Engineering, Saarland University, 66123 Saarbrücken, Germany

Stefanie Arnold – INM - Leibniz Institute for New Materials, 66123 Saarbrücken, Germany; Department of Materials Science & Engineering, Saarland University, 66123 Saarbrücken, Germany

Panyu Ren – INM - Leibniz Institute for New Materials, 66123 Saarbrücken, Germany; Department of Materials Science & Engineering, Saarland University, 66123 Saarbrücken, Germany

Qingsong Wang – INM - Leibniz Institute for New Materials, 66123 Saarbrücken, Germany; Present Address: Bavarian Center for Battery Technology (BayBatt), University of Bayreuth, Universitätsstrasse 30, 95447 Bayreuth, Germany and Department of Chemistry, University of

Bayreuth, Universitätsstrasse 30, 95447 Bayreuth, Germany; orcid.org/0000-0001-5879-8009

Jun Jin – CAS Key Laboratory of Materials for Energy Conversion, Shanghai Institute of Ceramics, Chinese Academy of Sciences, Shanghai 200050, P. R. China

Complete contact information is available at:

<https://pubs.acs.org/10.1021/acseenergylett.2c01746>

Notes

The authors declare no competing financial interest.

ACKNOWLEDGMENTS

The authors thank Eduard Arzt (INM) for his continuing support. L.W. acknowledges funding from the China Scholarship Council (CSC) via award number 201906260277. We acknowledge support for the eLiRec project and eWeWa project by the European Union from the European Regional Development Fund (EFRE) and the State of Saarland, Germany.

REFERENCES

- (1) Greim, P.; Solomon, A. A.; Breyer, C. Assessment of lithium criticality in the global energy transition and addressing policy gaps in transportation. *Nat. Commun.* **2020**, *11* (1), 4570.
- (2) Yang, S.; Zhang, F.; Ding, H.; He, P.; Zhou, H. Lithium metal extraction from seawater. *Joule* **2018**, *2* (9), 1648–1651.
- (3) Diallo, M. S.; Kotte, M. R.; Cho, M. Mining critical metals and elements from seawater: Opportunities and challenges. *Environ. Sci. Technol.* **2015**, *49* (16), 9390–9399.
- (4) Zhao, X.; Yang, H.; Wang, Y.; Sha, Z. Review on the electrochemical extraction of lithium from seawater/brine. *J. Electroanal. Chem.* **2019**, *850*, 113389.
- (5) Um, N.; Hirato, T. Precipitation behavior of $\text{Ca}(\text{OH})_2$, $\text{Mg}(\text{OH})_2$, and $\text{Mn}(\text{OH})_2$ from CaCl_2 , MgCl_2 , and MnCl_2 in $\text{NaOH-H}_2\text{O}$ solutions and study of lithium recovery from seawater via two-stage precipitation process. *Hydrometallurgy* **2014**, *146*, 142–148.
- (6) Liu, C.; Tao, B.; Wang, Z.; Wang, D.; Guo, R.; Chen, L. Preparation and characterization of lithium ion sieves embedded in a hydroxyethyl cellulose cryogel for the continuous recovery of lithium from brine and seawater. *Chem. Eng. Sci.* **2021**, *229*, 115984.
- (7) Harvianto, G. R.; Kim, S.-H.; Ju, C.-S. Solvent extraction and stripping of lithium ion from aqueous solution and its application to seawater. *Rare Metals* **2016**, *35* (12), 948–953.
- (8) Yu, C.; Lu, J.; Dai, J.; Dong, Z.; Lin, X.; Xing, W.; Wu, Y.; Ma, Z. Bio-inspired fabrication of Ester-functionalized imprinted composite membrane for rapid and high-efficient recovery of lithium ion from seawater. *J. Colloid Interface Sci.* **2020**, *572*, 340–353.
- (9) Liu, C.; Li, Y.; Lin, D.; Hsu, P.-C.; Liu, B.; Yan, G.; Wu, T.; Cui, Y.; Chu, S. Lithium extraction from seawater through pulsed electrochemical intercalation. *Joule* **2020**, *4* (7), 1459–1469.
- (10) Joo, H.; Lee, J.; Yoon, J. Short review: Timeline of the electrochemical lithium recovery system using the spinel LiMn_2O_4 as a positive electrode. *Energies* **2020**, *13* (23), 6235.
- (11) Santos, C.; La Mantia, F. Recent advances in reactor design and control for lithium recovery by means of electrochemical ion pumping. *Current Opinion in Electrochemistry* **2022**, *35*, 101089.
- (12) Swain, B. Recovery and recycling of lithium: A review. *Sep. Purif. Technol.* **2017**, *172*, 388–403.
- (13) Li, X.; Mo, Y.; Qing, W.; Shao, S.; Tang, C. Y.; Li, J. Membrane-based technologies for lithium recovery from water lithium resources: A review. *J. Membr. Sci.* **2019**, *591*, 117317.
- (14) Joo, H.; Kim, S.; Kim, S.; Choi, M.; Kim, S.-H.; Yoon, J. Pilot-scale demonstration of an electrochemical system for lithium recovery from the desalination concentrate. *Environ. Sci.: Water Res. Technol.* **2020**, *6* (2), 290–295.
- (15) Wang, L.; Frisella, K.; Srimuk, P.; Janka, O.; Kickelbick, G.; Presser, V. Electrochemical lithium recovery with lithium iron phosphate: what causes performance degradation and how can we improve the stability? *Sustainable Energy & Fuels* **2021**, *5* (12), 3124–3133.
- (16) Zhang, H.; Ren, Y.; Wu, X.; Wang, N. An interface-modified solid-state electrochemical device for lithium extraction from seawater. *J. Power Sources* **2021**, *482*, 228938.
- (17) Kim, N.; Su, X.; Kim, C. Electrochemical lithium recovery system through the simultaneous lithium enrichment via sustainable redox reaction. *Chemical Engineering Journal* **2021**, *420*, 127715.
- (18) Li, Z.; Li, C.; Liu, X.; Cao, L.; Li, P.; Wei, R.; Li, X.; Guo, D.; Huang, K.-W.; Lai, Z. Continuous electrical pumping membrane process for seawater lithium mining. *Energy Environ. Sci.* **2021**, *14* (5), 3152–3159.
- (19) Wang, Q.; Jin, J.; Wu, X.; Ma, G.; Yang, J.; Wen, Z. A shuttle effect free lithium sulfur battery based on a hybrid electrolyte. *Phys. Chem. Chem. Phys.* **2014**, *16* (39), 21225–21229.
- (20) Xu, X.; Wen, Z.; Wu, X.; Yang, X.; Gu, Z. Lithium ion-conducting glass-ceramics of $\text{Li}_{1.5}\text{Al}_{0.5}\text{Ge}_{1.5}(\text{PO}_4)_3\text{-xLi}_2\text{O}$ ($x = 0.0\text{--}0.20$) with good electrical and electrochemical properties. *J. Am. Ceram. Soc.* **2007**, *90* (9), 2802–2806.
- (21) Fu, L.; Teng, Y.; Liu, P.; Xin, W.; Qian, Y.; Yang, L.; Lin, X.; Hu, Y.; Kong, X.-Y.; Jiang, L.; et al. Electrochemical ion-pumping-assisted transfer system featuring a heterogeneous membrane for lithium recovery. *Chemical Engineering Journal* **2022**, *435*, 134955.
- (22) Zhang, M.; Takahashi, K.; Uechi, I.; Takeda, Y.; Yamamoto, O.; Im, D.; Lee, D.-J.; Chi, B.; Pu, J.; Li, J.; et al. Water-stable lithium anode with $\text{Li}_{1.4}\text{Al}_{0.4}\text{Ge}_{1.6}(\text{PO}_4)_3\text{-TiO}_2$ sheet prepared by tape casting method for lithium-air batteries. *J. Power Sources* **2013**, *235*, 117–121.
- (23) Zhang, P.; Wang, H.; Lee, Y.-G.; Matsui, M.; Takeda, Y.; Yamamoto, O.; Imanishi, N. Tape-cast water-stable NASICON-type high lithium ion conducting solid electrolyte films for aqueous lithium-air batteries. *J. Electrochem. Soc.* **2015**, *162* (7), A1265–A1271.
- (24) Nikodimos, Y.; Abrha, L. H.; Weldeyohannes, H. H.; Shitaw, K. N.; Temesgen, N. T.; Olbasa, B. W.; Huang, C.-J.; Jiang, S.-K.; Wang, C.-H.; Sheu, H.-S.; et al. A new high- Li^+ -conductivity Mg-doped $\text{Li}_{1.5}\text{Al}_{0.5}\text{Ge}_{1.5}(\text{PO}_4)_3$ solid electrolyte with enhanced electrochemical performance for solid-state lithium metal batteries. *Journal of Materials Chemistry A* **2020**, *8* (48), 26055–26065.
- (25) Luo, J.; Sam, A.; Hu, B.; DeBruiler, C.; Wei, X.; Wang, W.; Liu, T. L. Unraveling pH dependent cycling stability of ferricyanide/ferricyanide in redox flow batteries. *Nano Energy* **2017**, *42*, 215–221.
- (26) Sun, Q.; He, L.; Zheng, F.; Wang, Z.; An Oh, S.-J.; Sun, J.; Zhu, K.; Lu, L.; Zeng, K. Decomposition failure of $\text{Li}_{1.5}\text{Al}_{0.5}\text{Ge}_{1.5}(\text{PO}_4)_3$ solid electrolytes induced by electric field: A multi-scenario study using Scanning Probe Microscopy-based techniques. *J. Power Sources* **2020**, *471*, 228468.
- (27) Paoletta, A.; Zhu, W.; Xu, G.-L.; La Monaca, A.; Savoie, S.; Girard, G.; Vijh, A.; Demers, H.; Perea, A.; Delaporte, N.; et al. Understanding the reactivity of a thin $\text{Li}_{1.5}\text{Al}_{0.5}\text{Ge}_{1.5}(\text{PO}_4)_3$ solid-state electrolyte toward metallic lithium anode. *Adv. Energy Mater.* **2020**, *10* (32), 2001497.
- (28) Liu, G.; Zhao, Z.; He, L. Highly selective lithium recovery from high Mg/Li ratio brines. *Desalination* **2020**, *474*, 114185.
- (29) Zhao, X.; Zhang, H.; Yuan, Y.; Ren, Y.; Wang, N. Ultra-fast and stable extraction of Li metal from seawater. *Chem. Commun.* **2020**, *56* (10), 1577–1580.
- (30) Zhang, F.; Yang, S.; Du, Y.; Li, C.; Bao, J.; He, P.; Zhou, H. A low-cost anodic catalyst of transition metal oxides for lithium extraction from seawater. *Chem. Commun.* **2020**, *56* (47), 6396–6399.
- (31) Guo, Z.-Y.; Ji, Z.-Y.; Chen, Q.-B.; Liu, J.; Zhao, Y.-Y.; Li, F.; Liu, Z.-Y.; Yuan, J.-S. Prefractionation of LiCl from concentrated seawater/salt lake brines by electrodialysis with monovalent selective ion exchange membranes. *Journal of Cleaner Production* **2018**, *193*, 338–350.
- (32) Ji, P.-Y.; Ji, Z.-Y.; Chen, Q.-B.; Liu, J.; Zhao, Y.-Y.; Wang, S.-Z.; Li, F.; Yuan, J.-S. Effect of coexisting ions on recovering lithium from

high Mg^{2+}/Li^{+} ratio brines by selective-electrodialysis. *Sep. Purif. Technol.* **2018**, *207*, 1–11.

(33) Gmar, S.; Chagnes, A. Recent advances on electrodialysis for the recovery of lithium from primary and secondary resources. *Hydrometallurgy* **2019**, *189*, 105124.

(34) Calvo, E. J. Direct lithium recovery from aqueous electrolytes with electrochemical ion pumping and lithium intercalation. *ACS Omega* **2021**, *6* (51), 35213–35220.

(35) Battistel, A.; Palagonia, M. S.; Brogioli, D.; La Mantia, F.; Trócoli, R. Electrochemical methods for lithium recovery: A comprehensive and critical review. *Adv. Mater.* **2020**, *32* (23), 1905440.

(36) Safanama, D.; Adams, S. Flexible light-weight lithium-ion-conducting inorganic-organic composite electrolyte membrane. *ACS Energy Letters* **2017**, *2* (5), 1130–1136.

(37) Smith, K. C.; Dmello, R. Na-ion desalination (NID) enabled by Na-blocking membranes and symmetric na-intercalation: Porous-electrode modeling. *J. Electrochem. Soc.* **2016**, *163* (3), A530–A539.

(38) Kim, K.; Candeago, R.; Rim, G.; Raymond, D.; Park, A.-H. A.; Su, X. Electrochemical approaches for selective recovery of critical elements in hydrometallurgical processes of complex feedstocks. *iScience* **2021**, *24* (5), 102374.

(39) Vieceli, N.; Nogueira, C. A.; Guimarães, C.; Pereira, M. F. C.; Durão, F. O.; Margarido, F. Hydrometallurgical recycling of lithium-ion batteries by reductive leaching with sodium metabisulphite. *Waste Management* **2018**, *71*, 350–361.

(40) Weiss, M.; Weber, D. A.; Senyshyn, A.; Janek, J.; Zeier, W. G. Correlating transport and structural properties in $Li_{1+x}Al_xGe_{2-x}(PO_4)_3$ (LAGP) prepared from aqueous solution. *ACS Appl. Mater. Interfaces* **2018**, *10* (13), 10935–10944.

(41) Kim, S.; Kim, J.; Kim, S.; Lee, J.; Yoon, J. Electrochemical lithium recovery and organic pollutant removal from industrial wastewater of a battery recycling plant. *Environ. Sci.: Water Res. Technol.* **2018**, *4* (2), 175–182.

Recommended by ACS

A Lithium Feedstock Pathway: Coupled Electrochemical Extraction and Direct Battery Materials Manufacturing

Jiangtao Hu, Dongping Lu, *et al.*

JUNE 30, 2022
ACS ENERGY LETTERS

READ 

Mechanochemical Lithium Extraction and Zeolite Synthesis from End-of-Life Glass–Ceramics

Tobias Necke, Anke Weidenkaff, *et al.*

AUGUST 11, 2022
ACS SUSTAINABLE CHEMISTRY & ENGINEERING

READ 

Lithium-Ion Battery Recycling—Influence of Recycling Processes on Component Liberation and Flotation Separation Efficiency

Anna Vanderbruggen, Martin Rudolph, *et al.*

SEPTEMBER 29, 2022
ACS ES&T ENGINEERING

READ 

Optimal Diafiltration Membrane Cascades Enable Green Recycling of Spent Lithium-Ion Batteries

Noah P. Wamble, Alexander W. Dowling, *et al.*

SEPTEMBER 02, 2022
ACS SUSTAINABLE CHEMISTRY & ENGINEERING

READ 

Get More Suggestions >

Supporting Information

Redox Flow Battery for Continuous and Energy-Effective

Lithium Recovery from Aqueous Solution

Lei Wang,^{1,2} Stefanie Arnold,^{1,2} Panyu Ren,^{1,2}

Qingsong Wang^{1,||}, Jun Jin³, Zhaoyin Wen^{3,4,*}, Volker Presser,^{1,2,5,*}

¹ *INM - Leibniz Institute for New Materials, D2 2, 66123, Saarbrücken, Germany*

² *Department of Materials Science & Engineering, Saarland University, Campus D2 2, 66123, Saarbrücken, Germany*

³ *CAS Key Laboratory of Materials for Energy Conversion, Shanghai Institute of Ceramics, Chinese Academy of Sciences, Shanghai, 200050 P. R. China*

⁴ *State Key Lab of High Performance Ceramics and Superfine Microstructure, Shanghai Institute of Ceramics, Chinese Academy of Sciences, Shanghai, 200050 P. R. China*

⁵ *Saarene, Saarland Center for Energy Materials and Sustainability, Campus C4 2, 66123 Saarbrücken, Germany*

* Corresponding author's email: zywen@mail.sic.ac.cn volker.presser@leibniz-inm.de

|| *Current address: Bavarian Center for Battery Technology (BayBatt), University of Bayreuth, Universitätsstrasse 30, 95447 Bayreuth, Germany and Department of Chemistry, University of Bayreuth, Universitätsstrasse 30, 95447 Bayreuth, Germany*

Experimental Methods

Synthesis and manufacturing of the LISICON membranes

Briefly, a mixture of precursors containing lithium carbonate Li_2CO_3 , alumina Al_2O_3 , germanium oxide GeO_2 (99.99%), and ammonium dihydrogen phosphate $(\text{NH}_4)\text{H}_2\text{PO}_4$ was dispersed in isopropanol and thoroughly mixed by planetary ball-milling with ZrO_2 balls for 6 h at 400 rpm. The well-mixed precursor was dried and calcinated at 800 °C for 6 h. Afterward, the synthesized powder was pressed into pellets (thickness of 0.8 mm) and sintered in a Pt crucible at 900 °C for 12 h. The obtained ceramic pellets were further polished before use.

Component and operation of the LE-RFB system

Two commercial symmetric carbon felt electrodes (discs with a diameter of 14 mm, SGL Carbon) were employed as the cathode and anode, contacting with the redox electrolyte channels. The redox electrolyte with the volume of 50 mL contained 280 mM $\text{K}_3[\text{Fe}(\text{CN})_6]$, 280 mM $\text{K}_4[\text{Fe}(\text{CN})_6]$, and 10 mM LiCl (to increase the lithium extraction rate), which is maintained in a brown bottle to avoid the deterioration of $\text{K}_3[\text{Fe}(\text{CN})_6]$ when exposed to light. A 10 L tank of simulated seawater prepared according to the concentration of primary cations from the norm D1141-98 (Ref. ¹) of the American Society for Testing and Materials (**Table S2**) was applied as the feed water. The anions were chloride ions. The recovery solution consisted of 65 mL of 10 mM NaCl solution. The feed water and recovery solution were separated by an anion exchange membrane (diameter 50 mm, FAS-PET-130, Fumatech). These two solutions were separated from the redox electrolyte by the LISICON membrane (effective area 1.5 cm², thickness ~500 μm, geometric density 3.26 g/cm³). All these three solutions were circulated from and back to the reservoirs through the peristaltic pump (Masterflex L/S) with a flow rate of 5 mL/min. The recovery solution and redox electrolyte reservoirs were constantly stirred at 400 rpm by magnetic stirring (Variomag, MULTIPOINT magnetic HP6). The setup of the LE-RFB system was operated in a climate chamber (Binder) at a constant temperature of 25±1 °C, shown in **Figure S1**. The LE-RFB was first charged at a constant current density of 1 mA/cm² limited to 0.6 V by VSP300 potentiostat/galvanostat (Bio-Logic). Subsequently, the battery was held at 0.6 V for 5 h. The concentration of all the cations in the recovery solution at various charging times was tested by an inductively coupled plasma optical emission spectrometer (ICP-OES, ARCOS FHX22, SPECTRO Analytical Instruments). The experiment of recovering lithium from brines water was complemented with the same LISICON membranes, and the other experimental conditions were the same except for the composition of the feed water (100 mL, prepared according to Ref. ²) and the volume of recovery solution (75 mL). The chemical composition of the redox electrolyte and of the seawater and brine is provided in **Table S1** and **Table S2**, respectively.

Characterization

X-ray diffraction (XRD) analysis was carried out via a D8 Advanced diffractometer (Bruker AXS) with a copper X-ray source (Cu-K α , $\lambda = 1.5406 \text{ \AA}$; 40 kV, 40 mA). The samples were examined in the range of 10° to 70° 2 θ and with 1 s per step: Scanning electron microscopy (SEM) was conducted using a ZEISS Gemini 500 system at acceleration voltages of 1-3 kV. A small piece of the LISICON membrane was vertically mounted on an aluminum sample holder and analyzed without the aid of an additional, conductive sputter coating. Energy-dispersive X-ray spectroscopy (EDX) spectra were obtained with an in-lens secondary electron (SE) detector at 15 kV employing an X-Max Silicon Detector from Oxford Instruments attached to the electron microscope.

Ionic conductivity measurement

To measure the ionic conductivity of ceramic pellets, we applied a thin layer via gold sputtering as ion conducting blocking electrode. The electrochemical impedance spectroscopy was measured in the frequency range of 100 kHz to 0.1 Hz with a perturbation voltage of 10 mV.

Calculations

The extraction ratio of all the cations is calculated according to **Equation S1**.

$$\text{Extraction ratio (\%)} = \frac{\Delta c_x}{\Delta c_{all}} \times 100 \quad (\text{Eq. S1})$$

where, Δc_x and Δc_{all} are the concentration change of x (x = Li⁺, K⁺, Mg²⁺ or Na⁺) and all the cations in the recovery solution.

We also calculated the selectivity factors ($K_{Li/M}$) between Li⁺ and other cations M (M = Na⁺, K⁺, Mg²⁺), which involves the initial concentration of cations, according to the **Equation S2**

$$K_{Li/M} = \frac{\Delta c_{Li}}{\Delta c_M} \times \frac{c_{M-initial}}{c_{Li-initial}} \quad (\text{Eq. S2})$$

where, Δc_{Li} and Δc_M are the concentration change of Li⁺ and M in the recovery solution, respectively. $c_{M-initial}$ and $c_{Li-initial}$ are the concentration of M and Li⁺ in the initial feed water, respectively.

The lithium retraction rate and energy consumption are also important indexes to evaluate the system's performance, calculated by **Equation S3** and **Equation S4**, respectively.

$$\text{Lithium extraction rate} = \frac{\Delta c_{Li} \times V}{t \times A \times M_{Li}} \quad (\text{Eq. S3})$$

where Δc_{Li} is the concentration change of Li⁺ in the recovery solution, V is the volume, t is the time, A the effective area of LISICON membrane, M_{Li} is the molar mass of Li.

$$\text{Energy consumption} = \frac{E}{V \times \Delta c_{Li} \times M_{Li}} \quad (\text{Eq. S4})$$

where E is the consumed electrical energy during the charging operation, Δc_{Li} is the concentration change of Li⁺ in the recovery solution, V is the volume, M_{Li} is the molar mass of Li

Supporting Figures

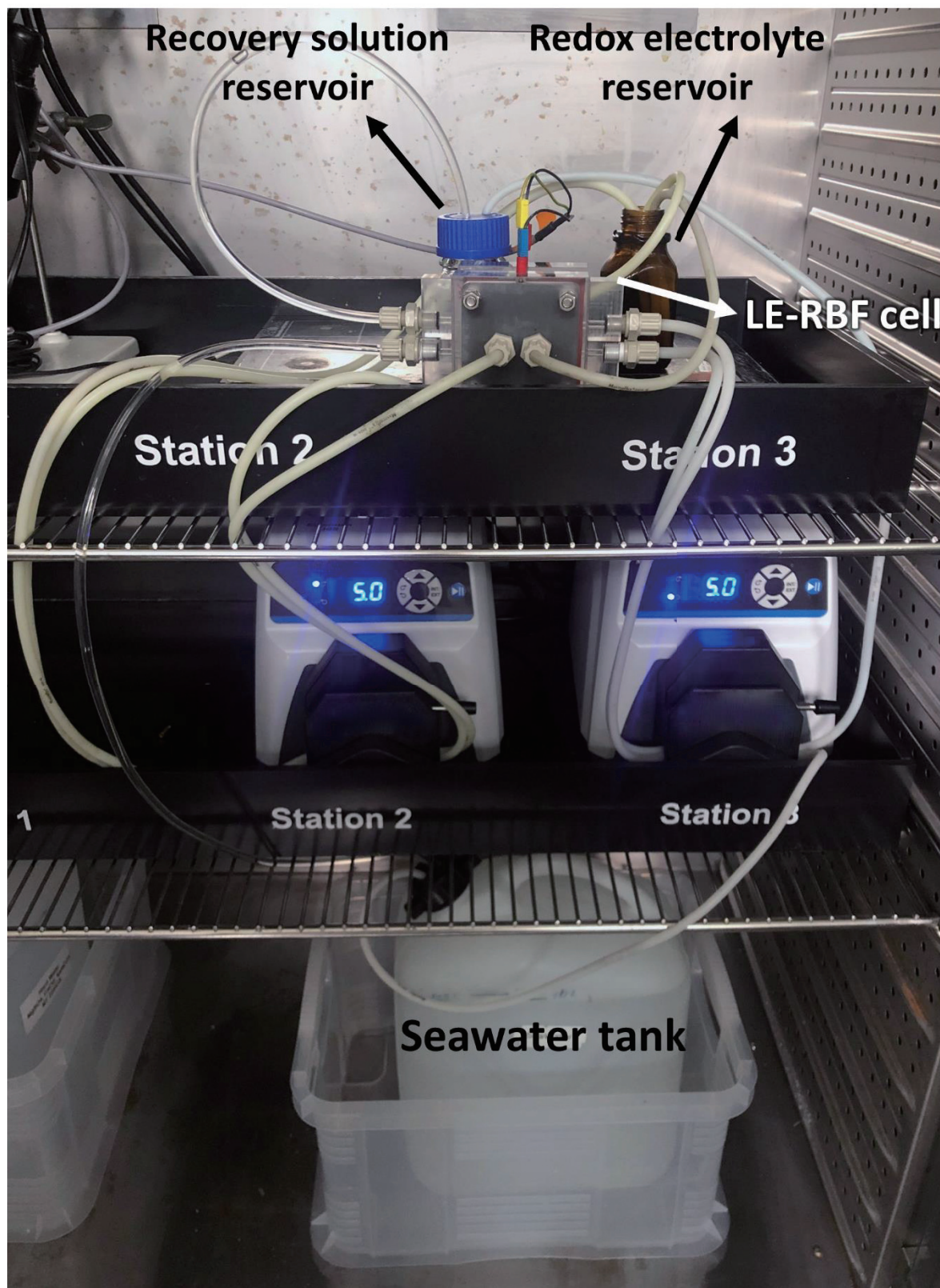


Figure S1: Photograph of the setup of lithium-extraction redox flow battery system.

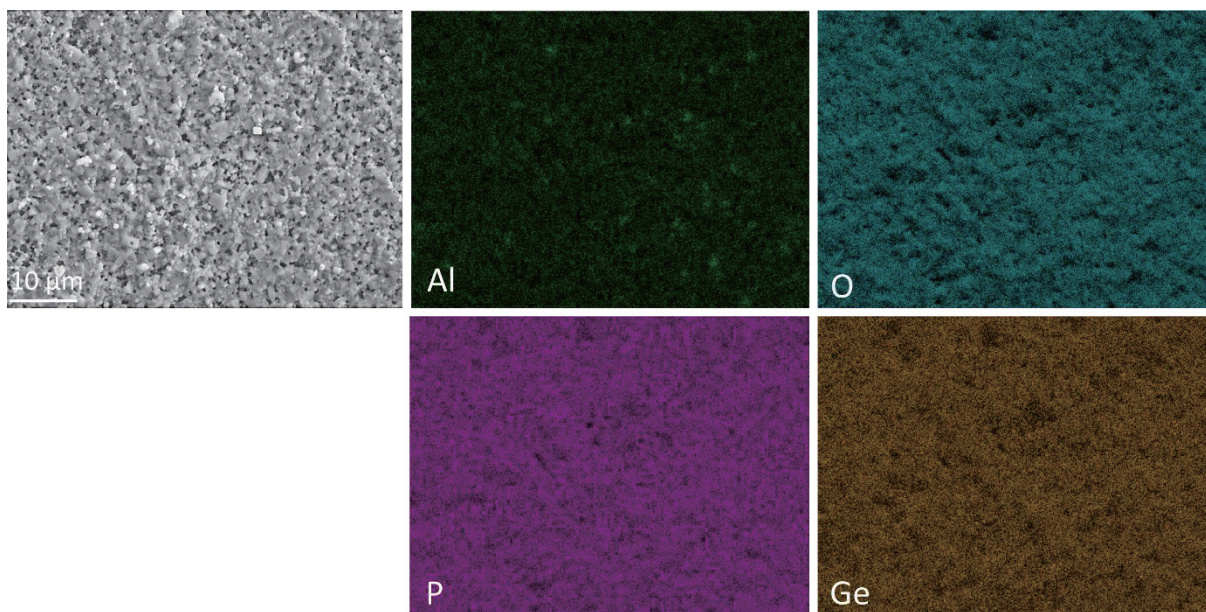


Figure S2: A cross-sectional scanning electron micrograph of the LISICON membrane and corresponding EDX mapping of Al, Ge, P, and O. All elemental maps show the same area (with same resolution) as the electron micrograph.

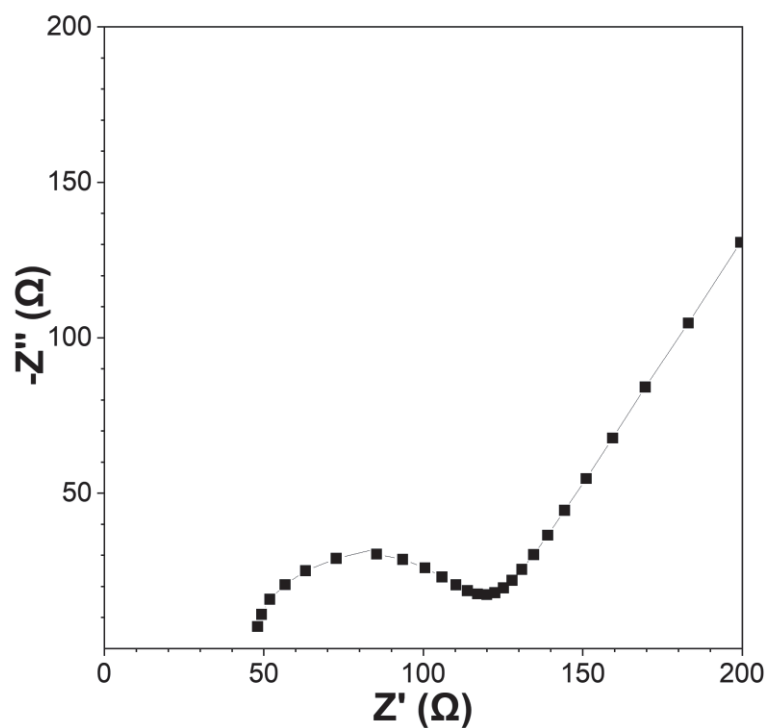


Figure S3: The electrochemical impedance spectrum of the LAGP membrane with an area of 323.5 mm².

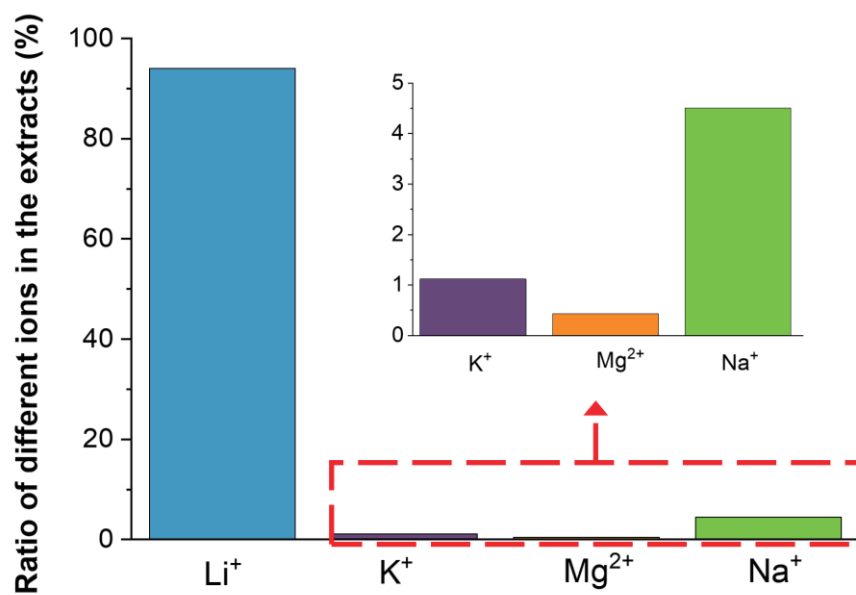


Figure S4: The percentage of all cations in the cations extracted from seawater. Insert: magnification of column graph for the K⁺, Mg²⁺, and Na⁺.

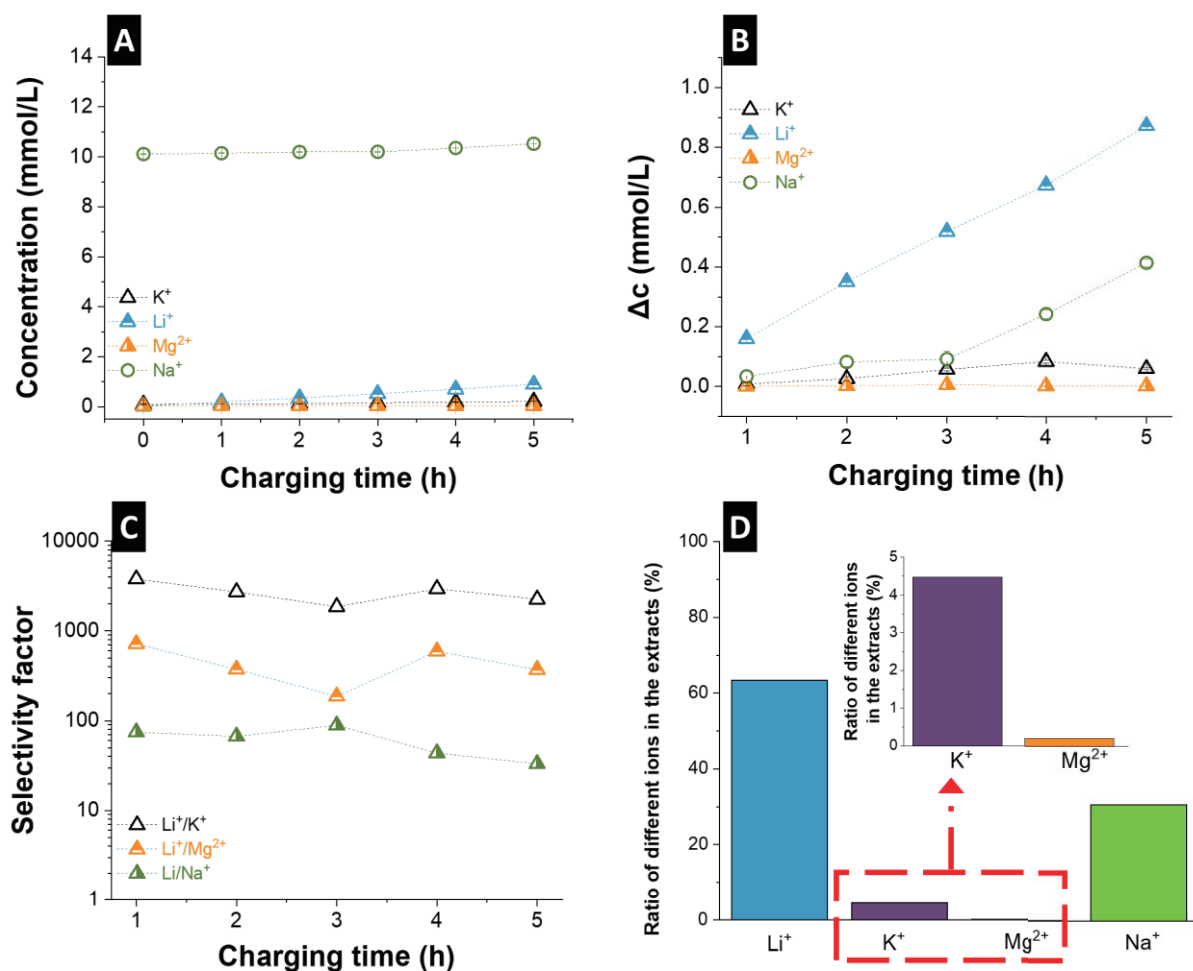


Figure S5: Lithium extraction from seawater by lithium-extraction redox flow battery: (A) the concentration and (B) concentration change of cations in the recovery solution at different times; (C) the selectivity factors between Li^+ and other cations; (D) The percentage of all cations in the cations extracted from brine. Inset: magnification of column graph for the K^+ and Mg^{2+} .

Supporting Tables

Table S1: The concentration of main cations and Li⁺ in the redox electrolyte in the experiment for lithium extraction from seawater. No calcium was detected.

Concentration (mM)	Initial	After
Li ⁺	9.35±0.01	9.37±0.01
Na ⁺	0.95±0.01	1.13±0.01
K ⁺	2095.2±3.8	2119.4±2.1
Ca ²⁺	-	-
Mg ²⁺	3.6·10 ⁻³ ±3.3·10 ⁻⁵	1.0·10 ⁻² ±4.8·10 ⁻⁵
Fe ³⁺	571.7±0.6	579.8±0.9
pH	6.75	6.25

Table S2: The concentration of main cations and Li⁺ in the simulated seawater (Ref. ¹) and brine water (Ref. ²).

Concentration (mM)	Seawater	Brine water
Li ⁺	0.024	210
Na ⁺	477.5	3300
K ⁺	9.3	460
Ca ²⁺	10.5	7.75
Mg ²⁺	54.6	400

Table S3: Key economic and technical price assumption for a simplified techno-economic analysis of LE-RFB system with an effective area of 1 m².

Price assumption		Economic assumptions		Technical assumptions
LISICON membrane (\$/m ²) Ref. ³	461	Depreciation (% yr ⁻¹ of fixed capital)	10	1.1 times as the effective area
Anion exchange membrane (\$/m ²)	780	Depreciation (% yr ⁻¹ of fixed capital)	5	1.5 times as the effective area
Graphite block (\$/kg)	3	Processing fee (%)	20	
PMMA (\$/kg)	4	Processing fee (%)	20	
Carbon felt (\$/m ²)	30			
Other components of the LE-RFB system (\$)	200			Including gasket, O-rings, screws
Tax (%)	19			
Na ₂ CO ₃ (\$/kg) Ref. ³	0.3			
Li ₂ CO ₃ (\$/kg)*	68			
Electricity (\$/kWh)**	0.13			The power of the pump is 1 kW

* <https://www.chemanalyst.com/Pricing-data/lithium-carbonate-1269>

** https://www.globalpetrolprices.com/electricity_prices

Supporting References

- (1) ASTM. *D1141-98 Standard Practice for the Preparation of Substitute Ocean Water*; 2013. Access date: 14.09.2022
- (2) Liu, G.; Zhao, Z.; He, L. Highly selective lithium recovery from high Mg/Li ratio brines. *Desalination* **2020**, *474*, 114185. DOI: 10.1016/j.desal.2019.114185.
- (3) Hu, J.; Jiang, Y.; Li, L.; Yu, Z.; Wang, C.; Gill, G.; Xiao, J.; Cavagnaro, R. J.; Kuo, L.-J.; Asmussen, R. M.; et al. A Lithium Feedstock Pathway: Coupled Electrochemical Extraction and Direct Battery Materials Manufacturing. *ACS Energy Letters* **2022**, *7* (8), 2420-2427. DOI: 10.1021/acseenergylett.2c01216.

5. Conclusion and outlook

My doctoral work investigated the performance of Faradaic materials (pseudocapacitive and battery behavior) in water purification (i.e., ion/water separation) and ion-selective extraction (among alkali and alkaline earth metal ions). The study of pseudocapacitive materials focused on $\text{Ti}_3\text{C}_2\text{T}_x$ MXene, an interesting layered material with unique characteristics. Moreover, battery behavior materials included solid electrodes and redox electrolytes. The ion storage mechanism determined by the lattice structure and elements components strongly influence the ion-storage capacity and selectivity. We could find that pseudocapacitive materials with fast and reversible charge transfer processes show better stability. In contrast, the charge storage capacity is generally lower than battery materials which could store ions in bulk. Regarding the intercalation type redox reactions (both pseudocapacitive and battery behavior), stronger and narrower interstitial sites generally are better for isolating one ion from other ions.

The ion/water separation performance of $\text{Ti}_3\text{C}_2\text{T}_x$ MXene was explored paired with activated carbon in both low-salinity (20°mM NaCl) and high-salinity water (600°mM NaCl). The asymmetric system exhibits a stable desalination capacity of 10-12°mg_{NaCl}/g for 100 cycles with charge efficiencies of over 80% in both feed water. In contrast, the symmetric cell with both activated carbon shows a desalination capacity lower than 4°mgNaCl/g with charge efficiencies lower than 50% (< 10% in high salinity water). The high ion storage capacity is due to the pseudocapacitance of $\text{Ti}_3\text{C}_2\text{T}_x$. The high charge efficiency of the system benefits from the permselectivity of $\text{Ti}_3\text{C}_2\text{T}_x$ towards cations, which originates from negatively charged terminal groups on $\text{Ti}_3\text{C}_2\text{T}_x$. In low-salinity feed water, where the co-ion expulsion effect is limited, the contribution of chemical charge (regenerated by discharging to the slightly positive potential) leads to a charge efficiency higher than 1. In the feed water with high concentration, the permselectivity of $\text{Ti}_3\text{C}_2\text{T}_x$ forces activated carbon to have the permselectivity towards Cl^- , which common activated carbon does not possess.

The work also explored alloying materials, which store ions through multi-charge transfer reactions, to obtain a higher ion storage capacity. However, the potential of redox reactions of alloying materials is beyond the safe window potential of aqueous electrolytes. A NASICON membrane is utilized to isolate the Sb (a high-performance Na alloying material) and the organic electrolyte from the feed water to address the cell-voltage issue. With a cell voltage from -2.0°V to +2.0°V, Sb exhibits a superior Na^+ storage capacity of 294°mg_{Na}/g_{Sb} after 40 cycles, much higher than the reported pseudocapacitive and other battery behavior material, including intercalation and conversion materials. However, due to the high volume extension, the retention of this capacity is ca. 50%. Suffering from side reactions (e.g., oxidation of carbon materials) and degradation of the NASICON membrane, the charge efficiency of the system is ca. 70%.

Besides water purification, Faradaic materials could also extract specific ions from the mixture by utilizing the interplay between characteristics of ions and inherent crystal structures of the Faradaic materials. For example, $\text{Ti}_3\text{C}_2\text{T}_x$ has a two-dimensional structure with an intercalation distance of ca. 0.57 nm (without considering the terminal functional groups). In the mixture of equimolar Li^+ , Na^+ , K^+ , Ca^{2+} and Mg^{2+} (10 mM), $\text{Ti}_3\text{C}_2\text{T}_x$ exhibits a time depended selectivity. Since the intercalation distance of $\text{Ti}_3\text{C}_2\text{T}_x$ is lower than the hydration diameters of all the cations, they need to (partially) dehydrate before intercalating into the $\text{Ti}_3\text{C}_2\text{T}_x$ layers. Therefore, at the beginning of the charging process in the second cycle, the uptake capacity of K^+ is the highest, while Li^+ is the lowest, following the same order of dehydration energy (normalized by charge). However, with the increase in charging time, the uptake capacity of monovalent cations reduces, but that of divalent continuously rises, indicating that the divalent cations replace monovalent cations. This is because the divalent cations carry more charges. Since the intercalation distance of $\text{Ti}_3\text{C}_2\text{T}_x$ is flexible (i.e., changing with the intercalation/deintercalation of the cations) and not narrower than the ionic diameter of some cations, $\text{Ti}_3\text{C}_2\text{T}_x$ does not show a high affinity for one specific ion among Li^+ , Na^+ , K^+ , Ca^{2+} , and Mg^{2+} ; the highest selectivity factor is less than 5.

Unlike MXenes, LiFePO_4 has narrower interstitial sites and a robust structure with slight structure changes after the intercalation/deintercalation of Li^+ . Due to the distinct properties of ions (e.g., ionic diameter, valence, and electronegativity), the redox potential (intercalation reaction) of Li^+ , Na^+ , Ca^{2+} , and Mg^{2+} are different. With the potential window of -0.4 V to +0.8 V vs. Ag/AgCl , only the redox peaks representing Li^+ intercalation occur in the single-cation solution (10 mM); that suggests LiFePO_4 has superior selectivity towards Li^+ under this potential range. In a mixed solution containing 5 mM LiCl and 50 mM NaCl , LiFePO_4 shows a Li^+ uptake capacity of ca. 25 mg/g, and no Na^+ uptake is detected. However, less than 50% capacity retents after 10 cycles due to the irreversible oxidation of Fe by the dissolved oxygen in the electrolyte. After continuously bubbling N_2 gas in the feed water to expel the O_2 , the capacity retention increased to ca. 70% after 10 cycles. Additionally, coating carbon on the surface of LiFePO_4 particles could further improve the stability of LiFePO_4 (by reducing the contact between the O_2 and LiFePO_4 particles) and decrease the energy consumption of Li^+ extraction due to the enhanced conductivity.

The typical electrochemical separation process with Faradaic materials requires the charging and discharging process to regenerate the material. Moreover, the electrolyte would switch from the feed water to the recovery solution to enrich the target cations, which is time-intense and labor-consuming. An electrochemical separation process that could continuously extract the target ions is more favorable for practical applications. Thus, we designed a lithium-extraction redox flow battery, where the redox couple of $\text{Fe}(\text{CN})_6^{4-}/\text{Fe}(\text{CN})_6^{3-}$ provides the driving force for the migration of cations, and the LISICON membrane plays the role of selectively extracting Li^+ for the lowest diffusion barriers of Li^+

than other cations. The redox electrolyte is oxidized at the anode area and carried to the cathode area by the pump, accomplishing regeneration (i.e., reduction); that means the oxidation and reduction coincide, and the system could continuously work. The system could extract Li^+ from seawater with an energy consumption of $2.5^\circ\text{Wh/g}_{\text{Li}^+}$ and a superior selectivity of 500000 (Li/Mg). However, due to the sluggish diffusion rate of Li^+ in the LISICON membrane, the extraction rate of the system is limited to $0.04^\circ\text{mg/cm}^2/\text{h}$. Higher values are important to make this technology relevant for the actual application.

Faradaic materials show stupendous potential in both water purification and valuable ion extraction. Although many Faradaic materials have been investigated, there are still many unknowns to be explored and some challenges to be overcome. For instance, the interaction between the lattice structure of materials and their selectivity is unclear. The performance of current Faradaic materials, such as stability and cost, still can not meet the demand of the industrial application. Further studies include but are not limited to the following aspect. (1) Fabricating a database containing the performance, operation conditions, and structural characteristics of Faradaic materials. By machine learning, the relationship between the material characteristics and its selectivity performance could be predicted, directing the design of materials. (2) Exploring and designing new cell architecture or electrochemical separation processes. The novel system may enhance the performance or endow bi-/multi- functions. For example, the combination of catalytic electrodes and Faradaic materials could remove organic pollutants and extract valuable ions at the same time. (3) Developing new Faradaic materials with higher stability, capacity, and selectivity and optimizing the synthesis process to reduce the cost. (4) Establishing the universal evaluation system for ion/ion selectivity work, benefiting in an easier and more scientific comparison between the new work and reported work.

6. References

- [1] U. Water, Sustainable Development Goal 6 synthesis report on water and sanitation, Published by the United Nations New York, New York, 10017 (2018).
- [2] M. Alsehli, J.-K. Choi, M. Aljuhan, A novel design for a solar powered multistage flash desalination, *Solar Energy*, 153 (2017) 348-359.
- [3] H. Sayyaadi, A. Saffari, Thermo-economic optimization of multi effect distillation desalination systems, *Applied Energy*, 87 (2010) 1122-1133.
- [4] Y. Yao, P. Zhang, C. Jiang, R.M. DuChanois, X. Zhang, M. Elimelech, High performance polyester reverse osmosis desalination membrane with chlorine resistance, *Nature Sustainability*, 4 (2021) 138-146.
- [5] S. Al-Amshawee, M.Y.B.M. Yunus, A.A.M. Azoddein, D.G. Hassell, I.H. Dakhil, H.A. Hasan, Electrodialysis desalination for water and wastewater: A review, *Chemical Engineering Journal*, 380 (2020) 122231.
- [6] M. Qasim, M. Badrelzaman, N.N. Darwish, N.A. Darwish, N. Hilal, Reverse osmosis desalination: A state-of-the-art review, *Desalination*, 459 (2019) 59-104.
- [7] G.L. Meerganz von Medeazza, "Direct" and socially-induced environmental impacts of desalination, *Desalination*, 185 (2005) 57-70.
- [8] K. Park, J. Kim, D.R. Yang, S. Hong, Towards a low-energy seawater reverse osmosis desalination plant: A review and theoretical analysis for future directions, *Journal of Membrane Science*, 595 (2020) 117607.
- [9] S. Porada, R. Zhao, A. van der Wal, V. Presser, P.M. Biesheuvel, Review on the science and technology of water desalination by capacitive deionization, *Progress in Materials Science*, 58 (2013) 1388-1442.
- [10] L. Wang, Y. Zhang, K. Moh, V. Presser, From capacitive deionization to desalination batteries and desalination fuel cells, *Current Opinion in Electrochemistry*, 29 (2021) 100758.
- [11] M.E. Suss, S. Porada, X. Sun, P.M. Biesheuvel, J. Yoon, V. Presser, Water desalination via capacitive deionization: what is it and what can we expect from it?, *Energy & Environmental Science*, 8 (2015) 2296-2319.
- [12] Y. Zhang, P. Ren, L. Wang, E.P. Yambou, S. Husmann, V. Presser, Selectivity toward heavier monovalent cations of carbon ultramicropores used for capacitive deionization, *Desalination*, 542 (2022) 116053.
- [13] M.E. Suss, V. Presser, Water Desalination with Energy Storage Electrode Materials, *Joule*, 2 (2018) 10-15.
- [14] M. Pasta, C.D. Wessells, Y. Cui, F. La Mantia, A Desalination Battery, *Nano Letters*, 12 (2012) 839-843.
- [15] Z. Chen, X. Xu, Z. Ding, K. Wang, X. Sun, T. Lu, M. Konarova, M. Eguchi, J.G. Shapter, L. Pan, Y. Yamauchi, Ti_3C_2 MXenes-derived $NaTi_2(PO_4)_3$ /MXene nanohybrid for fast and efficient hybrid capacitive deionization performance, *Chemical Engineering Journal*, 407 (2021) 127148.
- [16] F. Chen, Y. Huang, L. Guo, L. Sun, Y. Wang, H.Y. Yang, Dual-ions electrochemical deionization: a desalination generator, *Energy & Environmental Science*, 10 (2017) 2081-2089.
- [17] P. Srimuk, F. Kaasik, B. Krüner, A. Tolosa, S. Fleischmann, N. Jäckel, M.C. Tekeli, M. Aslan, M.E. Suss, V. Presser, MXene as a novel intercalation-type pseudocapacitive cathode and anode for capacitive deionization, *Journal of Materials Chemistry A*, 4 (2016) 18265-18271.
- [18] L. Guo, R. Mo, W. Shi, Y. Huang, Z.Y. Leong, M. Ding, F. Chen, H.Y. Yang, A Prussian blue anode for high performance electrochemical deionization promoted by the faradaic mechanism, *Nanoscale*, 9 (2017) 13305-13312.
- [19] Q. Li, Y. Zheng, D. Xiao, T. Or, R. Gao, Z. Li, M. Feng, L. Shui, G. Zhou, X. Wang, Z. Chen, Faradaic Electrodes Open a New Era for Capacitive Deionization, *Advanced Science*, 7 (2020) 2002213.
- [20] H. Yoon, J. Lee, S. Kim, J. Yoon, Review of concepts and applications of electrochemical ion separation (EIONS) process, *Separation and Purification Technology*, 215 (2019) 190-207.

- [21] M. Panayotova, B. Velikov, Influence of Zeolite Transformation in a Homoionic Form on the Removal of Some Heavy Metal Ions from Wastewater, *Journal of Environmental Science and Health, Part A*, 38 (2003) 545-554.
- [22] H. Nassrullah, S.F. Anis, R. Hashaikeh, N. Hilal, Energy for desalination: A state-of-the-art review, *Desalination*, 491 (2020) 114569.
- [23] F. Alvarado-Revilla, *Desalination markets 2016: Global perspective and opportunities for growth*, Media Analytics Limited, 2015.
- [24] P. Catrini, A. Cipollina, F. Giacalone, G. Micale, A. Piacentino, A. Tamburini, Chapter 12 - Thermodynamic, Exergy, and Thermo-economic analysis of Multiple Effect Distillation Processes, in: V.G. Gude (Ed.) *Renewable Energy Powered Desalination Handbook*, Butterworth-Heinemann, 2018, pp. 445-489.
- [25] M. Al-Shammiri, M. Safar, Multi-effect distillation plants: state of the art, *Desalination*, 126 (1999) 45-59.
- [26] M.W. Shahzad, M. Burhan, L. Ang, K.C. Ng, Energy-water-environment nexus underpinning future desalination sustainability, *Desalination*, 413 (2017) 52-64.
- [27] A. Al-Karaghoul, L.L. Kazmerski, Energy consumption and water production cost of conventional and renewable-energy-powered desalination processes, *Renewable and Sustainable Energy Reviews*, 24 (2013) 343-356.
- [28] M. Pace, Microfiltration vs. Ultrafiltration vs. Nanofiltration vs. Reverse Osmosis, in.
- [29] C. Tang, M.L. Bruening, Ion separations with membranes, *Journal of Polymer Science*, 58 (2020) 2831-2856.
- [30] A. Al-Amoudi, R.W. Lovitt, Fouling strategies and the cleaning system of NF membranes and factors affecting cleaning efficiency, *Journal of Membrane Science*, 303 (2007) 4-28.
- [31] M.A. Abdelkareem, M. El Haj Assad, E.T. Sayed, B. Soudan, Recent progress in the use of renewable energy sources to power water desalination plants, *Desalination*, 435 (2018) 97-113.
- [32] G. IDA, *IDA Desalination Yearbook 2017–2018*, Media Analytics Ltd.: Oxford, UK, (2017).
- [33] M.T. Mito, X. Ma, H. Albuflasa, P.A. Davies, Reverse osmosis (RO) membrane desalination driven by wind and solar photovoltaic (PV) energy: State of the art and challenges for large-scale implementation, *Renewable and Sustainable Energy Reviews*, 112 (2019) 669-685.
- [34] A.J. Schunke, G.A. Hernandez Herrera, L. Padhye, T.-A. Berry, Energy Recovery in SWRO Desalination: Current Status and New Possibilities, *Frontiers in Sustainable Cities*, 2 (2020).
- [35] Y. Shatilla, 7 - Nuclear desalination, in: S.U.-D. Khan, A. Nakhobov (Eds.) *Nuclear Reactor Technology Development and Utilization*, Woodhead Publishing, 2020, pp. 247-270.
- [36] J. Kim, K. Park, D.R. Yang, S. Hong, A comprehensive review of energy consumption of seawater reverse osmosis desalination plants, *Applied Energy*, 254 (2019) 113652.
- [37] T.Y. Cath, A.E. Childress, M. Elimelech, Forward osmosis: Principles, applications, and recent developments, *Journal of Membrane Science*, 281 (2006) 70-87.
- [38] S. Yadav, H. Saleem, I. Ibrar, O. Naji, A.A. Hawari, A.A. Alanezi, S.J. Zaidi, A. Altaee, J. Zhou, Recent developments in forward osmosis membranes using carbon-based nanomaterials, *Desalination*, 482 (2020) 114375.
- [39] N. Akther, A. Sodiq, A. Giwa, S. Daer, H.A. Arafat, S.W. Hasan, Recent advancements in forward osmosis desalination: A review, *Chemical Engineering Journal*, 281 (2015) 502-522.
- [40] J. Zhou, H.-L. He, F. Sun, Y. Su, H.-Y. Yu, J.-S. Gu, Structural parameters reduction in polyamide forward osmosis membranes via click modification of the polysulfone support, *Colloids and Surfaces A: Physicochemical and Engineering Aspects*, 585 (2020) 124082.
- [41] X. Fan, Y. Liu, X. Quan, A novel reduced graphene oxide/carbon nanotube hollow fiber membrane with high forward osmosis performance, *Desalination*, 451 (2019) 117-124.
- [42] C.H. Worthley, K.T. Constantopoulos, M. Ginic-Markovic, E. Markovic, S. Clarke, A study into the effect of POSS nanoparticles on cellulose acetate membranes, *Journal of Membrane Science*, 431 (2013) 62-71.
- [43] Y. Wang, R. Ou, Q. Ge, H. Wang, T. Xu, Preparation of polyethersulfone/carbon nanotube substrate for high-performance forward osmosis membrane, *Desalination*, 330 (2013) 70-78.

- [44] M.J. Park, S. Phuntsho, T. He, G.M. Nisola, L.D. Tijing, X.-M. Li, G. Chen, W.-J. Chung, H.K. Shon, Graphene oxide incorporated polysulfone substrate for the fabrication of flat-sheet thin-film composite forward osmosis membranes, *Journal of Membrane Science*, 493 (2015) 496-507.
- [45] N. Niksefat, M. Jahanshahi, A. Rahimpour, The effect of SiO₂ nanoparticles on morphology and performance of thin film composite membranes for forward osmosis application, *Desalination*, 343 (2014) 140-146.
- [46] X. Wu, M. Ding, H. Xu, W. Yang, K. Zhang, H. Tian, H. Wang, Z. Xie, Scalable Ti₃C₂T_x MXene Interlayered Forward Osmosis Membranes for Enhanced Water Purification and Organic Solvent Recovery, *ACS Nano*, 14 (2020) 9125-9135.
- [47] H. Liu, H. Wang, X. Zhang, Facile Fabrication of Freestanding Ultrathin Reduced Graphene Oxide Membranes for Water Purification, *Advanced Materials*, 27 (2015) 249-254.
- [48] P. Cruz-Tato, N. Rivera-Fuentes, M. Flynn, E. Nicolau, Anti-Fouling Electroconductive Forward Osmosis Membranes: Electrochemical and Chemical Properties, *ACS Applied Polymer Materials*, 1 (2019) 1061-1070.
- [49] N.A. Thompson, P.G. Nicoll, Forward osmosis desalination: a commercial reality, in: *IDA World Congress—Perth Convention and Exhibition Centre (PCEC)*, Perth, Western Australia September, 2011, pp. 4-9.
- [50] W. Suwaileh, N. Pathak, H. Shon, N. Hilal, Forward osmosis membranes and processes: A comprehensive review of research trends and future outlook, *Desalination*, 485 (2020) 114455.
- [51] F.A. AlMarzooqi, A.A. Al Ghaferi, I. Saadat, N. Hilal, Application of Capacitive Deionisation in water desalination: A review, *Desalination*, 342 (2014) 3-15.
- [52] H. Rabiee, K.R. Khalilpour, J.M. Betts, N. Tapper, Chapter 13 - Energy-Water Nexus: Renewable-Integrated Hybridized Desalination Systems, in: K.R. Khalilpour (Ed.) *Polygeneration with Polystorage for Chemical and Energy Hubs*, Academic Press, 2019, pp. 409-458.
- [53] Y. Wang, W. Zhang, X. Zeng, T. Deng, J. Wang, Membranes for separation of alkali/alkaline earth metal ions: A review, *Separation and Purification Technology*, 278 (2021) 119640.
- [54] J.W. Jorgenson, K.D. Lukacs, High-resolution separations based on electrophoresis and electroosmosis, *Journal of Chromatography A*, 218 (1981) 209-216.
- [55] A. Weston, P.R. Brown, P. Jandik, W.R. Jones, A.L. Heckenberg, Factors affecting the separation of inorganic metal cations by capillary electrophoresis, *Journal of Chromatography A*, 593 (1992) 289-295.
- [56] W.R. Jones, P. Jandik, Controlled changes of selectivity in the separation of ions by capillary electrophoresis, *Journal of Chromatography A*, 546 (1991) 445-458.
- [57] T. Wang, S.F.Y. Li, Migration behaviour of alkali and alkaline-earth metal ion-EDTA complexes and quantitative analysis of magnesium in real samples by capillary electrophoresis with indirect ultraviolet detection, *Journal of Chromatography A*, 707 (1995) 343-353.
- [58] T.I. Lin, Y.H. Lee, Y.C. Chen, Capillary electrophoretic analysis of inorganic cations: Role of complexing agent and buffer pH, *Journal of Chromatography A*, 654 (1993) 167-176.
- [59] X. Xu, Y. Chen, P. Wan, K. Gasem, K. Wang, T. He, H. Adidharma, M. Fan, Extraction of lithium with functionalized lithium ion-sieves, *Progress in Materials Science*, 84 (2016) 276-313.
- [60] G. He, L. Zhang, D. Zhou, Y. Zou, F. Wang, The optimal condition for H₂TiO₃-lithium adsorbent preparation and Li⁺ adsorption confirmed by an orthogonal test design, *Ionics*, 21 (2015) 2219-2226.
- [61] Q. Feng, Y. Miyai, H. Kanoh, K. Ooi, Lithium(1+) extraction/insertion with spinel-type lithium manganese oxides. Characterization of redox-type and ion-exchange-type sites, *Langmuir*, 8 (1992) 1861-1867.
- [62] O. Kenta, M. Yoshitaka, K. Shunsaku, M. Hiroshi, A. Mitsuo, Lithium-ion Insertion/Extraction Reaction with λ-MnO₂ in the Aqueous Phase, *Chemistry Letters*, 17 (1988) 989-992.
- [63] L. Li, W. Qu, F. Liu, T. Zhao, X. Zhang, R. Chen, F. Wu, Surface modification of spinel λ-MnO₂ and its lithium adsorption properties from spent lithium ion batteries, *Applied Surface Science*, 315 (2014) 59-65.
- [64] R. Chitrakar, H. Kanoh, Y. Miyai, K. Ooi, A New Type of Manganese Oxide (MnO₂·0.5H₂O) Derived from Li_{1.6}Mn_{1.6}O₄ and Its Lithium Ion-Sieve Properties, *Chemistry of Materials*, 12 (2000) 3151-3157.
- [65] J.-L. Xiao, S.-Y. Sun, J. Wang, P. Li, J.-G. Yu, Synthesis and Adsorption Properties of Li_{1.6}Mn_{1.6}O₄ Spinel, *Industrial & Engineering Chemistry Research*, 52 (2013) 11967-11973.

- [66] R. Chitrakar, Y. Makita, K. Ooi, A. Sonoda, Lithium recovery from salt lake brine by H_2TiO_3 , *Dalton Transactions*, 43 (2014) 8933-8939.
- [67] B. Zhao, Z. Qian, Y. Qiao, J. Li, Z. Wu, Z. Liu, The $\text{Li}(\text{H}_2\text{O})_n$ dehydration behavior influences the Li^+ ion adsorption on $\text{H}_4\text{Ti}_5\text{O}_{12}$ with different facets exposed, *Chemical Engineering Journal*, 451 (2023) 138870.
- [68] D. Weng, H. Duan, Y. Hou, J. Huo, L. Chen, F. Zhang, J. Wang, Introduction of manganese based lithium-ion Sieve-A review, *Progress in Natural Science: Materials International*, 30 (2020) 139-152.
- [69] O. Murphy, M.N. Haji, A review of technologies for direct lithium extraction from low Li^+ concentration aqueous solutions, *Frontiers in Chemical Engineering*, 4 (2022).
- [70] C.P. Lawagon, G.M. Nisola, J. Mun, A. Tron, R.E.C. Torrejos, J.G. Seo, H. Kim, W.-J. Chung, Adsorptive Li^+ mining from liquid resources by H_2TiO_3 : Equilibrium, kinetics, thermodynamics, and mechanisms, *Journal of Industrial and Engineering Chemistry*, 35 (2016) 347-356.
- [71] J. Yuan, Y. Zhao, Q. Li, Z. Ji, X. Guo, Preparation of potassium ionic sieve membrane and its application on extracting potash from seawater, *Separation and Purification Technology*, 99 (2012) 55-60.
- [72] L. Pan, A.-B. Zhang, J. Sun, Y. Ye, X.-G. Chen, M.-S. Xia, Application of ocean manganese nodules for the adsorption of potassium ions from seawater, *Minerals Engineering*, 49 (2013) 121-127.
- [73] G. Liu, Z. Zhao, A. Ghahreman, Novel approaches for lithium extraction from salt-lake brines: A review, *Hydrometallurgy*, 187 (2019) 81-100.
- [74] X. Li, Y. Mo, W. Qing, S. Shao, C.Y. Tang, J. Li, Membrane-based technologies for lithium recovery from water lithium resources: A review, *Journal of Membrane Science*, 591 (2019) 117317.
- [75] T. Luo, S. Abdu, M. Wessling, Selectivity of ion exchange membranes: A review, *Journal of Membrane Science*, 555 (2018) 429-454.
- [76] Y. Guo, Y. Ying, Y. Mao, X. Peng, B. Chen, Polystyrene Sulfonate Threaded through a Metal–Organic Framework Membrane for Fast and Selective Lithium-Ion Separation, *Angewandte Chemie International Edition*, 55 (2016) 15120-15124.
- [77] X. Pang, Y. Tao, Y. Xu, J. Pan, J. Shen, C. Gao, Enhanced monovalent selectivity of cation exchange membranes via adjustable charge density on functional layers, *Journal of Membrane Science*, 595 (2020) 117544.
- [78] T. Sata, T. Sata, W. Yang, Studies on cation-exchange membranes having permselectivity between cations in electrodialysis, *Journal of Membrane Science*, 206 (2002) 31-60.
- [79] Y. Kim, W.S. Walker, D.F. Lawler, Competitive separation of di- vs. mono-valent cations in electrodialysis: Effects of the boundary layer properties, *Water Research*, 46 (2012) 2042-2056.
- [80] Y. Du, B.K. Pramanik, Y. Zhang, L. Dumée, V. Jegatheesan, Recent Advances in the Theory and Application of Nanofiltration: a Review, *Current Pollution Reports*, 8 (2022) 51-80.
- [81] N. García Doménech, F. Purcell-Milton, Y.K. Gun'ko, Recent progress and future prospects in development of advanced materials for nanofiltration, *Materials Today Communications*, 23 (2020) 100888.
- [82] J.J. Richardson, M. Björnmalm, F. Caruso, Technology-driven layer-by-layer assembly of nanofilms, *Science*, 348 (2015) aaa2491.
- [83] X. Li, C. Zhang, S. Zhang, J. Li, B. He, Z. Cui, Preparation and characterization of positively charged polyamide composite nanofiltration hollow fiber membrane for lithium and magnesium separation, *Desalination*, 369 (2015) 26-36.
- [84] H.-Z. Zhang, Z.-L. Xu, H. Ding, Y.-J. Tang, Positively charged capillary nanofiltration membrane with high rejection for Mg^{2+} and Ca^{2+} and good separation for Mg^{2+} and Li^+ , *Desalination*, 420 (2017) 158-166.
- [85] R. Epsztein, R.M. DuChanois, C.L. Ritt, A. Noy, M. Elimelech, Towards single-species selectivity of membranes with subnanometre pores, *Nature Nanotechnology*, 15 (2020) 426-436.
- [86] X. Li, M.R. Hill, H. Wang, H. Zhang, Metal–Organic Framework-Based Ion-Selective Membranes, *Advanced Materials Technologies*, 6 (2021) 2000790.
- [87] Q. Wen, D. Yan, F. Liu, M. Wang, Y. Ling, P. Wang, P. Kluth, D. Schauries, C. Trautmann, P. Apel, W. Guo, G. Xiao, J. Liu, J. Xue, Y. Wang, Highly Selective Ionic Transport through Subnanometer Pores in Polymer Films, *Advanced Functional Materials*, 26 (2016) 5796-5803.

- [88] J. Abraham, K.S. Vasu, C.D. Williams, K. Gopinadhan, Y. Su, C.T. Cherian, J. Dix, E. Prestat, S.J. Haigh, I.V. Grigorieva, P. Carbone, A.K. Geim, R.R. Nair, Tunable sieving of ions using graphene oxide membranes, *Nature Nanotechnology*, 12 (2017) 546-550.
- [89] A. Noy, Kinetic Model of Gas Transport in Carbon Nanotube Channels, *The Journal of Physical Chemistry C*, 117 (2013) 7656-7660.
- [90] J.C. Bachman, S. Muy, A. Grimaud, H.-H. Chang, N. Pour, S.F. Lux, O. Paschos, F. Maglia, S. Lupart, P. Lamp, L. Giordano, Y. Shao-Horn, Inorganic Solid-State Electrolytes for Lithium Batteries: Mechanisms and Properties Governing Ion Conduction, *Chemical Reviews*, 116 (2016) 140-162.
- [91] L. Wang, S. Arnold, P. Ren, Q. Wang, J. Jin, Z. Wen, V. Presser, Redox Flow Battery for Continuous and Energy-Effective Lithium Recovery from Aqueous Solution, *ACS Energy Letters*, 7 (2022) 3539-3544.
- [92] Z. Li, C. Li, X. Liu, L. Cao, P. Li, R. Wei, X. Li, D. Guo, K.-W. Huang, Z. Lai, Continuous electrical pumping membrane process for seawater lithium mining, *Energy & Environmental Science*, 14 (2021) 3152-3159.
- [93] L. Fu, Y. Teng, P. Liu, W. Xin, Y. Qian, L. Yang, X. Lin, Y. Hu, X.-Y. Kong, L. Jiang, L. Wen, Electrochemical ion-pumping-assisted transfer system featuring a heterogeneous membrane for lithium recovery, *Chemical Engineering Journal*, 435 (2022) 134955.
- [94] A. Schmidt, F. Mestmäcker, L. Brückner, T. Elwert, J. Strube, Liquid-Liquid Extraction and Chromatography Process Routes for the Purification of Lithium, *Materials Science Forum*, 959 (2019) 79-99.
- [95] R.E.C. Torrejos, G.M. Nisola, H.S. Song, J.W. Han, C.P. Lawagon, J.G. Seo, S. Koo, H. Kim, W.-J. Chung, Liquid-liquid extraction of lithium using lipophilic dibenzo-14-crown-4 ether carboxylic acid in hydrophobic room temperature ionic liquid, *Hydrometallurgy*, 164 (2016) 362-371.
- [96] X. Zhao, H. Wu, M. Duan, X. Hao, Q. Yang, Q. Zhang, X. Huang, Liquid-liquid extraction of lithium from aqueous solution using novel ionic liquid extractants via COSMO-RS and experiments, *Fluid Phase Equilibria*, 459 (2018) 129-137.
- [97] Q. Sun, H. Chen, J. Yu, Investigation on the Lithium Extraction Process with the TBP-FeCl₃ Solvent System Using Experimental and DFT Methods, *Industrial & Engineering Chemistry Research*, 61 (2022) 4672-4682.
- [98] B.P. Czech, D.A. Babb, B. Son, R.A. Bartsch, Functionalized 13-crown-4, 14-crown-4, 15-crown-4, and 16-crown-4 compounds: synthesis and lithium ion complexation, *The Journal of Organic Chemistry*, 49 (1984) 4805-4810.
- [99] A. Chagnes, J. Swiatowska, *Lithium process chemistry: Resources, extraction, batteries, and recycling*, Elsevier, 2015.
- [100] B. Swain, Separation and purification of lithium by solvent extraction and supported liquid membrane, analysis of their mechanism: a review, *Journal of Chemical Technology & Biotechnology*, 91 (2016) 2549-2562.
- [101] N.M. Kocherginsky, Q. Yang, L. Seelam, Recent advances in supported liquid membrane technology, *Separation and Purification Technology*, 53 (2007) 171-177.
- [102] P. Ma, X.D. Chen, M.M. Hossain, Lithium Extraction from a Multicomponent Mixture Using Supported Liquid Membranes, *Separation Science and Technology*, 35 (2000) 2513-2533.
- [103] A.D. Sharma, N.D. Patil, A.W. Patwardhan, R.K. Moorthy, P.K. Ghosh, Synergistic interplay between D2EHPA and TBP towards the extraction of lithium using hollow fiber supported liquid membrane, *Separation Science and Technology*, 51 (2016) 2242-2254.
- [104] G. Zante, M. Boltoeva, A. Masmoudi, R. Barillon, D. Trébouet, Lithium extraction from complex aqueous solutions using supported ionic liquid membranes, *Journal of Membrane Science*, 580 (2019) 62-76.
- [105] W.M. Haynes, *CRC Handbook of Chemistry and Physics*
Lanthanum, 95th ed., CRC Press, Boca Raton, FL, 2014.
- [106] J.W. An, D.J. Kang, K.T. Tran, M.J. Kim, T. Lim, T. Tran, Recovery of lithium from Uyuni salar brine, *Hydrometallurgy*, 117-118 (2012) 64-70.
- [107] A.H. Hamzaoui, H. Hammi, A. M'nif, Operating conditions for lithium recovery from natural brines, *Russian Journal of Inorganic Chemistry*, 52 (2007) 1859-1863.

- [108] H. Helmholtz, Studies on electrical boundary layers, *Annalen der Physik*, 243 (1879) 337-382.
- [109] M. Gouy, Constitution of the electric charge at the surface of an electrolyte, *J. Phys. Theor. Appl.*, 9 (1910) 457-468.
- [110] D.L. Chapman, LI. A contribution to the theory of electrocapillarity, *The London, Edinburgh, and Dublin philosophical magazine and journal of science*, 25 (1913) 475-481.
- [111] H. Wang, L. Pilon, Accurate Simulations of Electric Double Layer Capacitance of Ultramicroelectrodes, *The Journal of Physical Chemistry C*, 115 (2011) 16711-16719.
- [112] O. Stern, ON THE THEORY OF THE ELECTROLYTIC DOUBLE LAYER, *Zeitschrift für Elektrochemie und angewandte physikalische Chemie*, 30 (1924) 508-516.
- [113] R. Zhao, P.M. Biesheuvel, H. Miedema, H. Bruning, A. van der Wal, Charge Efficiency: A Functional Tool to Probe the Double-Layer Structure Inside of Porous Electrodes and Application in the Modeling of Capacitive Deionization, *The Journal of Physical Chemistry Letters*, 1 (2010) 205-210.
- [114] P.M. Biesheuvel, R. Zhao, S. Porada, A. van der Wal, Theory of membrane capacitive deionization including the effect of the electrode pore space, *Journal of Colloid and Interface Science*, 360 (2011) 239-248.
- [115] R. Zhao, M. van Soestbergen, H.H.M. Rijnaarts, A. van der Wal, M.Z. Bazant, P.M. Biesheuvel, Time-dependent ion selectivity in capacitive charging of porous electrodes, *Journal of Colloid and Interface Science*, 384 (2012) 38-44.
- [116] S. Porada, M. Bryjak, A. van der Wal, P.M. Biesheuvel, Effect of electrode thickness variation on operation of capacitive deionization, *Electrochimica Acta*, 75 (2012) 148-156.
- [117] R. Zhao, P.M. Biesheuvel, A. van der Wal, Energy consumption and constant current operation in membrane capacitive deionization, *Energy & Environmental Science*, 5 (2012) 9520-9527.
- [118] Y. Jiang, J. Liu, Definitions of Pseudocapacitive Materials: A Brief Review, *ENERGY & ENVIRONMENTAL MATERIALS*, 2 (2019) 30-37.
- [119] T.S. Mathis, N. Kurra, X. Wang, D. Pinto, P. Simon, Y. Gogotsi, Energy Storage Data Reporting in Perspective—Guidelines for Interpreting the Performance of Electrochemical Energy Storage Systems, *Advanced Energy Materials*, 9 (2019) 1902007.
- [120] E. Frackowiak, Carbon materials for supercapacitor application, *Physical Chemistry Chemical Physics*, 9 (2007) 1774-1785.
- [121] P. Simon, Y. Gogotsi, Materials for electrochemical capacitors, *Nature Materials*, 7 (2008) 845-854.
- [122] J. Xie, P. Yang, Y. Wang, T. Qi, Y. Lei, C.M. Li, Puzzles and confusions in supercapacitor and battery: Theory and solutions, *Journal of Power Sources*, 401 (2018) 213-223.
- [123] S. Fleischmann, J.B. Mitchell, R. Wang, C. Zhan, D.-e. Jiang, V. Presser, V. Augustyn, Pseudocapacitance: From Fundamental Understanding to High Power Energy Storage Materials, *Chemical Reviews*, 120 (2020) 6738-6782.
- [124] B.E. Conway, H. Angerstein-Kozłowska, The electrochemical study of multiple-state adsorption in monolayers, *Accounts of Chemical Research*, 14 (1981) 49-56.
- [125] S. Hadzi-Jordanov, H. Angerstein-Kozłowska, M. Vukovič, B.E. Conway, Reversibility and Growth Behavior of Surface Oxide Films at Ruthenium Electrodes, *Journal of The Electrochemical Society*, 125 (1978) 1471.
- [126] B.E. Conway, Two-dimensional and quasi-two-dimensional isotherms for Li intercalation and upd processes at surfaces, *Electrochimica Acta*, 38 (1993) 1249-1258.
- [127] V. Augustyn, P. Simon, B. Dunn, Pseudocapacitive oxide materials for high-rate electrochemical energy storage, *Energy & Environmental Science*, 7 (2014) 1597-1614.
- [128] Y. Yang, C. Huang, Effect of synthetical conditions, morphology, and crystallographic structure of MnO₂ on its electrochemical behavior, *Journal of Solid State Electrochemistry*, 14 (2010) 1293-1301.
- [129] J.W. Kim, V. Augustyn, B. Dunn, The Effect of Crystallinity on the Rapid Pseudocapacitive Response of Nb₂O₅, *Advanced Energy Materials*, 2 (2012) 141-148.
- [130] M. Okubo, E. Hosono, J. Kim, M. Enomoto, N. Kojima, T. Kudo, H. Zhou, I. Honma, Nanosize Effect on High-Rate Li-Ion Intercalation in LiCoO₂ Electrode, *Journal of the American Chemical Society*, 129 (2007) 7444-7452.

- [131] T. Brousse, D. Bélanger, J.W. Long, To Be or Not To Be Pseudocapacitive?, *Journal of The Electrochemical Society*, 162 (2015) A5185.
- [132] Y. Ando, M. Okubo, A. Yamada, M. Otani, Capacitive versus Pseudocapacitive Storage in MXene, *Advanced Functional Materials*, 30 (2020) 2000820.
- [133] B.E. Conway, Transition from “Supercapacitor” to “Battery” Behavior in Electrochemical Energy Storage, *Journal of The Electrochemical Society*, 138 (1991) 1539.
- [134] X. Yu, S. Yun, J.S. Yeon, P. Bhattacharya, L. Wang, S.W. Lee, X. Hu, H.S. Park, Emergent Pseudocapacitance of 2D Nanomaterials, *Advanced Energy Materials*, 8 (2018) 1702930.
- [135] P. Simon, Y. Gogotsi, B. Dunn, Where Do Batteries End and Supercapacitors Begin?, *Science*, 343 (2014) 1210-1211.
- [136] R.R. Gaddam, L. Katzenmeier, X. Lamprecht, A.S. Bandarenka, Review on physical impedance models in modern battery research, *Physical Chemistry Chemical Physics*, 23 (2021) 12926-12944.
- [137] N. Yabuuchi, K. Kubota, M. Dahbi, S. Komaba, Research Development on Sodium-Ion Batteries, *Chemical Reviews*, 114 (2014) 11636-11682.
- [138] M.R. Palacín, Recent advances in rechargeable battery materials: a chemist’s perspective, *Chemical Society Reviews*, 38 (2009) 2565-2575.
- [139] Y. Zhu, T. Gao, X. Fan, F. Han, C. Wang, Electrochemical Techniques for Intercalation Electrode Materials in Rechargeable Batteries, *Accounts of Chemical Research*, 50 (2017) 1022-1031.
- [140] Y. Zhang, Q.-y. Huo, P.-p. Du, L.-z. Wang, A.-q. Zhang, Y.-h. Song, Y. Lv, G.-y. Li, Advances in new cathode material LiFePO₄ for lithium-ion batteries, *Synthetic Metals*, 162 (2012) 1315-1326.
- [141] E. de la Llave, E. Talaie, E. Levi, P.K. Nayak, M. Dixit, P.T. Rao, P. Hartmann, F. Chesneau, D.T. Major, M. Greenstein, D. Aurbach, L.F. Nazar, Improving Energy Density and Structural Stability of Manganese Oxide Cathodes for Na-Ion Batteries by Structural Lithium Substitution, *Chemistry of Materials*, 28 (2016) 9064-9076.
- [142] P. Nie, L. Shen, H. Luo, B. Ding, G. Xu, J. Wang, X. Zhang, Prussian blue analogues: a new class of anode materials for lithium ion batteries, *Journal of Materials Chemistry A*, 2 (2014) 5852-5857.
- [143] J. Cabana, L. Monconduit, D. Larcher, M.R. Palacín, Beyond Intercalation-Based Li-Ion Batteries: The State of the Art and Challenges of Electrode Materials Reacting Through Conversion Reactions, *Advanced Materials*, 22 (2010) E170-E192.
- [144] L. Fang, N. Bahlawane, W. Sun, H. Pan, B.B. Xu, M. Yan, Y. Jiang, Conversion-Alloying Anode Materials for Sodium Ion Batteries, *Small*, 17 (2021) 2101137.
- [145] J. Cui, H. Zheng, K. He, In Situ TEM Study on Conversion-Type Electrodes for Rechargeable Ion Batteries, *Advanced Materials*, 33 (2021) 2000699.
- [146] Y. Sun, N. Liu, Y. Cui, Promises and challenges of nanomaterials for lithium-based rechargeable batteries, *Nature Energy*, 1 (2016) 16071.
- [147] M. Lao, Y. Zhang, W. Luo, Q. Yan, W. Sun, S.X. Dou, Alloy-Based Anode Materials toward Advanced Sodium-Ion Batteries, *Advanced Materials*, 29 (2017) 1700622.
- [148] J.W. Wang, X.H. Liu, S.X. Mao, J.Y. Huang, Microstructural Evolution of Tin Nanoparticles during In Situ Sodium Insertion and Extraction, *Nano Letters*, 12 (2012) 5897-5902.
- [149] L. Wu, H. Lu, L. Xiao, X. Ai, H. Yang, Y. Cao, Electrochemical properties and morphological evolution of pitaya-like Sb@C microspheres as high-performance anode for sodium ion batteries, *Journal of Materials Chemistry A*, 3 (2015) 5708-5713.
- [150] S. Imtiaz, I.S. Amiinu, Y. Xu, T. Kennedy, C. Blackman, K.M. Ryan, Progress and perspectives on alloying-type anode materials for advanced potassium-ion batteries, *Materials Today*, 48 (2021) 241-269.
- [151] C.-X. Zu, H. Li, Thermodynamic analysis on energy densities of batteries, *Energy & Environmental Science*, 4 (2011) 2614-2624.
- [152] F. Wu, G. Yushin, Conversion cathodes for rechargeable lithium and lithium-ion batteries, *Energy & Environmental Science*, 10 (2017) 435-459.
- [153] H. Kim, J. Hong, K.-Y. Park, H. Kim, S.-W. Kim, K. Kang, Aqueous Rechargeable Li and Na Ion Batteries, *Chemical Reviews*, 114 (2014) 11788-11827.

- [154] J. Lin, C. Liu, H. Cao, R. Chen, Y. Yang, L. Li, Z. Sun, Environmentally benign process for selective recovery of valuable metals from spent lithium-ion batteries by using conventional sulfation roasting, *Green Chemistry*, 21 (2019) 5904-5913.
- [155] Y. Zhang, C. Prehal, H. Jiang, Y. Liu, G. Feng, V. Presser, Ionophobicity of carbon sub-nanometer pores enables efficient desalination at high salinity, *Cell Reports Physical Science*, 3 (2022) 100689.
- [156] A.N. Shocron, R.S. Roth, E.N. Gueyes, R. Epsztein, M.E. Suss, Comparison of Ion Selectivity in Electrodialysis and Capacitive Deionization, *Environmental Science & Technology Letters*, (2022).
- [157] J.E. Dykstra, J. Dijkstra, A. van der Wal, H.V.M. Hamelers, S. Porada, On-line method to study dynamics of ion adsorption from mixtures of salts in capacitive deionization, *Desalination*, 390 (2016) 47-52.
- [158] C.-H. Hou, C.-Y. Huang, A comparative study of electrosorption selectivity of ions by activated carbon electrodes in capacitive deionization, *Desalination*, 314 (2013) 124-129.
- [159] M.E. Suss, Size-Based Ion Selectivity of Micropore Electric Double Layers in Capacitive Deionization Electrodes, *Journal of The Electrochemical Society*, 164 (2017) E270.
- [160] E.N. Gueyes, A.N. Shocron, Y. Chen, C.E. Diesendruck, M.E. Suss, Long-lasting, monovalent-selective capacitive deionization electrodes, *npj Clean Water*, 4 (2021) 22.
- [161] B. Corry, Mechanisms of selective ion transport and salt rejection in carbon nanostructures, *MRS Bulletin*, 42 (2017) 306-310.
- [162] L. Eliad, G. Salitra, A. Soffer, D. Aurbach, Ion Sieving Effects in the Electrical Double Layer of Porous Carbon Electrodes: Estimating Effective Ion Size in Electrolytic Solutions, *The Journal of Physical Chemistry B*, 105 (2001) 6880-6887.
- [163] P. Srimuk, J. Lee, Ö. Budak, J. Choi, M. Chen, G. Feng, C. Prehal, V. Presser, In Situ Tracking of Partial Sodium Desolvation of Materials with Capacitive, Pseudocapacitive, and Battery-like Charge/Discharge Behavior in Aqueous Electrolytes, *Langmuir*, 34 (2018) 13132-13143.
- [164] J.G. Gamaethiralalage, K. Singh, S. Sahin, J. Yoon, M. Elimelech, M.E. Suss, P. Liang, P.M. Biesheuvel, R.L. Zornitta, L.C.P.M. de Smet, Recent advances in ion selectivity with capacitive deionization, *Energy & Environmental Science*, 14 (2021) 1095-1120.
- [165] P. Srimuk, J. Lee, S. Fleischmann, M. Aslan, C. Kim, V. Presser, Potential-Dependent, Switchable Ion Selectivity in Aqueous Media Using Titanium Disulfide, *ChemSusChem*, 11 (2018) 2091-2100.
- [166] Z.-w. Zhao, X.-f. Si, X.-x. Liang, X.-h. Liu, L.-h. He, Electrochemical behavior of Li^+ , Mg^{2+} , Na^+ and K^+ in $\text{LiFePO}_4/\text{FePO}_4$ structures, *Transactions of Nonferrous Metals Society of China*, 23 (2013) 1157-1164.
- [167] S.P. Ong, V.L. Chevrier, G. Hautier, A. Jain, C. Moore, S. Kim, X. Ma, G. Ceder, Voltage, stability and diffusion barrier differences between sodium-ion and lithium-ion intercalation materials, *Energy & Environmental Science*, 4 (2011) 3680-3688.
- [168] R. Trócoli, A. Battistel, F.L. Mantia, Selectivity of a Lithium-Recovery Process Based on LiFePO_4 , *Chemistry – A European Journal*, 20 (2014) 9888-9891.
- [169] W. Xu, D. Liu, X. Liu, D. Wang, L. He, Z. Zhao, Highly selective and efficient lithium extraction from brines by constructing a novel multiple-crack-porous $\text{LiFePO}_4/\text{FePO}_4$ electrode, *Desalination*, 546 (2023) 116188.
- [170] Y. Cai, W. Zhang, R. Fang, D. Zhao, Y. Wang, J. Wang, Well-dispersed few-layered MoS_2 connected with robust 3D conductive architecture for rapid capacitive deionization process and its specific ion selectivity, *Desalination*, 520 (2021) 115325.
- [171] L. Wang, M. Torkamanzadeh, A. Majed, Y. Zhang, Q. Wang, B. Breitung, G. Feng, M. Naguib, V. Presser, Time-Dependent Cation Selectivity of Titanium Carbide MXene in Aqueous Solution, *Advanced Sustainable Systems*, 6 (2022) 2100383.
- [172] P. Liu, T. Yan, J. Zhang, L. Shi, D. Zhang, Separation and recovery of heavy metal ions and salt ions from wastewater by 3D graphene-based asymmetric electrodes via capacitive deionization, *Journal of Materials Chemistry A*, 5 (2017) 14748-14757.
- [173] J. Kim, A. Jain, K. Zuo, R. Verduzco, S. Walker, M. Elimelech, Z. Zhang, X. Zhang, Q. Li, Removal of calcium ions from water by selective electrosorption using target-ion specific nanocomposite electrode, *Water Research*, 160 (2019) 445-453.

- [174] W. Tang, J. Liang, D. He, J. Gong, L. Tang, Z. Liu, D. Wang, G. Zeng, Various cell architectures of capacitive deionization: Recent advances and future trends, *Water Research*, 150 (2019) 225-251.
- [175] D. Ma, Y. Cai, Y. Wang, S. Xu, J. Wang, M.U. Khan, Grafting the Charged Functional Groups on Carbon Nanotubes for Improving the Efficiency and Stability of Capacitive Deionization Process, *ACS Applied Materials & Interfaces*, 11 (2019) 17617-17628.
- [176] F. Dixit, K. Zimmermann, R. Dutta, N.J. Prakash, B. Barbeau, M. Mohseni, B. Kandasubramanian, Application of MXenes for water treatment and energy-efficient desalination: A review, *Journal of Hazardous Materials*, 423 (2022) 127050.
- [177] X. Gao, A. Omosebi, Z. Ma, F. Zhu, J. Landon, M. Ghorbanian, N. Kern, K. Liu, Capacitive deionization using symmetric carbon electrode pairs, *Environmental Science: Water Research & Technology*, 5 (2019) 660-671.
- [178] R. Uwayid, C.E. Diesendruck, M.E. Suss, Emerging investigator series: a comparison of strong and weak-acid functionalized carbon electrodes in capacitive deionization, *Environmental Science: Water Research & Technology*, 8 (2022) 949-956.
- [179] X. Gao, A. Omosebi, J. Landon, K. Liu, Surface charge enhanced carbon electrodes for stable and efficient capacitive deionization using inverted adsorption-desorption behavior, *Energy & Environmental Science*, 8 (2015) 897-909.
- [180] J. Lee, S.-H. Yu, C. Kim, Y.-E. Sung, J. Yoon, Highly selective lithium recovery from brine using a λ - MnO_2 -Ag battery, *Physical Chemistry Chemical Physics*, 15 (2013) 7690-7695.
- [181] F. Chen, Y. Huang, L. Guo, M. Ding, H.Y. Yang, A dual-ion electrochemistry deionization system based on $\text{AgCl-Na}_{0.44}\text{MnO}_2$ electrodes, *Nanoscale*, 9 (2017) 10101-10108.
- [182] K. Wang, Y. Liu, Z. Ding, Z. Chen, X. Xu, M. Wang, T. Lu, L. Pan, Chloride pre-intercalated CoFe -layered double hydroxide as chloride ion capturing electrode for capacitive deionization, *Chemical Engineering Journal*, 433 (2022) 133578.
- [183] J. Lee, S. Kim, C. Kim, J. Yoon, Hybrid capacitive deionization to enhance the desalination performance of capacitive techniques, *Energy & Environmental Science*, 7 (2014) 3683-3689.
- [184] Z. Ding, X. Xu, Y. Li, K. Wang, T. Lu, L. Pan, Significantly improved stability of hybrid capacitive deionization using nickel hexacyanoferrate/reduced graphene oxide cathode at low voltage operation, *Desalination*, 468 (2019) 114078.
- [185] J.-B. Lee, K.-K. Park, H.-M. Eum, C.-W. Lee, Desalination of a thermal power plant wastewater by membrane capacitive deionization, *Desalination*, 196 (2006) 125-134.
- [186] N. Kim, J. Lee, S. Kim, S.P. Hong, C. Lee, J. Yoon, C. Kim, Short Review of Multichannel Membrane Capacitive Deionization: Principle, Current Status, and Future Prospect, *Applied Sciences-Basel*, 10 (2020).
- [187] Y. Zhang, P. Srimuk, M. Aslan, M. Gallei, V. Presser, Polymer ion-exchange membranes for capacitive deionization of aqueous media with low and high salt concentration, *Desalination*, 479 (2020) 114331.
- [188] C. Kim, P. Srimuk, J. Lee, V. Presser, Enhanced desalination via cell voltage extension of membrane capacitive deionization using an aqueous/organic bi-electrolyte, *Desalination*, 443 (2018) 56-61.
- [189] Y. Zhang, S.T. Senthilkumar, J. Park, J. Park, Y. Kim, A New Rechargeable Seawater Desalination Battery System, *Batteries & Supercaps*, 1 (2018) 6-10.
- [190] N. Kim, S. Jeong, W. Go, Y. Kim, A Na^+ ion-selective desalination system utilizing a NASICON ceramic membrane, *Water Research*, 215 (2022) 118250.
- [191] S. Yang, F. Zhang, H. Ding, P. He, H. Zhou, Lithium Metal Extraction from Seawater, *Joule*, 2 (2018) 1648-1651.
- [192] D.G. Kwabi, Y. Ji, M.J. Aziz, Electrolyte Lifetime in Aqueous Organic Redox Flow Batteries: A Critical Review, *Chemical Reviews*, 120 (2020) 6467-6489.
- [193] P. Srimuk, S. Husmann, V. Presser, Low voltage operation of a silver/silver chloride battery with high desalination capacity in seawater, *RSC Advances*, 9 (2019) 14849-14858.
- [194] R. Trócoli, A. Battistel, F. La Mantia, Nickel Hexacyanoferrate as Suitable Alternative to Ag for Electrochemical Lithium Recovery, *ChemSusChem*, 8 (2015) 2514-2519.

- [195] S.-i. Jeon, H.-r. Park, J.-g. Yeo, S. Yang, C.H. Cho, M.H. Han, D.K. Kim, Desalination via a new membrane capacitive deionization process utilizing flow-electrodes, *Energy & Environmental Science*, 6 (2013) 1471-1475.
- [196] P. Nativ, O. Lahav, Y. Gendel, Separation of divalent and monovalent ions using flow-electrode capacitive deionization with nanofiltration membranes, *Desalination*, 425 (2018) 123-129.
- [197] K.B. Hatzell, E. Iwama, A. Ferris, B. Daffos, K. Urita, T. Tzedakis, F. Chauvet, P.-L. Taberna, Y. Gogotsi, P. Simon, Capacitive deionization concept based on suspension electrodes without ion exchange membranes, *Electrochemistry Communications*, 43 (2014) 18-21.
- [198] P. Nativ, Y. Badash, Y. Gendel, New insights into the mechanism of flow-electrode capacitive deionization, *Electrochemistry Communications*, 76 (2017) 24-28.
- [199] F. Yang, Y. He, L. Rosentsvit, M.E. Suss, X. Zhang, T. Gao, P. Liang, Flow-electrode capacitive deionization: A review and new perspectives, *Water Research*, 200 (2021) 117222.
- [200] G. Folaranmi, M. Tauk, M. Bechelany, P. Sizat, M. Cretin, F. Zaviska, Investigation of fine activated carbon as a viable flow electrode in capacitive deionization, *Desalination*, 525 (2022) 115500.
- [201] S. Sasi, A. Murali, S.V. Nair, A.S. Nair, K.R.V. Subramanian, The effect of graphene on the performance of an electrochemical flow capacitor, *Journal of Materials Chemistry A*, 3 (2015) 2717-2725.
- [202] K.-Y. Chen, Y.-Y. Shen, D.-M. Wang, C.-H. Hou, Carbon nanotubes/activated carbon hybrid as a high-performance suspension electrode for the electrochemical desalination of wastewater, *Desalination*, 522 (2022) 115440.
- [203] Y. Sun, Y. Cheng, F. Yu, J. Ma, Enhanced Salt Removal Performance Using Graphene-Modified Sodium Vanadium Fluorophosphate in Flow Electrode Capacitive Deionization, *ACS Applied Materials & Interfaces*, 13 (2021) 53850-53858.
- [204] Y. Xu, F. Duan, Y. Li, H. Cao, J. Chang, H. Pang, J. Chen, Enhanced desalination performance in asymmetric flow electrode capacitive deionization with nickel hexacyanoferrate and activated carbon electrodes, *Desalination*, 514 (2021) 115172.
- [205] S. Porada, D. Weingarh, H.V.M. Hamelers, M. Bryjak, V. Presser, P.M. Biesheuvel, Carbon flow electrodes for continuous operation of capacitive deionization and capacitive mixing energy generation, *Journal of Materials Chemistry A*, 2 (2014) 9313-9321.
- [206] Y.-U. Shin, J. Lim, C. Boo, S. Hong, Improving the feasibility and applicability of flow-electrode capacitive deionization (FCDI): Review of process optimization and energy efficiency, *Desalination*, 502 (2021) 114930.
- [207] J.W. Campos, M. Beidaghi, K.B. Hatzell, C.R. Dennison, B. Musci, V. Presser, E.C. Kumbur, Y. Gogotsi, Investigation of carbon materials for use as a flowable electrode in electrochemical flow capacitors, *Electrochimica Acta*, 98 (2013) 123-130.
- [208] J. Lee, D. Weingarh, I. Grobelsek, V. Presser, Use of Surfactants for Continuous Operation of Aqueous Electrochemical Flow Capacitors, *Energy Technology*, 4 (2016) 75-84.
- [209] G.J. Doornbusch, J.E. Dykstra, P.M. Biesheuvel, M.E. Suss, Fluidized bed electrodes with high carbon loading for water desalination by capacitive deionization, *Journal of Materials Chemistry A*, 4 (2016) 3642-3647.
- [210] N.A.T. Tran, T.M. Khoi, N.M. Phuoc, H.B. Jung, Y. Cho, A review of recent advances in electrode materials and applications for flow-electrode desalination systems, *Desalination*, 541 (2022) 116037.
- [211] C. Zhang, J. Ma, L. Wu, J. Sun, L. Wang, T. Li, T.D. Waite, Flow Electrode Capacitive Deionization (FCDI): Recent Developments, Environmental Applications, and Future Perspectives, *Environmental Science & Technology*, 55 (2021) 4243-4267.
- [212] D. Moreno, M.C. Hatzell, Influence of Feed-Electrode Concentration Differences in Flow-Electrode Systems for Capacitive Deionization, *Industrial & Engineering Chemistry Research*, 57 (2018) 8802-8809.
- [213] J. Ma, C. Zhang, F. Yang, X. Zhang, M.E. Suss, X. Huang, P. Liang, Carbon Black Flow Electrode Enhanced Electrochemical Desalination Using Single-Cycle Operation, *Environmental Science & Technology*, 54 (2020) 1177-1185.
- [214] A. Rommerskirchen, Y. Gendel, M. Wessling, Single module flow-electrode capacitive deionization for continuous water desalination, *Electrochemistry Communications*, 60 (2015) 34-37.

- [215] X. Hou, Q. Liang, X. Hu, Y. Zhou, Q. Ru, F. Chen, S. Hu, Coupling desalination and energy storage with redox flow electrodes, *Nanoscale*, 10 (2018) 12308-12314.
- [216] G. Mohandass, W. Chen, S. Krishnan, T. Kim, Asymmetric and Symmetric Redox Flow Batteries for Energy-Efficient, High-Recovery Water Desalination, *Environmental Science & Technology*, 56 (2022) 4477-4488.
- [217] D.-H. Nam, M.A. Lumley, K.-S. Choi, Electrochemical Redox Cells Capable of Desalination and Energy Storage: Addressing Challenges of the Water–Energy Nexus, *ACS Energy Letters*, 6 (2021) 1034-1044.
- [218] K. Ramalingam, Q. Wei, F. Chen, K. Shen, M. Liang, J. Dai, X. Hou, Q. Ru, G. Babu, Q. He, P.M. Ajayan, Achieving High-Quality Freshwater from a Self-Sustainable Integrated Solar Redox-Flow Desalination Device, *Small*, 17 (2021) 2100490.
- [219] F. Chen, J. Wang, C. Feng, J. Ma, T. David Waite, Low energy consumption and mechanism study of redox flow desalination, *Chemical Engineering Journal*, 401 (2020) 126111.
- [220] C. Debruler, W. Wu, K. Cox, B. Vanness, T.L. Liu, Integrated Saltwater Desalination and Energy Storage through a pH Neutral Aqueous Organic Redox Flow Battery, *Advanced Functional Materials*, 30 (2020) 2000385.
- [221] Q. Liang, F. Chen, S. Wang, Q. Ru, Q. He, X. Hou, C.-y. Su, Y. Shi, An organic flow desalination battery, *Energy Storage Materials*, 20 (2019) 203-207.
- [222] E.S. Beh, M.A. Benedict, D. Desai, J.B. Rivest, A Redox-Shuttled Electrochemical Method for Energy-Efficient Separation of Salt from Water, *ACS Sustainable Chemistry & Engineering*, 7 (2019) 13411-13417.
- [223] Y. Zhang, L. Liu, J. Xi, Z. Wu, X. Qiu, The benefits and limitations of electrolyte mixing in vanadium flow batteries, *Applied Energy*, 204 (2017) 373-381.
- [224] Q. Luo, L. Li, W. Wang, Z. Nie, X. Wei, B. Li, B. Chen, Z. Yang, V. Sprenkle, Capacity Decay and Remediation of Nafion-based All-Vanadium Redox Flow Batteries, *ChemSusChem*, 6 (2013) 268-274.
- [225] D. Desai, E.S. Beh, S. Sahu, V. Vedharathinam, Q. van Overmeere, C.F. de Lannoy, A.P. Jose, A.R. Völkel, J.B. Rivest, Electrochemical Desalination of Seawater and Hypersaline Brines with Coupled Electricity Storage, *ACS Energy Letters*, 3 (2018) 375-379.
- [226] J. Luo, A.P. Wang, M. Hu, T.L. Liu, Materials challenges of aqueous redox flow batteries, *MRS Energy & Sustainability*, 9 (2022) 1-12.
- [227] W. Xiao, D. Wang, X.W. Lou, Shape-Controlled Synthesis of MnO₂ Nanostructures with Enhanced Electrocatalytic Activity for Oxygen Reduction, *The Journal of Physical Chemistry C*, 114 (2010) 1694-1700.
- [228] Z.Y. Leong, H.Y. Yang, A Study of MnO₂ with Different Crystalline Forms for Pseudocapacitive Desalination, *ACS Applied Materials & Interfaces*, 11 (2019) 13176-13184.
- [229] P. Ragupathy, H.N. Vasan, N. Munichandraiah, Synthesis and Characterization of Nano- MnO₂ for Electrochemical Supercapacitor Studies, *Journal of The Electrochemical Society*, 155 (2008) A34.
- [230] B.W. Byles, D.A. Cullen, K.L. More, E. Pomerantseva, Tunnel structured manganese oxide nanowires as redox active electrodes for hybrid capacitive deionization, *Nano Energy*, 44 (2018) 476-488.
- [231] S. Xu, S.-P. Li, T. Wang, C.-F. Wang, Effect of Surface Ionization of Doped MnO₂ on Capacitive Deionization Efficiency, *Langmuir*, 35 (2019) 628-640.
- [232] Z.-h. Liu, K. Ooi, Preparation and Alkali-Metal Ion Extraction/Insertion Reactions with Nanofibrous Manganese Oxide Having 2 × 4 Tunnel Structure, *Chemistry of Materials*, 15 (2003) 3696-3703.
- [233] Y. Wang, J. Liu, B. Lee, R. Qiao, Z. Yang, S. Xu, X. Yu, L. Gu, Y.-S. Hu, W. Yang, K. Kang, H. Li, X.-Q. Yang, L. Chen, X. Huang, Ti-substituted tunnel-type Na_{0.44}MnO₂ oxide as a negative electrode for aqueous sodium-ion batteries, *Nature Communications*, 6 (2015) 6401.
- [234] M.S. Chae, H.J. Kim, H. Bu, J. Lyoo, R. Attias, B. Dlugatch, M. Oliei, Y. Gofer, S.-T. Hong, D. Aurbach, The Sodium Storage Mechanism in Tunnel-Type Na_{0.44}MnO₂ Cathodes and the Way to Ensure Their Durable Operation, *Advanced Energy Materials*, 10 (2020) 2000564.
- [235] H. Yoon, J. Lee, S. Kim, J. Yoon, Electrochemical sodium ion impurity removal system for producing high purity KCl, *Hydrometallurgy*, 175 (2018) 354-358.

- [236] D.J. Kim, R. Ponraj, A.G. Kannan, H.-W. Lee, R. Fathi, R. Ruffo, C.M. Mari, D.K. Kim, Diffusion behavior of sodium ions in $\text{Na}_{0.44}\text{MnO}_2$ in aqueous and non-aqueous electrolytes, *Journal of Power Sources*, 244 (2013) 758-763.
- [237] J.F. Whitacre, A. Tevar, S. Sharma, $\text{Na}_4\text{Mn}_9\text{O}_{18}$ as a positive electrode material for an aqueous electrolyte sodium-ion energy storage device, *Electrochemistry Communications*, 12 (2010) 463-466.
- [238] Z. Li, D. Young, K. Xiang, W.C. Carter, Y.-M. Chiang, Towards High Power High Energy Aqueous Sodium-Ion Batteries: The $\text{NaTi}_2(\text{PO}_4)_3/\text{Na}_{0.44}\text{MnO}_2$ System, *Advanced Energy Materials*, 3 (2013) 290-294.
- [239] Y. Cao, L. Xiao, W. Wang, D. Choi, Z. Nie, J. Yu, L.V. Saraf, Z. Yang, J. Liu, Reversible Sodium Ion Insertion in Single Crystalline Manganese Oxide Nanowires with Long Cycle Life, *Advanced Materials*, 23 (2011) 3155-3160.
- [240] S. Kim, H. Yoon, D. Shin, J. Lee, J. Yoon, Electrochemical selective ion separation in capacitive deionization with sodium manganese oxide, *Journal of Colloid and Interface Science*, 506 (2017) 644-648.
- [241] P.P. Michałowski, M. Anayee, T.S. Mathis, S. Kozdra, A. Wójcik, K. Hantanasirisakul, I. Jóźwik, A. Piątkowska, M. Możdżonek, A. Malinowska, R. Diduszko, E. Wierzbicka, Y. Gogotsi, Oxycarbide MXenes and MAX phases identification using monoatomic layer-by-layer analysis with ultralow-energy secondary-ion mass spectrometry, *Nature Nanotechnology*, 17 (2022) 1192-1197.
- [242] D. Xiong, X. Li, Z. Bai, S. Lu, Recent Advances in Layered $\text{Ti}_3\text{C}_2\text{T}_x$ MXene for Electrochemical Energy Storage, *Small*, 14 (2018) 1703419.
- [243] S.K. Nemani, B. Zhang, B.C. Wyatt, Z.D. Hood, S. Manna, R. Khaledialidusti, W. Hong, M.G. Sternberg, S.K.R.S. Sankaranarayanan, B. Anasori, High-Entropy 2D Carbide MXenes: TiVNbMoC_3 and TiVCrMoC_3 , *ACS Nano*, 15 (2021) 12815-12825.
- [244] A. VahidMohammadi, J. Rosen, Y. Gogotsi, The world of two-dimensional carbides and nitrides (MXenes), *Science*, 372 (2021) eabf1581.
- [245] R. Meshkian, H. Lind, J. Halim, A. El Ghazaly, J. Thörnberg, Q. Tao, M. Dahlgqvist, J. Palisaitis, P.O.Å. Persson, J. Rosen, Theoretical Analysis, Synthesis, and Characterization of 2D $\text{W}_{1.33}\text{C}$ (MXene) with Ordered Vacancies, *ACS Applied Nano Materials*, 2 (2019) 6209-6219.
- [246] J. Yang, G. Yao, S. Sun, Z. Chen, S. Yuan, K. Wu, X. Fu, Q. Wang, W. Cui, Structural, magnetic properties of in-plane chemically ordered $(\text{Mo}_{2/3}\text{R}_{1/3})_2\text{AlC}$ (R = Gd, Tb, Dy, Ho, Er and Y) MAX phase and enhanced capacitance of $\text{Mo}_{1.33}\text{C}$ MXene derivatives, *Carbon*, 179 (2021) 104-110.
- [247] M. Naguib, V.N. Mochalin, M.W. Barsoum, Y. Gogotsi, 25th Anniversary Article: MXenes: A New Family of Two-Dimensional Materials, *Advanced Materials*, 26 (2014) 992-1005.
- [248] Q. Tao, M. Dahlgqvist, J. Lu, S. Kota, R. Meshkian, J. Halim, J. Palisaitis, L. Hultman, M.W. Barsoum, P.O.Å. Persson, J. Rosen, Two-dimensional $\text{Mo}_{1.33}\text{C}$ MXene with divacancy ordering prepared from parent 3D laminate with in-plane chemical ordering, *Nature Communications*, 8 (2017) 14949.
- [249] A. Mockute, Q. Tao, M. Dahlgqvist, J. Lu, S. Calder, E.N. Caspi, L. Hultman, J. Rosen, Materials synthesis, neutron powder diffraction, and first-principles calculations of $(\text{Mo}_x\text{Sc}_{1-x})_2\text{AlC}$ i-MAX phase used as parent material for MXene derivation, *Physical Review Materials*, 3 (2019) 113607.
- [250] M. Torkamanzadeh, L. Wang, Y. Zhang, Ö. Budak, P. Srimuk, V. Presser, MXene/Activated-Carbon Hybrid Capacitive Deionization for Permselective Ion Removal at Low and High Salinity, *ACS Applied Materials & Interfaces*, 12 (2020) 26013-26025.
- [251] S. Ren, J.-L. Xu, L. Cheng, X. Gao, S.-D. Wang, Amine-Assisted Delaminated 2D $\text{Ti}_3\text{C}_2\text{T}_x$ MXenes for High Specific Capacitance in Neutral Aqueous Electrolytes, *ACS Applied Materials & Interfaces*, 13 (2021) 35878-35888.
- [252] P. Srimuk, J. Halim, J. Lee, Q. Tao, J. Rosen, V. Presser, Two-Dimensional Molybdenum Carbide (MXene) with Divacancy Ordering for Brackish and Seawater Desalination via Cation and Anion Intercalation, *ACS Sustainable Chemistry & Engineering*, 6 (2018) 3739-3747.
- [253] X. Ma, X. Zhu, C. Huang, J. Fan, Revealing the effects of terminal groups of MXene on the water desalination performance, *Journal of Membrane Science*, 647 (2022) 120334.
- [254] J. Xu, T. Peng, Q. Zhang, H. Zheng, H. Yu, S. Shi, Intercalation Effects on the Electrochemical Properties of $\text{Ti}_3\text{C}_2\text{T}_x$ MXene Nanosheets for High-Performance Supercapacitors, *ACS Applied Nano Materials*, 5 (2022) 8794-8803.

- [255] B. Chen, A. Feng, R. Deng, K. Liu, Y. Yu, L. Song, MXene as a Cation-Selective Cathode Material for Asymmetric Capacitive Deionization, *ACS Applied Materials & Interfaces*, 12 (2020) 13750-13758.
- [256] L. Guo, X. Wang, Z.Y. Leong, R. Mo, L. Sun, H.Y. Yang, Ar plasma modification of 2D MXene $Ti_3C_2T_x$ nanosheets for efficient capacitive desalination, *FlatChem*, 8 (2018) 17-24.
- [257] J. Ma, Y. Cheng, L. Wang, X. Dai, F. Yu, Free-standing $Ti_3C_2T_x$ MXene film as binder-free electrode in capacitive deionization with an ultrahigh desalination capacity, *Chemical Engineering Journal*, 384 (2020) 123329.
- [258] W. Bao, X. Tang, X. Guo, S. Choi, C. Wang, Y. Gogotsi, G. Wang, Porous Cryo-Dried MXene for Efficient Capacitive Deionization, *Joule*, 2 (2018) 778-787.
- [259] Z. Chen, X. Xu, Y. Liu, J. Li, K. Wang, Z. Ding, F. Meng, T. Lu, L. Pan, Ultra-durable and highly-efficient hybrid capacitive deionization by MXene confined MoS_2 heterostructure, *Desalination*, 528 (2022) 115616.
- [260] K. Wang, L. Chen, G. Zhu, X. Xu, L. Wan, T. Lu, L. Pan, Ferroferric oxide@titanium carbide MXene heterostructure with enhanced sodium storage ability for efficient hybrid capacitive deionization, *Desalination*, 522 (2022) 115420.
- [261] Q. Li, X. Xu, J. Guo, J.P. Hill, H. Xu, L. Xiang, C. Li, Y. Yamauchi, Y. Mai, Two-Dimensional MXene-Polymer Heterostructure with Ordered In-Plane Mesochannels for High-Performance Capacitive Deionization, *Angewandte Chemie International Edition*, 60 (2021) 26528-26534.
- [262] Y. Gogotsi, B. Anasori, The Rise of MXenes, *ACS Nano*, 13 (2019) 8491-8494.
- [263] S. Buczek, M.L. Barsoum, S. Uzun, N. Kurra, R. Andris, E. Pomerantseva, K.A. Mahmoud, Y. Gogotsi, Rational Design of Titanium Carbide MXene Electrode Architectures for Hybrid Capacitive Deionization, *ENERGY & ENVIRONMENTAL MATERIALS*, 3 (2020) 398-404.
- [264] J. Come, J.M. Black, M.R. Lukatskaya, M. Naguib, M. Beidaghi, A.J. Rondinone, S.V. Kalinin, D.J. Wesolowski, Y. Gogotsi, N. Balke, Controlling the actuation properties of MXene paper electrodes upon cation intercalation, *Nano Energy*, 17 (2015) 27-35.
- [265] J. Qian, C. Wu, Y. Cao, Z. Ma, Y. Huang, X. Ai, H. Yang, Prussian Blue Cathode Materials for Sodium-Ion Batteries and Other Ion Batteries, *Advanced Energy Materials*, 8 (2018) 1702619.
- [266] H. Yi, R. Qin, S. Ding, Y. Wang, S. Li, Q. Zhao, F. Pan, Structure and Properties of Prussian Blue Analogues in Energy Storage and Conversion Applications, *Advanced Functional Materials*, 31 (2021) 2006970.
- [267] X. Wu, C. Wu, C. Wei, L. Hu, J. Qian, Y. Cao, X. Ai, J. Wang, H. Yang, Highly Crystallized $Na_2CoFe(CN)_6$ with Suppressed Lattice Defects as Superior Cathode Material for Sodium-Ion Batteries, *ACS Applied Materials & Interfaces*, 8 (2016) 5393-5399.
- [268] J. Song, L. Wang, Y. Lu, J. Liu, B. Guo, P. Xiao, J.-J. Lee, X.-Q. Yang, G. Henkelman, J.B. Goodenough, Removal of Interstitial H_2O in Hexacyanometallates for a Superior Cathode of a Sodium-Ion Battery, *Journal of the American Chemical Society*, 137 (2015) 2658-2664.
- [269] C. Xu, Z. Yang, X. Zhang, M. Xia, H. Yan, J. Li, H. Yu, L. Zhang, J. Shu, Prussian Blue Analogues in Aqueous Batteries and Desalination Batteries, *Nano-Micro Letters*, 13 (2021) 166.
- [270] B. Wang, Y. Han, X. Wang, N. Bahlawane, H. Pan, M. Yan, Y. Jiang, Prussian Blue Analogs for Rechargeable Batteries, *iScience*, 3 (2018) 110-133.
- [271] F. Yu, L. Wang, Y. Wang, X. Shen, Y. Cheng, J. Ma, Faradaic reactions in capacitive deionization for desalination and ion separation, *Journal of Materials Chemistry A*, 7 (2019) 15999-16027.
- [272] M. Pasta, R.Y. Wang, R. Ruffo, R. Qiao, H.-W. Lee, B. Shyam, M. Guo, Y. Wang, L.A. Wray, W. Yang, M.F. Toney, Y. Cui, Manganese-cobalt hexacyanoferrate cathodes for sodium-ion batteries, *Journal of Materials Chemistry A*, 4 (2016) 4211-4223.
- [273] F. Scholz, A. Dostal, The Formal Potentials of Solid Metal Hexacyanometallates, *Angewandte Chemie International Edition in English*, 34 (1996) 2685-2687.
- [274] K.C. Smith, Theoretical evaluation of electrochemical cell architectures using cation intercalation electrodes for desalination, *Electrochimica Acta*, 230 (2017) 333-341.
- [275] J. Lee, S. Kim, J. Yoon, Rocking Chair Desalination Battery Based on Prussian Blue Electrodes, *ACS Omega*, 2 (2017) 1653-1659.
- [276] X. Zhang, J. Dutta, X-Fe (X = Mn, Co, Cu) Prussian Blue Analogue-Modified Carbon Cloth Electrodes for Capacitive Deionization, *ACS Applied Energy Materials*, 4 (2021) 8275-8284.

- [277] E. Sebti, M.M. Besli, M. Metzger, S. Hellstrom, M.J. Schultz-Neu, J. Alvarado, J. Christensen, M. Doeff, S. Kuppan, C.V. Subban, Removal of Na⁺ and Ca²⁺ with Prussian blue analogue electrodes for brackish water desalination, *Desalination*, 487 (2020) 114479.
- [278] S. Wang, G. Wang, Y. Wang, H. Song, S. Lv, T. Li, C. Li, In Situ Formation of Prussian Blue Analogue Nanoparticles Decorated with Three-Dimensional Carbon Nanosheet Networks for Superior Hybrid Capacitive Deionization Performance, *ACS Applied Materials & Interfaces*, 12 (2020) 44049-44057.
- [279] S. Wang, Z. Li, G. Wang, Y. Wang, Z. Ling, C. Li, Freestanding Ti₃C₂T_x MXene/Prussian Blue Analogues Films with Superior Ion Uptake for Efficient Capacitive Deionization by a Dual Pseudocapacitance Effect, *ACS Nano*, 16 (2022) 1239-1249.
- [280] W. Shi, X. Liu, T. Deng, S. Huang, M. Ding, X. Miao, C. Zhu, Y. Zhu, W. Liu, F. Wu, C. Gao, S.-W. Yang, H.Y. Yang, J. Shen, X. Cao, Enabling Superior Sodium Capture for Efficient Water Desalination by a Tubular Polyaniline Decorated with Prussian Blue Nanocrystals, *Advanced Materials*, 32 (2020) 1907404.
- [281] S. Choi, B. Chang, S. Kim, J. Lee, J. Yoon, J.W. Choi, Battery Electrode Materials with Omnivalent Cation Storage for Fast and Charge-Efficient Ion Removal of Asymmetric Capacitive Deionization, *Advanced Functional Materials*, 28 (2018) 1802665.
- [282] K. Singh, Z. Qian, P.M. Biesheuvel, H. Zuilhof, S. Porada, L.C.P.M. de Smet, Nickel hexacyanoferrate electrodes for high mono/divalent ion-selectivity in capacitive deionization, *Desalination*, 481 (2020) 114346.
- [283] S. Porada, A. Shrivastava, P. Bukowska, P.M. Biesheuvel, K.C. Smith, Nickel Hexacyanoferrate Electrodes for Continuous Cation Intercalation Desalination of Brackish Water, *Electrochimica Acta*, 255 (2017) 369-378.
- [284] S. Qiu, Y. Xu, X. Wu, X. Ji, Prussian Blue Analogues as Electrodes for Aqueous Monovalent Ion Batteries, *Electrochemical Energy Reviews*, 5 (2022) 242-262.
- [285] D. Morgan, A. Van der Ven, G. Ceder, Li Conductivity in Li_x MPO₄ (M = Mn , Fe , Co , Ni) Olivine Materials, *Electrochemical and Solid-State Letters*, 7 (2004) A30.
- [286] S.-i. Nishimura, G. Kobayashi, K. Ohoyama, R. Kanno, M. Yashima, A. Yamada, Experimental visualization of lithium diffusion in Li_xFePO₄, *Nature Materials*, 7 (2008) 707-711.
- [287] R. Malik, D. Burch, M. Bazant, G. Ceder, Particle Size Dependence of the Ionic Diffusivity, *Nano Letters*, 10 (2010) 4123-4127.
- [288] J. Yang, J.S. Tse, Li Ion Diffusion Mechanisms in LiFePO₄: An ab Initio Molecular Dynamics Study, *The Journal of Physical Chemistry A*, 115 (2011) 13045-13049.
- [289] B. Zhang, Y. Xu, J. Wang, X. Ma, W. Hou, X. Xue, Electrochemical performance of LiFePO₄/graphene composites at low temperature affected by preparation technology, *Electrochimica Acta*, 368 (2021) 137575.
- [290] S.-Y. Chung, S.-Y. Choi, T. Yamamoto, Y. Ikuhara, Orientation-Dependent Arrangement of Antisite Defects in Lithium Iron(II) Phosphate Crystals, *Angewandte Chemie International Edition*, 48 (2009) 543-546.
- [291] J. Hu, W. Huang, L. Yang, F. Pan, Structure and performance of the LiFePO₄ cathode material: from the bulk to the surface, *Nanoscale*, 12 (2020) 15036-15044.
- [292] L. Wang, K. Frisella, P. Srimuk, O. Janka, G. Kickelbick, V. Presser, Electrochemical lithium recovery with lithium iron phosphate: what causes performance degradation and how can we improve the stability?, *Sustainable Energy & Fuels*, 5 (2021) 3124-3133.
- [293] G. Yan, M. Wang, G.T. Hill, S. Zou, C. Liu, Defining the challenges of Li extraction with olivine host: The roles of competitor and spectator ions, *Proceedings of the National Academy of Sciences*, 119 (2022) e2200751119.
- [294] G. Oyama, S.-i. Nishimura, S.-C. Chung, M. Okubo, A. Yamada, Electrochemical Properties of Heterosite FePO₄ in Aqueous Mg²⁺ Electrolytes, *Electrochemistry*, 82 (2014) 855-858.
- [295] P. Shan, Y. Gu, L. Yang, T. Liu, J. Zheng, F. Pan, Olivine FePO₄ Cathode Material for Rechargeable Mg-Ion Batteries, *Inorganic Chemistry*, 56 (2017) 13411-13416.
- [296] M. Pasta, A. Battistel, F. La Mantia, Batteries for lithium recovery from brines, *Energy & Environmental Science*, 5 (2012) 9487-9491.

- [297] J.-S. Kim, Y.-H. Lee, S. Choi, J. Shin, H.-C. Dinh, J.W. Choi, An Electrochemical Cell for Selective Lithium Capture from Seawater, *Environmental Science & Technology*, 49 (2015) 9415-9422.
- [298] C. Liu, Y. Li, D. Lin, P.-C. Hsu, B. Liu, G. Yan, T. Wu, Y. Cui, S. Chu, Lithium Extraction from Seawater through Pulsed Electrochemical Intercalation, *Joule*, 4 (2020) 1459-1469.
- [299] Z. Jian, Y.-S. Hu, X. Ji, W. Chen, NASICON-Structured Materials for Energy Storage, *Advanced Materials*, 29 (2017) 1601925.
- [300] S. Chen, C. Wu, L. Shen, C. Zhu, Y. Huang, K. Xi, J. Maier, Y. Yu, Challenges and Perspectives for NASICON-Type Electrode Materials for Advanced Sodium-Ion Batteries, *Advanced Materials*, 29 (2017) 1700431.
- [301] S. Qiu, X. Wu, M. Wang, M. Lucero, Y. Wang, J. Wang, Z. Yang, W. Xu, Q. Wang, M. Gu, J. Wen, Y. Huang, Z.J. Xu, Z. Feng, NASICON-type $\text{Na}_3\text{Fe}_2(\text{PO}_4)_3$ as a low-cost and high-rate anode material for aqueous sodium-ion batteries, *Nano Energy*, 64 (2019) 103941.
- [302] J. Cao, Y. Wang, L. Wang, F. Yu, J. Ma, $\text{Na}_3\text{V}_2(\text{PO}_4)_3@C$ as Faradaic Electrodes in Capacitive Deionization for High-Performance Desalination, *Nano Letters*, 19 (2019) 823-828.
- [303] F. Chen, Y. Huang, D. Kong, M. Ding, S. Huang, H.Y. Yang, $\text{NaTi}_2(\text{PO}_4)_3\text{-Ag}$ electrodes based desalination battery and energy recovery, *FlatChem*, 8 (2018) 9-16.
- [304] W. Zhao, L. Guo, M. Ding, Y. Huang, H.Y. Yang, Ultrahigh-Desalination-Capacity Dual-Ion Electrochemical Deionization Device Based on $\text{Na}_3\text{V}_2(\text{PO}_4)_3@C\text{-AgCl}$ Electrodes, *ACS Applied Materials & Interfaces*, 10 (2018) 40540-40548.
- [305] K. Wang, Y. Liu, Z. Ding, Z. Chen, G. Zhu, X. Xu, T. Lu, L. Pan, Controlled synthesis of $\text{NaTi}_2(\text{PO}_4)_3/\text{Carbon}$ composite derived from Metal-organic-frameworks as highly-efficient electrodes for hybrid capacitive deionization, *Separation and Purification Technology*, 278 (2021) 119565.
- [306] M. Wu, W. Ni, J. Hu, J. Ma, NASICON-Structured $\text{NaTi}_2(\text{PO}_4)_3$ for Sustainable Energy Storage, *Nano-Micro Letters*, 11 (2019) 44.
- [307] T. Zhang, D. Li, Z. Tao, J. Chen, Understanding electrode materials of rechargeable lithium batteries via DFT calculations, *Progress in Natural Science: Materials International*, 23 (2013) 256-272.
- [308] A. Battistel, M.S. Palagonia, D. Brogioli, F. La Mantia, R. Trócoli, Electrochemical Methods for Lithium Recovery: A Comprehensive and Critical Review, *Advanced Materials*, 32 (2020) 1905440.
- [309] Y.-L. Ding, J. Xie, G.-S. Cao, T.-J. Zhu, H.-M. Yu, X.-B. Zhao, Single-Crystalline LiMn_2O_4 Nanotubes Synthesized Via Template-Engaged Reaction as Cathodes for High-Power Lithium Ion Batteries, *Advanced Functional Materials*, 21 (2011) 348-355.
- [310] B. Ammundsen, D.J. Jones, J. Rozière, G.R. Burns, Effect of Chemical Extraction of Lithium on the Local Structure of Spinel Lithium Manganese Oxides Determined by X-ray Absorption Spectroscopy, *Chemistry of Materials*, 8 (1996) 2799-2808.
- [311] N. Xie, Y. Li, Y. Lu, J. Gong, X. Hu, Electrochemically Controlled Reversible Lithium Capture and Release Enabled by LiMn_2O_4 Nanorods, *ChemElectroChem*, 7 (2020) 105-111.
- [312] S. Kim, J. Lee, J.S. Kang, K. Jo, S. Kim, Y.-E. Sung, J. Yoon, Lithium recovery from brine using a $\lambda\text{-MnO}_2/\text{activated carbon}$ hybrid supercapacitor system, *Chemosphere*, 125 (2015) 50-56.
- [313] H. Kanoh, K. Ooi, Y. Miyai, S. Katoh, Electrochemical Recovery of Lithium Ions in the Aqueous Phase, *Separation Science and Technology*, 28 (1993) 643-651.
- [314] M.-Y. Zhao, Z.-Y. Ji, Y.-G. Zhang, Z.-Y. Guo, Y.-Y. Zhao, J. Liu, J.-S. Yuan, Study on lithium extraction from brines based on $\text{LiMn}_2\text{O}_4/\text{Li}_{1-x}\text{Mn}_2\text{O}_4$ by electrochemical method, *Electrochimica Acta*, 252 (2017) 350-361.
- [315] H. Joo, S. Kim, S. Kim, M. Choi, S.-H. Kim, J. Yoon, Pilot-scale demonstration of an electrochemical system for lithium recovery from the desalination concentrate, *Environmental Science: Water Research & Technology*, 6 (2020) 290-295.
- [316] X. Shang, J. Liu, B. Hu, P. Nie, J. Yang, B. Zhang, Y. Wang, F. Zhan, J. Qiu, CNT-Strung LiMn_2O_4 for Lithium Extraction with High Selectivity and Stability, *Small Methods*, 6 (2022) 2200508.
- [317] R. Benedek, Role of Disproportionation in the Dissolution of Mn from Lithium Manganate Spinel, *The Journal of Physical Chemistry C*, 121 (2017) 22049-22053.
- [318] K.Y. Chung, K.-B. Kim, Investigations into capacity fading as a result of a Jahn–Teller distortion in 4V LiMn_2O_4 thin film electrodes, *Electrochimica Acta*, 49 (2004) 3327-3337.

- [319] S. Kim, J. Lee, S. Kim, S. Kim, J. Yoon, Electrochemical Lithium Recovery with a LiMn_2O_4 –Zinc Battery System using Zinc as a Negative Electrode, *Energy Technology*, 6 (2018) 340-344.
- [320] G. Xu, Z. Liu, C. Zhang, G. Cui, L. Chen, Strategies for improving the cyclability and thermo-stability of LiMn_2O_4 -based batteries at elevated temperatures, *Journal of Materials Chemistry A*, 3 (2015) 4092-4123.
- [321] G. Zhou, L. Chen, X. Li, G. Luo, Z. Yu, J. Yin, L. Fan, Y. Chao, L. Jiang, W. Zhu, Construction of truncated-octahedral LiMn_2O_4 for battery-like electrochemical lithium recovery from brine, *Green Energy & Environment*, (2022).
- [322] S. Arnold, L. Wang, V. Presser, Dual-Use of Seawater Batteries for Energy Storage and Water Desalination, *Small*, 18 (2022) 2107913.
- [323] S. Arnold, L. Wang, Ö. Budak, M. Aslan, P. Srimuk, V. Presser, Antimony alloying electrode for high-performance sodium removal: how to use a battery material not stable in aqueous media for saline water remediation, *Journal of Materials Chemistry A*, 9 (2021) 585-596.